Calibration Report for the Imagers of the Descent Imager/Spectral Radiometer Instrument aboard the Huygens Probe of the Cassini Mission

L. R. Doose, B. Rizk, E. Karkoschka, and E. McFarlane

Table of Contents

Table of Figures

Table of Tables

1.0 Introduction

The DISR includes three imaging cameras, named the High Resolution Imager (HRI), Medium Resolution Imager (MRI), and Side-Looking Imager (SLI). The three cameras have adjacent fields of view in nadir angle. All three are centered at the same instrumental azimuth, namely out the front of the sensor head.

The three imagers may be exposed simultaneously, yielding a field of view extended from nearly the nadir to above the horizon with an extent in azimuth of about 30°. Twelve sets of exposures equidistant in azimuth cover nearly all the visible downward hemisphere, and these sets of 36 images are called panoramas. During its descent, DISR should acquire approximately 12 panoramas.

The imaging cameras are wide field, as opposed to telephoto, in order to cover the hemisphere. Nominally the pixels subtend angular sizes of 0.06 milliradians (mr) (HRI), 0.12 mr (MRI), and 0.20 mr (SLI). The optical point spread function covers roughly 2 pixels to satisfy the sampling theorem, so the actual resolution is somewhat less. High spatial resolution on the ground is achieved by being close to it. The last image above the ground is taken from about 200m with the HRI, providing a resolution of approximately 24 cm per line pair.

All three imagers have very nearly the same spectral bandpass, which extends from about 640 to 1050 nm. This near-infrared bandpass was chosen to improve visibility through the haze in Titan's atmosphere. The optical thickness of the atmospheric aerosols decreases markedly toward the infrared. The varying optical depth with altitude of methane in several bands complicates the effective bandpass of the instrument-atmosphere combination.

In the sections below we discuss the imager optics and detector. Image display, including the construction of panoramic display from individual images, is discussed. A section covering image sharpening by taking advantage of knowledge of the image system point spread function follows. Photometry using the imagers is covered in sections on the relative spectral responsivity, absolute responsivity, and the on-board processing of the images. The final sections cover an improved method of decompressing DISR images and a tradeoff study of image compression ratios.

1.1 Overview of Optical Systems

The imagers are unconventional, because the light is carried from the objective lens to the focal plane via a fiber optic conduit. The optical path is shown very schematically in figure 1. The objective lenses are compound lenses, normally used as eyepieces. They are also shown in figure 1.1-1.

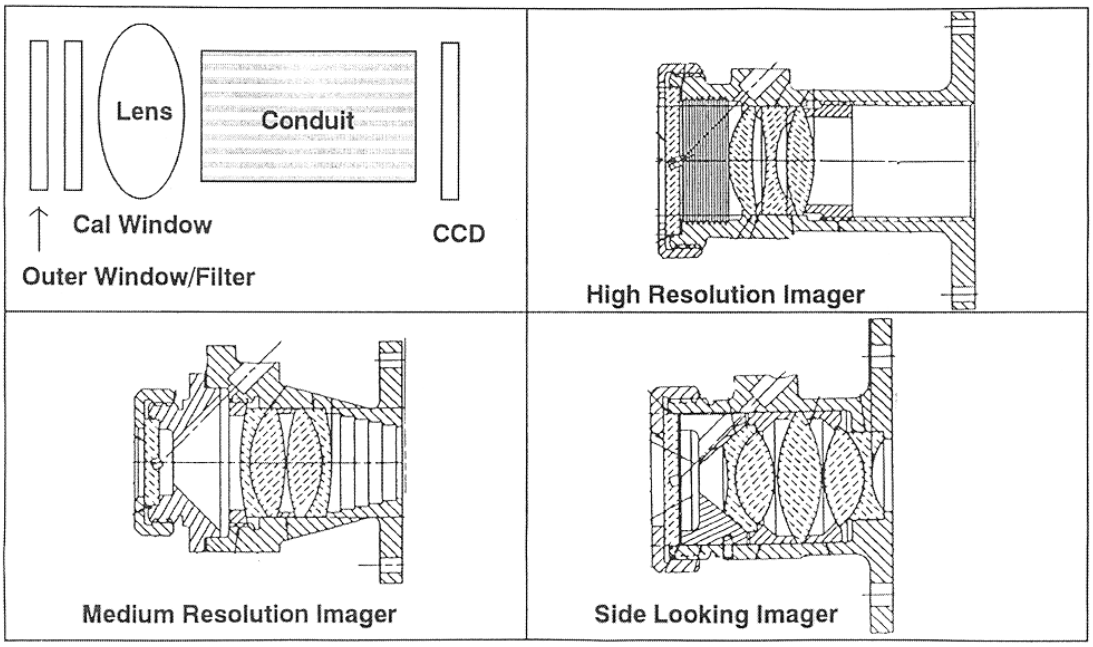

Figure 1.1-1 Drawing of the front end of the optics of the imagers showing window, filter, lenses, etc.

The high resolution imager objective is a modified Cooke-triplet design. The medium resolution imager is a conventional Plössl eyepiece design. The side-looking imager objective is a conventional Erfle eyepiece design.

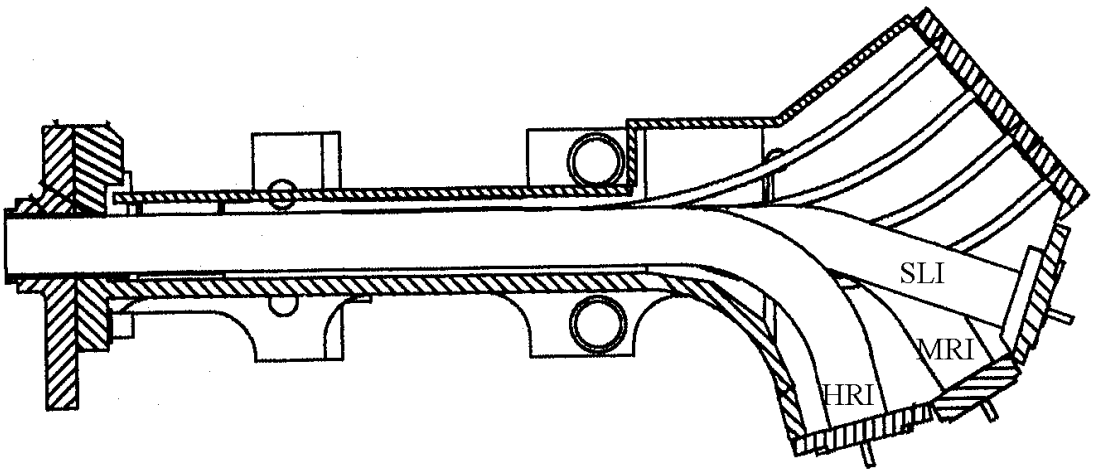

Figure 1.1-2 Diagram of the fiber optic image conduits, which carry the image to the CCD.

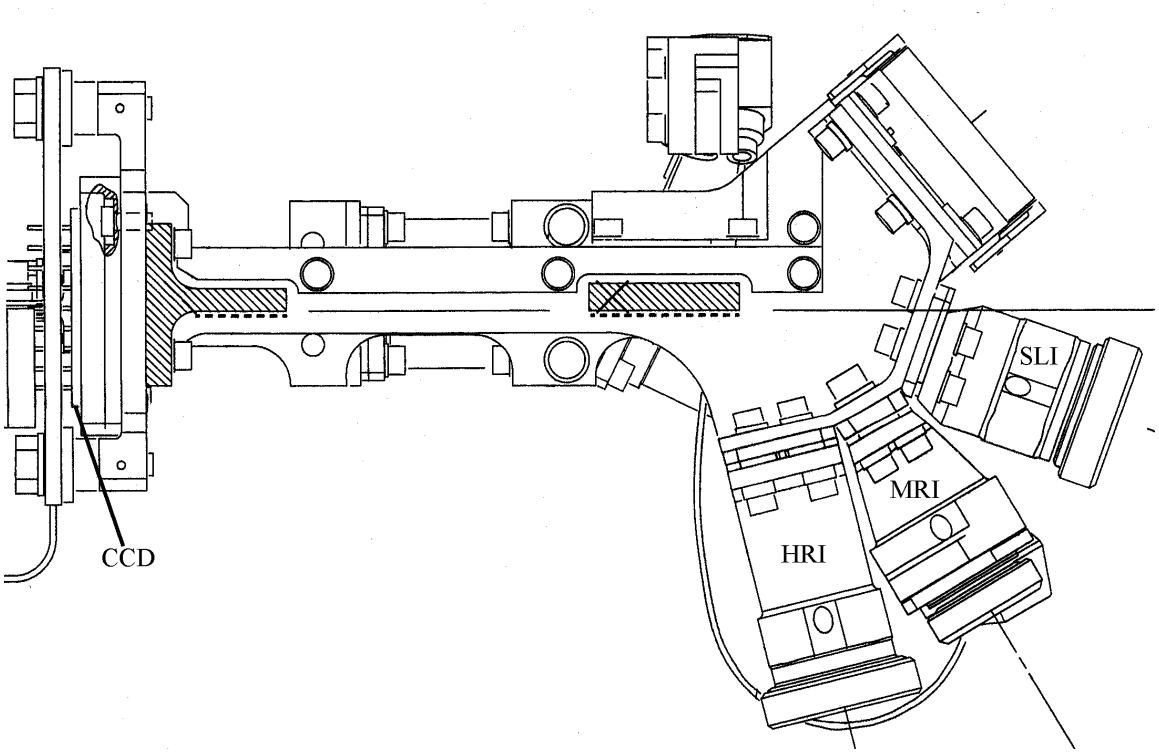

Figure 1.1-3 The imager objective lenses are attached to an optical bench, which holds the fiber optic conduit.

Figure 1.1-2 shows the fiber optic conduits, which carry the images from the objective focal planes to the CCD. Figure 1.1-3 shows the objective lenses in their housings as well as the optical bench, which supports the conduits. The conduits actually end about 20 μm from the surface of the CCD. A looping fiber is shown entering the MRI. This is a fiber, which carries light from an internal calibration system, shown near the top of figure 3. The fiber actually enters the lens housing through the oval holes shown. Light from the fiber reflects off a very small mirror in the center of each outer window. In reality separate fibers run to each of three imager objective housings. This calibration light provides a nearly constant optical stimulus, which can be used to check to stability and health of the imagers.

The CCD is an image transfer type. Anti-blooming gates inhibit the spread of excess charge over the chip when overexposure occurs. The pixels are 23 μm squares. The CCD contains 512×512 pixels, but one half of the surface is covered by an aluminum mask, which is opaque. The images are formed in three subsections of the CCD, and it is then rapidly shifted under the opaque mask. Each row of the image is deposited into a serial register, and a 12-bit analog-to-digital converter digitizes the amount of charge in each pixel in that register. The result is stored in computer memory. Subsequent processing of the image data is discussed below.

The HRI uses an area of 160 columns by 254 rows on the CCD. 256 rows are not used, because the first and last rows contain corrupted pixels. This is true for all three imagers.

The MRI uses an area of 176 columns by 254 rows. The SLI uses an area of 128 columns by 254 rows.

In the sections below we discuss calibration of the DISR imagers in detail, including image distortion and geometry calibrations, relative spectral response calibrations, absolute response calibrations, on-board image processing, image compression ratio optimization, compression defect removal, image sharpening, and finally considerations of using DISR imager data for photometry.

2.0 DISR Image Distortion and Geometry Calibrations

Bashar Rizk

2.1 Introduction

In this document the calibration results characterizing the optical distortion of the DISR 2 and 3 near-IR imagers and their geometrical mapping to the upper and lower hemispheres of object space are presented and discussed. This calibration has recently (July-September 2001) been completely re-performed in order to take advantage of the improvement in resolution created by E. Karkoschka's image sharpening algorithm (see image sharpening section of the image calibration document.)

The main results of this effort are the absolute assignment of each pixel contained within each of the 6 imagers to a direction in object space, which is conveniently represented as a sphere at infinity. We will call this sphere the object sphere. Its center is near the DISR sensor head front housing, e.g. the entrance pupils of each of the imagers or some other instrument-related point. In practice, because anticipated object distances are so much larger than image-related distances, the exact choice of center is assumed not to matter. This approximation is slightly violated in many of the laboratory and field images acquired by the HRI and MRI. In those cases, the center is assumed to be the entrance pupil of the imager in question and the resulting parallax observed in the imaging results.

The direction on the object sphere associated with a specific pixel is absolutely located, just as in any standard spherical coordinate system, by two angles, usually zenith angle θ (co-latitude) and counterclockwise azimuth ϕ. Often, and especially in this work, nadir angle N is used instead of zenith angle, and clockwise azimuth ϕ (positive to the right as seen from the point of view of the imager) is used instead of azimuths that are positive to the left. With respect to each imager, pixels can also located by the dihedral angels α and β, which resemble x and y Cartesian coordinates within each field of view and run parallel to columns and rows, respectively.

The absolute assignments are presented in abbreviated form below and the paths to the complete transformations are provided. These assignments are accomplished for each imager by two separate polynomial transformations, one which largely removes the effects of optical distortion and one which absolutely assigns each pixel to an absolute object location. The matrix elements for each of these transformations are presented.

The methods by which these maps were derived are subsequently described, first the distortion transformation, then the absolute transformation. Details concerning the

actual procedures, relevant details and other data important for those required to re-perform the calibration are given in the appendices.

2.2 Summary of Results

DISR's three near-IR imagers are designed to image the instrument's lower hemisphere as efficiently as possible within the spacecraft mission's constraints on data rate, power, mass and size. Their fields of view and relative arrangement enable them to image a 90^o-high continuous vertical slice of the lower hemisphere, one at least 23.5^o wide, from 6^o above the horizon to 6^o above the nadir. They represent a more or less successful compromise between the contradictory Huygens Probe goals of maximizing field of view and maximizing resolution.

The nominal fields of view of each imager were designed and specified as 9.6×15.2^o for the HRI, 21.1×30.5^o for the MRI and 25.6×51.8^o for the SLI. The nominal centers of each field were intended to be 166^o for the HRI, 148.5^o for the MRI and 109.4^o for the SLI. These correspond to nadir angles of 14^o, 31.5^o and 70.6^o, respectively. The actual fields of view are displayed in Figs. 1 and 2 for each imager, mapped to an object sphere coordinate system spanned by nadir angle N and clockwise azimuth ϕ.

As built, the dihedral fields of view of the imagers are rectangular for the MRI and HRI and slightly trapezoidal in the case of the SLI, and correspond to 9.8×15.4^o for the HRI, 21.5×30.4^o for the MRI and 25.9×50.4^o for the SLI, where the dihedral angles quoted are averages of the top and bottom sides for the width and the left and right sides for the height. The dimensions given are those of DISR 3, the flight unit. Table 2.2-1 gives the locations for the corner and edge pixels, those indicated by squares in Figs. 2.2-1 and 2.2-2. The centers of each field of view are also included. The SLI, in both DISR models, can be seen to be some 4^o longer on the left side than the right.

As built, the system of three imagers can roughly image the lower object sphere below a nadir angle of 58^o in one 12-around cycle, but need 2 12-around cycles to fully image nadir angles between 58 and 96^o. The region covering nadir angles from 16-23^o also needs more than just one 12-around cycle (the top of the HRI) and there is a small 1-3^o nadir angle region at 45^o nadir angle (the top of the MRI, just below the SLI) which also needs more than just one 12-around cycle.

The actual matrix elements enabling the transformation from a raw, distorted image to an undistorted one are displayed in Table 2.2-1 for DISR#2 and #3. Those facilitating the mapping of the undistorted images onto object sphere azimuth and nadir angles are given in Tables 2.3-2. As presented the transformations assume the input images have been sharpened using the DISR#2 and #3 imager-sharpening algorithm developed by Erich Karkoschka.

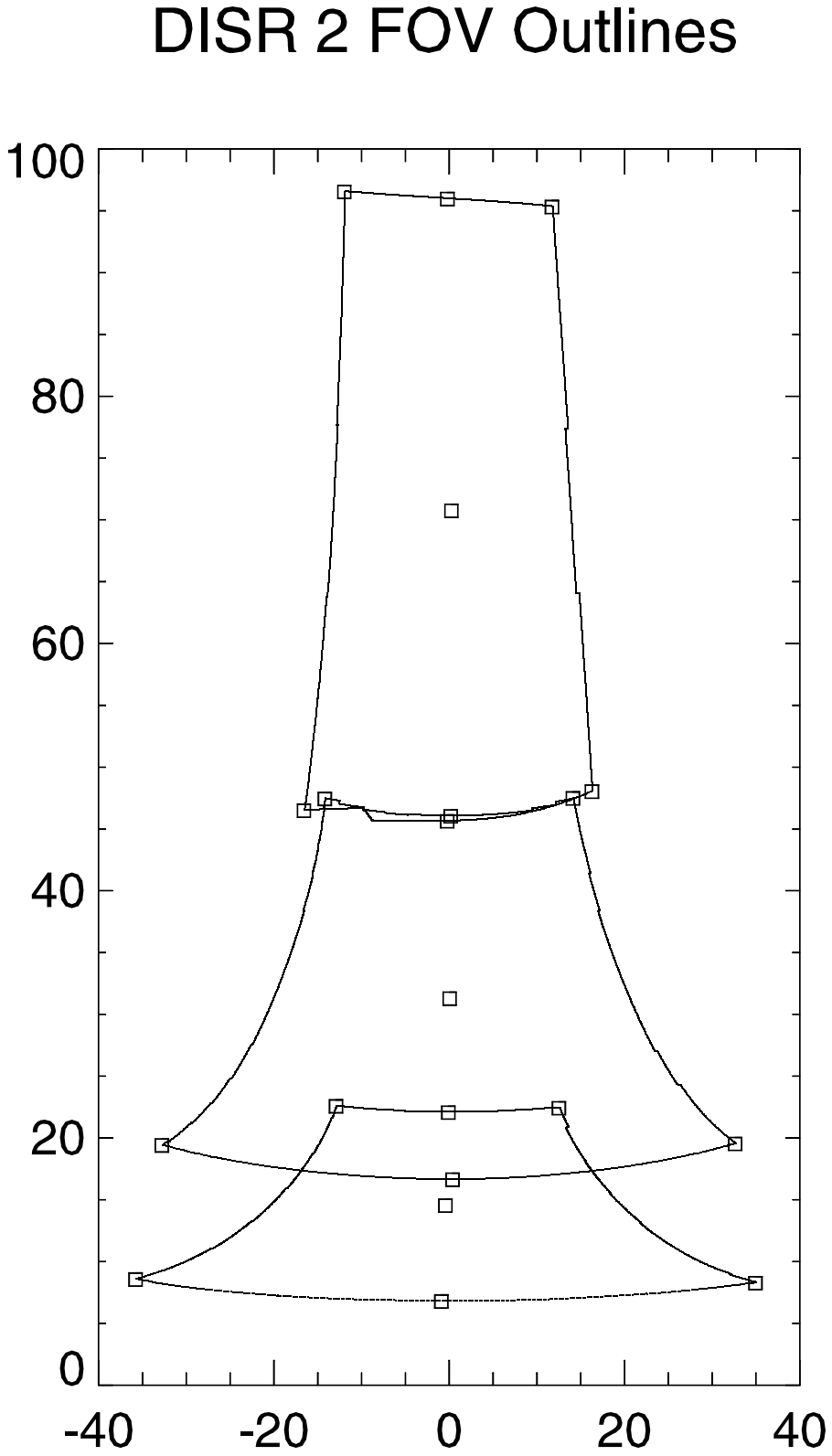

Figure 2.2-1 Outline of DISR 2 Field of View; Corners, centers and halfway points are indicated by squares.

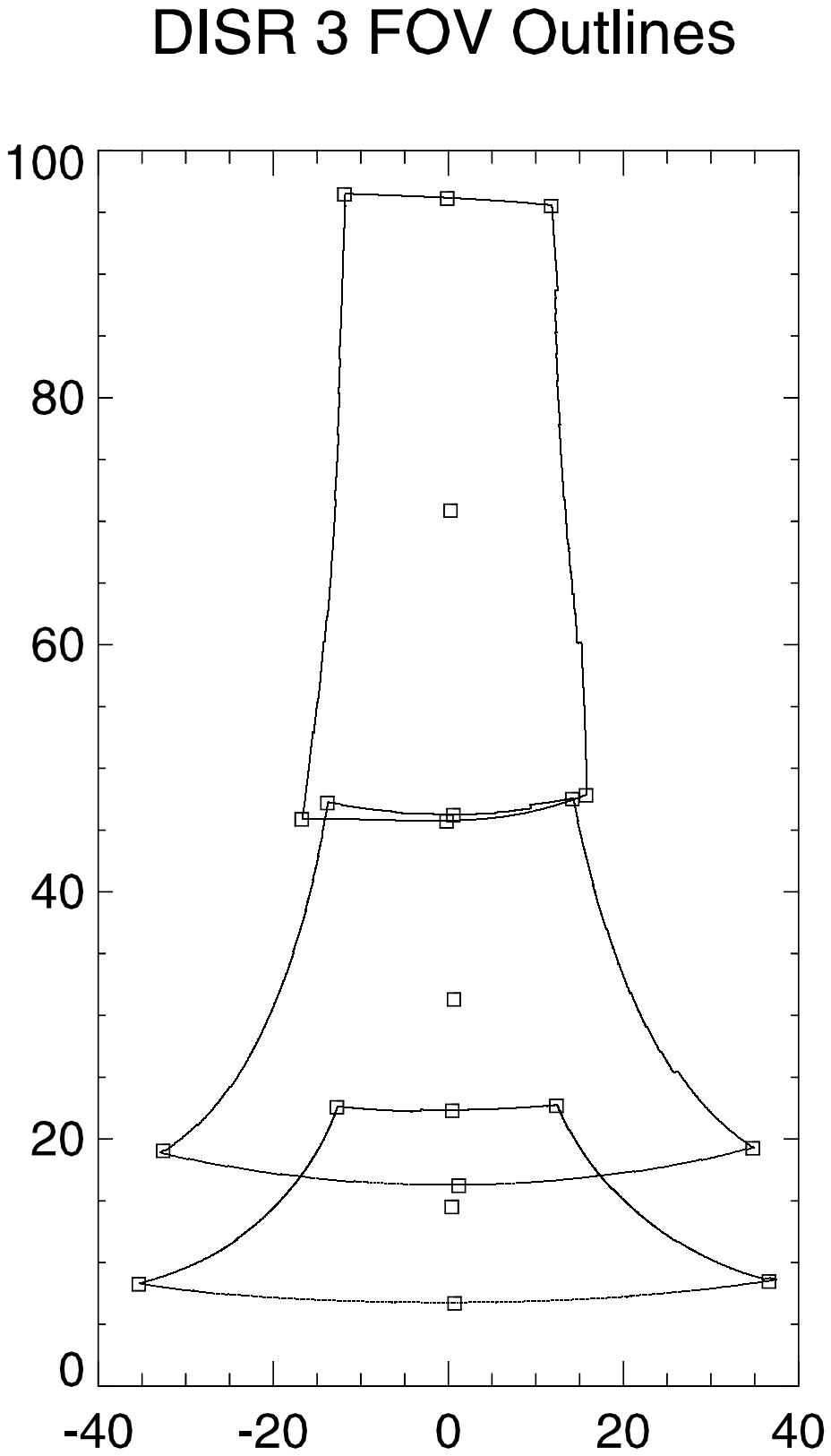

Figure 2.2-2 Outline of DISR 3 Field of View; Corners, centers and halfway points are indicated by squares.

Table 2.2-1

Azimuth and nadir coordinates for the corners of the DISR#2 and DISR#3 fields of view

LOCATION	DISR 2 Spherical Azimuth ϕ	DISR 2 Nadir Angle **N**	DISR 3 Spherical Azimuth ϕ	DISR 3 Nadir Angle **N**
MRI bottom left corner	-32.78	19.39	-32.58	19.04
MRI bottom right corner	32.62	19.52	34.79	19.23
MRI top left corner	-14.19	47.42	-13.81	47.19
MRI top right corner	14.10	47.47	14.18	47.52
MRI bottom center	0.38	16.62	1.20	15.98
MRI top center	0.17	46.02	0.58	46.21
MRI center	0.05	31.27	0.63	31.29
SLI bottom left corner	-16.58	46.47	-16.75	45.87
SLI bottom right corner	16.28	48.02	15.73	47.82
SLI top left corner	-11.97	96.54	-11.88	96.45
SLI top right corner	11.72	95.31	11.74	95.51
SLI bottom center	-0.23	45.61	-0.21	45.70
SLI top center	-0.20	95.95	-0.13	96.12
SLI center	0.24	70.74	0.26	70.85
HRI bottom left corner	-35.77	8.54	-35.37	8.24
HRI bottom right corner	34.94	8.27	36.91	8.42
HRI top left corner	-12.92	22.56	-12.74	22.57
HRI top right corner	12.52	22.41	12.36	22.69
HRI bottom center	-0.90	6.78	0.72	6.71
HRI top center	-0.10	22.06	0.45	22.29
HRI center	-0.42	14.53	0.40	14.50

Table 2.2-2

Matrix elements to transform raw DISR frames to undistorted ones

DISR 2 MRI K^X

0.716	-0.0435	8.487E-05	2.789E-10
0.9907	2.748E-04	-5.754E-07	2.395E-11
-9.099E-06	4.246E-08	2.808E-10	-2.360E-13
3.697E-08	-4.488E-10	1.116E-13	4.828E-16

DISR 3 MRI K^X

-1.892	-0.0284	7.194E-05	-1.418E-09
1.00602	4.048E-05	-2.585E-08	-1.557E-12
-8.047E-05	1.729E-06	-3.487E-09	-5.479E-15
1.317E-07	-3.432E-09	6.895E-12	-3.558E-17

DISR 2 MRI K^Y

-0.766	0.9895	8.728E-05	-1.157E-07
-0.03018	5.430E-05	2.715E-07	-2.259E-10
8.629E-05	-8.044E-08	-1.262E-09	1.306E-12
2.255E-09	-5.540E-11	2.798E-13	-3.784E-16

DISR 3 MRI K^Y

0.955	0.988	1.026E-04	-1.377E-07
-0.04804	7.644E-05	3.634E-07	-4.294E-10
1.243E-04	-3.394E-07	-9.257E-10	1.191E-12
-4.978E-09	4.945E-11	-6.037E-14	-7.363E-18

DISR 2 SLI K^X

11.674	-0.0974	1.956E-04	8.849E-10
0.90449	6.741E-04	-1.382E-06	4.272E-11
-6.961E-05	1.577E-06	-2.112E-09	-7.209E-13
4.184E-07	-5.167E-09	7.237E-12	1.740E-15

DISR 3 SLI K^X

6.462	-0.0940	2.034E-04	-6.373E-09
0.91545	7.480E-04	-1.421E-06	2.418E-12
5.187E-05	8.090E-07	-1.250E-09	3.980E-14
-3.253E-08	-2.167E-09	3.509E-12	-7.781E-16

DISR 2 SLI K^Y

13.499	0.8957	3.552E-04	-4.588E-07
-0.07393	4.646E-05	1.283E-06	-1.598E-09
2.873E-04	-2.669E-07	-5.015E-09	6.491E-12
8.447E-08	-6.095E-10	1.607E-12	-1.886E-15

DISR 3 SLI K^Y

9.973	0.909	3.403E-04	-4.589E-07
-0.08724	1.159E-04	1.021E-06	-1.288E-09
3.557E-04	-6.453E-07	-4.005E-09	5.502E-12
4.106E-08	-1.843E-10	2.295E-13	-2.961E-16

DISR 2 HRI K^X

0.680	-0.011	1.045E-06	-1.148E-09
1.02755	-6.880E-05	1.105E-07	2.903E-12
-1.431E-04	6.256E-07	-1.009E-09	8.920E-15
3.093E-07	-1.365E-09	2.178E-12	-5.801E-17

DISR 3 HRI K^X

-1.002	2.272E-03	7.734E-06	3.441E-10
1.01017	3.693E-05	-7.635E-08	-4.397E-13
-7.332E-05	-1.220E-07	2.402E-10	1.507E-15
1.625E-07	2.051E-10	-3.396E-13	3.262E-18

DISR 2 HRI K^Y

-4.551	1.034	-9.468E-05	1.106E-07
0.01621	-1.025E-04	4.632E-07	-5.586E-10
-1.265E-05	2.911E-07	-1.367E-09	1.641E-12
3.908E-09	-2.149E-11	4.899E-14	-3.021E-17

DISR 3 HRI K^Y

0.4571	1.015	-6.036E-05	7.205E-08
-6.768E-03	-9.192E-06	1.047E-07	-1.809E-10
4.226E-06	2.271E-08	-2.899E-10	4.667E-13
-8.969E-10	-1.596E-12	4.994E-15	-7.583E-18

Table 2.2-3

Matrix elements to transform undistorted images onto object sphere azimuth and nadir angles

DISR 2 MRI K^X

-1.585	0.0893	-1.456E-03	3.595E-06
-0.4715	-5.453E-02	1.754E-03	-1.799E-05
-7.078E-04	2.269E-04	-1.247E-05	1.785E-07
-1.472E-03	1.520E-04	-4.999E-06	5.214E-08

DISR 3 MRI K^X

-3.394	0.1928	-4.522E-03	3.573E-05
-0.65334	-3.526E-02	1.046E-03	-9.695E-06
-1.812E-03	2.787E-04	-1.177E-05	1.459E-07
-8.786E-04	8.232E-05	-2.375E-06	2.100E-08

DISR 2 MRI K^Y

0.425	0.9402	1.836E-03	-1.811E-05
-0.01852	2.377E-03	-8.371E-05	8.860E-07
-3.479E-03	3.870E-04	-1.339E-05	1.495E-07
5.390E-05	-5.835E-06	2.004E-07	-2.142E-09

DISR 3 MRI K^Y

0.218	0.943	2.059E-03	-2.106E-05
0.02725	-2.339E-03	8.040E-05	-9.245E-07
-2.379E-04	6.081E-05	-2.687E-06	3.619E-08
-7.452E-05	8.233E-06	-2.933E-07	3.386E-09

DISR 2 SLI K^X

2.860	-0.0822	4.429E-04	1.258E-06
-0.58137	-1.765E-02	2.439E-04	-1.107E-06
2.697E-02	-1.169E-03	1.614E-05	-7.237E-08
-1.579E-03	5.971E-05	-7.780E-07	3.343E-09

DISR 3 SLI K^X

3.135	-0.0977	7.072E-04	-2.136E-07
-0.65301	-1.547E-02	2.288E-04	-1.118E-06
3.166E-02	-1.252E-03	1.597E-05	-6.678E-08
-1.803E-04	1.265E-05	-3.218E-07	2.233E-09

DISR 2 SLI K^Y

1.128	0.9832	3.948E-05	1.383E-07
-0.26821	1.266E-02	-1.737E-04	6.885E-07
-3.156E-02	1.446E-03	-2.132E-05	1.016E-07
5.188E-03	-2.076E-04	2.743E-06	-1.199E-08

DISR 3 SLI K^Y

-0.174	1.048	-9.235E-04	4.785E-06
-0.48880	2.299E-02	-3.269E-04	1.423E-06
-5.545E-03	2.380E-04	-3.160E-06	1.321E-08
4.709E-03	-1.982E-04	2.736E-06	-1.236E-08

DISR 2 HRI K^X

0.846	0.022	-6.510E-03	1.760E-04
-0.62246	-7.017E-02	4.981E-03	-1.170E-04
2.591E-03	-6.725E-04	3.728E-05	-3.667E-07
-7.608E-04	2.043E-04	-1.754E-05	4.558E-07

DISR 3 HRI K^X

-1.950	2.572E-01	-1.437E-02	2.587E-04
-0.68931	-5.616E-02	3.958E-03	-9.309E-05
1.807E-03	-3.334E-04	4.320E-06	5.092E-07
-6.707E-04	1.835E-04	-1.600E-05	4.199E-07

DISR 2 HRI K^Y

0.404	1.029	-1.897E-03	3.715E-05
-0.00555	1.444E-03	-1.382E-04	4.079E-06
-1.053E-03	2.416E-04	-1.582E-05	2.837E-07
6.957E-05	-1.974E-05	1.791E-06	-5.052E-08

DISR 3 HRI K^Y

0.5265	0.996	4.609E-04	-1.661E-05
-8.277E-04	1.053E-03	-1.046E-04	3.119E-06
-1.015E-03	2.241E-04	-1.352E-05	2.042E-07
5.178E-05	-1.498E-05	1.389E-06	-3.960E-08

2.3 Distortion Calibration

The purpose of the calibration of the optical distortion of the 6 near-IR imaging systems of DISR 2 and 3 was to determine the extent to which magnification changed for off-axis image points. The significant barrel distortion possessed especially by the SLI made this calibration an important one.

The distortion calibration data for the DISR 3 imagers was acquired on August 19, 1996. For the DISR 2 imagers it was acquired on March 4, 1997. Square grid-like targets printed on drafting paper were mounted in front of the imagers on a rigid surface. These targets consisted of black bars separated by white space, oriented both in a horizontal and vertical configuration. An alignment laser mounted on the altitude-azimuth yoke, parallel to the imaging system, and a mirror mounted on the rigid target surface enabled the surface to be adjusted perpendicular to each imaging system. The distance to the imaging system was also measured. The distance of each target, the thickness and separation of the black bars for each target and the assumed angular pixel size in degrees are listed in Table 2.3-1.

Table 2.3-1

Imager distortion measurement parameters

	MRI 2	SLI 2	HRI 2	MRI 3	SLI 3	HRI 3
Distance of distortion target (mm.)	1486	1168	4693	1486	1168	4685
Width of black bars (mm.)	31.60	40.21	54.51	31.60	40.21	54.51
Separation of black bars (mm.)	92.61	119.5	162.0	92.61	119.5	162.0
Size of sharpened pixel (^{o})	0.06	0.1	0.0308	0.06	0.1	0.0308
Nominal Zenith Angle of Central Pixel (^{o})	148.5	109.4	166	148.5	109.4	166
Number of Columns (sharpened)	353	257	321	353	257	321
Number of Rows (sharpened)	509	509	509	509	509	509

The target images used for the final analysis are shown in Figures 2.3-1 through 2.3-6 for the 6 imagers. For each image an accompanying dark, bias and flat-field was acquired and used to reduce the image. The transition boundaries between black and white were identified and traced by a procedure originally written by Mike Bushroe and the intersections of these boundaries determined. This data is listed in Tables 2.3-3 through 2.3-8, and consists of the pixel locations of the corners of the black boxes making up the target grid system. The actual locations of these objects were assumed to be determined by the distances from Table 2.3-2, centrally projected to the image axis, i.e., as they would have been seen from the distance of each image in an undistorted view.

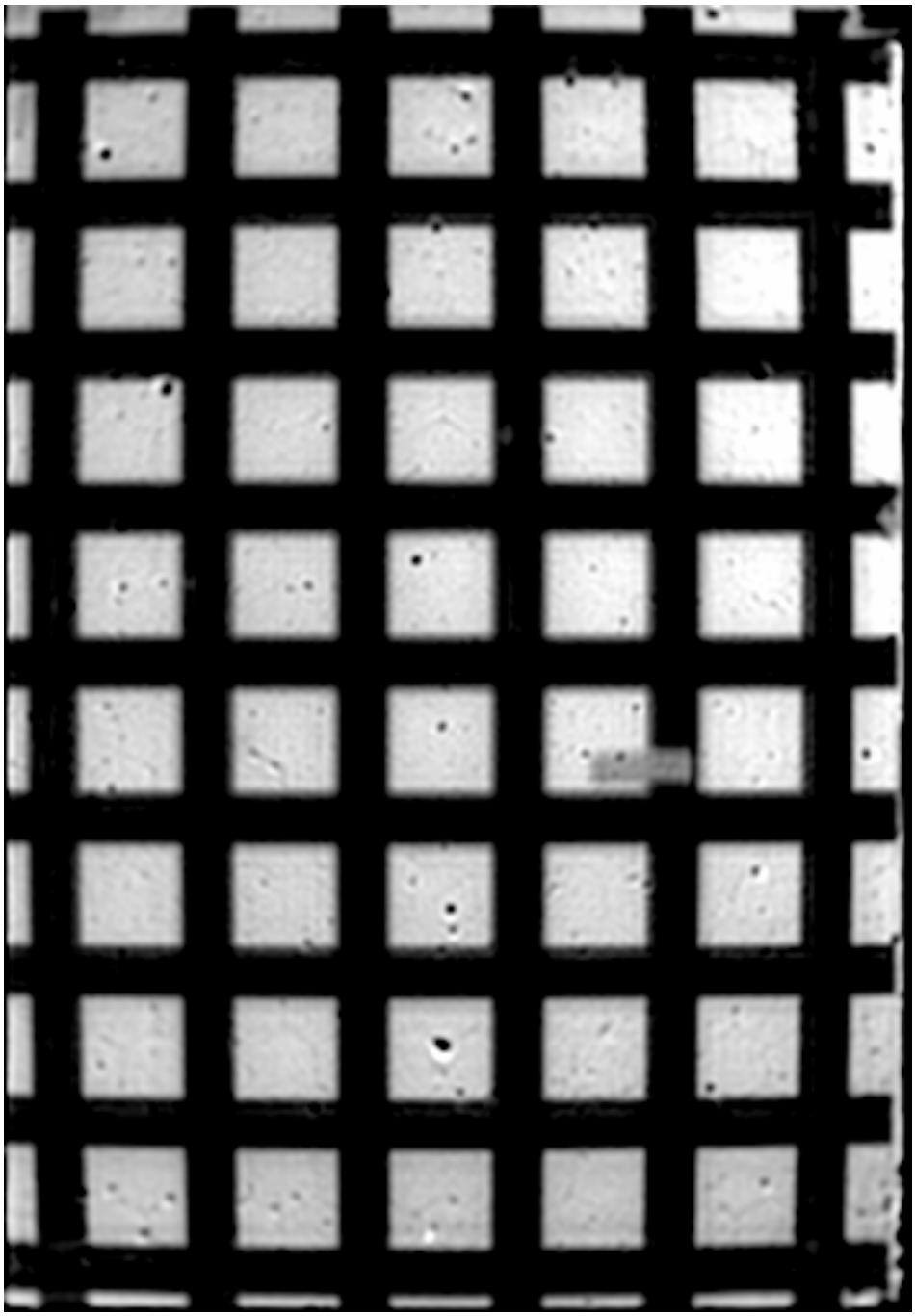

Figure 2.3-1 DISR 2 MRI Target Grid (sharpened)

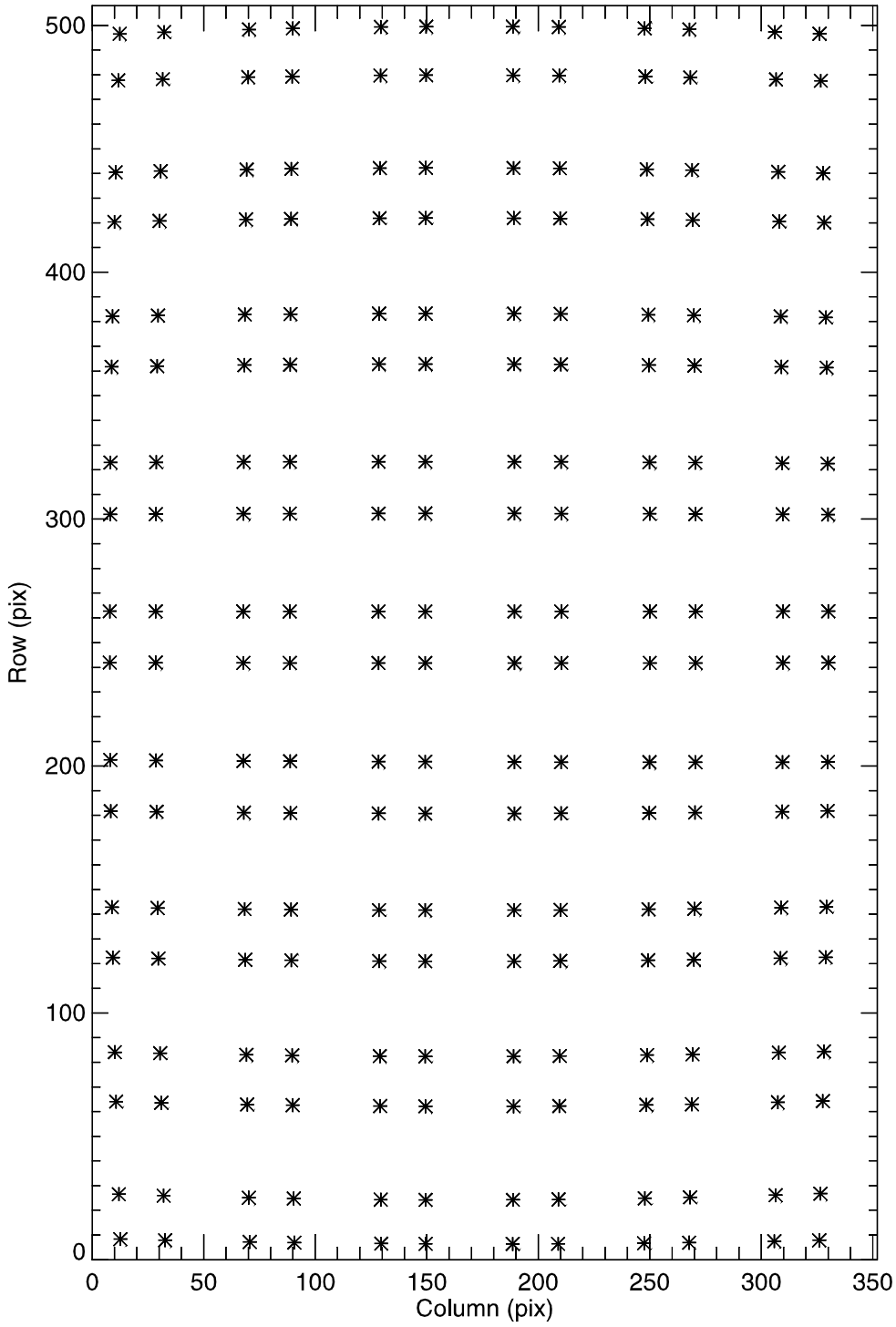

Figure 2.3-2 Location of Observed Vertices for DISR 2 MRI

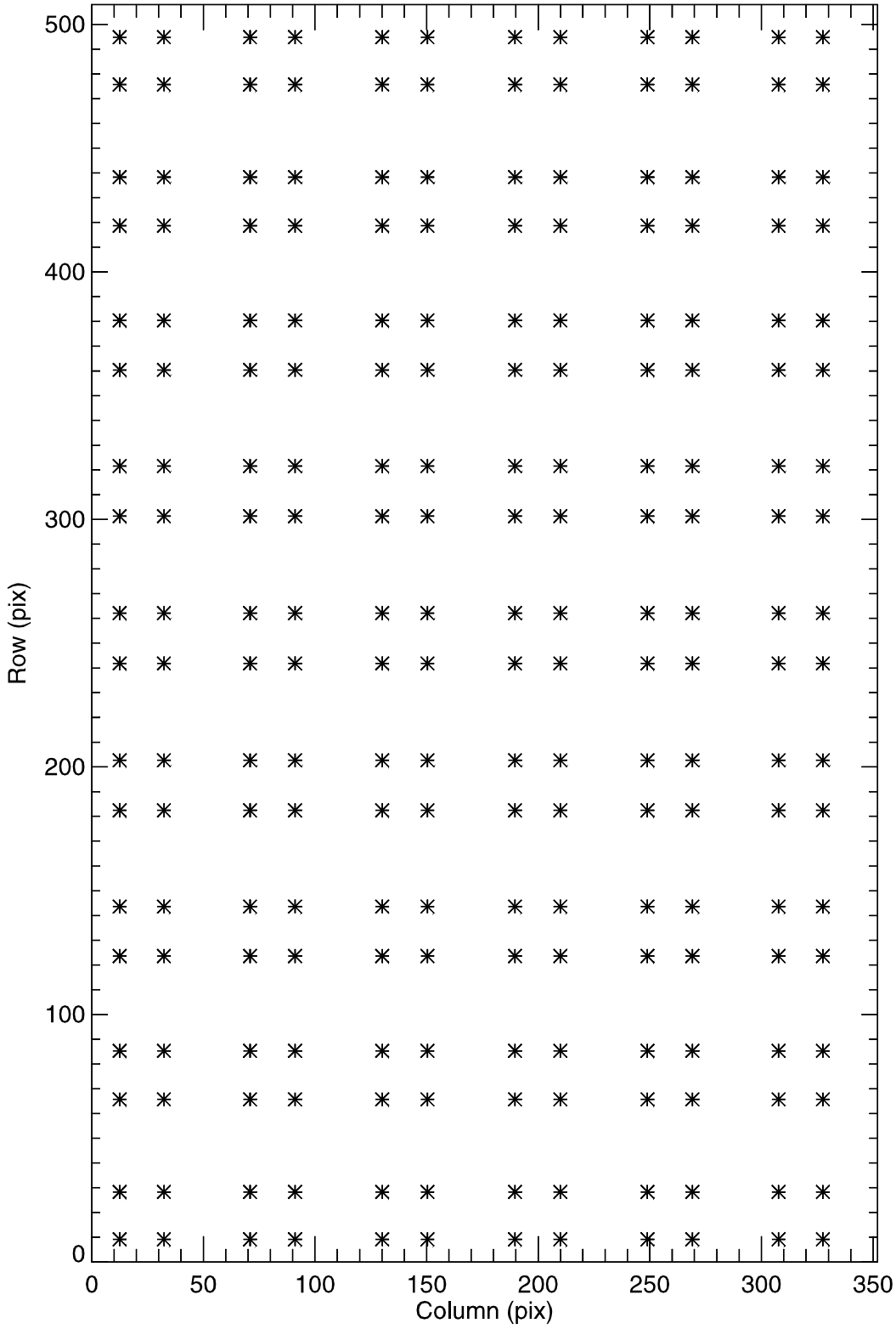

Figure 2.3-3 Location of Desired Vertices for DISR 2 MRI

Table 2.3-2

Vertex Information for DISR 2 MRI Distortion Fit

	C = Column	R=Row						
Point ID	Observed C	Observed R	Desired C	Desired R	Computed C	Computed R	C Residual	R Residual
0	12.60	8.34	12.50	9.16	12.74	7.95	0.14	-0.39
1	11.93	26.52	12.50	28.28	12.03	26.94	0.10	0.41
2	10.71	64.04	12.50	65.70	10.80	64.28	0.10	0.24
3	10.14	84.08	12.50	85.32	10.25	83.94	0.11	-0.14
4	9.24	122.39	12.50	123.60	9.34	122.41	0.10	0.02
5	8.85	142.77	12.50	143.59	8.95	142.56	0.11	-0.21
6	8.28	181.71	12.50	182.45	8.39	181.82	0.11	0.11
7	8.07	202.41	12.50	202.68	8.18	202.29	0.11	-0.12
8	7.87	241.89	12.50	241.85	7.97	241.96	0.11	0.06
9	7.85	262.67	12.50	262.15	7.95	262.53	0.10	-0.13
10	8.01	301.96	12.50	301.32	8.11	302.20	0.10	0.25
11	8.19	322.95	12.50	321.55	8.28	322.67	0.09	-0.27
12	8.71	361.69	12.50	360.41	8.79	361.95	0.08	0.26
13	9.08	382.19	12.50	380.41	9.15	382.11	0.07	-0.07
14	9.93	420.40	12.50	418.68	10.00	420.61	0.07	0.21
15	10.48	440.52	12.50	438.30	10.53	440.28	0.05	-0.24
16	11.64	477.71	12.50	475.73	11.70	477.65	0.06	-0.06
17	12.32	496.59	12.50	494.84	12.39	496.66	0.07	0.07
18	32.63	7.89	32.33	9.16	32.42	7.43	-0.20	-0.46
19	32.04	25.96	32.33	28.28	31.81	26.45	-0.23	0.49
20	30.97	63.57	32.33	65.70	30.75	63.84	-0.22	0.27
21	30.47	83.66	32.33	85.32	30.27	83.53	-0.20	-0.13
22	29.67	122.03	32.33	123.60	29.48	122.07	-0.19	0.04
23	29.33	142.48	32.33	143.59	29.14	142.26	-0.18	-0.22
24	28.82	181.47	32.33	182.45	28.65	181.61	-0.17	0.14
25	28.64	202.27	32.33	202.68	28.47	202.12	-0.17	-0.15
26	28.44	241.85	32.33	241.85	28.28	241.88	-0.16	0.03
27	28.43	262.64	32.33	262.15	28.26	262.51	-0.16	-0.14
28	28.55	302.04	32.33	301.32	28.38	302.28	-0.17	0.24
29	28.70	323.05	32.33	321.55	28.53	322.81	-0.18	-0.24
30	29.14	361.97	32.33	360.41	28.96	362.19	-0.18	0.21
31	29.45	382.47	32.33	380.41	29.26	382.41	-0.19	-0.06
32	30.19	420.79	32.33	418.68	29.99	421.01	-0.20	0.22
33	30.65	440.96	32.33	438.30	30.44	440.73	-0.21	-0.22
34	31.66	478.23	32.33	475.73	31.44	478.22	-0.21	-0.01
35	32.24	497.29	32.33	494.84	32.03	497.28	-0.21	-0.01
36	70.61	7.21	70.93	9.16	70.74	6.63	0.13	-0.58
37	70.21	25.11	70.93	28.28	70.31	25.68	0.10	0.57
38	69.46	62.85	70.93	65.70	69.58	63.16	0.11	0.31
39	69.12	83.02	70.93	85.32	69.24	82.90	0.13	-0.12
40	68.56	121.49	70.93	123.60	68.69	121.55	0.13	0.06
41	68.32	142.04	70.93	143.59	68.46	141.80	0.13	-0.24
42	67.98	181.11	70.93	182.45	68.11	181.27	0.13	0.16
43	67.85	202.05	70.93	202.68	67.98	201.85	0.13	-0.19
44	67.71	241.79	70.93	241.85	67.84	241.76	0.13	-0.03
45	67.70	262.61	70.93	262.15	67.82	262.46	0.12	-0.14
46	67.79	302.17	70.93	301.32	67.90	302.39	0.11	0.22
47	67.89	323.20	70.93	321.55	68.00	323.00	0.10	-0.19
48	68.20	362.40	70.93	360.41	68.28	362.55	0.09	0.15

49	68.41	382.89	70.93	380.41	68.49	382.86	0.07	-0.03
50	68.92	421.38	70.93	418.68	68.98	421.63	0.06	0.26
51	69.25	441.62	70.93	438.30	69.29	441.44	0.04	-0.18
52	69.94	479.01	70.93	475.73	69.97	479.09	0.03	0.08
53	70.35	498.35	70.93	494.84	70.37	498.24	0.02	-0.11
54	90.64	6.93	91.06	9.16	90.72	6.31	0.07	-0.61
55	90.38	24.78	91.06	28.28	90.39	25.38	0.01	0.60
56	89.88	62.57	91.06	65.70	89.82	62.89	-0.06	0.33
57	89.64	82.77	91.06	85.32	89.56	82.65	-0.08	-0.12
58	89.26	121.27	91.06	123.60	89.14	121.34	-0.12	0.07
59	89.09	141.87	91.06	143.59	88.96	141.62	-0.13	-0.25
60	88.83	180.96	91.06	182.45	88.68	181.14	-0.15	0.18
61	88.73	201.94	91.06	202.68	88.58	201.75	-0.14	-0.20
62	88.60	241.76	91.06	241.85	88.47	241.71	-0.13	-0.05
63	88.57	262.59	91.06	262.15	88.46	262.44	-0.11	-0.15
64	88.58	302.22	91.06	301.32	88.52	302.43	-0.06	0.22
65	88.62	323.25	91.06	321.55	88.59	323.08	-0.03	-0.17
66	88.76	362.56	91.06	360.41	88.81	362.69	0.04	0.12
67	88.87	383.05	91.06	380.41	88.96	383.03	0.09	-0.02
68	89.14	421.60	91.06	418.68	89.34	421.87	0.20	0.27
69	89.32	441.88	91.06	438.30	89.57	441.72	0.26	-0.16
70	89.70	479.32	91.06	475.73	90.10	479.44	0.39	0.12
71	89.93	498.77	91.06	494.84	90.40	498.62	0.47	-0.14
72	129.56	6.54	130.11	9.16	129.47	5.89	-0.08	-0.65
73	129.39	24.35	130.11	28.28	129.33	24.99	-0.06	0.64
74	129.07	62.22	130.11	65.70	129.09	62.55	0.01	0.34
75	128.93	82.46	130.11	85.32	128.97	82.34	0.05	-0.12
76	128.69	121.00	130.11	123.60	128.79	121.08	0.10	0.08
77	128.59	141.66	130.11	143.59	128.71	141.39	0.12	-0.27
78	128.44	180.78	130.11	182.45	128.59	180.97	0.15	0.19
79	128.39	201.78	130.11	202.68	128.55	201.61	0.16	-0.17
80	128.33	241.72	130.11	241.85	128.50	241.64	0.17	-0.09
81	128.33	262.58	130.11	262.15	128.49	262.41	0.16	-0.17
82	128.36	302.28	130.11	301.32	128.51	302.47	0.15	0.20
83	128.41	323.30	130.11	321.55	128.54	323.15	0.14	-0.14
84	128.53	362.76	130.11	360.41	128.63	362.84	0.10	0.08
85	128.62	383.24	130.11	380.41	128.70	383.23	0.08	0.00
86	128.84	421.89	130.11	418.68	128.86	422.16	0.02	0.27
87	128.98	442.20	130.11	438.30	128.96	442.06	-0.01	-0.14
88	129.27	479.72	130.11	475.73	129.19	479.88	-0.08	0.16
89	129.44	499.33	130.11	494.84	129.32	499.12	-0.12	-0.21
90	149.51	6.43	150.40	9.16	149.61	5.78	0.10	-0.65
91	149.47	24.25	150.40	28.28	149.56	24.89	0.09	0.63
92	149.41	62.13	150.40	65.70	149.48	62.47	0.07	0.34
93	149.39	82.39	150.40	85.32	149.44	82.26	0.06	-0.13
94	149.35	120.94	150.40	123.60	149.38	121.02	0.03	0.08
95	149.33	141.61	150.40	143.59	149.35	141.33	0.02	-0.27
96	149.32	180.74	150.40	182.45	149.31	180.93	-0.01	0.19
97	149.31	201.71	150.40	202.68	149.29	201.57	-0.02	-0.14
98	149.32	241.71	150.40	241.85	149.28	241.61	-0.05	-0.10
99	149.33	262.57	150.40	262.15	149.27	262.39	-0.06	-0.18
100	149.37	302.29	150.40	301.32	149.28	302.47	-0.09	0.19
101	149.39	323.29	150.40	321.55	149.29	323.16	-0.10	-0.13
102	149.45	362.80	150.40	360.41	149.32	362.87	-0.13	0.07

103	149.49	383.27	150.40	380.41	149.34	383.27	-0.14	0.00
104	149.57	421.96	150.40	418.68	149.40	422.23	-0.17	0.27
105	149.61	442.27	150.40	438.30	149.43	442.14	-0.18	-0.13
106	149.72	479.82	150.40	475.73	149.51	479.99	-0.21	0.17
107	149.77	499.47	150.40	494.84	149.55	499.25	-0.22	-0.22
108	188.53	6.37	189.60	9.16	188.55	5.76	0.01	-0.60
109	188.64	24.28	189.60	28.28	188.67	24.88	0.03	0.60
110	188.85	62.16	189.60	65.70	188.89	62.48	0.04	0.32
111	188.95	82.42	189.60	85.32	188.99	82.28	0.04	-0.15
112	189.10	120.96	189.60	123.60	189.15	121.04	0.05	0.08
113	189.17	141.63	189.60	143.59	189.22	141.35	0.05	-0.28
114	189.27	180.75	189.60	182.45	189.33	180.93	0.06	0.18
115	189.30	201.61	189.60	202.68	189.37	201.57	0.06	-0.04
116	189.34	241.71	189.60	241.85	189.41	241.60	0.07	-0.11
117	189.34	262.58	189.60	262.15	189.41	262.37	0.07	-0.21
118	189.32	302.27	189.60	301.32	189.39	302.43	0.08	0.16
119	189.29	323.24	189.60	321.55	189.36	323.12	0.08	-0.12
120	189.20	362.76	189.60	360.41	189.28	362.82	0.08	0.06
121	189.14	383.21	189.60	380.41	189.22	383.22	0.08	0.01
122	188.99	421.93	189.60	418.68	189.08	422.18	0.08	0.25
123	188.90	442.23	189.60	438.30	188.99	442.10	0.09	-0.12
124	188.70	479.80	189.60	475.73	188.79	479.98	0.08	0.18
125	188.59	499.47	189.60	494.84	188.67	499.25	0.08	-0.22
126	208.90	6.42	209.89	9.16	208.70	5.86	-0.20	-0.56
127	209.09	24.41	209.89	28.28	208.91	24.98	-0.17	0.57
128	209.45	62.28	209.89	65.70	209.28	62.58	-0.17	0.30
129	209.61	82.53	209.89	85.32	209.45	82.37	-0.16	-0.16
130	209.88	121.04	209.89	123.60	209.72	121.12	-0.16	0.08
131	210.00	141.70	209.89	143.59	209.84	141.42	-0.16	-0.28
132	210.17	180.80	209.89	182.45	210.02	180.98	-0.16	0.17
133	210.24	201.58	209.89	202.68	210.08	201.60	-0.16	0.03
134	210.32	241.71	209.89	241.85	210.15	241.60	-0.17	-0.11
135	210.33	262.58	209.89	262.15	210.16	262.35	-0.17	-0.23
136	210.30	302.24	209.89	301.32	210.12	302.39	-0.18	0.15
137	210.26	323.18	209.89	321.55	210.08	323.06	-0.19	-0.11
138	210.14	362.68	209.89	360.41	209.94	362.74	-0.20	0.06
139	210.05	383.11	209.89	380.41	209.84	383.13	-0.21	0.01
140	209.83	421.83	209.89	418.68	209.59	422.07	-0.23	0.24
141	209.69	442.11	209.89	438.30	209.44	441.98	-0.24	-0.12
142	209.38	479.68	209.89	475.73	209.10	479.85	-0.28	0.17
143	209.20	499.33	209.89	494.84	208.90	499.13	-0.29	-0.20
144	247.44	6.68	248.94	9.16	247.54	6.24	0.10	-0.44
145	247.80	24.89	248.94	28.28	247.90	25.36	0.11	0.48
146	248.45	62.69	248.94	65.70	248.54	62.94	0.08	0.25
147	248.76	82.91	248.94	85.32	248.82	82.71	0.07	-0.20
148	249.24	121.34	248.94	123.60	249.30	121.40	0.06	0.06
149	249.46	141.96	248.94	143.59	249.50	141.67	0.05	-0.28
150	249.76	181.00	248.94	182.45	249.80	181.15	0.04	0.15
151	249.88	201.55	248.94	202.68	249.91	201.73	0.04	0.19
152	250.00	241.74	248.94	241.85	250.03	241.64	0.03	-0.10
153	250.01	262.61	248.94	262.15	250.04	262.34	0.04	-0.27
154	249.93	302.15	248.94	301.32	249.98	302.28	0.04	0.13
155	249.84	323.01	248.94	321.55	249.89	322.90	0.05	-0.12
156	249.58	362.40	248.94	360.41	249.64	362.48	0.06	0.08

157	249.39	382.81	248.94	380.41	249.47	382.82	0.07	0.01
158	248.95	421.49	248.94	418.68	249.04	421.69	0.09	0.21
159	248.67	441.70	248.94	438.30	248.77	441.57	0.11	-0.13
160	248.06	479.25	248.94	475.73	248.18	479.39	0.13	0.14
161	247.69	498.79	248.94	494.84	247.83	498.64	0.14	-0.15
162	267.67	6.90	269.07	9.16	267.57	6.54	-0.10	-0.36
163	268.09	25.25	269.07	28.28	268.01	25.66	-0.08	0.41
164	268.85	63.00	269.07	65.70	268.77	63.22	-0.07	0.22
165	269.19	83.19	269.07	85.32	269.12	82.97	-0.08	-0.22
166	269.75	121.58	269.07	123.60	269.68	121.62	-0.07	0.05
167	269.99	142.15	269.07	143.59	269.93	141.87	-0.07	-0.29
168	270.34	181.15	269.07	182.45	270.28	181.29	-0.05	0.13
169	270.46	201.55	269.07	202.68	270.41	201.84	-0.05	0.29
170	270.59	241.76	269.07	241.85	270.55	241.67	-0.04	-0.09
171	270.59	262.62	269.07	262.15	270.57	262.33	-0.03	-0.29
172	270.49	302.08	269.07	301.32	270.48	302.20	-0.01	0.12
173	270.37	322.90	269.07	321.55	270.38	322.78	0.01	-0.12
174	270.04	362.20	269.07	360.41	270.07	362.30	0.03	0.10
175	269.81	382.60	269.07	380.41	269.86	382.60	0.04	0.01
176	269.27	421.23	269.07	418.68	269.34	421.41	0.06	0.18
177	268.93	441.40	269.07	438.30	269.01	441.26	0.08	-0.14
178	268.20	478.92	269.07	475.73	268.30	479.03	0.10	0.11
179	267.76	498.37	269.07	494.84	267.88	498.27	0.11	-0.11
180	305.83	7.47	307.67	9.16	306.03	7.32	0.20	-0.15
181	306.39	26.16	307.67	28.28	306.60	26.42	0.21	0.26
182	307.39	63.78	307.67	65.70	307.58	63.92	0.19	0.14
183	307.86	83.90	307.67	85.32	308.02	83.63	0.17	-0.26
184	308.59	122.16	307.67	123.60	308.75	122.18	0.16	0.02
185	308.91	142.63	307.67	143.59	309.06	142.35	0.14	-0.28
186	309.38	181.53	307.67	182.45	309.51	181.63	0.13	0.09
187	309.54	201.58	307.67	202.68	309.67	202.09	0.13	0.52
188	309.71	241.81	307.67	241.85	309.83	241.75	0.12	-0.06
189	309.73	262.66	307.67	262.15	309.84	262.33	0.12	-0.34
190	309.60	301.92	307.67	301.32	309.71	302.01	0.12	0.09
191	309.45	322.64	307.67	321.55	309.57	322.50	0.12	-0.14
192	309.03	361.70	307.67	360.41	309.16	361.84	0.13	0.14
193	308.73	382.06	307.67	380.41	308.87	382.06	0.14	-0.01
194	308.03	420.58	307.67	418.68	308.17	420.70	0.15	0.12
195	307.59	440.65	307.67	438.30	307.75	440.48	0.16	-0.17
196	306.63	478.10	307.67	475.73	306.80	478.12	0.17	0.03
197	306.07	497.31	307.67	494.84	306.24	497.31	0.17	0.00
198	325.96	7.86	327.50	9.16	325.81	7.82	-0.15	-0.04
199	326.56	26.75	327.50	28.28	326.44	26.91	-0.12	0.15
200	327.62	64.28	327.50	65.70	327.51	64.37	-0.10	0.09
201	328.10	84.35	327.50	85.32	328.00	84.05	-0.10	-0.30
202	328.88	122.53	327.50	123.60	328.80	122.53	-0.08	0.00
203	329.21	142.94	327.50	143.59	329.13	142.66	-0.08	-0.28
204	329.69	181.78	327.50	182.45	329.62	181.84	-0.08	0.06
205	329.86	201.61	327.50	202.68	329.79	202.26	-0.07	0.65
206	330.04	241.85	327.50	241.85	329.96	241.81	-0.08	-0.04
207	330.05	262.69	327.50	262.15	329.97	262.33	-0.08	-0.36
208	329.90	301.81	327.50	301.32	329.81	301.90	-0.09	0.08
209	329.74	322.48	327.50	321.55	329.65	322.32	-0.09	-0.16
210	329.28	361.38	327.50	360.41	329.17	361.55	-0.11	0.17

211	328.96	381.72	327.50	380.41	328.85	381.71	-0.12	-0.01
212	328.20	420.17	327.50	418.68	328.07	420.26	-0.14	0.09
213	327.73	440.17	327.50	438.30	327.59	439.98	-0.14	-0.19
214	326.70	477.56	327.50	475.73	326.52	477.54	-0.18	-0.02
215	326.11	496.61	327.50	494.84	325.91	496.69	-0.20	0.08

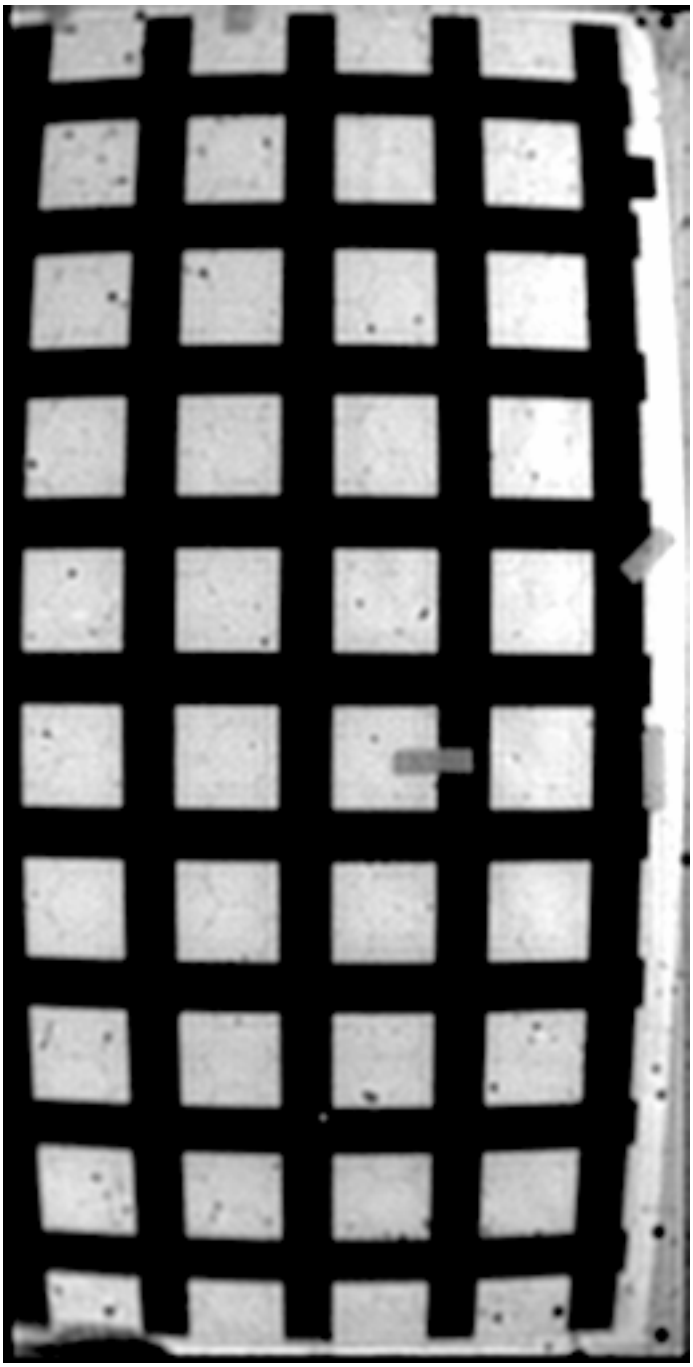

Figure 2.3-4 DISR 2 SLI Target Grid (sharpened)

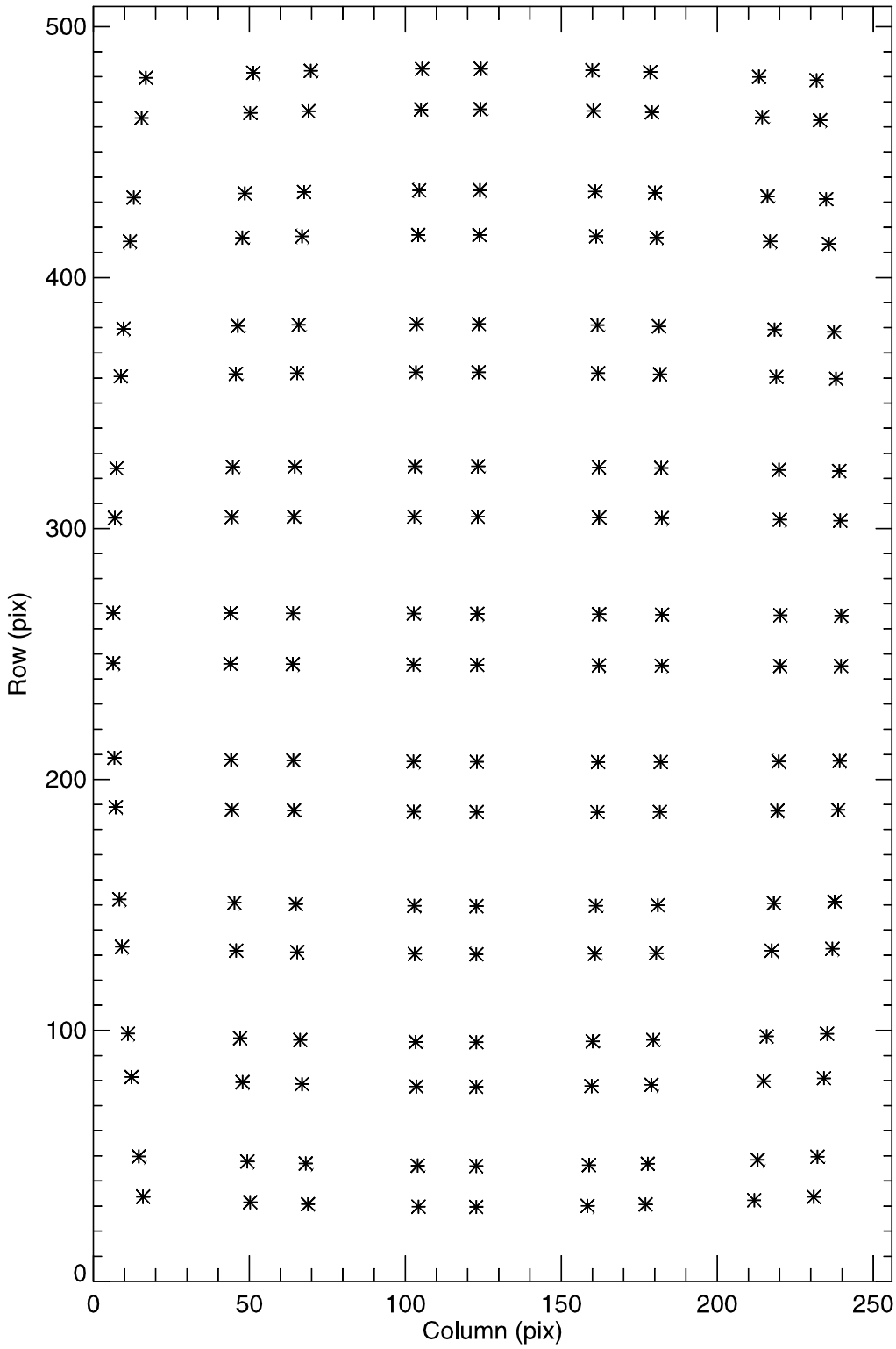

Figure 2.3-5 Location of Observed Vertices for DISR 2 SLI

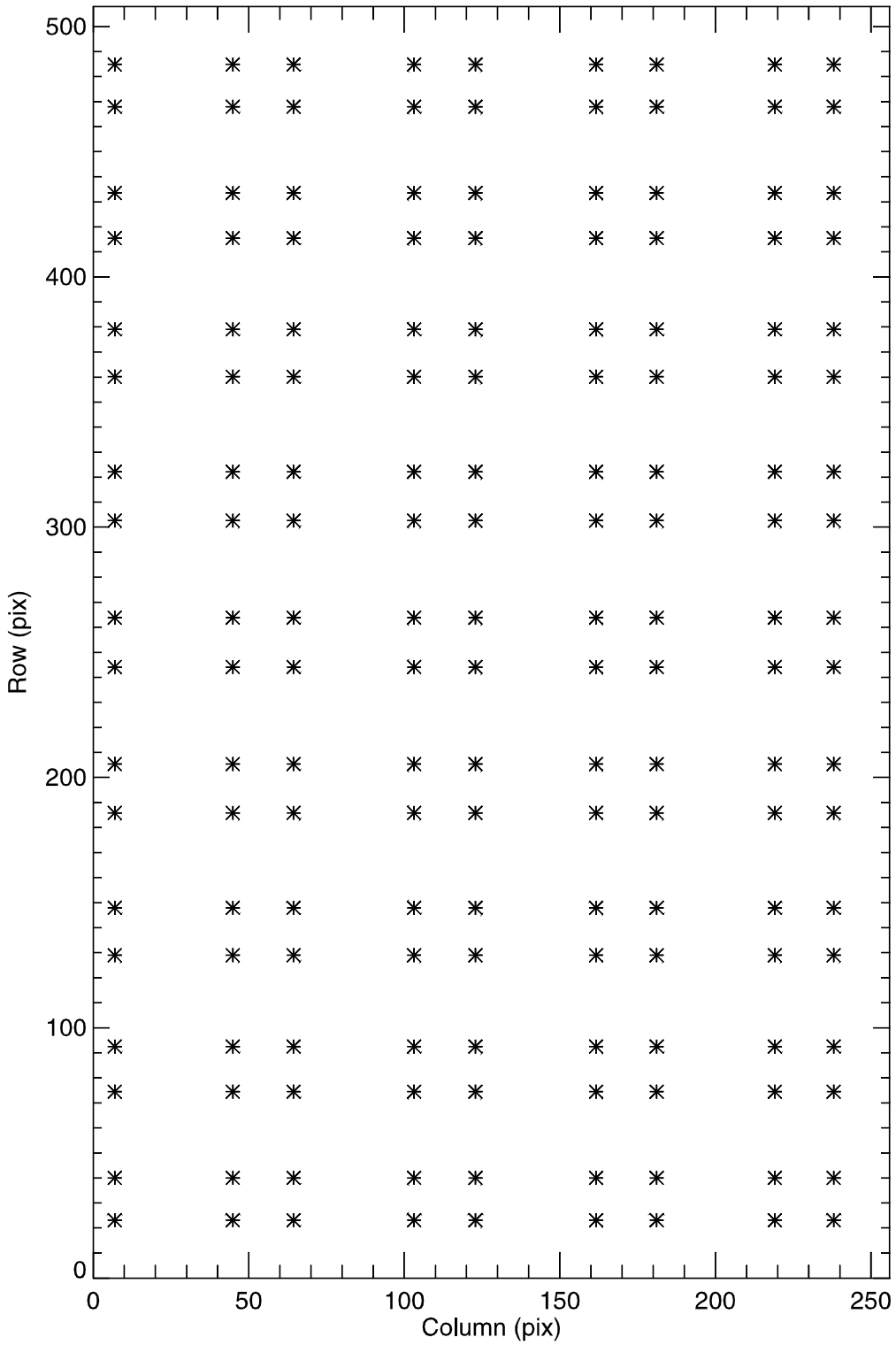

Figure 2.3-6 Location of Desired Vertices for DISR#2 SLI

Table 2.3-3

Vertex Information for DISR#2 SLI Distortion Fit

	C = Column	R=Row						
Point ID	Observed C	Observed R	Desired C	Desired R	Computed C	Computed R	C Residual	R Residual
0	15.94	33.70	6.91	23.14	15.87	33.92	-0.07	0.23
1	14.59	49.77	6.91	40.03	14.50	49.42	-0.08	-0.35
2	12.22	81.42	6.91	74.48	12.04	81.57	-0.18	0.15
3	11.09	98.74	6.91	92.50	10.93	98.63	-0.16	-0.11
4	9.20	133.31	6.91	128.98	9.06	133.62	-0.14	0.31
5	8.37	152.24	6.91	147.91	8.28	151.97	-0.09	-0.27
6	7.16	188.98	6.91	185.87	7.12	189.11	-0.04	0.13
7	6.74	208.57	6.91	205.38	6.73	208.31	-0.01	-0.25
8	6.37	246.30	6.91	244.14	6.39	246.62	0.02	0.32
9	6.40	266.35	6.91	263.86	6.42	266.14	0.02	-0.21
10	6.92	304.21	6.91	302.62	6.93	304.47	0.00	0.26
11	7.42	323.95	6.91	322.13	7.39	323.70	-0.03	-0.25
12	8.77	360.64	6.91	360.09	8.70	360.91	-0.07	0.28
13	9.68	379.54	6.91	379.02	9.56	379.32	-0.12	-0.23
14	11.73	414.35	6.91	415.50	11.59	414.44	-0.14	0.09
15	12.94	431.85	6.91	433.52	12.77	431.57	-0.16	-0.27
16	15.44	463.59	6.91	467.97	15.38	463.88	-0.06	0.29
17	16.85	479.59	6.91	484.86	16.82	479.47	-0.04	-0.12
18	50.31	31.53	44.87	23.14	50.74	31.74	0.43	0.20
19	49.39	47.74	44.87	40.03	49.79	47.30	0.39	-0.45
20	47.82	79.35	44.87	74.48	48.08	79.62	0.26	0.27
21	47.06	96.88	44.87	92.50	47.31	96.80	0.25	-0.08
22	45.79	131.78	44.87	128.98	46.01	132.09	0.22	0.31
23	45.24	150.86	44.87	147.91	45.47	150.61	0.24	-0.25
24	44.44	188.02	44.87	185.87	44.68	188.13	0.24	0.11
25	44.17	207.87	44.87	205.38	44.41	207.55	0.25	-0.31
26	43.94	246.05	44.87	244.14	44.19	246.30	0.25	0.24
27	43.98	266.28	44.87	263.86	44.22	266.05	0.24	-0.23
28	44.37	304.58	44.87	302.62	44.59	304.83	0.23	0.25
29	44.72	324.49	44.87	322.13	44.93	324.29	0.21	-0.20
30	45.67	361.62	44.87	360.09	45.87	361.92	0.19	0.30
31	46.31	380.71	44.87	379.02	46.48	380.52	0.17	-0.19
32	47.73	415.87	44.87	415.50	47.92	415.98	0.19	0.11
33	48.57	433.50	44.87	433.52	48.76	433.27	0.19	-0.23
34	50.31	465.54	44.87	467.97	50.61	465.81	0.30	0.27
35	51.29	481.62	44.87	484.86	51.63	481.50	0.34	-0.12
36	68.80	30.71	64.38	23.14	68.65	30.94	-0.14	0.23
37	68.10	46.97	64.38	40.03	67.94	46.51	-0.16	-0.46
38	66.89	78.55	64.38	74.48	66.65	78.89	-0.24	0.34
39	66.31	96.18	64.38	92.50	66.07	96.12	-0.24	-0.06
40	65.34	131.18	64.38	128.98	65.09	131.50	-0.25	0.32
41	64.91	150.31	64.38	147.91	64.69	150.09	-0.22	-0.22
42	64.31	187.63	64.38	185.87	64.10	187.75	-0.21	0.12
43	64.11	207.57	64.38	205.38	63.91	207.25	-0.19	-0.33
44	63.94	245.93	64.38	244.14	63.77	246.15	-0.18	0.22
45	63.98	266.23	64.38	263.86	63.81	265.98	-0.18	-0.24
46	64.29	304.69	64.38	302.62	64.11	304.93	-0.18	0.24
47	64.57	324.67	64.38	322.13	64.38	324.47	-0.19	-0.19
48	65.32	361.96	64.38	360.09	65.13	362.26	-0.20	0.30

49	65.82	381.12	64.38	379.02	65.61	380.93	-0.21	-0.19
50	66.93	416.41	64.38	415.50	66.73	416.52	-0.20	0.10
51	67.59	434.10	64.38	433.52	67.39	433.86	-0.20	-0.24
52	68.94	466.25	64.38	467.97	68.83	466.50	-0.11	0.25
53	69.70	482.37	64.38	484.86	69.62	482.22	-0.08	-0.15
54	104.22	29.79	103.14	23.14	104.32	30.00	0.09	0.22
55	103.97	46.10	103.14	40.03	104.07	45.59	0.10	-0.51
56	103.54	77.64	103.14	74.48	103.65	78.02	0.11	0.39
57	103.34	95.40	103.14	92.50	103.46	95.29	0.12	-0.11
58	103.01	130.46	103.14	128.98	103.16	130.78	0.15	0.32
59	102.87	149.64	103.14	147.91	103.04	149.43	0.17	-0.21
60	102.70	187.12	103.14	185.87	102.89	187.24	0.19	0.12
61	102.65	207.16	103.14	205.38	102.86	206.82	0.21	-0.34
62	102.65	245.71	103.14	244.14	102.87	245.91	0.22	0.20
63	102.70	266.09	103.14	263.86	102.93	265.84	0.22	-0.26
64	102.90	304.74	103.14	302.62	103.12	304.97	0.22	0.24
65	103.04	324.79	103.14	322.13	103.26	324.61	0.21	-0.18
66	103.41	362.28	103.14	360.09	103.61	362.57	0.20	0.29
67	103.64	381.49	103.14	379.02	103.83	381.33	0.18	-0.16
68	104.15	416.96	103.14	415.50	104.32	417.07	0.17	0.11
69	104.45	434.73	103.14	433.52	104.60	434.48	0.16	-0.25
70	105.05	466.99	103.14	467.97	105.21	467.23	0.16	0.24
71	105.38	483.13	103.14	484.86	105.54	482.99	0.16	-0.14
72	122.73	29.66	122.86	23.14	122.52	29.88	-0.22	0.22
73	122.73	45.97	122.86	40.03	122.52	45.46	-0.21	-0.51
74	122.74	77.48	122.86	74.48	122.53	77.88	-0.20	0.40
75	122.75	95.28	122.86	92.50	122.55	95.14	-0.20	-0.14
76	122.78	130.31	122.86	128.98	122.59	130.63	-0.19	0.32
77	122.81	149.49	122.86	147.91	122.62	149.29	-0.19	-0.20
78	122.88	186.98	122.86	185.87	122.69	187.11	-0.19	0.13
79	122.93	207.02	122.86	205.38	122.74	206.70	-0.19	-0.32
80	123.04	245.61	122.86	244.14	122.84	245.81	-0.19	0.20
81	123.10	266.00	122.86	263.86	122.90	265.74	-0.20	-0.26
82	123.25	304.67	122.86	302.62	123.04	304.91	-0.21	0.23
83	123.33	324.74	122.86	322.13	123.11	324.56	-0.22	-0.18
84	123.50	362.26	122.86	360.09	123.26	362.55	-0.24	0.29
85	123.60	381.47	122.86	379.02	123.35	381.32	-0.25	-0.15
86	123.80	416.96	122.86	415.50	123.52	417.08	-0.28	0.12
87	123.90	434.77	122.86	433.52	123.61	434.50	-0.29	-0.27
88	124.11	467.03	122.86	467.97	123.79	467.27	-0.31	0.24
89	124.22	483.17	122.86	484.86	123.89	483.05	-0.33	-0.13
90	158.42	30.07	161.62	23.14	158.49	30.32	0.07	0.25
91	158.88	46.33	161.62	40.03	158.95	45.85	0.08	-0.48
92	159.68	77.80	161.62	74.48	159.81	78.18	0.13	0.38
93	160.08	95.65	161.62	92.50	160.21	95.39	0.13	-0.26
94	160.77	130.47	161.62	128.98	160.91	130.78	0.14	0.31
95	161.08	149.59	161.62	147.91	161.21	149.39	0.13	-0.20
96	161.58	186.95	161.62	185.87	161.71	187.10	0.13	0.16
97	161.78	206.92	161.62	205.38	161.91	206.64	0.12	-0.28
98	162.05	245.43	161.62	244.14	162.17	245.65	0.12	0.22
99	162.12	265.80	161.62	263.86	162.24	265.54	0.13	-0.26
100	162.12	304.37	161.62	302.62	162.25	304.61	0.14	0.24
101	162.05	324.42	161.62	322.13	162.20	324.22	0.14	-0.20
102	161.81	361.87	161.62	360.09	161.96	362.13	0.16	0.27

103	161.62	380.99	161.62	379.02	161.79	380.87	0.16	-0.13
104	161.17	416.46	161.62	415.50	161.33	416.58	0.17	0.12
105	160.88	434.31	161.62	433.52	161.05	433.98	0.17	-0.33
106	160.28	466.45	161.62	467.97	160.41	466.71	0.13	0.26
107	159.94	482.57	161.62	484.86	160.05	482.47	0.11	-0.10
108	177.05	30.64	181.13	23.14	176.72	30.89	-0.33	0.25
109	177.72	46.85	181.13	40.03	177.40	46.39	-0.32	-0.46
110	178.89	78.28	181.13	74.48	178.66	78.63	-0.24	0.35
111	179.48	96.14	181.13	92.50	179.24	95.80	-0.25	-0.34
112	180.47	130.78	181.13	128.98	180.24	131.08	-0.23	0.30
113	180.92	149.84	181.13	147.91	180.68	149.63	-0.24	-0.21
114	181.62	187.06	181.13	185.87	181.37	187.23	-0.25	0.17
115	181.89	206.95	181.13	205.38	181.63	206.71	-0.26	-0.24
116	182.22	245.34	181.13	244.14	181.97	245.59	-0.25	0.25
117	182.29	265.68	181.13	263.86	182.04	265.42	-0.25	-0.26
118	182.21	304.13	181.13	302.62	181.99	304.37	-0.23	0.24
119	182.07	324.13	181.13	322.13	181.86	323.93	-0.21	-0.21
120	181.62	361.48	181.13	360.09	181.44	361.74	-0.19	0.26
121	181.30	380.53	181.13	379.02	181.13	380.43	-0.17	-0.10
122	180.53	415.92	181.13	415.50	180.37	416.05	-0.16	0.13
123	180.05	433.78	181.13	433.52	179.91	433.42	-0.14	-0.37
124	179.06	465.81	181.13	467.97	178.87	466.10	-0.19	0.29
125	178.50	481.90	181.13	484.86	178.28	481.84	-0.22	-0.06
126	211.84	32.35	219.09	23.14	212.49	32.71	0.65	0.36
127	212.95	48.41	219.09	40.03	213.56	48.10	0.61	-0.31
128	214.88	79.79	219.09	74.48	215.50	80.10	0.62	0.30
129	215.85	97.61	219.09	92.50	216.39	97.12	0.54	-0.49
130	217.44	131.78	219.09	128.98	217.92	132.10	0.48	0.32
131	218.17	150.68	219.09	147.91	218.58	150.48	0.41	-0.20
132	219.28	187.49	219.09	185.87	219.60	187.72	0.32	0.23
133	219.70	207.15	219.09	205.38	219.97	207.01	0.27	-0.14
134	220.18	245.21	219.09	244.14	220.40	245.52	0.22	0.31
135	220.26	265.41	219.09	263.86	220.47	265.16	0.21	-0.25
136	220.06	303.51	219.09	302.62	220.28	303.75	0.22	0.24
137	219.78	323.39	219.09	322.13	220.03	323.12	0.24	-0.26
138	218.95	360.41	219.09	360.09	219.23	360.61	0.29	0.21
139	218.36	379.26	219.09	379.02	218.69	379.15	0.33	-0.11
140	216.98	414.41	219.09	415.50	217.36	414.52	0.38	0.11
141	216.13	432.27	219.09	433.52	216.56	431.77	0.43	-0.50
142	214.39	463.98	219.09	467.97	214.79	464.26	0.39	0.28
143	213.40	479.98	219.09	484.86	213.79	479.93	0.39	-0.05
144	230.95	33.64	238.02	23.14	230.49	33.97	-0.47	0.32
145	232.13	49.59	238.02	40.03	231.72	49.29	-0.41	-0.30
146	234.20	80.92	238.02	74.48	233.95	81.12	-0.25	0.20
147	235.23	98.69	238.02	92.50	234.97	98.05	-0.26	-0.64
148	236.90	132.53	238.02	128.98	236.72	132.82	-0.18	0.29
149	237.67	151.31	238.02	147.91	237.47	151.09	-0.20	-0.22
150	238.81	187.84	238.02	185.87	238.62	188.09	-0.19	0.25
151	239.23	207.33	238.02	205.38	239.03	207.26	-0.20	-0.08
152	239.69	245.15	238.02	244.14	239.49	245.51	-0.20	0.36
153	239.74	265.26	238.02	263.86	239.54	265.02	-0.20	-0.24
154	239.45	303.10	238.02	302.62	239.27	303.36	-0.18	0.25
155	239.11	322.90	238.02	322.13	238.96	322.61	-0.16	-0.29
156	238.13	359.68	238.02	360.09	237.99	359.87	-0.14	0.19

157	237.45	378.39	238.02	379.02	237.33	378.31	-0.12	-0.08
158	235.87	413.37	238.02	415.50	235.73	413.49	-0.14	0.12
159	234.91	431.21	238.02	433.52	234.78	430.66	-0.13	-0.55
160	232.95	462.69	238.02	467.97	232.67	463.03	-0.29	0.34
161	231.84	478.62	238.02	484.86	231.49	478.64	-0.35	0.02

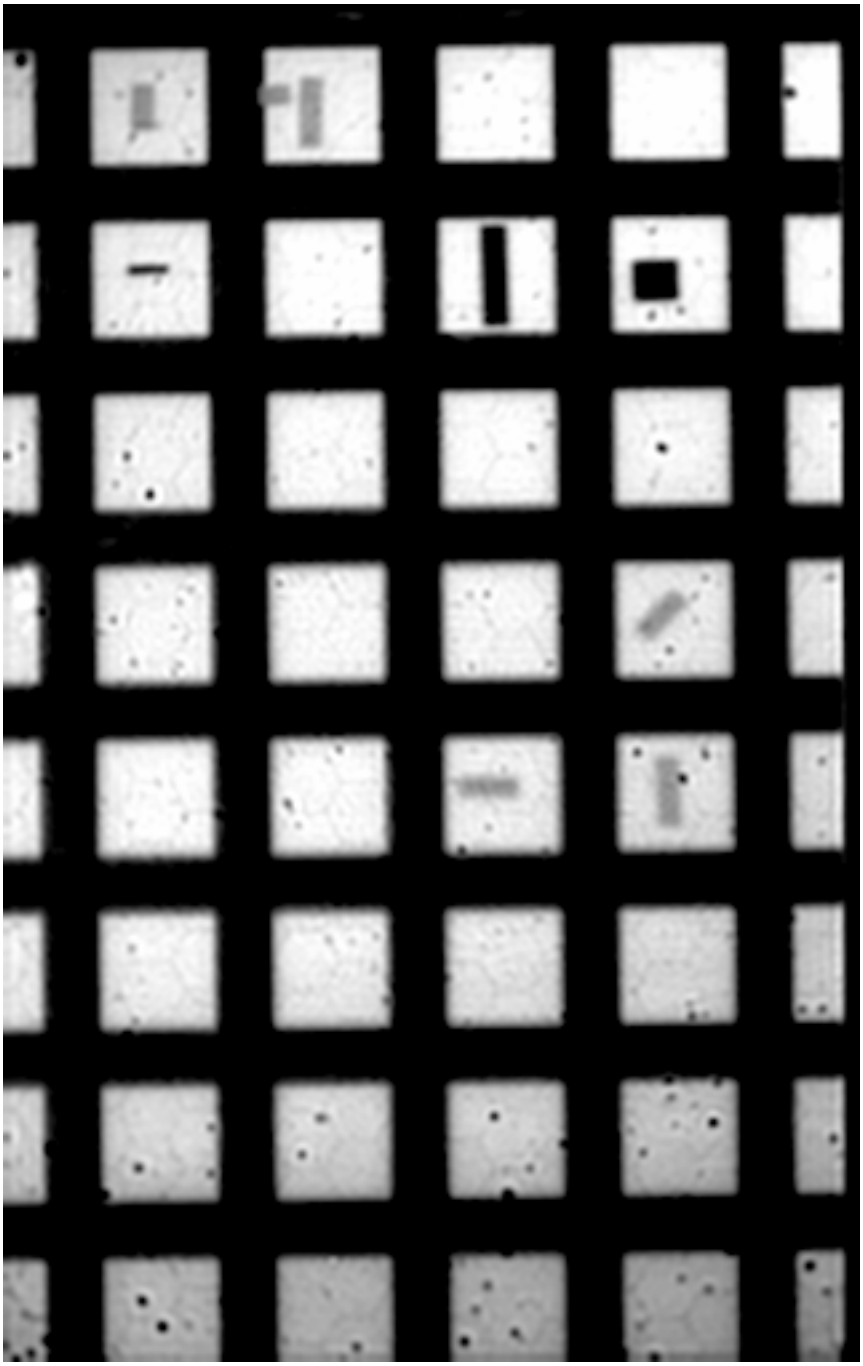

Figure 2.3-7 DISR 2 HRI Target Grid (sharpened)

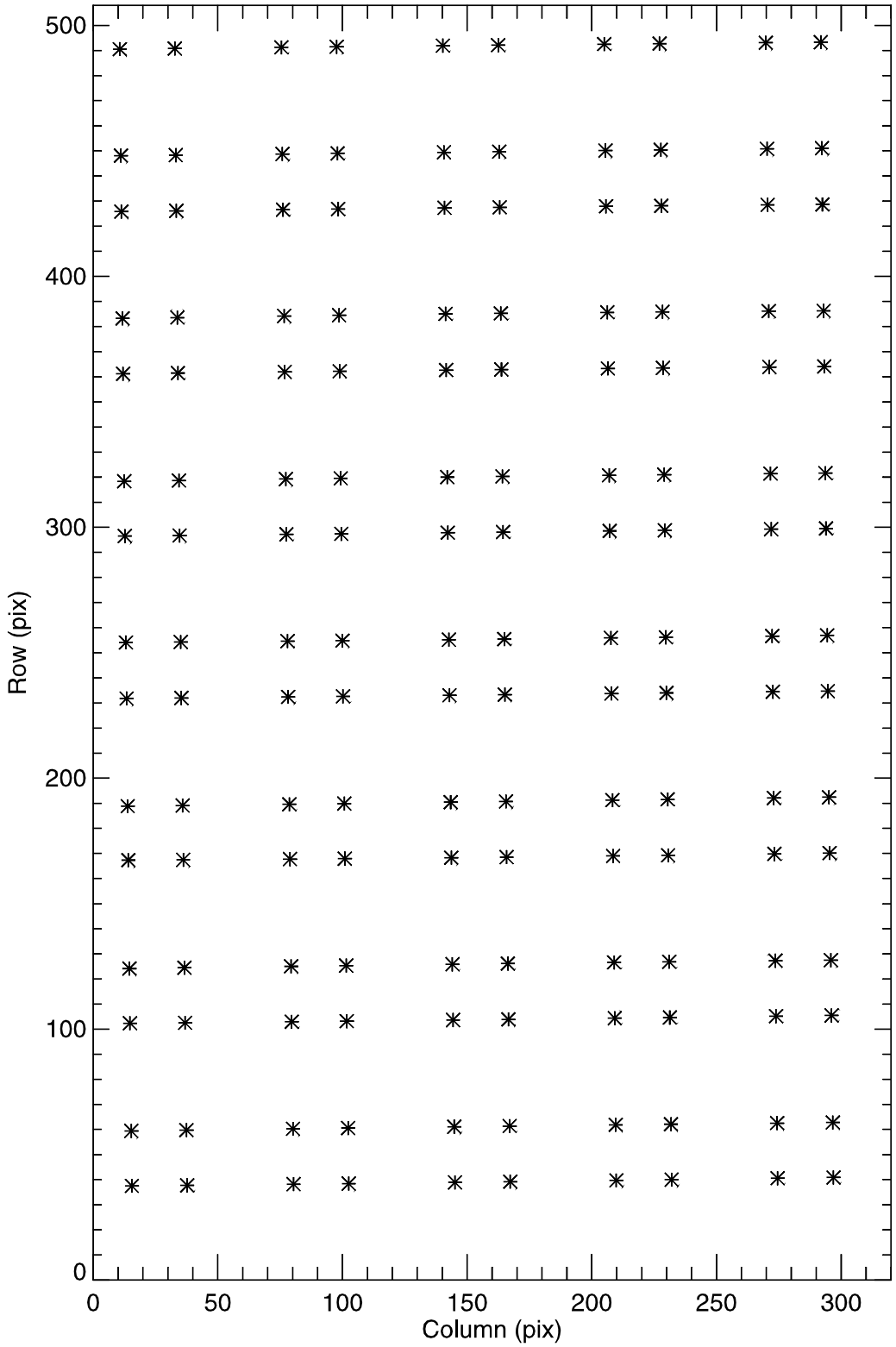

Figure 2.3-8 Location of Observed Vertices for DISR 2 HRI

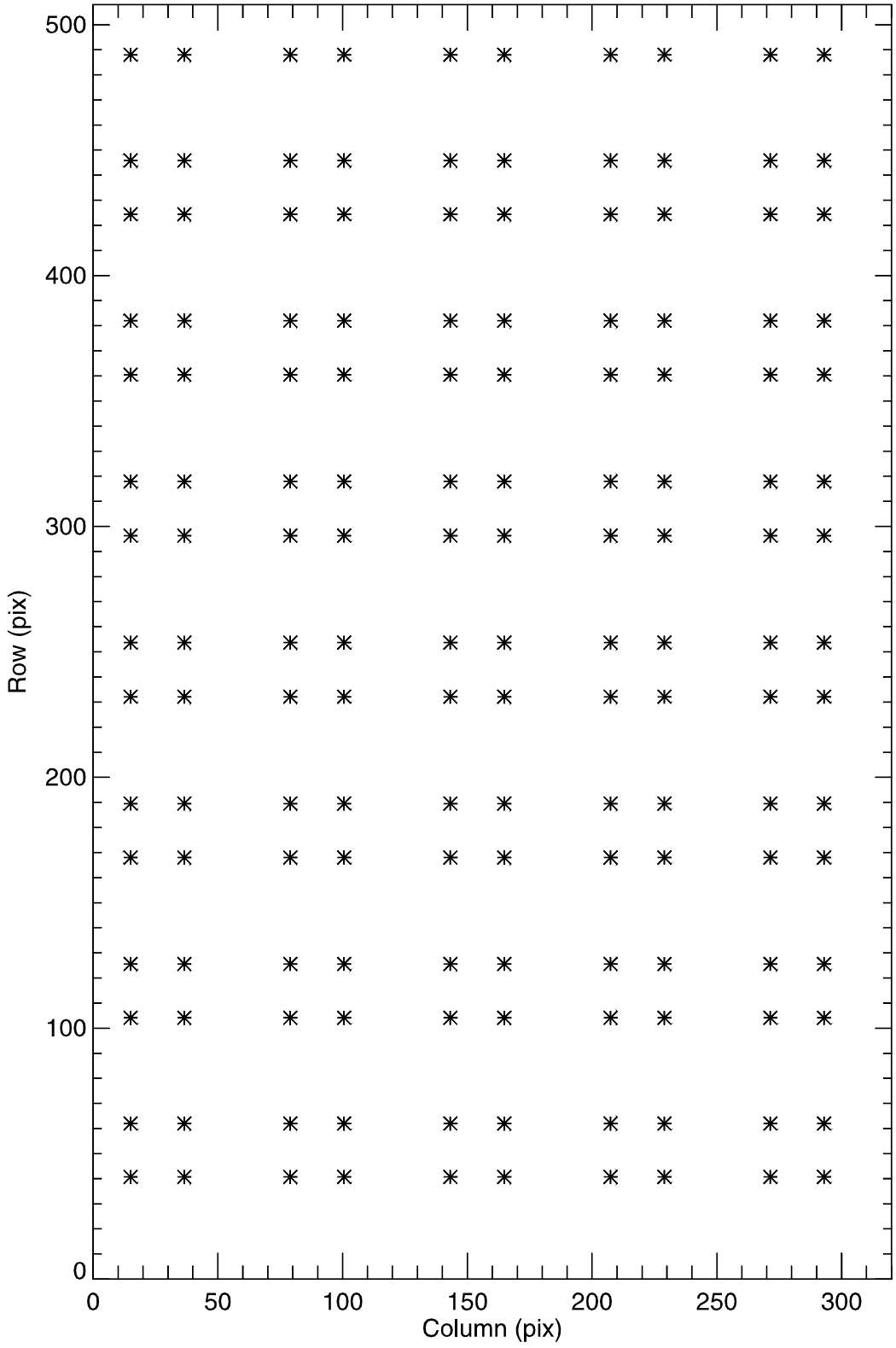

Figure 2.3-9 Location of Desired Vertices for DISR 2 HRI

Table 2.3-4

Vertex Information for DISR#2 HRI Distortion Fit

	C = Column	R=Row						
Point ID	Observed C	Observed R	Desired C	Desired R	Computed C	Computed R	C Residual	R Residual
0	15.53	37.52	15.01	40.67	15.60	37.55	0.07	0.03
1	15.28	59.45	15.01	61.97	15.35	59.37	0.07	-0.08
2	14.80	102.32	15.01	104.13	14.87	102.39	0.07	0.07
3	14.56	124.14	15.01	125.58	14.62	124.19	0.07	0.06
4	14.08	167.35	15.01	167.98	14.15	167.17	0.06	-0.17
5	13.85	188.85	15.01	189.53	13.91	188.96	0.06	0.12
6	13.38	231.76	15.01	232.09	13.44	231.92	0.06	0.16
7	13.14	254.10	15.01	253.70	13.20	253.70	0.06	-0.40
8	12.69	296.51	15.01	296.31	12.74	296.63	0.06	0.13
9	12.46	318.31	15.01	317.91	12.51	318.40	0.05	0.09
10	12.01	361.16	15.01	360.47	12.06	361.32	0.05	0.17
11	11.78	383.24	15.01	382.02	11.84	383.08	0.06	-0.16
12	11.34	425.81	15.01	424.42	11.39	425.99	0.05	0.18
13	11.12	448.07	15.01	445.87	11.17	447.75	0.06	-0.32
14	10.69	490.54	15.01	488.03	10.74	490.65	0.05	0.11
15	37.70	37.75	36.52	40.67	37.52	37.83	-0.18	0.08
16	37.42	59.75	36.52	61.97	37.26	59.62	-0.16	-0.12
17	36.89	102.52	36.52	104.13	36.74	102.61	-0.15	0.09
18	36.63	124.45	36.52	125.58	36.49	124.40	-0.14	-0.05
19	36.12	167.47	36.52	167.98	35.99	167.38	-0.12	-0.09
20	35.87	189.11	36.52	189.53	35.75	189.18	-0.12	0.07
21	35.38	231.97	36.52	232.09	35.27	232.15	-0.11	0.17
22	35.13	254.27	36.52	253.70	35.03	253.93	-0.10	-0.33
23	34.67	296.73	36.52	296.31	34.57	296.89	-0.10	0.16
24	34.44	318.63	36.52	317.91	34.34	318.66	-0.10	0.04
25	33.99	361.43	36.52	360.47	33.89	361.60	-0.10	0.17
26	33.77	383.59	36.52	382.02	33.67	383.36	-0.10	-0.23
27	33.35	426.09	36.52	424.42	33.24	426.27	-0.11	0.19
28	33.13	448.30	36.52	445.87	33.02	448.02	-0.11	-0.28
29	32.73	490.79	36.52	488.03	32.61	490.90	-0.12	0.11
30	80.39	38.20	79.02	40.67	80.60	38.36	0.21	0.16
31	80.14	60.30	79.02	61.97	80.33	60.11	0.19	-0.18
32	79.65	102.93	79.02	104.13	79.81	103.05	0.15	0.12
33	79.40	125.03	79.02	125.58	79.55	124.84	0.14	-0.19
34	78.93	167.76	79.02	167.98	79.04	167.81	0.12	0.05
35	78.68	189.63	79.02	189.53	78.79	189.61	0.11	-0.02
36	78.21	232.40	79.02	232.09	78.30	232.60	0.09	0.20
37	77.97	254.62	79.02	253.70	78.06	254.40	0.09	-0.23
38	77.51	297.17	79.02	296.31	77.60	297.38	0.09	0.21
39	77.27	319.21	79.02	317.91	77.37	319.17	0.10	-0.04
40	76.82	361.94	79.02	360.47	76.93	362.12	0.11	0.19
41	76.59	384.23	79.02	382.02	76.71	383.89	0.12	-0.34
42	76.14	426.59	79.02	424.42	76.28	426.79	0.14	0.20
43	75.92	448.76	79.02	445.87	76.08	448.53	0.16	-0.23
44	75.48	491.26	79.02	488.03	75.67	491.36	0.19	0.10
45	102.52	38.44	100.60	40.67	102.40	38.62	-0.13	0.18
46	102.25	60.57	100.60	61.97	102.13	60.37	-0.12	-0.21
47	101.72	103.16	100.60	104.13	101.61	103.28	-0.11	0.13
48	101.46	125.32	100.60	125.58	101.35	125.06	-0.11	-0.25

49	100.96	167.93	100.60	167.98	100.85	168.04	-0.11	0.11
50	100.71	189.90	100.60	189.53	100.60	189.83	-0.11	-0.06
51	100.23	232.62	100.60	232.09	100.12	232.83	-0.11	0.21
52	99.99	254.82	100.60	253.70	99.88	254.63	-0.11	-0.18
53	99.53	297.40	100.60	296.31	99.42	297.62	-0.12	0.22
54	99.30	319.49	100.60	317.91	99.19	319.42	-0.12	-0.08
55	98.87	362.19	100.60	360.47	98.74	362.38	-0.13	0.19
56	98.65	384.52	100.60	382.02	98.52	384.15	-0.13	-0.38
57	98.25	426.84	100.60	424.42	98.10	427.05	-0.15	0.21
58	98.04	449.00	100.60	445.87	97.89	448.78	-0.15	-0.22
59	97.65	491.50	100.60	488.03	97.48	491.59	-0.17	0.10
60	145.11	38.93	143.20	40.67	145.31	39.14	0.20	0.21
61	144.85	61.10	143.20	61.97	145.06	60.87	0.21	-0.23
62	144.36	103.61	143.20	104.13	144.57	103.76	0.21	0.15
63	144.11	125.85	143.20	125.58	144.33	125.53	0.22	-0.32
64	143.63	168.31	143.20	167.98	143.85	168.50	0.21	0.19
65	143.39	190.43	143.20	189.53	143.60	190.29	0.22	-0.14
66	142.92	233.06	143.20	232.09	143.14	233.29	0.22	0.23
67	142.68	255.22	143.20	253.70	142.90	255.10	0.22	-0.12
68	142.23	297.85	143.20	296.31	142.44	298.10	0.21	0.25
69	142.00	320.02	143.20	317.91	142.21	319.89	0.21	-0.12
70	141.56	362.65	143.20	360.47	141.76	362.86	0.21	0.21
71	141.33	385.04	143.20	382.02	141.54	384.63	0.21	-0.41
72	140.91	427.30	143.20	424.42	141.10	427.52	0.20	0.22
73	140.69	449.45	143.20	445.87	140.88	449.24	0.20	-0.21
74	140.28	491.93	143.20	488.03	140.46	492.03	0.18	0.10
75	167.31	39.19	164.80	40.67	167.06	39.40	-0.25	0.21
76	167.05	61.36	164.80	61.97	166.82	61.12	-0.23	-0.24
77	166.56	103.86	164.80	104.13	166.35	104.01	-0.21	0.15
78	166.31	126.11	164.80	125.58	166.11	125.78	-0.20	-0.34
79	165.83	168.53	164.80	167.98	165.64	168.74	-0.18	0.21
80	165.58	190.71	164.80	189.53	165.41	190.53	-0.17	-0.18
81	165.11	233.29	164.80	232.09	164.94	233.53	-0.17	0.24
82	164.87	255.45	164.80	253.70	164.71	255.34	-0.16	-0.11
83	164.42	298.09	164.80	296.31	164.25	298.33	-0.16	0.25
84	164.18	320.27	164.80	317.91	164.02	320.13	-0.16	-0.14
85	163.74	362.88	164.80	360.47	163.57	363.09	-0.17	0.21
86	163.51	385.28	164.80	382.02	163.35	384.86	-0.16	-0.42
87	163.08	427.52	164.80	424.42	162.90	427.75	-0.18	0.23
88	162.86	449.69	164.80	445.87	162.68	449.47	-0.18	-0.22
89	162.45	492.15	164.80	488.03	162.24	492.25	-0.21	0.10
90	209.83	39.71	207.40	40.67	209.97	39.91	0.14	0.20
91	209.62	61.85	207.40	61.97	209.75	61.63	0.13	-0.22
92	209.19	104.36	207.40	104.13	209.30	104.52	0.11	0.16
93	208.97	126.60	207.40	125.58	209.08	126.28	0.11	-0.32
94	208.53	169.00	207.40	167.98	208.63	169.23	0.10	0.23
95	208.30	191.26	207.40	189.53	208.40	191.02	0.10	-0.24
96	207.86	233.74	207.40	232.09	207.95	234.01	0.09	0.26
97	207.62	255.90	207.40	253.70	207.72	255.81	0.10	-0.10
98	207.16	298.55	207.40	296.31	207.26	298.79	0.10	0.24
99	206.92	320.74	207.40	317.91	207.03	320.58	0.11	-0.16
100	206.45	363.30	207.40	360.47	206.58	363.53	0.13	0.22
101	206.20	385.67	207.40	382.02	206.34	385.29	0.14	-0.39
102	205.72	427.93	207.40	424.42	205.88	428.17	0.16	0.24

103	205.47	450.14	207.40	445.87	205.65	449.89	0.18	-0.26
104	204.98	492.55	207.40	488.03	205.19	492.66	0.21	0.12
105	232.00	40.00	228.98	40.67	231.76	40.17	-0.23	0.17
106	231.76	62.10	228.98	61.97	231.54	61.90	-0.22	-0.20
107	231.31	104.62	228.98	104.13	231.10	104.78	-0.21	0.16
108	231.08	126.84	228.98	125.58	230.88	126.55	-0.20	-0.29
109	230.63	169.27	228.98	167.98	230.43	169.49	-0.19	0.22
110	230.39	191.55	228.98	189.53	230.21	191.28	-0.18	-0.27
111	229.94	233.98	228.98	232.09	229.76	234.25	-0.18	0.27
112	229.71	256.15	228.98	253.70	229.53	256.04	-0.18	-0.10
113	229.26	298.79	228.98	296.31	229.07	299.01	-0.19	0.23
114	229.02	320.97	228.98	317.91	228.84	320.80	-0.18	-0.17
115	228.57	363.51	228.98	360.47	228.38	363.74	-0.19	0.23
116	228.33	385.85	228.98	382.02	228.14	385.49	-0.19	-0.36
117	227.89	428.13	228.98	424.42	227.68	428.37	-0.21	0.24
118	227.65	450.38	228.98	445.87	227.44	450.09	-0.21	-0.30
119	227.20	492.75	228.98	488.03	226.97	492.87	-0.23	0.12
120	274.53	40.56	271.48	40.67	274.84	40.67	0.31	0.12
121	274.32	62.56	271.48	61.97	274.61	62.42	0.29	-0.14
122	273.90	105.16	271.48	104.13	274.15	105.32	0.25	0.16
123	273.68	127.27	271.48	125.58	273.92	127.09	0.24	-0.18
124	273.25	169.84	271.48	167.98	273.46	170.02	0.21	0.18
125	273.03	192.11	271.48	189.53	273.23	191.80	0.20	-0.32
126	272.59	234.44	271.48	232.09	272.77	234.74	0.17	0.30
127	272.36	256.65	271.48	253.70	272.53	256.52	0.17	-0.14
128	271.91	299.26	271.48	296.31	272.07	299.45	0.15	0.19
129	271.68	321.37	271.48	317.91	271.83	321.22	0.15	-0.15
130	271.22	363.88	271.48	360.47	271.36	364.13	0.14	0.24
131	270.97	386.13	271.48	382.02	271.12	385.88	0.15	-0.26
132	270.51	428.49	271.48	424.42	270.66	428.74	0.15	0.25
133	270.26	450.84	271.48	445.87	270.42	450.46	0.16	-0.38
134	269.78	493.11	271.48	488.03	269.95	493.26	0.17	0.15
135	296.93	40.86	292.99	40.67	296.76	40.93	-0.17	0.06
136	296.67	62.80	292.99	61.97	296.51	62.69	-0.15	-0.11
137	296.16	105.45	292.99	104.13	296.03	105.60	-0.13	0.15
138	295.90	127.49	292.99	125.58	295.78	127.37	-0.12	-0.12
139	295.40	170.16	292.99	167.98	295.30	170.30	-0.10	0.14
140	295.15	192.41	292.99	189.53	295.05	192.07	-0.09	-0.35
141	294.66	234.69	292.99	232.09	294.58	234.99	-0.09	0.30
142	294.41	256.93	292.99	253.70	294.34	256.76	-0.07	-0.17
143	293.93	299.51	292.99	296.31	293.86	299.67	-0.07	0.16
144	293.69	321.57	292.99	317.91	293.62	321.43	-0.06	-0.14
145	293.22	364.07	292.99	360.47	293.15	364.32	-0.07	0.25
146	292.98	386.25	292.99	382.02	292.92	386.06	-0.06	-0.19
147	292.52	428.66	292.99	424.42	292.45	428.92	-0.07	0.25
148	292.29	451.08	292.99	445.87	292.22	450.64	-0.07	-0.44
149	291.84	493.29	292.99	488.03	291.76	493.45	-0.08	0.16

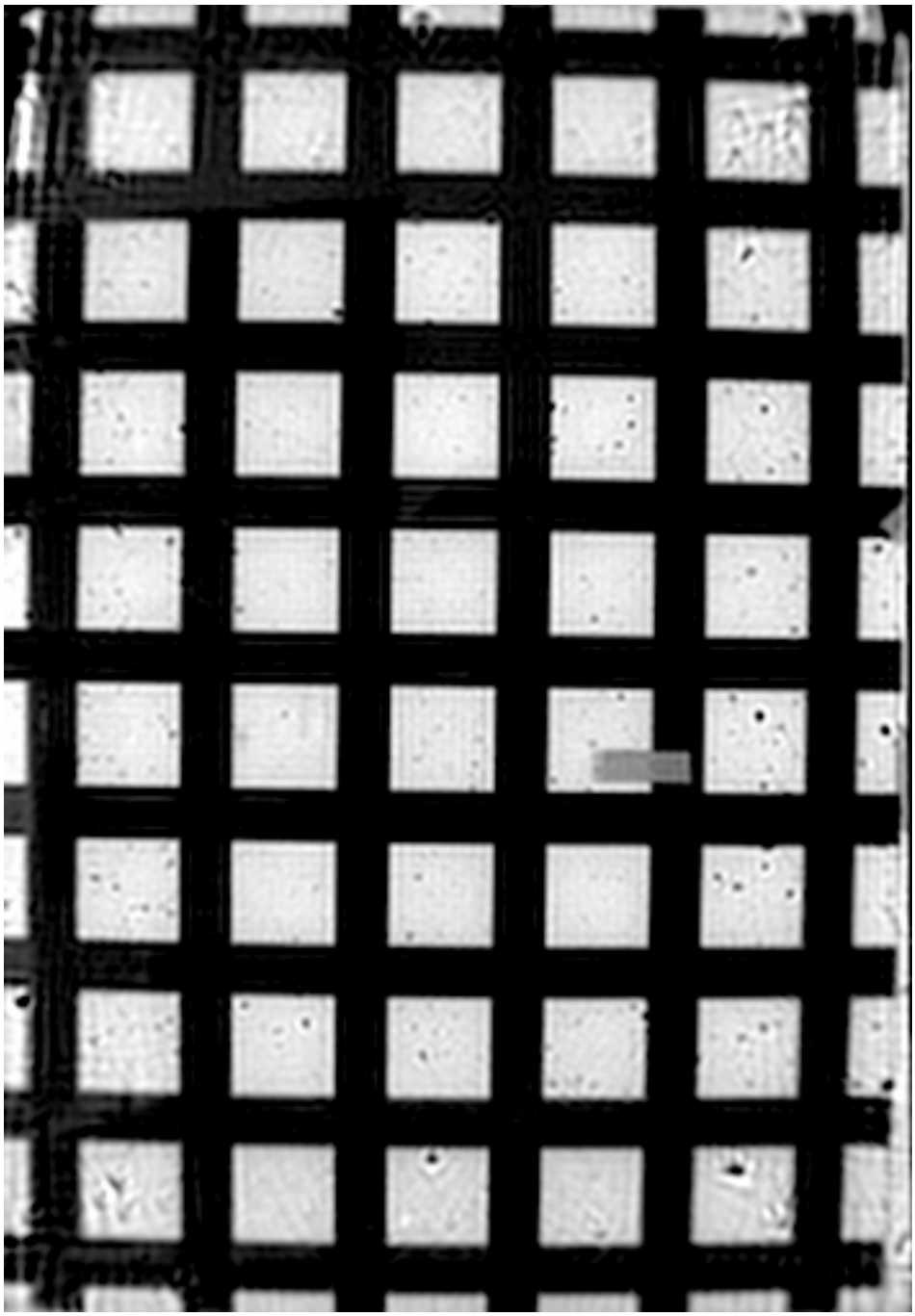

Figure 2.3-10 DISR 3 MRI Target Grid (sharpened)

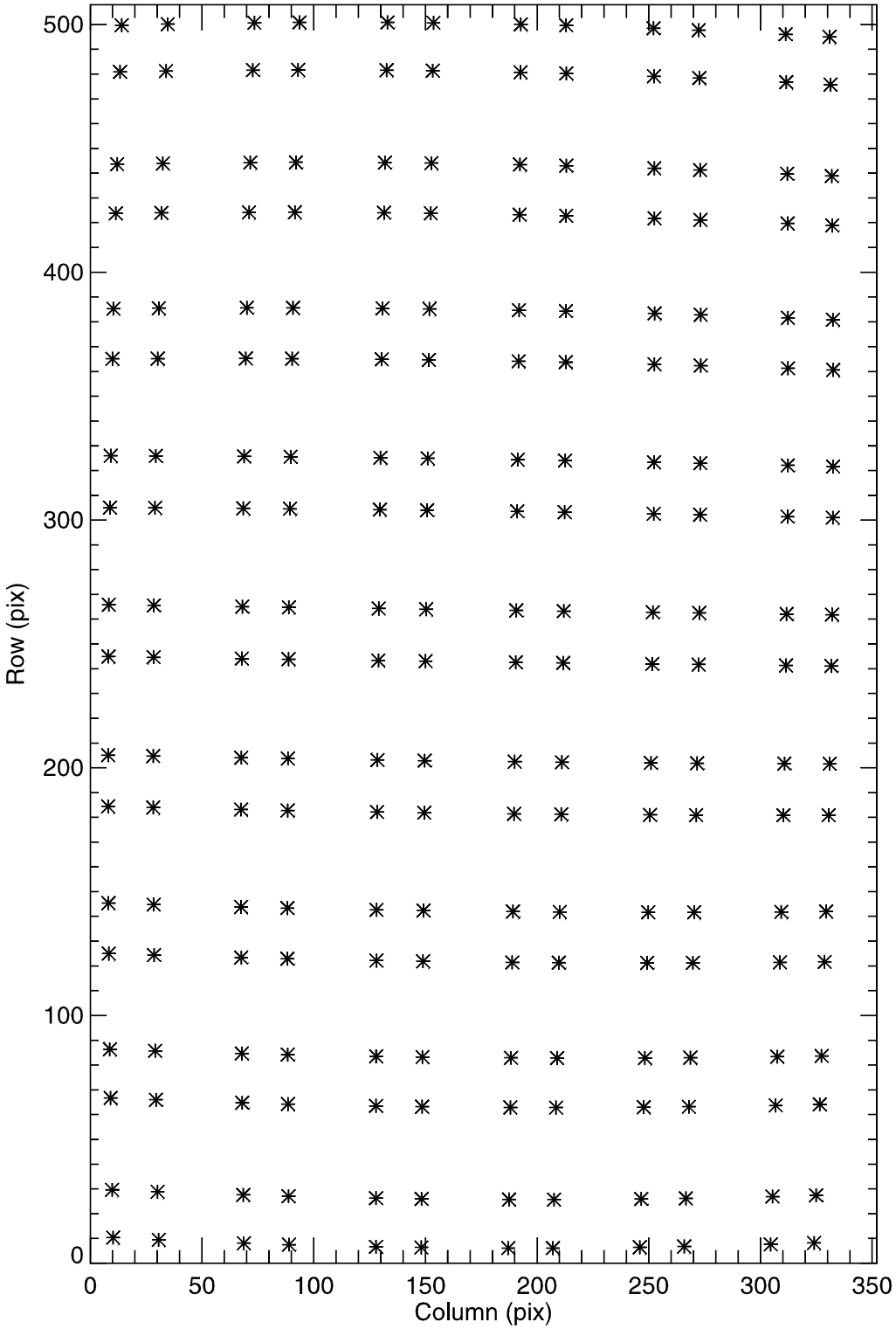

Figure 2.3-11 Location of Observed Vertices for DISR 3 MRI

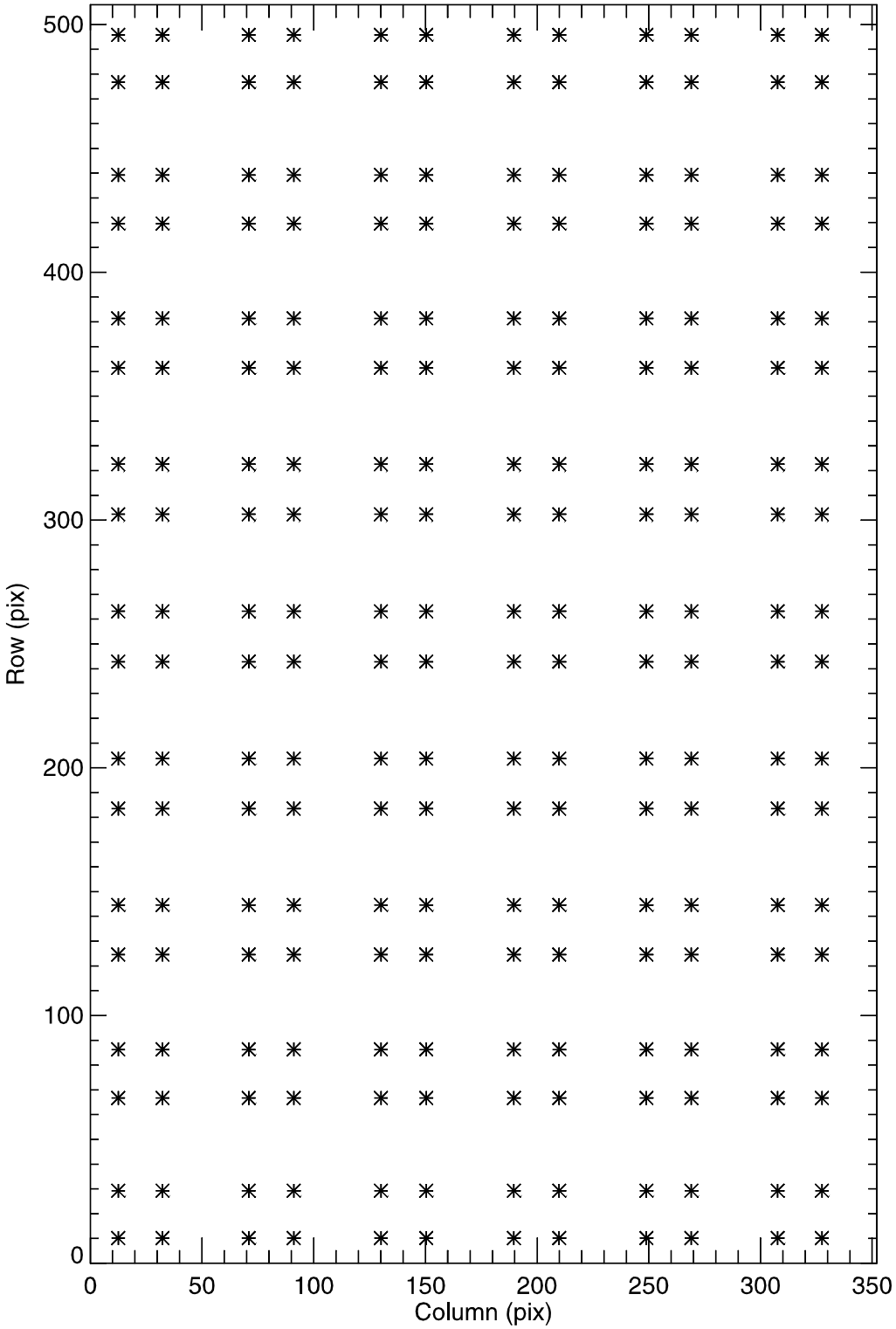

Figure 2.3-12 Location of Desired Vertices for DISR 3 MRI

Table 2.3-5

Vertex Information for DISR#3 MRI Distortion Fit

	C = Column	R=Row						
Point ID	Observed C	Observed R	Desired C	Desired R	Computed C	Computed R	C Residual	R Residual
0	10.20	10.35	12.50	10.16	10.40	10.43	0.19	0.09
1	9.77	29.64	12.50	29.28	9.92	29.42	0.16	-0.21
2	9.06	66.72	12.50	66.70	9.14	66.79	0.08	0.08
3	8.75	86.38	12.50	86.32	8.81	86.47	0.06	0.09
4	8.31	125.02	12.50	124.60	8.32	125.02	0.02	0.00
5	8.15	145.35	12.50	144.59	8.15	145.22	0.00	-0.13
6	8.00	184.42	12.50	183.45	7.98	184.58	-0.02	0.16
7	8.00	205.08	12.50	203.68	7.97	205.10	-0.02	0.02
8	8.15	244.90	12.50	242.85	8.12	244.88	-0.03	-0.02
9	8.32	265.82	12.50	263.15	8.29	265.51	-0.03	-0.31
10	8.78	305.00	12.50	302.32	8.76	305.28	-0.02	0.28
11	9.11	325.94	12.50	322.55	9.09	325.80	-0.02	-0.14
12	9.88	365.05	12.50	361.41	9.89	365.14	0.01	0.09
13	10.36	385.32	12.50	381.41	10.38	385.32	0.02	0.01
14	11.41	423.75	12.50	419.68	11.47	423.83	0.06	0.09
15	12.03	443.61	12.50	439.30	12.11	443.50	0.08	-0.12
16	13.33	480.89	12.50	476.73	13.48	480.82	0.15	-0.07
17	14.05	499.71	12.50	495.84	14.25	499.78	0.20	0.07
18	30.64	9.46	32.33	10.16	30.30	9.60	-0.34	0.15
19	30.15	28.84	32.33	29.28	29.86	28.62	-0.29	-0.21
20	29.37	65.97	32.33	66.70	29.15	66.06	-0.22	0.09
21	29.04	85.74	32.33	86.32	28.86	85.78	-0.18	0.04
22	28.54	124.40	32.33	124.60	28.43	124.41	-0.11	0.01
23	28.36	144.78	32.33	144.59	28.28	144.66	-0.08	-0.11
24	28.18	183.96	32.33	183.45	28.15	184.13	-0.03	0.17
25	28.18	204.70	32.33	203.68	28.16	204.71	-0.01	0.01
26	28.33	244.62	32.33	242.85	28.34	244.60	0.01	-0.02
27	28.51	265.55	32.33	263.15	28.51	265.29	0.01	-0.26
28	29.00	304.92	32.33	302.32	29.00	305.18	0.00	0.26
29	29.36	325.87	32.33	322.55	29.34	325.76	-0.02	-0.11
30	30.18	365.14	32.33	361.41	30.13	365.22	-0.06	0.08
31	30.70	385.49	32.33	381.41	30.61	385.46	-0.09	-0.03
32	31.83	423.98	32.33	419.68	31.69	424.08	-0.15	0.10
33	32.50	443.92	32.33	439.30	32.31	443.79	-0.19	-0.14
34	33.90	481.23	32.33	476.73	33.65	481.20	-0.26	-0.03
35	34.69	500.16	32.33	495.84	34.40	500.20	-0.29	0.04
36	68.76	8.08	70.93	10.16	68.93	8.26	0.17	0.18
37	68.46	27.58	70.93	29.28	68.62	27.32	0.17	-0.26
38	68.00	64.77	70.93	66.70	68.14	64.85	0.15	0.08
39	67.81	84.68	70.93	86.32	67.95	84.63	0.14	-0.06
40	67.57	123.37	70.93	124.60	67.70	123.39	0.14	0.02
41	67.50	143.81	70.93	144.59	67.64	143.72	0.14	-0.09
42	67.50	183.15	70.93	183.45	67.63	183.34	0.13	0.19
43	67.57	204.02	70.93	203.68	67.69	204.00	0.13	-0.02
44	67.82	244.09	70.93	242.85	67.94	244.07	0.12	-0.01
45	68.02	265.04	70.93	263.15	68.13	264.86	0.11	-0.18
46	68.53	304.71	70.93	302.32	68.62	304.93	0.10	0.21
47	68.86	325.67	70.93	322.55	68.94	325.60	0.08	-0.07
48	69.62	365.17	70.93	361.41	69.68	365.23	0.07	0.06

49	70.07	385.65	70.93	381.41	70.12	385.56	0.05	-0.10
50	71.05	424.21	70.93	419.68	71.09	424.33	0.04	0.12
51	71.62	444.29	70.93	439.30	71.64	444.12	0.02	-0.17
52	72.80	481.63	70.93	476.73	72.82	481.67	0.02	0.05
53	73.46	500.72	70.93	495.84	73.47	500.74	0.02	0.01
54	88.96	7.49	91.06	10.16	89.02	7.70	0.06	0.21
55	88.76	27.04	91.06	29.28	88.81	26.77	0.04	-0.27
56	88.48	64.25	91.06	66.70	88.48	64.33	0.00	0.08
57	88.38	84.22	91.06	86.32	88.37	84.13	-0.01	-0.09
58	88.27	122.91	91.06	124.60	88.24	122.94	-0.03	0.03
59	88.26	143.37	91.06	144.59	88.22	143.29	-0.04	-0.08
60	88.34	182.77	91.06	183.45	88.30	182.97	-0.04	0.20
61	88.43	203.70	91.06	203.68	88.39	203.67	-0.04	-0.03
62	88.71	243.82	91.06	242.85	88.67	243.80	-0.04	-0.01
63	88.91	264.77	91.06	263.15	88.87	264.62	-0.04	-0.15
64	89.38	304.56	91.06	302.32	89.36	304.76	-0.02	0.19
65	89.68	325.52	91.06	322.55	89.67	325.46	-0.01	-0.06
66	90.35	365.11	91.06	361.41	90.36	365.16	0.01	0.05
67	90.74	385.65	91.06	381.41	90.77	385.52	0.03	-0.12
68	91.58	424.23	91.06	419.68	91.65	424.36	0.07	0.13
69	92.06	444.36	91.06	439.30	92.15	444.18	0.09	-0.18
70	93.05	481.70	91.06	476.73	93.20	481.78	0.15	0.08
71	93.60	500.87	91.06	495.84	93.78	500.87	0.18	0.00
72	127.89	6.66	130.11	10.16	127.92	6.90	0.03	0.24
73	127.88	26.26	130.11	29.28	127.91	25.97	0.03	-0.29
74	127.90	63.48	130.11	66.70	127.94	63.56	0.05	0.08
75	127.94	83.51	130.11	86.32	127.99	83.37	0.05	-0.14
76	128.06	122.17	130.11	124.60	128.13	122.23	0.07	0.06
77	128.16	142.67	130.11	144.59	128.23	142.61	0.07	-0.06
78	128.40	182.13	130.11	183.45	128.49	182.35	0.09	0.22
79	128.56	203.14	130.11	203.68	128.65	203.09	0.09	-0.05
80	128.92	243.31	130.11	242.85	129.01	243.29	0.09	-0.02
81	129.14	264.26	130.11	263.15	129.23	264.15	0.09	-0.11
82	129.61	304.21	130.11	302.32	129.70	304.37	0.09	0.16
83	129.89	325.15	130.11	322.55	129.97	325.11	0.09	-0.03
84	130.47	364.86	130.11	361.41	130.55	364.89	0.08	0.03
85	130.80	385.45	130.11	381.41	130.87	385.29	0.07	-0.16
86	131.48	424.05	130.11	419.68	131.54	424.20	0.06	0.15
87	131.86	444.25	130.11	439.30	131.91	444.05	0.05	-0.20
88	132.62	481.58	130.11	476.73	132.66	481.71	0.04	0.13
89	133.04	500.86	130.11	495.84	133.07	500.83	0.03	-0.03
90	148.19	6.37	150.40	10.16	148.09	6.62	-0.10	0.25
91	148.30	25.98	150.40	29.28	148.20	25.69	-0.10	-0.29
92	148.54	63.19	150.40	66.70	148.43	63.27	-0.10	0.08
93	148.68	83.24	150.40	86.32	148.57	83.09	-0.11	-0.15
94	148.97	121.87	150.40	124.60	148.87	121.94	-0.11	0.07
95	149.14	142.37	150.40	144.59	149.03	142.33	-0.11	-0.05
96	149.49	181.85	150.40	183.45	149.39	182.08	-0.11	0.23
97	149.69	202.88	150.40	203.68	149.58	202.81	-0.11	-0.06
98	150.11	243.05	150.40	242.85	149.99	243.03	-0.11	-0.02
99	150.33	263.99	150.40	263.15	150.22	263.90	-0.11	-0.10
100	150.80	303.98	150.40	302.32	150.68	304.13	-0.12	0.15
101	151.05	324.91	150.40	322.55	150.93	324.88	-0.12	-0.02
102	151.57	364.64	150.40	361.41	151.44	364.67	-0.13	0.03

103	151.85	385.26	150.40	381.41	151.71	385.08	-0.13	-0.17
104	152.40	423.84	150.40	419.68	152.26	424.01	-0.14	0.17
105	152.70	444.07	150.40	439.30	152.55	443.86	-0.15	-0.20
106	153.28	481.38	150.40	476.73	153.13	481.54	-0.15	0.15
107	153.59	500.70	150.40	495.84	153.44	500.66	-0.15	-0.04
108	187.12	6.11	189.60	10.16	187.04	6.36	-0.08	0.25
109	187.44	25.71	189.60	29.28	187.37	25.41	-0.07	-0.30
110	188.03	62.88	189.60	66.70	188.01	62.94	-0.02	0.07
111	188.34	82.91	189.60	86.32	188.33	82.74	-0.01	-0.17
112	188.90	121.45	189.60	124.60	188.92	121.55	0.02	0.10
113	189.19	141.95	189.60	144.59	189.22	141.92	0.03	-0.03
114	189.71	181.40	189.60	183.45	189.77	181.63	0.05	0.24
115	189.98	202.44	189.60	203.68	190.04	202.36	0.06	-0.09
116	190.46	242.57	189.60	242.85	190.53	242.54	0.07	-0.03
117	190.70	263.49	189.60	263.15	190.77	263.40	0.07	-0.10
118	191.13	303.48	189.60	302.32	191.21	303.60	0.08	0.13
119	191.33	324.36	189.60	322.55	191.42	324.34	0.08	-0.02
120	191.70	364.09	189.60	361.41	191.79	364.11	0.08	0.03
121	191.88	384.70	189.60	381.41	191.96	384.51	0.08	-0.18
122	192.19	423.24	189.60	419.68	192.26	423.42	0.07	0.18
123	192.34	443.47	189.60	439.30	192.40	443.27	0.06	-0.20
124	192.59	480.74	189.60	476.73	192.64	480.93	0.05	0.18
125	192.71	500.12	189.60	495.84	192.74	500.04	0.04	-0.08
126	207.08	6.12	209.89	10.16	207.18	6.37	0.10	0.25
127	207.58	25.70	209.89	29.28	207.63	25.40	0.05	-0.30
128	208.48	62.83	209.89	66.70	208.46	62.89	-0.02	0.06
129	208.93	82.83	209.89	86.32	208.87	82.67	-0.06	-0.16
130	209.73	121.32	209.89	124.60	209.62	121.44	-0.11	0.12
131	210.12	141.81	209.89	144.59	209.98	141.78	-0.14	-0.03
132	210.81	181.21	209.89	183.45	210.63	181.45	-0.18	0.24
133	211.14	202.25	209.89	203.68	210.94	202.15	-0.20	-0.10
134	211.69	242.33	209.89	242.85	211.47	242.30	-0.22	-0.03
135	211.95	263.23	209.89	263.15	211.72	263.13	-0.22	-0.10
136	212.36	303.17	209.89	302.32	212.14	303.30	-0.21	0.13
137	212.54	324.03	209.89	322.55	212.33	324.02	-0.21	-0.01
138	212.81	363.71	209.89	361.41	212.63	363.75	-0.18	0.04
139	212.91	384.31	209.89	381.41	212.76	384.13	-0.16	-0.17
140	213.04	422.81	209.89	419.68	212.94	423.01	-0.11	0.20
141	213.08	443.04	209.89	439.30	213.00	442.84	-0.08	-0.20
142	213.08	480.28	209.89	476.73	213.06	480.47	-0.02	0.19
143	213.05	499.67	209.89	495.84	213.06	499.57	0.02	-0.10
144	245.97	6.44	248.94	10.16	245.95	6.67	-0.02	0.23
145	246.61	25.94	248.94	29.28	246.60	25.64	-0.01	-0.30
146	247.74	62.96	248.94	66.70	247.79	63.02	0.04	0.05
147	248.30	82.87	248.94	86.32	248.36	82.73	0.05	-0.14
148	249.28	121.22	248.94	124.60	249.37	121.38	0.09	0.16
149	249.75	141.68	248.94	144.59	249.84	141.65	0.09	-0.02
150	250.55	180.96	248.94	183.45	250.67	181.20	0.11	0.24
151	250.93	201.95	248.94	203.68	251.04	201.83	0.11	-0.12
152	251.53	241.89	248.94	242.85	251.65	241.84	0.12	-0.04
153	251.80	262.75	248.94	263.15	251.92	262.61	0.12	-0.14
154	252.19	302.53	248.94	302.32	252.32	302.65	0.13	0.12
155	252.34	323.33	248.94	322.55	252.47	323.30	0.13	-0.03
156	252.53	362.87	248.94	361.41	252.65	362.91	0.13	0.04

157	252.57	383.40	248.94	381.41	252.69	383.24	0.12	-0.16
158	252.55	421.79	248.94	419.68	252.66	422.00	0.11	0.21
159	252.49	441.97	248.94	439.30	252.59	441.78	0.10	-0.19
160	252.28	479.12	248.94	476.73	252.35	479.32	0.07	0.20
161	252.13	498.51	248.94	495.84	252.18	498.38	0.05	-0.13
162	265.83	6.74	269.07	10.16	265.95	6.96	0.12	0.22
163	266.60	26.18	269.07	29.28	266.69	25.89	0.09	-0.29
164	267.94	63.15	269.07	66.70	268.02	63.19	0.08	0.04
165	268.60	82.98	269.07	86.32	268.66	82.87	0.07	-0.11
166	269.74	121.25	269.07	124.60	269.79	121.43	0.05	0.18
167	270.29	141.68	269.07	144.59	270.32	141.66	0.03	-0.02
168	271.21	180.88	269.07	183.45	271.22	181.11	0.01	0.23
169	271.63	201.83	269.07	203.68	271.62	201.70	-0.01	-0.14
170	272.29	241.67	269.07	242.85	272.27	241.62	-0.02	-0.05
171	272.57	262.50	269.07	263.15	272.54	262.33	-0.03	-0.17
172	272.97	302.16	269.07	302.32	272.93	302.28	-0.03	0.12
173	273.10	322.92	269.07	322.55	273.07	322.89	-0.03	-0.03
174	273.23	362.36	269.07	361.41	273.20	362.41	-0.03	0.06
175	273.23	382.83	269.07	381.41	273.21	382.69	-0.03	-0.14
176	273.11	421.15	269.07	419.68	273.08	421.38	-0.02	0.23
177	272.98	441.29	269.07	439.30	272.96	441.12	-0.02	-0.17
178	272.62	478.39	269.07	476.73	272.59	478.59	-0.02	0.20
179	272.37	497.76	269.07	495.84	272.34	497.61	-0.02	-0.14
180	304.55	7.62	307.67	10.16	304.33	7.78	-0.22	0.16
181	305.37	26.92	307.67	29.28	305.19	26.63	-0.18	-0.29
182	306.81	63.73	307.67	66.70	306.75	63.76	-0.06	0.03
183	307.51	83.37	307.67	86.32	307.49	83.33	-0.02	-0.05
184	308.73	121.46	307.67	124.60	308.78	121.69	0.05	0.23
185	309.31	141.83	307.67	144.59	309.38	141.81	0.08	-0.02
186	310.27	180.81	307.67	183.45	310.40	181.04	0.12	0.23
187	310.72	201.67	307.67	203.68	310.84	201.51	0.13	-0.16
188	311.41	241.27	307.67	242.85	311.55	241.20	0.15	-0.07
189	311.69	262.04	307.67	263.15	311.84	261.79	0.15	-0.25
190	312.08	301.39	307.67	302.32	312.23	301.51	0.15	0.12
191	312.21	322.07	307.67	322.55	312.35	322.01	0.14	-0.06
192	312.31	361.24	307.67	361.41	312.43	361.32	0.11	0.07
193	312.29	381.59	307.67	381.41	312.38	381.49	0.09	-0.10
194	312.11	419.73	307.67	419.68	312.15	419.98	0.03	0.25
195	311.95	439.77	307.67	439.30	311.95	439.63	0.00	-0.14
196	311.52	476.74	307.67	476.73	311.41	476.93	-0.10	0.19
197	311.22	496.04	307.67	495.84	311.07	495.87	-0.15	-0.17
198	323.95	8.20	327.50	10.16	324.07	8.34	0.12	0.14
199	324.90	27.41	327.50	29.28	324.97	27.14	0.07	-0.27
200	326.56	64.13	327.50	66.70	326.59	64.16	0.03	0.02
201	327.36	83.67	327.50	86.32	327.36	83.67	0.00	0.00
202	328.75	121.65	327.50	124.60	328.70	121.90	-0.04	0.25
203	329.40	141.97	327.50	144.59	329.33	141.96	-0.08	-0.01
204	330.48	180.83	327.50	183.45	330.38	181.05	-0.11	0.22
205	330.97	201.61	327.50	203.68	330.84	201.44	-0.13	-0.17
206	331.71	241.07	327.50	242.85	331.57	240.99	-0.14	-0.07
207	332.01	261.81	327.50	263.15	331.87	261.51	-0.14	-0.29
208	332.39	300.96	327.50	302.32	332.27	301.09	-0.13	0.13
209	332.50	321.59	327.50	322.55	332.39	321.51	-0.12	-0.07
210	332.53	360.59	327.50	361.41	332.45	360.68	-0.08	0.09

211	332.46	380.85	327.50	381.41	332.40	380.79	-0.06	-0.06
212	332.16	418.90	327.50	419.68	332.14	419.15	-0.02	0.26
213	331.91	438.87	327.50	439.30	331.92	438.74	0.02	-0.12
214	331.30	475.77	327.50	476.73	331.36	475.94	0.06	0.17
215	330.89	495.03	327.50	495.84	330.98	494.84	0.09	-0.19

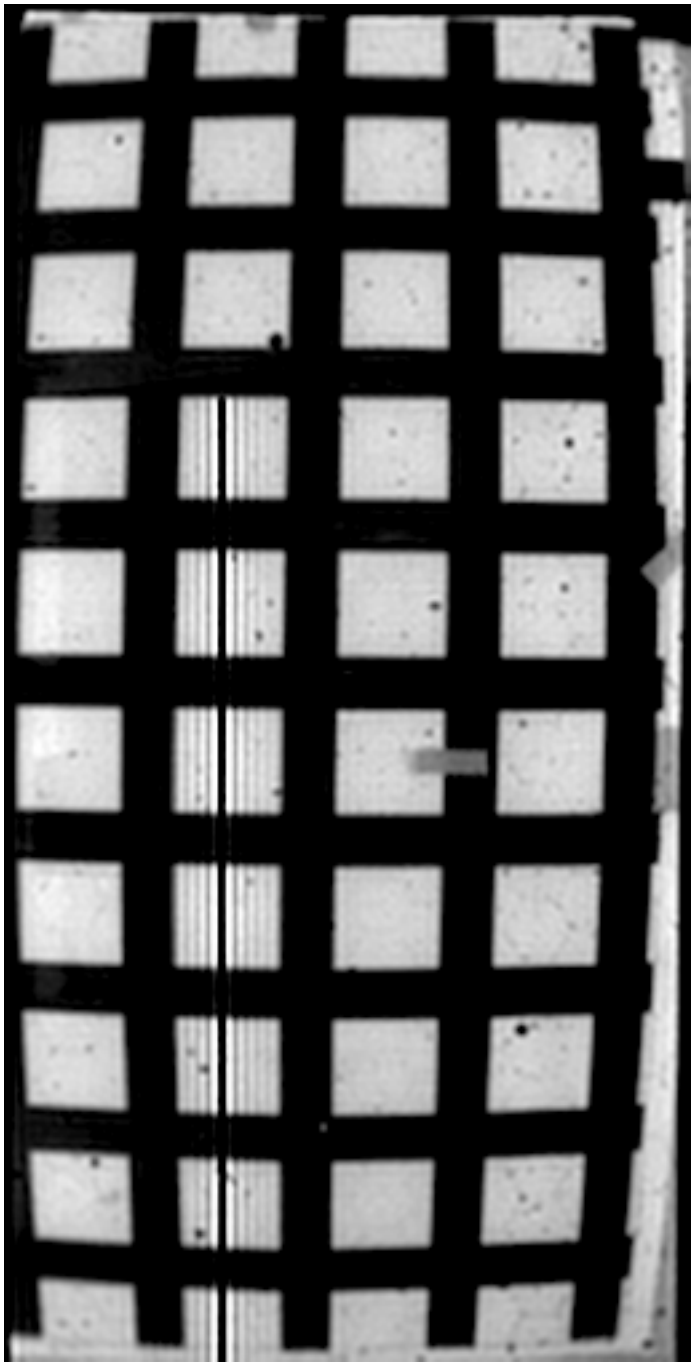

Figure 2.3-13 DISR 3 SLI Target Grid (sharpened)

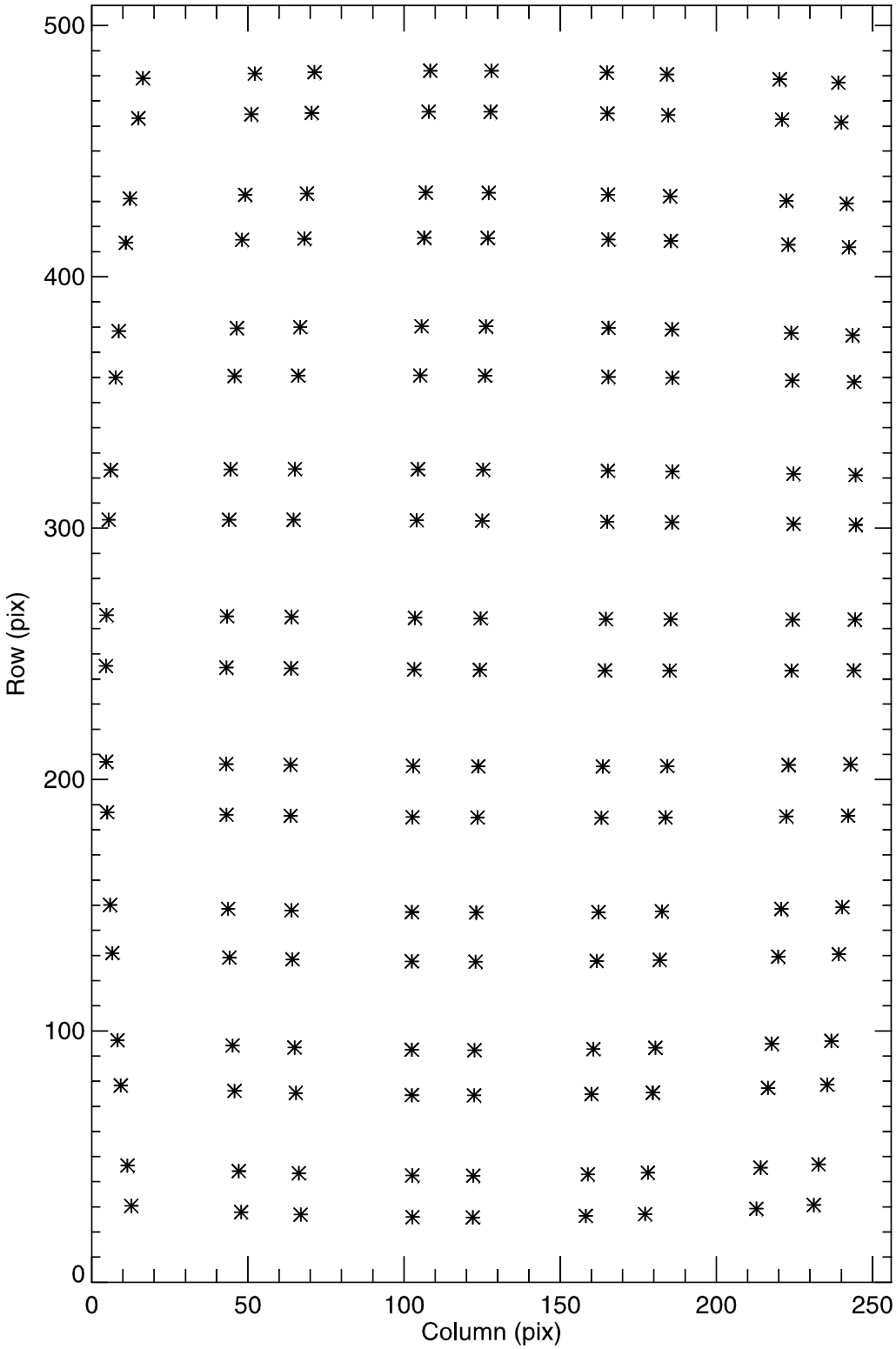

Figure 2.3-14 Location of Observed Vertices for DISR 3 SLI

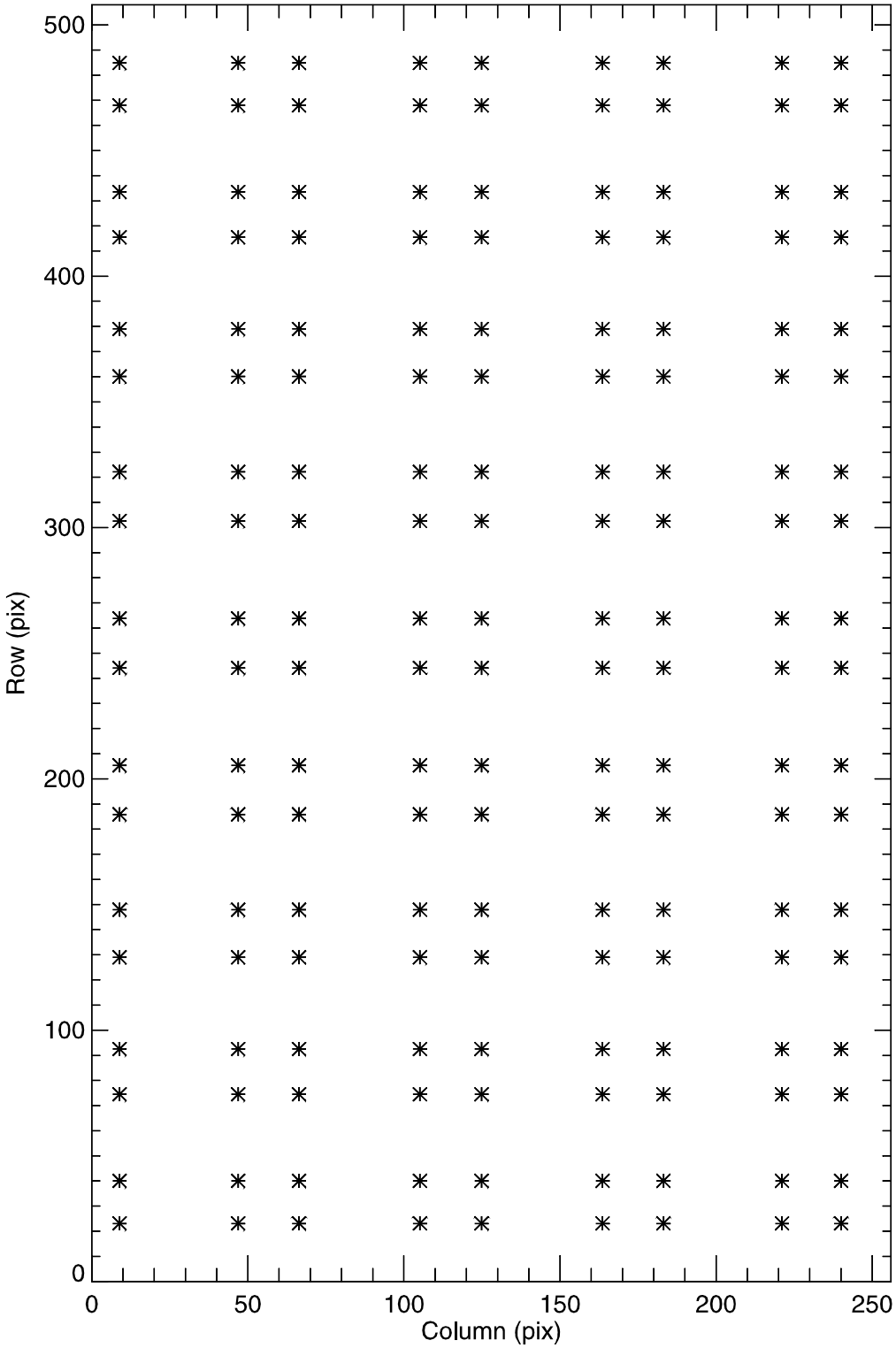

Figure 2.3-15 Location of Desired Vertices for DISR 3 SLI

Table 2.3-6

Vertex Information for DISR 3 SLI Distortion Fit

	C = Column	R=Row						
Point ID	Observed C	Observed R	Desired C	Desired R	Computed C	Computed R	C Residual	R Residual
0	12.70	30.40	8.91	23.14	12.70	30.46	0.00	0.06
1	11.46	46.48	8.91	40.03	11.43	46.17	-0.03	-0.30
2	9.31	78.29	8.91	74.48	9.17	78.73	-0.13	0.44
3	8.26	96.31	8.91	92.50	8.17	96.00	-0.09	-0.31
4	6.61	130.98	8.91	128.98	6.52	131.37	-0.09	0.39
5	5.90	150.11	8.91	147.91	5.86	149.90	-0.04	-0.20
6	4.94	186.96	8.91	185.87	4.94	187.37	0.00	0.41
7	4.65	207.06	8.91	205.38	4.68	206.73	0.03	-0.33
8	4.53	245.17	8.91	244.14	4.58	245.31	0.05	0.14
9	4.71	265.40	8.91	263.86	4.74	264.95	0.04	-0.45
10	5.47	303.35	8.91	302.62	5.49	303.48	0.02	0.14
11	6.10	323.15	8.91	322.13	6.07	322.80	-0.03	-0.35
12	7.68	359.96	8.91	360.09	7.61	360.15	-0.06	0.20
13	8.67	378.40	8.91	379.02	8.58	378.61	-0.10	0.20
14	10.93	413.56	8.91	415.50	10.81	413.79	-0.12	0.23
15	12.25	431.16	8.91	433.52	12.09	430.95	-0.15	-0.21
16	14.94	463.12	8.91	467.97	14.87	463.26	-0.07	0.15
17	16.43	479.04	8.91	484.86	16.40	478.84	-0.03	-0.19
18	47.85	27.88	46.87	23.14	48.23	27.99	0.38	0.10
19	47.06	44.22	46.87	40.03	47.40	43.78	0.34	-0.44
20	45.72	76.13	46.87	74.48	45.95	76.55	0.23	0.42
21	45.08	94.20	46.87	92.50	45.32	93.95	0.24	-0.25
22	44.09	129.16	46.87	128.98	44.30	129.63	0.21	0.47
23	43.68	148.58	46.87	147.91	43.91	148.34	0.23	-0.25
24	43.17	185.98	46.87	185.87	43.42	186.18	0.24	0.21
25	43.05	206.20	46.87	205.38	43.31	205.75	0.26	-0.45
26	43.13	244.53	46.87	244.14	43.39	244.75	0.26	0.22
27	43.33	264.91	46.87	263.86	43.58	264.61	0.25	-0.30
28	44.00	303.39	46.87	302.62	44.25	303.58	0.25	0.20
29	44.51	323.45	46.87	322.13	44.73	323.12	0.22	-0.33
30	45.74	360.54	46.87	360.09	45.95	360.87	0.22	0.33
31	46.51	379.60	46.87	379.02	46.70	379.52	0.19	-0.08
32	48.18	414.78	46.87	415.50	48.39	415.05	0.21	0.27
33	49.16	432.61	46.87	433.52	49.35	432.36	0.20	-0.25
34	51.12	464.67	46.87	467.97	51.42	464.94	0.30	0.27
35	52.21	480.83	46.87	484.86	52.54	480.62	0.33	-0.21
36	66.88	26.93	66.38	23.14	66.55	27.10	-0.33	0.17
37	66.32	43.37	66.38	40.03	65.96	42.92	-0.36	-0.45
38	65.38	75.32	66.38	74.48	64.94	75.76	-0.43	0.44
39	64.93	93.39	66.38	92.50	64.51	93.20	-0.42	-0.19
40	64.26	128.46	66.38	128.98	63.84	128.98	-0.43	0.52
41	64.00	147.98	66.38	147.91	63.59	147.75	-0.40	-0.24
42	63.70	185.57	66.38	185.87	63.33	185.72	-0.38	0.15
43	63.66	205.85	66.38	205.38	63.30	205.36	-0.36	-0.48
44	63.81	244.25	66.38	244.14	63.48	244.51	-0.33	0.27
45	64.02	264.68	66.38	263.86	63.69	264.45	-0.33	-0.23
46	64.63	303.35	66.38	302.62	64.32	303.57	-0.31	0.22
47	65.07	323.51	66.38	322.13	64.75	323.19	-0.32	-0.33
48	66.09	360.71	66.38	360.09	65.81	361.09	-0.29	0.37

49	66.74	380.01	66.38	379.02	66.44	379.80	-0.30	-0.20
50	68.10	415.19	66.38	415.50	67.85	415.46	-0.25	0.26
51	68.89	433.11	66.38	433.52	68.64	432.83	-0.25	-0.28
52	70.47	465.21	66.38	467.97	70.33	465.50	-0.13	0.29
53	71.34	481.47	66.38	484.86	71.24	481.23	-0.10	-0.23
54	102.72	25.93	105.14	23.14	103.07	26.13	0.35	0.20
55	102.62	42.48	105.14	40.03	102.96	41.97	0.34	-0.52
56	102.50	74.46	105.14	74.48	102.83	74.85	0.33	0.39
57	102.47	92.49	105.14	92.50	102.80	92.33	0.33	-0.16
58	102.48	127.67	105.14	128.98	102.82	128.19	0.34	0.53
59	102.53	147.27	105.14	147.91	102.87	147.02	0.34	-0.25
60	102.72	185.04	105.14	185.87	103.07	185.12	0.35	0.08
61	102.88	205.39	105.14	205.38	103.22	204.83	0.34	-0.56
62	103.26	243.81	105.14	244.14	103.61	244.13	0.35	0.32
63	103.52	264.31	105.14	263.86	103.85	264.15	0.33	-0.16
64	104.10	303.17	105.14	302.62	104.41	303.43	0.32	0.26
65	104.45	323.44	105.14	322.13	104.74	323.13	0.29	-0.31
66	105.19	360.78	105.14	360.09	105.46	361.19	0.27	0.41
67	105.62	380.34	105.14	379.02	105.86	379.99	0.24	-0.35
68	106.48	415.53	105.14	415.50	106.70	415.79	0.22	0.26
69	106.96	433.51	105.14	433.52	107.16	433.23	0.19	-0.29
70	107.89	465.69	105.14	467.97	108.09	466.02	0.20	0.33
71	108.39	482.04	105.14	484.86	108.57	481.81	0.18	-0.23
72	122.01	25.81	124.86	23.14	121.70	26.04	-0.32	0.23
73	122.14	42.39	124.86	40.03	121.84	41.86	-0.30	-0.53
74	122.41	74.35	124.86	74.48	122.16	74.73	-0.25	0.37
75	122.58	92.35	124.86	92.50	122.34	92.20	-0.24	-0.15
76	122.92	127.52	124.86	128.98	122.72	128.05	-0.20	0.53
77	123.12	147.12	124.86	147.91	122.93	146.87	-0.19	-0.25
78	123.54	184.88	124.86	185.87	123.37	184.97	-0.17	0.09
79	123.78	205.27	124.86	205.38	123.61	204.68	-0.17	-0.59
80	124.25	243.64	124.86	244.14	124.10	243.98	-0.15	0.34
81	124.52	264.14	124.86	263.86	124.36	264.00	-0.16	-0.13
82	125.06	303.02	124.86	302.62	124.89	303.30	-0.17	0.28
83	125.35	323.30	124.86	322.13	125.16	323.00	-0.19	-0.30
84	125.92	360.67	124.86	360.09	125.71	361.08	-0.21	0.41
85	126.23	380.27	124.86	379.02	125.99	379.88	-0.24	-0.39
86	126.81	415.46	124.86	415.50	126.54	415.71	-0.27	0.25
87	127.12	433.43	124.86	433.52	126.82	433.16	-0.30	-0.27
88	127.69	465.65	124.86	467.97	127.35	465.98	-0.34	0.34
89	127.99	482.00	124.86	484.86	127.62	481.78	-0.37	-0.22
90	158.20	26.39	163.62	23.14	158.40	26.66	0.20	0.27
91	158.85	42.94	163.62	40.03	159.04	42.42	0.18	-0.51
92	160.03	74.85	163.62	74.48	160.24	75.17	0.22	0.31
93	160.63	92.73	163.62	92.50	160.83	92.57	0.20	-0.16
94	161.72	127.80	163.62	128.98	161.92	128.28	0.19	0.48
95	162.27	147.26	163.62	147.91	162.43	147.03	0.16	-0.23
96	163.19	184.81	163.62	185.87	163.34	184.98	0.15	0.17
97	163.63	205.25	163.62	205.38	163.75	204.62	0.12	-0.62
98	164.32	243.42	163.62	244.14	164.45	243.78	0.13	0.36
99	164.63	263.88	163.62	263.86	164.75	263.74	0.12	-0.14
100	165.07	302.60	163.62	302.62	165.21	302.91	0.13	0.31
101	165.24	322.84	163.62	322.13	165.37	322.56	0.14	-0.28
102	165.42	360.20	163.62	360.09	165.58	360.54	0.16	0.34

103	165.45	379.69	163.62	379.02	165.62	379.30	0.17	-0.39
104	165.40	414.86	163.62	415.50	165.59	415.06	0.19	0.20
105	165.33	432.72	163.62	433.52	165.52	432.49	0.19	-0.23
106	165.09	464.99	163.62	467.97	165.28	465.29	0.18	0.30
107	164.93	481.27	163.62	484.86	165.11	481.09	0.18	-0.18
108	177.16	27.11	183.13	23.14	176.92	27.38	-0.25	0.27
109	178.06	43.61	183.13	40.03	177.79	43.09	-0.26	-0.51
110	179.64	75.47	183.13	74.48	179.44	75.73	-0.20	0.26
111	180.45	93.26	183.13	92.50	180.23	93.07	-0.22	-0.19
112	181.88	128.23	183.13	128.98	181.67	128.66	-0.21	0.43
113	182.58	147.57	183.13	147.91	182.33	147.34	-0.25	-0.23
114	183.74	184.90	183.13	185.87	183.47	185.15	-0.26	0.25
115	184.27	205.35	183.13	205.38	183.97	204.71	-0.29	-0.63
116	185.05	243.37	183.13	244.14	184.77	243.73	-0.28	0.36
117	185.37	263.78	183.13	263.86	185.08	263.61	-0.29	-0.16
118	185.77	302.33	183.13	302.62	185.50	302.65	-0.27	0.32
119	185.87	322.50	183.13	322.13	185.62	322.24	-0.26	-0.26
120	185.87	359.81	183.13	360.09	185.65	360.10	-0.23	0.29
121	185.78	379.15	183.13	379.02	185.57	378.82	-0.21	-0.33
122	185.43	414.31	183.13	415.50	185.24	414.49	-0.19	0.19
123	185.17	432.06	183.13	433.52	184.99	431.89	-0.18	-0.17
124	184.56	464.36	183.13	467.97	184.36	464.63	-0.20	0.27
125	184.18	480.55	183.13	484.86	183.97	480.41	-0.22	-0.13
126	212.81	29.24	221.09	23.14	213.00	29.56	0.19	0.32
127	214.16	45.56	221.09	40.03	214.33	45.15	0.18	-0.42
128	216.54	77.30	221.09	74.48	216.81	77.49	0.27	0.19
129	217.74	94.89	221.09	92.50	217.98	94.66	0.24	-0.23
130	219.82	129.55	221.09	128.98	220.08	129.89	0.26	0.34
131	220.81	148.55	221.09	147.91	221.02	148.37	0.21	-0.18
132	222.41	185.30	221.09	185.87	222.60	185.78	0.20	0.47
133	223.11	205.75	221.09	205.38	223.26	205.13	0.15	-0.62
134	224.08	243.38	221.09	244.14	224.24	243.73	0.16	0.35
135	224.42	263.65	221.09	263.86	224.58	263.40	0.16	-0.25
136	224.72	301.71	221.09	302.62	224.91	302.03	0.20	0.32
137	224.69	321.67	221.09	322.13	224.92	321.42	0.23	-0.25
138	224.33	358.82	221.09	360.09	224.61	358.94	0.28	0.12
139	223.97	377.70	221.09	379.02	224.29	377.50	0.32	-0.20
140	223.03	412.82	221.09	415.50	223.39	412.90	0.36	0.09
141	222.42	430.28	221.09	433.52	222.80	430.18	0.38	-0.10
142	221.05	462.63	221.09	467.97	221.39	462.76	0.34	0.13
143	220.26	478.58	221.09	484.86	220.58	478.48	0.32	-0.10
144	231.18	30.73	240.02	23.14	231.00	31.03	-0.17	0.30
145	232.72	46.92	240.02	40.03	232.56	46.54	-0.16	-0.38
146	235.47	78.57	240.02	74.48	235.43	78.69	-0.03	0.12
147	236.84	96.05	240.02	92.50	236.78	95.76	-0.05	-0.28
148	239.21	130.50	240.02	128.98	239.19	130.75	-0.02	0.26
149	240.33	149.27	240.02	147.91	240.26	149.11	-0.07	-0.16
150	242.13	185.62	240.02	185.87	242.05	186.24	-0.08	0.62
151	242.93	206.06	240.02	205.38	242.79	205.45	-0.14	-0.61
152	243.99	243.44	240.02	244.14	243.85	243.77	-0.14	0.33
153	244.36	263.61	240.02	263.86	244.20	263.30	-0.16	-0.31
154	244.63	301.34	240.02	302.62	244.49	301.66	-0.15	0.32
155	244.57	321.15	240.02	322.13	244.43	320.92	-0.13	-0.23
156	244.07	358.18	240.02	360.09	243.95	358.20	-0.11	0.03

157	243.62	376.73	240.02	379.02	243.52	376.65	-0.10	-0.07
158	242.44	411.82	240.02	415.50	242.33	411.87	-0.12	0.06
159	241.70	429.09	240.02	433.52	241.57	429.08	-0.13	-0.02
160	240.02	461.45	240.02	467.97	239.78	461.53	-0.24	0.08
161	239.06	477.23	240.02	484.86	238.75	477.20	-0.31	-0.03

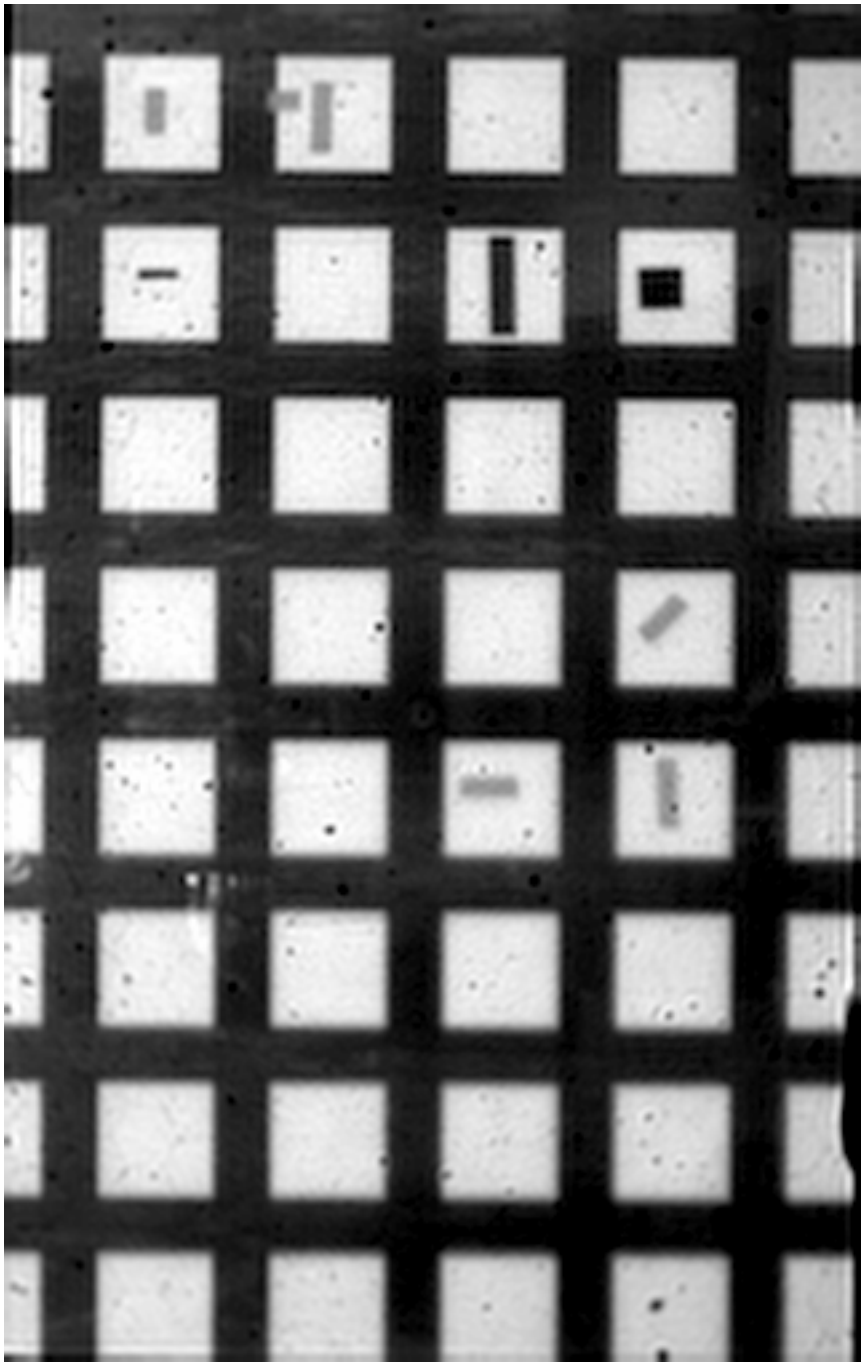

Figure 2.3-16 DISR#3 HRI Target Grid (sharpened)

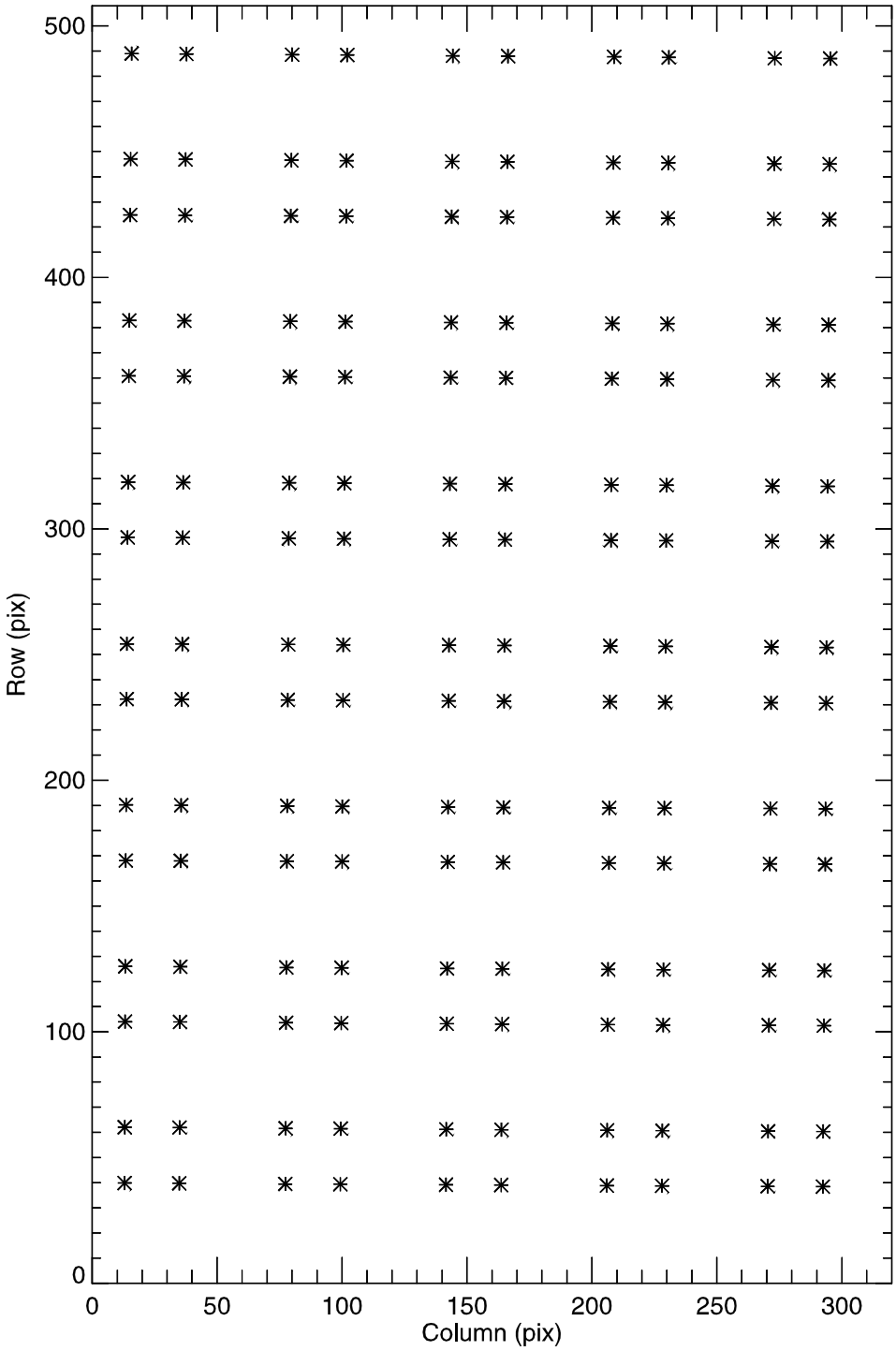

Figure 2.3-17 Location of Observed Vertices for DISR 3 HRI

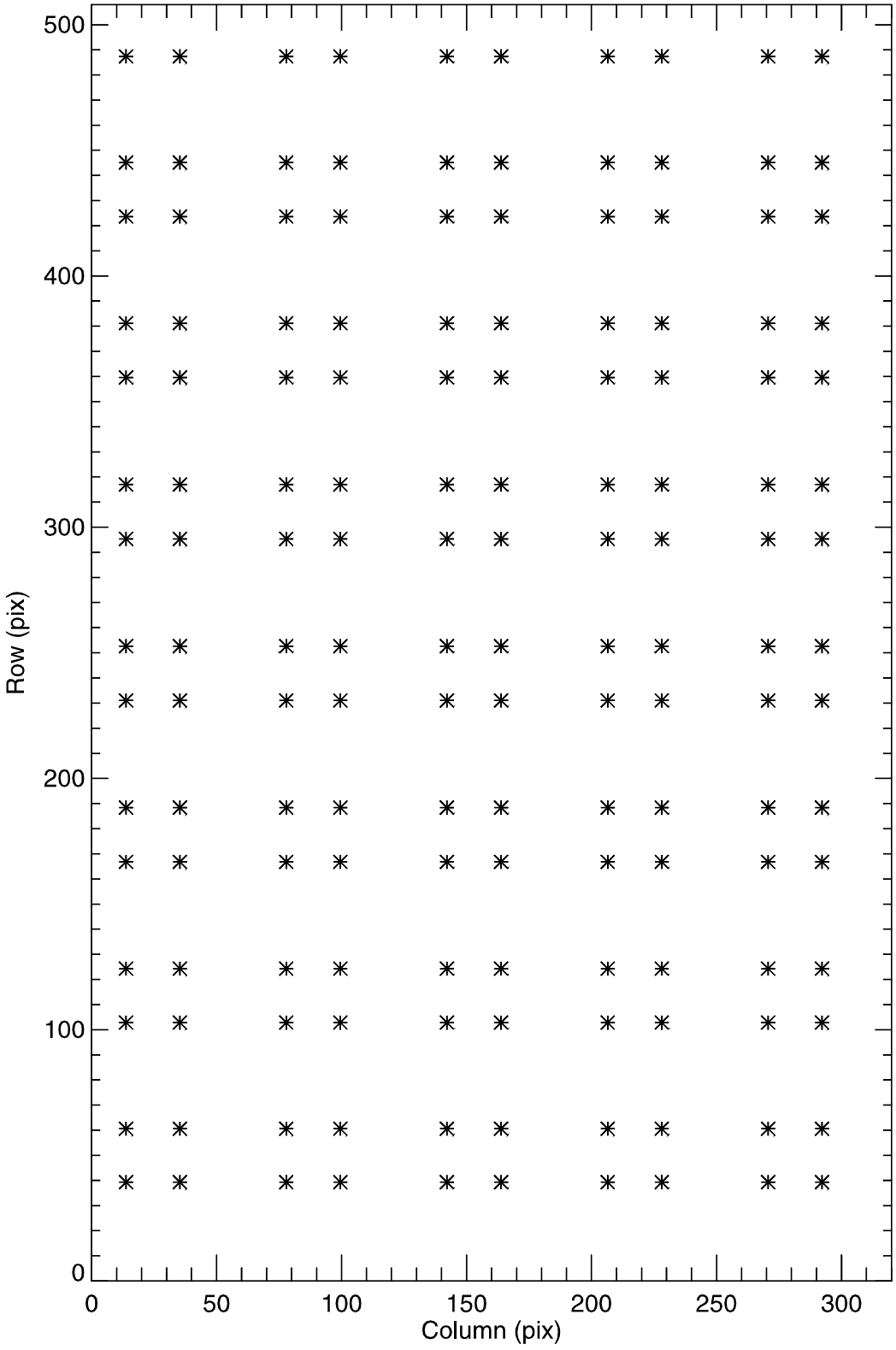

Figure 2.3-18 Location of Desired Vertices for DISR 3 HRI

Table 2.3-7

Vertex Information for DISR#3 HRI Distortion Fit

	C = Column	R=Row						
Point ID	Observed C	Observed R	Desired C	Desired R	Computed C	Computed R	C Residual	R Residual
0	12.97	39.86	13.78	39.28	13.02	40.15	0.05	0.28
1	13.04	62.05	13.78	60.61	13.10	61.69	0.06	-0.37
2	13.19	104.04	13.78	102.84	13.26	104.20	0.08	0.16
3	13.27	126.02	13.78	124.32	13.35	125.78	0.08	-0.24
4	13.46	168.11	13.78	166.80	13.55	168.36	0.09	0.25
5	13.57	190.23	13.78	188.39	13.67	189.96	0.09	-0.27
6	13.80	232.30	13.78	231.02	13.91	232.57	0.10	0.27
7	13.94	254.27	13.78	252.66	14.04	254.18	0.10	-0.08
8	14.21	296.62	13.78	295.34	14.31	296.80	0.10	0.18
9	14.37	318.58	13.78	316.98	14.47	318.41	0.10	-0.18
10	14.68	360.82	13.78	359.61	14.78	361.00	0.10	0.18
11	14.86	382.89	13.78	381.20	14.95	382.59	0.09	-0.30
12	15.22	424.78	13.78	423.68	15.31	425.13	0.09	0.35
13	15.42	447.07	13.78	445.16	15.50	446.68	0.08	-0.39
14	15.81	489.01	13.78	487.39	15.89	489.14	0.07	0.14
15	34.86	39.74	35.32	39.28	34.74	40.00	-0.12	0.27
16	34.96	61.90	35.32	60.61	34.82	61.54	-0.14	-0.35
17	35.16	103.88	35.32	102.84	35.00	104.06	-0.15	0.18
18	35.27	125.86	35.32	124.32	35.10	125.64	-0.16	-0.22
19	35.49	168.01	35.32	166.80	35.32	168.23	-0.18	0.22
20	35.62	190.07	35.32	188.39	35.43	189.83	-0.19	-0.23
21	35.87	232.19	35.32	231.02	35.68	232.45	-0.19	0.26
22	36.01	254.18	35.32	252.66	35.81	254.07	-0.20	-0.11
23	36.28	296.48	35.32	295.34	36.08	296.69	-0.20	0.21
24	36.43	318.48	35.32	316.98	36.23	318.30	-0.20	-0.18
25	36.73	360.72	35.32	359.61	36.53	360.89	-0.20	0.17
26	36.90	382.76	35.32	381.20	36.70	382.47	-0.20	-0.28
27	37.22	424.68	35.32	423.68	37.03	425.00	-0.19	0.33
28	37.40	446.91	35.32	445.16	37.21	446.55	-0.19	-0.36
29	37.75	488.86	35.32	487.39	37.57	488.98	-0.18	0.12
30	77.30	39.50	77.89	39.28	77.49	39.73	0.19	0.23
31	77.41	61.60	77.89	60.61	77.60	61.27	0.19	-0.33
32	77.61	103.59	77.89	102.84	77.81	103.79	0.20	0.20
33	77.73	125.57	77.89	124.32	77.92	125.38	0.20	-0.19
34	77.95	167.82	77.89	166.80	78.15	167.97	0.20	0.16
35	78.07	189.77	77.89	188.39	78.27	189.58	0.20	-0.19
36	78.31	231.97	77.89	231.02	78.52	232.22	0.21	0.25
37	78.44	254.01	77.89	252.66	78.65	253.84	0.21	-0.17
38	78.70	296.22	77.89	295.34	78.92	296.46	0.22	0.25
39	78.84	318.27	77.89	316.98	79.06	318.07	0.22	-0.20
40	79.11	360.50	77.89	359.61	79.35	360.66	0.23	0.16
41	79.26	382.50	77.89	381.20	79.50	382.24	0.23	-0.26
42	79.55	424.46	77.89	423.68	79.80	424.75	0.25	0.29
43	79.71	446.59	77.89	445.16	79.96	446.28	0.25	-0.31
44	80.01	488.58	77.89	487.39	80.28	488.67	0.26	0.10
45	99.33	39.38	99.51	39.28	99.15	39.59	-0.18	0.21
46	99.45	61.45	99.51	60.61	99.26	61.13	-0.19	-0.32
47	99.67	103.45	99.51	102.84	99.48	103.66	-0.19	0.21
48	99.79	125.42	99.51	124.32	99.60	125.25	-0.19	-0.18

49	100.03	167.71	99.51	166.80	99.84	167.85	-0.19	0.14
50	100.16	189.63	99.51	188.39	99.96	189.46	-0.20	-0.17
51	100.41	231.85	99.51	231.02	100.21	232.10	-0.20	0.25
52	100.54	253.91	99.51	252.66	100.35	253.72	-0.20	-0.19
53	100.81	296.08	99.51	295.34	100.61	296.35	-0.20	0.26
54	100.95	318.15	99.51	316.98	100.75	317.96	-0.20	-0.20
55	101.22	360.38	99.51	359.61	101.03	360.54	-0.19	0.16
56	101.37	382.36	99.51	381.20	101.17	382.12	-0.20	-0.24
57	101.65	424.34	99.51	423.68	101.46	424.62	-0.19	0.27
58	101.81	446.43	99.51	445.16	101.61	446.14	-0.19	-0.29
59	102.10	488.43	99.51	487.39	101.92	488.52	-0.19	0.09
60	141.60	39.16	142.18	39.28	141.83	39.34	0.23	0.19
61	141.71	61.18	142.18	60.61	141.95	60.88	0.24	-0.30
62	141.94	103.19	142.18	102.84	142.20	103.41	0.26	0.22
63	142.06	125.16	142.18	124.32	142.32	125.00	0.26	-0.16
64	142.30	167.49	142.18	166.80	142.57	167.60	0.27	0.11
65	142.43	189.37	142.18	188.39	142.70	189.22	0.27	-0.16
66	142.68	231.61	142.18	231.02	142.96	231.85	0.28	0.24
67	142.81	253.71	142.18	252.66	143.09	253.48	0.28	-0.23
68	143.07	295.83	142.18	295.34	143.35	296.11	0.28	0.27
69	143.21	317.91	142.18	316.98	143.48	317.71	0.27	-0.20
70	143.49	360.13	142.18	359.61	143.75	360.29	0.26	0.16
71	143.63	382.10	142.18	381.20	143.89	381.86	0.26	-0.23
72	143.92	424.10	142.18	423.68	144.16	424.35	0.25	0.25
73	144.07	446.12	142.18	445.16	144.30	445.86	0.23	-0.26
74	144.36	488.13	142.18	487.39	144.58	488.21	0.22	0.08
75	163.68	39.05	163.82	39.28	163.47	39.22	-0.22	0.18
76	163.82	61.04	163.82	60.61	163.59	60.76	-0.22	-0.29
77	164.07	103.06	163.82	102.84	163.85	103.29	-0.22	0.22
78	164.20	125.03	163.82	124.32	163.98	124.87	-0.22	-0.16
79	164.45	167.37	163.82	166.80	164.23	167.48	-0.22	0.11
80	164.58	189.25	163.82	188.39	164.36	189.09	-0.22	-0.16
81	164.84	231.48	163.82	231.02	164.62	231.73	-0.22	0.25
82	164.98	253.60	163.82	252.66	164.75	253.35	-0.22	-0.24
83	165.23	295.70	163.82	295.34	165.01	295.98	-0.22	0.28
84	165.37	317.78	163.82	316.98	165.15	317.59	-0.22	-0.19
85	165.63	359.99	163.82	359.61	165.41	360.16	-0.22	0.17
86	165.77	381.95	163.82	381.20	165.55	381.73	-0.22	-0.23
87	166.03	423.97	163.82	423.68	165.81	424.20	-0.22	0.24
88	166.17	445.96	163.82	445.16	165.95	445.71	-0.22	-0.24
89	166.43	487.97	163.82	487.39	166.21	488.05	-0.22	0.08
90	205.98	38.84	206.49	39.28	206.15	38.99	0.17	0.16
91	206.11	60.79	206.49	60.61	206.29	60.53	0.17	-0.26
92	206.37	102.84	206.49	102.84	206.56	103.05	0.18	0.22
93	206.51	124.79	206.49	124.32	206.69	124.64	0.18	-0.15
94	206.77	167.13	206.49	166.80	206.96	167.24	0.19	0.11
95	206.91	189.03	206.49	188.39	207.09	188.85	0.18	-0.17
96	207.18	231.23	206.49	231.02	207.36	231.49	0.18	0.26
97	207.32	253.37	206.49	252.66	207.49	253.10	0.17	-0.26
98	207.59	295.46	206.49	295.34	207.76	295.73	0.17	0.26
99	207.73	317.51	206.49	316.98	207.89	317.33	0.16	-0.18
100	208.01	359.71	206.49	359.61	208.15	359.89	0.14	0.18
101	208.15	381.68	206.49	381.20	208.28	381.45	0.13	-0.23
102	208.43	423.70	206.49	423.68	208.54	423.92	0.11	0.22

103	208.57	445.66	206.49	445.16	208.67	445.42	0.09	-0.24
104	208.85	487.66	206.49	487.39	208.92	487.74	0.07	0.07
105	228.05	38.73	228.11	39.28	227.81	38.88	-0.24	0.15
106	228.20	60.67	228.11	60.61	227.95	60.42	-0.25	-0.25
107	228.49	102.73	228.11	102.84	228.23	102.94	-0.26	0.21
108	228.64	124.68	228.11	124.32	228.37	124.53	-0.27	-0.15
109	228.92	167.00	228.11	166.80	228.64	167.12	-0.27	0.12
110	229.06	188.92	228.11	188.39	228.78	188.73	-0.28	-0.19
111	229.32	231.09	228.11	231.02	229.05	231.36	-0.27	0.28
112	229.46	253.24	228.11	252.66	229.19	252.98	-0.27	-0.26
113	229.71	295.34	228.11	295.34	229.45	295.59	-0.26	0.25
114	229.84	317.36	228.11	316.98	229.58	317.19	-0.25	-0.17
115	230.08	359.56	228.11	359.61	229.84	359.75	-0.23	0.19
116	230.20	381.53	228.11	381.20	229.97	381.31	-0.22	-0.23
117	230.42	423.55	228.11	423.68	230.23	423.77	-0.20	0.22
118	230.54	445.50	228.11	445.16	230.35	445.26	-0.18	-0.24
119	230.75	487.50	228.11	487.39	230.60	487.58	-0.15	0.08
120	270.34	38.54	270.68	39.28	270.57	38.68	0.23	0.14
121	270.50	60.44	270.68	60.61	270.72	60.21	0.23	-0.23
122	270.80	102.54	270.68	102.84	271.02	102.73	0.22	0.19
123	270.95	124.47	270.68	124.32	271.17	124.31	0.22	-0.16
124	271.24	166.74	270.68	166.80	271.46	166.89	0.22	0.15
125	271.39	188.73	270.68	188.39	271.60	188.50	0.21	-0.23
126	271.67	230.81	270.68	231.02	271.88	231.11	0.22	0.30
127	271.81	252.99	270.68	252.66	272.02	252.72	0.22	-0.27
128	272.07	295.11	270.68	295.34	272.30	295.32	0.22	0.21
129	272.21	317.06	270.68	316.98	272.43	316.91	0.22	-0.15
130	272.46	359.25	270.68	359.61	272.69	359.46	0.24	0.21
131	272.59	381.25	270.68	381.20	272.82	381.01	0.24	-0.24
132	272.83	423.25	270.68	423.68	273.08	423.46	0.25	0.21
133	272.95	445.21	270.68	445.16	273.20	444.95	0.25	-0.26
134	273.17	487.18	270.68	487.39	273.44	487.27	0.27	0.09
135	292.40	38.44	292.22	39.28	292.28	38.58	-0.11	0.14
136	292.56	60.33	292.22	60.61	292.44	60.11	-0.11	-0.21
137	292.86	102.45	292.22	102.84	292.76	102.63	-0.10	0.18
138	293.01	124.37	292.22	124.32	292.91	124.20	-0.10	-0.17
139	293.30	166.60	292.22	166.80	293.21	166.78	-0.09	0.18
140	293.46	188.64	292.22	188.39	293.36	188.38	-0.10	-0.27
141	293.74	230.66	292.22	231.02	293.65	230.98	-0.09	0.32
142	293.89	252.84	292.22	252.66	293.79	252.59	-0.10	-0.26
143	294.17	294.99	292.22	295.34	294.07	295.18	-0.10	0.19
144	294.31	316.89	292.22	316.98	294.20	316.76	-0.10	-0.13
145	294.58	359.08	292.22	359.61	294.47	359.30	-0.11	0.23
146	294.72	381.10	292.22	381.20	294.60	380.85	-0.12	-0.25
147	294.98	423.09	292.22	423.68	294.85	423.30	-0.13	0.21
148	295.11	445.06	292.22	445.16	294.98	444.79	-0.14	-0.27
149	295.37	487.01	292.22	487.39	295.22	487.11	-0.15	0.10

Having established a mapping between the set of points in Tables 2.3-2 through 2.3-7, the mapping was modeled to third order by two-dimensional polynomial transformations between the original MRI, SLI and HRI image coordinates in pixels to the new image coordinates. The coefficients of the fit (i.e., the multipliers of the *xy*-

looking terms which store the column and row positions of the image signal) rest in two matrices, one which gives the new x (column) position and one which gives the new y (row) position. They are called K_x and K_y.

The mapping is expressed mathematically as

$$x_i = \sum_{k=0}^{3}\sum_{j=0}^{3} K^X{}_{jk} x_o{}^k y_o{}^j$$

$$y_i = \sum_{k=0}^{3}\sum_{j=0}^{3} K^Y{}_{jk} x_o{}^k y_o{}^j$$

and is computed by the IDL procedure **polywarp**. It is applied to an image by the IDL procedure **poly_2d**. The original coordinates are given by x_o and y_o and the measured resulting coordinates in x_i and y_i. A concrete example of the equations applied to the DISR2 MRI *x* coordinate is shown below, where the matrix of numbers is K^X.

$$x_i = \begin{bmatrix} 1 & x_o & x_o{}^2 & x_o{}^3 \end{bmatrix} \begin{bmatrix} 0.716 & -0.0435 & 8.5\times10^{-5} & 2.8\times10^{-10} \\ 0.991 & 2.7\times10^{-4} & -5.8\times10^{-7} & 2.4\times10^{-11} \\ -9.1\times10^{-6} & 4.2\times10^{-8} & 2.8\times10^{-10} & -2.4\times10^{-13} \\ 3.7\times10^{-8} & -4.5\times10^{-10} & 1.1\times10^{-13} & 4.8\times10^{-16} \end{bmatrix} \begin{bmatrix} 1 \\ y_o \\ y_o{}^2 \\ y_o{}^3 \end{bmatrix}$$

The description of the mapping in the notes of the IDL polywarp and poly_2d procedures is somewhat counter-intuitive in that the pixel coordinates for the desired geometry (x_o and y_o) are treated as the inputs and those for the observed geometry (x_i and y_i) are treated as the outputs, with the implication that the derived matrices will transform from an undistorted system to a distorted. In fact, the exact opposite happens, which is what is needed. Inputting the observed coordinates for the vertices of the raw MRI, SLI and HRI images into the x_i and y_i slots of the polywarp and poly_2d arguments and providing the desired (unwarped) coordinates for the vertices into the x_o and y_o slots produces an *un*distortion model, a transformation that converts a raw image where orthogonal lines are curved into barrel distortion into an undistorted image.

The conceptual solution to this paradox lies in the fact that a warping *is* going on: the distorted pixel coordinates of the original raw image are being elevated to the status of the correct coordinates, and the resultant image being displayed in a way where this coordinate system has primacy, i.e., where it is completely orthogonal. This has the effect of unwarping or undistorting the image.

2.4 Geometry Calibration

The purpose of the calibration of absolute geometry of the 6 near-IR imaging systems of DISR 2 and 3 was to assign each pixel in a sharpened and undistorted image to a single point on the object sphere.

The data contributing to the geometry calibrations was acquired on May 6, 1996 for DISR 2 and August 9, 1996 for DISR 3. The essence of the calibration was to image point sources at infinity, sources that were precisely located on the object sphere. Their images were injected into the imagers' field of views by back-illuminated pinholes at the focus of the laboratory collimator system. The DISR Sensor Head was mounted on the altitude-azimuth mount and the window of the imager being calibrated was placed at the

center of rotation. The camera was oriented into several dozen positions, enough to sample all regions of the relevant imager's field of view. The resulting composite for each imager is shown in Figs. 2.4-1 through 2.4-6.

Tables 2.4-1 through 2.4-6 show the relevant data for each system. Columns 2 and 3 provide the laboratory altitude-azimuth mount azimuth and elevation as each point was imaged. The illumination pattern of a single "point" is generally smeared out over a group of more than two dozen pixels. Identifying the maximum and the nearest two dozen surrounding the maximum, the centroid of each point in pixels was computed. These are provide in Columns 4 and 5 as the column and row number of each point. The "observed" points are the laboratory azimuth and elevation from Columns 2 and 3 were converted to a spherical coordinate system of clockwise azimuth and nadir angle, where the azimuth coordinate was centered at the center of the image.

The conversion between laboratory azimuth and elevation and the image-based spherical system is given by

$$N = 180.0 - \cos^{-1}\left(\sin e \cos a\right)$$

$$\phi = \sin^{-1}\left(\frac{-\sin a}{\sqrt{1-\sin^2 e \cos^2 a}}\right)$$

where e and a are laboratory elevation and azimuth. The results are given in Columns 6 and 7 as x_i (clockwise azimuth) and y_i (nadir angle). The x_i and y_i correspond to the IDL polywarp formalism explained in the previous section.

The indexed counterclockwise azimuth and nadir angles are given in Columns 8 and 9 as x_o and y_o and are calculated by assuming the pixel sizes and zenith angles for image centers assumed in Table 2.3-1 and computing the counterclockwise azimuth and nadir angles, assuming the azimuth angles at image center are 0.0. The expressions for the conversion are given by

$$\phi = \tan^{-1}\left(\frac{\tan\alpha}{\sin\theta_0 - \tan\beta\sin\theta_0}\right)$$

$$N = 180.0 - \tan^{-1}\left(\frac{\sqrt{\tan^2\alpha + \left(\sin\theta_0 - \tan\beta\cos\theta_0\right)^2}}{\cos\theta_0 + \tan\beta\sin\theta_0}\right)$$

where α and β are the dihedral angles associated with the pixel columns and rows and θ_0 is the central zenith angle. The angles α and β are given by

$$\alpha = m\left(c - \frac{n_c}{2}\right)$$

$$\beta = m\left(r - \frac{n_r}{2}\right)$$

where m is the pixel size from Table 2.3-1 and n_c and n_r are the number of columns and rows in each image (also from Table 2.3-1). The specific column and row c and r of each point are given in Columns 2 and 3.

Just as for the distortion maps, the model derived to match the indexed azimuth and nadir angles (x_o and y_o) to the observed angles (x_i and y_i) are third-order two-dimensional polynomial transformations constructed by the IDL procedure polywarp and

applied by the procedure poly_2d. The coefficients of the relevant matrices are given in Table 2.2-3.

The observed points x_n and y_n computed by the model are given in Columns 10 and 11 and should be compared with x_i and y_i in Columns 6 and 7. The residuals between the observed points and resulting synthetic observed points are given in Columns 12 and 13. The root-mean-square residual for azimuth and nadir angle for each imager is listed in Table 2.5-1.

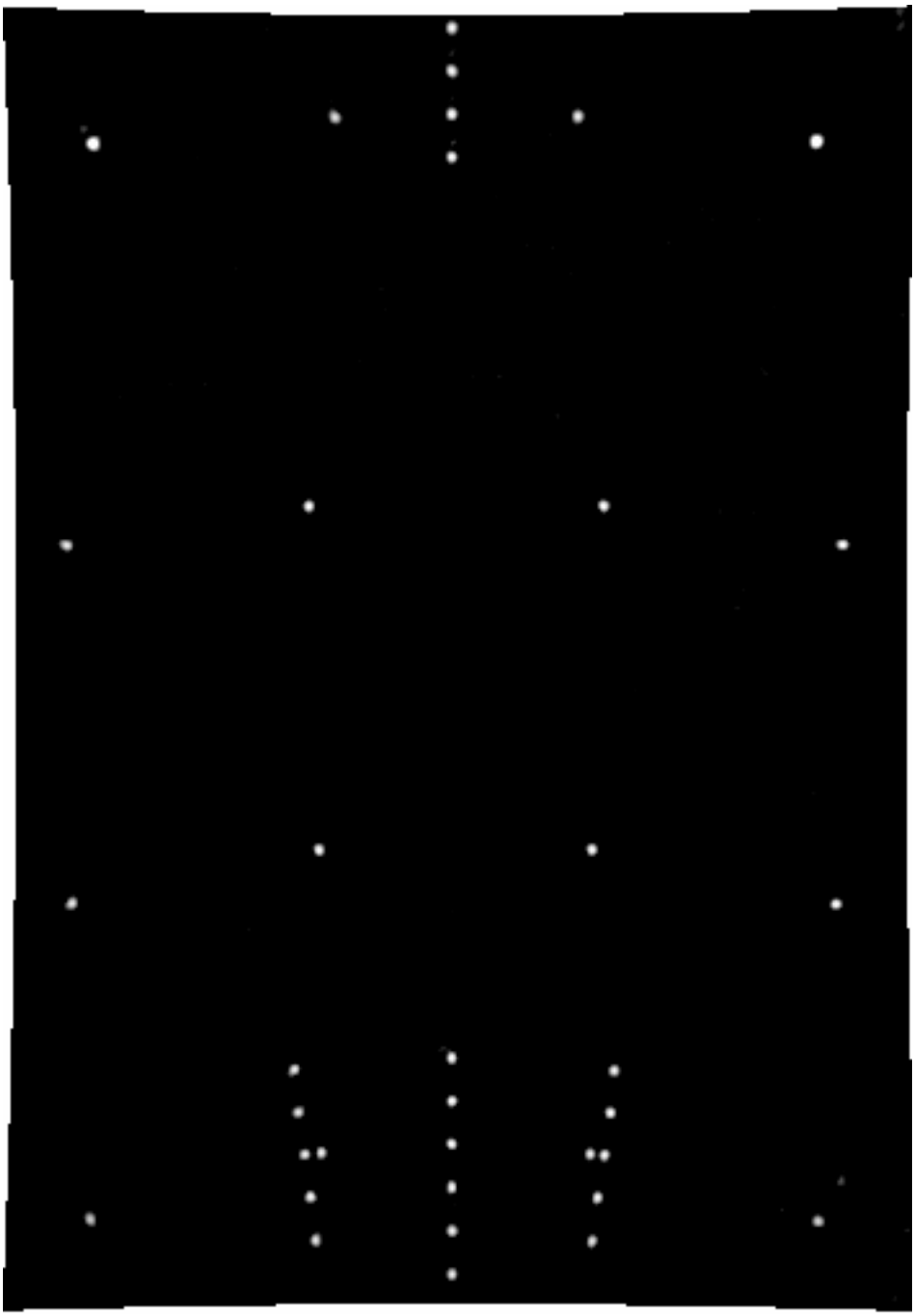

Figure 2.4-1 DISR#2 MRI Geometry Calibration Bright Point Composite Image

Table 2.4-1
Point Information for DISR 2 MRI Absolute Location Fit

line	cal_az	cal_el	col	row	x_i	y_i	x_o	y_o	x_n	y_n	xresid	y_resid
0	0	-68	173.8732	99.0505	0	22	-0.4121	22.1736	0.1358	21.9756	0.1358	-0.0244
1	0	-69	173.8799	82.2321	0	21	-0.4284	21.1645	0.1192	20.9723	0.1192	-0.0277
2	0	-70	173.8828	65.7089	0	20	-0.4465	20.1731	0.1018	19.988	0.1018	-0.012
3	0	-71	173.9029	48.8376	0	19	-0.4638	19.1609	0.0796	18.9846	0.0796	-0.0154
4	0	-72	173.9391	31.9262	0	18	-0.48	18.1462	0.0526	17.9803	0.0526	-0.0197
5	0	-73	173.9408	15.0427	0	17	-0.5049	17.1332	0.0307	16.9795	0.0307	-0.0205
6	-3.73	-68.3	112.7295	94.6148	9.9995	22.003	-10.0234	22.2137	9.891	22.0048	-0.1085	0.0018
7	-3.57	-69.29	114.1555	78.0096	10.0052	21.0021	-10.2075	21.2172	10.0237	21.0121	0.0185	0.01
8	-3.4	-70.28	116.8015	61.6681	9.9858	19.9995	-10.1989	20.2243	9.9497	20.0239	-0.0361	0.0244
9	-3.24	-71.27	118.9501	44.9859	9.9981	18.9983	-10.2896	19.2161	9.9629	19.0214	-0.0352	0.0231
10	-3.08	-72.26	121.0005	28.203	10.0149	17.9969	-10.4144	18.2027	9.9966	18.0147	-0.0183	0.0177
11	3.73	-68.3	236.9379	94.0603	-9.9995	22.003	9.5206	22.1498	-9.9182	21.9917	0.0813	-0.0113
12	3.57	-69.29	235.5519	77.7609	-10.0052	21.0021	9.6835	21.1711	-10.0787	21.0182	-0.0735	0.0161
13	3.4	-70.28	232.9494	61.1265	-9.9858	19.9995	9.6669	20.1613	-10.0519	20.0129	-0.0661	0.0134
14	3.24	-71.27	230.4169	44.7402	-9.9981	18.9983	9.6579	19.1666	-10.0263	19.023	-0.0282	0.0247
15	3.08	-72.26	228.1572	27.9557	-10.0149	17.9969	9.7133	18.1508	-10.057	18.0124	-0.0421	0.0155
16	8.3	-46.63	315.3425	455.1982	-11.9936	44.0016	11.7435	44.1474	-11.9895	43.9992	0.0041	-0.0024
17	2.78	-46.07	222.8437	465.0479	-4.0037	44	3.8937	44.1991	-4.0932	44.0055	-0.0895	0.0055
18	-2.78	-46.07	128.2845	464.8581	4.0037	44	-4.0517	44.1932	3.919	44.0036	-0.0847	0.0036
19	8.3	-46.63	315.3658	455.288	-11.9936	44.0016	11.7441	44.1529	-11.9902	44.0047	0.0034	0.0031
20	9.1	-56.06	325.3377	298.6641	-16.0073	34.9971	15.6222	35.1586	-16.0014	34.9929	0.0059	-0.0042
21	3.44	-55.15	232.8657	313.7224	-6.0051	34.998	5.8634	35.1948	-5.9865	35.0015	0.0186	0.0035
22	-3.44	-55.15	118.3063	313.7001	6.0051	34.998	-6.0528	35.2028	5.9704	35.0074	-0.0347	0.0094
23	-9.1	-56.06	24.0925	298.2975	16.0073	34.9971	-15.9929	35.1857	16.011	34.9917	0.0037	-0.0054
24	8.93	-64.42	323.0425	158.8522	-19.9977	26.9945	19.4991	27.1099	-20.0017	26.9995	-0.004	0.005
25	3.17	-63.17	228.2193	180.0418	-6.9957	27.0028	6.7818	27.1957	-7.075	27.0073	-0.0793	0.0045
26	-3.17	-63.17	122.3837	180.0756	6.9957	27.0028	-7.0931	27.2132	7.0522	26.997	0.0565	-0.0058
27	-8.93	-64.42	26.2768	159.1668	19.9977	26.9945	-19.9462	27.1946	19.9963	27.0008	-0.0014	0.0063
28	8.31	-71.74	315.9376	35.7708	-24.9932	20.0032	24.4328	20.0456	-24.9497	19.9903	0.0435	-0.0129
29	3.07	-70.23	227.5781	61.8476	-9.0099	19.9975	8.7437	20.1566	-9.1253	20.004	-0.1154	0.0065
30	-3.07	-70.23	123.1584	62.1098	9.0099	19.9975	-9.1193	20.1916	8.8528	19.9921	-0.1571	-0.0054
31	-8.31	-71.74	33.7168	36.7339	24.9932	20.0032	-24.8948	20.1763	25.0384	19.9892	0.0452	-0.014
32	0	-44	173.8593	499.6712	0	46	-0.2123	46.2105	0.0033	46.0031	0.0033	0.0031
33	0	-45	173.8447	482.8487	0	45	-0.2181	45.2011	0.0291	44.9994	0.0291	-0.0006
34	0	-46	173.806	465.9901	0	44	-0.2262	44.1896	0.0556	43.9923	0.0556	-0.0077
35	0	-47	173.8183	449.2585	0	43	-0.2302	43.1858	0.076	42.9916	0.076	-0.0084
36	-8.3	-46.63	34.7301	454.727	11.9936	44.0016	-11.9948	44.1455	12.0029	44.0027	0.0093	0.0011

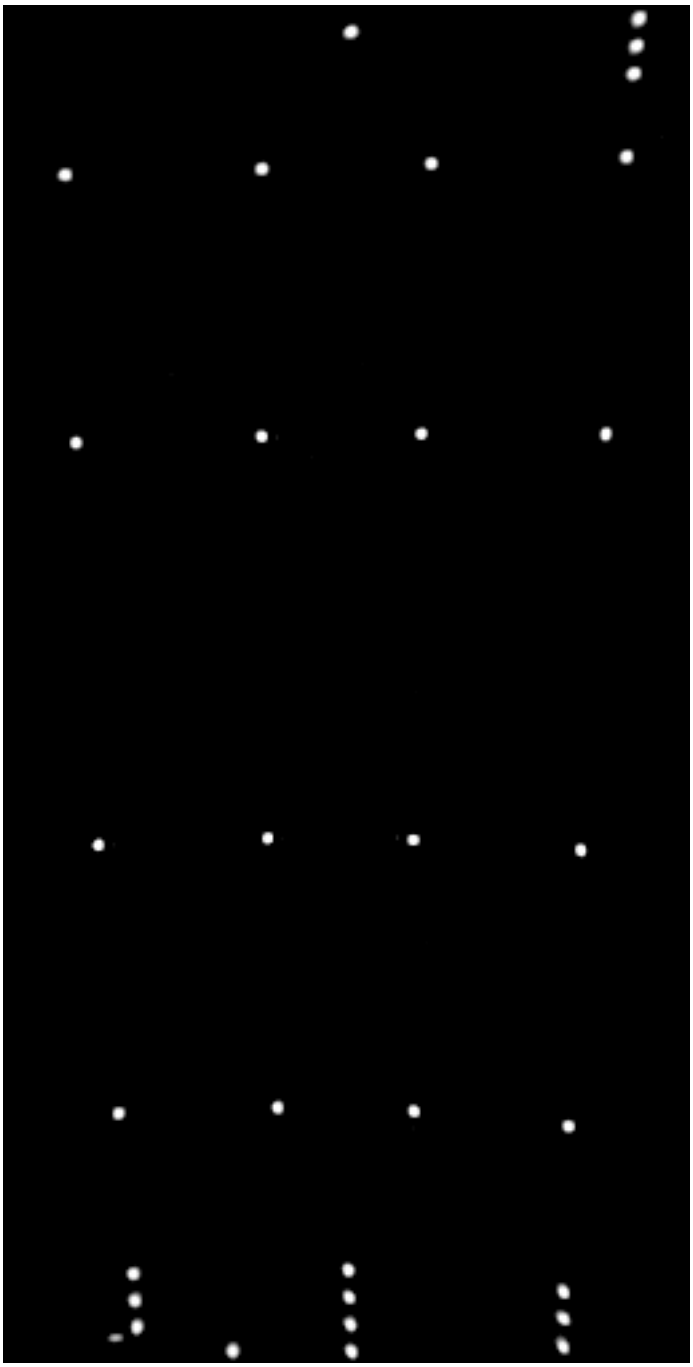

Figure 2.4-2 DISR 2 SLI Geometry Calibration Bright Point Composite Image

Table 2.4-2

Point Information for DISR 2 SLI Absolute Location Fit

line	cal_az	cal_el	col	row	x_i	y_i	x_o	y_o	x_n	y_n	xresid	y_resid
0	0	-41	128.8229	34.2458	0	49	0.0399	48.5746	0.0151	48.996	0.0151	-0.004
1	0	-42	129.0983	24.1056	0	48	0.0746	47.5606	0.0122	47.9947	0.0122	-0.0053
2	0	-43	129.3305	13.9742	0	47	0.1045	46.5475	0.0155	46.9943	0.0155	-0.0057

3	0	-44	129.9156	3.8477	0	46	0.1797	45.5349	-0.0243	45.995	-0.0243	-0.005
4	-7.53	-41.43	48.228	32.9523	9.9986	49.0046	-9.9007	48.8716	9.9719	48.9441	-0.0267	-0.0605
5	-7.41	-42.44	48.8919	22.8706	9.9946	47.996	-9.9019	47.8652	10.0049	47.9212	0.0103	-0.0747
6	-7.3	-43.44	49.7631	12.9818	10.0056	46.9982	-9.8769	46.8752	10.0115	46.9158	0.0059	-0.0824
7	7.53	-41.43	209.1895	26.0535	-9.9986	49.0046	10.0087	48.1923	-9.9717	48.9857	0.0269	-0.0189
8	7.41	-42.44	209.1602	16.0848	-9.9946	47.996	10.0895	47.2039	-10.0005	48.0252	-0.0059	0.0293
9	7.3	-43.44	209.1121	5.3533	-10.0056	46.9982	10.1774	46.1395	-10.0283	46.9914	-0.0227	-0.0068
10	8.18	-35.41	211.1155	88.1819	-10.0024	55.0034	9.7614	54.3648	-9.9804	55.0006	0.022	-0.0028
11	2.46	-35.04	153.2805	93.8822	-3.0037	54.997	2.9229	54.5735	-3.029	54.9805	-0.0253	-0.0165
12	-2.46	-35.04	102.2648	95.1597	3.0037	54.997	-3.0915	54.7053	2.9764	55.0022	-0.0273	0.0052
13	-8.18	-35.41	42.8315	93.0205	10.0024	55.0034	-10.0844	54.873	9.9964	55.006	-0.006	0.0026
14	9.05	-25.34	215.732	191.733	-9.9949	64.9973	9.605	64.6378	-10.0186	65.0016	-0.0237	0.0043
15	2.72	-25.03	153.0577	195.593	-3.0014	65.0001	2.7014	64.7339	-2.9805	65.0069	0.0209	0.0068
16	-2.72	-25.03	98.5828	196.1687	3.0014	65.0001	-3.2896	64.8033	3.0245	65.0149	0.0231	0.0148
17	-9.05	-25.34	35.2019	193.6412	9.9949	64.9973	-10.2581	64.8709	10.0095	65.0434	0.0146	0.0461
18	9.85	-10.15	225.0851	347.7345	-10.0035	80.0012	9.6798	80.064	-10.0075	80.0016	-0.004	0.0004
19	2.95	-10.01	156.0445	347.7962	-2.9955	80.0034	2.7605	79.9411	-3.0039	80.0072	-0.0084	0.0038
20	-2.95	-10.01	96.3257	346.8146	2.9955	80.0034	-3.2264	79.8473	2.9806	79.9977	-0.0149	-0.0057
21	-9.85	-10.15	26.8575	344.3359	10.0035	80.0012	-10.2069	79.7449	9.9943	79.9658	-0.0092	-0.0354
22	10	0	232.8836	451.7332	-10	90	9.8385	90.3186	-9.9784	90.0003	0.0216	0.0003
23	3	0	159.8093	449.0475	-3	90	2.9525	90.0547	-2.9967	89.9906	0.0033	-0.0094
24	-3	0	96.249	447.0421	3	90	-3.0451	89.8544	3.0073	89.9927	0.0073	-0.0073
25	-10	0	22.8708	444.8398	10	90	-9.9976	89.6395	10.003	90.014	0.003	0.014
26	9.96	5.08	237.7451	503.7632	-9.9985	95.0032	9.9736	95.4433	-10.0154	95.0155	-0.0169	0.0123
27	9.98	4.06	236.7078	493.1216	-10.0046	93.9985	9.9446	94.3954	-10.0058	93.9887	-0.0012	-0.0098
28	9.99	3.05	235.7304	482.8695	-10.0039	93.0037	9.9173	93.3857	-9.9976	92.9999	0.0063	-0.0038
29	-8	-44.2	41.7687	8.7342	11.0914	46.3398	-10.9111	46.5455	11.0968	46.4737	0.0054	0.1339
30	-4	-44.2	85.2708	3.9844	5.571	45.9356	-5.4798	45.6796	5.5769	46.0056	0.0059	0.07
31	0	5	129.8659	498.5912	0	95	0.1249	95.0091	-0.0024	95.0102	-0.0024	0.0102

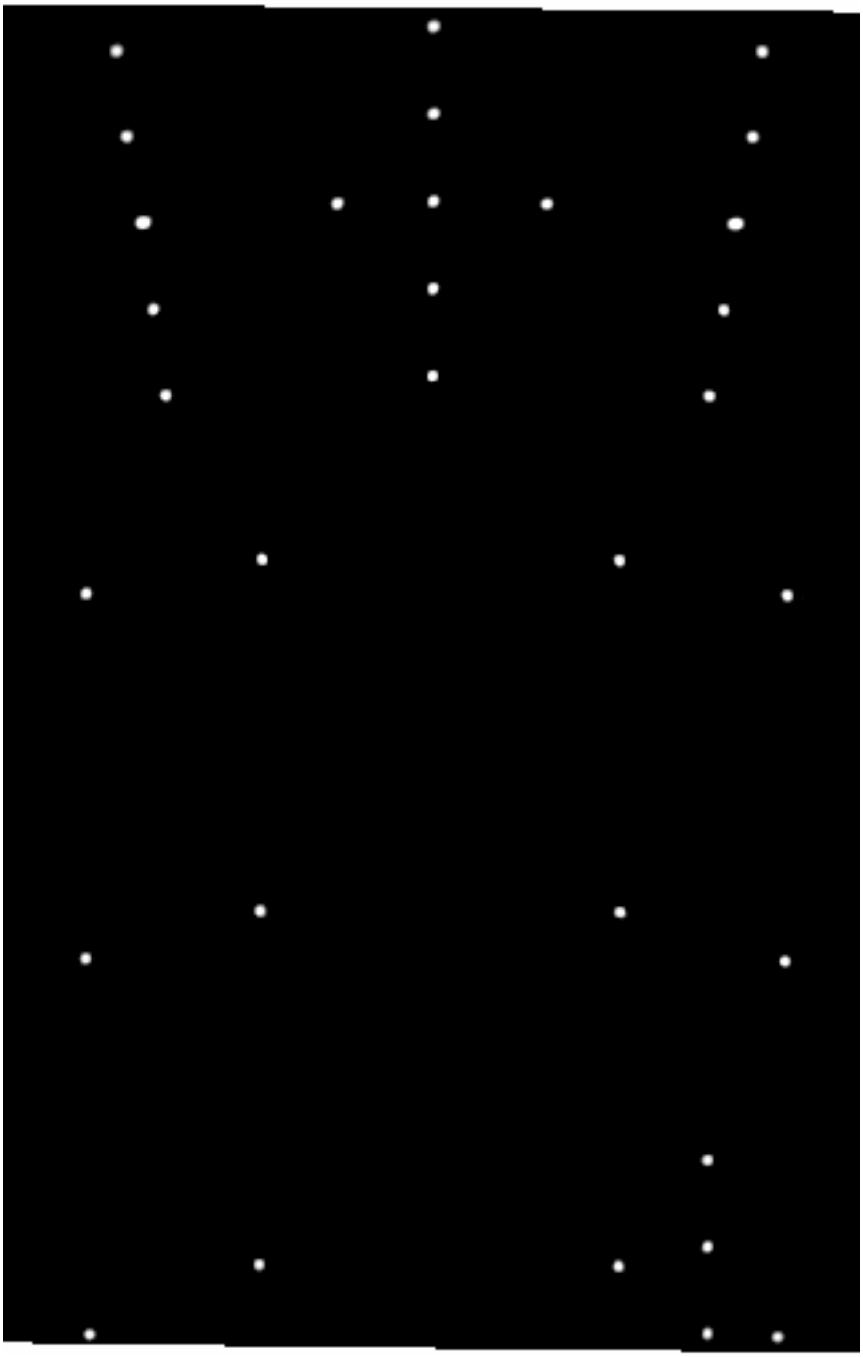

Figure 2.4-3 DISR 2 HRI Geometry Calibration Bright Point Composite Image

Table 2.4-3

Point Information for DISR 2 HRI Absolute Location Fit

line	cal_az	cal_el	col	row	x_i	y_i	x_o	y_o	x_n	y_n	xresid	y_resid
0	3.4	-70.28	273.0043	423.2419	-9.9858	19.9995	10.3921	19.4934	-9.8893	19.9903	0.0965	-0.0092
1	1.2	-70.03	203.2394	430.9192	-3.5097	20.0046	3.9332	19.4761	-3.6764	20.0039	-0.1667	-0.0007
2	-1.2	-70.03	124.8073	431.051	3.5097	20.0046	-3.2854	19.4674	3.2838	19.9948	-0.2259	-0.0098

3	-3.4	-70.28	52.9553	423.9641	9.9858	19.9995	-9.9311	19.49	9.836	20.0013	-0.1498	0.0018
4	4.09	-74.52	293.2812	284.1229	-14.9979	15.9984	15.5255	15.4506	-14.9264	15.9838	0.0715	-0.0146
5	2.06	-74.13	230.5174	297.2361	-7.4934	15.9997	8.1112	15.4637	-7.4932	15.9959	0.0002	-0.0038
6	-2.06	-74.13	96.5422	297.7012	7.4934	15.9997	-7.4101	15.4536	7.3437	15.9991	-0.1497	-0.0006
7	-4.09	-74.52	30.752	284.932	14.9979	15.9984	-15.1626	15.4507	14.9959	15.9784	-0.002	-0.02
8	4.08	-78.7	292.4067	147.0639	-20.003	12.005	20.9185	11.4261	-19.9995	12.0045	0.0035	-0.0005
9	2.07	-78.18	230.7032	165.3409	-10.007	11.9974	10.9373	11.4567	-10.0065	12.0042	0.0005	0.0068
10	-2.07	-78.18	95.9148	165.9093	10.007	11.9974	-10.065	11.443	10.0141	12.0045	0.0071	0.0071
11	-4.08	-78.7	30.6029	148.1301	20.003	12.005	-20.5693	11.4354	20.008	12.0086	0.005	0.0036
12	3.99	-83.06	289.7889	6.2016	-29.9965	8.0004	31.9463	7.4744	-29.8615	8.004	0.135	0.0036
13	2.06	-82.27	230.1078	32.7666	-14.9717	7.9982	16.5826	7.4783	-14.7401	7.9999	0.2316	0.0017
14	-2.06	-82.27	95.3974	33.3132	14.9717	7.9982	-15.5281	7.4567	14.9306	7.9945	-0.0411	-0.0037
15	-3.99	-83.06	31.9652	7.1532	29.9965	8.0004	-31.6798	7.4874	30.0108	8.0009	0.0143	0.0005
16	0	-68	160.8631	497.3835	0	22	0.0303	21.4808	0.0282	22.0086	0.0282	0.0086
17	0	-69	160.8713	464.7743	0	21	0.0325	20.4765	0.0455	21.0055	0.0455	0.0055
18	0	-70	160.7636	431.946	0	20	0.0243	19.4653	0.0815	19.9963	0.0815	-0.0037
19	0	-71	160.6327	399.2119	0	19	0.0129	18.4571	0.128	18.9906	0.128	-0.0094
20	0	-72	160.4581	366.4062	0	18	-0.0043	17.4467	0.1864	17.9831	0.1864	-0.0169
21	-3.73	-68.3	42.0356	488.1948	9.9995	22.003	-9.9243	21.4906	10.0116	21.9904	0.0121	-0.0126
22	-3.57	-69.29	45.915	456.179	10.0052	21.0021	-10.0632	20.5014	10.0438	21.0059	0.0386	0.0038
23	-3.4	-70.28	51.0587	423.914	9.9858	19.9995	-10.1038	19.498	10.0097	20.0088	0.0239	0.0093
24	-3.24	-71.27	55.8668	391.4109	9.9981	18.9983	-10.1832	18.4887	10.0436	19.0067	0.0455	0.0084
25	-3.08	-72.26	60.4036	359.1645	10.0149	17.9969	-10.2932	17.4884	10.1321	18.0141	0.1172	0.0172
26	3.73	-68.3	283.9307	488.0068	-9.9995	22.003	10.3355	21.5098	-9.9443	21.9906	0.0552	-0.0124
27	3.57	-69.29	280.26	455.988	-10.0052	21.0021	10.512	20.5222	-10.0534	21.0089	-0.0482	0.0068
28	3.4	-70.28	274.9318	423.6396	-9.9858	19.9995	10.56	19.5156	-10.0526	20.011	-0.0668	0.0115
29	3.24	-71.27	269.489	391.1222	-9.9981	18.9983	10.6037	18.5029	-10.0554	19.0075	-0.0573	0.0092
30	3.08	-72.26	264.1176	358.9026	-10.0149	17.9969	10.6527	17.4992	-10.0678	18.0129	-0.0529	0.016
31	3.08	-83	263.3215	7.6696	-23.8225	7.6446	26.2056	7.1234	-24.0116	7.6399	-0.1891	-0.0047
32	3.08	-82	263.3635	39.9887	-21.1378	8.5688	23.1375	8.0316	-21.2206	8.564	-0.0828	-0.0048
33	3.08	-81	263.3439	72.5948	-18.9814	9.5083	20.6637	8.9656	-19.0763	9.5129	-0.0949	0.0046

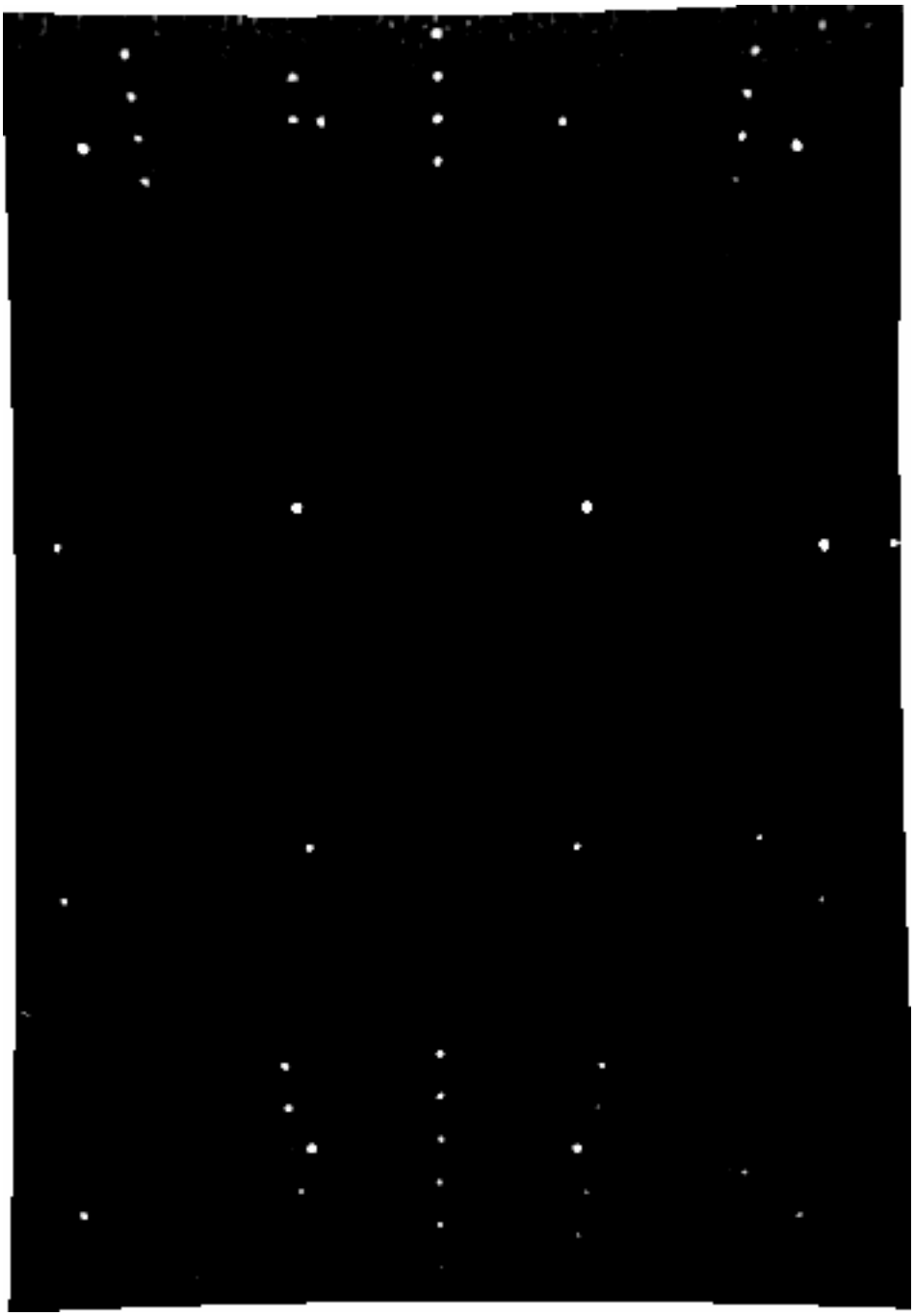

Figure 2.4-4 DISR 3 MRI Geometry Calibration Bright Point Composite Image

Table 2.4-4

Point Information for DISR 3 MRI Absolute Location Fit

line	cal_az	cal_el	col	row	x_i	y_i	x_o	y_o	x_n	y_n	xresid	y_resid
0	0	-68	169.6838	100.165	0	22	-1.0664	22.2434	0.1447	21.9835	0.1447	-0.0165
1	0	-69	169.6859	83.5225	0	21	-1.1103	21.245	0.1393	20.9817	0.1393	-0.0183
2	0	-70	169.7386	66.8424	0	20	-1.1499	20.2443	0.1235	19.979	0.1235	-0.021
3	0	-71	169.7397	49.9966	0	19	-1.2033	19.2337	0.115	18.9679	0.115	-0.0321
4	0	-72	169.7503	33.3116	0	18	-1.2599	18.2328	0.1035	17.968	0.1035	-0.032
5	0	-73	169.8088	16.848	0	17	-1.3126	17.2452	0.0819	16.9831	0.0819	-0.0169
6	-3.73	-68.3	109.0635	95.4031	9.9995	22.003	-10.569	22.2962	9.9146	22.0101	-0.0849	0.0071
7	-3.57	-69.29	110.8201	79.021	10.0052	21.0021	-10.7159	21.3103	9.9965	21.0202	-0.0087	0.0181
8	-3.4	-70.28	113.1006	62.3875	9.9858	19.9995	-10.7981	20.3041	9.9988	20.0112	0.013	0.0117
9	-3.24	-71.27	115.6862	46.0976	9.9981	18.9983	-10.8281	19.3149	9.9365	19.0203	-0.0616	0.022
10	-3.08	-72.26	117.8077	29.8279	10.0149	17.9969	-10.949	18.3316	9.9553	18.0365	-0.0596	0.0396
11	3.73	-68.3	232.161	95.4768	-9.9995	22.003	8.7489	22.1922	-9.9163	21.9938	0.0832	-0.0092
12	3.57	-69.29	230.8061	79.1704	-10.0052	21.0021	8.8852	21.2125	-10.0747	21.0139	-0.0695	0.0118
13	3.4	-70.28	228.1991	62.7982	-9.9858	19.9995	8.8264	20.2183	-10.033	20.0194	-0.0472	0.0199
14	3.24	-71.27	225.9523	46.1906	-9.9981	18.9983	8.8344	19.213	-10.0582	19.0162	-0.0601	0.0179
15	3.08	-72.26	223.7919	29.7655	-10.0149	17.9969	8.8577	18.2191	-10.0971	18.0264	-0.0822	0.0295
16	8.3	-46.63	308.1146	453.2779	-11.9936	44.0016	11.1677	43.9738	-11.9348	43.9567	0.0588	-0.0449
17	2.78	-46.07	217.0392	463.1001	-4.0037	44	3.4153	44.0669	-4.0598	43.9932	-0.0561	-0.0068
18	-2.78	-46.07	123.152	462.8583	4.0037	44	-4.4939	44.0897	3.9038	44.0084	-0.0999	0.0084
19	8.3	-46.63	308.1397	453.8037	-11.9936	44.0016	11.1622	44.0048	-11.9288	43.9877	0.0648	-0.0139
20	9.1	-56.06	318.7089	298.2591	-16.0073	34.9971	14.9573	35.0485	-16.0085	34.9991	-0.0012	0.002
21	3.44	-55.15	226.7403	312.8784	-6.0051	34.998	5.2355	35.1153	-6.0096	34.9974	-0.0045	-0.0006
22	-3.44	-55.15	113.8696	312.6257	6.0051	34.998	-6.5225	35.1625	6.0013	34.9981	-0.0038	0.0001
23	-8.31	-71.74	31.0919	37.195	24.9932	20.0032	-25.2723	20.2635	25.0238	19.9953	0.0306	-0.0079
24	8.31	-71.74	310.3185	37.7519	-24.9932	20.0032	23.4252	20.0292	-24.9618	19.9965	0.0314	-0.0067
25	3.07	-70.23	222.8212	63.3504	-9.0099	19.9975	7.9076	20.2079	-9.0983	20.0013	-0.0884	0.0038
26	-3.07	-70.23	119.29	63.0547	9.0099	19.9975	-9.7457	20.2826	8.9161	19.9909	-0.0938	-0.0066
27	-8.3	-46.63	30.9491	452.1719	11.9936	44.0016	-12.3504	44.0304	11.9373	43.9664	-0.0563	-0.0352
28	9.1	-56.06	318.7068	298.2287	-16.0073	34.9971	14.9578	35.0467	-16.0091	34.9972	-0.0018	0.0001
29	3.44	-55.15	226.7207	312.8483	-6.0051	34.998	5.2337	35.1135	-6.0078	34.9956	-0.0027	-0.0024
30	-3.44	-55.15	113.8524	312.5976	6.0051	34.998	-6.5246	35.161	6.0035	34.9965	-0.0016	-0.0015
31	-3.44	-45	111.8394	480.0388	4.8591	45.1031	-5.3241	45.1562	4.7491	45.0821	-0.11	-0.021
32	-3.44	-46	112.0406	463.7608	4.9457	44.1068	-5.421	44.184	4.842	44.1045	-0.1037	-0.0023
33	9.1	-56.06	318.6888	298.2512	-16.0073	34.9971	14.9555	35.0477	-16.0067	34.9982	0.0006	0.0011
34	3.44	-55.15	226.7091	312.8742	-6.0051	34.998	5.2323	35.115	-6.0063	34.9971	-0.0012	-0.0009
35	-3.44	-55.15	113.8408	312.6193	6.0051	34.998	-6.5256	35.1623	6.0045	34.9979	-0.0006	-0.0001
36	-9.1	-56.06	20.7378	297.1546	16.0073	34.9971	-16.3605	35.1663	16.0335	34.9965	0.0262	-0.0006
37	8.93	-64.42	317.5248	160.0051	-19.9977	26.9945	18.7657	27.0783	-20.0066	26.9977	-0.0089	0.0032
38	3.17	-63.17	222.8054	180.6324	-6.9957	27.0028	6.0693	27.1987	-7.0454	27.0087	-0.0497	0.0059
39	-3.17	-63.17	118.6003	180.2169	6.9957	27.0028	-7.5825	27.2473	7.05	26.9992	0.0543	-0.0036
40	-8.93	-64.42	23.4903	159.3338	19.9977	26.9945	-20.2856	27.2556	19.9761	27.0013	-0.0216	0.0068
41	8.31	-71.74	310.3076	37.7295	-24.9932	20.0032	23.4249	20.0277	-24.9617	19.995	0.0315	-0.0082
42	3.07	-70.23	222.8626	63.3258	-9.0099	19.9975	7.9151	20.2067	-9.1059	20.0001	-0.096	0.0026
43	-3.07	-70.23	119.6747	63.0693	9.0099	19.9975	-9.6808	20.2799	8.8492	19.9883	-0.1607	-0.0092

44	-8.31	-71.74	31.0643	37.1627	24.9932	20.0032	-25.2787	20.2624	25.0305	19.9942	0.0373	-0.009
45	0	-44	168.0405	497.1564	0	46	-0.6823	46.0614	0.0684	45.9811	0.0684	-0.0189
46	0	-44.999	168.1268	480.714	0	45.001	-0.6898	45.0749	0.0725	44.9943	0.0725	-0.0067
47	0	-46	168.1987	464.0941	0	44	-0.6988	44.0778	0.0791	43.9953	0.0791	-0.0047
48	0	-47	168.2731	447.7045	0	43	-0.7078	43.0945	0.0864	43.0088	0.0864	0.0088
49	-8.3	-46.63	30.8747	452.243	11.9936	44.0016	-12.3555	44.0352	11.9427	43.9713	-0.0509	-0.0303
50	-7.18	-44.44	46.9716	489.1903	10.0062	45.999	-10.5001	46.065	10.0641	46.0157	0.0579	0.0167
51	-7.05	-45.44	49.6935	472.8254	9.996	44.9982	-10.4973	45.0831	10.0383	45.0245	0.0423	0.0263
52	-6.93	-46.439	51.921	456.1902	10.0027	43.9994	-10.5379	44.0883	10.0637	44.0199	0.061	0.0205
53	-6.8	-47.44	54.7907	439.8388	9.9985	42.9971	-10.5198	43.1046	10.0346	43.0258	0.0361	0.0287
54	7.18	-44.44	291.9113	490.7425	-10.0062	45.999	9.3471	46.0573	-10.0515	46.0199	-0.0453	0.0209
55	7.05	-45.44	289.1129	473.9658	-9.996	44.9982	9.3192	45.0486	-10.0306	45.0126	-0.0346	0.0144
56	6.93	-46.439	286.8018	457.2849	-10.0027	43.9994	9.3282	44.0482	-10.0494	44.0121	-0.0467	0.0127
57	6.8	-47.44	284.0685	440.9361	-9.9985	42.9971	9.296	43.0639	-10.028	43.0259	-0.0295	0.0288

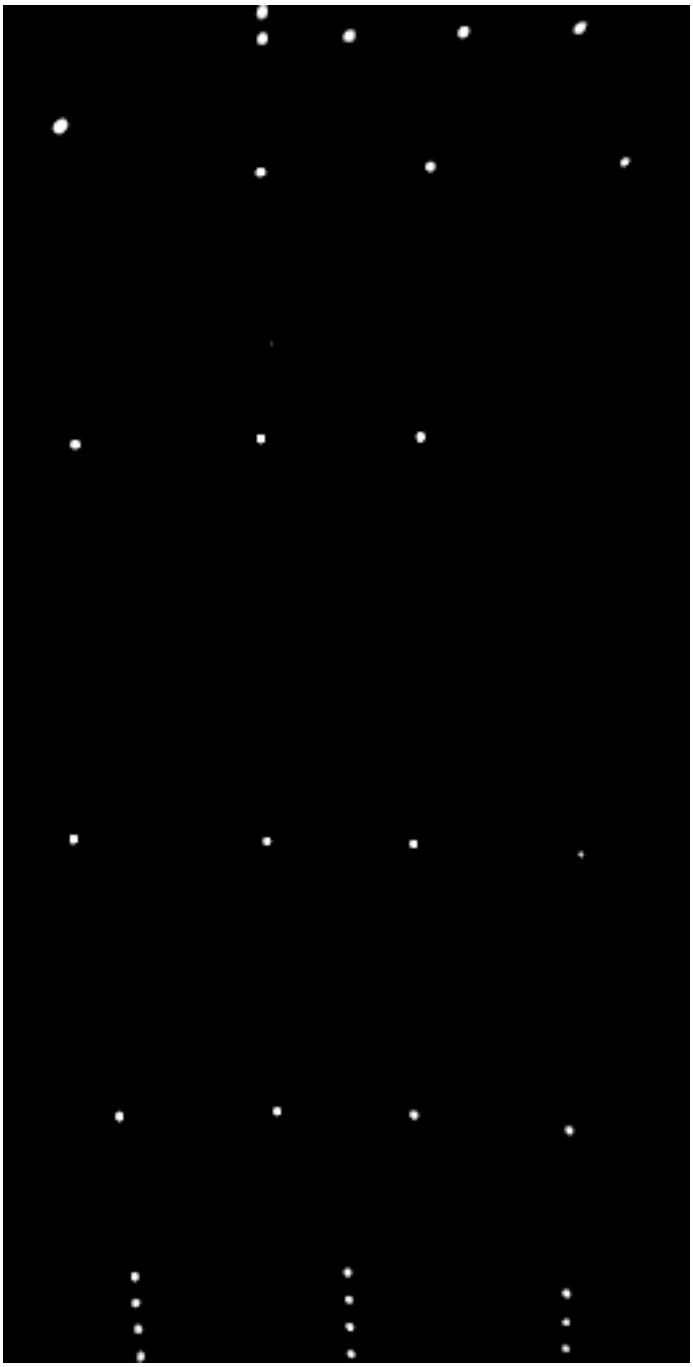

Figure 2.4-5 DISR 3 SLI Geometry Calibration Bright Point Composite Image

Table 2.4-5

Point Information for DISR 3 SLI Absolute Location Fit

line	cal_az	cal_el	col	row	x_i	y_i	x_o	y_o	x_n	y_n	xresid	y_resid
0	0	-41	128.4253	33.2868	0	49	-0.0092	48.4787	0.0448	49.0108	0.0448	0.0108
1	0	-42	128.948	23.1042	0	48	0.0559	47.4604	0.0122	48.0013	0.0122	0.0013
2	0	-43	129.2843	12.9379	0	47	0.0987	46.4438	0.0032	46.9924	0.0032	-0.0076
3	0	-44	129.7982	2.9398	0	46	0.1649	45.4441	-0.028	45.9999	-0.028	-0.0001
4	-7.53	-41.43	48.851	31.8856	9.9986	49.0046	-9.833	48.7593	9.9408	48.9905	-0.0578	-0.0141
5	-7.41	-42.44	49.2074	21.9629	9.9946	47.996	-9.8704	47.7718	10.0125	48.0001	0.0179	0.0042
6	-7.3	-43.44	50.1846	11.9607	10.0056	46.9982	-9.833	46.7694	10.0089	46.999	0.0033	0.0008
7	-7.18	-44.44	50.9546	2.0601	10.0062	45.999	-9.8215	45.7789	10.0327	46.0083	0.0265	0.0093
8	7.53	-41.43	210.2068	25.3284	-9.9986	49.0046	10.1401	48.1315	-9.9879	49.0013	0.0107	-0.0033
9	7.41	-42.44	210.0955	14.9517	-9.9946	47.996	10.2155	47.102	-9.9936	47.9886	0.001	-0.0074
10	7.3	-43.44	210.2039	4.8866	-10.0056	46.9982	10.3183	46.1055	-10.0233	47.0102	-0.0177	0.012
11	8.18	-35.41	211.4398	86.8223	-10.0024	55.0034	9.8093	54.2333	-9.9739	54.9953	0.0285	-0.0081
12	2.46	-35.04	153.2278	92.641	-3.0037	54.997	2.9194	54.4493	-3.0373	54.9987	-0.0336	0.0017
13	-2.46	-35.04	102.1465	93.9611	3.0037	54.997	-3.1082	54.586	2.9778	54.9923	-0.0259	-0.0047
14	-8.18	-35.41	43.112	91.9885	10.0024	55.0034	-10.0591	54.7682	9.9975	54.9958	-0.0049	-0.0076
15	9.05	-25.34	215.6277	190.0814	-9.9949	64.9973	9.6036	64.474	-10.0204	65.0077	-0.0255	0.0104
16	2.72	-25.03	153.0704	194.0388	-3.0014	65.0001	2.7055	64.5787	-2.9927	64.991	0.0087	-0.0091
17	-2.72	-25.03	98.3623	195.0092	3.0014	65.0001	-3.3163	64.6881	3.0263	65.0079	0.0249	0.0078
18	-10	-25.03	25.945	195.7694	11.0123	65.3758	-11.2564	65.154	11.0338	65.3861	0.0215	0.0103
19	2.95	-10.01	155.5841	346.6533	-2.9955	80.0034	2.7162	79.8265	-2.9855	80.0057	0.01	0.0023
20	-2.95	-10.01	95.9194	345.867	2.9955	80.0034	-3.269	79.7531	2.9945	80.0104	-0.001	0.007
21	-9.85	-10.15	26.7265	343.6903	10.0035	80.0012	-10.2239	79.6819	9.9849	79.9941	-0.0186	-0.0071
22	10	0	232.1162	449.6865	-10	90	9.778	90.1169	-9.9805	89.9925	0.0195	-0.0075
23	3	0	159.34	447.7899	-3	90	2.9105	89.9291	-3.0228	90.002	-0.0228	0.002
24	-3	0	96.0063	445.8297	3	90	-3.0703	89.7334	2.9952	89.9884	-0.0048	-0.0116
25	-3	6	96.6319	505.8495	3.0165	95.9918	-2.9001	95.7277	3.0219	95.9967	0.0054	0.0049
26	-3	5	96.5803	495.8878	3.0114	94.9931	-2.9233	94.7327	3.0083	94.9982	-0.0031	0.0051
27	4	5	171.8739	498.27	-4.0152	94.9878	3.9669	94.9651	-3.985	94.9833	0.0302	-0.0045
28	8	5	215.6777	499.9947	-8.0302	94.9512	7.972	95.1	-8.056	94.9601	-0.0258	0.0089
29	0	5	129.0424	496.8497	0	95	0.0496	94.835	-0.0044	94.9958	-0.0044	-0.0042
30	-10	2	21.8467	463.9483	10.006	91.9696	-9.9788	91.5215	9.9998	91.9811	-0.0062	0.0115
31	-10.15	1.849	20.1234	462.2125	10.1552	91.8201	-10.1512	91.3498	10.1675	91.8108	0.0123	-0.0093

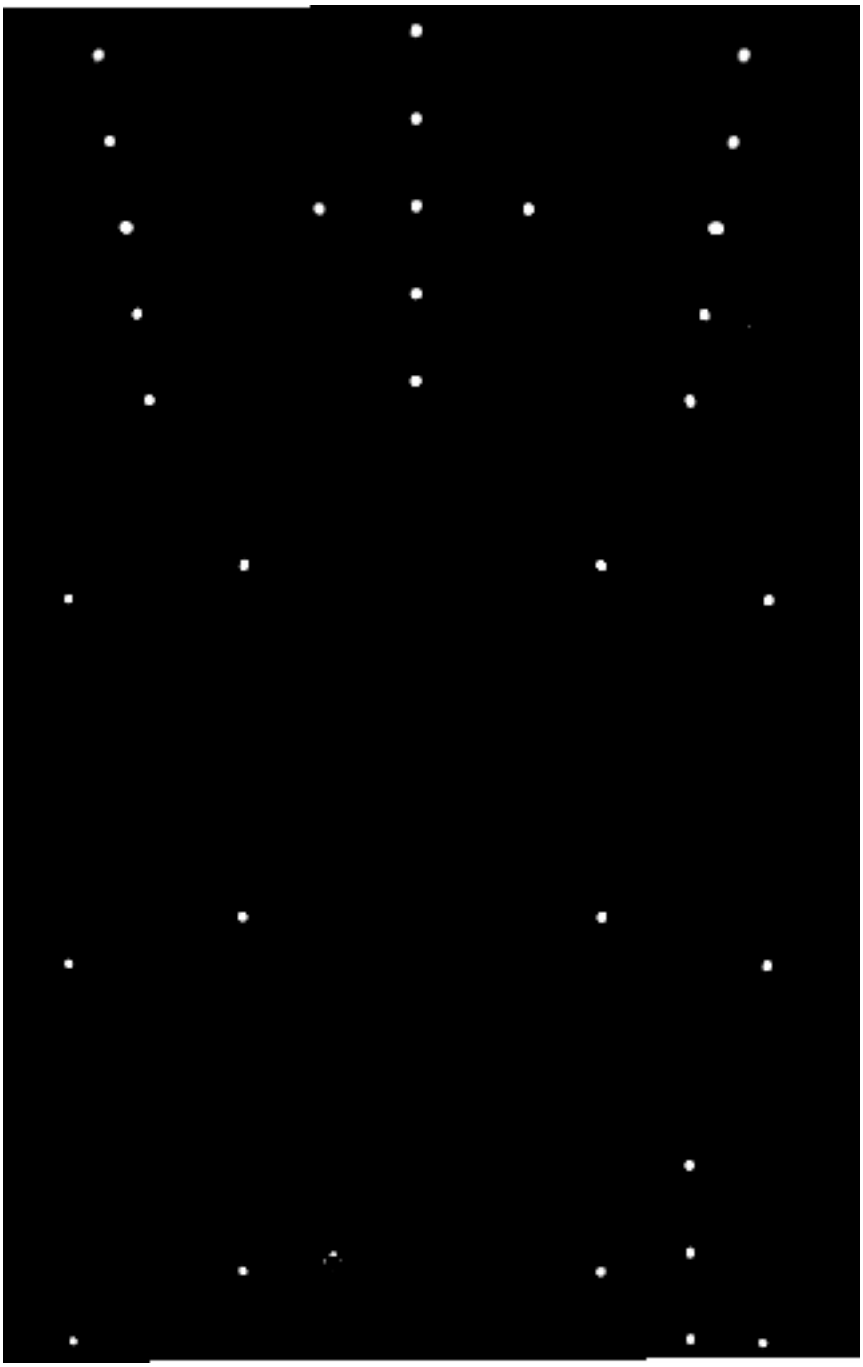

Figure 2.4-6 DISR 3 HRI Geometry Calibration Bright Point Composite Image

Table 2.4-6

Point Information for DISR 3 HRI Absolute Location Fit

line	cal_az	cal_el	col	row	x_i	y_i	x_o	y_o	x_n	y_n	xresid	y_resid
0	3.4	-70.28	265.6574	424.775	-9.9858	19.9995	9.7021	19.5028	-9.8753	19.9986	0.1105	-0.0009
1	1.2	-70.03	196.3839	431.9562	-3.5097	20.0046	3.2983	19.4955	-3.6734	19.9995	-0.1637	-0.0051
2	-1.2	-70.03	117.9797	432.0021	3.5097	20.0046	-3.9064	19.509	3.3211	19.9903	-0.1886	-0.0143
3	-3.4	-70.28	46.715	424.9585	9.9858	19.9995	-10.48	19.5521	9.8329	19.9936	-0.1529	-0.0059
4	4.09	-74.519	286.3105	285.3601	-14.997	15.9994	14.7091	15.4333	-14.9337	15.9859	0.0633	-0.0135
5	2.06	-74.13	223.5197	298.3319	-7.4934	15.9997	7.2936	15.4693	-7.4851	15.9951	0.0083	-0.0046
6	-2.06	-74.13	89.8796	298.6345	7.4934	15.9997	-8.158	15.5088	7.3708	15.9982	-0.1226	-0.0015
7	-4.09	-74.519	24.2804	285.9049	14.997	15.9994	-15.8544	15.5311	15.0102	15.9797	0.0132	-0.0197
8	4.08	-78.7	285.7664	148.2529	-20.003	12.005	19.8861	11.3906	-19.9968	12.0043	0.0062	-0.0007
9	2.07	-78.18	223.9659	166.5439	-10.007	11.9974	9.8775	11.4564	-10.0164	12.0033	-0.0094	0.0059
10	-2.07	-78.18	89.2131	166.7876	10.007	11.9974	-11.0604	11.5066	10.0109	12.0029	0.0039	0.0055
11	-4.08	-78.7	24.1916	149.069	20.003	12.005	-21.4456	11.5319	20.0008	12.0086	-0.0022	0.0036
12	3.99	-83.06	283.9912	6.9692	-29.9965	8.0004	30.683	7.4033	-29.8699	8.0071	0.1266	0.0067
13	2.06	-82.27	223.463	33.7841	-14.9717	7.9982	15.0125	7.4536	-14.7439	8.0056	0.2278	0.0074
14	-2.06	-82.27	89.2929	33.9789	14.9717	7.9982	-16.8612	7.5281	14.9306	7.994	-0.0411	-0.0042
15	-3.99	-83.06	25.9256	7.7053	29.9965	8.0004	-32.8033	7.5996	30.0119	8.0012	0.0154	0.0008
16	0	-68	154.2608	498.9758	0	22	-0.5191	21.5307	0.0231	22.0127	0.0231	0.0127
17	0	-69	154.2721	465.9307	0	21	-0.5439	20.5129	0.0444	21.0022	0.0444	0.0022
18	0	-70	154.2681	433.1337	0	20	-0.5723	19.5028	0.0738	19.9981	0.0738	-0.0019
19	0	-71	154.2288	400.2557	0	19	-0.6072	18.4902	0.1124	18.9904	0.1124	-0.0096
20	0	-71.999	154.0582	367.6858	0	18.001	-0.6591	17.4872	0.1682	17.9912	0.1682	-0.0098
21	-3.73	-68.3	35.2682	489.8702	9.9995	22.003	-10.4558	21.5755	10.0147	21.9922	0.0152	-0.0108
22	-3.57	-69.29	39.3587	457.6263	10.0052	21.0021	-10.605	20.579	10.0505	21.0074	0.0453	0.0053
23	-3.4	-70.28	44.8495	425.0905	9.9858	19.9995	-10.6462	19.566	10.0011	20.0063	0.0153	0.0068
24	-3.24	-71.27	49.7173	392.7951	9.9981	18.9983	-10.7451	18.5632	10.0309	19.014	0.0328	0.0157
25	-3.08	-72.26	54.3348	360.2796	10.0149	17.9969	-10.8831	17.5548	10.1143	18.0151	0.0994	0.0182
26	3.73	-68.3	277.0097	489.7414	-9.9995	22.003	9.7418	21.528	-9.948	21.9958	0.0515	-0.0072
27	3.57	-69.29	273.0652	457.0184	-10.0052	21.0021	9.8766	20.5168	-10.057	20.9983	-0.0518	-0.0038
28	3.4	-70.28	267.6936	424.7712	-9.9858	19.9995	9.8868	19.5127	-10.0551	20.0076	-0.0693	0.0081
29	3.24	-71.27	262.2548	392.3739	-9.9981	18.9983	9.8925	18.5033	-10.0536	19.0101	-0.0555	0.0118
30	3.08	-72.26	256.9058	360.0118	-10.0149	17.9969	9.9062	17.495	-10.0637	18.0121	-0.0488	0.0152
31	3.08	-83	257.0316	8.3546	-23.8225	7.6446	24.7275	7.0604	-24.0024	7.6342	-0.1799	-0.0104
32	3.08	-82	256.8348	40.9238	-21.1378	8.5688	21.7331	7.9827	-21.219	8.5642	-0.0812	-0.0046
33	3.08	-80.999	256.6499	73.6285	-18.9795	9.5093	19.3537	8.9261	-19.0683	9.5116	-0.0888	0.0023

2.5. Error Analysis

Table 2.5-1

Propagated and Observed Errors in Degrees and Pixels

	DISR 2			DISR 3		
	MRI	SLI	HRI	MRI	SLI	HRI
Calibration Alt-Az Mount Azimuth Error (°)	0.055	0.014	0.025	0.031	0.019	0.023

Calibration Alt-Az Mount Elevation Error (°)	0.025	0.039	0.007	0.017	0.008	0.008
Propagated Observed Azimuth Error (°)	0.068	0.016	0.104	0.069	0.022	0.097
RMS Residual Error in Observed Azimuth (°)	0.068	0.016	0.104	0.070	0.022	0.097
Propagated Observed Nadir Angle Error (°)	0.013	0.038	0.009	0.017	0.008	0.009
RMS Residual Error in Observed Nadir Angle (°)	0.013	0.038	0.009	0.018	0.008	0.009
RMS Residual Error in Observed Azimuth (pixels)	**0.252**	**0.087**	**0.440**	**0.294**	**0.130**	**0.411**
RMS Residual Error in Observed Nadir Angle (pixels)	**0.108**	**0.185**	**0.147**	**0.140**	**0.038**	**0.143**

The propagated errors listed in Table 2.5-1 were computed based on the assumption that the major source of error for the rms residuals between the modeled and observed bright points in the imager geometry calibrations was inaccuracies in the pointing of the altitude-azimuth mount itself. These errors have often observed and estimated in the laboratory as ranging from 0.01 to 0.05°. The formulae for computing these errors are given as

$$\sigma_\phi = \sqrt{\left(\frac{\cos e}{1-\sin^2 e\cos^2 a}\right)^2 \sigma_a^{\,2} + \left(\frac{\sin a\cos a\sin e}{1-\sin^2 e\cos^2 a}\right)^2 \sigma_e^{\,2}}$$

$$\sigma_N = \sqrt{\left(\frac{\sin e\sin a}{1-\sin^2 e\cos^2 a}\right)^2 \sigma_a^{\,2} + \left(\frac{\cos e\cos a}{1-\sin^2 e\cos^2 a}\right)^2 \sigma_e^{\,2}}$$

where a and e are the cal azimuth and elevation and σ_a and σ_e are the cal azimuth and elevation errors (rows 1 and 2 in Table 2.5-1), respectively.

The data in Table 2.5-1 are complete agreement with the *a priori* estimates of cal azimuth and elevation error, as can be seen by the agreement between Row 3 and Row 4 for observed clockwise azimuth and the agreement between Row 5 and Row 6 for observed nadir angle. The average cal azimuth error implied by the rms residuals in azimuth was 0.028° and the average cal elevation error implied by the rms residuals in nadir angle was 0.017° for the geometrical calibration of the 6 imagers, in total agreement with previously observed cal pointing error estimates of 0.03° for cal azimuth and 0.02° for cal elevation.

The rms residuals in clockwise azimuth and nadir angle were converted to pixel errors, a non-trivial conversion because of the varying dimensions of the pixels of each imager over the range of its field of view. The average column dihedral pixel error implied for all 6 imagers was less than 0.3 pixels and the average row dihedral pixel error was less than 0.15 pixels. A more detailed breakdown, imager by imager, confirms that the average cal azimuth and elevation errors of 0.028 and 0.017° simply translate to similar dihedral pixel angle errors of 0.028 and 0.17°.

The agreement observed between the pointing errors of the calibration test-bed and the measured discrepancies between the modeled and the observed locations of the images of the bright point sources confirm that the essential results of the calibration—the matrix coefficients of Table 2.3-1—are working as well as can be expected. In other words, no other significant sources of systematic error, e.g., mis-assignment of points, coding errors, spurious points throwing off the fit, seem to be present.

The sources of the largest discrepancies still evident in some of the pictures are the degree of the polywarp used to actually tile the image panels into the final mosaic and the presence of parallax in the near-field, especially between panels.

2.6. Sample Mosaics

Another confirmation of the validity of the absolute assignment information contained in the plots of Figures 2.2-1 and 2.2-2 and the matrix coefficients of Tables 2.2-2 and 2.2-3 is the construction of sample mosaics that demonstrate the alignment of the three imagers. Several are pictured in Figures 2.6-1 through 2.6-6. They show good alignment at the boundaries between SLI and MRI and between MRI and HRI. Some of the visible discrepancies can be explained by the parallax between the three imagers. The displacements between the three imager windows are given in Table 2.6-1, basically the same for both models of the instrument. A vertical displacement of 10 mm, such as occurs between the MRI and the HRI, leads to a nadir angle displacement of 0.03^{o} at a range of 20 m, or half an HRI pixel. Between panels, the horizontal displacements were of the order of 50 mm horizontally, translating to angular displacements of about 0.13^{o} in azimuth and somewhat less than that in nadir angle.

Table 2.6-1

Displacements between imager windows (mm). In DISR coordinate system, X is vertical, Z is along direction in which Sensor Head points and Y is perpendicular to this direction.

(mm)	X_{SH}	Y_{SH}	Z_{SH}	ΔX	ΔY	ΔZ
MRI	17.6	49.2	208.3	-28.8	-3.6	-16.2
SLI	46.4	52.8	224.5	38.3	-3.4	37.4
HRI	8.1	56.2	187.1	-9.6	7.0	-21.2

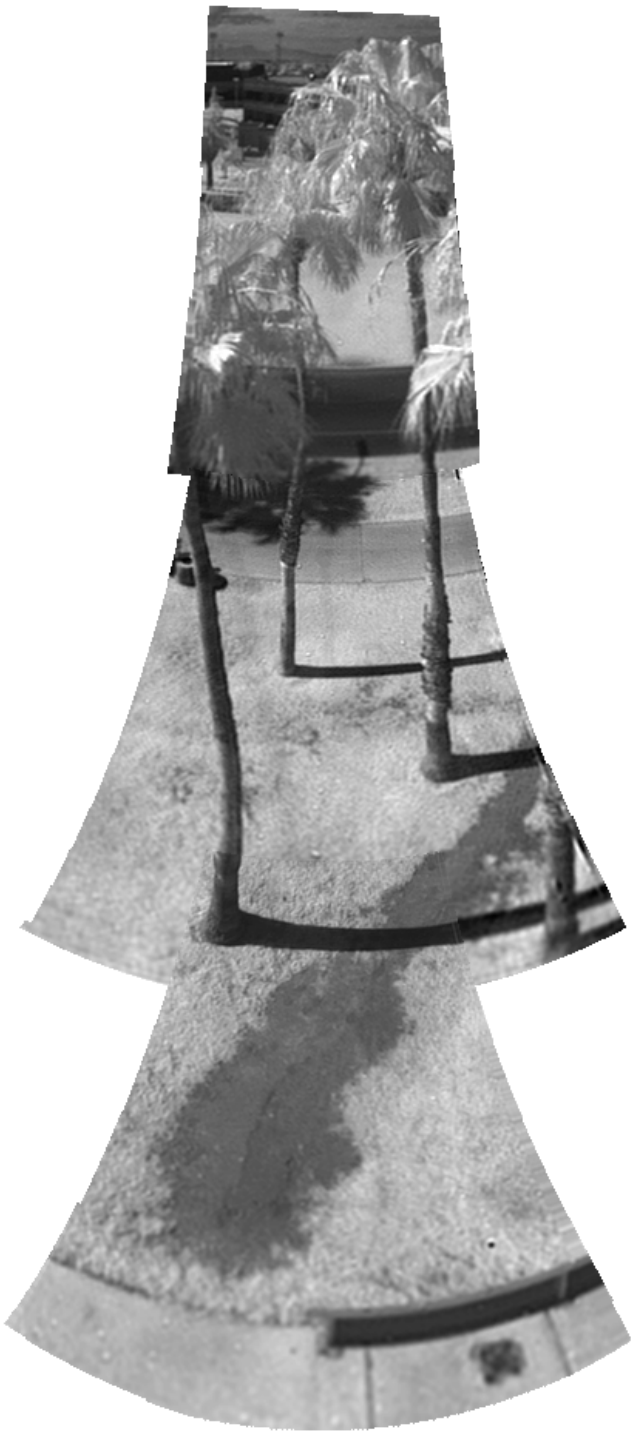

Figure 2.6-1 Detail from LPL Rooftop Manual Rotating Test, 18 July 1998, SE corner of LPL Rooftop. DISR 2 in Single Measurement Mode. Images sharpened (wc=0.7, we=1.0). Azimuth = 90.0^{o}.

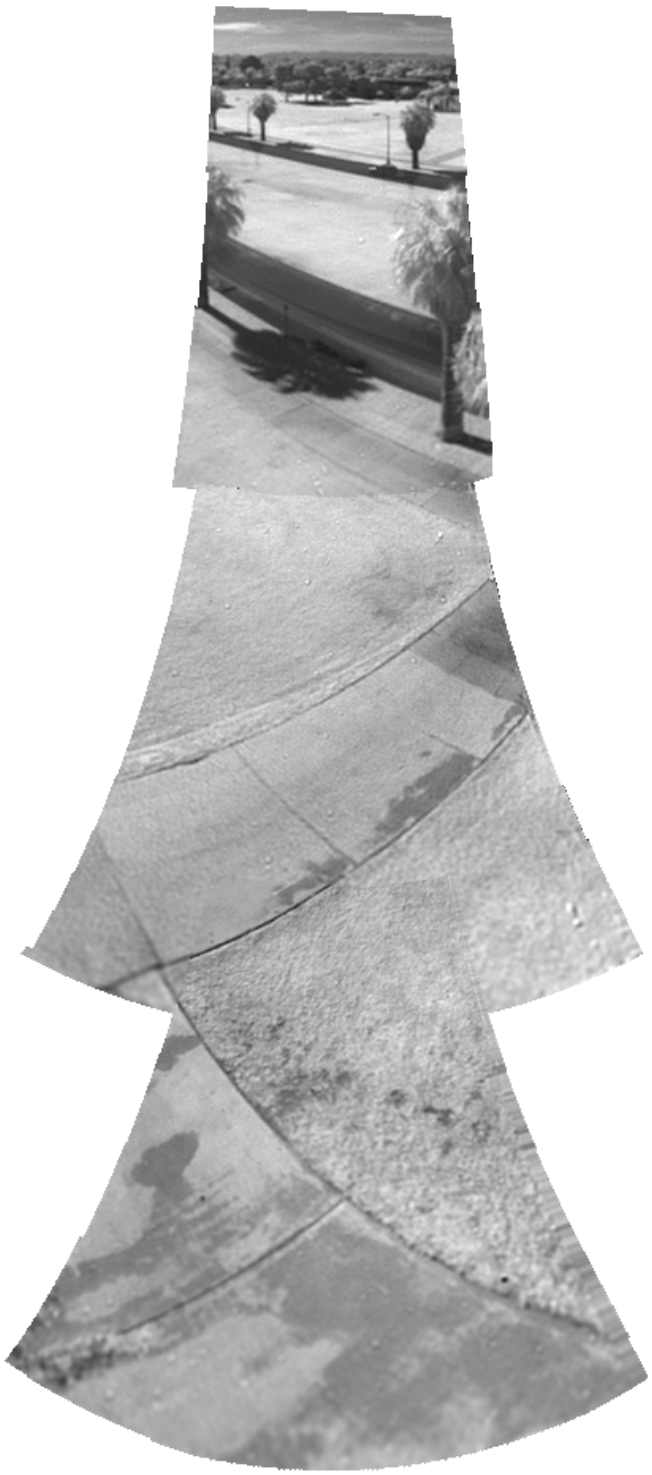

Figure 2.6-2 Detail from LPL Rooftop Manual Rotating Test, 18 July 1998, SE corner of LPL Rooftop. DISR 2 in Single Measurement Mode. Images sharpened (wc=0.7, we=1.0). Azimuth = 45.0^{o}.

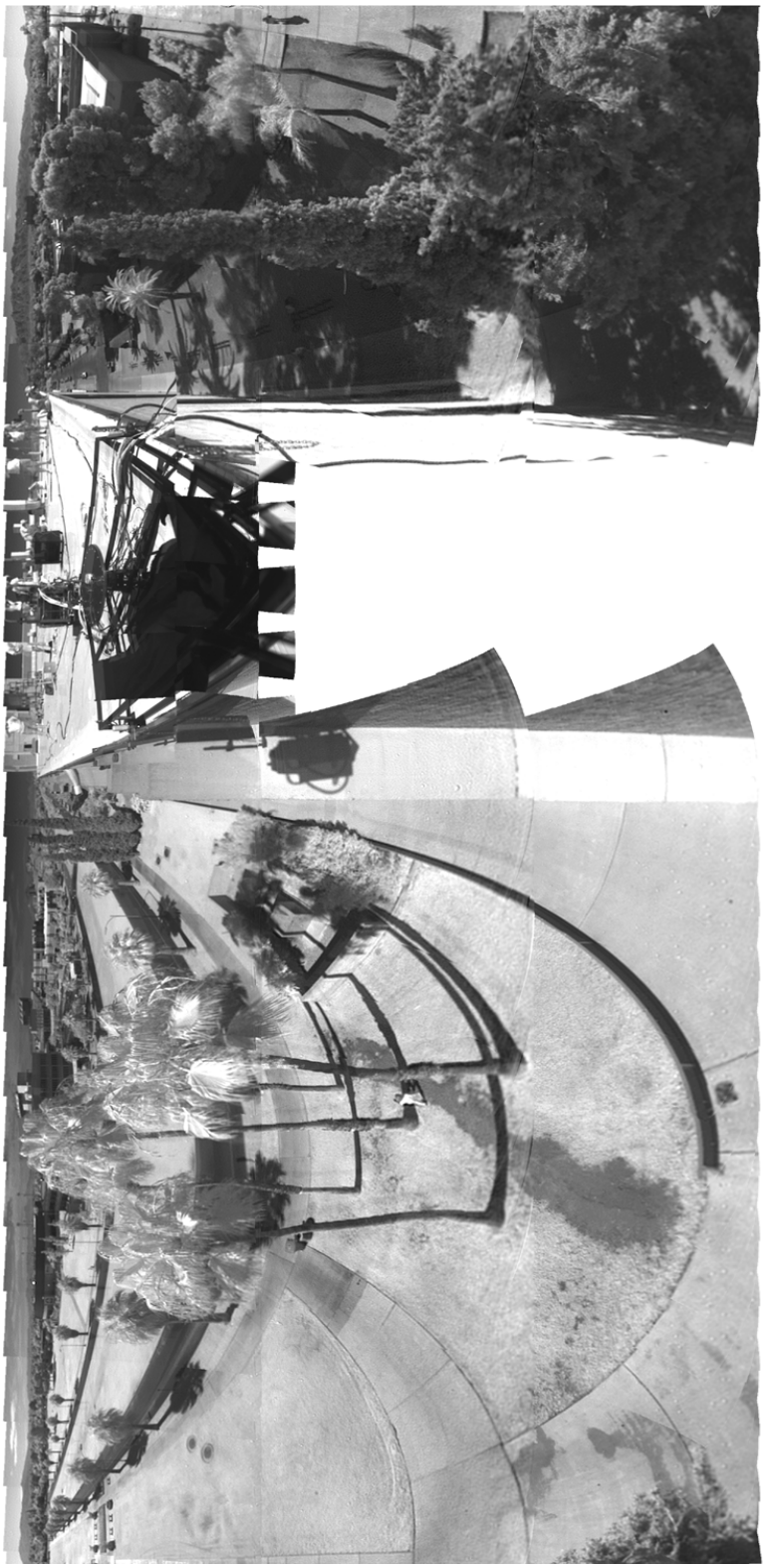

Figure 2.6-3 LPL Rooftop Manual Rotating Test, 18 July 1998, SE corner of LPL Rooftop. DISR 2 in Single Measurement Mode. Images sharpened (wc=0.7, we=1.0).

Figure 2.6-4 Mt. Bigelow Fire Observation Tower Test, 9 June 1999, Mt. Bigelow, Arizona. DISR 2 Sensor Head in Descent Mode, alternating 3-6 hardware compression ratios. Images sharpened (wc=0.7, we=1.0).

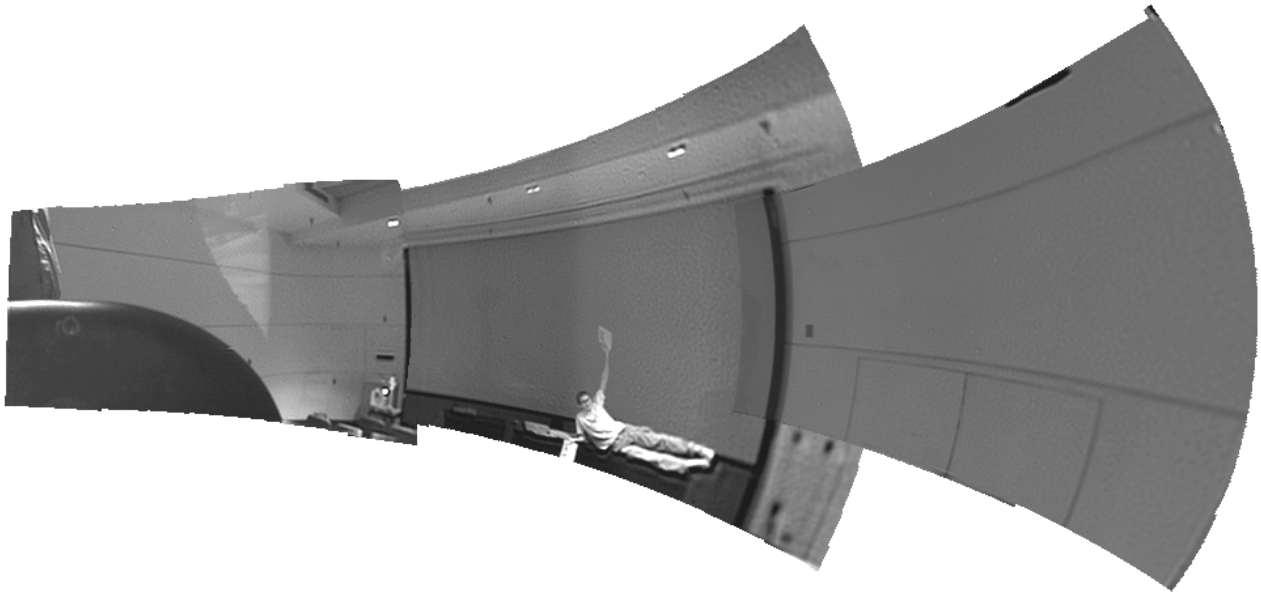

Figure 2.6-5 Imaging Cool-Down Test, 18 September 1996, LPL Auditorium. DISR 3 Sensor Head on its side in Single Measurement Mode. Mercator Projection with HRI on the right and SLI on the left. Images sharpened (wc=0.7, we=1.0).

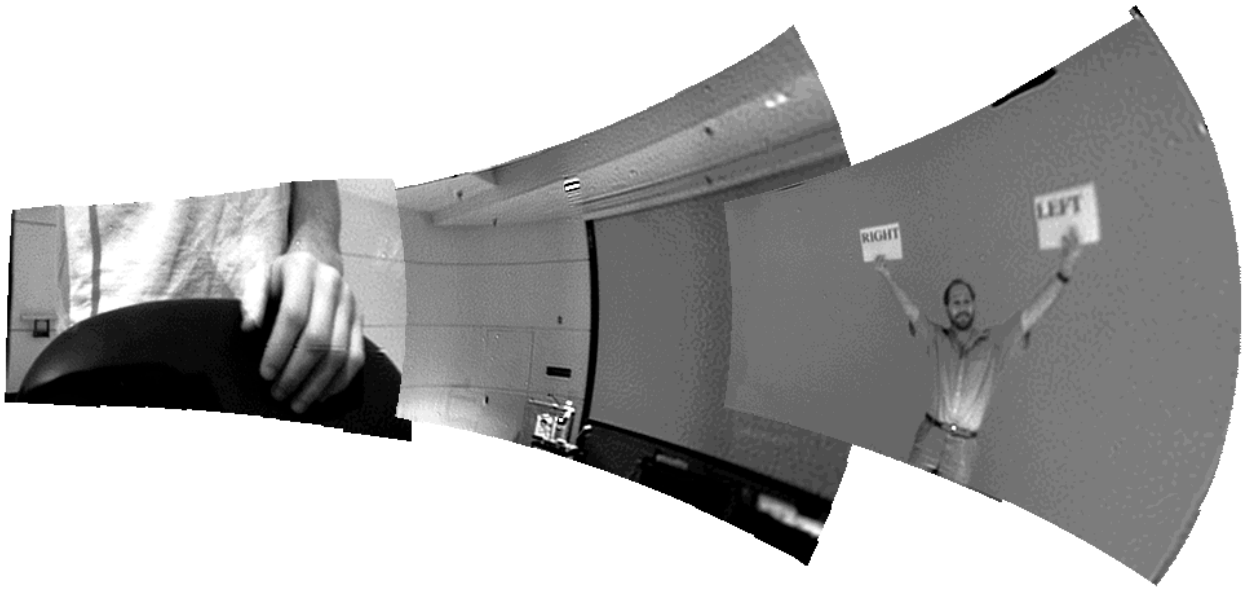

Figure 2.6-6 Imaging Cool-Down Test, 18 September 1996, LPL Auditorium. DISR 3 Sensor Head on its side in Single Measurement Mode. Mercator Projection with HRI on the right and SLI on the left. Parallax evident in overlap of MRI with SLI; otherwise alignment good. Images sharpened (wc=0.7, we=1.0).

3.0. Deconvolution of DISR Images

Erich Karkoschka May 2001

3.1. Abstract

For the DISR #2/3 instruments, a total of 28 point spread functions (PSF) sampled at quarter-pixels are available. These data were fitted by optical aberrations in order to calculate PSFs for each location across the field of views. Software was written to generate PSFs and deconvolve images.

3.2. Introduction

The information in an image can fully be evaluated only if the size and shape of the PSF is known for every location in the image. The size and shape of PSFs of DISR imagers varies across the field of views of each CCD. This is especially true for the MRIs. The best characterization of the PSFs comes from 28 laboratory measurements for the DISR #2 and #3 instruments, between two and six PSFs for each of the six cameras: HRI3, MRI3, SLI3 (the flight cameras on Cassini) and HRI2, MRI2, and SLI2. Due to the variations across the field of views, these data are not sufficient to characterize the PSF for every location without further knowledge of the spatial variations.

Lyn Doose performed some ray tracing calculations with a commercial software package using the parameters of the optical design. These theoretical PSFs showed the expected variation of the PSFs. They were consistent with some of the observed features, but they were sufficiently different from the observed PSFs that they could not be used directly. However, I noticed that these theoretical PSFs look like examples of the primary optical aberrations. Indeed, I performed some calculations with the primary optical aberrations which approximated the calculations using the design quite well. The hope was that the measured PSFs would also be fitted well by primary optical aberrations with some parameters such as the focus location changed somewhat with respect to Lyn's calculations. This would then allow us to calculate PSFs for every location across the field of views.

Table 3.0-1 lists equations for the four aberrations: defocus, spherical aberration, astigmatism, and coma. The equations describe the coordinates of a beam at the CCD as function of the coordinates of the beam at the aperture. The following quantity need to be specified: R, the distance of the center of light from the optical axis in the focal plane, which uniquely corresponds to the angle of the incoming beam. In order to build up an image for an aberration, one typically calculates some 1000 beams spread across the aperture.

Coma is assumed to vary with a linear and cubic dependence on R. Astigmatism is assumed to vary with the square of R. The defocus term is a constant defocus combined with a term dependent on the square of R, called field curvature. Spherical aberration is assumed to have the same kind of dependence on R as the defocus term.

When fitting theoretical PSFs to the measured ones, the parameters for the defocus term were allowed to be different for the #2 and #3 instruments. The other four

optical aberrations were assumed to be identical for both instruments and changed only between HRI, MRI, and SLI. For a better fit, three pairs of parameters were added for each camera, the location of the interception of the image plane with the optical axis, the slope of the image plane (not necessarily perpendicular to the optical axis), and the decentering of the aperture obstruction. The size and shape of the obstruction was taken from the instrument design drawings.

The smearing of the image by the fibers, the spacing between fibers and CCD, and the finite pixel size were modeled in the following way. The observed SLI3 and SLI2 PSFs in the center of the field of view had the sharpest PSFs. Their elongation in the vertical direction can be explained by sensitive pixel areas of 23x15 mm (DISR#3) and 23x14 mm (DISR#2), accurate to about 1 mm. The adopted area was 23x15.

While an aperture with isotropic illumination causes an intensity distribution proportional to $\cos^4 a$ (a is the angle of the beam in the spacing between fibers and CCD with respect to the normal on the image plane), the wings of the measured PSFs indicate that the exponent is at least 5 and probably closer to 6 (a value somewhat above 4 is expected due to reflection at the end of the fibers). The adopted exponent was 6. The distance between fibers and CCD based on this dependence is then 1.02±0.1 and 1.20±0.1 pixels for DISR3 and DISR2, respectively, about 23 and 28 mm. I tested the data for a possible variation of the spacing with location or imager, but no significant variation was found. Note that the measured PSFs do not constrain the physical spacing. They only show that the smearing due to fibers and spacing is similar to that of a $\cos^6 a$ dependence and a 23 or 28 mm spacing. Table 3.0-2 lists the adopted parameters derived by least-square fitting of the PSFs.

PSFs generated with the adopted parameter are very similar to the 28 observed ones. There are some small deviations unlikely to be noise. However, deviations are so different in different parts of the field of view that it seems close to impossible to achieve a better understanding of the true PSFs across the field of view. Even for especially accurate photometric measurements of small features where knowledge of PSFs are critical, the generated PSFs probably approximate the true PSFs sufficiently well.

PSFs were generated for a grid every 9 pixels in both coordinates for each of the six investigated cameras. Each PSF was sampled in 0.6 pixel steps, the largest step size which essentially preserves all spatial information. All PSFs were centered according to their center of light. These PSFs were Fourier transformed for the deconvolution process using the Fourier or Wiener method. The specified PSFs in the deconvolution program have Fourier transforms of the form $(1 - f_x^2/4 - f_y^2/4)^e$ where f_x and f_y are the spatial frequencies in cycles/pixel and the exponent e can be chosen freely to control sharpness. In the program, e is a function of the distance from the center of the image.

In principle, a specified PSF should not contain any spatial frequencies which are not contained in the PSF of the camera, since such a case causes a division by zero and an infinite boost factor for the amplitude of that frequency. In reality, such cases will happen, especially near the corners of the MRI where the PSF does not contain some moderately high frequencies. The software then modifies the specified PSF so that boost factors remain finite. A free parameter allows the choice between s small modification of the specified PSF with large boost factors and thus noisy deconvolved images versus a large modification of the specified PSF with more pleasing looking results.

3.3. Distortion

Since the locations of the 28 measured PSFs are also known in the azimuth-elevation system of the mount, one can explore the approximate mapping between these coordinates and the pixel coordinates. For each of the six cameras, four parameters were determined: the azimuth and elevation for the center of the image, the scale (in the center), and the rotation angle with respect to the vertical. For both HRIs, this gives an almost perfect mapping. For the MRI, a standard radial distortion is obvious. Considering this distortion, the mapping is also almost perfect. The radial distortion is even more obvious for the SLI. Yet, the simple distortion gives a mapping only accurate to about 1 pixel. For purposes which don't require higher precision, a subroutine was written which converts the coordinates for all six cameras in both ways, pixels coordinates into azimuth/elevation and vise versa.

3.4. Smear due to Rotation of the Probe

The finite integration times and the rotation of the probe cause a smear which is typically about 1.5 pixels. This smear can be deconvolved. A program was written which calculates smear lengths and smear orientations based on one input parameter, the angular rotation during the exposure, which is the product of the integration time and spin rate. It is assumed that the rotation occurs around the axis azimuth = 0° and elevation = ±90°. The program then smears the synthetic PSFs. For deconvolution of smeared images, the deconvolution program needs this file.

Table 3.0-1

Aberrations

Defocus	$r = d\,\rho\cos\phi$ $t = d\,\rho\sin\phi$	$d = d_0 + d_2R^2 + (d_x x + d_y y)/100$
Spherical Aberration	$r = s(3\rho^2 - 2)\rho\cos\phi$ $t = s(3\rho^2 - 2)\rho\sin\phi$	$s = s_0 + s_2R^2$
Astigmatism	$r = a\,\rho\cos\phi$ $t = -a\,\rho\sin\phi$	$a = a_2R^2$
Coma	$r = c(\rho^2\cos2\phi + 2\rho^2 - 1)$ $t = c(\rho^2\sin2\phi)$	$c = c_1R + c_3R^3$

Table 3.0-2
Adopted Parameters

Parameter	HRI3	HRI2	MRI3	MRI2	SLI3	SLI2
d_0	-0.50	-0.31	-0.76	0.50	-0.03	-0.03
d_2	-0.46	-0.23	1.54	2.30	-0.50	-0.50
d_x	-0.04	0.09	0.12	0	-0.05	0
d_y	-0.15	0.25	-0.03	0	-0.05	0
s_0	0.73	0.73	-0.64	-0.64	-0.56	-0.56
s_2	-0.87	-0.87	0.56	0.56	0	0
a_2	-0.23	-0.23	2.71	2.71	0.65	0.65
c_1	-1.26	-1.26	1.45	1.45	-0.93	-0.93
c_3	0.68	0.68	-0.56	-0.56	1.15	1.15
o_x	0.55	-0.35	0.38	0	0.20	0
o_y	0.35	-0.20	-0.05	0	0.05	0
x_a	-10	54	-4	3	0	0
y_a	-5	38	0	1	0	0

Table 3.0-3
Explanation of Parameters

x	(pixels)	x-coordinate in image, from center to right
y	(pixels)	y-coordinate in image, from center up
x_a	(pixels)	x-coordinate of optical axis
y_a	(pixels)	y-coordinate of optical axis
R	0 ... 1	normalized distance from optical axis R = 1 in image corner if $x_a = y_a = 0$
ρ	0 ... 1	normalized distance from center of aperture ρ = 1 at edge of aperture stop
ϕ	0 ... 2π	azimuthal angle in aperture (radial=0°)
r	(pixels)	radial distance from center of light
t	(pixels)	tangential distance from center of light
c	(pixels)	1/3-diameter of coma
a	(pixels)	half-diameter of astigmatism
d	(pixels)	half-diameter of defocused image
s	(pixels)	half-diameter of spherical aberration
o_x, o_y		relative offset of aperture obstruction
c_1, c_3, a_2, d_0, d_2, d_x, d_y, s_0, s_2, o_x, o_y, x_a, y_a	(pixels)	constants for each camera (cf. Table 3.0-2)

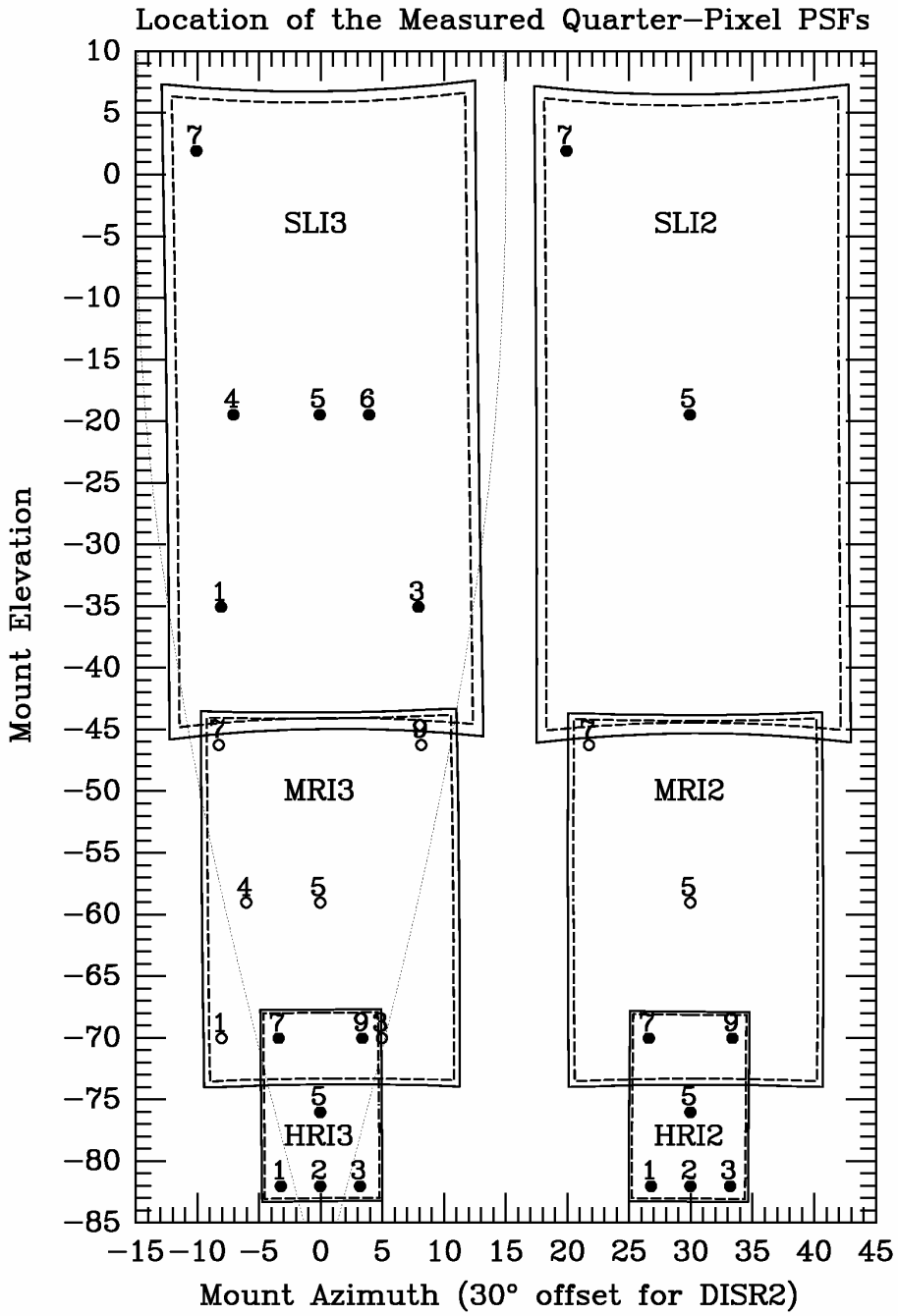

Figure 3.0-1 Location of the Measured Quarter-Pixel PSFs. Displayed are the 28 measured PSFs in the azimuth-elevation system of the mount. Positions are numbered within each camera from bottom (1-3) to top (7-9) and from left to right. The thin dotted lines are meridians separated by 30° of probe rotation, corresponding to a panorama of 12 images.

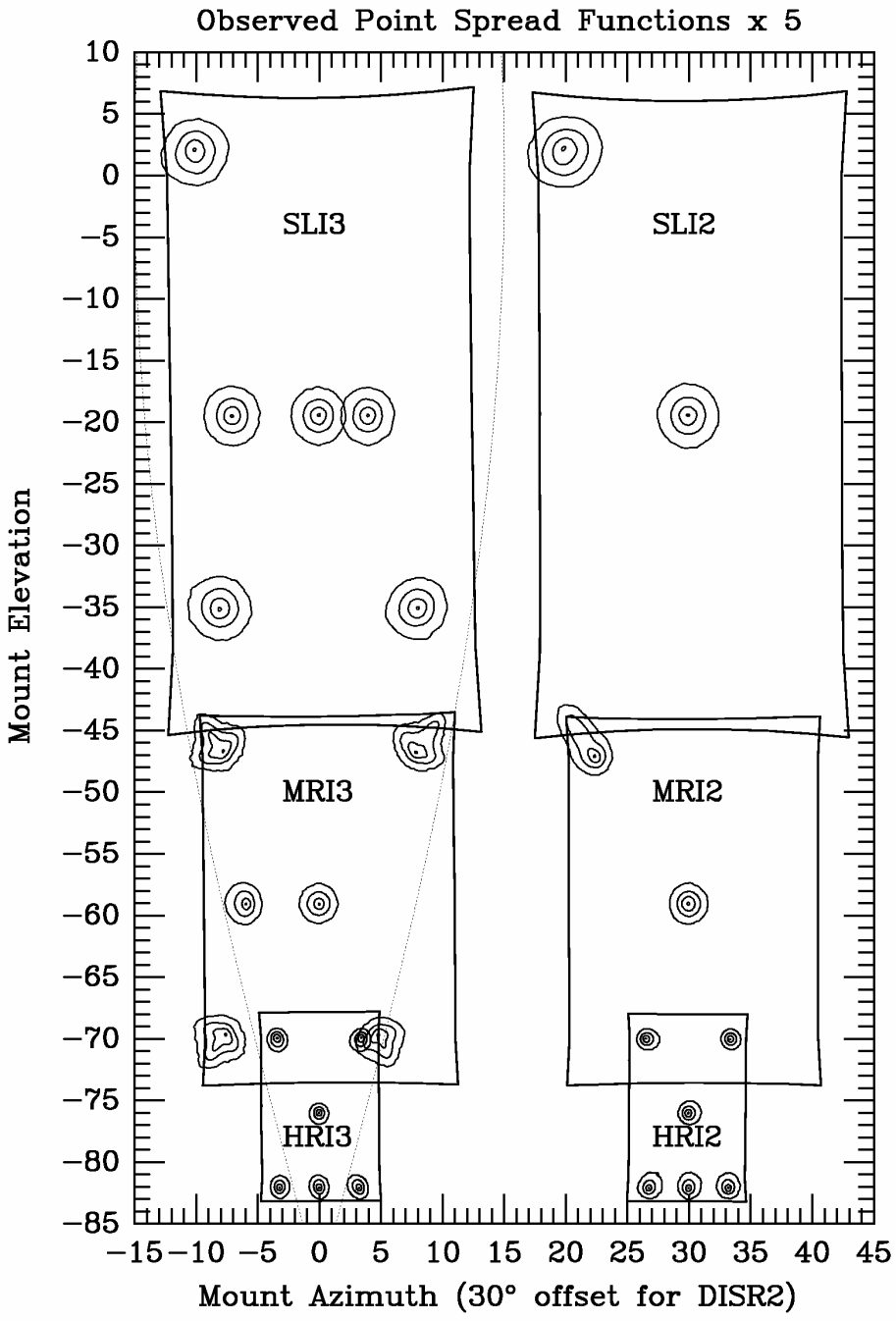

Figure 3.0-2 Observed Point Spread Functions x 5. Contour lines for the observed PSFs magnified five times are shown for 50%, 10%, and 1% of maximum intensity.

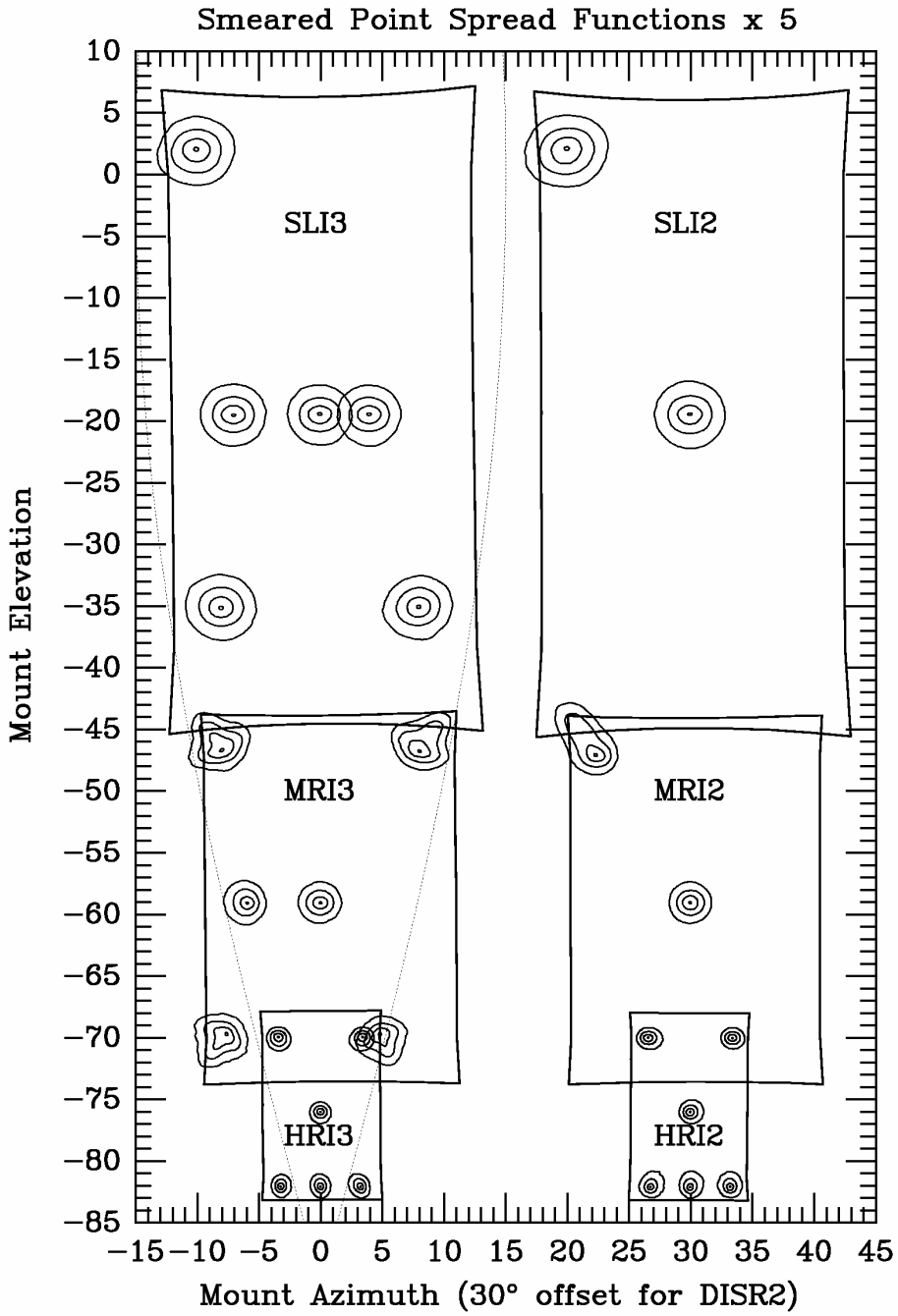

Figure 3.0-3 Smeared Point Spread Functions x 5. Same as Fig. 2 except that the PSFs are smeared according to a probe rotation of 0.36°.

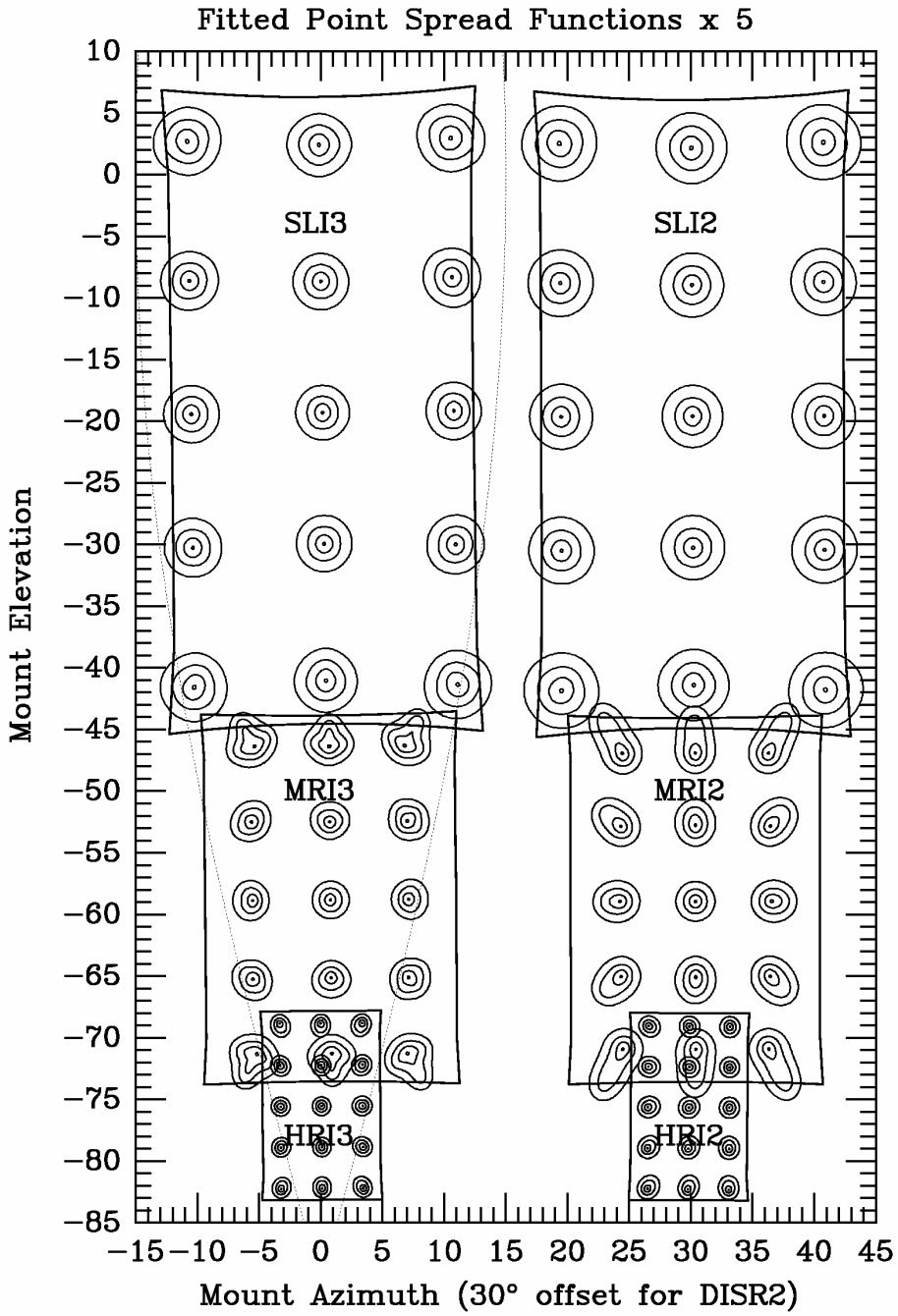

Figure 3.0-4 Fitted Point Spread Functions x 5. Same as Fig. 2 except that the synthetic PSFs are displayed.

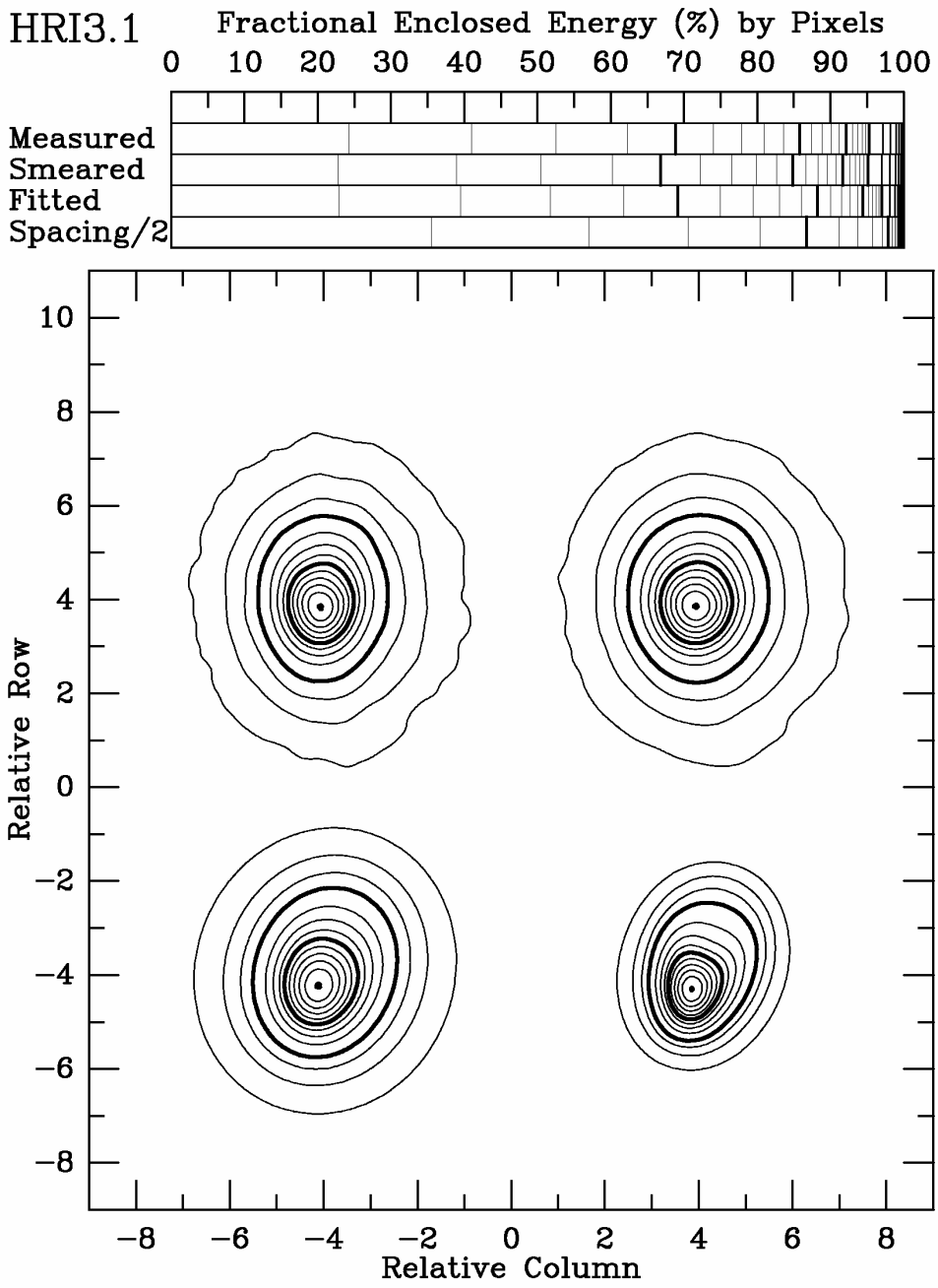

Figures 3.0-5 to 3.0-32 Fractional Enclosed Energy (%) by Pixels for each of the 28 PSFs locations for measured, smeared, standard synthetic, and alternative synthetic PSFs. The alternative synthetic PSFs are calculated with a spacing between the fibers and the CCD of half the actual spacing. The top panel shows the enclosed energy for the brightest pixel, the brightest two pixels, etc. After 20 pixels, only every fifth pixel is marked. The bottom panel shows contours of 0.5, 2, 5, 10, **20, 30, 40,** 50, **60, 70, 80, 90, and 100% (central dot). The order is measured PSF (top left), smeared PSF (top right), fitted PSF (bottom left), and spacing/2 (bottom right).**

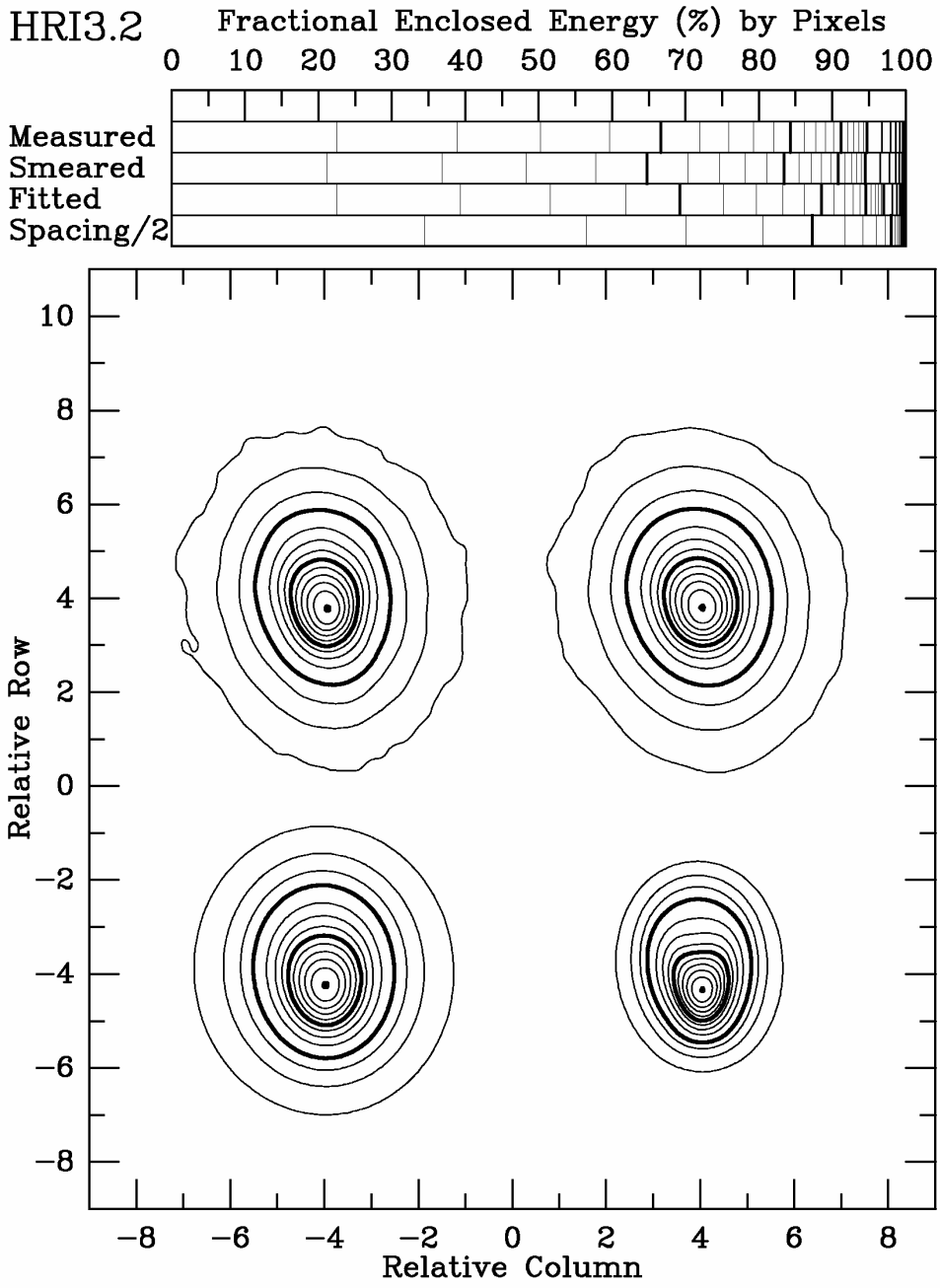
HRI3.2
Fractional Enclosed Energy (%) by Pixels
0 10 20 30 40 50 60 70 80 90 100
Measured
Smeared
Fitted
Spacing/2
Relative Row
10
8
6
4
2
0
−2
−4
−6
−8
−8 −6 −4 −2 0 2 4 6 8
Relative Column

Figure 3.0-6

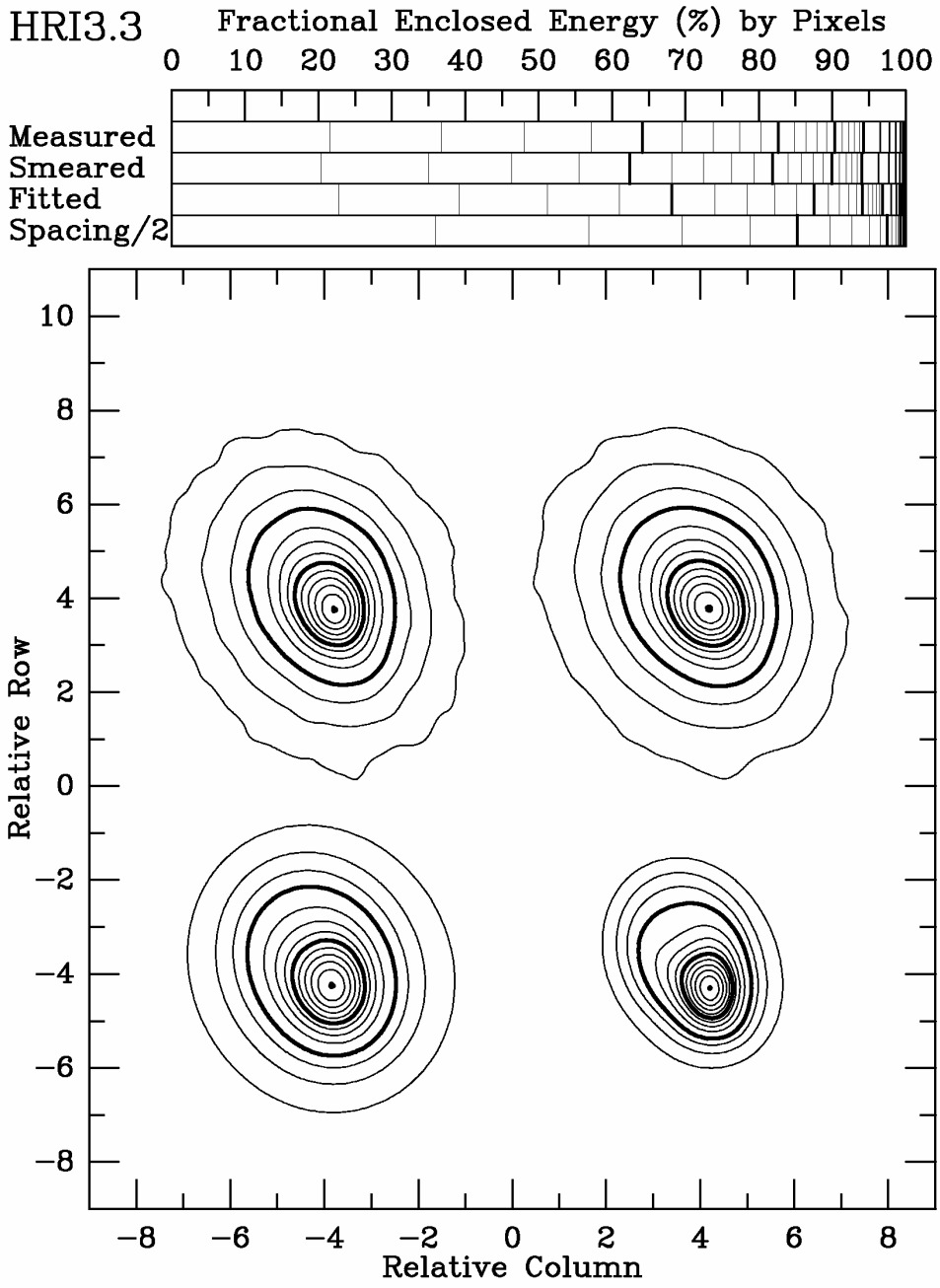
HRI3.3
Fractional Enclosed Energy (%) by Pixels
0 10 20 30 40 50 60 70 80 90 100
Measured
Smeared
Fitted
Spacing/2
10
8
6
4
2
0
−2
−4
−6
−8
Relative Row
−8 −6 −4 −2 0 2 4 6 8
Relative Column

Figure 3.0-7

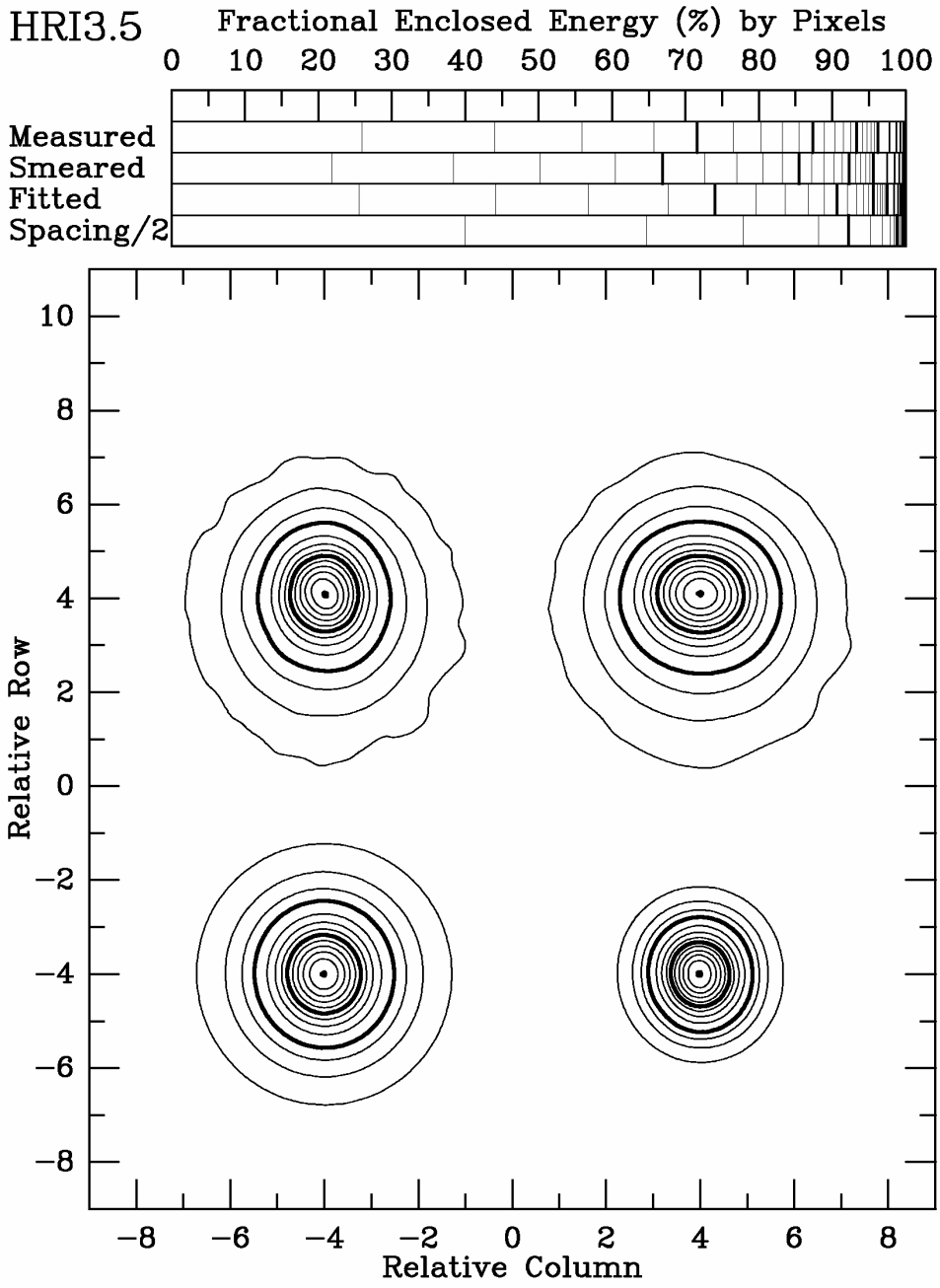
HRI3.5
Fractional Enclosed Energy (%) by Pixels
0 10 20 30 40 50 60 70 80 90 100
Measured
Smeared
Fitted
Spacing/2
Relative Row
Relative Column
10
8
6
4
2
0
−2
−4
−6
−8
−8 −6 −4 −2 0 2 4 6 8

Figure 3.0-8

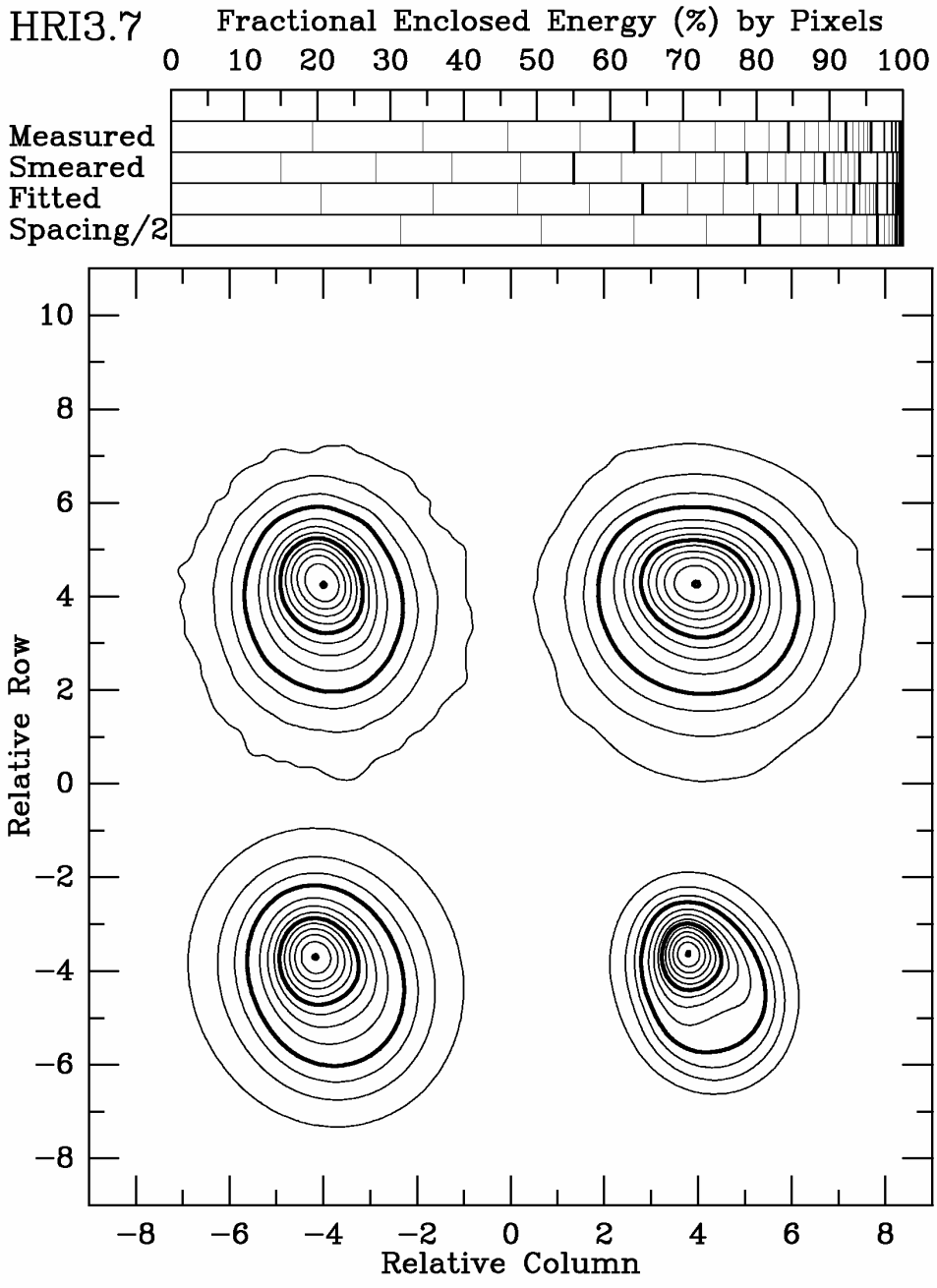
HRI3.7
Fractional Enclosed Energy (%) by Pixels
0 10 20 30 40 50 60 70 80 90 100
Measured
Smeared
Fitted
Spacing/2
10
8
6
4
2
0
−2
−4
−6
−8
Relative Row
−8 −6 −4 −2 0 2 4 6 8
Relative Column

Figure 3.0-9

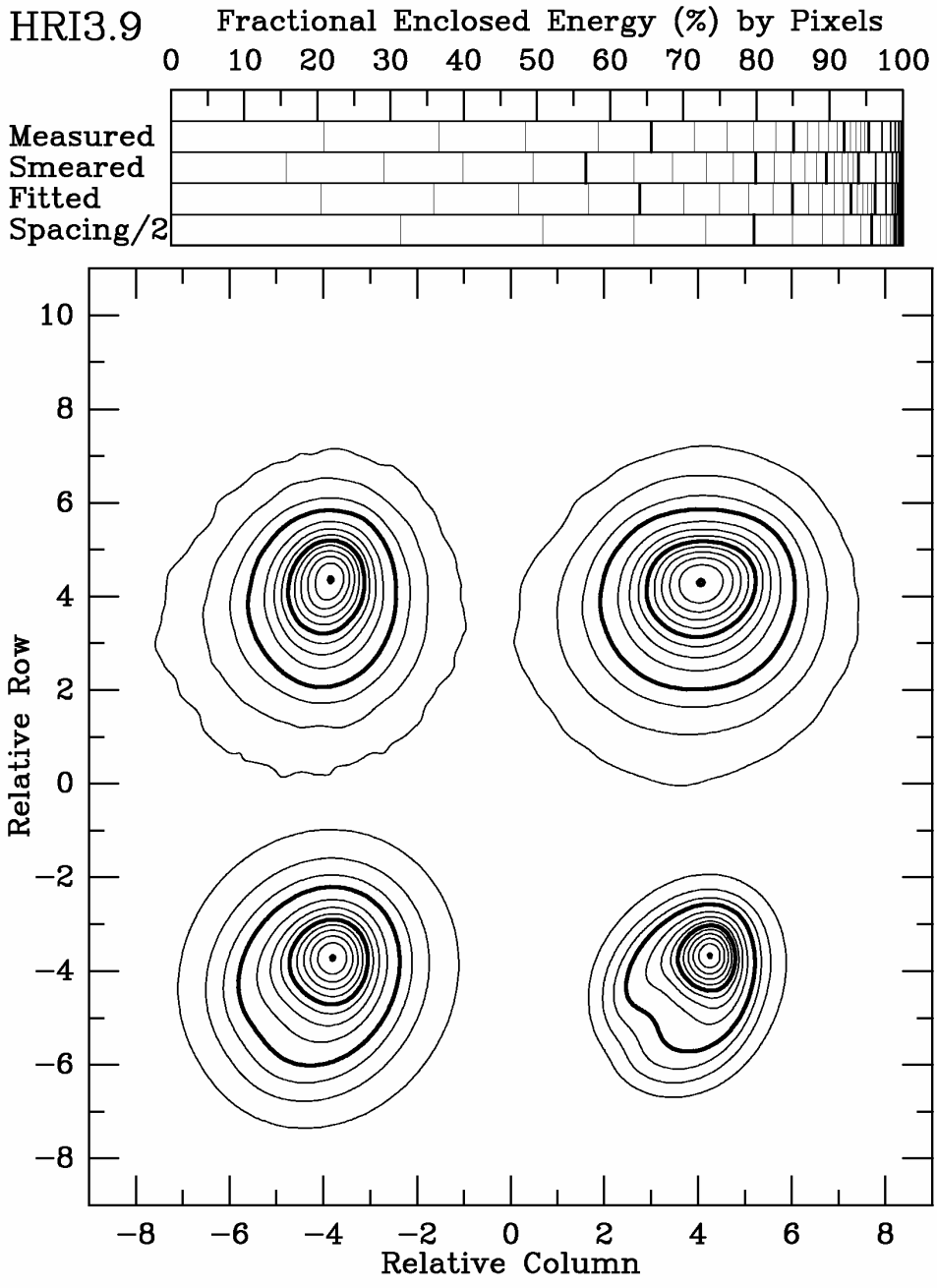
HRI3.9
Fractional Enclosed Energy (%) by Pixels
0 10 20 30 40 50 60 70 80 90 100
Measured
Smeared
Fitted
Spacing/2
10
8
6
4
2
0
−2
−4
−6
−8
Relative Row
−8 −6 −4 −2 0 2 4 6 8
Relative Column

Figure 3.0-10

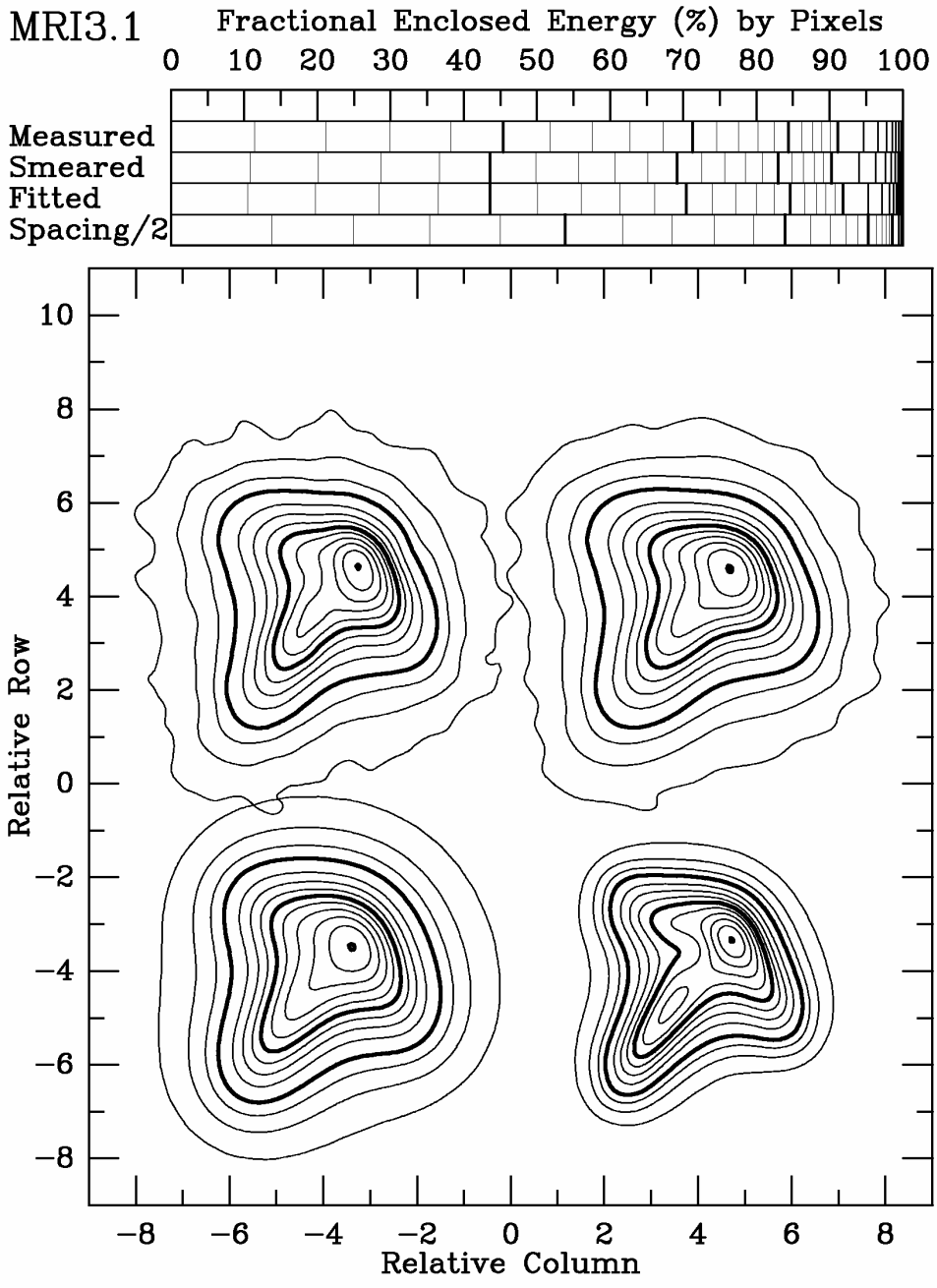
MRI3.1
Fractional Enclosed Energy (%) by Pixels
0 10 20 30 40 50 60 70 80 90 100
Measured
Smeared
Fitted
Spacing/2
10
8
6
4
2
0
−2
−4
−6
−8
Relative Row
−8 −6 −4 −2 0 2 4 6 8
Relative Column

Figure 3.0-11

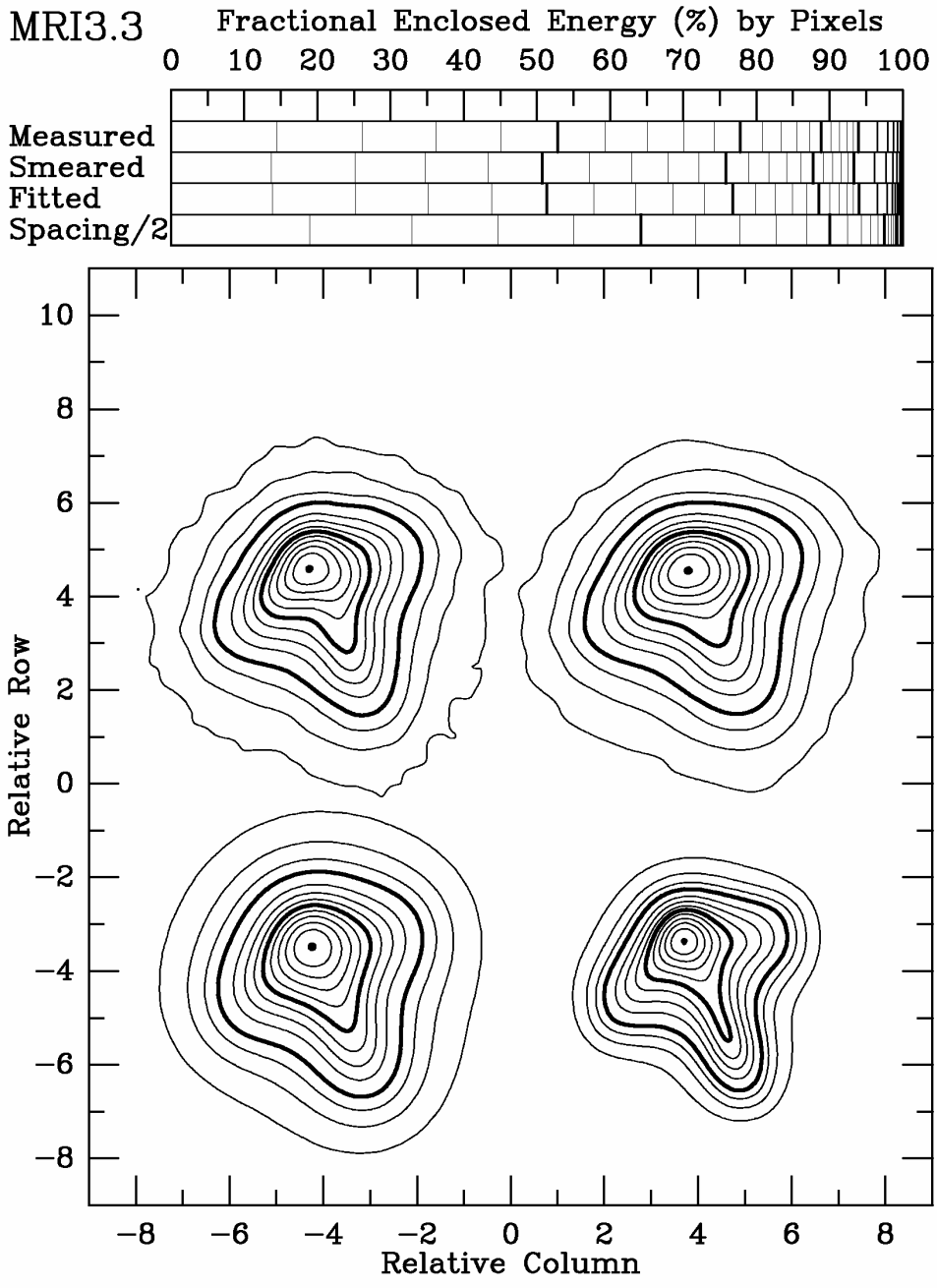
MRI3.3
Fractional Enclosed Energy (%) by Pixels
0 10 20 30 40 50 60 70 80 90 100
Measured
Smeared
Fitted
Spacing/2
10
8
6
4
2
0
−2
−4
−6
−8
Relative Row
−8 −6 −4 −2 0 2 4 6 8
Relative Column

Figure 3.0-12

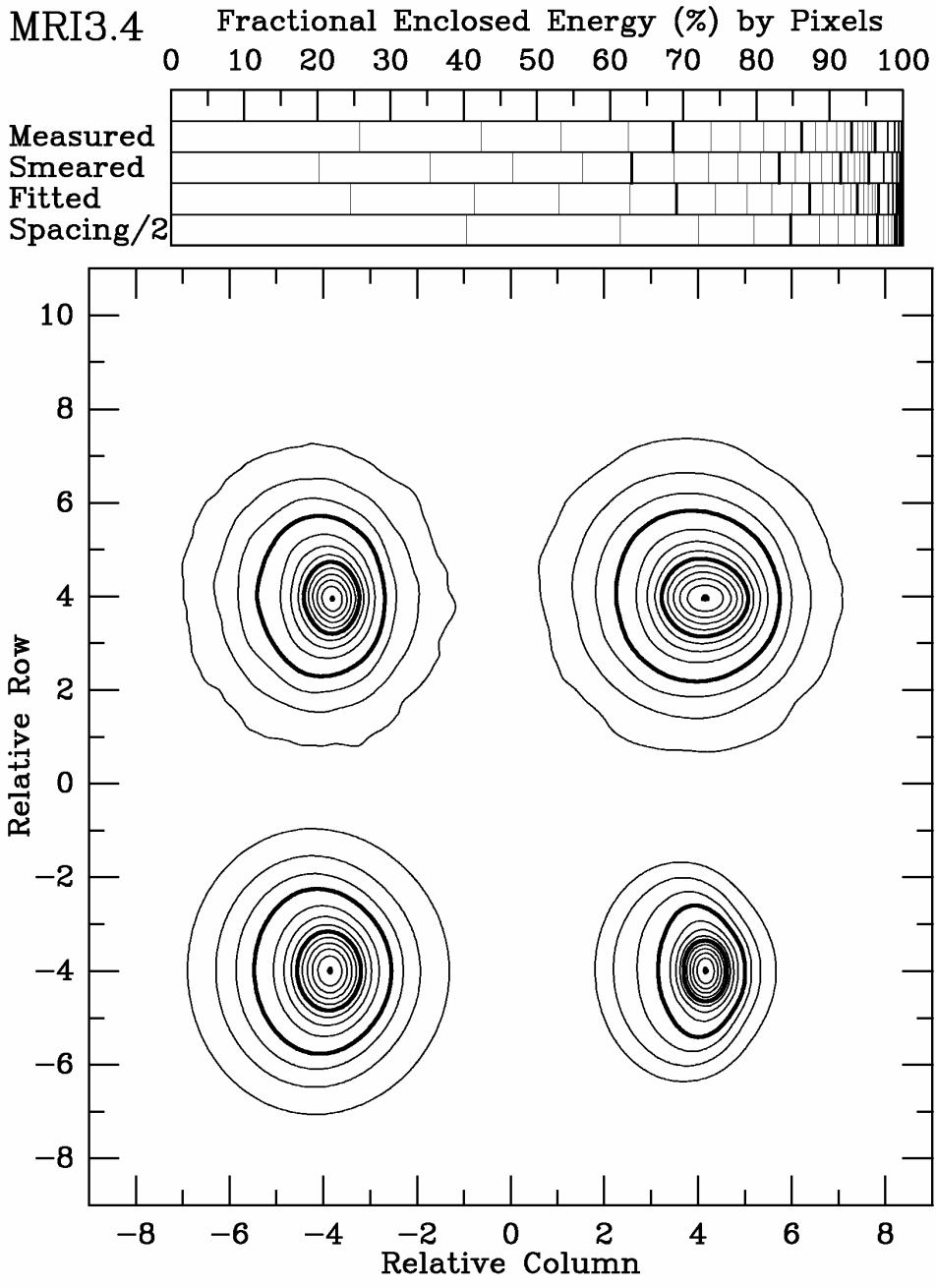
MRI3.4
Fractional Enclosed Energy (%) by Pixels
0 10 20 30 40 50 60 70 80 90 100
Measured
Smeared
Fitted
Spacing/2
10
8
6
4
2
0
−2
−4
−6
−8
Relative Row
−8 −6 −4 −2 0 2 4 6 8
Relative Column

Figure 3.0-13

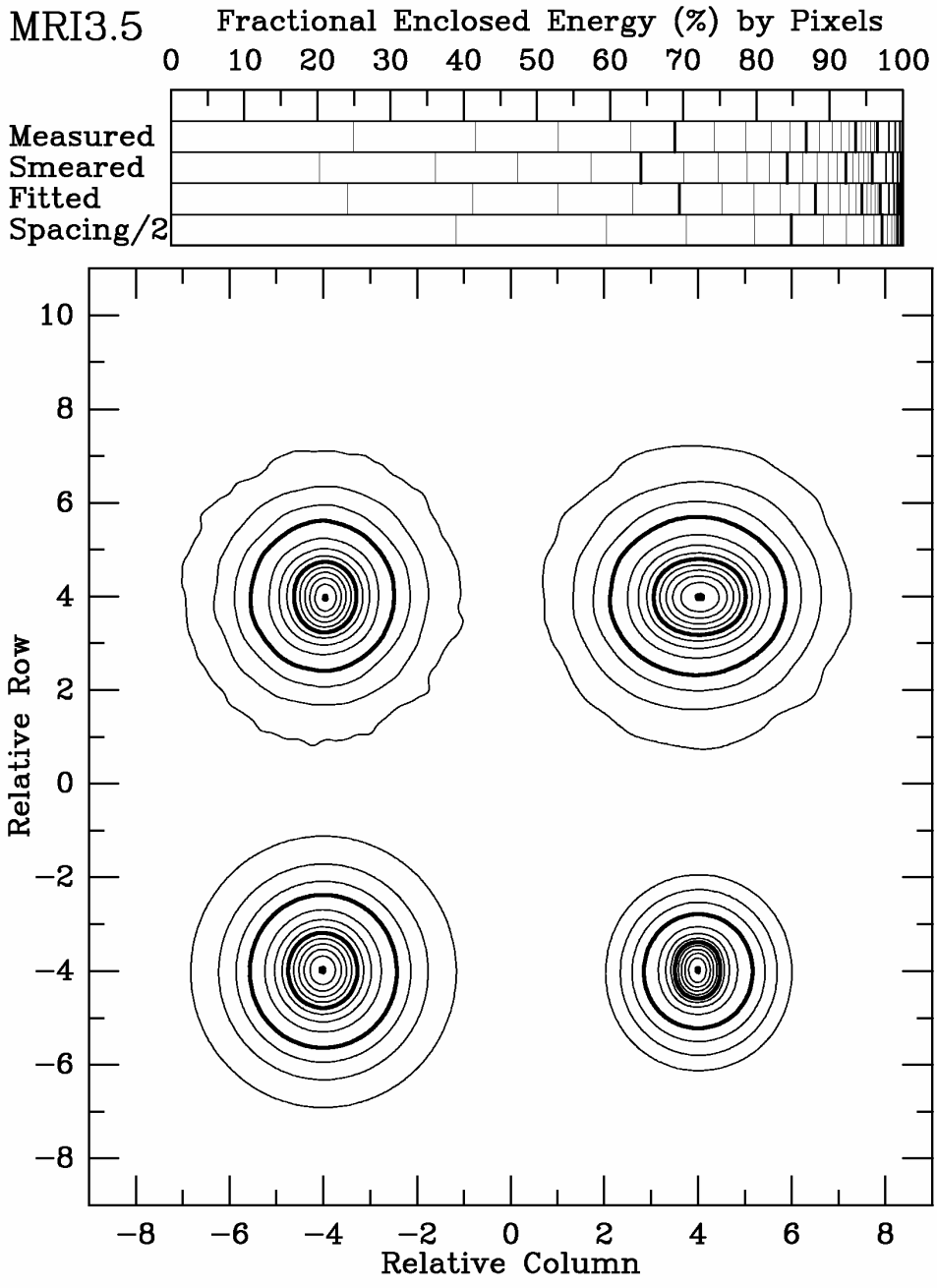
MRI3.5
Fractional Enclosed Energy (%) by Pixels
0 10 20 30 40 50 60 70 80 90 100
Measured
Smeared
Fitted
Spacing/2
10
8
6
4
2
0
−2
−4
−6
−8
Relative Row
−8 −6 −4 −2 0 2 4 6 8
Relative Column

Figure 3.0-14

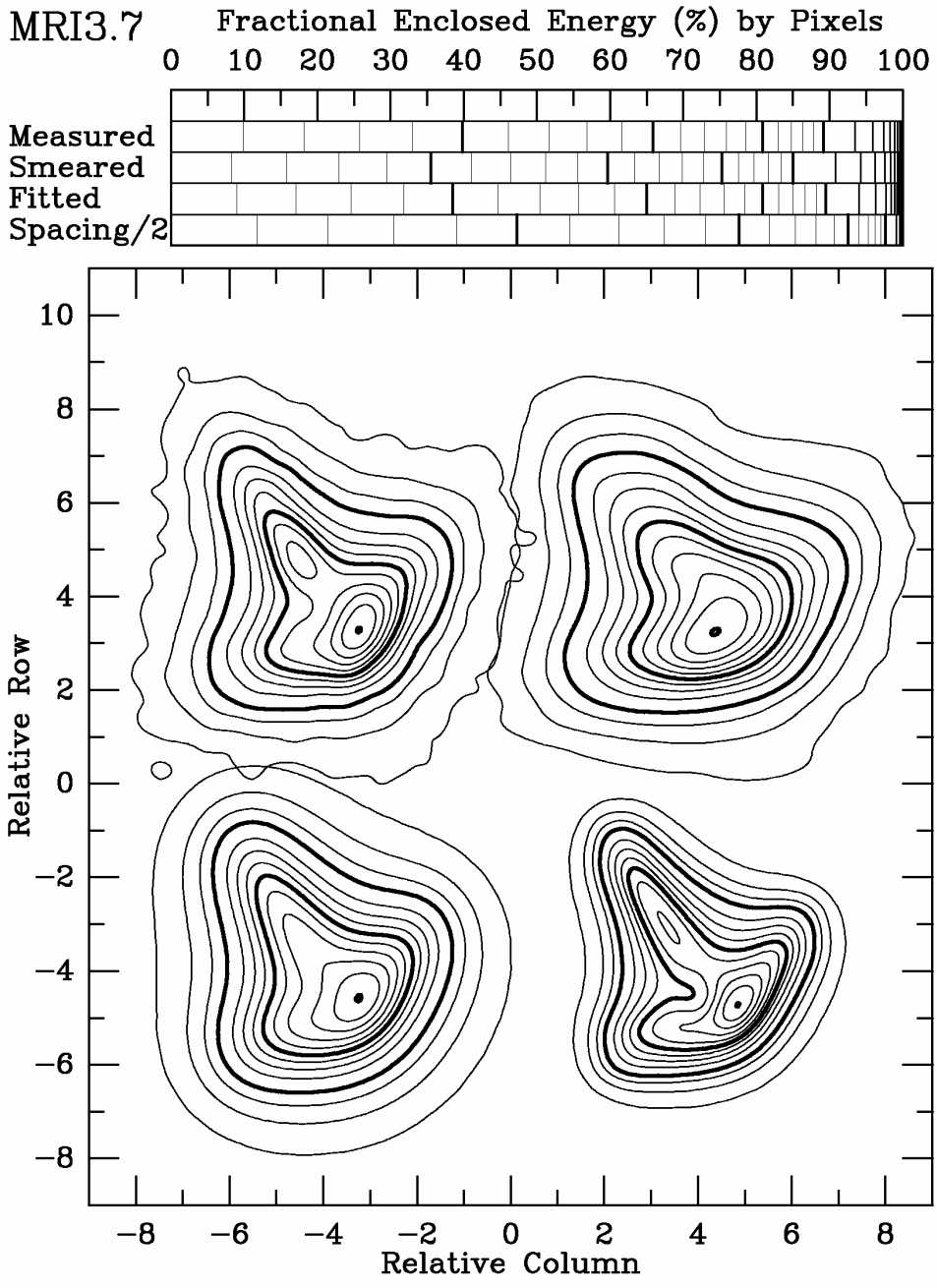
MRI3.7
Fractional Enclosed Energy (%) by Pixels
0 10 20 30 40 50 60 70 80 90 100
Measured
Smeared
Fitted
Spacing/2
Relative Row
Relative Column
10
8
6
4
2
0
−2
−4
−6
−8
−8 −6 −4 −2 0 2 4 6 8

Figure 3.0-15

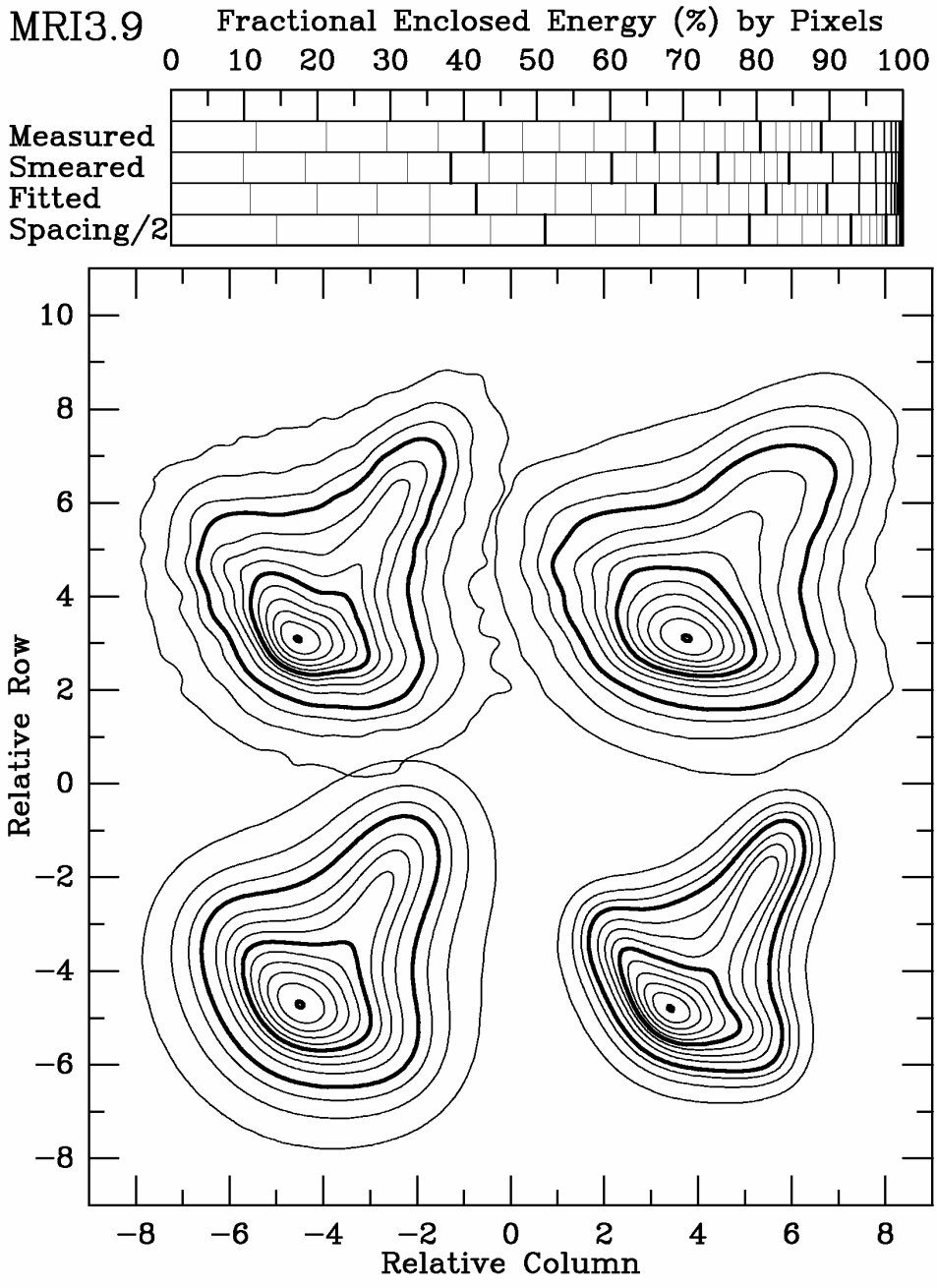
MRI3.9
Fractional Enclosed Energy (%) by Pixels
0 10 20 30 40 50 60 70 80 90 100
Measured
Smeared
Fitted
Spacing/2
10
8
6
4
2
0
−2
−4
−6
−8
Relative Row
−8 −6 −4 −2 0 2 4 6 8
Relative Column

Figure 3.0-16

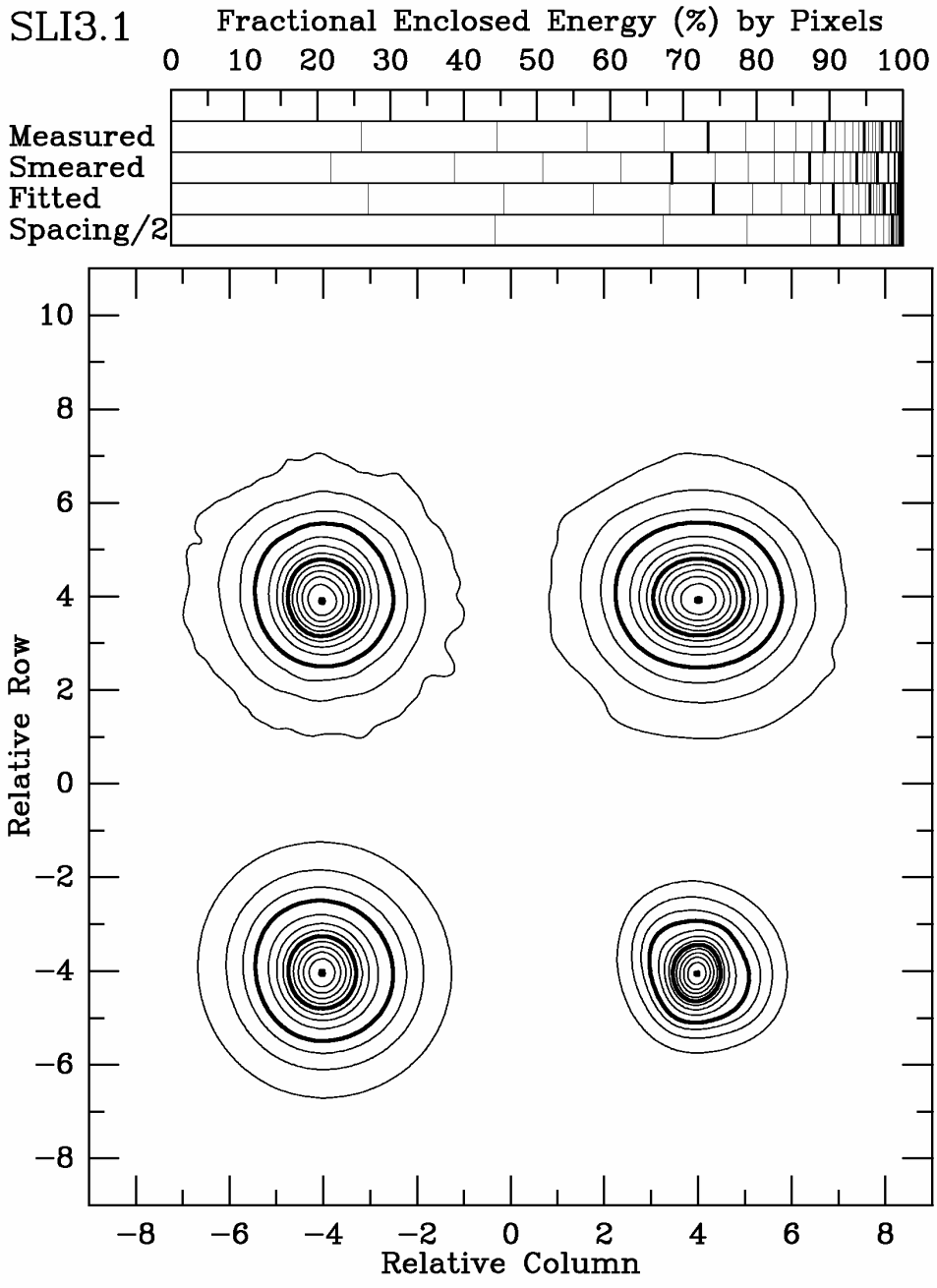
SLI3.1
Fractional Enclosed Energy (%) by Pixels
0 10 20 30 40 50 60 70 80 90 100
Measured
Smeared
Fitted
Spacing/2
Relative Row
Relative Column
10
8
6
4
2
0
−2
−4
−6
−8
−8 −6 −4 −2 0 2 4 6 8

Figure 3.0-17

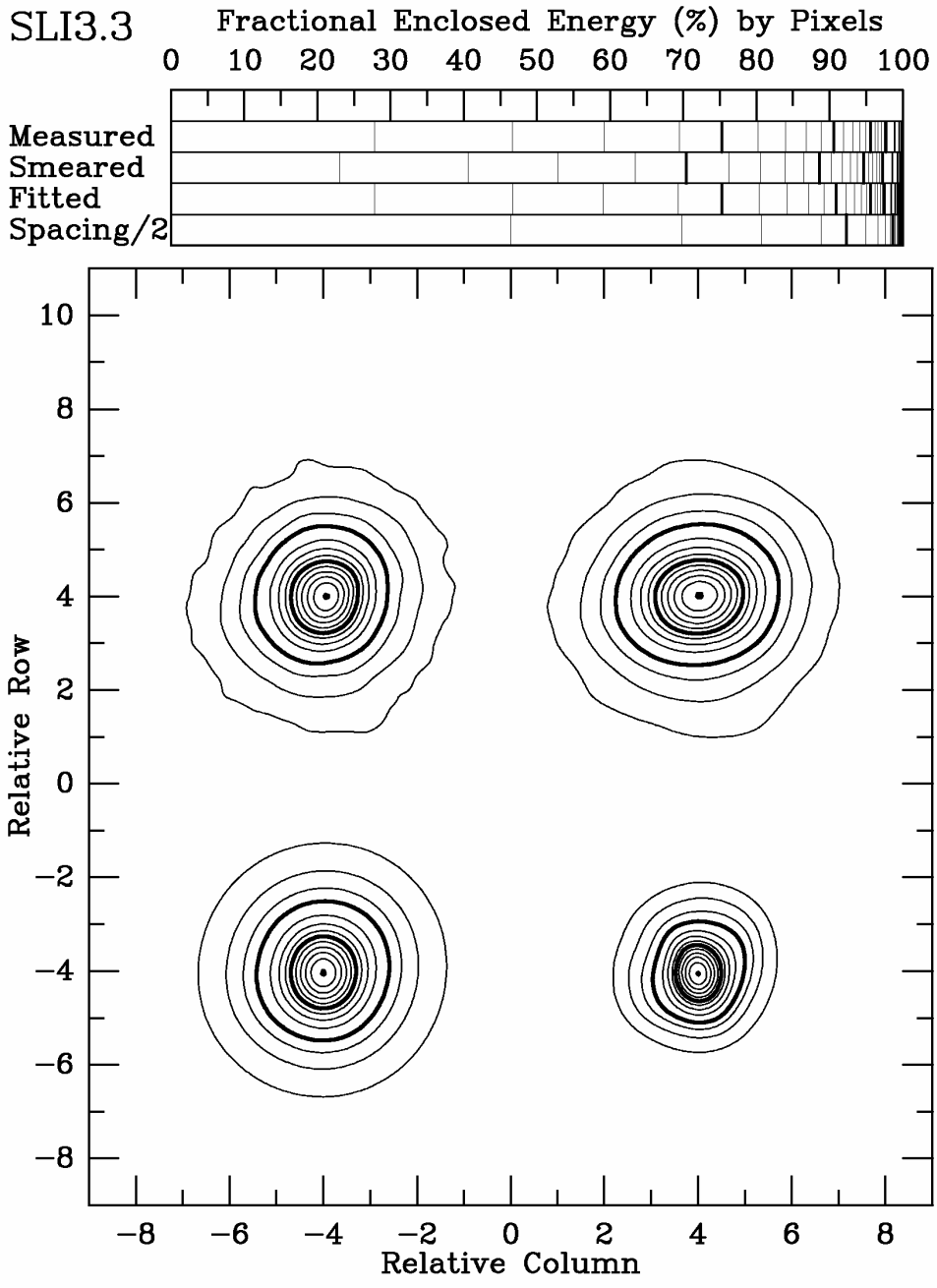
SLI3.3
Fractional Enclosed Energy (%) by Pixels
0 10 20 30 40 50 60 70 80 90 100
Measured
Smeared
Fitted
Spacing/2
Relative Row
10
8
6
4
2
0
−2
−4
−6
−8
−8 −6 −4 −2 0 2 4 6 8
Relative Column

Figure 3.0-18

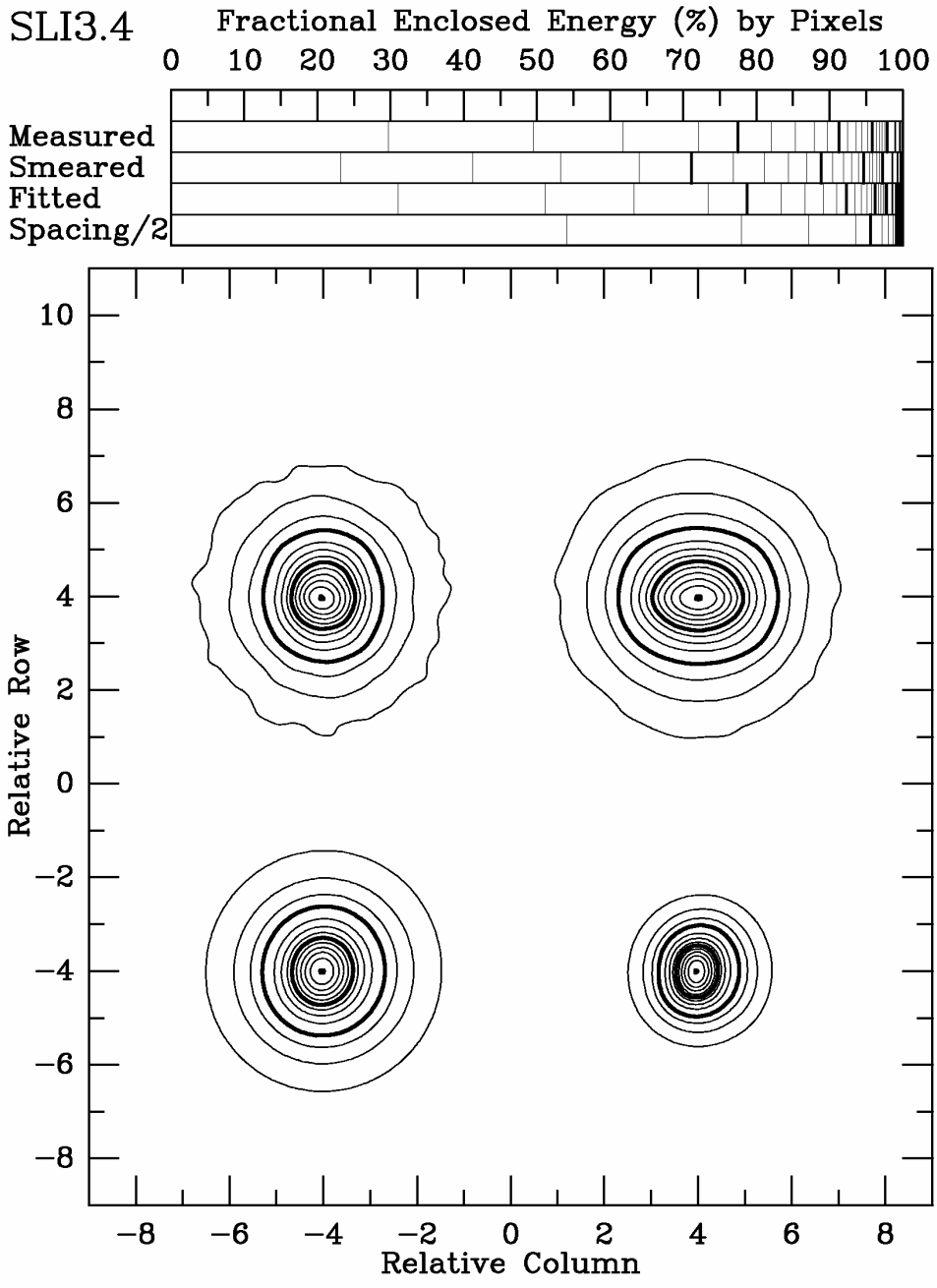
SLI3.4
Fractional Enclosed Energy (%) by Pixels
0 10 20 30 40 50 60 70 80 90 100
Measured
Smeared
Fitted
Spacing/2
Relative Row
10
8
6
4
2
0
−2
−4
−6
−8
−8 −6 −4 −2 0 2 4 6 8
Relative Column

Figure 3.0-19

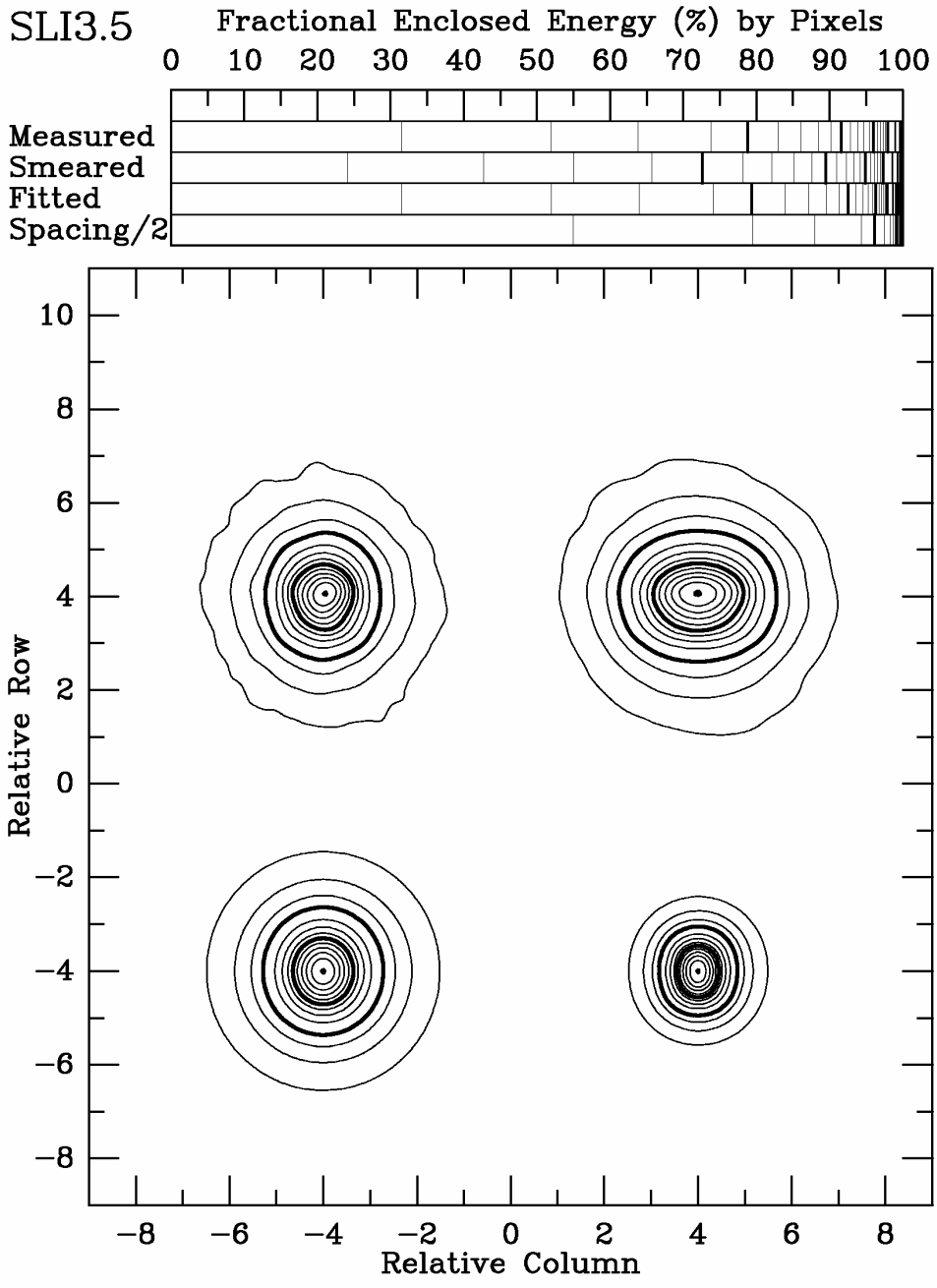
SLI3.5
Fractional Enclosed Energy (%) by Pixels
0 10 20 30 40 50 60 70 80 90 100
Measured
Smeared
Fitted
Spacing/2
Relative Row
10
8
6
4
2
0
−2
−4
−6
−8
−8 −6 −4 −2 0 2 4 6 8
Relative Column

Figure 3.0-20

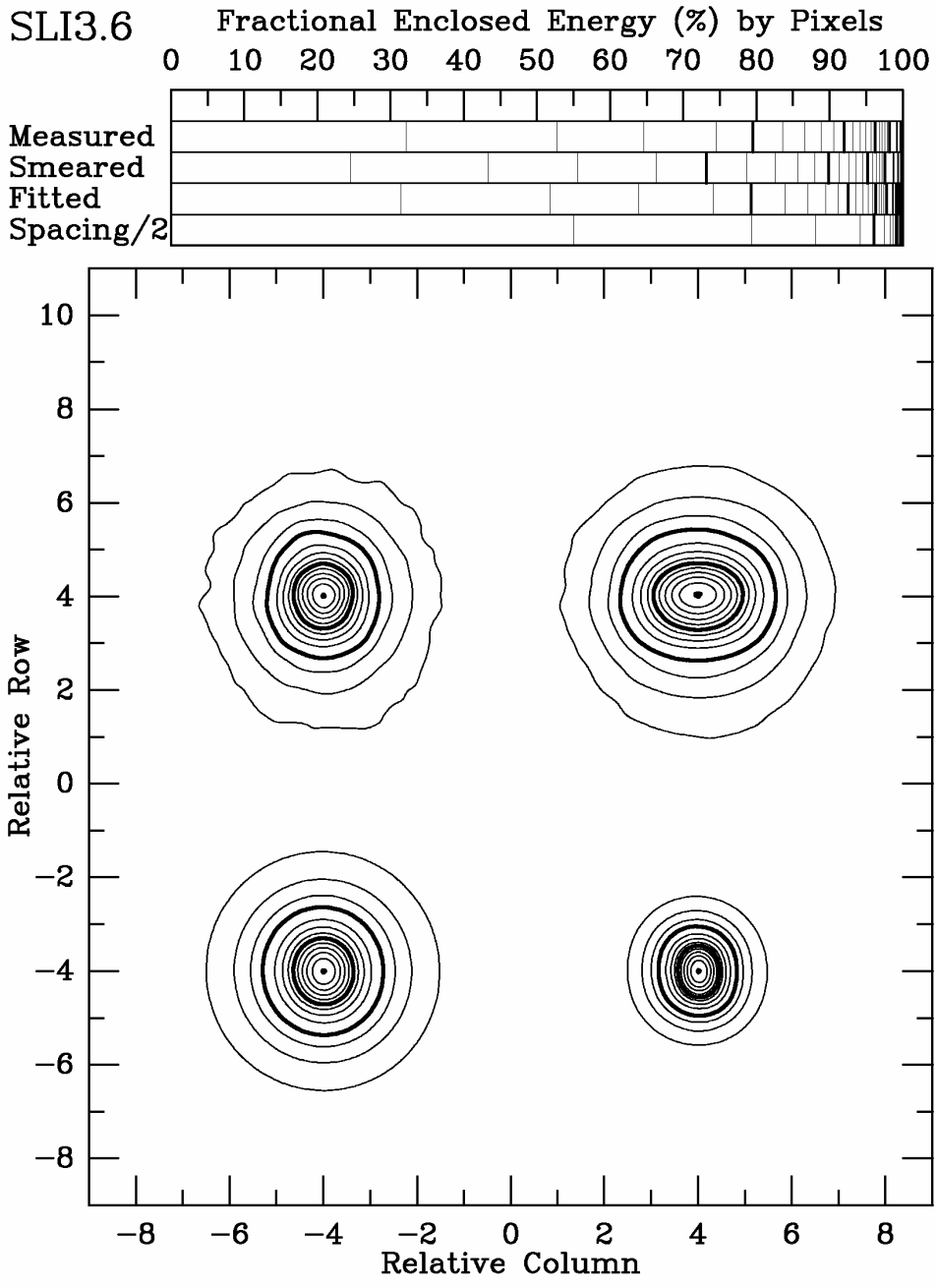
SLI3.6
Fractional Enclosed Energy (%) by Pixels
0 10 20 30 40 50 60 70 80 90 100
Measured
Smeared
Fitted
Spacing/2
10
8
6
4
2
0
−2
−4
−6
−8
Relative Row
−8 −6 −4 −2 0 2 4 6 8
Relative Column

Figure 3.0-21

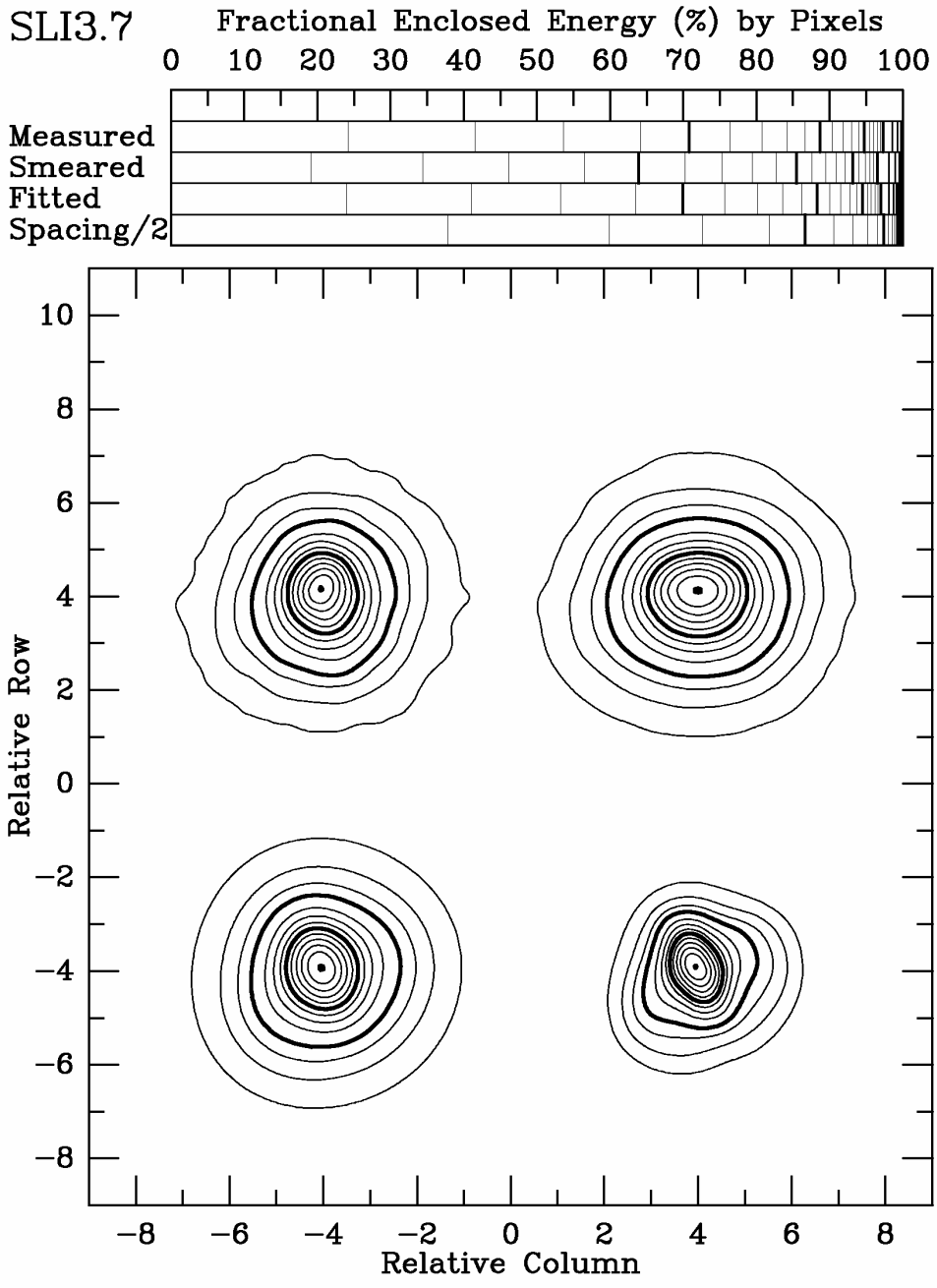
SLI3.7
Fractional Enclosed Energy (%) by Pixels
0 10 20 30 40 50 60 70 80 90 100
Measured
Smeared
Fitted
Spacing/2
10
8
6
4
2
0
−2
−4
−6
−8
Relative Row
−8 −6 −4 −2 0 2 4 6 8
Relative Column

Figure 3.0-22

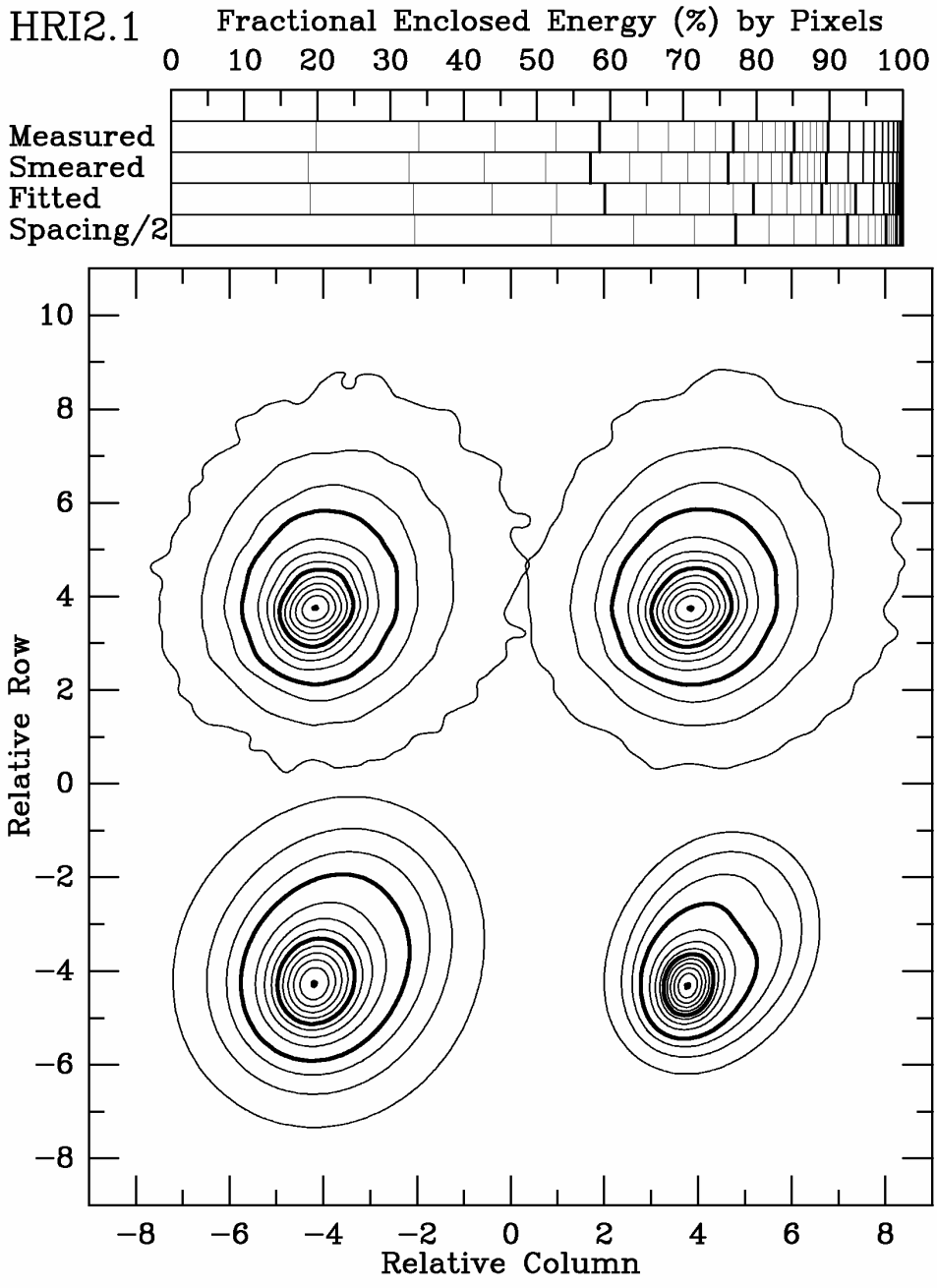
HRI2.1
Fractional Enclosed Energy (%) by Pixels
0 10 20 30 40 50 60 70 80 90 100
Measured
Smeared
Fitted
Spacing/2
10
8
6
4
2
0
−2
−4
−6
−8
Relative Row
−8 −6 −4 −2 0 2 4 6 8
Relative Column

Figure 3.0-23

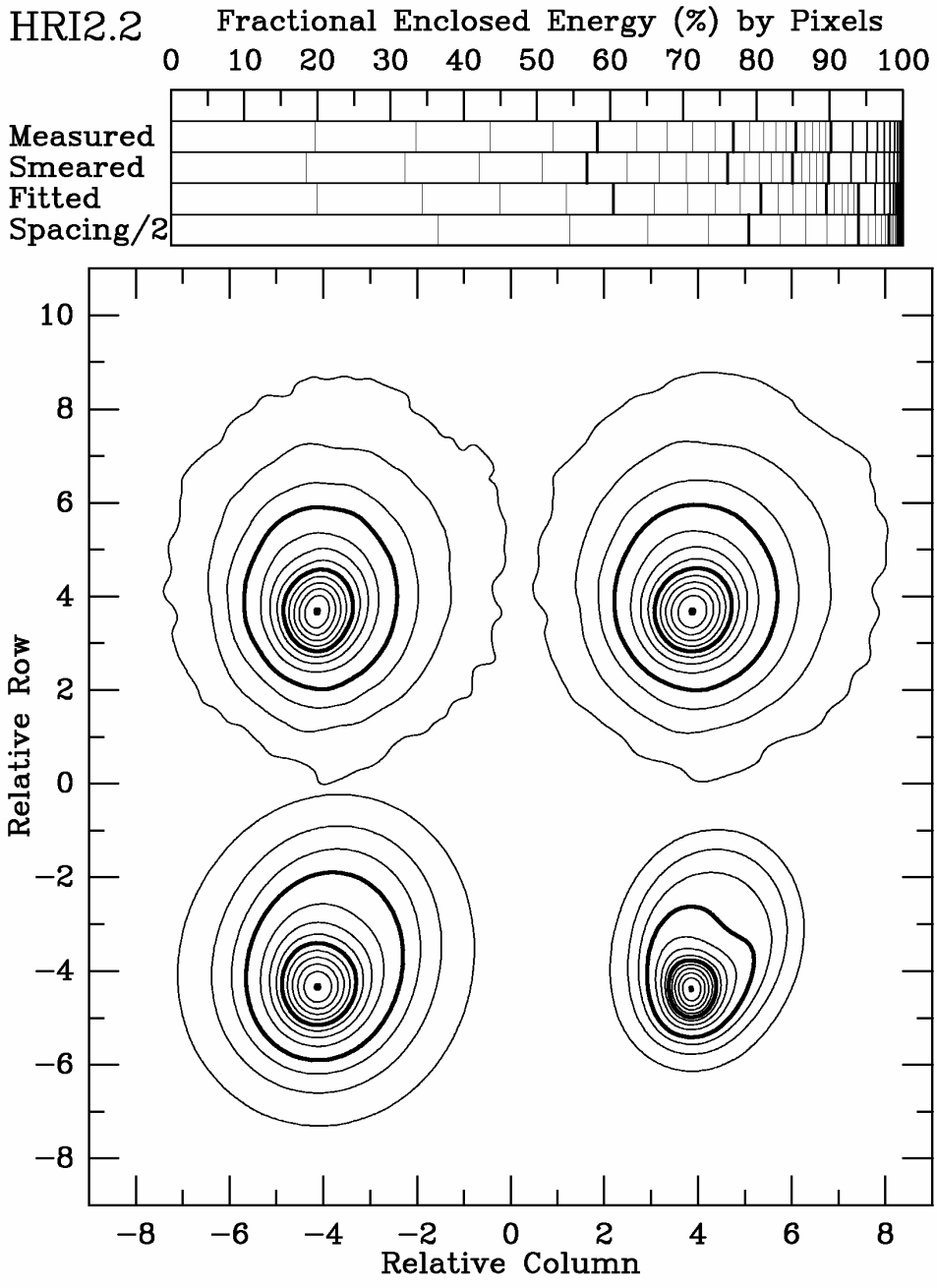
HRI2.2
Fractional Enclosed Energy (%) by Pixels
0 10 20 30 40 50 60 70 80 90 100
Measured
Smeared
Fitted
Spacing/2
Relative Row
Relative Column
10
8
6
4
2
0
−2
−4
−6
−8
−8 −6 −4 −2 0 2 4 6 8

Figure 3.0-24

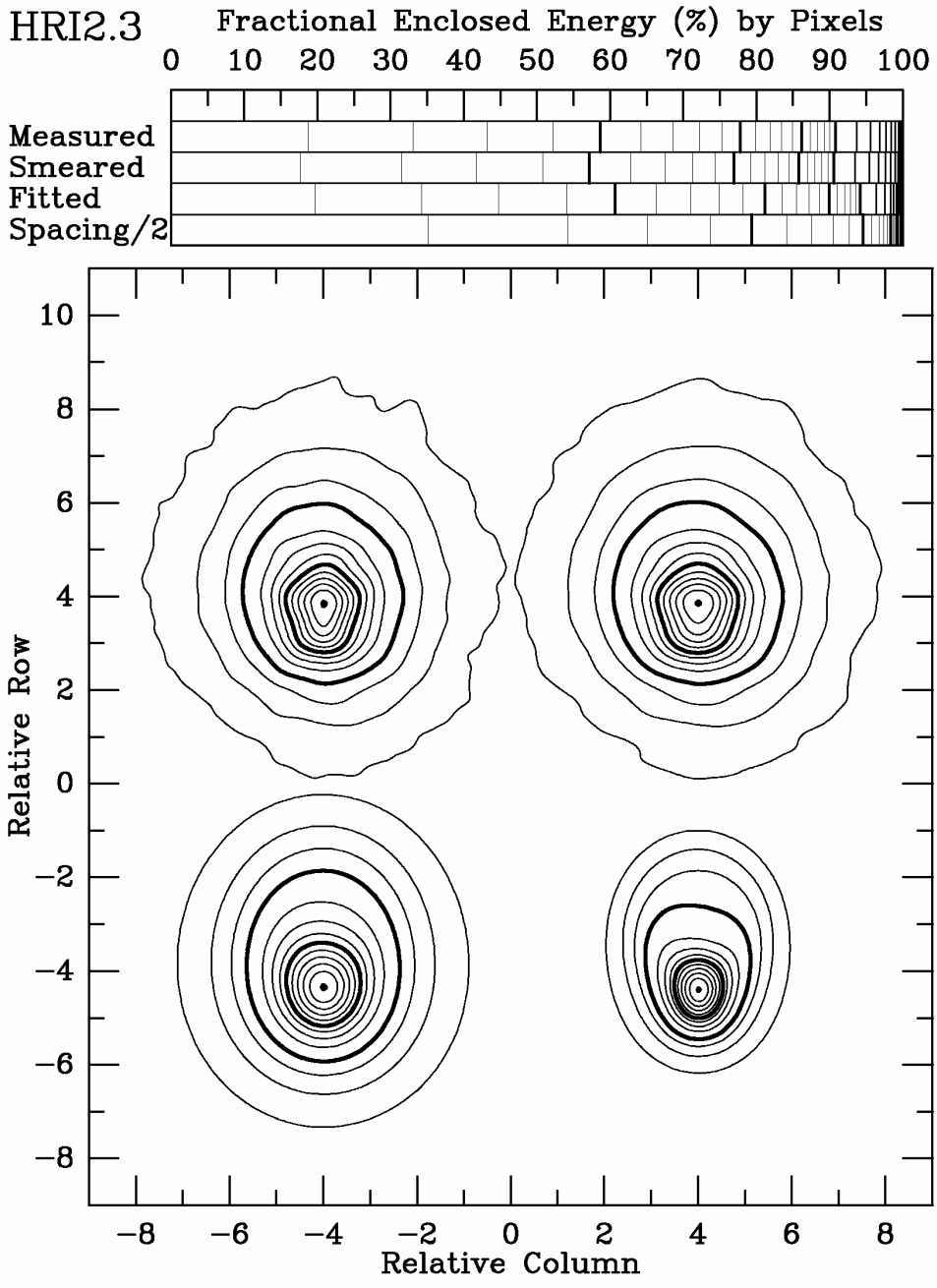
HRI2.3
Fractional Enclosed Energy (%) by Pixels
0 10 20 30 40 50 60 70 80 90 100
Measured
Smeared
Fitted
Spacing/2
10
8
6
4
2
0
−2
−4
−6
−8
Relative Row
−8 −6 −4 −2 0 2 4 6 8
Relative Column

Figure 3.0-25

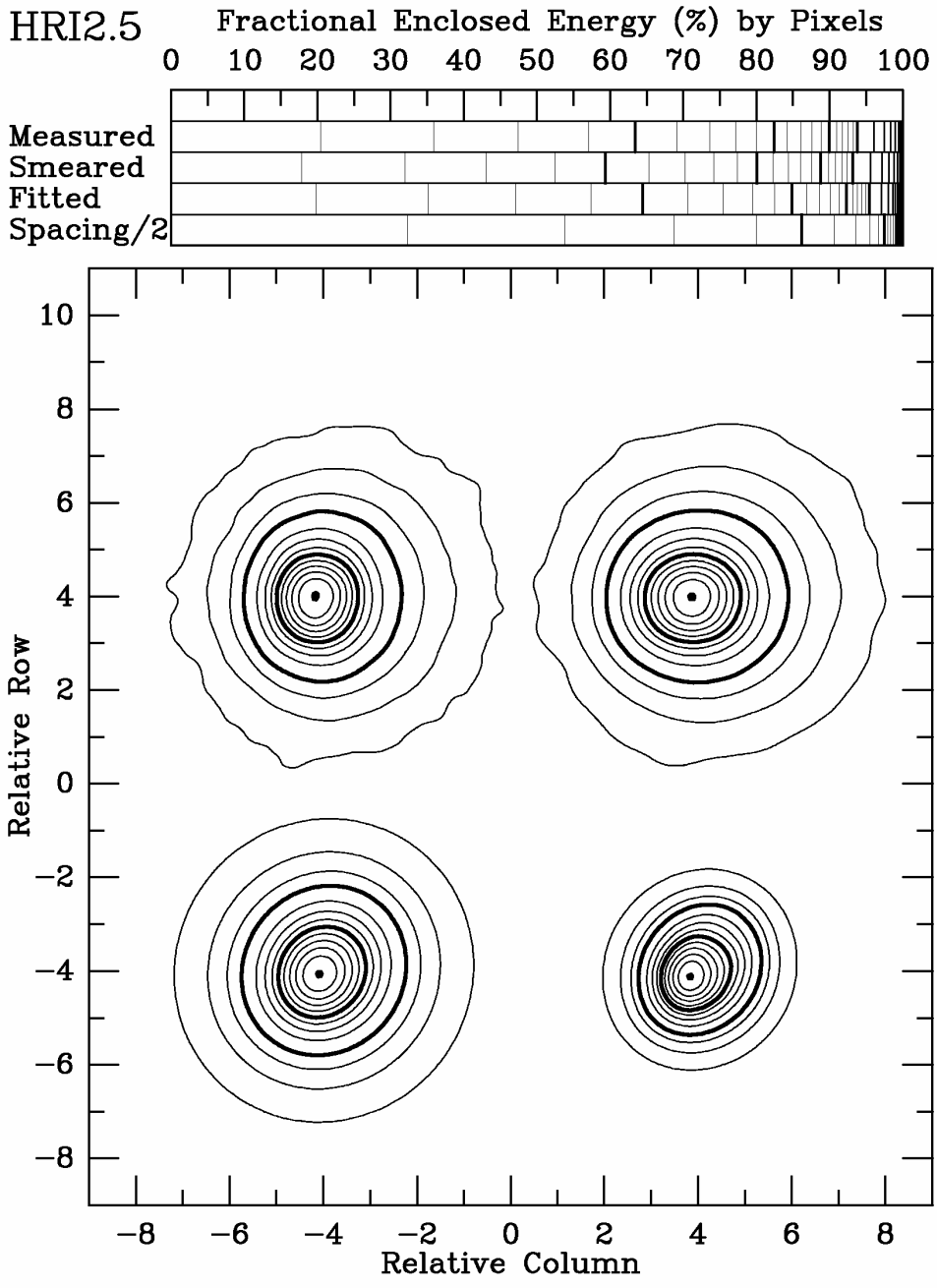
HRI2.5
Fractional Enclosed Energy (%) by Pixels
0 10 20 30 40 50 60 70 80 90 100
Measured
Smeared
Fitted
Spacing/2
10
8
6
4
2
0
−2
−4
−6
−8
Relative Row
−8 −6 −4 −2 0 2 4 6 8
Relative Column

Figure 3.0-26

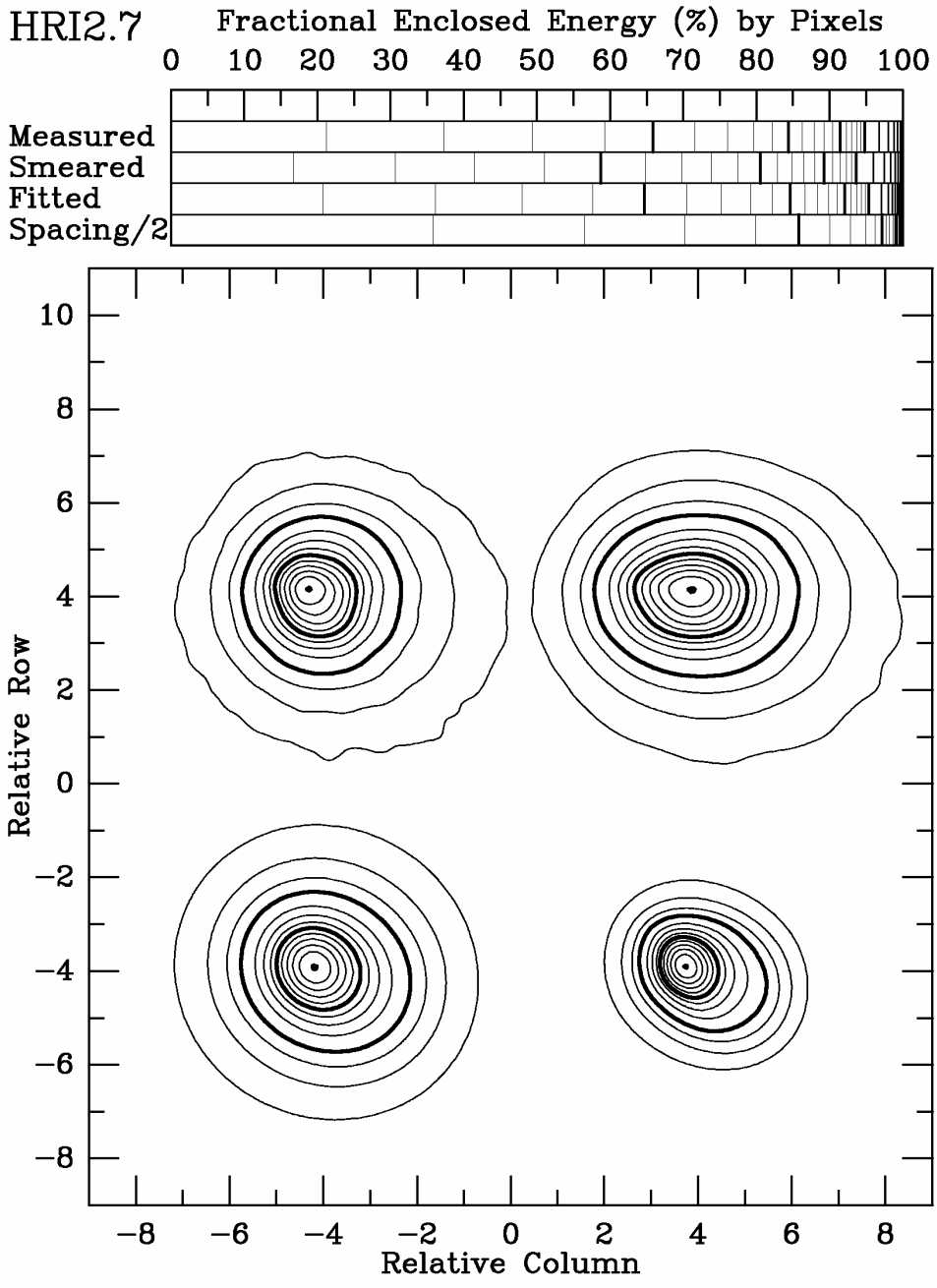
HRI2.7
Fractional Enclosed Energy (%) by Pixels
0 10 20 30 40 50 60 70 80 90 100
Measured
Smeared
Fitted
Spacing/2
10
8
6
4
2
0
−2
−4
−6
−8
Relative Row
−8 −6 −4 −2 0 2 4 6 8
Relative Column

Figure 3.0-27

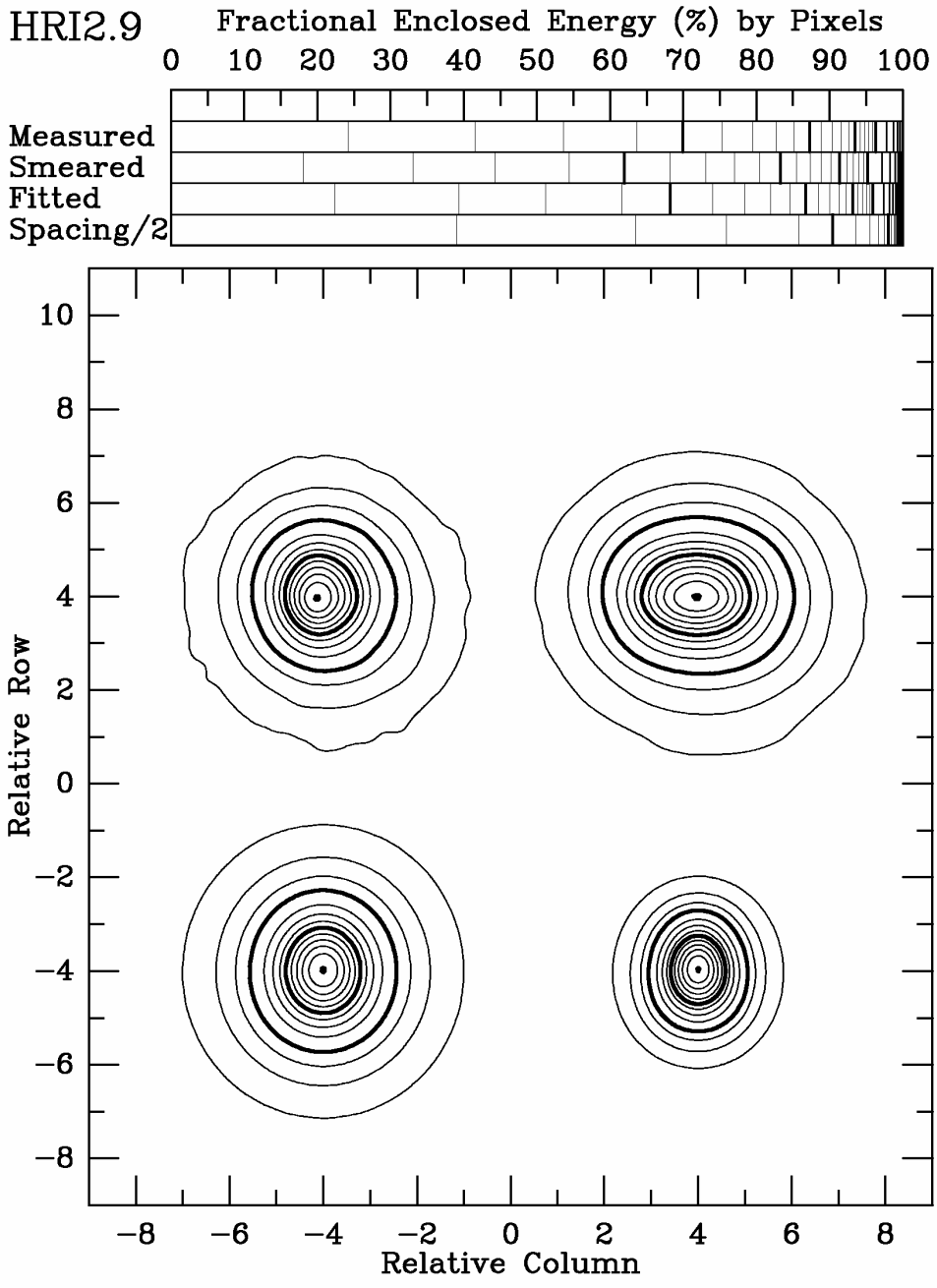
HRI2.9
Fractional Enclosed Energy (%) by Pixels
0 10 20 30 40 50 60 70 80 90 100
Measured
Smeared
Fitted
Spacing/2
10
8
6
4
2
0
−2
−4
−6
−8
Relative Row
−8 −6 −4 −2 0 2 4 6 8
Relative Column

Figure 3.0-28

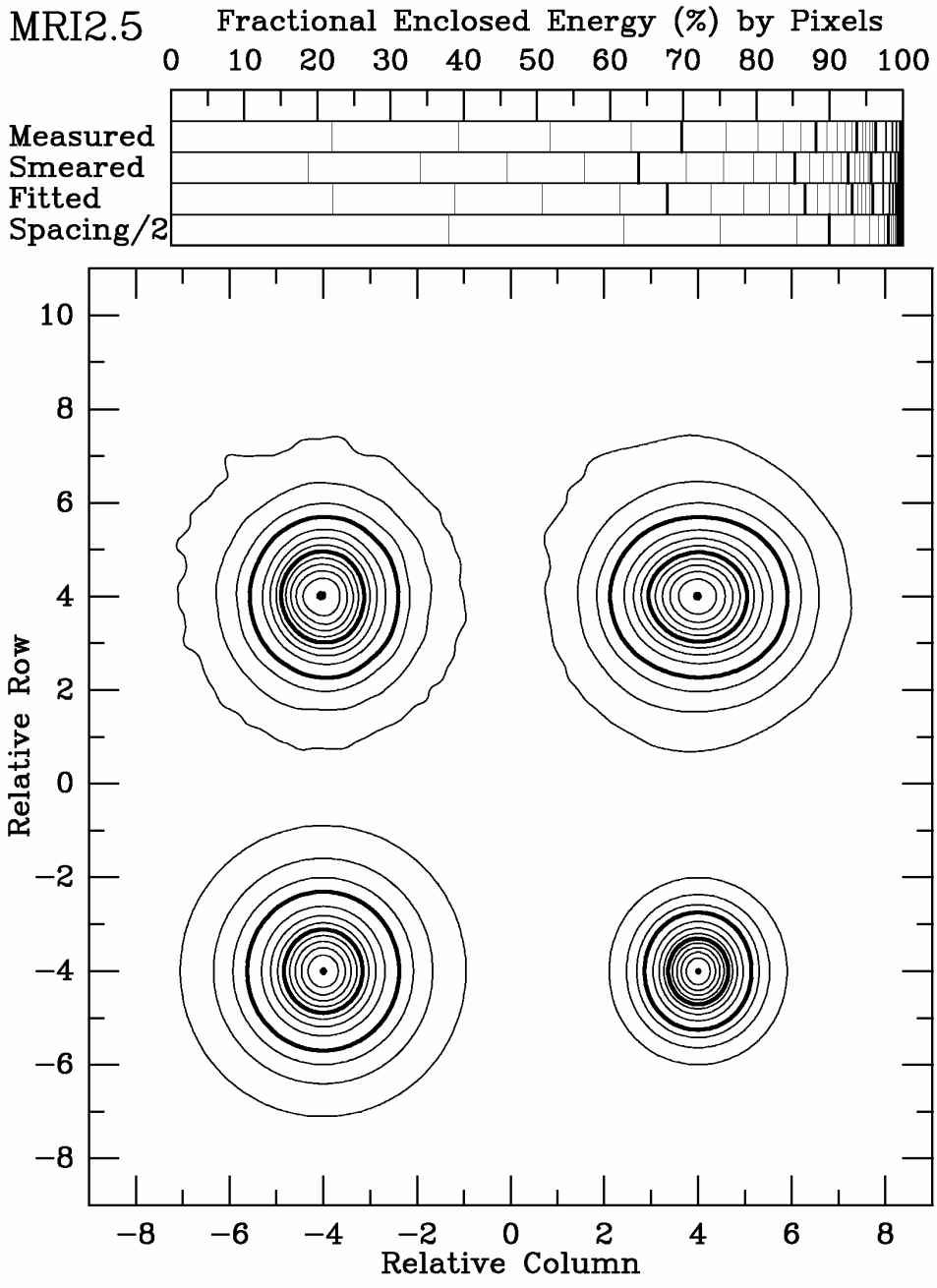
MRI2.5
Fractional Enclosed Energy (%) by Pixels
0 10 20 30 40 50 60 70 80 90 100
Measured
Smeared
Fitted
Spacing/2
10
8
6
4
2
0
−2
−4
−6
−8
Relative Row
−8 −6 −4 −2 0 2 4 6 8
Relative Column

Figure 3.0-29

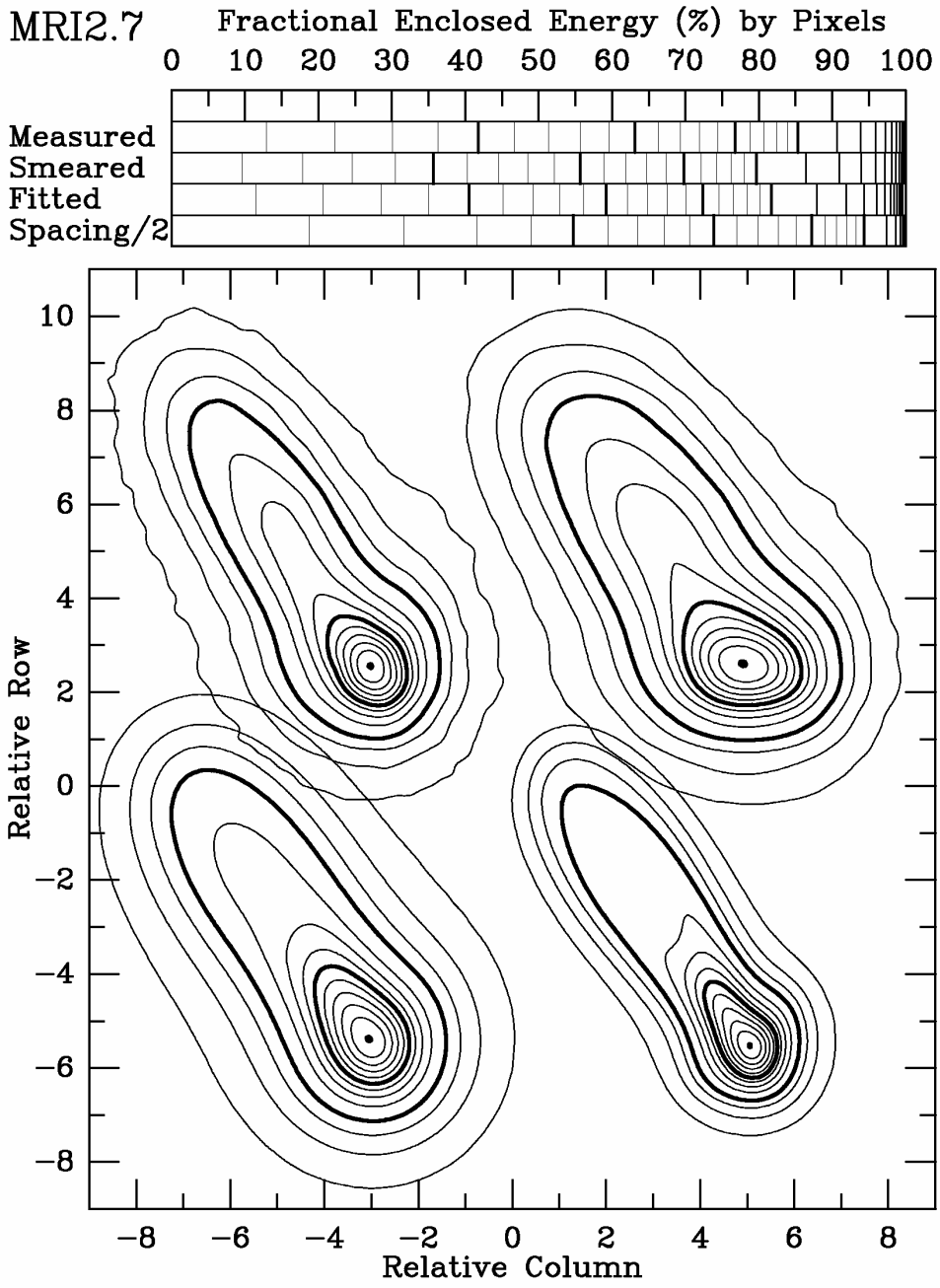
MRI2.7
Fractional Enclosed Energy (%) by Pixels
0 10 20 30 40 50 60 70 80 90 100
Measured
Smeared
Fitted
Spacing/2
Relative Row
Relative Column
10
8
6
4
2
0
−2
−4
−6
−8
−8 −6 −4 −2 0 2 4 6 8

Figure 3.0-30

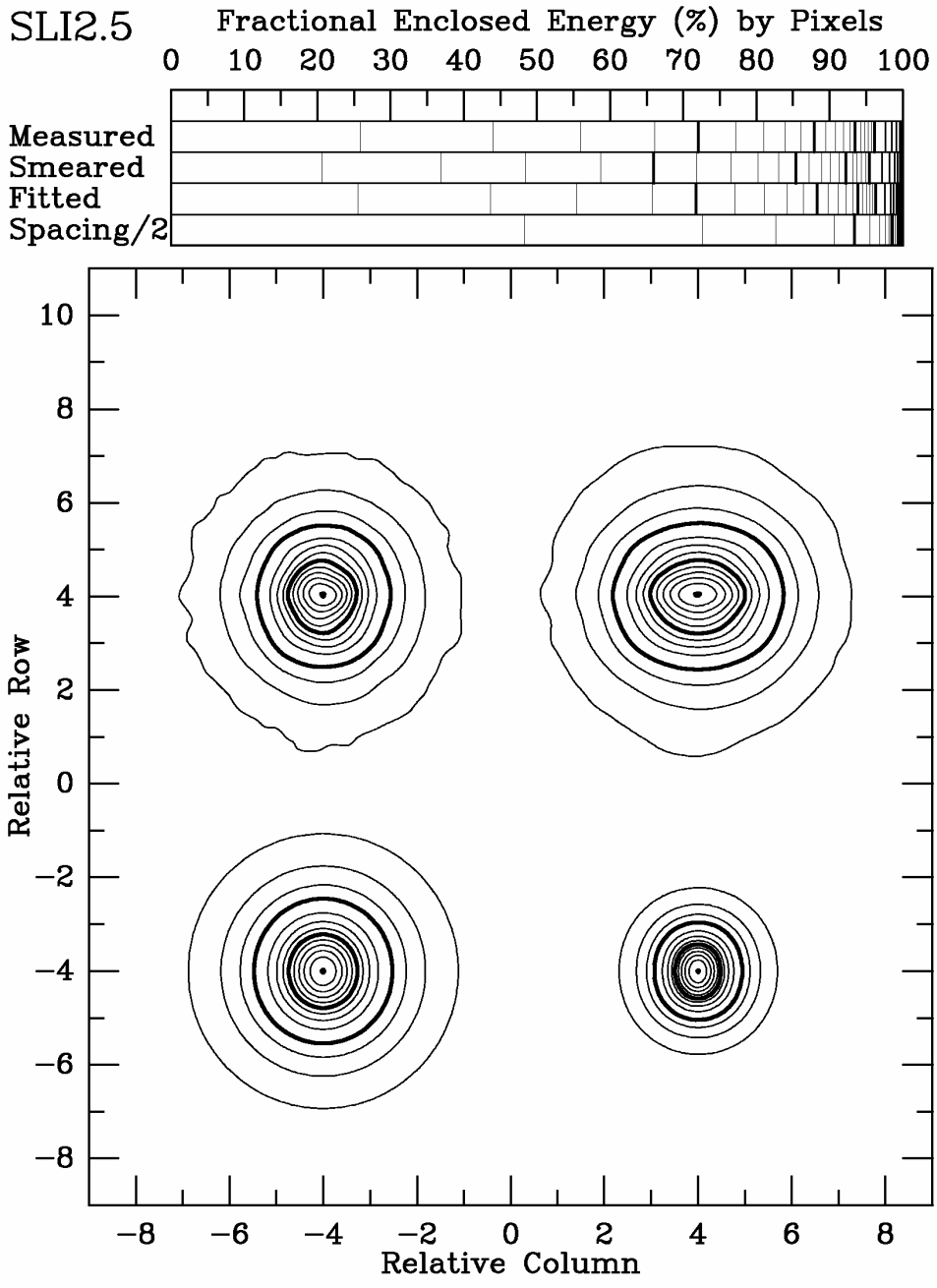
SLI2.5
Fractional Enclosed Energy (%) by Pixels
0 10 20 30 40 50 60 70 80 90 100
Measured
Smeared
Fitted
Spacing/2
10
8
6
4
2
0
−2
−4
−6
−8
Relative Row
−8 −6 −4 −2 0 2 4 6 8
Relative Column

Figure 3.0-31

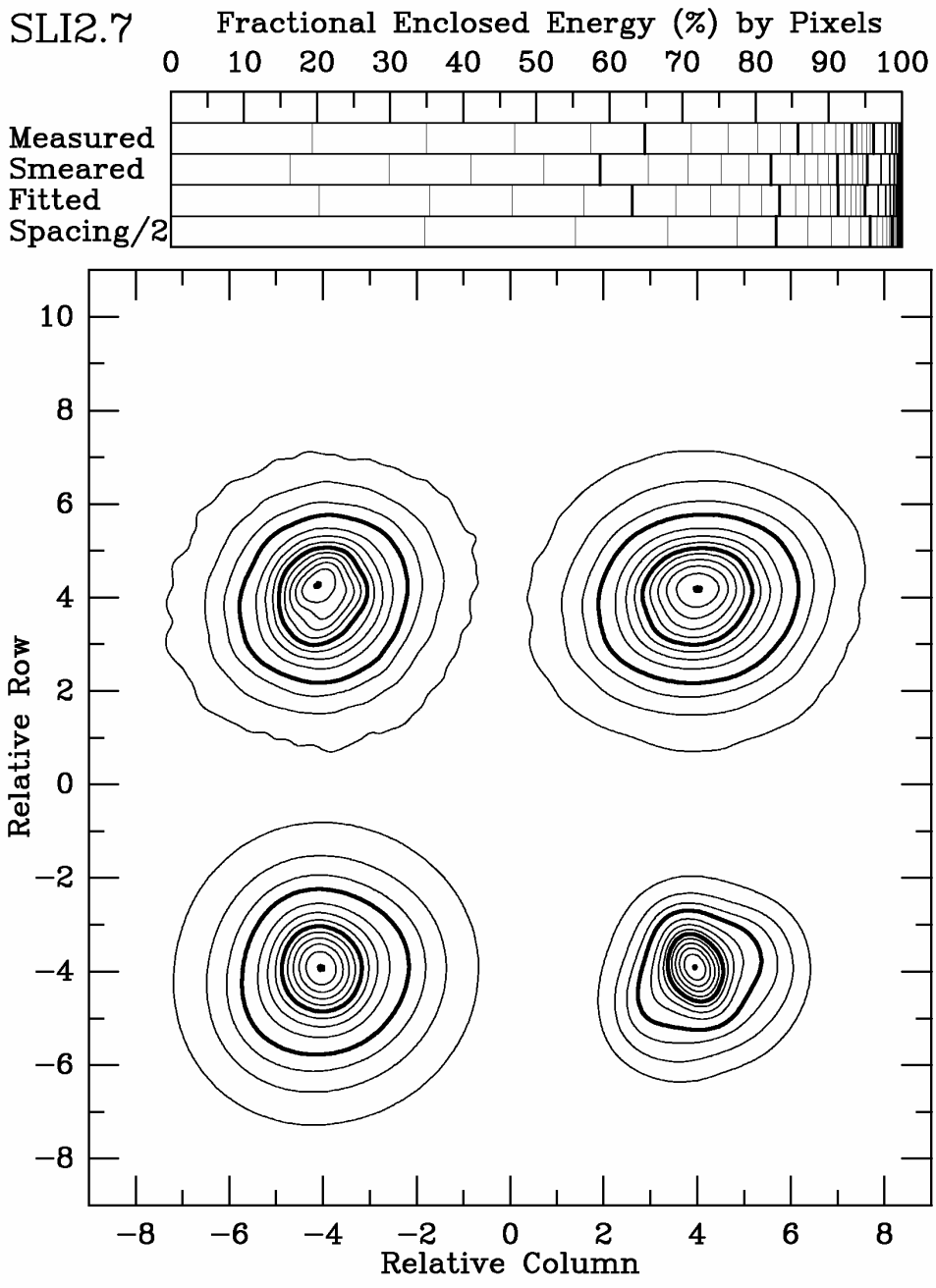
SLI2.7
Fractional Enclosed Energy (%) by Pixels
0 10 20 30 40 50 60 70 80 90 100
Measured
Smeared
Fitted
Spacing/2
10
8
6
4
2
0
−2
−4
−6
−8
Relative Row
−8 −6 −4 −2 0 2 4 6 8
Relative Column

Figure 3.0-32

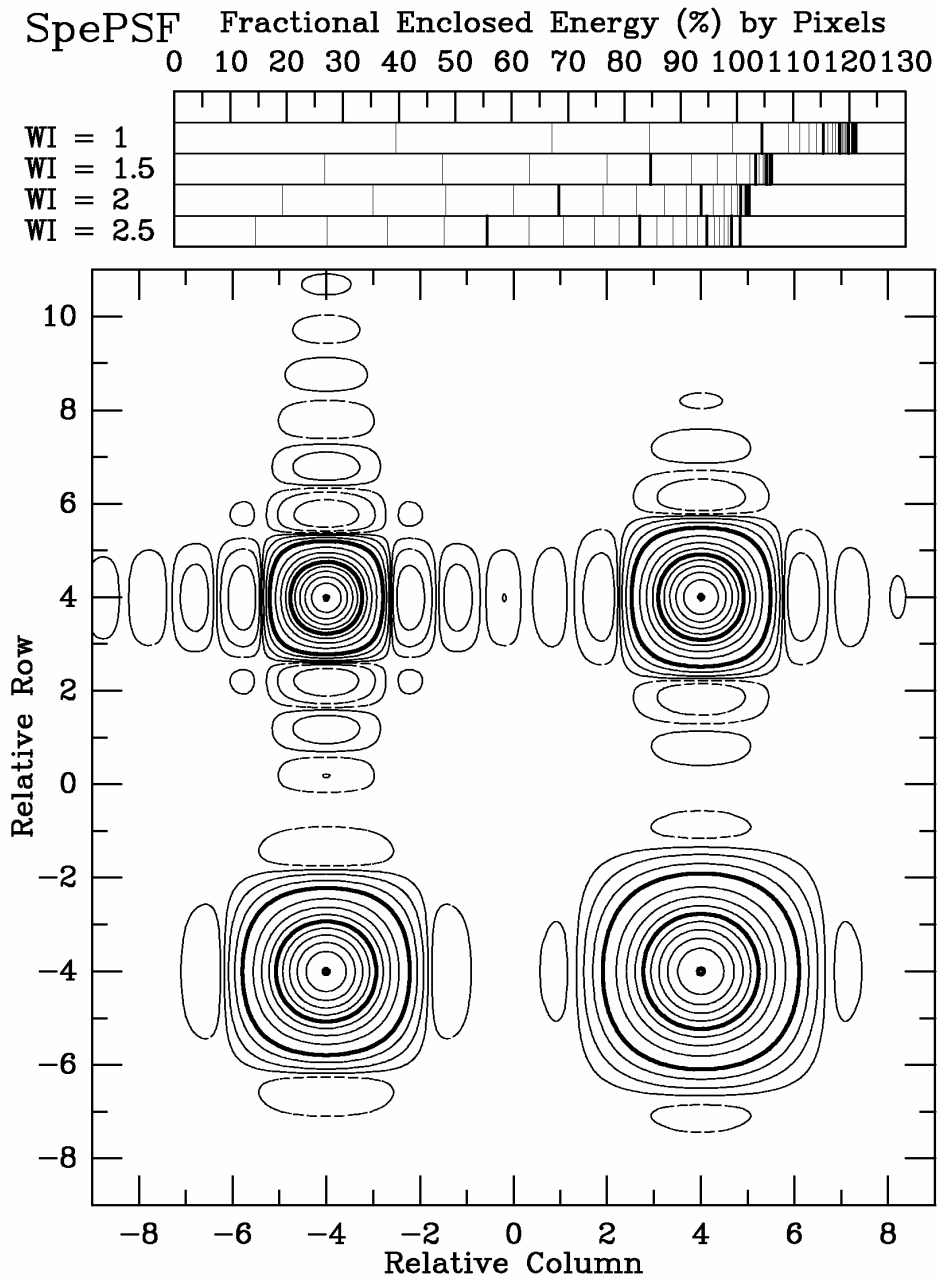

Figures 3.0-33 to 3.0-35 Fractional Enclosed Energy (%) by Pixels for the PSFs after deconvolution. The display is the same as in Figs. 5-32. SpePSF is the specified PSF in the deconvolution program for the widths 1, 1.5, 2, and 2.5. SLI3.c is the actual PSF after deconvolution in the center of the SLI3. It is slightly different because the SLI3 PSF does not contain all frequencies with the required amplitude for the deconvolution with limited amplitude boosts. MRI3.e is the actual PSF after deconvolution in the corner of the MRI3. It is quite different because the MRI3 PSF does not contain many frequencies with the required amplitude for the deconvolution with limited amplitude boosts.

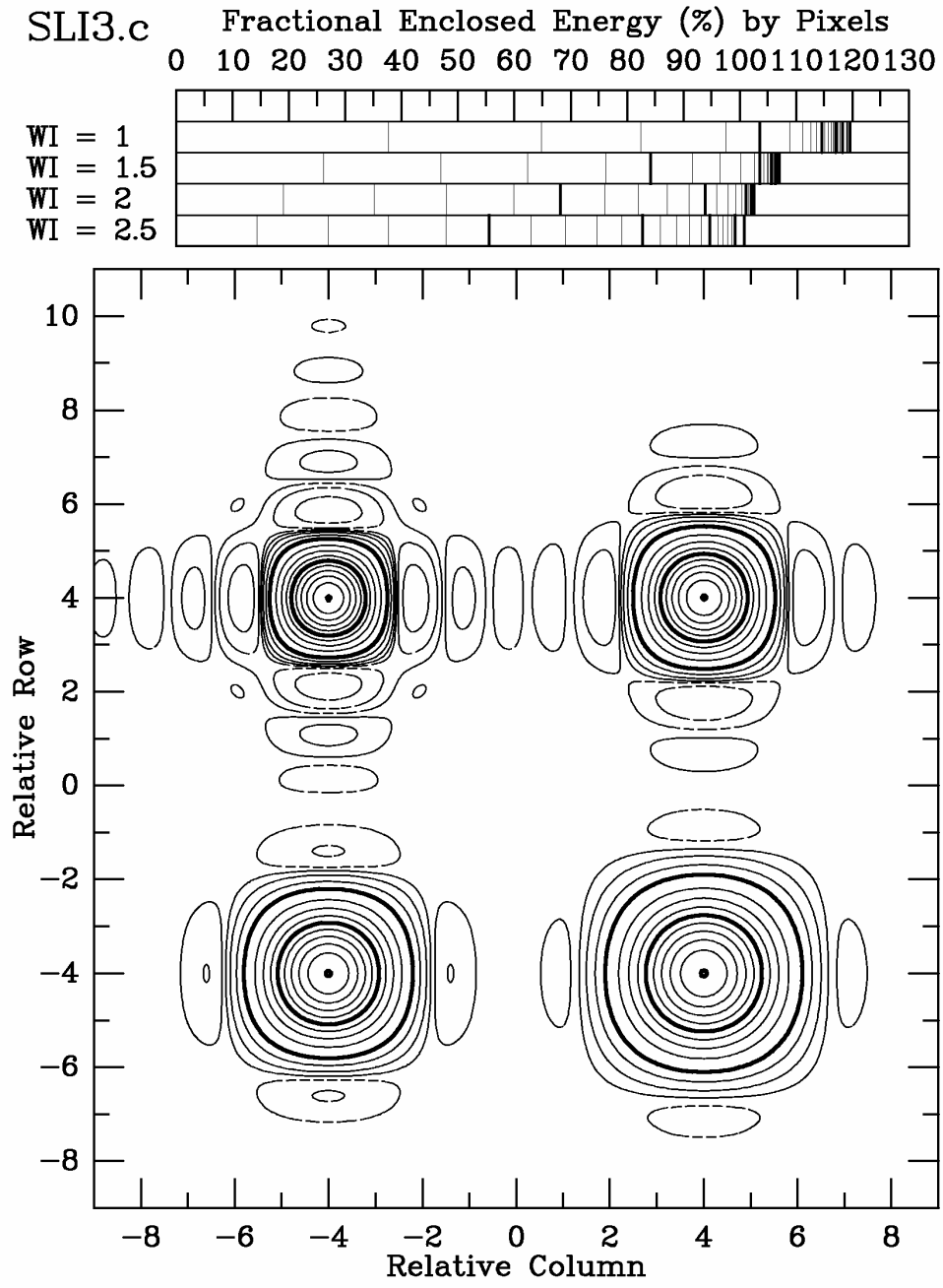
SLI3.c
Fractional Enclosed Energy (%) by Pixels
0 10 20 30 40 50 60 70 80 90 100 110 120 130
WI = 1
WI = 1.5
WI = 2
WI = 2.5
Relative Row
Relative Column
10
8
6
4
2
0
−2
−4
−6
−8
−8 −6 −4 −2 0 2 4 6 8

Figure 3.0-34

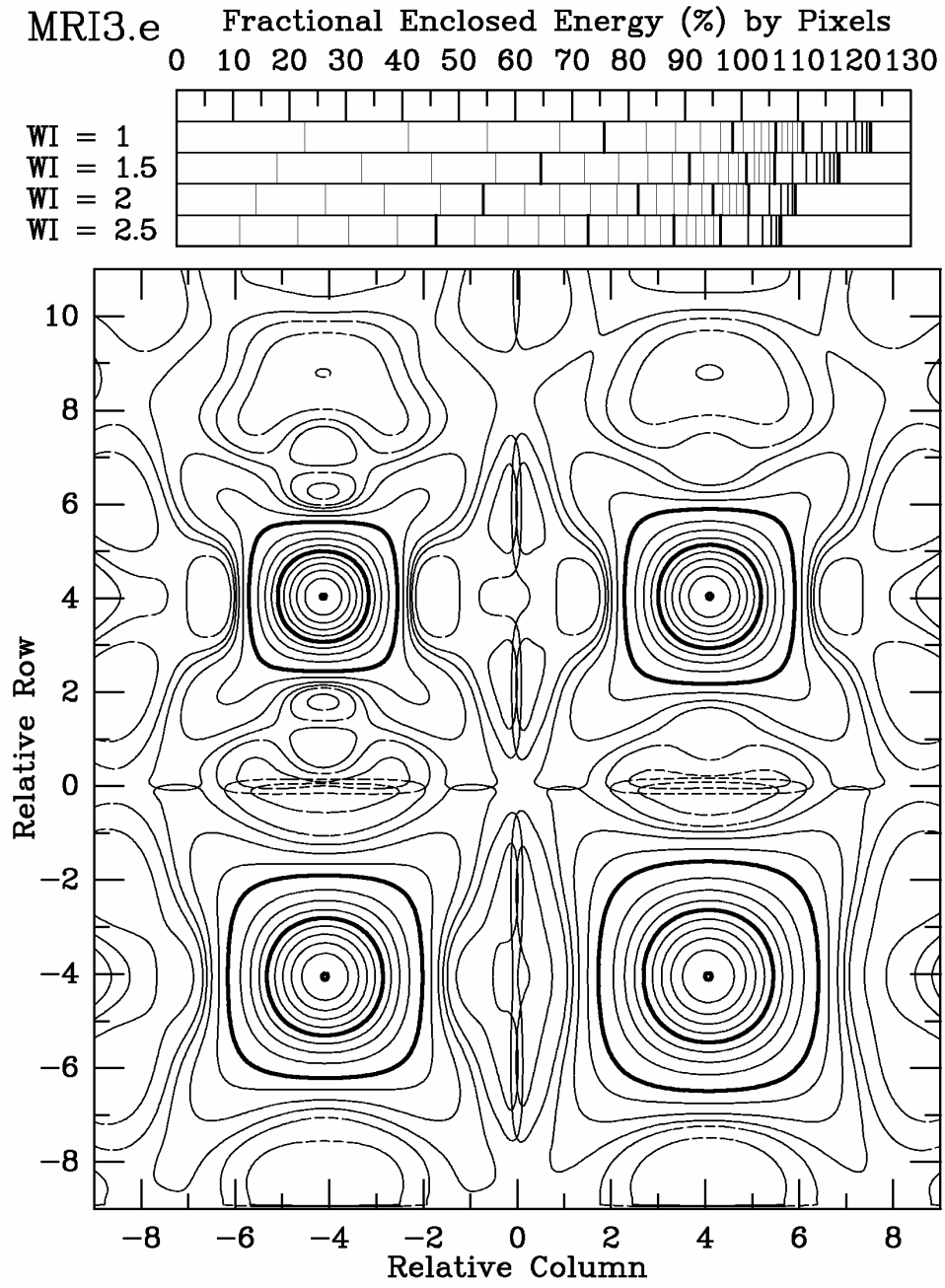
MRI3.e
Fractional Enclosed Energy (%) by Pixels
0 10 20 30 40 50 60 70 80 90 100110120130
WI = 1
WI = 1.5
WI = 2
WI = 2.5
Relative Row
Relative Column
10
8
6
4
2
0
−2
−4
−6
−8
−8 −6 −4 −2 0 2 4 6 8

Figure 3.0-35

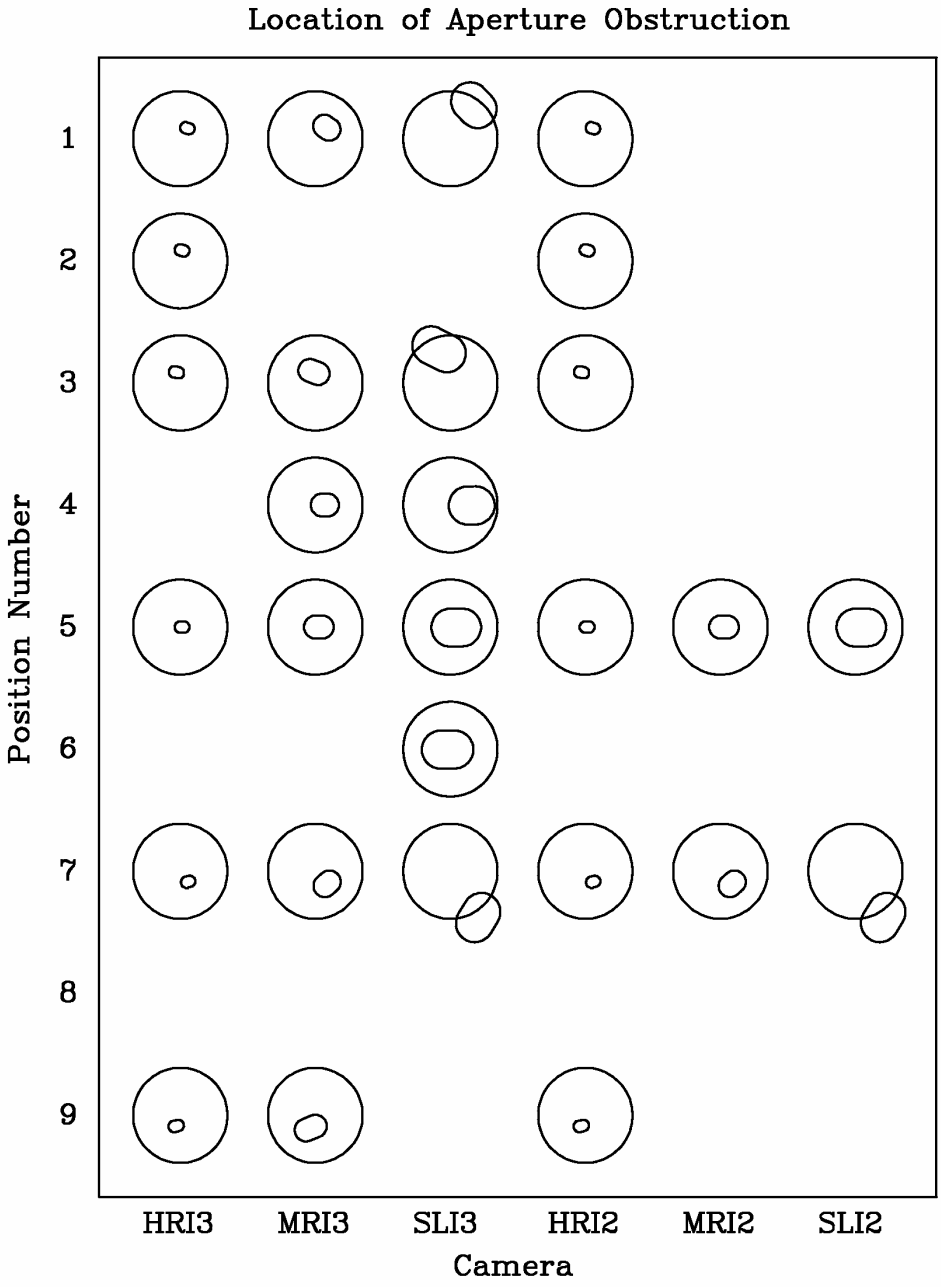

Figure 3.0-36 Location of Aperture Obstruction. For each of the 28 measured PSF locations, the location of the aperture obstruction is shown according to the design. The fitting of the observed PSFs suggested that the actual locations may be slightly different although other effects such as slight lens misalignments could cause similar deviations.

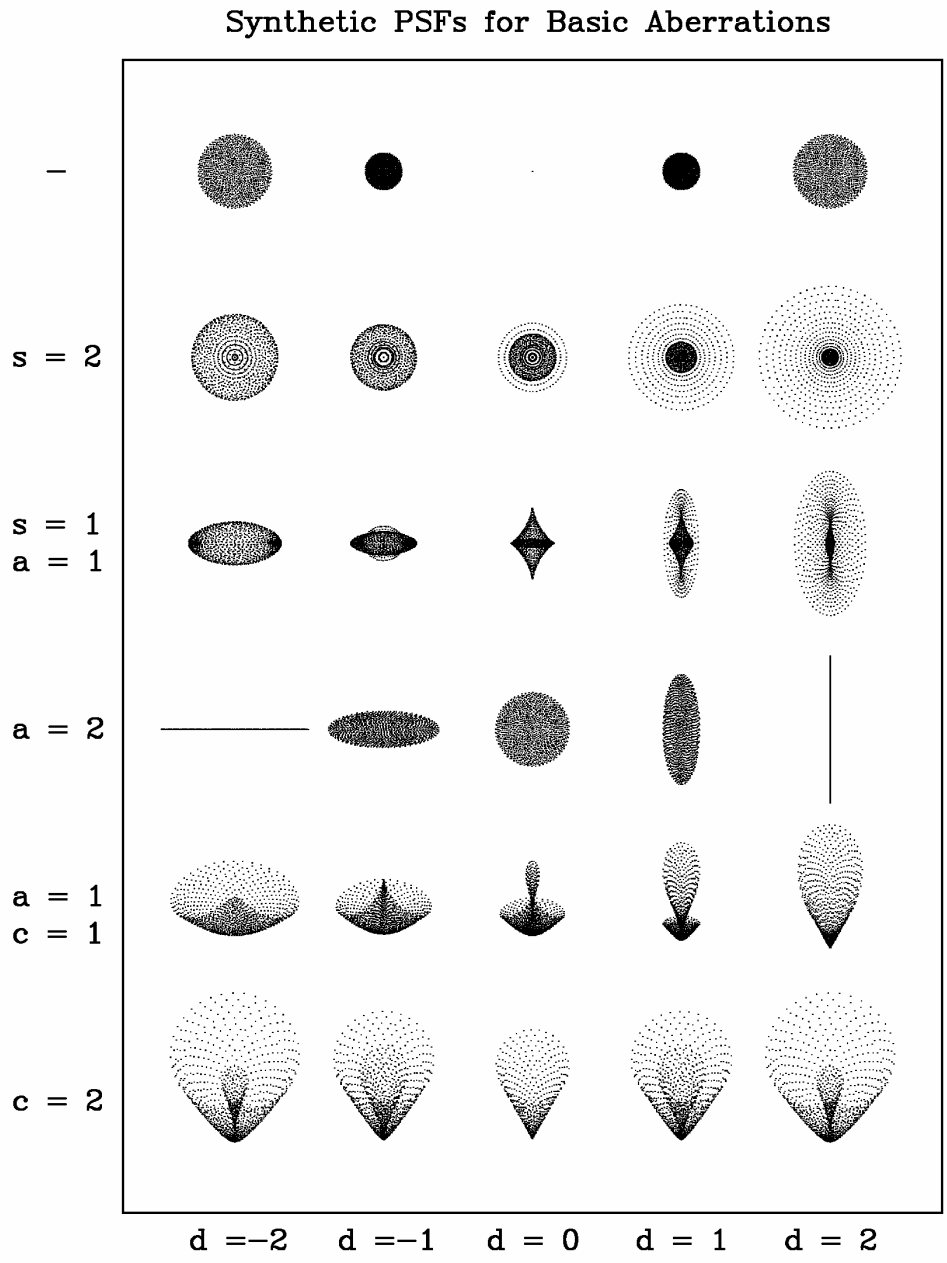

Figure 3.0-37 Synthetic PSFs for Basic Aberrations. Displayed are spot diagrams without aperture obstructions. The central column is the focused image while the left and right columns show it defocused on either side. The top row is for a perfect system. The second, fourth, and sixth rows show spherical aberration, astigmatism, and coma, respectively. The rows in between show the mix of two aberrations.

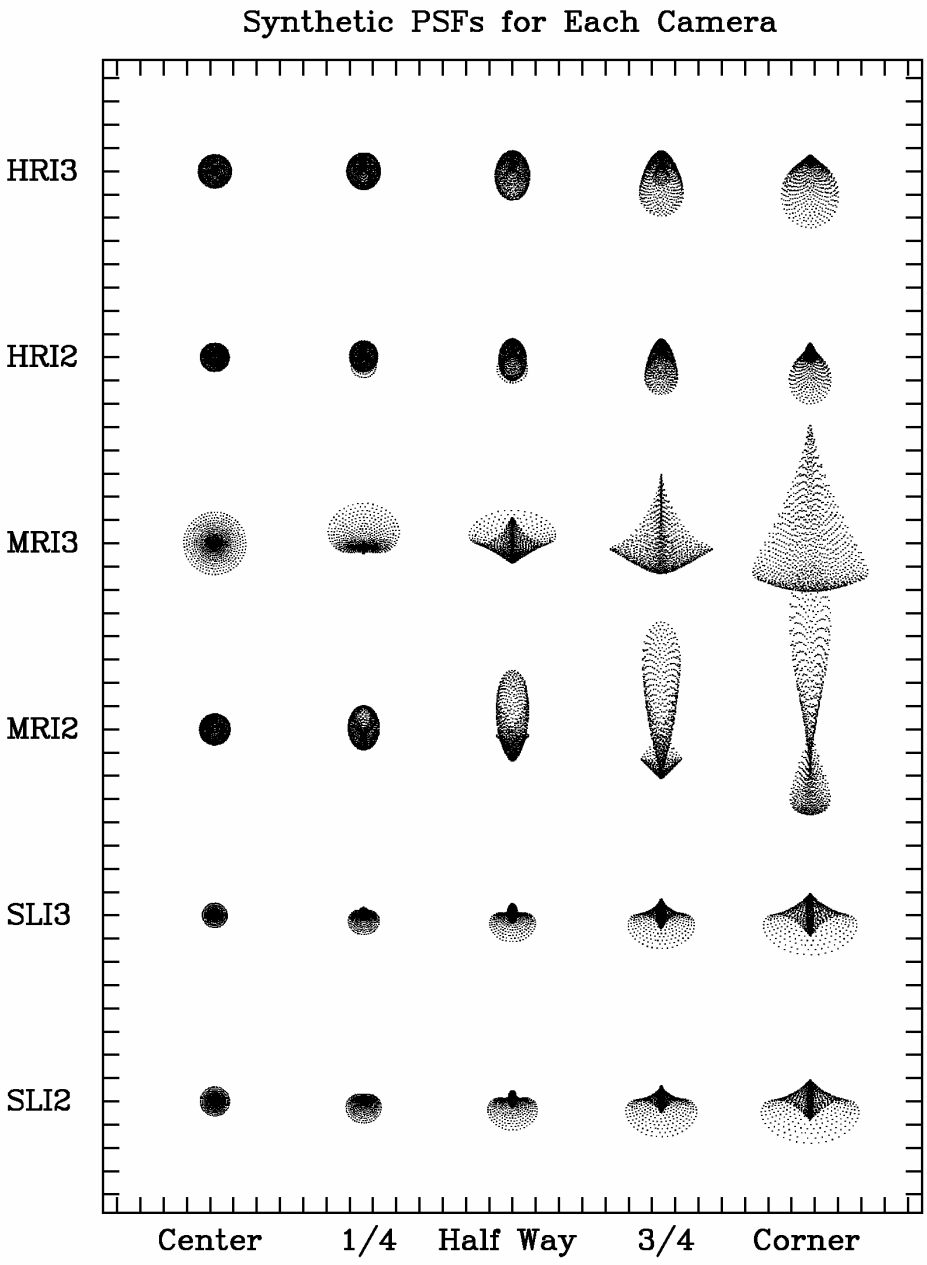

Figure 3.0-38 Synthetic PSFs for Each Camera. Spot diagrams are displayed for each camera and for five equally spaced positions from the optical axis to the corner of the field of view. No obstruction is included. The image plane is assumed to be perpendicular to the optical axis for this plot. The tick marks show the size of pixels.

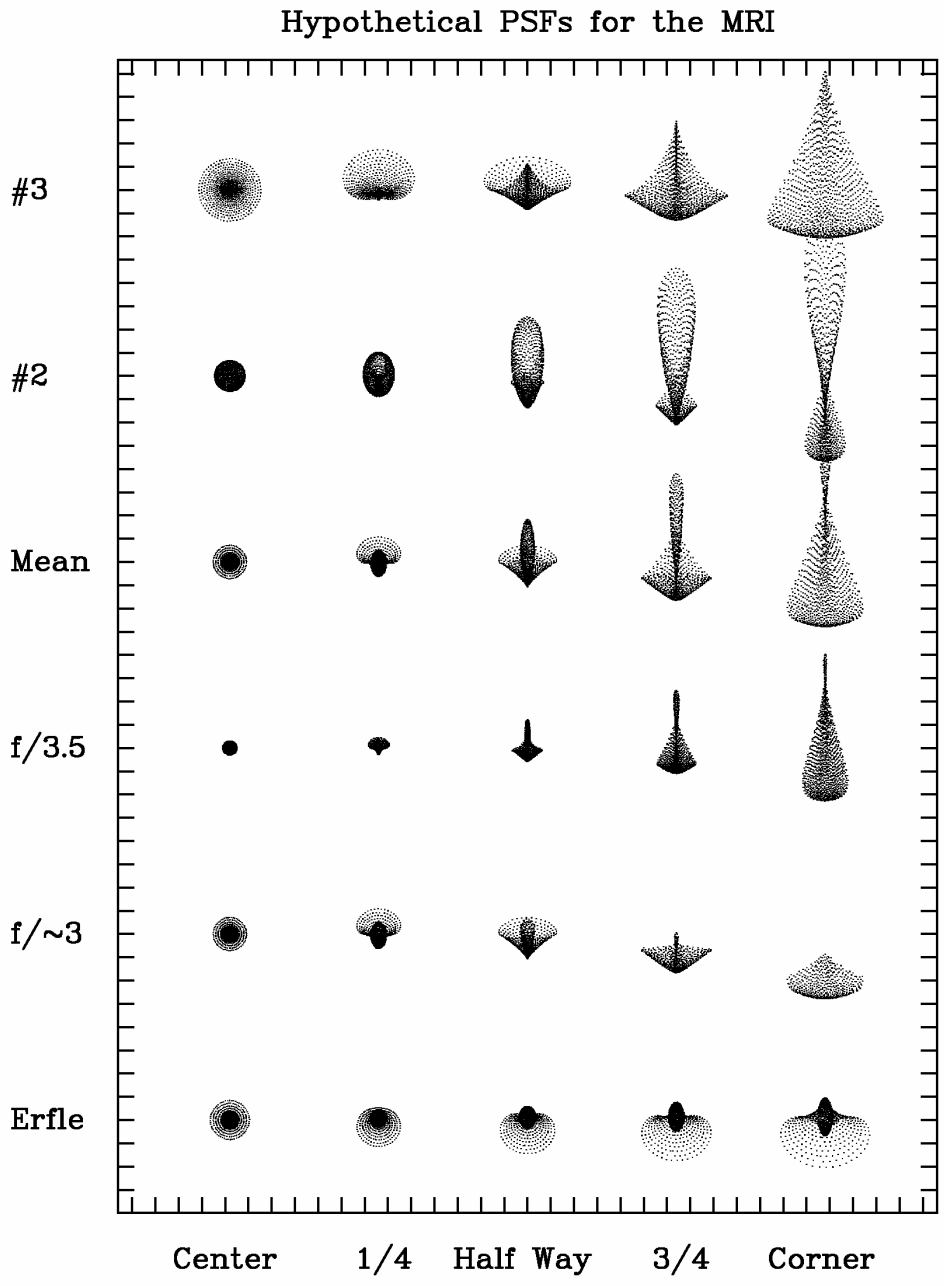

Figure 3.0-39 Hypothetical PSFs for the MRI. Spot diagrams as in Fig. 38 but for various designs of the MRI, from top to bottom: MRI3, MRI2, focus parameters half way between those of the MRI3 and MRI2, the same for the system stopped down to f/3.5, a design with two f/2.5 field stops (the additional stop is placed such that the central beam in the actual stop grazes the edge of the additional stop for the corner of the field,

which causes vignetting and thus an average effective f/3), and a design with an Erfle eyepiece as for the SLI.

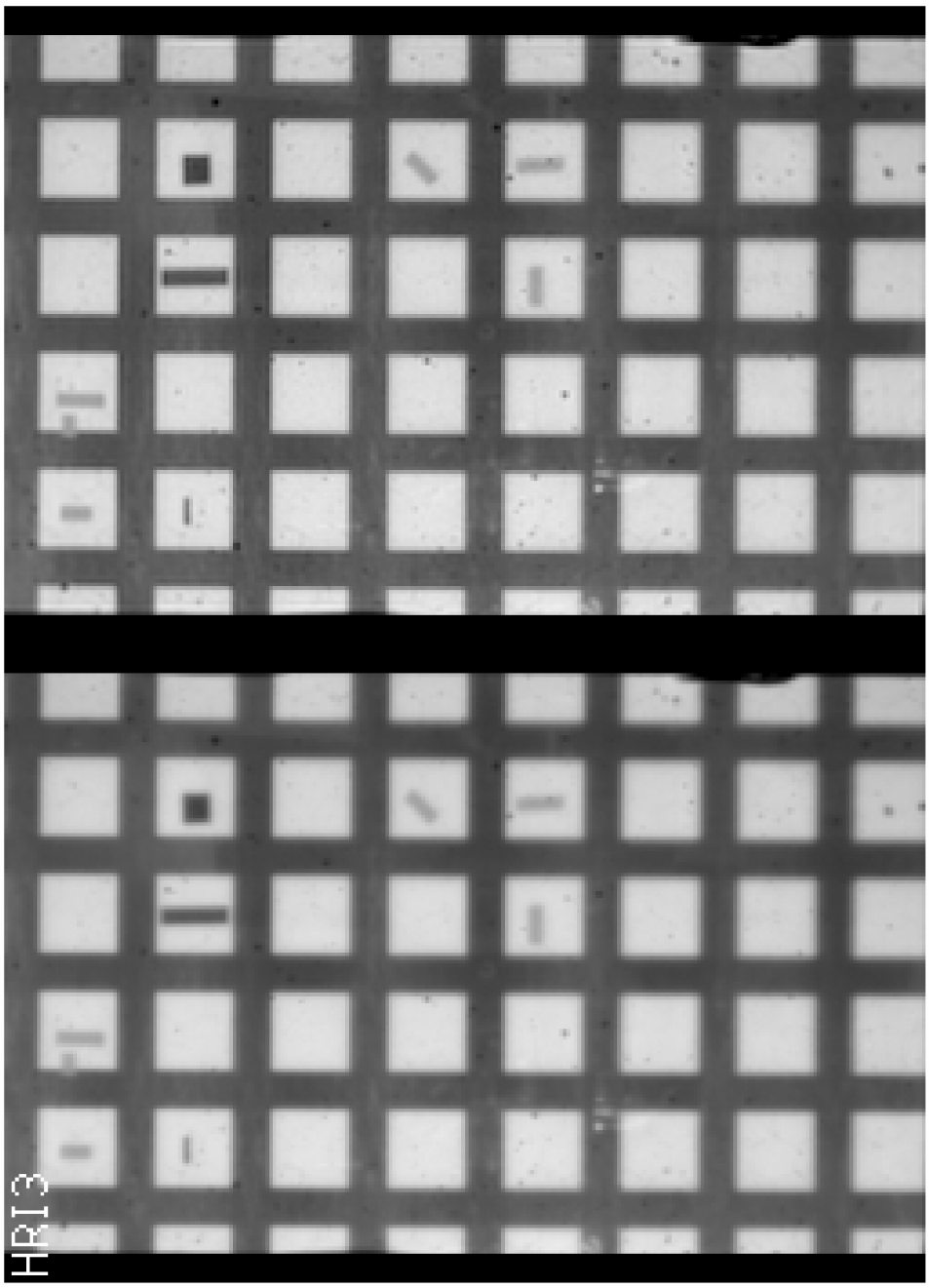

Figures 3.0-40 to 3.0-54: Examples of original images (top) and deconvolved images (bottom) with the width set at 1.0 (center) and 1.5 (corner). The geometric pattern of SLI3 comes in four versions, smeared by 0, 2, 3, and 4 pixels, respectively, and the deconvolution included similar amount of smear.

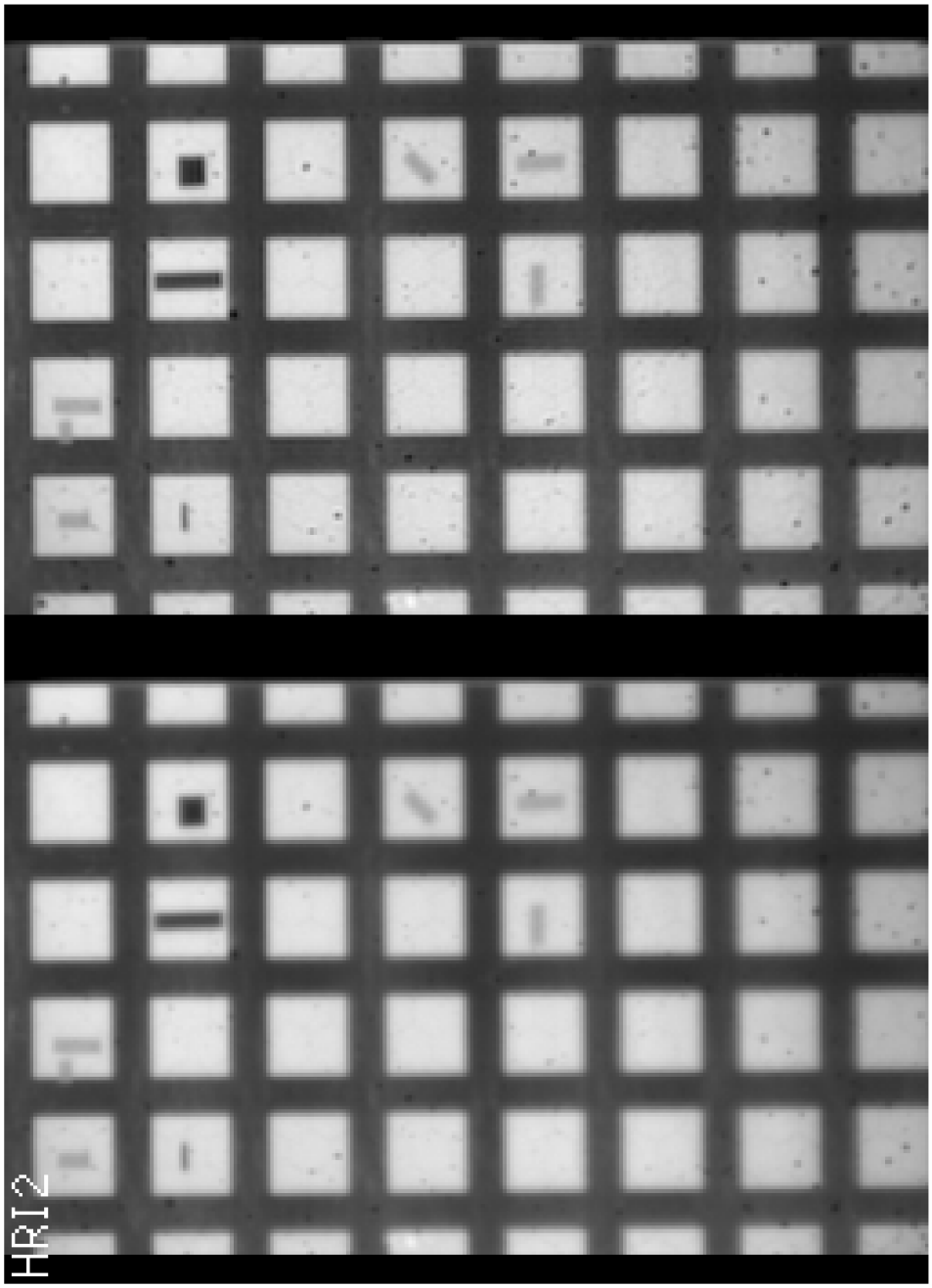

Figure 3.0-41

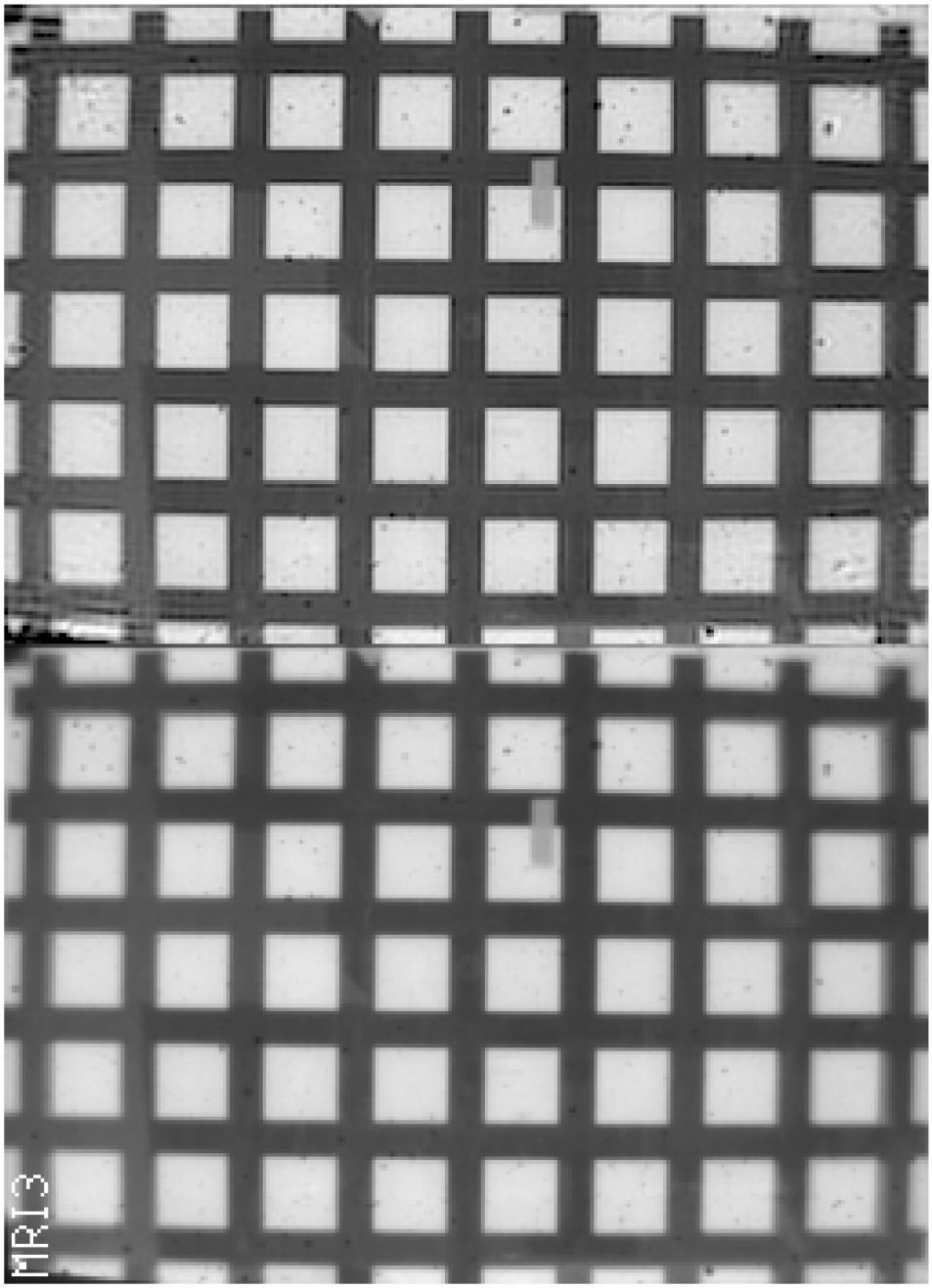

Figure 3.0-42

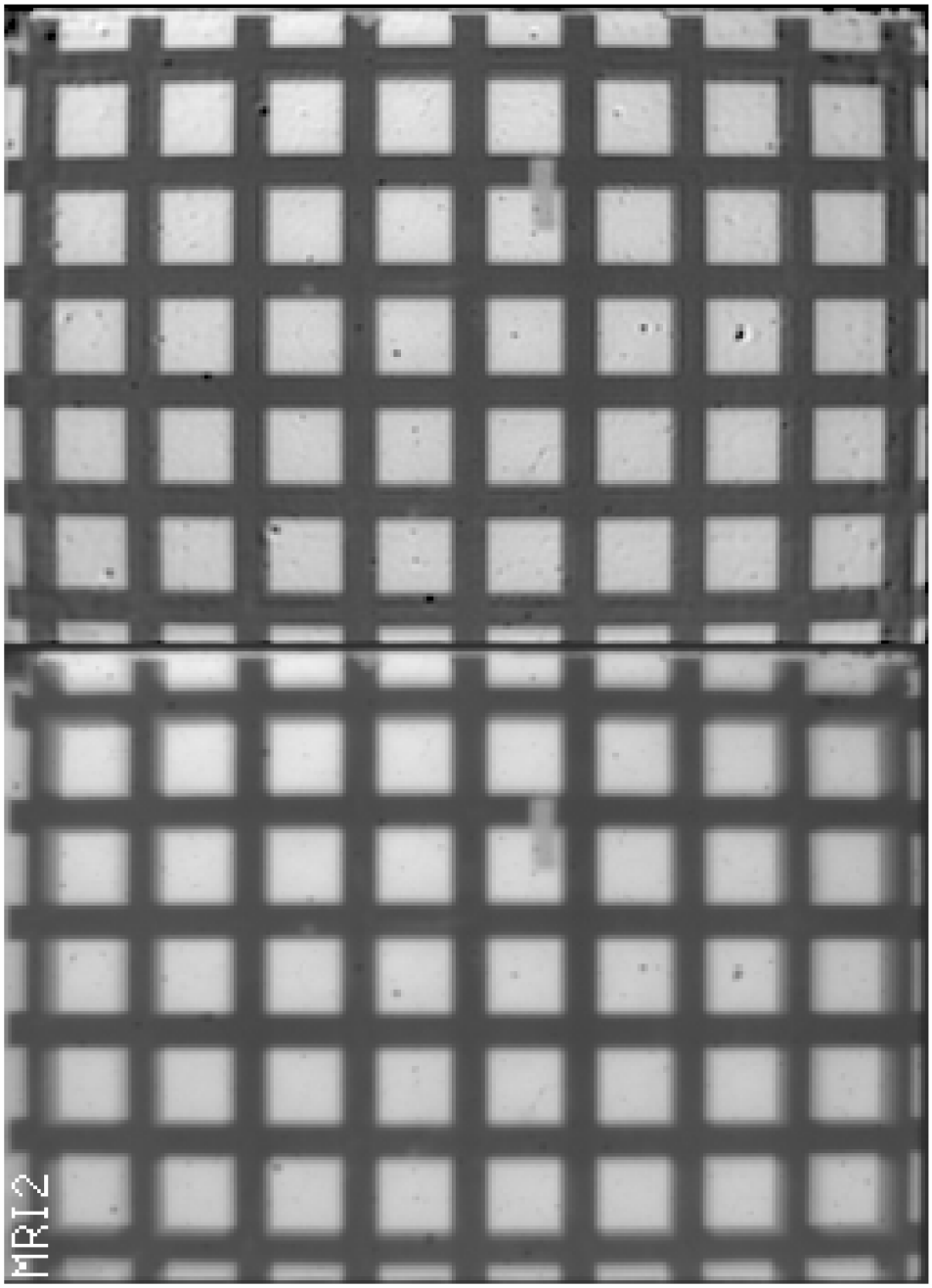

Figure 3.0-43

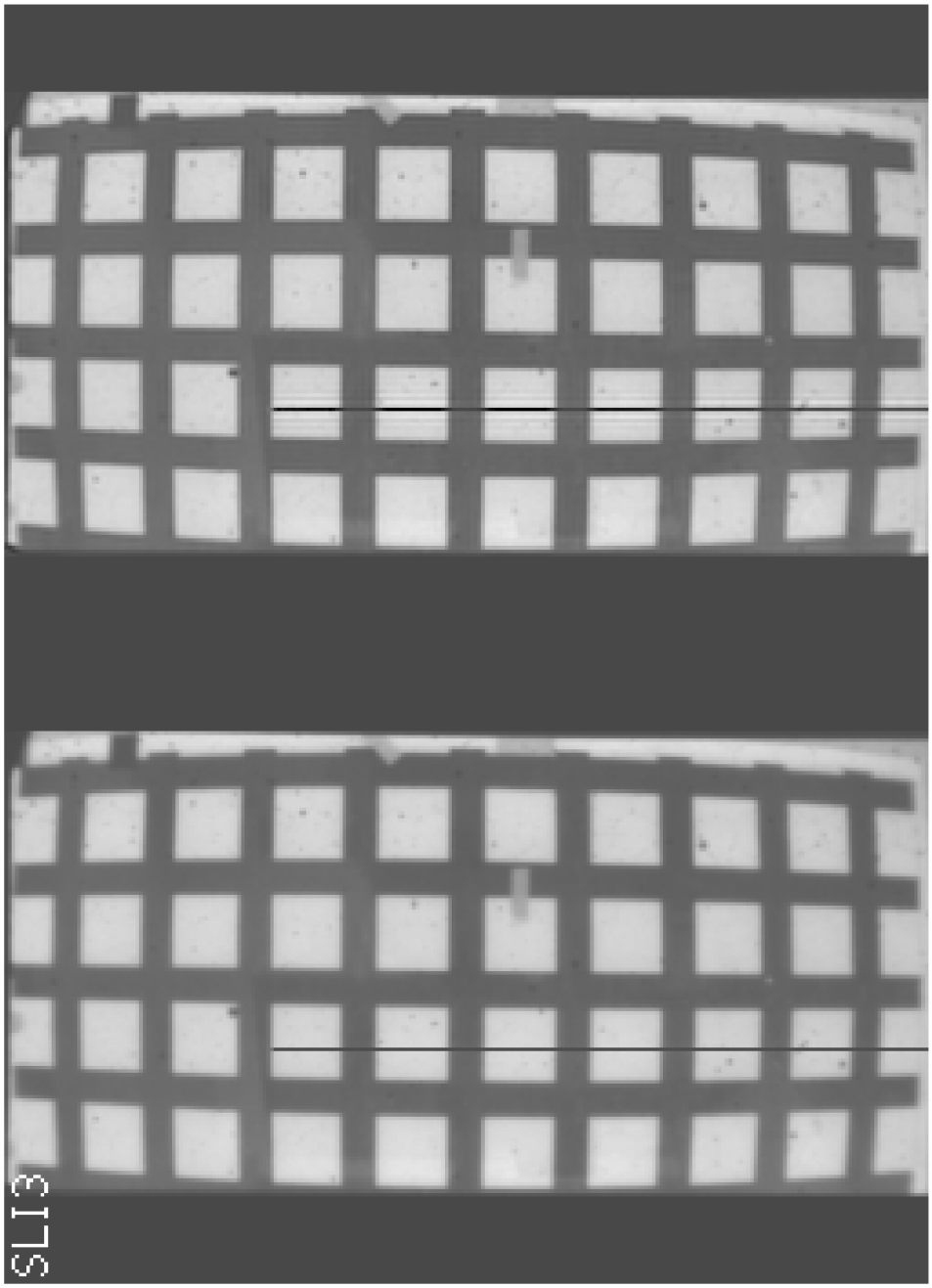

Figure 3.0-44

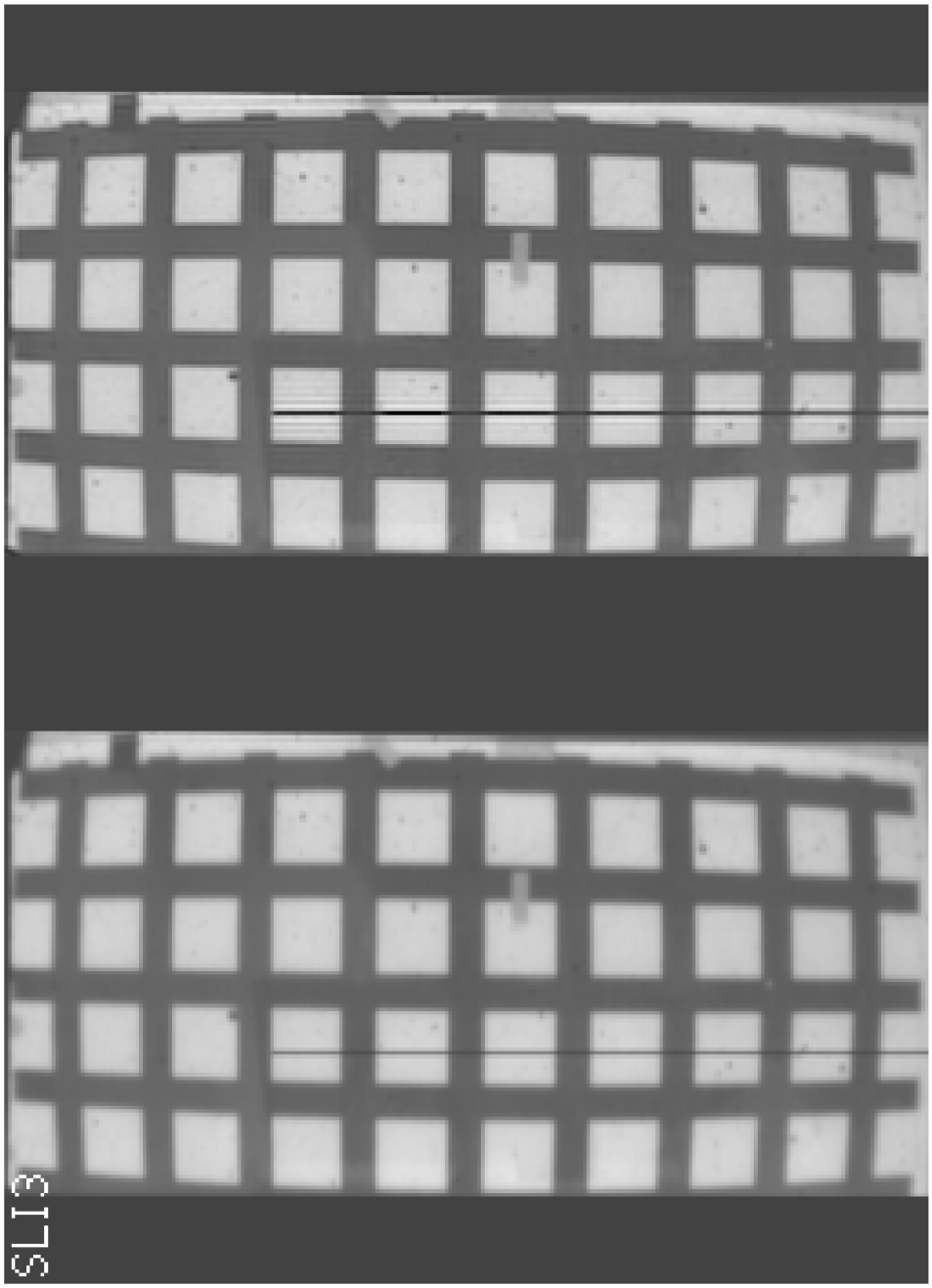

Figure 3.0-45

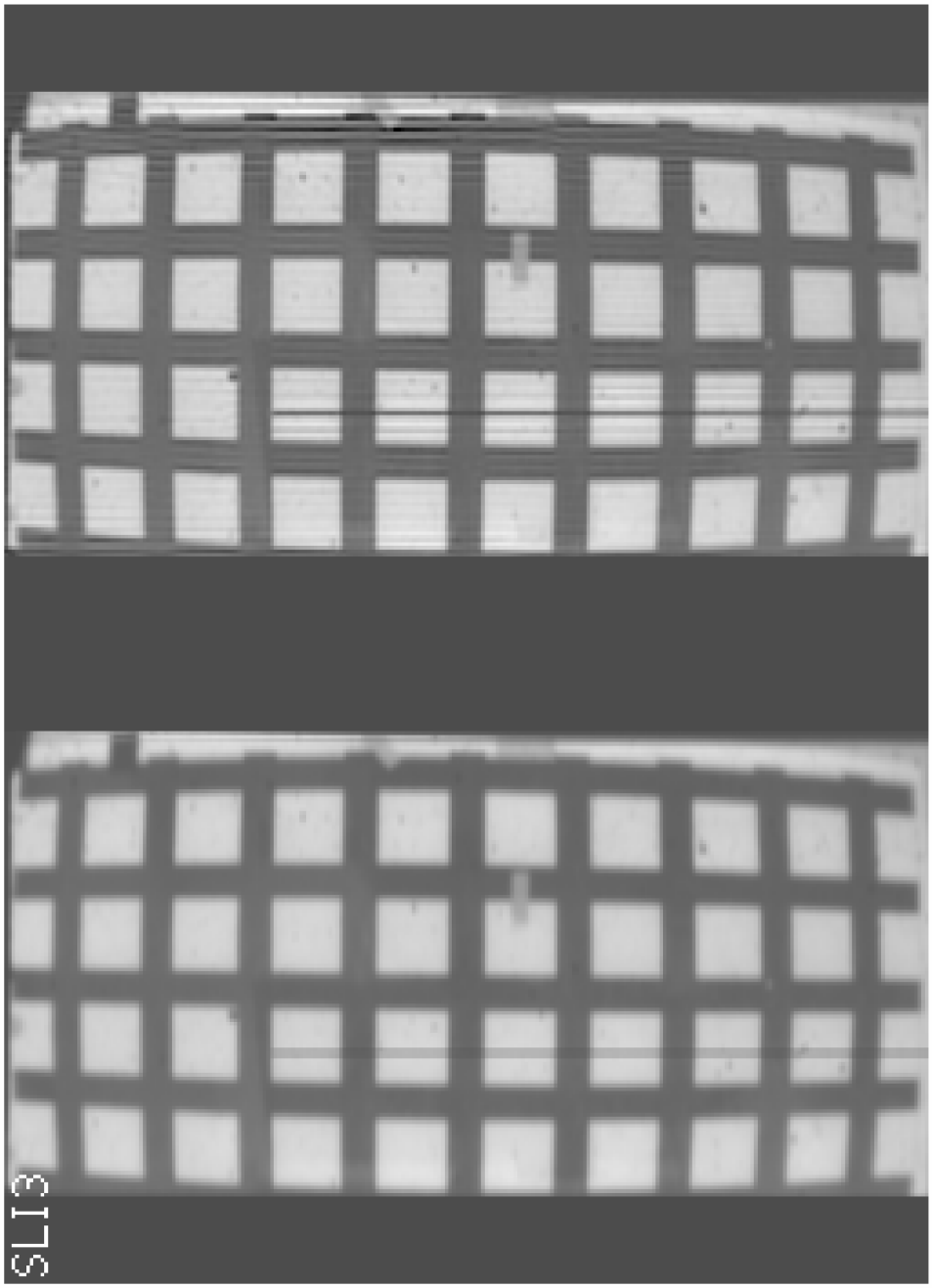

Figure 3.0-46

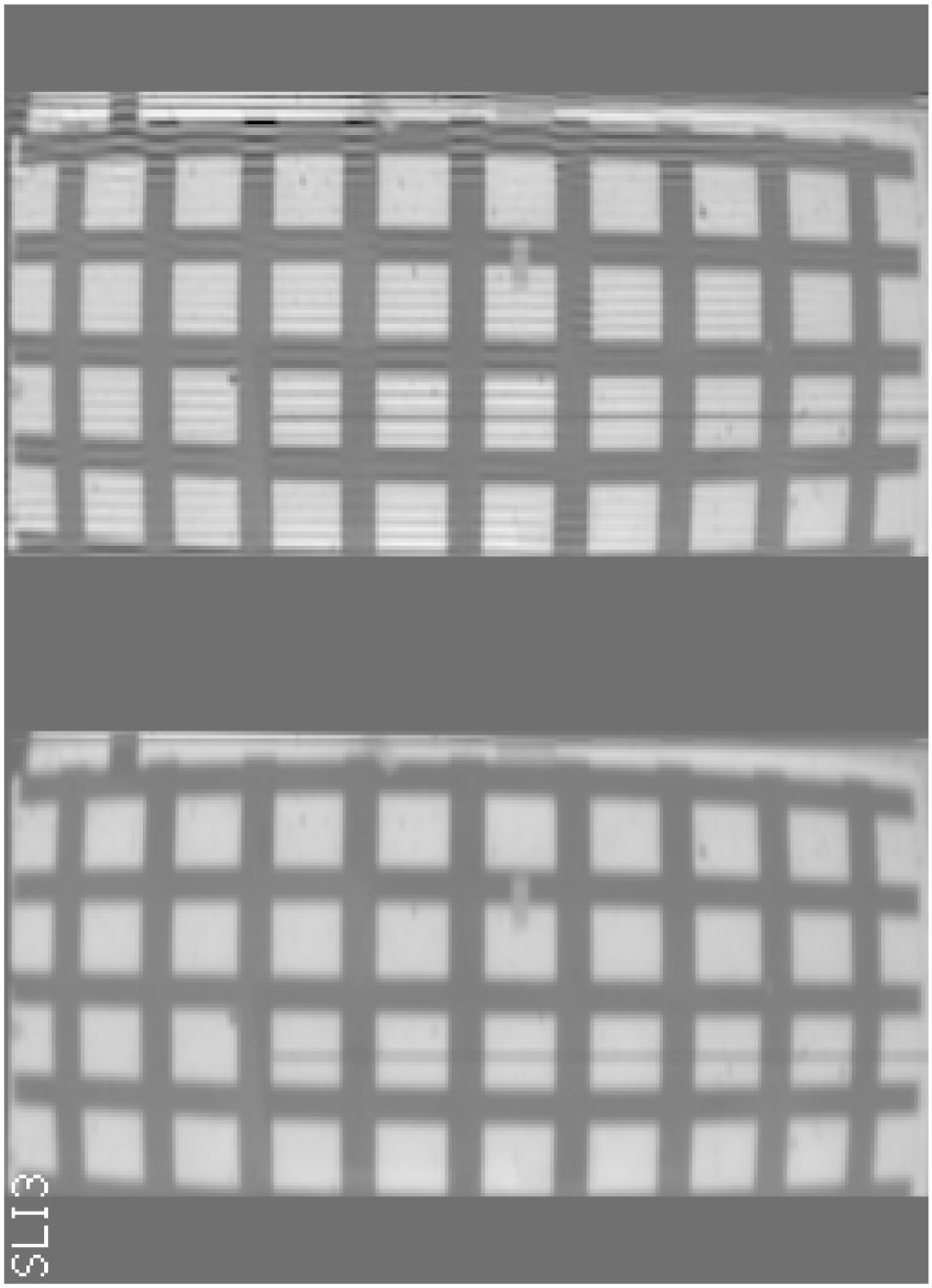

Figure 3.0-47

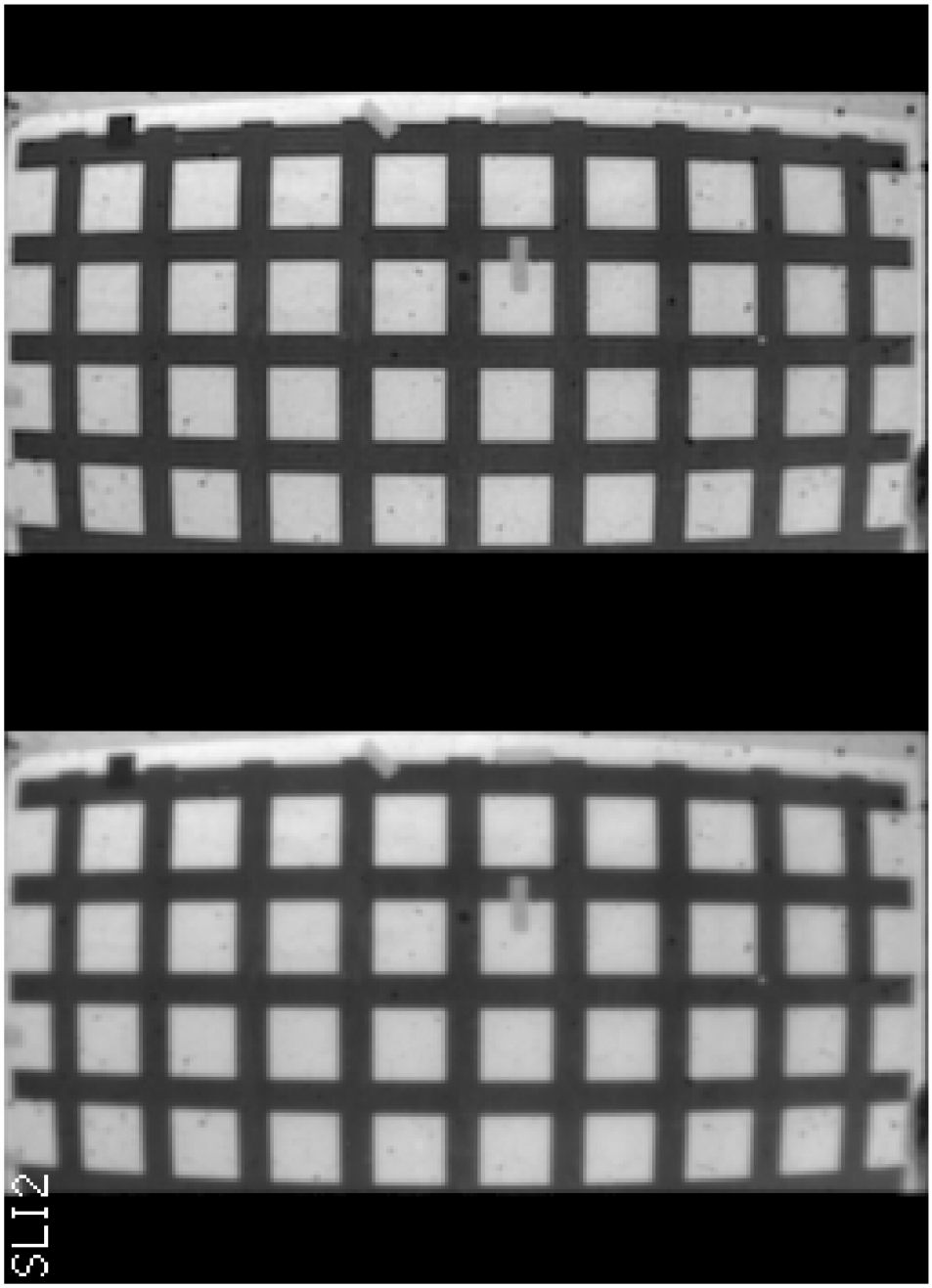

Figure 3.0-48

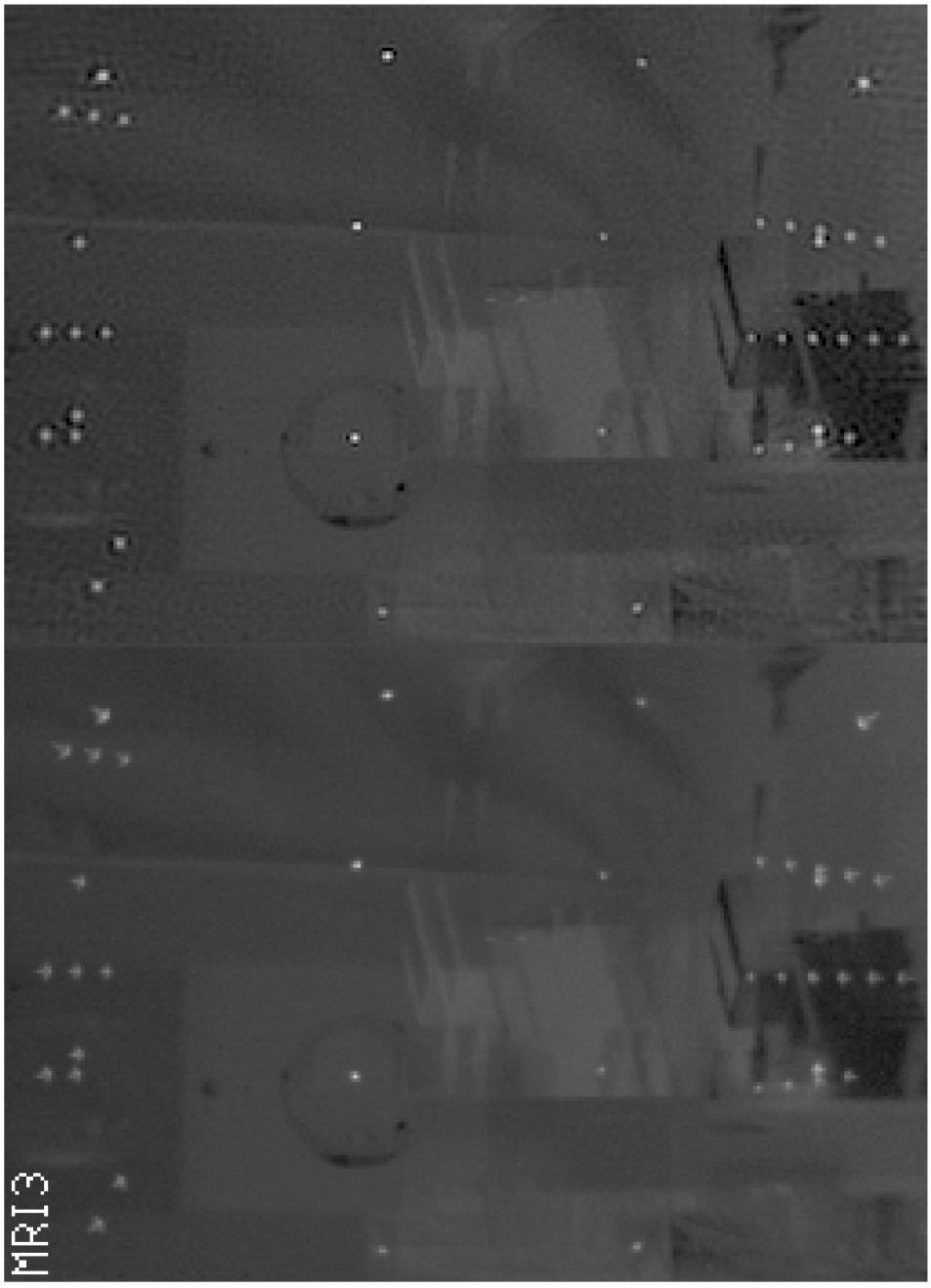

Figure 3.0-49

Figure 3.0-50

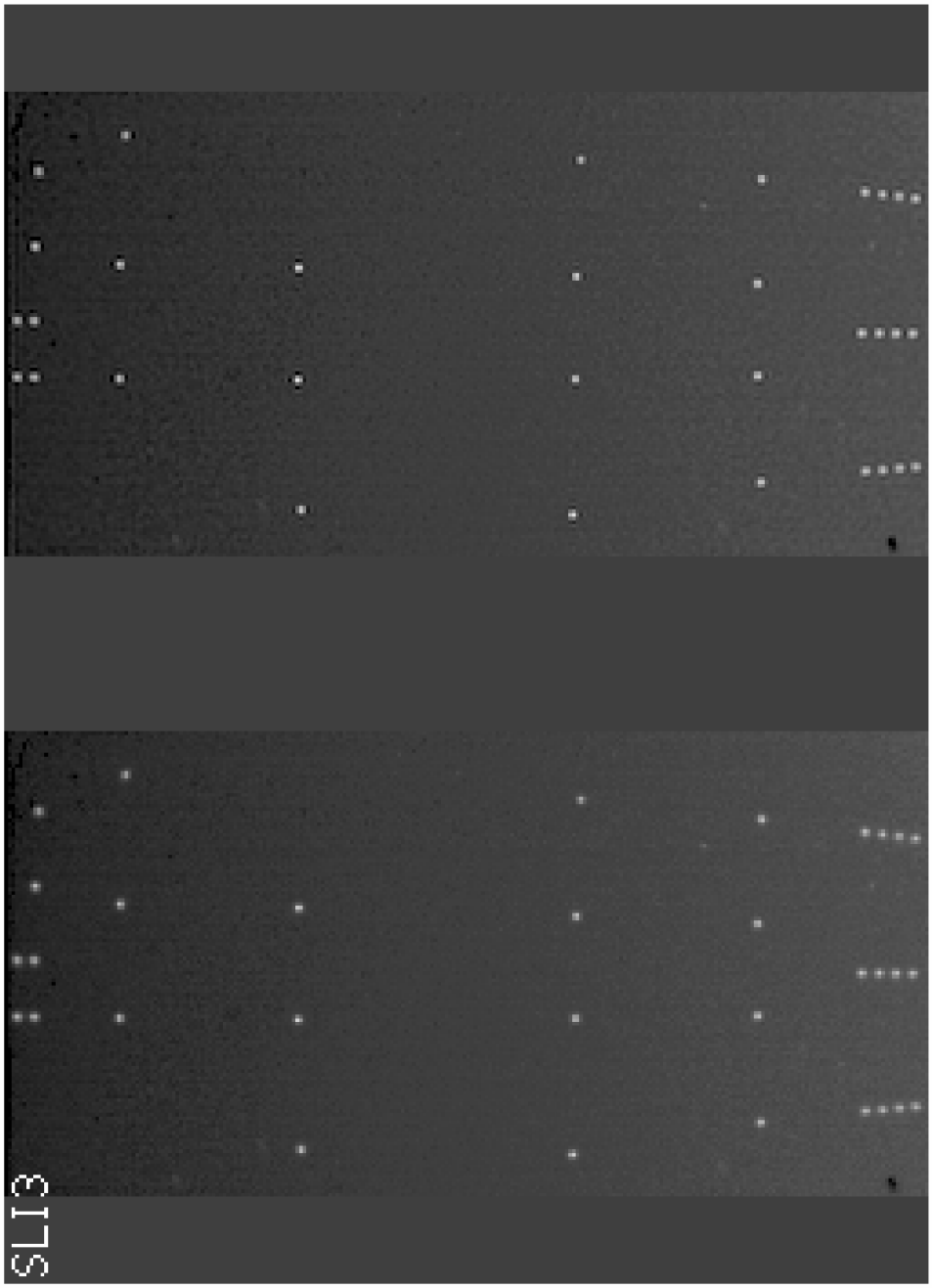

Figure 3.0-51

Figure 3.0-52

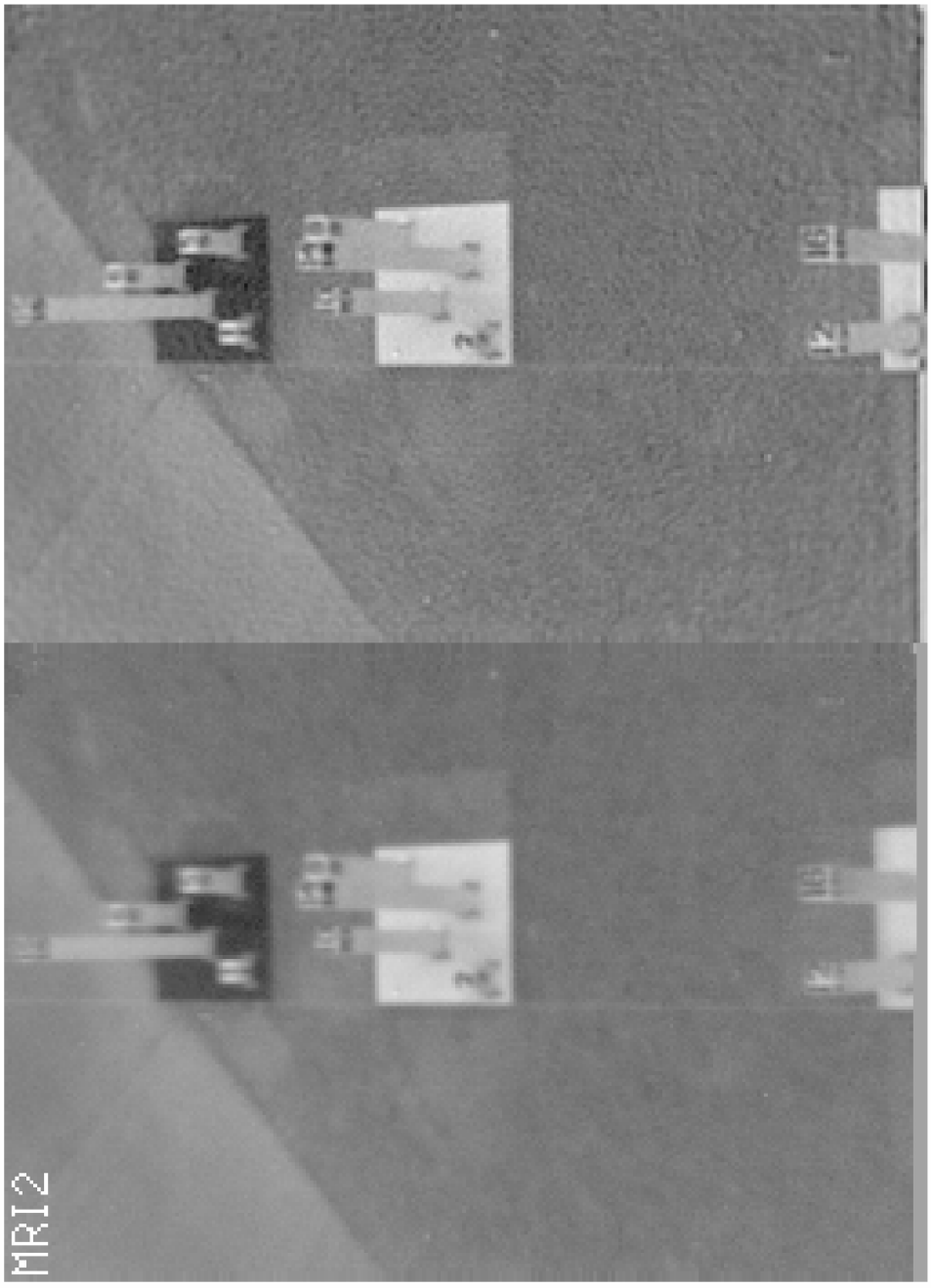

Figure 3.0-53

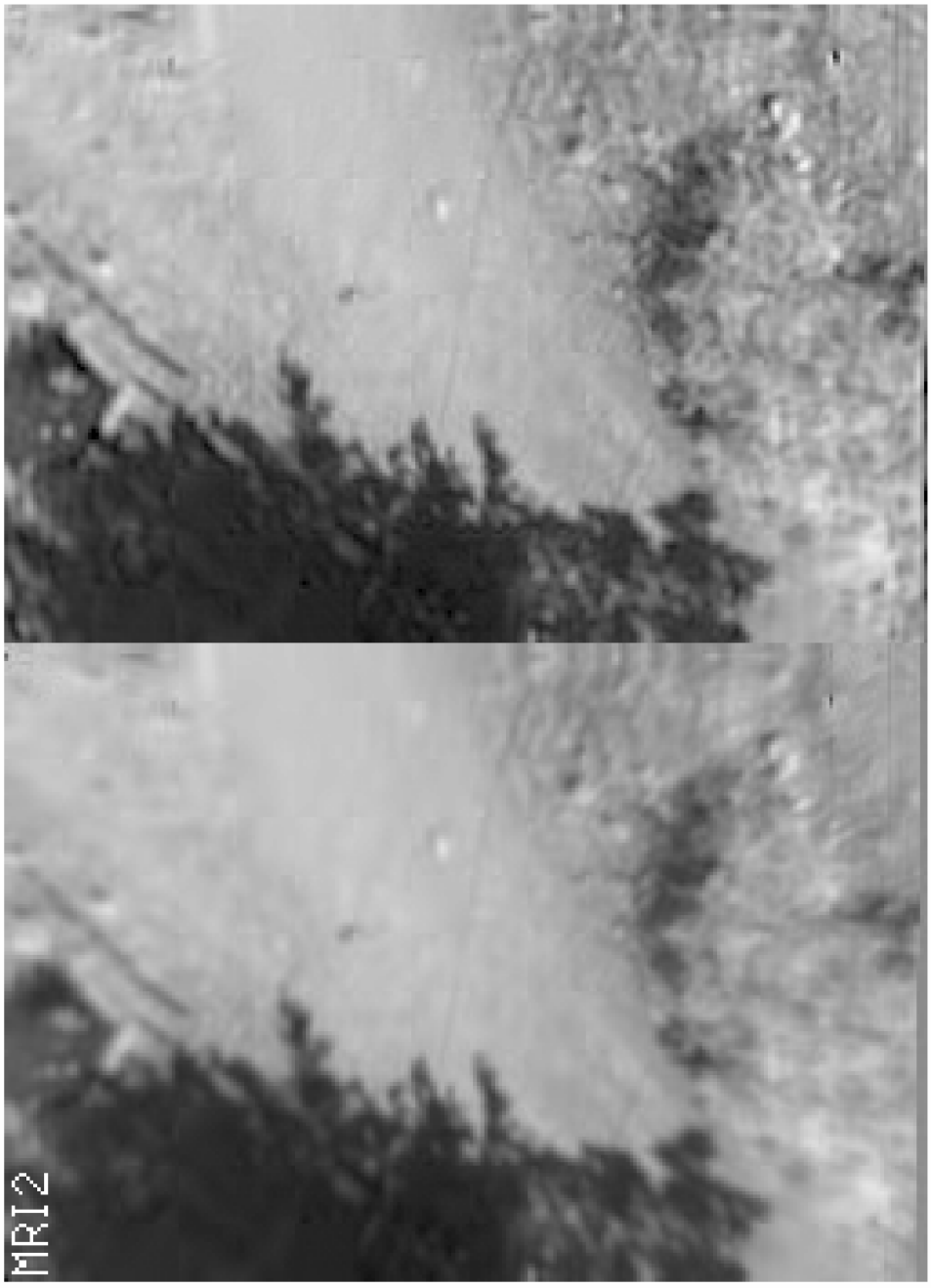

Figure 3.0-54

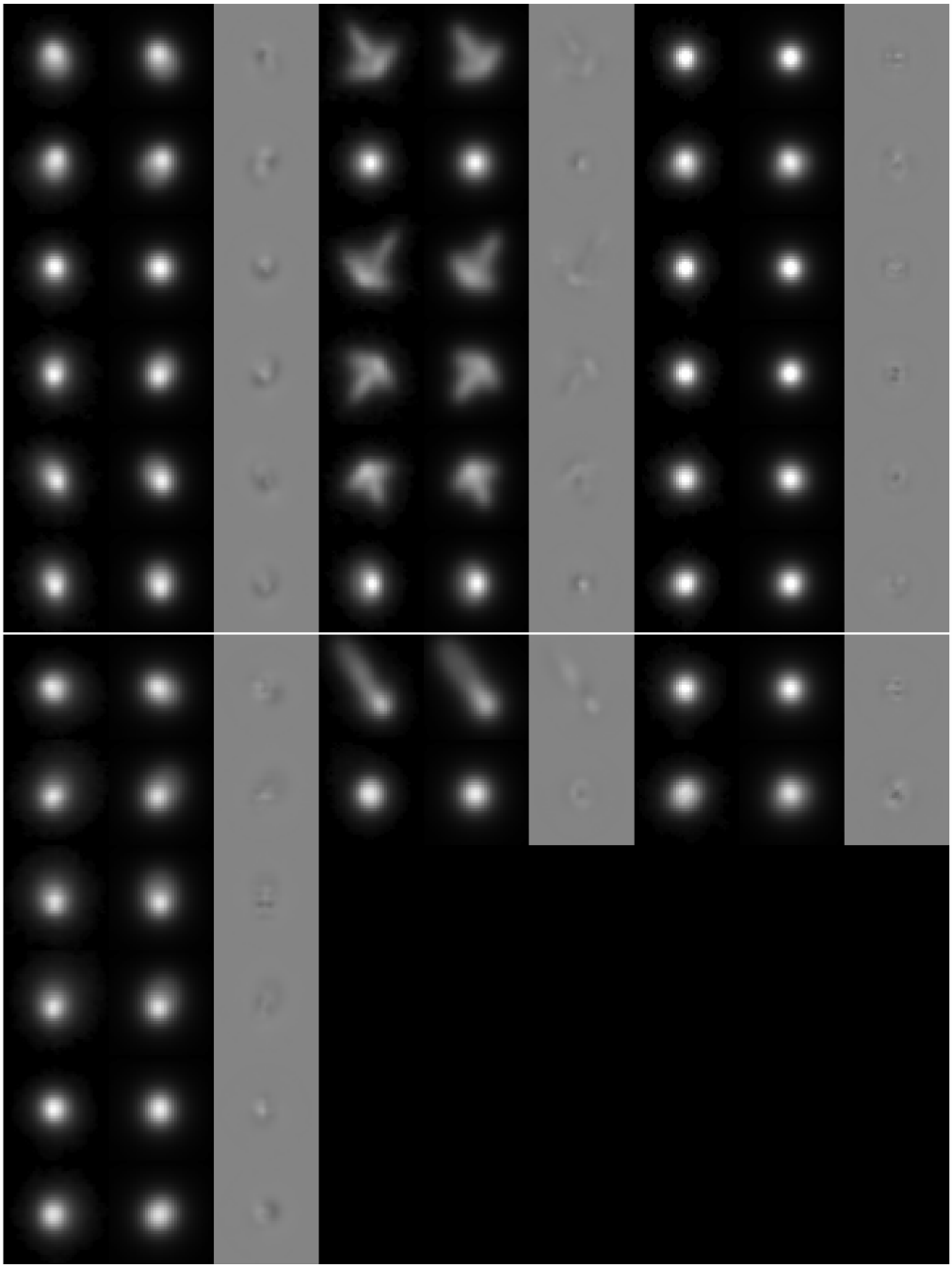

Figure 3.0-55 Images of the observed PSFs, the fitted PSFs, and their difference, from left to right in each case. The top panel is for DISR3, the bottom panel for DISR2. The left three columns are for the HRI, the middle three for the MRI, and the right three for the SLI. (the figure is oriented correctly if the big black rectangle shows up at bottom right)

4.0. Image Photometric Calibration

4.1. Relative Spectral Response

The relative spectral response (RSR) defines the wavelength-dependent response of the entire imaging system, including all component transmissions and the CCD response. By definition it is normalized to 1 at the peak.

The RSR of the DISR imagers was measured in the lab using the large integrating sphere. The interior of the sphere is illuminated through the monochromator with an incandescent light source, producing near-monochromatic illumination on the interior of the sphere. The brightness of the illuminated interior is measured with the monochromator standard detector, and the three imagers are exposed nearly simultaneously. This procedure is repeated at 10 nm intervals from 600 nm to 1050 nm. At each wavelength the relative spectral response of the standard detector, R_{ref}, is known. The measured current from the standard detector is I_{ref}. The data number per second from a pixel in the DISR imagers is r. The relative spectral response of the pixel at the current wavelength is given by

$$RSR(\lambda, col, row) = r(col, row)\frac{R_{ref}(\lambda)}{I_{ref}(\lambda)}$$

Corrections must be applied for dark current by exposing a dark image, and the result for each pixel is normalized to 1 at the wavelength where the peak occurs. The values of R_{ref} can be found on cassini in the file /local/cal.cal/si.std.

Measurements using this procedure were taken for DISR#3 from July 26, 1996, until August 1, 1996, at 7 temperatures. The results of these measurements are stored on cassini in the directory /local/Imagers/Rel_Spectral_Resp/output/DISR#3 in DISRSOFT files with the naming convention *imager_temperature*, i.e., mri_185, e.g. Data returned by executing a d_read statement on these files returns an array of floating point numbers with dimensions number-of-columns × number-of-rows (254) × 50 wavelengths (600 nm – 1050 nm in increments of 10 nm).

To make access to the RSR data more tractable, a parametric model has been developed to describe the RSR of each pixel at all wavelengths and temperatures. This model is discussed below.

4.1.1. A Model for the relative spectral response of the imagers

4.1.1.1. Motivation for a Model

The relative spectral response (RSR) measurements for the imagers represent an enormous amount of data. There are three imagers (HRI, MRI and SLI) with 40,640,

44,704 and 32,512 pixels respectively for a total of 117,856 pixels. In addition, relative spectral response data (as the name implies) depends upon wavelength, and measurements were made from 600 nm to 1090 nm in increments of ten corresponding to 50 wavelengths. Finally, the relative response data is also a function of temperature, and measurements were made at 7 temperatures encompassing a range from 171 to 294 K. Thus, well over 41 million numbers [(40,640 + 44,704 + 32,512) × 50 × 7] would be required to fully represent the relative spectral response data for each pixel of all three imagers. The sheer size of this data set was motivation for development of a parametric model for the RSR. The ultimate goal is to find a model that works not only for the majority of pixels but for all pixels in all imagers at all temperatures with small deviations from the measurements.

4.1.1.2. General Description of RSR data

Displayed in Figure 4.1.1.1-1 is the average RSR for all pixels for the 7 measured

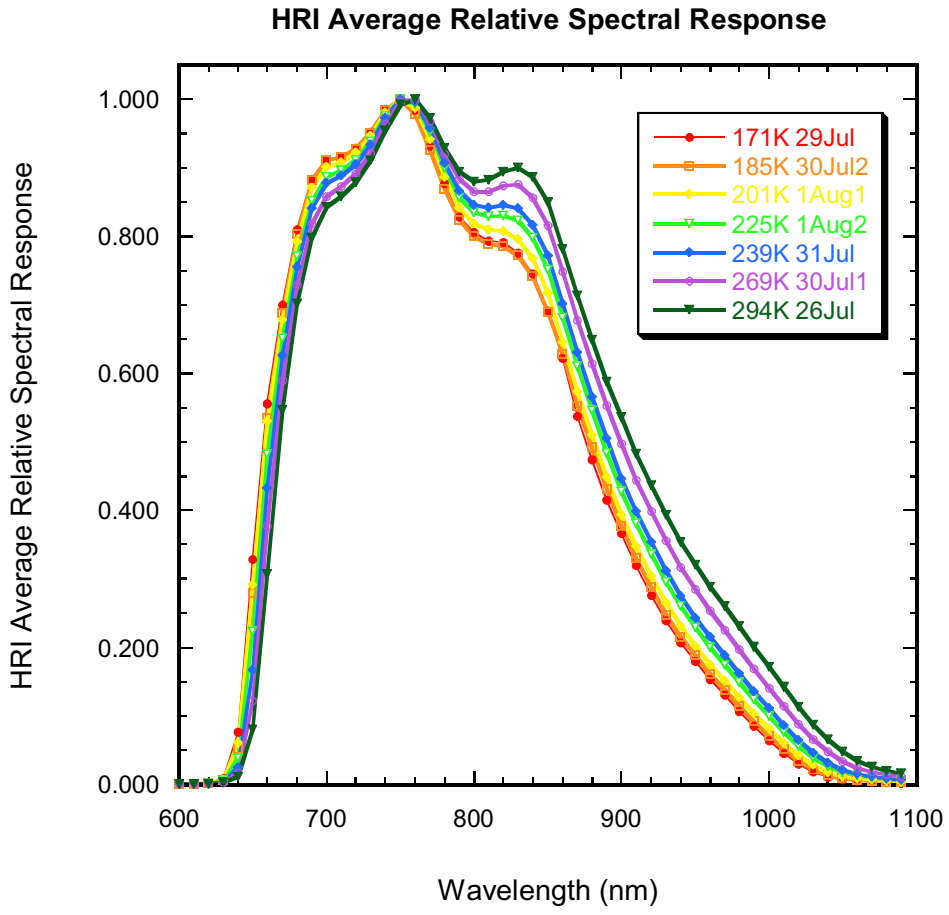

Figure 4.1.1.1-1 RSR averaged over all the pixels for the HRI at measured temperatures versus wavelength for the HRI. The RSR bandpass has a characteristic shape, similar in appearance to a normal distribution

skewed toward shorter wavelengths with 3 "humps", the middle of which is the highest.

temperatures.

Plots of RSR curves at different temperatures show a systematic shift in shape, its left and right humps increasing and decreasing with temperature. At shorter wavelengths, at the blue edge of the bandpass, lower temperatures show a higher RSR while the higher temperatures show a lower RSR. The opposite is true at longer wavelengths near the red end of the bandpass, where the higher temperatures show higher RSR.

Figure 4.1.1.1-2 is a drawing of the front end of the optics for all three imagers, showing window, filter, lenses, etc. The general shape of the RSR curve is caused principally by the bandpass filter, which defines the blue edge, and by the decreasing detector responsivity with wavelength, which defines the red end. Variations in the shape of the RSR curve are caused by different affects. At short wavelengths, the bandpass filter changes transmission with temperature, while at long wavelengths, change with temperature of the detector responsivity is the dominant effect.

On a pixel-by-pixel level at least two factors act to shift the RSR curve: 1) different amounts of silicon doping on the CCD itself, and 2) variations in the transmission of the fiber optic conduit. The fiber optic conduit has blemishes, and is yellowish in color and so absorbs in the blue.

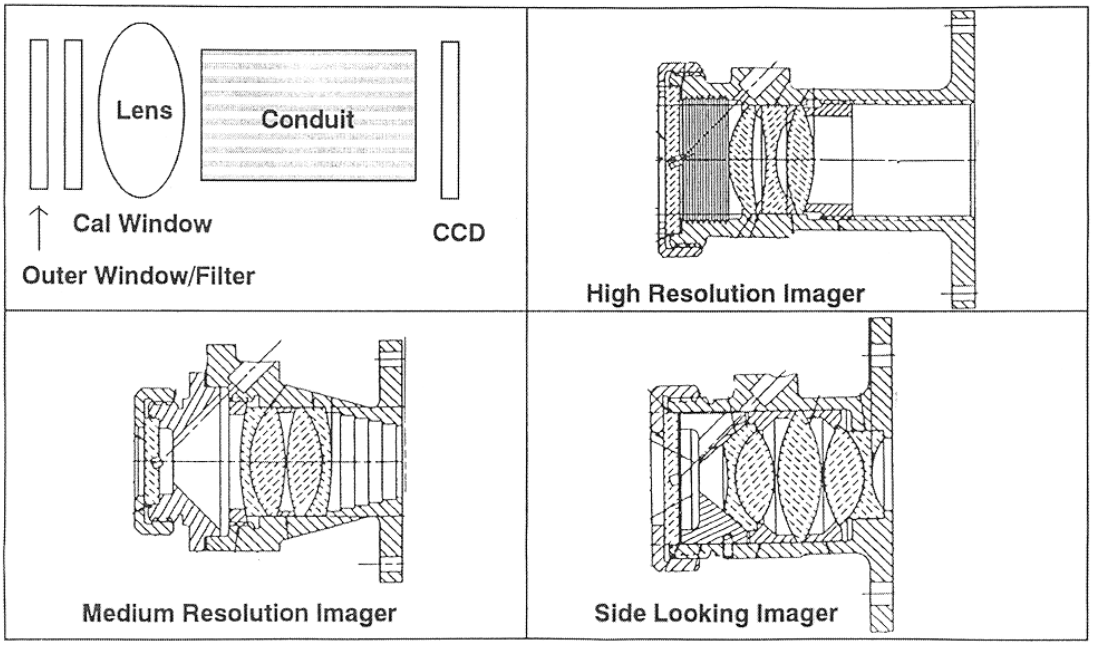

Figure 4.1.1.1-2 Drawing of the front end of the optics of the imagers showing window, filter, lenses, etc.

4.1.1.3. Suspected Correlation: AR and RSR

Every pixel in an imager has a unique Absolute Responsivity (AR), but there is no variation with wavelength to consider, and the temperature dependence of the AR can be described by a simple polynomial. Thus, the number of values needed to fully represent the Absolute Responsivity measurements is roughly 100 times less (assuming 3 coefficients replace the 50 wavelengths × 7 temperatures) than the over 41 million numbers required to fully represent the RSR data for each pixel of all three imagers.

In our first attempt to develop a parametric model we hypothesized that pixels with a relatively lower AR may be fed by relatively more fibers with extramural absorption and have a different shaped RSR. It was speculated that pixels that have a low overall AR would tend to be more responsive in the red end of the spectrum and less responsive in the blue. If there was a correlation between the AR and RSR we sought to parameterize this relationship to enable determination of RSR values when AR values are known. Thus, we initially sought a quantifiable relationship between the AR and the RSR of the imager pixels.

4.1.1.4. Absolute Responsivity Measurements

The frequency of AR values for the HRI is shown in a histogram plot in Figure 3. The

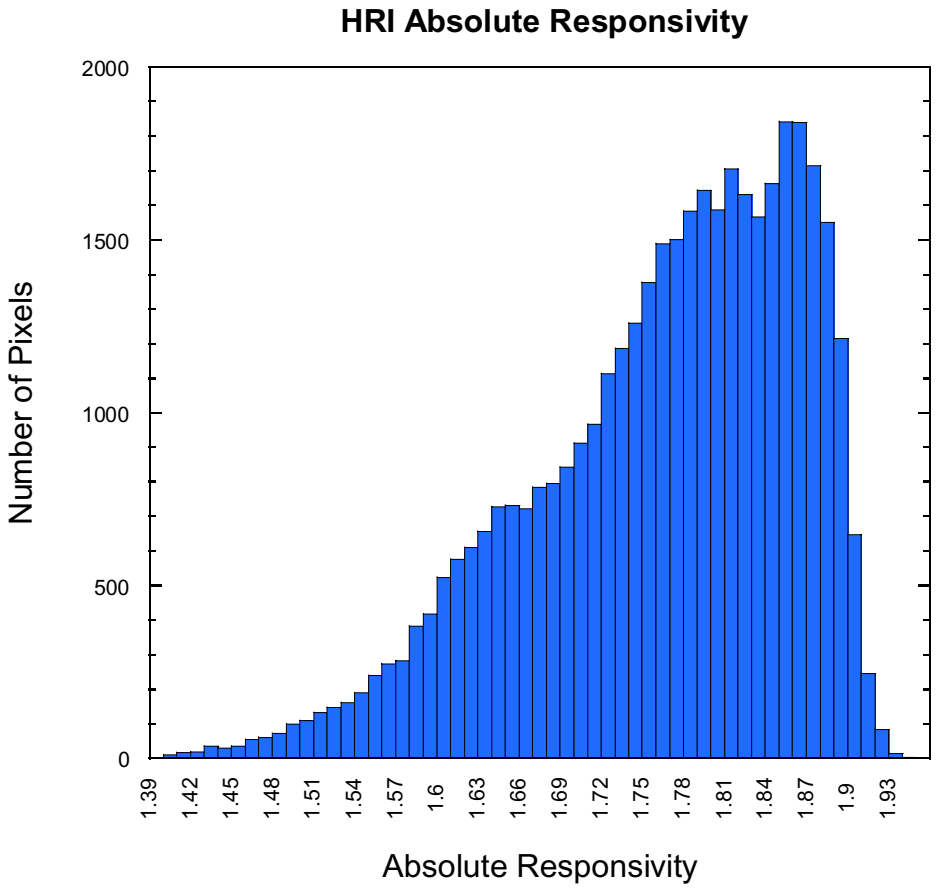

Figure 4.1.1.4-1 Histogram showing numbers of pixels and AR values in units of (1×10^6 DN/sec)/ Watt m2 □m str.

Pixel AR values show a somewhat normal distribution skewed toward higher values of AR, with a hump of more pixels evident towards the high end. The average AR value is 1.736 x10^6, or 1.759 x10^6 if the bad pixels are excluded (there are 511 bad pixels in the HRI). The AR curves for the MRI and SLI are similar.

4.1.1.5. Absolute Responsivity bins

In the interest of seeking a correlation between AR and RSR, ten groupings of pixels were chosen to represent 10 bins based upon average AR levels. The average of the good pixels for the AR array was computed and all individual AR values were divided by this average. The resulting normalized AR ratios were sorted from large to small, grouping pixels into bins that are most responsive, slightly less responsive, less responsive still, etc., to see if different groupings of pixels based on AR may have a different RSR character.

The RSR data were examined for the imager of interest using AR measurements at a temperature of 237.75 K and RSR measurements for a temperature of 239 K. Most of the

variation in the RSR occurs in the left and right "humps". While initial samples of populations seemed to indicate a trend, when considering all the data trends become much less clear as there is a tremendous amount of scatter (Figure 4.1.1.5-1). There is

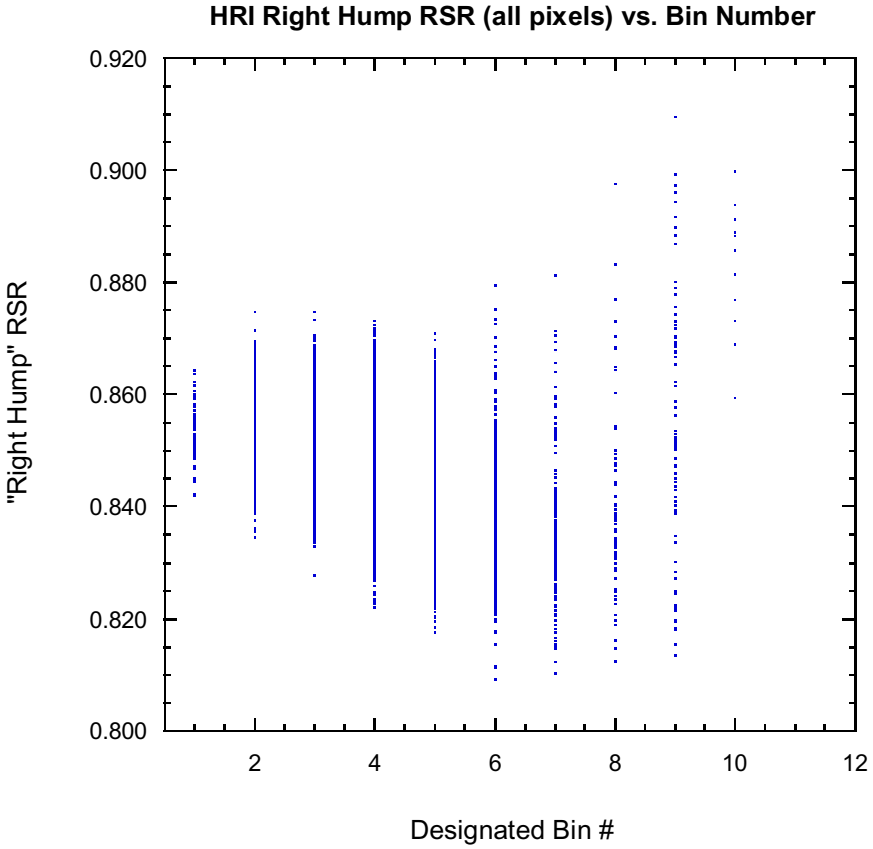

Figure 4.1.1.5-1 The HRI RSR at 820 nm vs. AR bin number. This plot shows all the pixels in the HRI imager encompassing all possible bin values (1-10).

considerable spread in the value of the RSR within each bin, and the correlation between AR and RSR is weak. However, there is some correlation and so we proceeded with the development of a RSR model based on AR.

Coefficients were determined that describe how the RSR varies with wavelength within each of these ten AR bins by fitting a second order polynomial to the ratio of the average RSR within a bin to the average RSR for the entire imager versus wavelength:

$$\frac{RSR_i(\lambda)}{\overline{RSR(\lambda)}} = a_i + b_i\lambda + c_i\lambda^2 \text{, where } i \text{ indicates the bin number} \qquad (1)$$

Polynomial fits for a_i, b_i, and c_i as a function of AR_i were then made. Because these fits were not adequate when a single polynomial was used, the fits were made in two pieces.

Thus, a different set of coefficients is used depending upon whether or not the AR of the pixel of interest exceeded a threshold value.

Thus, 3 groups (one per imager) of 6 (constant, linear and quadratic terms of both the low AR and high AR variety) sets of coefficients were determined, and basically, three equations were used to derive a_i, b_i, and c_i. The RSR could then be determined from the AR of any pixel using equation (1).

The root mean square (RMS) difference between the measured and modeled RSR was computed for each good pixel for each of the 7 temperatures at which the RSR measurements were made (171,185,201,225, 239, 269,294). Figure Figure 4.1.1.5-2 shows the computed RMS values plotted versus AR. The conclusion from figure Figure 4.1.1.5-2 is that the model is not very successful, because the RSR and AR of pixels are not very well correlated.

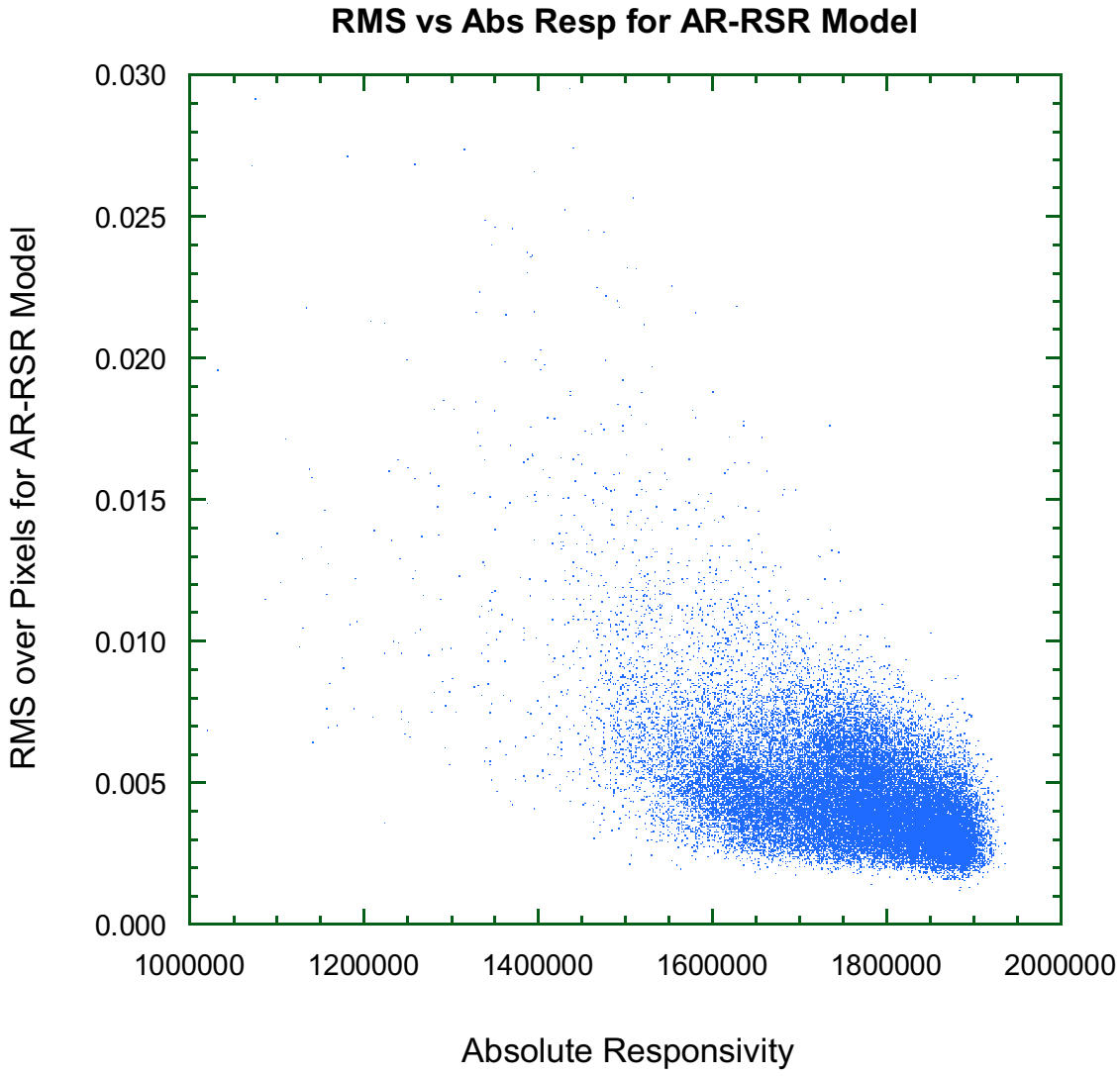

Figure 4.1.1.5-2 Resultant Root Mean Square (RMS) difference values between the measured and model RSR values for each of the pixels in the HRI

imager when using the AR-RSR model for computing RSR. Note the significant scatter.

Figure 4.1.1.5-3 shows a probability plot of RMS difference values for both the AR-RSR model and a model called Ave that simply uses the average RSR within each bin for the RSR of each pixel in that bin. The simple average performs better for a majority of pixels, while the AR-RSR model does better for a small percentage of pixels. The cross over occurs just beyond 99.9 % of the pixels. The conclusion is that the AR-RSR model is not successful when compared to a much simpler model of using the average RSR within each bin for the RSR of the pixel of interest, although the AR-RSR model performs better for a subset of pixels.

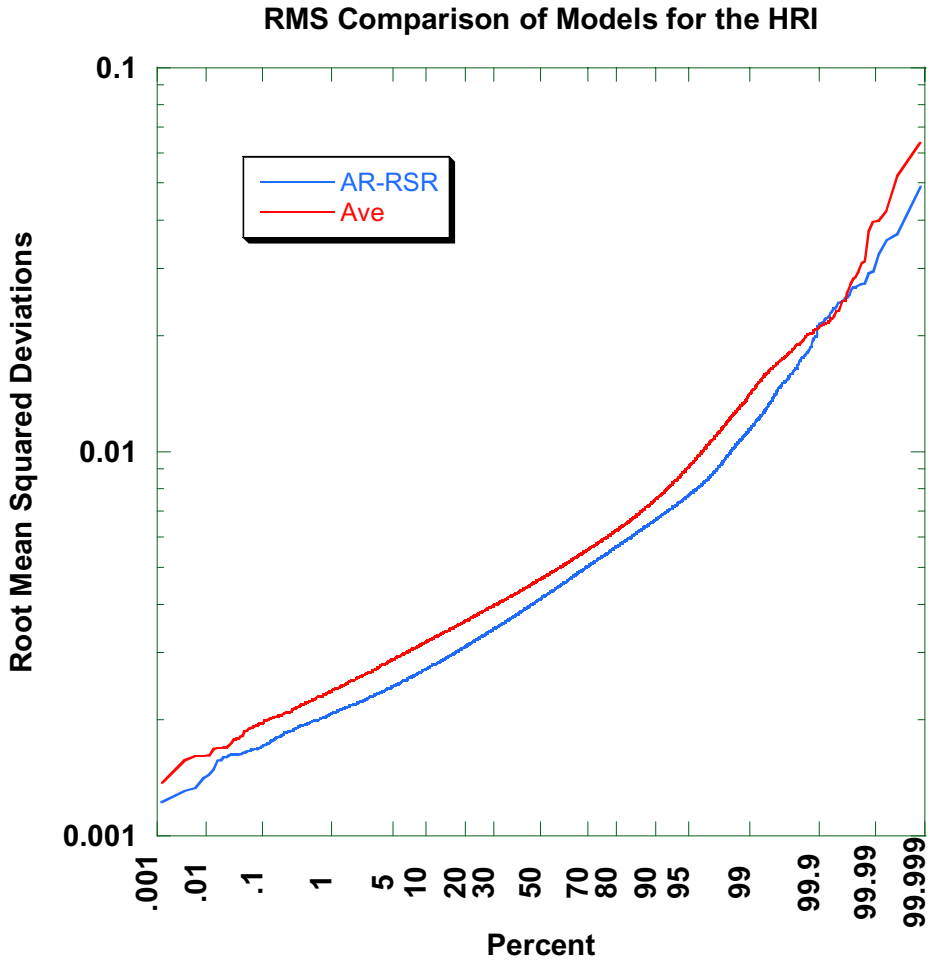

Figure 4.1.1.5-3 A probability plot for the HRI comparing the over all Root Mean Square (RMS) differences for the AR-RSR model versus a simple model using only the average within each bin. Generally the models are similar, with the AR-RSR model yielding better results (lower RMS deviations) for the vast majority of pixels. For a small subset of pixels toward the right of the graph, the Ave model gives a result preferable to using the AR-RSR model.

4.1.1.6. Limitation of the AR-RSR Method

Thus, while there is some relationship between AR and the RSR, there is significant scatter in this relationship. For the majority of pixels, the AR-RSR model performs better than a simple average to represent the RSR of a pixel. However for the AR-RSR model and the Ave model the RMS deviation of some pixels approaches 5% and almost 7% respectively for the HRI at 239K. The implication is that the correlation between the AR and the RSR is not sufficiently strong for the development of a successful RSR model. Our goal was to develop a model for which the RMS deviations are lower than some threshold for all pixels within an imager. Such a model that does not employ the AR has now been developed and is explained below.

4.1.2. The Hump Ratio Model for determination of RSR

4.1.2.1. Development of the model at 239K

As was mentioned previously, the RSR array is composed of a peak with two "humps" on either side of the peak. For the purposes of constructing a parametric model, the left hump is defined to be at a wavelength of 700 nm and the right hump is defined to exist at 820 nm. It was noticed that large variations in the RSR versus wavelength curve generally occurs in the close vicinity of these two humps. The RSR model is based on the ratio of the RSR at these two wavelengths (700 and 820 nm) at a temperature of 239K for each pixel. The hump ratio or "h ratio" is defined as the RSR of the left hump divided by the RSR of the right hump, and every pixel is assigned to one of 10 bins based upon this ratio (see Tables 4.1.2.1-1 through 4.1.2.1-3).

Initially, 20 bins were arbitrarily chosen, but the choice of ten bins was ultimately made as fewer than ten bins increased root mean square (RMS) deviations, while more than ten bins did not offer improvement in the RMS. The h ratio limits for the bins are the same for all three imagers, and are given in table 4.1.2.1-1:

Table 4.1.2.1-1

h ratio bin limit values

bin	h ratio lower limit	h ratio upper limit
1	1.12	1.17
2	1.10	1.12
3	1.06	1.10
4	1.04	1.06
5	1.02	1.04
6	1.00	1.02
7	0.96	1.00
8	0.93	0.96
9	0.90	0.93
10	0.75	0.90

Bad pixels (as defined by the bad pixel map) are assigned a flag value of 255.

Four plots at different temperatures (171K, 185K, 201K and 225K) comprise Figure 4.1.2.1-1. On each graph the average RSR within a bin, normalized to the RSR of all the good pixels at 239K, is plotted versus wavelength, for each of the ten bins. Figure 4.1.2.1-2 shows the equivalent graph for the three remaining temperatures at which RSR measurements were taken (239K, 269K and 294K). The left vertical line (at 700 nm) shows the position of the left hump and the right vertical line (at 820 nm) shows the position of the right hump.

These seven graphs demonstrate that there are groups of pixels, assigned to one of ten bins that show different spectral responses from one another. Thus, the pixels within these ten bins behave distinctly from one another in terms of their average RSR within a bin.

In addition, the bins are persistent over temperature. In other words, bin1 (the red line) is always highest left of the peak (or crossover point) in the lower wavelength portion of the spectrum, while bin 10 (the black line) is always lowest in this region. Likewise, bin 10 is always higher than bin 1 in the longer wavelength portion of the spectrum.

There is a large spike at an approximate wavelength of 640 nm that appears to be a real feature. The RSR at this wavelength differs greatly with temperature, although the response at 640 nm is so low that this does not have a large effect on the overall RSR curve.

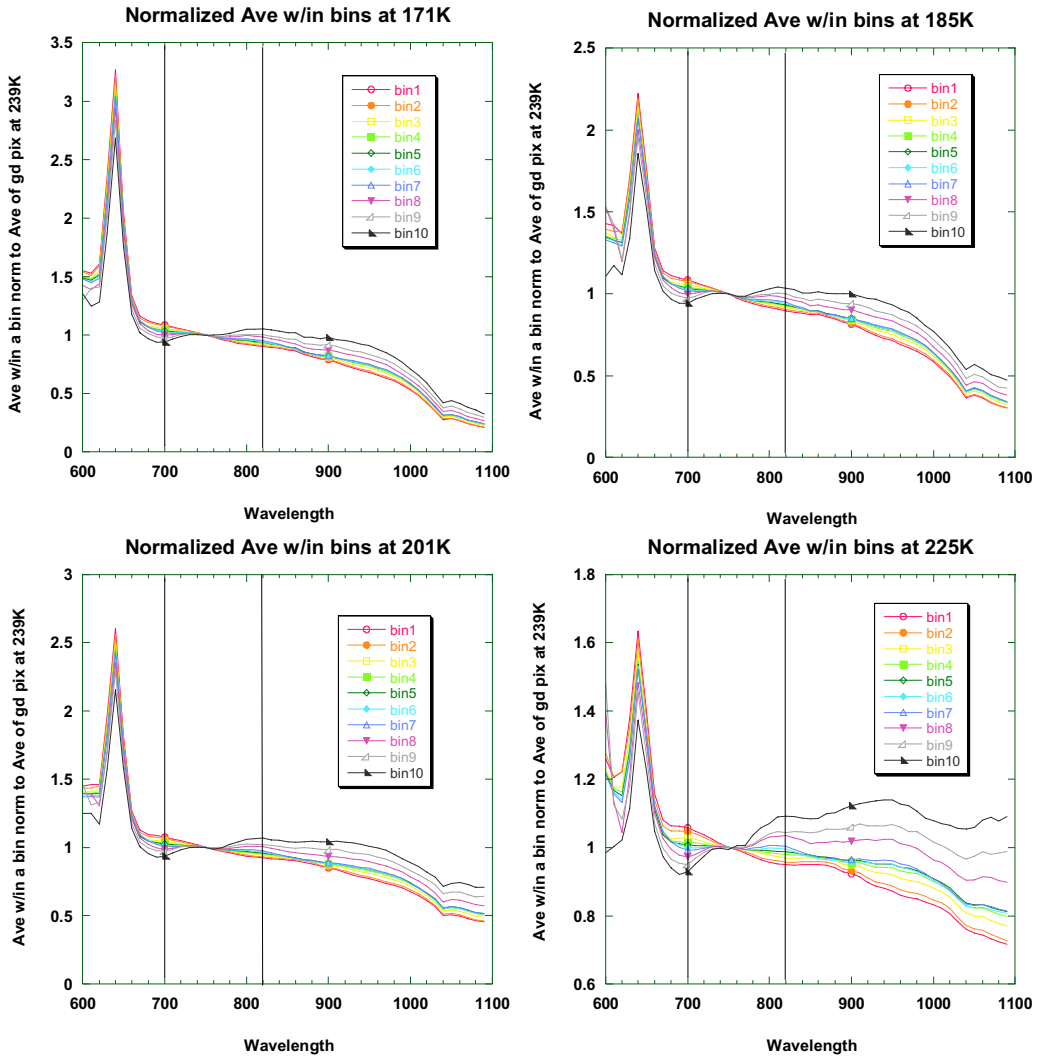

Figure 4.1.2.1-1 The average within a bin normalized to the average of all the good pixels at 239K plotted versus wavelength for 171K, 185K, 201K and 225K.

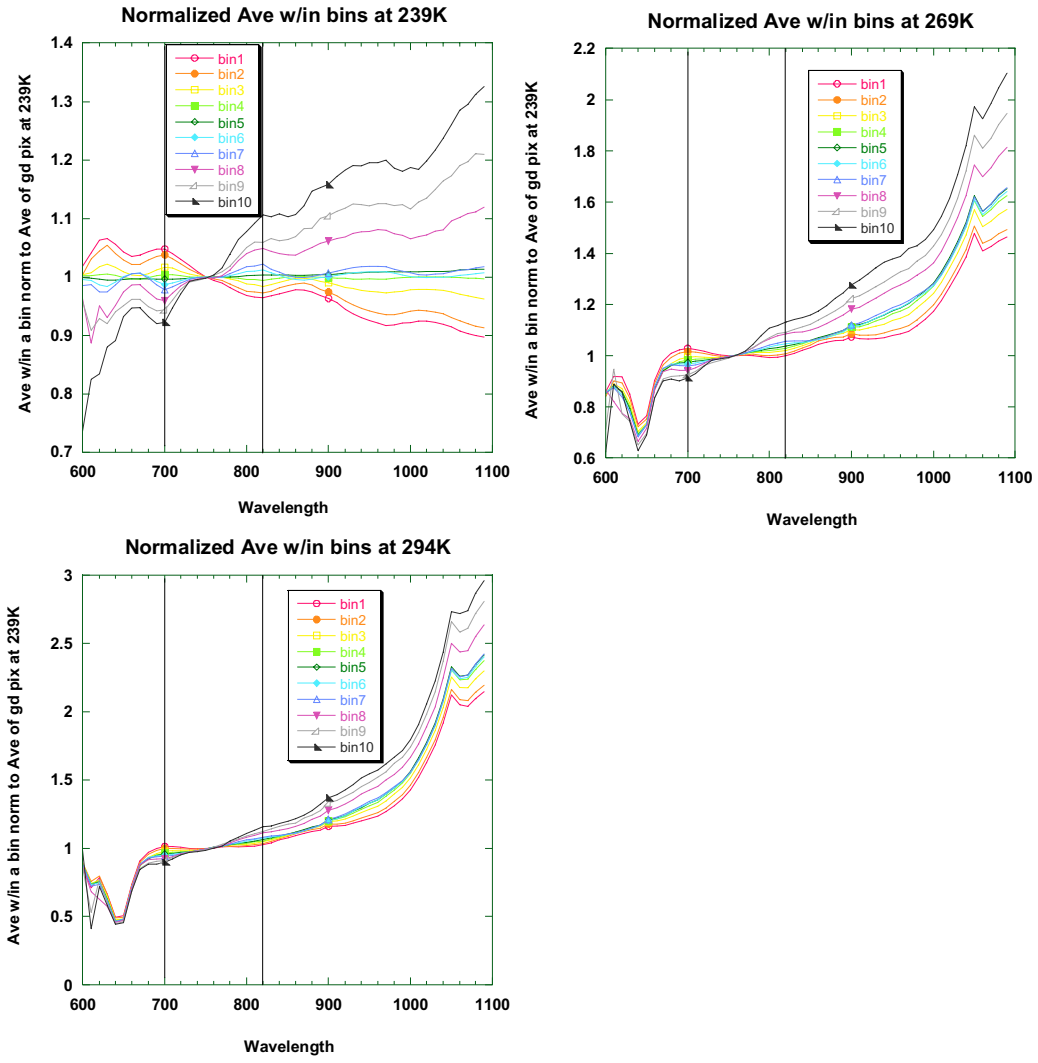

Figure 4.1.2.1-2 The average within a bin normalized to the average of all the good pixels at 239K plotted versus wavelength for 171K, 185K, 201K and 225K.

Tables 1, 2 and 3 in appendix A show the bin assignments for each pixel in the HRI, MRI and SLI respectively. The bin values range from 1 to 10 for all three imagers, with the caveat that the MRI has 10 "out of family" pixels. Each of the ten "out of family" pixels for the MRI is assigned a value from 20-29.

The model was developed at a base temperature of 239K. Thus, obtaining the representative RSR for a given pixel at 239K simply requires looking up the bin for that pixel, then using the RSR for that bin.

4.1.2.2. Development of the model at all Temperatures

Although the RSR data was originally taken at seven temperatures (171K, 185K, 201K, 225K, 239K, 269K, 294K), the RSR of any temperature can be computed with the model. Temperature coefficients that enable the computation of the RSR at other temperatures are derived as follows: for each of the temperatures and for each bin (recall the bin of each pixel is defined by the RSR "h ratio" at 239K) we compute the mean RSR of the pixels within each bin. Figure 4.1.2.2-1 is a plot of the average RSR within a bin normalized to

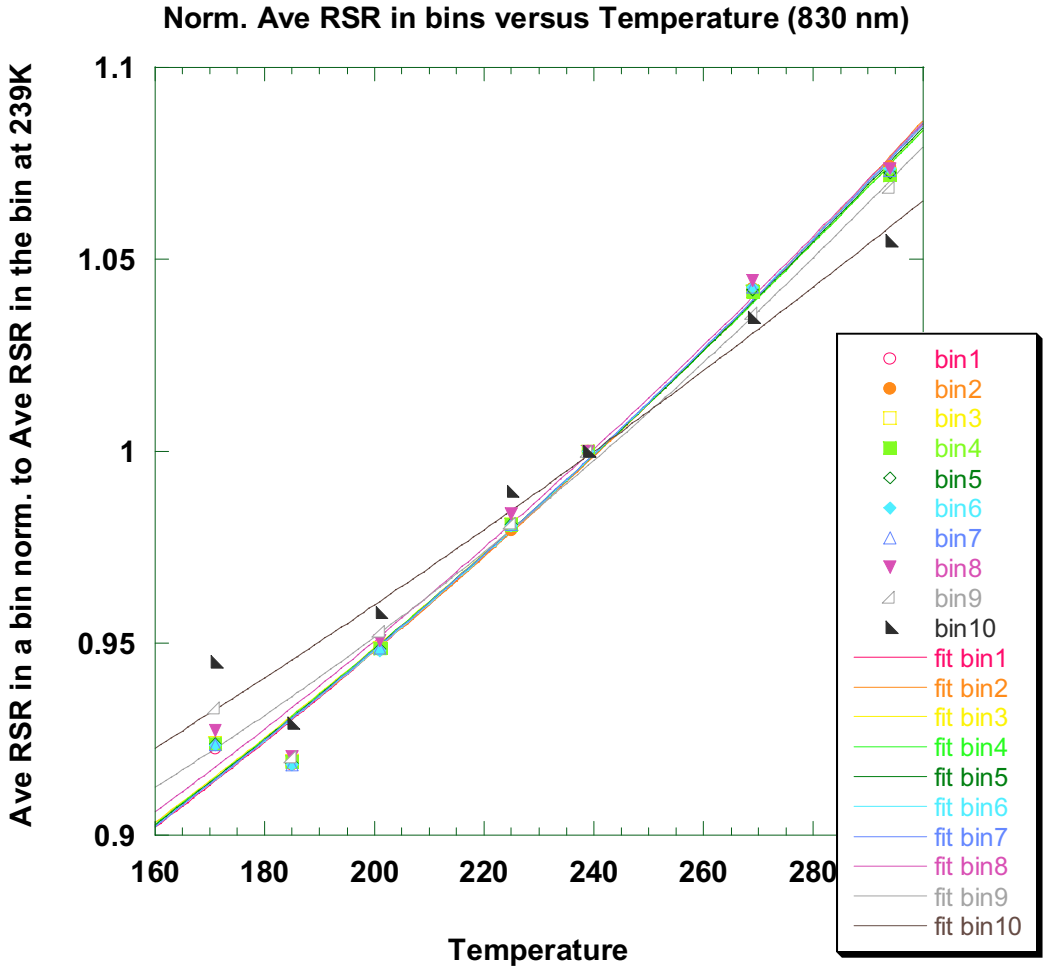

Figure 4.1.2.2-1 Normalized average RSR versus Temperature for all 10 bins with polynomial fits.

the average RSR in the same bin at 239K for one wavelength (830 nm), all plotted versus temperature for all ten bins. Coefficients are determined by doing a second order polynomial fit of the above-mentioned normalized average RSR versus temperature. As can be seen in Figure 4.1.2.2-1, the temperature dependence of the RSR is well fit by a 2nd order polynomial.

The result is three coefficients (multipliers in the constant, linear and quadratic terms). Such coefficients are computed for each of the 10 bins at each wavelength. A weighted coefficient is then computed for each of the three terms based upon the numbers of pixels within each bin multiplied by its coefficients. Thus, the result is a weighted coefficient expressed as a 2nd order polynomial in temperature for each wavelength (see Table 4.1.2.4-2). Figure 4.1.2.2-2 shows the same graph as Figure 4.1.2.2-1, but with only the weighted fit shown. Clearly there is very little variation in temperature dependence among the bins.

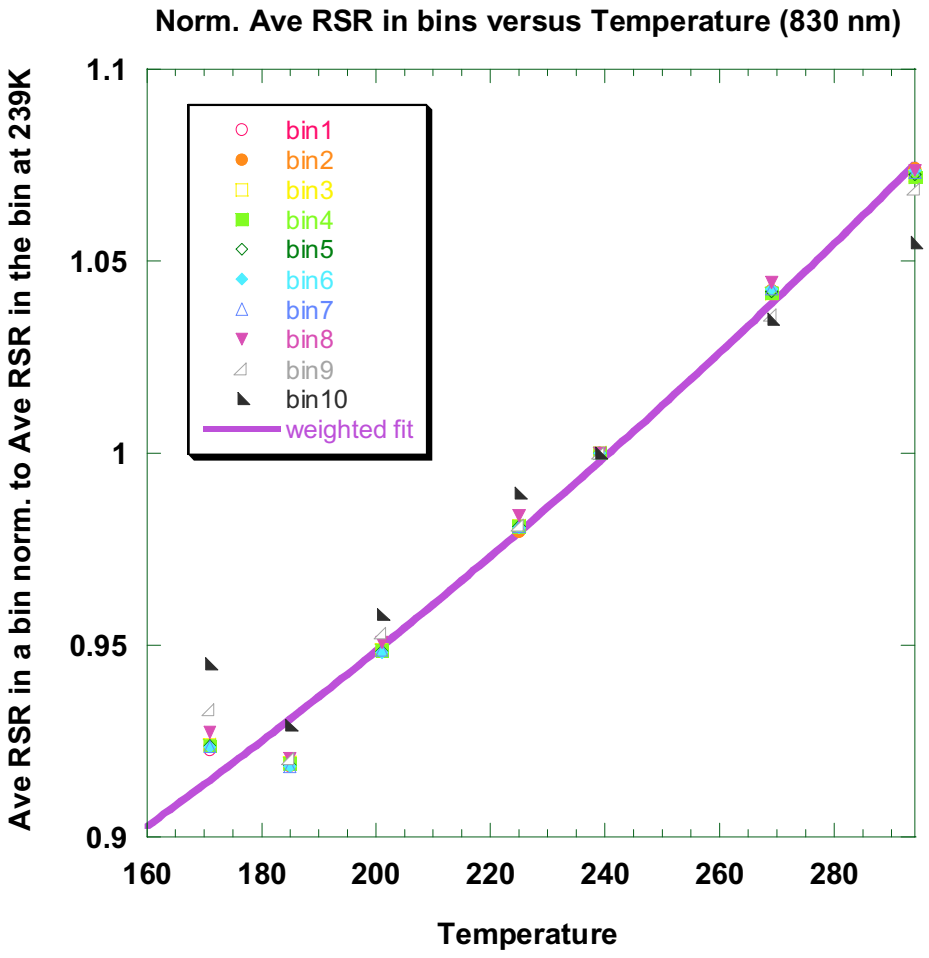

Figure 4.1.2.2-2 Normalized average RSR versus temperature for all bins with weighted fit.

Coefficients at one wavelength (830 nm) are included below to enable a sense of the variations between the bins and the resultant weighted coefficient (see Table 4.1.2.2-1).

Table 4.1.2.2-1

Coefficients for each of the 10 bins for the constant, linear and quadratic terms at 830 nm. The lowest line is the weighted coefficient used in this model as it appears in Table 4.1.2.4-2.

bin	a	b	c
1	0.771737	5.50036E-04	1.65102E-06
2	0.785720	4.29481E-04	1.90630E-06
3	0.769909	5.90394E-04	1.51800E-06
4	0.767452	6.08742E-04	1.48339E-06
5	0.769370	5.85084E-04	1.54880E-06
6	0.772336	5.48266E-04	1.65152E-06
7	0.767795	5.93230E-04	1.54627E-06
8	0.782577	4.98224E-04	1.70743E-06
9	0.823810	2.12714E-04	2.12991E-06
10	0.801691	6.16234E-04	8.73406E-07
830	0.769592	4289E-04	1.548489E-06

A second order polynomial is used to describe the temperature variation of the RSR. The temperature of interest and the weighted coefficients from Table 4.1.2.4-2 for the appropriate imager are used to compute the polynomial fit as shown in equation 2, where a, b, and c are given in Table 4.1.2.4-2.

$$RSR(\lambda,T) = RSR(\lambda,T_0)\left(a + b \cdot T + c \cdot T^2\right) \qquad (2)$$

The RSR for any pixel at any temperature is obtained by multiplying this polynomial by the average RSR within the bin for that pixel, normalized by the average RSR at the base temperature of 239K (see Tables 6-8 for these normalized averages).

While only bins 1-10 are possible for the HRI and SLI, the MRI has several anomalous pixels designated by bins 20-29 and there is a separate table for the normalized averages within a bin for these pixels (see Table 7b).

4.1.2.3. Use of the model (or how to get the RSR for any pixel)

There are three steps to obtaining the RSR for a temperature, imager and pixel of interest:

1) Find the bin of the pixel of interest (Appendix A, Tables 1-3)

2) Find the temperature coefficients for the imager of interest (Table 4.1.2.4-2, or appropriate table from Appendix A)
3) Use equation 2 for the temperature of interest and the average within a bin for each wavelength (Tables 6-8)

4.1.2.4. Sample Calculation

For example, assume we are interested in knowing the RSR for the pixel in column 14 and row 24 of the HRI at a temperature of 208K and a wavelength of 700 nm. Since we are interested in the HRI in columns 0-32 we go to Table 4.1.2.4-1a. The "h ratio" bin designator is a value of 7.

Next, go to Table 4.1.2.4-2 and get the weighted coefficients for the HRI at 700 nm. These are the polynomial coefficients:

1.095146	-8.66387E-05	-1.270609E-06

Thus, the $\left(a + b \cdot T + c \cdot T^2\right)$ portion is:

$\left(a + b \cdot T + c \cdot T^2\right)$=1.095146 –8.66387E-05*(208.0) – 1.270609E-06*(208.0)^2
= 1.02215

Finally, go to Table 6 for the average within bin 7 at 700 nm (normalized to the average with a bin at 239K) for the HRI.

0.857343

Thus, the RSR for pixel HRI (14,24) at 700 nm and a temperature of 208K is: 0.876333

Tables giving the bin designators for each imager pixel are too large to fit on a single page. In figure 4.1.2.4-1a we reproduce such a table from Appendix A, in order to illustrate a calculation. Each imager has a distinct number of columns (HRI: 160; MRI: 176; SLI: 128) such that each table is divided up by column and designated by letter as follows: HRI (Table 1a-1e), MRI (Table 2a-2f), and SLI (Table 3a-3d). The designated letter and associated columns in parentheses are: a (0-32), b (33-64), c (65-96), d (97-128), e (129-160) and f (129-159). All three tables are color coded in the identical manner for readability, but the top left cell of each page designates the imager. Note that columns and rows are numbered from zero.

Table 4.1.2.4-1a

Columns 0-32 of the H ratio bin designator for the HRI

HRI	0	1	2	3	4	5	6	7	8	9	10	11	12	13	14	15	16	17	18	19	20	21	22	23	24	25	26	27	28	29	30	31	32
0	3	4	4	4	3	4	4	4	4	5	5	4	4	4	6	4	5	4	4	5	4	4	4	4	4	4	4	4	4	5	5	4	4
1	5	5	5	5	6	5	6	6	5	6	6	5	5	5	6	5	6	6	6	5	6	6	6	5	5	6	6	5	6	6	6	6	5
2	6	6	5	5	6	6	6	6	5	6	6	6	5	5	5	5	6	6	5	6	6	6	6	5	6	6	6	6	6	7	6	6	6
3	5	5	5	6	6	5	6	6	6	6	5	5	6	5	5	6	6	6	5	7	5	6	6	7	7	6	6	6	6	6	6	6	7
4	5	6	6	5	5	6	6	5	6	5	5	5	6	5	5	5	6	6	6	5	6	6	6	5	5	6	6	7	6	5	6	6	6
5	5	5	5	5	6	6	5	5	6	5	5	5	5	6	6	5	5	6	7	6	6	6	5	5	6	6	6	6	6	6	7	6	6
6	6	6	6	5	5	6	6	6	6	6	5	6	6	6	7	6	7	6	6	6	7	6	6	6	5	6	6	7	6	6	6	6	6
7	6	6	6	6	6	6	5	5	6	5	6	6	6	5	6	6	6	6	6	6	6	7	5	6	6	6	6	6	7	6	6	6	6
8	5	6	6	6	5	5	6	5	6	6	5	5	5	6	6	6	6	6	6	6	6	6	6	6	6	6	5	6	5	6	6	5	7
9	6	5	5	6	6	6	5	6	6	5	5	4	6	5	6	7	6	7	6	6	6	5	6	6	6	7	6	6	7	6	6	6	6
10	5	6	6	5	5	5	4	5	5	5	6	5	6	6	5	6	7	6	6	7	7	6	5	6	6	6	5	6	6	6	6	6	5
11	5	6	5	5	6	5	5	5	6	5	5	6	5	6	5	6	6	7	6	6	6	5	6	6	7	6	5	6	6	6	6	6	6
12	5	6	6	5	5	5	5	5	5	5	5	6	5	5	6	6	6	6	6	6	6	6	6	6	7	6	6	6	7	7	6	6	7
13	5	6	5	5	6	6	6	6	5	6	6	6	6	5	5	6	6	6	6	6	6	7	6	6	6	5	6	6	6	6	6	6	6
14	5	6	6	6	6	5	6	5	5	6	5	5	6	6	5	5	6	6	6	6	6	6	6	6	6	6	6	7	7	6	6	5	6
15	6	5	5	6	5	6	6	5	5	6	5	5	6	6	6	6	5	6	6	6	6	6	6	6	6	6	6	6	6	6	7	6	6
16	5	5	5	5	5	6	6	6	6	5	6	7	6	6	5	5	6	5	6	5	6	6	5	5	6	5	7	6	6	6	5	6	5
17	5	6	6	6	6	6	5	6	6	5	5	6	6	5	6	7	5	5	6	7	6	6	6	6	6	7	6	6	7	6	6	6	6
18	6	6	5	6	6	5	5	6	5	6	5	5	5	6	5	5	6	6	6	7	6	7	6	6	6	6	6	6	6	6	7	6	6
19	5	6	6	6	6	5	6	6	5	6	6	5	6	6	5	6	6	6	7	6	6	6	6	6	6	6	7	6	6	5	7	7	5
20	6	6	7	6	6	6	5	5	5	5	5	5	5	6	6	6	6	6	6	6	6	6	6	6	6	6	6	6	5	6	6	6	6
21	6	6	6	6	6	6	5	5	6	6	6	5	6	6	6	6	6	6	7	6	6	6	6	6	6	6	6	6	6	6	6	6	6
22	5	5	5	6	5	5	6	5	5	5	5	5	6	6	6	6	6	6	6	6	7	5	6	6	6	6	6	6	6	6	6	6	5
23	5	5	5	6	6	5	5	6	6	6	6	5	6	5	6	6	6	6	6	7	6	6	7	6	6	6	6	7	5	6	6	6	6
24	5	6	6	6	7	6	6	5	6	5	6	5	5	5	7	6	6	6	6	6	6	6	6	6	6	6	6	7	6	7	6	6	6
25	6	5	6	5	6	5	6	6	6	6	6	6	6	6	6	6	6	6	6	6	6	6	6	5	6	7	6	5	7	6	6	7	6
26	4	6	5	5	6	6	6	5	7	5	6	6	6	6	6	5	6	6	6	6	7	6	6	5	6	6	7	6	6	7	7	6	6
27	4	6	6	6	5	6	6	6	6	5	5	6	7	6	6	5	6	6	6	6	7	6	6	6	6	6	6	6	7	6	7	6	7

28	5	5	5	6	6	5	6	6	6	6	6	5	5	6	6	6	6	6	6	7	6	6	6	7	6	5	6	6	6	5	7	6	6
29	5	6	6	6	6	6	6	6	6	6	5	6	6	6	6	6	6	6	7	6	6	6	7	6	6	6	6	6	6	7	6	6	6
HRI	0	1	2	3	4	5	6	7	8	9	10	11	12	13	14	15	16	17	18	19	20	21	22	23	24	25	26	27	28	29	30	31	32
30	5	6	6	6	6	6	6	6	5	6	5	6	6	6	6	6	6	6	6	7	6	6	7	7	6	6	7	6	6	6	6	6	7
31	4	5	6	6	6	6	5	6	5	5	6	6	6	6	6	6	6	6	6	7	6	7	6	7	6	6	5	7	6	6	6	6	6
32	5	5	6	6	5	6	6	6	6	6	6	6	6	6	6	6	6	7	7	7	6	7	6	6	6	6	6	6	6	6	6	5	6
33	4	6	6	5	6	6	6	5	5	6	6	5	5	5	6	6	7	7	6	7	6	7	6	5	6	6	7	6	6	6	7	6	6
34	255	6	7	6	6	6	6	6	6	5	5	5	8	6	6	7	7	6	6	6	6	6	6	6	5	6	6	6	6	6	7	6	6
35	255	5	6	5	6	6	6	4	6	6	6	5	6	5	6	6	6	6	7	6	6	6	6	6	6	6	6	5	6	6	6	6	7
36	255	5	6	6	6	6	5	6	5	6	5	5	5	6	6	6	6	5	6	7	7	7	6	6	6	6	6	7	5	6	7	6	6
37	255	6	7	6	6	6	6	6	7	5	6	6	5	6	6	6	6	6	5	6	6	6	6	6	6	6	6	6	6	6	7	6	6
38	255	6	6	6	6	5	5	5	6	5	6	6	6	6	6	7	5	6	8	6	6	6	6	7	6	6	6	6	6	6	6	7	6
39	255	6	6	5	6	6	6	6	5	5	5	5	5	6	6	6	6	6	6	6	6	6	6	6	7	6	6	6	6	6	6	6	6
40	255	5	6	5	6	6	5	6	5	6	6	5	6	6	5	4	5	7	6	6	6	6	6	6	6	6	6	6	6	6	6	6	6
41	255	5	5	6	6	6	6	5	5	6	6	5	6	5	5	6	7	6	7	7	6	6	6	6	6	5	6	6	6	6	6	6	5
42	255	5	6	5	6	6	6	6	5	5	6	6	6	6	6	6	6	6	6	6	7	6	6	7	5	6	6	6	7	7	7	6	6
43	255	5	6	6	5	6	5	5	5	5	6	6	6	6	6	7	6	6	7	6	6	6	6	6	5	6	6	6	6	6	6	6	6
44	255	255	6	5	5	6	5	5	5	5	6	6	6	6	6	6	6	6	6	6	6	6	6	6	6	6	6	6	5	6	6	6	6
45	255	255	6	6	6	5	6	6	5	5	5	6	6	6	5	6	6	5	6	6	6	6	6	6	6	7	6	6	7	6	6	6	6
46	255	255	6	6	6	5	5	5	6	6	6	6	5	6	6	6	6	6	6	6	7	6	6	6	6	6	6	6	6	6	6	6	7
47	255	255	5	5	5	5	5	6	5	5	7	5	5	5	6	5	6	6	7	6	7	6	6	6	5	6	6	6	6	6	6	6	6
48	255	255	5	5	6	5	6	6	5	6	6	6	6	5	5	5	6	5	7	6	6	5	6	6	5	6	6	6	7	6	6	6	6
49	255	255	5	6	6	5	6	6	5	5	6	5	5	5	5	5	5	6	6	6	5	6	6	6	6	6	6	6	6	6	5	6	6
50	255	255	6	5	5	6	5	5	5	5	6	6	5	6	6	6	6	6	6	6	6	6	6	6	6	6	5	6	6	6	5	6	6
51	255	255	4	6	5	6	6	6	5	5	5	6	6	5	6	5	5	6	6	6	6	6	6	6	5	6	6	6	5	6	6	6	6
52	255	255	6	5	5	5	4	6	6	6	5	6	6	6	6	6	6	6	6	6	5	6	6	5	7	6	6	6	6	6	6	6	6
53	255	255	5	5	6	6	6	5	5	5	5	5	6	5	6	6	6	6	6	6	6	6	6	5	6	5	6	6	6	6	5	6	5
54	255	255	6	6	6	6	6	5	5	6	6	5	5	6	5	6	6	6	6	6	6	7	5	7	6	6	6	6	7	6	6	6	6
55	255	255	6	5	5	6	5	6	5	6	5	4	6	6	6	6	6	6	5	5	6	6	6	6	6	6	6	6	6	5	6	6	6
56	255	255	5	6	6	6	6	5	5	5	5	5	5	5	6	6	5	5	5	5	5	6	6	5	6	6	6	6	5	5	6	6	5
57	255	255	6	6	5	6	5	5	5	4	5	5	5	5	6	6	5	7	10	7	5	6	7	6	5	6	6	6	5	6	6	6	6
58	255	255	6	6	6	5	4	5	6	5	5	4	5	5	6	6	5	7	10	8	6	6	6	6	7	6	6	6	6	6	6	6	6
59	255	255	6	6	5	5	6	5	5	6	5	5	5	5	5	6	5	5	6	5	6	7	6	6	7	6	6	6	5	6	5	6	5

60	255	255	6	5	6	5	5	6	6	5	6	6	5	5	5	5	5	6	6	6	6	5	6	6	7	5	5	6	6	6	5	5	5
61	255	255	5	5	6	5	6	6	5	6	5	5	6	5	6	5	5	6	6	6	6	6	6	6	6	6	6	6	5	6	6	6	6
HRI	0	1	2	3	4	5	6	7	8	9	10	11	12	13	14	15	16	17	18	19	20	21	22	23	24	25	26	27	28	29	30	31	32
62	255	255	6	6	4	5	5	5	5	6	5	5	6	5	5	4	5	6	5	6	5	6	6	6	6	6	5	7	6	6	6	6	6
63	255	255	5	5	5	5	5	5	5	6	6	4	5	5	5	5	5	5	6	6	6	6	6	6	5	5	6	5	7	5	6	6	6
64	255	255	5	5	5	5	5	5	5	5	4	5	5	5	5	6	5	5	6	6	6	6	5	6	6	5	5	6	6	6	7	7	5
65	255	255	5	6	5	5	5	5	4	5	5	5	5	5	6	5	6	6	5	6	5	5	5	6	5	6	5	6	6	6	6	6	6
66	255	255	6	6	5	5	5	5	6	5	5	5	4	6	5	6	6	6	6	6	6	6	6	5	6	6	6	5	5	6	5	6	6
67	255	255	5	5	5	6	5	5	4	5	5	5	5	5	5	5	5	6	6	5	6	5	6	6	6	6	7	5	6	6	6	6	5
68	255	255	5	5	6	5	6	5	5	6	6	5	6	6	6	6	5	6	5	5	6	6	5	6	7	6	6	6	6	5	6	5	5
69	255	255	6	5	6	4	5	5	6	6	6	5	5	5	5	5	6	5	6	6	6	5	5	6	6	6	5	6	6	6	6	5	6
70	255	255	6	5	5	5	6	5	6	6	5	5	5	5	5	5	6	5	6	5	6	5	6	5	6	6	6	6	6	6	6	6	6
71	255	255	5	6	6	5	6	5	6	5	5	6	6	6	6	5	5	5	6	5	5	6	5	5	5	6	6	6	6	5	6	5	6
72	255	255	5	5	6	5	5	5	5	5	5	6	5	5	6	4	6	5	5	6	5	6	6	5	5	6	6	6	6	6	6	6	6
73	255	255	4	5	6	5	5	5	5	5	6	5	6	6	5	5	5	5	6	6	6	6	6	6	6	5	6	6	5	6	5	6	6
74	255	255	5	6	4	5	5	5	5	5	5	5	5	5	5	6	6	6	5	5	6	6	5	6	6	5	5	6	6	5	6	6	5
75	255	3	5	4	5	6	5	5	5	5	6	5	5	5	5	6	5	6	6	5	5	5	6	4	6	6	6	6	5	6	5	6	5
76	255	4	6	5	5	6	6	5	6	5	6	5	6	6	5	6	6	6	5	5	5	6	6	6	8	5	6	5	6	6	6	5	6
77	255	5	5	5	6	5	5	6	6	6	6	6	5	5	6	5	6	6	6	6	6	6	5	5	6	5	6	6	5	6	6	5	5
78	255	5	6	5	5	6	5	6	5	6	5	5	6	5	5	5	5	6	7	7	6	5	6	5	6	6	6	5	6	5	7	6	5
79	4	6	5	5	5	5	5	6	5	5	5	5	5	5	5	5	6	5	6	6	6	6	6	6	6	6	6	5	6	6	6	6	6
80	4	6	6	5	5	5	5	5	6	5	5	5	5	5	5	5	5	5	7	6	5	5	6	6	6	5	6	6	6	5	6	6	5
81	5	6	6	6	6	5	6	5	5	4	5	5	4	5	5	6	5	6	6	5	6	5	6	6	6	6	6	6	5	6	5	5	5
82	4	5	5	5	5	5	5	5	5	5	6	4	5	4	5	7	5	6	6	6	6	6	5	5	6	6	6	6	6	6	6	6	6
83	4	5	6	6	6	4	5	5	4	5	5	5	5	5	5	7	6	5	6	6	5	6	5	6	6	5	6	6	6	6	5	6	6
84	4	5	6	5	6	5	4	5	5	5	5	5	6	5	5	5	5	6	6	6	6	6	6	6	5	5	5	5	6	5	5	6	6
85	4	5	5	5	4	5	5	5	5	5	5	6	5	6	6	5	5	6	6	5	6	5	6	5	6	5	6	6	5	5	6	6	5
86	4	5	5	5	5	4	5	5	5	6	5	5	5	5	6	5	5	6	5	5	5	5	5	5	6	5	5	5	5	5	5	5	5
87	4	5	5	5	5	5	5	5	5	4	5	6	5	5	5	5	5	6	6	6	5	5	5	5	6	6	5	5	6	5	6	5	4
88	4	5	6	5	4	5	4	5	5	5	5	5	5	5	5	6	5	6	5	6	6	6	6	5	5	6	6	5	6	5	6	6	6
89	4	5	6	6	5	4	6	4	5	5	5	5	5	5	5	6	5	6	6	6	6	6	6	6	5	6	6	6	6	6	5	5	5
90	3	6	6	5	5	5	6	5	5	5	5	5	5	4	5	5	5	6	6	6	5	5	5	6	5	5	6	5	6	6	5	5	5
91	4	6	6	5	5	6	5	4	5	5	5	5	6	5	6	5	6	6	6	6	6	6	6	6	5	5	6	4	6	6	5	6	6

92	5	5	5	5	5	5	5	6	4	4	5	5	5	4	5	6	6	5	6	6	6	6	6	6	6	5	5	5	6	5	6	6	5
93	3	5	5	5	5	5	6	4	5	5	5	5	5	6	6	5	5	5	6	5	5	5	5	5	4	6	5	5	5	5	5	5	6
HRI	0	1	2	3	4	5	6	7	8	9	10	11	12	13	14	15	16	17	18	19	20	21	22	23	24	25	26	27	28	29	30	31	32
94	4	5	5	5	5	5	6	5	5	4	6	5	5	4	4	5	6	5	6	6	6	5	6	6	5	6	5	6	6	6	5	6	5
95	4	5	5	5	5	5	5	5	5	5	5	5	4	5	5	5	5	5	5	5	5	6	5	5	5	5	4	6	6	4	7	6	5
96	3	5	5	5	6	5	5	5	5	6	5	5	6	5	5	5	5	5	5	5	6	5	5	4	6	5	6	5	4	5	6	6	6
97	4	5	5	5	5	5	5	5	6	6	5	5	5	5	5	5	5	6	5	6	5	6	5	6	5	5	5	5	5	5	5	5	5
98	3	5	5	5	5	4	5	5	5	5	5	5	5	5	5	5	6	5	5	5	6	5	5	5	6	5	5	5	5	6	6	5	5
99	3	5	6	5	5	5	4	5	5	5	4	5	5	5	5	4	5	4	5	5	6	5	5	6	5	5	5	5	6	6	6	6	6
100	3	5	5	5	5	4	5	5	5	5	5	5	5	5	5	5	5	5	5	5	6	5	6	5	5	5	6	5	5	5	6	6	5
101	4	5	6	4	5	5	5	4	5	5	5	4	5	5	4	5	5	6	5	5	6	6	5	5	6	6	6	5	6	5	5	5	5
102	3	5	6	5	5	4	5	5	6	4	4	5	5	5	5	6	5	5	5	5	5	5	5	5	6	6	5	5	5	5	6	5	5
103	3	4	4	5	6	4	4	4	5	5	5	5	3	4	4	5	6	6	6	6	6	5	6	5	6	6	5	5	4	5	6	5	5
104	3	5	5	5	5	4	5	4	4	4	5	5	5	4	4	6	5	5	6	6	5	5	6	5	5	5	5	4	5	7	5	5	5
105	3	5	5	5	5	4	5	5	4	5	5	4	5	4	5	5	5	5	5	5	5	5	5	5	5	5	6	5	5	5	6	6	5
106	3	5	4	5	5	5	5	5	4	5	4	5	5	5	5	5	5	5	4	5	5	5	5	5	5	4	5	5	5	5	6	6	5
107	3	4	5	5	5	5	6	5	5	5	4	4	5	5	4	4	5	5	5	5	5	5	5	5	5	5	5	5	6	5	5	5	6
108	4	3	5	5	5	5	5	6	5	5	5	4	5	5	4	6	5	6	5	5	4	5	5	5	6	5	5	5	5	5	5	5	6
109	3	5	5	4	4	4	5	5	5	6	5	4	5	5	4	6	5	5	5	5	5	5	4	5	5	5	5	5	5	5	6	5	6
110	3	5	5	4	5	5	5	5	4	5	5	5	5	5	4	5	6	5	5	5	5	6	5	5	5	5	4	6	6	6	5	5	5
111	4	5	5	5	4	5	4	5	5	4	5	5	4	5	6	5	6	5	5	6	5	5	6	5	6	5	5	6	5	6	6	5	5
112	4	5	5	4	4	5	6	5	5	4	5	5	5	5	5	5	5	5	5	5	6	5	6	5	6	5	5	5	5	6	5	5	5
113	3	5	5	5	5	4	5	5	4	5	5	5	4	5	5	4	5	5	6	5	5	5	5	5	5	5	5	5	5	5	5	5	5
114	4	5	5	5	5	4	5	4	4	4	4	4	4	4	5	5	6	6	5	6	5	5	5	5	5	5	5	5	6	5	5	5	5
115	3	6	5	4	5	5	4	4	5	4	5	5	4	5	5	5	5	5	5	5	5	5	5	5	6	6	5	5	5	5	5	5	5
116	4	5	5	5	5	5	5	5	4	4	4	5	5	4	4	5	5	5	6	5	6	5	5	5	5	5	6	5	5	5	5	5	5
117	3	5	5	5	5	5	5	5	5	4	5	5	5	5	5	5	5	5	5	5	6	5	5	5	6	5	5	5	5	5	5	5	6
118	4	5	5	5	4	5	4	4	5	4	5	4	5	5	5	5	5	5	5	5	6	5	5	6	5	5	5	6	5	6	6	5	5
119	3	5	5	5	4	4	4	4	4	4	4	4	4	5	6	5	5	6	6	5	5	5	5	5	5	5	5	5	5	6	5	5	5
120	3	4	4	5	4	5	4	5	5	4	5	5	5	5	5	5	4	5	5	5	4	6	6	6	6	5	6	5	5	5	5	5	4
121	3	4	5	5	4	4	5	5	5	5	5	5	4	5	5	4	5	5	5	5	5	5	5	5	5	4	5	5	5	5	5	6	5
122	3	4	5	5	5	5	5	5	5	5	4	4	5	5	5	5	5	5	5	5	5	5	5	5	5	5	5	5	5	5	5	6	5
123	4	5	5	5	5	4	5	5	4	5	4	5	5	5	5	5	5	5	5	5	6	6	6	6	5	5	5	5	5	5	5	5	4

124	3	4	5	4	5	5	4	4	5	5	4	5	4	4	5	5	4	5	6	5	5	5	5	5	5	5	4	4	5	5	5	5	5
125	3	5	5	5	5	5	5	5	4	4	5	4	5	4	4	5	5	5	4	5	5	5	4	6	5	5	5	5	5	5	5	5	6
HRI	0	1	2	3	4	5	6	7	8	9	10	11	12	13	14	15	16	17	18	19	20	21	22	23	24	25	26	27	28	29	30	31	32
126	3	5	5	4	5	5	4	5	5	5	4	4	8	4	7	4	5	5	5	5	5	5	5	5	5	5	5	5	5	5	5	5	5
127	3	5	4	5	6	6	5	5	5	4	5	5	5	4	5	5	5	5	5	5	5	5	5	4	5	5	5	5	5	5	5	4	5
128	3	5	5	5	5	4	4	4	5	5	6	5	4	5	5	4	5	5	5	5	6	5	5	5	5	5	5	5	6	6	5	5	5
129	3	4	5	5	5	4	5	5	5	5	5	5	5	5	5	5	4	6	5	5	5	5	5	5	5	5	6	5	5	5	5	5	5
130	3	5	5	4	6	4	5	4	5	5	5	5	5	4	5	5	5	5	5	5	5	5	5	5	6	5	5	5	5	5	5	5	5
131	255	4	4	4	4	5	4	4	6	5	5	5	5	5	5	5	5	5	5	5	5	5	5	5	5	5	5	5	4	5	4	5	5
132	255	7	4	5	5	4	5	4	4	4	4	5	5	5	5	5	5	5	5	6	5	5	4	5	4	5	5	5	5	5	5	5	5
133	255	5	5	5	5	5	4	5	5	5	5	5	5	5	5	5	5	4	5	4	4	5	5	4	4	4	5	5	5	5	6	5	5
134	255	4	5	5	4	4	4	5	5	5	4	5	5	5	5	4	4	5	5	5	5	5	5	4	4	4	4	5	5	6	6	6	5
135	255	4	5	5	4	5	5	5	5	5	5	4	4	4	5	4	4	5	5	5	5	5	5	4	5	10	7	4	4	5	5	4	6
136	255	5	5	4	5	4	4	5	5	5	6	4	4	5	4	6	5	5	5	5	5	4	5	5	4	8	5	4	5	5	6	5	5
137	255	4	5	5	5	5	4	5	5	4	5	5	4	4	5	6	4	4	5	5	5	5	4	5	4	4	4	5	5	5	5	5	4
138	255	4	5	5	5	5	5	5	6	4	5	5	5	5	6	4	5	5	6	5	6	5	5	7	6	5	5	5	7	4	5	5	5
139	255	5	5	4	4	5	5	4	4	5	5	5	5	4	5	5	5	5	5	5	5	5	5	4	4	5	5	4	4	5	5	5	5
140	255	5	5	5	5	4	4	5	5	4	6	5	5	4	4	5	5	6	5	5	6	6	5	5	5	4	4	4	5	4	5	5	5
141	255	4	5	5	4	5	4	5	5	5	5	5	5	4	4	5	5	5	5	5	5	6	5	4	5	4	4	4	5	5	4	5	4
142	255	4	5	4	5	4	4	5	5	5	5	5	6	5	5	5	4	5	4	5	5	5	5	5	4	5	5	5	5	5	5	5	4
143	255	4	5	4	4	4	5	5	5	5	5	5	5	5	5	5	5	5	4	5	6	5	5	4	5	5	5	5	5	5	5	4	5
144	255	6	5	5	5	5	5	4	5	5	5	5	5	5	5	5	6	4	5	5	5	5	4	5	5	6	5	6	5	6	5	6	5
145	255	4	4	5	5	6	5	5	5	5	5	5	5	5	5	5	5	4	5	4	5	5	5	5	5	4	6	4	4	5	5	4	4
146	255	4	5	5	5	5	5	5	5	5	5	4	4	5	5	5	5	5	5	6	4	5	5	5	4	5	5	5	4	6	5	5	5
147	255	4	5	5	5	5	6	4	5	4	5	5	5	5	5	5	5	5	5	5	4	5	5	5	5	4	5	5	5	5	5	5	5
148	255	4	4	5	5	5	5	5	6	4	4	5	5	6	5	4	5	5	5	5	5	5	4	5	5	5	5	5	5	5	5	5	5
149	255	4	4	4	5	5	6	4	5	4	5	4	5	5	4	4	5	5	5	5	5	5	5	6	6	5	6	5	5	5	5	6	5
150	255	5	4	5	5	5	4	5	4	4	4	4	5	4	5	5	5	5	6	5	5	5	5	5	6	5	5	5	5	5	5	5	4
151	255	5	5	5	5	5	5	4	5	5	4	4	4	5	5	4	5	5	5	5	5	5	6	5	5	5	5	5	5	5	4	5	5
152	255	4	4	4	5	5	5	4	5	4	5	5	5	5	5	5	5	5	4	5	5	4	5	5	5	5	4	5	5	5	5	5	5
153	255	4	4	5	5	4	4	5	4	5	4	4	4	4	5	5	4	5	5	5	5	5	4	5	5	5	5	4	5	5	5	5	6
154	255	4	5	4	4	4	5	5	5	5	4	5	5	5	4	4	3	8	7	4	5	5	5	4	5	5	4	5	5	5	6	5	4
155	255	5	5	5	4	5	4	5	5	5	4	5	4	5	4	4	4	5	5	6	5	6	5	4	5	6	4	4	4	6	4	5	5

156	255	4	5	4	5	5	5	4	4	5	4	4	4	5	5	4	5	4	5	5	5	5	5	4	5	4	5	5	6	4	6	5	4
157	255	4	4	4	5	5	4	4	4	4	5	5	5	5	5	5	5	5	5	4	4	5	5	5	4	5	5	5	4	5	5	5	4
HRI	0	1	2	3	4	5	6	7	8	9	10	11	12	13	14	15	16	17	18	19	20	21	22	23	24	25	26	27	28	29	30	31	32
158	255	3	5	4	5	5	4	4	5	5	4	4	5	5	4	4	4	5	5	5	5	5	6	5	5	5	5	5	4	5	5	5	5
159	255	4	5	5	5	4	4	5	4	4	5	4	5	5	4	4	5	5	5	6	5	5	5	5	5	5	4	4	4	5	5	5	5
160	255	4	4	5	5	5	5	5	4	4	4	4	4	5	4	4	5	4	5	5	5	5	5	5	4	5	5	5	5	4	4	5	5
161	255	4	5	5	5	4	5	4	5	5	7	5	4	5	4	5	4	5	5	5	5	6	4	4	5	5	5	4	5	4	5	5	5
162	255	5	5	5	4	5	7	5	4	5	4	3	4	5	4	5	5	5	5	5	5	5	5	5	5	5	5	5	4	5	5	5	5
163	255	3	5	5	5	5	4	4	5	5	5	3	4	4	4	4	5	5	6	5	4	5	5	6	4	5	5	5	4	5	5	5	5
164	255	4	5	4	5	4	4	5	4	5	4	4	5	4	4	5	4	4	5	5	5	5	5	5	5	5	4	5	5	5	5	5	5
165	255	4	4	5	4	4	4	5	4	5	4	4	4	4	4	4	5	5	5	5	5	4	5	5	5	7	5	5	5	5	5	6	5
166	255	3	6	5	4	5	4	5	5	5	4	5	5	5	4	4	4	5	5	5	4	4	5	4	4	5	5	5	5	5	5	5	5
167	255	3	5	4	4	5	5	5	5	4	5	4	5	5	5	5	5	4	5	5	5	6	5	5	5	5	4	4	5	5	5	4	5
168	255	4	4	5	4	6	6	4	4	4	5	5	4	5	5	5	4	5	5	5	5	5	5	4	5	5	4	5	4	5	5	5	5
169	255	4	5	5	5	5	4	4	5	4	5	5	5	5	4	4	5	5	4	5	5	5	5	5	4	5	4	3	5	5	5	6	4
170	255	4	5	4	4	4	4	4	5	4	4	4	4	5	5	5	5	5	5	5	5	6	5	5	5	5	5	5	5	4	5	5	5
171	255	4	5	5	5	5	4	5	4	4	5	5	5	4	4	5	4	6	5	5	5	5	5	5	5	5	5	5	4	4	5	5	4
172	255	4	5	5	5	4	5	5	5	4	4	4	4	4	5	5	6	5	6	5	5	5	4	5	5	5	5	4	5	5	5	5	5
173	255	4	5	5	4	5	4	4	5	4	5	4	4	4	5	5	5	4	5	4	4	5	5	5	4	5	5	5	4	5	5	5	5
174	255	3	4	5	5	5	4	5	4	4	4	4	5	4	4	5	4	4	6	5	5	5	4	5	5	5	4	5	5	5	5	5	4
175	255	4	5	5	4	5	5	5	5	5	5	4	5	5	5	5	5	5	5	5	5	5	5	5	5	5	5	4	4	5	5	5	5
176	255	4	5	5	4	5	4	5	5	4	5	5	4	5	4	5	4	5	4	5	5	5	5	6	5	5	5	4	5	4	5	5	6
177	255	4	5	4	5	4	5	5	4	4	4	5	4	4	4	5	5	5	5	5	5	4	5	5	5	5	5	4	5	5	5	5	5
178	255	4	4	4	3	4	4	5	5	4	3	4	4	4	4	5	5	4	4	3	5	4	5	5	4	5	5	5	4	5	5	5	5
179	255	4	5	4	6	7	4	5	4	5	4	4	5	5	4	5	5	4	5	4	4	5	5	5	5	5	4	5	6	5	5	5	5
180	255	3	4	4	5	5	3	4	5	5	5	4	5	4	4	5	5	5	5	5	5	5	5	5	5	5	5	4	5	5	4	5	5
181	255	3	5	4	4	3	5	5	4	4	4	4	4	4	4	4	4	4	4	5	5	5	5	5	5	5	5	5	5	4	5	5	5
182	255	3	5	4	4	4	5	4	5	4	5	5	5	4	5	4	4	4	4	4	4	4	5	5	5	5	4	5	4	5	5	4	5
183	255	3	5	5	4	4	4	3	4	4	5	4	4	4	5	4	5	4	5	5	6	5	5	6	4	5	5	5	5	5	5	5	5
184	255	4	4	4	4	4	4	7	3	4	4	4	5	4	4	5	4	5	5	5	5	4	5	5	5	5	5	4	5	5	5	5	4
185	255	3	4	5	4	4	5	7	4	4	4	4	5	5	4	4	5	4	5	5	5	4	4	5	5	4	5	4	5	5	4	4	4
186	255	4	5	5	5	4	3	4	3	4	4	4	3	4	5	5	4	4	5	5	5	5	5	5	4	5	5	5	5	4	5	5	4
187	255	3	5	5	4	4	4	4	4	5	5	4	4	5	5	5	3	5	5	5	5	5	5	5	5	5	5	5	5	5	5	7	4

188	255	3	4	5	4	4	4	4	4	5	4	5	5	5	5	4	5	5	4	5	5	5	4	4	4	4	5	4	5	5	5	5	5
189	255	3	5	5	4	4	5	4	4	4	4	4	5	4	5	4	4	4	5	5	5	6	5	5	4	4	4	5	4	5	5	5	4
HRI	0	1	2	3	4	5	6	7	8	9	10	11	12	13	14	15	16	17	18	19	20	21	22	23	24	25	26	27	28	29	30	31	32
190	255	4	4	5	5	5	4	4	4	4	5	4	4	4	4	5	5	4	5	4	5	5	5	4	4	6	5	5	4	5	5	4	4
191	255	4	5	5	5	4	4	4	4	5	4	5	4	4	5	4	5	4	4	5	4	4	5	5	4	4	4	5	4	4	4	5	5
192	255	3	4	4	4	4	4	4	4	5	4	4	4	4	4	4	5	4	4	4	4	5	4	5	4	5	5	5	5	5	4	5	4
193	255	4	4	3	4	3	3	4	4	4	4	4	4	4	4	4	5	4	5	5	5	4	5	5	4	5	5	5	4	5	5	4	5
194	255	3	4	4	4	4	3	5	4	4	4	4	5	4	4	5	4	4	5	4	4	4	5	4	5	4	4	4	5	5	4	5	5
195	255	3	4	4	4	4	4	5	6	3	4	4	4	4	4	4	3	4	5	5	5	5	5	4	5	5	5	5	5	4	4	5	5
196	255	3	4	5	4	5	4	4	4	4	4	4	4	4	4	6	5	4	5	4	4	5	5	5	5	5	4	4	5	5	4	4	4
197	255	255	5	4	4	3	4	3	5	5	4	4	4	4	4	4	6	5	5	5	4	5	5	4	5	4	4	4	5	4	4	5	4
198	255	255	255	3	4	3	3	4	4	4	4	4	5	4	4	4	4	4	5	6	4	4	5	4	4	4	4	4	5	5	5	5	4
199	255	255	255	3	3	4	3	4	5	4	4	4	4	5	3	4	4	5	4	5	5	4	5	5	4	5	5	5	4	5	5	5	4
200	255	255	255	3	5	5	4	4	5	4	5	4	4	4	4	5	4	5	5	5	5	4	5	4	4	5	5	4	5	5	5	5	5
201	255	255	255	2	3	4	4	4	4	4	4	5	5	5	4	4	4	5	4	4	4	4	5	4	5	5	5	4	5	5	4	5	5
202	255	255	255	255	4	4	5	5	5	4	4	4	5	4	5	4	5	4	4	4	4	5	5	4	4	5	5	5	5	5	4	5	4
203	255	255	255	255	4	3	5	5	4	5	5	4	4	4	5	4	4	5	5	4	5	5	5	5	5	4	4	5	4	5	5	4	4
204	255	255	255	255	3	3	3	4	5	5	4	4	4	5	4	3	4	5	5	5	5	4	4	5	4	5	4	5	5	4	4	4	4
205	255	255	255	255	4	4	4	4	4	4	4	4	5	3	4	5	4	5	5	4	5	5	5	4	5	4	4	4	5	5	4	5	4
206	255	255	255	255	3	4	3	4	4	4	4	5	5	3	4	5	4	5	5	4	4	5	5	4	6	5	4	4	5	5	5	4	4
207	255	255	255	255	3	4	3	3	3	5	4	3	4	3	4	4	5	4	5	5	4	5	5	5	4	5	5	4	4	4	4	5	5
208	255	255	255	255	3	3	4	3	3	4	4	3	4	4	4	4	5	4	4	5	5	5	4	5	5	5	5	4	4	4	5	5	5
209	255	255	255	255	3	4	4	4	3	4	4	4	4	4	3	3	4	5	4	5	5	5	4	4	4	5	4	5	4	4	4	4	4
210	255	255	255	255	3	3	3	4	4	4	4	4	5	4	5	4	4	4	4	5	5	4	5	4	4	5	4	5	4	4	4	4	4
211	255	255	255	255	3	4	5	4	4	4	4	4	3	4	4	4	4	4	4	4	5	4	5	5	5	4	4	4	5	5	4	4	5
212	255	255	255	255	3	3	4	4	4	3	4	4	4	3	4	4	4	4	4	3	5	4	4	4	4	5	4	5	5	5	4	4	4
213	255	255	255	255	3	3	4	4	5	4	4	4	4	4	4	3	4	4	3	3	4	4	5	5	4	4	4	4	5	4	5	4	4
214	255	255	255	255	3	3	3	3	4	4	4	4	4	4	4	4	5	5	4	5	4	5	5	4	5	3	4	4	4	4	5	4	4
215	255	255	255	255	3	4	3	4	3	4	4	4	4	4	4	4	4	3	4	4	5	5	4	4	5	5	5	4	3	5	4	3	5
216	255	255	255	255	3	4	4	4	3	3	4	4	4	4	4	3	4	3	4	5	4	5	5	5	4	5	5	4	4	4	4	4	5
217	255	255	255	3	3	3	4	3	4	3	3	3	4	4	4	3	4	3	4	4	4	5	5	4	4	5	4	4	4	5	4	4	4
218	255	255	3	3	4	3	3	4	4	4	4	4	3	4	3	3	7	5	4	5	4	4	4	4	4	4	5	4	4	4	4	4	4
219	255	255	3	4	4	3	4	4	4	4	3	5	4	4	3	3	6	4	4	5	5	5	4	4	5	4	5	4	4	5	4	4	3

220	255	255	3	4	3	4	4	4	4	4	4	4	4	4	4	3	5	4	5	4	4	5	4	4	5	5	5	4	4	4	4	4	5
221	255	255	3	4	4	4	5	4	4	3	4	4	3	4	4	4	4	4	4	4	4	5	4	4	4	5	4	5	4	4	4	4	4
HRI	0	1	2	3	4	5	6	7	8	9	10	11	12	13	14	15	16	17	18	19	20	21	22	23	24	25	26	27	28	29	30	31	32
222	255	255	3	4	4	4	4	4	4	3	4	4	4	4	4	4	3	4	5	5	4	4	5	5	5	5	5	4	4	4	5	4	4
223	255	255	3	4	4	4	3	4	4	4	4	3	4	4	5	4	4	4	4	4	4	6	4	4	5	5	5	4	4	5	4	4	4
224	255	255	4	4	4	4	4	4	5	4	4	4	4	4	4	4	5	4	4	5	4	4	4	5	4	5	4	4	5	4	5	4	5
225	255	255	3	5	4	3	5	5	4	4	4	4	3	4	4	4	4	4	4	5	4	5	4	4	4	7	4	4	5	5	5	4	4
226	255	255	3	4	4	3	3	3	3	4	4	4	3	4	4	4	4	4	4	3	4	4	4	4	4	4	4	4	5	4	4	5	4
227	255	255	4	4	4	4	5	4	4	4	4	4	4	4	4	4	4	3	4	4	4	4	4	4	4	4	4	4	5	4	5	4	4
228	255	255	3	5	3	4	3	4	5	4	4	4	4	3	5	4	4	4	3	4	4	4	4	4	5	4	4	4	4	4	4	3	4
229	255	255	4	4	3	4	4	4	4	4	3	4	4	4	4	3	3	4	4	4	5	4	4	4	5	5	4	4	4	4	4	4	5
230	255	255	3	4	4	4	3	3	4	3	3	4	3	3	4	3	5	4	4	4	4	4	4	4	4	4	5	4	4	3	3	4	4
231	255	255	4	4	3	4	3	3	3	3	3	4	3	4	4	4	4	4	4	5	4	4	4	4	4	5	4	4	4	4	4	4	4
232	255	255	3	4	3	3	3	3	4	5	3	4	3	3	3	4	4	3	4	4	5	5	5	4	4	4	4	3	4	4	4	4	5
233	255	255	3	4	3	4	3	3	4	3	3	4	3	4	4	3	4	4	4	4	4	4	4	4	4	4	4	5	4	4	4	4	4
234	255	255	3	3	3	4	4	3	3	3	3	4	4	4	4	3	3	4	4	4	5	4	3	4	5	4	4	4	4	4	3	4	4
235	255	255	4	4	3	3	3	3	3	3	3	4	3	4	3	4	3	3	4	3	4	4	4	4	4	4	4	3	4	5	4	4	4
236	255	255	3	3	4	3	4	4	3	4	4	3	3	4	3	3	4	4	4	4	5	3	4	3	3	4	4	3	4	4	4	4	4
237	255	255	3	4	3	3	5	3	3	3	3	3	3	4	3	3	4	4	5	7	5	4	4	4	3	4	4	5	4	4	4	4	4
238	255	255	3	3	3	3	4	3	3	3	3	4	3	4	4	5	4	3	3	5	4	4	4	3	5	4	4	4	4	3	3	3	4
239	255	255	3	3	3	4	3	3	3	3	3	3	4	3	3	3	4	3	3	3	3	4	4	3	4	3	4	4	4	4	4	4	4
240	255	255	3	4	3	3	3	3	3	3	3	3	4	3	3	4	3	4	3	3	4	4	5	4	4	3	4	4	4	4	4	4	4
241	255	255	3	3	3	4	3	4	3	3	3	3	3	3	3	4	3	4	5	4	5	4	3	4	4	3	4	3	3	4	4	4	4
242	255	255	3	3	3	3	3	3	3	3	3	3	3	3	4	3	4	4	6	3	3	4	4	4	4	4	4	4	4	3	3	4	3
243	255	255	3	3	3	3	3	3	3	3	3	4	3	3	3	4	3	3	4	4	4	3	4	3	4	4	3	4	3	3	3	4	3
244	255	255	3	4	3	3	3	3	3	3	3	3	3	4	3	3	3	4	4	3	4	4	4	3	4	4	3	4	4	4	4	4	4
245	255	255	3	3	3	3	3	3	3	3	3	3	3	3	4	3	3	3	4	4	3	4	4	4	4	4	3	3	4	3	4	4	4
246	255	255	3	3	3	3	3	3	3	4	3	3	3	3	3	3	3	3	3	4	3	3	4	4	3	3	3	4	3	3	4	4	4
247	255	255	3	3	3	3	3	3	4	3	4	3	4	4	4	3	3	4	3	3	3	3	3	3	4	3	3	3	3	3	3	4	3
248	255	255	3	3	3	3	3	3	4	4	3	3	3	3	4	3	3	3	3	5	5	3	3	4	3	3	3	4	3	3	4	3	3
249	255	255	3	4	3	3	4	3	3	3	3	3	3	3	3	3	3	3	3	6	4	3	3	3	4	4	4	3	3	4	3	3	3
250	255	255	3	3	5	3	3	4	3	3	3	3	3	3	3	3	4	3	3	3	3	3	3	3	3	4	3	3	3	3	3	3	3
251	255	255	3	3	3	3	3	3	3	3	3	3	3	3	3	3	3	3	3	3	3	3	3	3	3	3	3	3	3	3	3	3	3

252	255	255	2	3	3	3	3	3	3	3	3	3	3	3	3	3	3	3	3	3	3	3	3	3	3	3	3	3	3	3	3	3
253	255	255	1	2	1	2	2	1	1	1	2	1	1	2	1	1	2	2	2	2	2	2	2	1	3	3	2	2	2	2	1	1	2

Table 1b. Columns 33-64 of the H ratio bin designator for the **HRI**.
Table 1c. Columns 65-96 of the H ratio bin designator for the **HRI**.
Table 1d. Columns 97-128 of the H ratio bin designator for the **HRI**.
Table 1e. Columns 129-159 of the H ratio bin designator for the **HRI**.

Table 2a. Columns 0-32 of the H ratio bin designator for the **MRI**.
Table 2b. Columns 33-64 of the H ratio bin designator for the **MRI**.
Table 2c. Columns 65-96 of the H ratio bin designator for the **MRI**.
Table 2d. Columns 97-128 of the H ratio bin designator for the **MRI**.
Table 2e. Columns 129-160 of the H ratio bin designator for the **MRI**.
Table 2f. Columns 161-175 of the H ratio bin designator for the **MRI**.

Table 3a. Columns 0-32 of the H ratio bin designator for the **SLI**.
Table 3b. Columns 33-64 of the H ratio bin designator for the **SLI**.
Table 3c. Columns 65-96 of the H ratio bin designator for the **SLI**.
Table 3d. Columns 97-128 of the H ratio bin designator for the **SLI**.

Table 4.1.2.4-2

Weighted coefficients for the HRI, MRI and SLI. Color has been added to this table to avoid confusion and facilitate reading of numbers. The HRI is coded green, the MRI pink and the SLI yellow. Wavelengths in increments of 50 nm are underlined.

Wave	HRI a	HRI b	HRI c	MRI a	MRI b	MRI c	SLI a	SLI b	SLI c
600	3.288974	-1.32550E-02	1.665190E-05	5.111286	-2.809130E-02	4.752022E-05	4.916132	-2.681690E-02	4.555899E-05
610	2.418571	-5.19748E-03	-1.911770E-06	2.120584	1.272830E-04	-1.805949E-05	1.894906	2.022280E-03	-2.202743E-05
620	3.036622	-1.04974E-02	9.139965E-06	3.864251	-1.649534E-02	1.951607E-05	3.786977	-1.582640E-02	1.810568E-05
630	6.932502	-3.73153E-02	5.388908E-05	8.363853	-4.863792E-02	7.649633E-05	8.709702	-5.101840E-02	8.062100E-05
640	11.550716	-6.75313E-02	1.011196E-04	18.958386	-1.220593E-01	2.003961E-04	19.757071	-1.272160E-01	2.084717E-04
650	4.280622	-1.43356E-02	4.494052E-06	9.466947	-4.964568E-02	6.302795E-05	9.767006	-5.147660E-02	6.560333E-05
660	1.218266	3.43220E-03	-1.758690E-05	1.783594	1.757473E-03	-1.995971E-05	1.846405	1.377690E-03	-1.943957E-05
670	1.13103	1.06200E-03	-6.576115E-06	1.119748	1.949033E-03	-1.001173E-05	1.128906	1.883840E-03	-9.890641E-06
680	1.14824	1.55337E-05	-2.600322E-06	1.169833	1.036833E-05	-2.951323E-06	1.178632	-7.962670E-05	-2.723885E-06
690	1.132828	-2.06158E-04	-1.417045E-06	1.170288	-4.830111E-04	-9.209733E-07	1.180867	-5.909070E-04	-6.526977E-07
700	1.095146	-8.66387E-05	-1.270609E-06	1.132769	-3.923761E-04	-6.570176E-07	1.144507	-5.056740E-04	-3.868393E-07
710	1.063243	5.74426E-05	-1.325585E-06	1.09917	-2.378110E-04	-7.248308E-07	1.111581	-3.528090E-04	-4.583687E-07
720	1.051643	6.57093E-05	-1.164638E-06	1.083889	-1.953717E-04	-6.395075E-07	1.093074	-2.935570E-04	-3.879672E-07
730	1.025303	1.90553E-04	-1.232495E-06	1.050522	-4.726235E-06	-8.583844E-07	1.058149	-9.856340E-05	-5.981789E-07
740	1.005586	2.18169E-04	-1.009786E-06	1.018717	1.166237E-04	-8.143735E-07	1.025921	2.198150E-05	-5.432133E-07
750	0.963112	3.84177E-04	-9.665908E-07	0.967982	3.423563E-04	-8.754751E-07	0.976417	2.372720E-04	-5.817663E-07
760	0.908761	5.94740E-04	-9.090922E-07	0.901442	6.413009E-04	-9.714695E-07	0.91181	5.295140E-04	-6.841600E-07
770	0.863176	7.54517E-04	-7.824690E-07	0.856536	8.049467E-04	-8.741732E-07	0.867289	6.878980E-04	-5.716742E-07
780	0.85718	6.48941E-04	-2.357488E-07	0.842646	7.681261E-04	-4.748638E-07	0.851954	6.652280E-04	-2.078589E-07
790	0.828506	7.47089E-04	-1.525834E-07	0.816895	8.593257E-04	-4.153557E-07	0.82361	7.673580E-04	-1.475281E-07
800	0.833012	5.98054E-04	3.903167E-07	0.811271	7.923628E-04	-3.375598E-08	0.820289	6.842670E-04	2.598304E-07

810	0.808892	6.40763E-04	6.342086E-07	0.784474	8.523508E-04	1.858560E-07	0.796538	7.196040E-04	5.305716E-07
820	0.804004	5.19249E-04	1.218913E-06	0.775586	7.501205E-04	7.592601E-07	0.782894	6.574500E-04	1.017625E-06
830	0.769592	5.84289E-04	1.548489E-06	0.741416	8.179728E-04	1.071970E-06	0.751243	7.056300E-04	1.370365E-06
840	0.768034	3.81093E-04	2.422684E-06	0.724258	7.302301E-04	1.739966E-06	0.729972	6.607260E-04	1.932139E-06
850	0.715047	5.58351E-04	2.603638E-06	0.676204	8.734291E-04	1.977582E-06	0.684124	7.785580E-04	2.234335E-06
860	0.746674	1.15022E-04	3.917412E-06	0.687043	6.302120E-04	2.817308E-06	0.69328	5.559430E-04	3.018810E-06
870	0.551166	1.42498E-03	1.902245E-06	0.534266	1.601658E-03	1.457453E-06	0.541877	1.511700E-03	1.703015E-06
880	0.538356	1.27811E-03	2.751388E-06	0.518945	1.458275E-03	2.336711E-06	0.525667	1.380230E-03	2.549068E-06
890	0.531977	1.02575E-03	3.889665E-06	0.506863	1.255058E-03	3.369906E-06	0.510508	1.191200E-03	3.578455E-06
900	0.705137	-8.16463E-04	8.586537E-06	0.664135	-4.605281E-04	7.821583E-06	0.674648	-5.741800E-04	8.117875E-06
910	0.59218	-8.57303E-05	7.513227E-06	0.54541	2.972283E-04	6.736824E-06	0.551387	2.246860E-04	6.941266E-06
920	0.560715	-1.62827E-04	8.374011E-06	0.507345	2.745011E-04	7.489396E-06	0.515397	1.744900E-04	7.769978E-06
930	0.605488	-9.09530E-04	1.069717E-05	0.531685	-3.019800E-04	9.462133E-06	0.536014	-3.668970E-04	9.661755E-06
940	0.621983	-1.40141E-03	1.249612E-05	0.540727	-7.312909E-04	1.113373E-05	0.547967	-8.261790E-04	1.140822E-05
950	0.646745	-1.95553E-03	1.441543E-05	0.544412	-1.134064E-03	1.279101E-05	0.54783	-1.194410E-03	1.299115E-05
960	0.611102	-2.11004E-03	1.565419E-05	0.52158	-1.389899E-03	1.422808E-05	0.525755	-1.452950E-03	1.442346E-05
970	0.675438	-3.15991E-03	1.892512E-05	0.577255	-2.363779E-03	1.733266E-05	0.578638	-2.412710E-03	1.751903E-05
980	0.683064	-3.86779E-03	2.178988E-05	0.600222	-3.184212E-03	2.039689E-05	0.60699	-3.275410E-03	2.066598E-05
990	0.676964	-4.55704E-03	2.478376E-05	0.596667	-3.909083E-03	2.349562E-05	0.596966	-3.934840E-03	2.360497E-05
1000	0.693957	-5.69615E-03	2.923833E-05	0.628506	-5.165556E-03	2.817695E-05	0.634181	-5.236900E-03	2.838410E-05
1010	0.80112	-7.82353E-03	3.630920E-05	0.742488	-7.332771E-03	3.529279E-05	0.747447	-7.390910E-03	3.545725E-05
1020	0.930916	-1.03893E-02	4.483759E-05	0.868927	-9.864173E-03	4.374059E-05	0.877364	-9.942390E-03	4.392786E-05
1030	1.119663	-1.38032E-02	5.583123E-05	1.050266	-1.317542E-02	5.442762E-05	1.056694	-1.322710E-02	5.454070E-05
1040	1.572806	-1.98429E-02	7.314089E-05	1.497343	-1.916700E-02	7.163924E-05	1.502572	-1.917750E-02	7.160510E-05
1050	2.91639	-3.29331E-02	1.047122E-04	2.818997	-3.202886E-02	1.026359E-04	2.78034	-3.163270E-02	1.016520E-04
1060	2.393062	-2.80499E-02	9.323775E-05	2.326112	-2.742079E-02	9.177578E-05	2.314316	-2.729240E-02	9.145683E-05
1070	2.199146	-2.67789E-02	9.133312E-05	2.089045	-2.571144E-02	8.878625E-05	2.056294	-2.537580E-02	8.795805E-05

1080	2.482303	-2.99791E-02	9.979281E-05		2.395833	-2.915238E-02	9.783855E-05		2.373029	-2.892280E-02	9.728562E-05
1090	2.732143	-3.27908E-02	1.072091E-04		2.560594	-3.113325E-02	1.032658E-04		2.513793	-3.067560E-02	1.021747E-04

In Tables 4.1.2.4-3 through 4.1.2.4-5, the HRI is again color coded green, the MRI pink and the SLI yellow, and wavelengths in increments of 50 nm are underlined.

Table 4.1.2.4-3

Mean within a bin for the HRI at a base temperature of 239K.

Wave	bin1	bin2	HRI bin3	bin4	239 bin5	bin6	bin7	HRI bin8	bin9	bin10
600	0.000409	0.000403	0.000403	0.000403	0.000401	0.000400	0.000396	0.000387	0.000385	0.000296
610	0.000630	0.000624	0.000610	0.000606	0.000604	0.000601	0.000597	0.000536	0.000550	0.000499
620	0.001248	0.001227	0.001195	0.001179	0.001170	0.001158	0.001144	0.001116	0.001091	0.000979
630	0.003808	0.003765	0.003650	0.003590	0.003552	0.003512	0.003481	0.003323	0.003287	0.003143
640	0.026109	0.025735	0.025155	0.024793	0.024607	0.024537	0.024395	0.023536	0.023267	0.022056
650	0.174333	0.172120	0.168724	0.167026	0.166515	0.167335	0.167036	0.163012	0.159064	0.155990
660	0.447086	0.441074	0.433138	0.430408	0.430460	0.434243	0.434258	0.425884	0.415512	0.408875
670	0.648236	0.638821	0.626193	0.622814	0.623542	0.629313	0.629097	0.617304	0.601251	0.592584
680	0.787447	0.777250	0.759335	0.753728	0.752734	0.755740	0.753524	0.734957	0.716742	0.704198
690	0.879738	0.868918	0.849413	0.840739	0.836303	0.833192	0.827833	0.807952	0.790720	0.772165
700	0.918463	0.909638	0.890858	0.879939	0.872526	0.865013	0.857343	0.840918	0.827005	0.808520
710	0.923696	0.915492	0.900927	0.891204	0.884286	0.877994	0.872686	0.862698	0.852849	0.840423
720	0.932059	0.925570	0.913844	0.906791	0.902232	0.898618	0.895133	0.891142	0.886042	0.878857
730	0.951119	0.945691	0.937716	0.933349	0.931049	0.930548	0.928845	0.926405	0.925087	0.925376
740	0.980878	0.977423	0.973106	0.971251	0.970386	0.971148	0.970291	0.968028	0.966026	0.966936
750	0.999771	0.999617	0.998925	0.998946	0.999117	0.999391	0.999161	0.997790	0.997351	0.997619
760	0.990232	0.993136	0.995833	0.995901	0.995648	0.994920	0.995460	0.993539	0.998128	0.998882
770	0.946463	0.950959	0.956434	0.957210	0.957326	0.956071	0.957144	0.958673	0.965342	0.971307
780	0.889420	0.895235	0.902805	0.904380	0.905862	0.906951	0.910360	0.915311	0.922163	0.940552
790	0.842642	0.849113	0.858790	0.862722	0.866081	0.869741	0.874523	0.888691	0.894859	0.920377
800	0.817516	0.824518	0.834855	0.840813	0.846278	0.852696	0.858932	0.878682	0.887412	0.910429
810	0.811005	0.818270	0.829138	0.836304	0.842207	0.848907	0.856188	0.878371	0.890237	0.917457
820	0.813526	0.820729	0.830570	0.839112	0.846843	0.854271	0.862701	0.885135	0.893815	0.933281
830	0.811992	0.819161	0.828532	0.836226	0.842058	0.845376	0.850877	0.876276	0.894654	0.925405

840	0.791726	0.799769	0.807962	0.813692	0.817752	0.817268	0.821787	0.848021	0.866133	0.902996
850	0.751840	0.759320	0.766570	0.770680	0.773018	0.769036	0.772069	0.800082	0.819727	0.850050
860	0.685450	0.692679	0.698824	0.701057	0.702244	0.697388	0.700049	0.726437	0.748975	0.775509
870	0.615174	0.622489	0.628267	0.630006	0.630846	0.625993	0.628488	0.657810	0.681479	0.706108
880	0.550480	0.557107	0.562798	0.565156	0.566730	0.562914	0.565744	0.593554	0.612059	0.648066
890	0.488361	0.493855	0.500562	0.503975	0.506348	0.503576	0.506393	0.533218	0.554863	0.581582
900	0.429571	0.434530	0.441399	0.445232	0.447702	0.445821	0.448710	0.473166	0.492249	0.516137
910	0.380195	0.384712	0.392209	0.396785	0.399630	0.398650	0.401828	0.423951	0.442078	0.465881
920	0.333609	0.338381	0.346722	0.352007	0.355087	0.354559	0.357606	0.376994	0.394518	0.417340
930	0.291900	0.296693	0.305195	0.310488	0.313647	0.313721	0.316598	0.334764	0.350289	0.370821
940	0.255753	0.260061	0.268504	0.273875	0.276902	0.277173	0.279744	0.296105	0.308798	0.327094
950	0.225063	0.229117	0.237275	0.242423	0.245097	0.245268	0.247577	0.262212	0.272715	0.290766
960	0.197572	0.201310	0.208936	0.213721	0.216247	0.216417	0.218428	0.231823	0.241326	0.256447
970	0.172548	0.176090	0.182990	0.187463	0.189821	0.189788	0.191375	0.203094	0.211734	0.225728
980	0.148439	0.151369	0.157534	0.161378	0.163168	0.162711	0.163906	0.173642	0.181464	0.191741
990	0.125264	0.127708	0.132802	0.135883	0.137257	0.136542	0.137426	0.145674	0.152766	0.160607
1000	0.102344	0.104458	0.108514	0.110924	0.111958	0.111095	0.111739	0.118226	0.123865	0.131732
1010	0.079881	0.081472	0.084592	0.086457	0.087217	0.086368	0.086771	0.092417	0.097469	0.102306
1020	0.059610	0.060790	0.063143	0.064521	0.065101	0.064398	0.064721	0.069085	0.073212	0.077240
1030	0.042432	0.043235	0.044994	0.046004	0.046447	0.045958	0.046235	0.049620	0.052846	0.055973
1040	0.029308	0.029857	0.031138	0.031877	0.032192	0.031850	0.032065	0.034439	0.037101	0.039436
1050	0.019027	0.019354	0.020257	0.020783	0.021020	0.020816	0.020988	0.022780	0.024377	0.026204
1060	0.014123	0.014390	0.015100	0.015541	0.015744	0.015600	0.015736	0.017142	0.018529	0.019987
1070	0.010434	0.010629	0.011178	0.011530	0.011699	0.011603	0.011705	0.012809	0.013832	0.014959
1080	0.007944	0.008083	0.008522	0.008809	0.008947	0.008881	0.008966	0.009807	0.010684	0.011587
1090	0.006110	0.006215	0.006556	0.006789	0.006901	0.006854	0.006925	0.007619	0.008236	0.009022

Table 4.1.2.4-4a

Mean within a bin at wavelength for the MRI. The MRI has 10 anomalous pixels, designated by bin numbers 20-29 and these are included in Table 7b.

Wave	bin1	bin2	MRI bin3	bin4	239 bin5	bin6	bin7	MRI bin8	bin9	bin10
600	0.00032	0.00024	0.00027	0.00025	0.00025	0.00025	0.00025	0.00026	0.00018	0.00031
610	0.00025	0.00025	0.00028	0.00027	0.00026	0.00026	0.00026	0.00026	0.00021	0.00031
620	0.00015	0.00029	0.00031	0.00031	0.00033	0.00033	0.00033	0.00033	0.00034	0.00037
630	0.00079	0.00067	0.00068	0.00067	0.00068	0.00069	0.00069	0.00068	0.00062	0.00069
640	0.00565	0.00594	0.00582	0.00577	0.00580	0.00585	0.00584	0.00571	0.00551	0.00527
650	0.07779	0.07776	0.07685	0.07600	0.07590	0.07615	0.07651	0.07573	0.07411	0.07298
660	0.34953	0.34653	0.34388	0.33971	0.33863	0.33901	0.34129	0.33931	0.33372	0.32781
670	0.60563	0.60701	0.60031	0.59236	0.58909	0.58883	0.59234	0.58904	0.57914	0.56809
680	0.77558	0.77094	0.76202	0.74995	0.74352	0.74088	0.74162	0.73410	0.72043	0.70245
690	0.87354	0.87191	0.85879	0.84479	0.83607	0.83041	0.82582	0.81247	0.79652	0.77555
700	0.92276	0.90942	0.89792	0.88473	0.87476	0.86641	0.85713	0.84295	0.82786	0.81085
710	0.91607	0.91268	0.90197	0.88976	0.88178	0.87550	0.86883	0.85944	0.84721	0.83612
720	0.92540	0.92249	0.91317	0.90281	0.89715	0.89276	0.88867	0.88436	0.87658	0.87428
730	0.95192	0.94522	0.93849	0.93151	0.92744	0.92440	0.92260	0.92075	0.91804	0.91480
740	0.97838	0.97701	0.97531	0.97160	0.96961	0.96824	0.96772	0.96741	0.96566	0.96430
750	0.99893	0.99992	0.99919	0.99891	0.99864	0.99863	0.99882	0.99783	0.99817	0.99534
760	0.99311	0.98808	0.99180	0.99357	0.99431	0.99431	0.99386	0.99493	0.99132	0.99378
770	0.94681	0.94055	0.94848	0.95126	0.95350	0.95503	0.95477	0.95870	0.95981	0.96839
780	0.88909	0.88175	0.89308	0.89791	0.90123	0.90367	0.90526	0.91317	0.91789	0.93217
790	0.83970	0.83750	0.85104	0.85794	0.86277	0.86688	0.87095	0.88273	0.89270	0.91558
800	0.81130	0.81497	0.82962	0.83918	0.84535	0.85104	0.85762	0.87281	0.88633	0.91356
810	0.81275	0.81167	0.82821	0.83895	0.84577	0.85242	0.85975	0.87662	0.89217	0.92306
820	0.81948	0.82058	0.83579	0.84491	0.85142	0.85874	0.86776	0.88693	0.90422	0.93574
830	0.83797	0.82700	0.84004	0.84961	0.85470	0.85915	0.86281	0.88052	0.89870	0.93518
840	0.80907	0.81289	0.82288	0.83104	0.83459	0.83676	0.83619	0.85206	0.87208	0.90484

850	0.77563	0.77312	0.78231	0.78942	0.79170	0.79183	0.78750	0.80261	0.82269	0.85805
860	0.70666	0.70776	0.71591	0.72235	0.72259	0.72140	0.71510	0.72949	0.75030	0.78191
870	0.64117	0.63618	0.64328	0.64902	0.65051	0.65016	0.64451	0.65983	0.67968	0.71331
880	0.57218	0.57310	0.57783	0.58241	0.58396	0.58453	0.58045	0.59477	0.61412	0.64837
890	0.51476	0.51156	0.51597	0.52026	0.52241	0.52346	0.52050	0.53423	0.55335	0.58589
900	0.45438	0.44996	0.45583	0.46079	0.46331	0.46506	0.46328	0.47631	0.49376	0.52519
910	0.39439	0.39966	0.40481	0.40985	0.41317	0.41560	0.41500	0.42703	0.44306	0.47365
920	0.35050	0.35166	0.35773	0.36330	0.36700	0.36950	0.36964	0.38095	0.39657	0.42162
930	0.31012	0.31035	0.31592	0.32181	0.32523	0.32754	0.32795	0.33845	0.35284	0.37572
940	0.27058	0.27222	0.27846	0.28435	0.28820	0.29079	0.29155	0.30147	0.31377	0.33515
950	0.23925	0.23924	0.24581	0.25165	0.25555	0.25836	0.25936	0.26794	0.27946	0.29863
960	0.20904	0.21077	0.21706	0.22232	0.22587	0.22836	0.22929	0.23675	0.24743	0.26385
970	0.18427	0.18578	0.19106	0.19587	0.19885	0.20102	0.20164	0.20804	0.21648	0.23164
980	0.16139	0.16112	0.16557	0.16952	0.17204	0.17372	0.17385	0.17921	0.18707	0.20029
990	0.13790	0.13639	0.14012	0.14337	0.14536	0.14669	0.14647	0.15070	0.15705	0.16773
1000	0.11222	0.11188	0.11471	0.11729	0.11882	0.11981	0.11936	0.12276	0.12791	0.13729
1010	0.08741	0.08796	0.08963	0.09158	0.09268	0.09335	0.09281	0.09546	0.09943	0.10670
1020	0.06634	0.06582	0.06717	0.06849	0.06929	0.06973	0.06922	0.07136	0.07449	0.08024
1030	0.04703	0.04710	0.04794	0.04892	0.04960	0.04994	0.04957	0.05118	0.05369	0.05806
1040	0.03232	0.03253	0.03313	0.03393	0.03446	0.03477	0.03452	0.03571	0.03749	0.04078
1050	0.02118	0.02103	0.02151	0.02208	0.02250	0.02274	0.02261	0.02348	0.02475	0.02698
1060	0.01561	0.01565	0.01599	0.01645	0.01682	0.01705	0.01699	0.01769	0.01877	0.02057
1070	0.01159	0.01153	0.01182	0.01219	0.01250	0.01270	0.01267	0.01321	0.01406	0.01549
1080	0.00874	0.00885	0.00905	0.00932	0.00958	0.00975	0.00974	0.01017	0.01084	0.01189
1090	0.00680	0.00685	0.00699	0.00721	0.00741	0.00754	0.00754	0.00790	0.00838	0.00929

Table 4.1.2.4-5a

Mean within a bin at wavelength for the 10 anomalous pixels for the MRI, designated by bin numbers 20-29.

Wave	bin20	bin21	bin22	bin23	bin24	MRI bin25	bin26	bin27	bin28	bin29
600	0.00019	0.00050	0.00000	0.00043	0.00040	0.00024	0.00036	0.00060	0.00019	0.00020
610	0.00016	0.00042	0.00023	0.00000	0.00034	0.00000	0.00000	0.00051	0.00049	0.00034
620	0.00016	0.00042	0.00000	0.00037	0.00069	0.00021	0.00061	0.00017	0.00033	0.00052
630	0.00051	0.00090	0.00025	0.00118	0.00074	0.00089	0.00065	0.00055	0.00053	0.00073
640	0.00543	0.00437	0.00520	0.00380	0.00509	0.00552	0.00540	0.00529	0.00583	0.00557
650	0.07792	0.06648	0.07295	0.06790	0.06986	0.07798	0.07191	0.07347	0.07537	0.07488
660	0.35368	0.31290	0.33316	0.30081	0.31384	0.34097	0.32264	0.33308	0.33270	0.33343
670	0.61599	0.53131	0.58563	0.51627	0.54163	0.59742	0.56518	0.56611	0.57903	0.59105
680	0.76333	0.65879	0.70882	0.62965	0.67614	0.74691	0.71446	0.71241	0.73516	0.73027
690	0.83620	0.71619	0.76448	0.71234	0.74533	0.81500	0.78088	0.80043	0.82869	0.82845
700	0.86097	0.77356	0.79310	0.75452	0.78568	0.86137	0.83964	0.85116	0.85581	0.86336
710	0.87148	0.79531	0.83475	0.80742	0.82472	0.86724	0.85768	0.84337	0.87398	0.88373
720	0.88532	0.85533	0.86644	0.81462	0.86097	0.88901	0.90309	0.88147	0.89649	0.89385
730	0.91467	0.90703	0.90819	0.88318	0.90535	0.94378	0.93590	0.91312	0.91930	0.93736
740	0.96455	0.97005	0.95892	0.95126	0.95151	0.97245	0.95526	0.96179	0.97036	0.98657
750	1.00000	0.97756	1.00000	0.96730	0.98806	1.00000	0.99582	0.99672	1.00000	1.00000
760	0.98868	0.98409	0.98503	1.00000	1.00000	0.99781	1.00000	1.00000	0.99888	0.99360
770	0.94455	0.97068	0.93358	0.97896	0.96872	0.96937	0.97377	0.96899	0.96711	0.96026
780	0.88503	0.96256	0.89471	0.96001	0.95408	0.90399	0.94711	0.92300	0.92206	0.89967
790	0.84680	0.94651	0.88902	0.93532	0.93112	0.87747	0.91606	0.89952	0.88701	0.88605
800	0.82821	0.95499	0.89276	0.95525	0.91963	0.88006	0.93455	0.87711	0.87026	0.86336
810	0.83233	0.98139	0.90376	0.97320	0.93150	0.88441	0.94809	0.88866	0.88741	0.86702
820	0.82161	0.99994	0.88891	0.97302	0.95744	0.89269	0.97253	0.88511	0.88851	0.88889
830	0.81634	1.00000	0.89233	0.99432	0.96249	0.90446	0.99241	0.89199	0.89148	0.89372
840	0.78558	0.97110	0.86272	0.97048	0.93138	0.88036	0.98284	0.87559	0.87491	0.88331
850	0.74165	0.91343	0.79595	0.91742	0.90342	0.83139	0.92178	0.82844	0.83784	0.82694
860	0.65909	0.84857	0.72277	0.84954	0.81117	0.77543	0.84765	0.75310	0.76597	0.75853

870	0.58560	0.76361	0.65707	0.77438	0.74233	0.69239	0.76555	0.68921	0.68385	0.70302
880	0.53390	0.69184	0.59308	0.71296	0.68110	0.62259	0.68577	0.61137	0.62834	0.62143
890	0.47054	0.63247	0.54250	0.64782	0.62339	0.55062	0.63346	0.55022	0.56794	0.55470
900	0.41900	0.58120	0.47861	0.58271	0.55235	0.49053	0.56265	0.49433	0.49583	0.48924
910	0.37569	0.52099	0.43834	0.53677	0.49722	0.43670	0.50652	0.44214	0.45027	0.44858
920	0.33330	0.46632	0.39273	0.46842	0.44971	0.38625	0.44965	0.39169	0.40067	0.39544
930	0.29370	0.41183	0.34889	0.43207	0.40375	0.34922	0.40693	0.35286	0.35003	0.34941
940	0.26295	0.37580	0.30487	0.37865	0.35402	0.30956	0.36132	0.31549	0.31146	0.31112
950	0.23153	0.33792	0.27169	0.33957	0.32104	0.27495	0.31845	0.27860	0.27906	0.27466
960	0.20022	0.29457	0.24227	0.29992	0.28769	0.24392	0.28222	0.24551	0.25121	0.24415
970	0.18177	0.26033	0.21273	0.26285	0.24503	0.21448	0.24786	0.21429	0.22044	0.21397
980	0.15202	0.22908	0.18247	0.22673	0.21510	0.18360	0.21977	0.18632	0.18990	0.18760
990	0.13011	0.18477	0.14852	0.19372	0.18449	0.15598	0.18086	0.15687	0.15891	0.15514
1000	0.10392	0.15429	0.12518	0.16031	0.14845	0.12751	0.14957	0.13035	0.13164	0.12649
1010	0.08001	0.11941	0.09601	0.12700	0.11806	0.09921	0.11726	0.10013	0.10353	0.10146
1020	0.05961	0.08989	0.07214	0.09395	0.08909	0.07343	0.08798	0.07647	0.07623	0.07587
1030	0.04262	0.06524	0.05143	0.06829	0.06524	0.05370	0.06454	0.05392	0.05451	0.05393
1040	0.02964	0.04737	0.03726	0.04814	0.04466	0.03672	0.04427	0.03838	0.03935	0.03683
1050	0.01888	0.03093	0.02363	0.03276	0.02945	0.02501	0.03067	0.02471	0.02558	0.02445
1060	0.01441	0.02492	0.01826	0.02518	0.02328	0.01814	0.02360	0.01885	0.01905	0.01840
1070	0.01071	0.01856	0.01351	0.01876	0.01761	0.01329	0.01732	0.01434	0.01428	0.01390
1080	0.00822	0.01449	0.01081	0.01457	0.01368	0.01033	0.01332	0.01067	0.01084	0.01049
1090	0.00631	0.01160	0.00810	0.01169	0.01063	0.00800	0.01051	0.00834	0.00865	0.00810

Table 4.1.2.4-6

Mean within a bin at wavelength for the SLI at 239K.

Wave	bin1	bin2	SLI bin3	bin4	239 bin5	bin6	bin7	SLI bin8	bin9	bin10
600	0.00022	0.00022	0.00024	0.00024	0.00024	0.00024	0.00023	0.00013	0.00044	0.00016
610	0.00023	0.00024	0.00024	0.00024	0.00024	0.00024	0.00026	0.00020	0.00038	0.00022
620	0.00031	0.00030	0.00029	0.00030	0.00030	0.00031	0.00031	0.00034	0.00019	0.00050
630	0.00057	0.00058	0.00060	0.00063	0.00063	0.00062	0.00063	0.00060	0.00040	0.00053
640	0.00528	0.00524	0.00539	0.00557	0.00555	0.00550	0.00550	0.00553	0.00509	0.00454
650	0.07757	0.07654	0.07618	0.07642	0.07635	0.07621	0.07575	0.07406	0.07306	0.07037
660	0.36147	0.35585	0.34943	0.34575	0.34580	0.34644	0.34481	0.34033	0.33652	0.32646
670	0.63748	0.62808	0.61247	0.60334	0.60308	0.60418	0.60102	0.59149	0.58921	0.57052
680	0.80040	0.78843	0.76804	0.75603	0.75366	0.75286	0.74752	0.73468	0.72620	0.70498
690	0.88591	0.87411	0.85339	0.84241	0.83715	0.83288	0.82588	0.80676	0.79854	0.78133
700	0.91507	0.90381	0.88652	0.87690	0.86900	0.86159	0.85420	0.83784	0.82828	0.80257
710	0.91908	0.90885	0.89391	0.88656	0.88080	0.87559	0.87071	0.86196	0.85985	0.83498
720	0.93256	0.92406	0.91136	0.90515	0.90110	0.89732	0.89399	0.89111	0.88838	0.87617
730	0.95809	0.95094	0.94099	0.93536	0.93281	0.93076	0.92936	0.92723	0.92655	0.91681
740	0.98678	0.98400	0.97871	0.97465	0.97318	0.97220	0.97122	0.97211	0.97949	0.97571
750	0.99986	0.99996	0.99982	0.99958	0.99944	0.99938	0.99883	0.99897	0.99970	0.99723
760	0.98057	0.98337	0.98796	0.99046	0.99131	0.99184	0.99265	0.99221	0.99195	0.99123
770	0.92944	0.93385	0.94257	0.94798	0.94938	0.95055	0.95294	0.95686	0.95938	0.96903
780	0.87267	0.87970	0.88888	0.89513	0.89834	0.90140	0.90485	0.91664	0.92727	0.92927
790	0.83168	0.83968	0.84964	0.85566	0.85971	0.86410	0.86977	0.88659	0.89833	0.90576
800	0.81268	0.82001	0.83056	0.83687	0.84164	0.84729	0.85451	0.87320	0.89013	0.90718
810	0.80792	0.81573	0.82756	0.83396	0.83869	0.84419	0.85189	0.87560	0.89814	0.91017
820	0.80719	0.81592	0.82745	0.83626	0.84301	0.85031	0.86010	0.88447	0.90618	0.91416
830	0.80024	0.81002	0.82248	0.83113	0.83424	0.83784	0.84661	0.87662	0.90457	0.90357
840	0.77198	0.78185	0.79438	0.80495	0.80688	0.80862	0.81753	0.84826	0.87179	0.88119
850	0.72303	0.73331	0.74589	0.75688	0.75770	0.75785	0.76677	0.80101	0.81883	0.83168
860	0.65497	0.66435	0.67543	0.68568	0.68616	0.68565	0.69377	0.72506	0.74801	0.75195

870	0.58580	0.59256	0.60385	0.61419	0.61489	0.61462	0.62329	0.65572	0.68685	0.67563
880	0.52243	0.52916	0.53971	0.54991	0.55147	0.55184	0.56019	0.59204	0.60801	0.61814
890	0.46445	0.46993	0.48057	0.49032	0.49204	0.49269	0.50058	0.53025	0.54593	0.55165
900	0.40910	0.41499	0.42464	0.43364	0.43541	0.43608	0.44351	0.47106	0.48566	0.49284
910	0.36275	0.36753	0.37778	0.38666	0.38879	0.38981	0.39636	0.42423	0.43838	0.44383
920	0.31915	0.32442	0.33448	0.34248	0.34450	0.34567	0.35170	0.37673	0.38852	0.39576
930	0.28166	0.28609	0.29557	0.30240	0.30411	0.30512	0.31072	0.33279	0.34458	0.35051
940	0.24717	0.25190	0.26104	0.26744	0.26890	0.26970	0.27502	0.29598	0.30396	0.31228
950	0.21771	0.22194	0.23062	0.23650	0.23780	0.23848	0.24307	0.26117	0.27277	0.27368
960	0.19139	0.19523	0.20285	0.20811	0.20930	0.20989	0.21382	0.22942	0.23823	0.23987
970	0.16745	0.17076	0.17757	0.18225	0.18316	0.18356	0.18696	0.20118	0.20801	0.21111
980	0.14397	0.14663	0.15252	0.15653	0.15704	0.15707	0.15996	0.17338	0.17888	0.18246
990	0.12069	0.12307	0.12784	0.13142	0.13178	0.13169	0.13416	0.14388	0.14960	0.15211
1000	0.09808	0.09975	0.10363	0.10675	0.10699	0.10682	0.10892	0.11735	0.12137	0.12326
1010	0.07585	0.07726	0.08019	0.08272	0.08291	0.08274	0.08441	0.09068	0.09344	0.09521
1020	0.05652	0.05734	0.05956	0.06147	0.06162	0.06149	0.06278	0.06815	0.06990	0.07225
1030	0.04007	0.04079	0.04241	0.04382	0.04393	0.04384	0.04479	0.04873	0.05044	0.05156
1040	0.02769	0.02812	0.02935	0.03040	0.03047	0.03041	0.03113	0.03409	0.03488	0.03657
1050	0.01797	0.01826	0.01912	0.01985	0.01991	0.01989	0.02041	0.02249	0.02301	0.02423
1060	0.01332	0.01353	0.01422	0.01481	0.01487	0.01488	0.01528	0.01697	0.01755	0.01884
1070	0.00981	0.00999	0.01053	0.01098	0.01104	0.01105	0.01136	0.01262	0.01312	0.01403
1080	0.00747	0.00762	0.00803	0.00838	0.00844	0.00845	0.00870	0.00976	0.01023	0.01085
1090	0.00577	0.00586	0.00619	0.00646	0.00650	0.00651	0.00672	0.00749	0.00778	0.00839

4.1.2.5. Location of Data and Supporting Programs

The location of the average RSR at each temperature is listed in Table 4.1.2.5-1. The program: yield_rsr.pro which exists in /users/lisa/RSR_model/ gives the RSR for any imager, any pixel and any temperature. To recreate the sample calculation in this document, type .run yield_rsr.pro then type: yield_rsr,'hri',208.,14,24,rsr The output (for all the wavelengths) is called rsr. The program g.pro and then o.pro were used initially as well.

Table 4.1.2.5-1. Complete path to the RSR data at temperature averaged over all pixels.

Temperature	Data Path
171	/misc/RSR_03/SH3/29Jul96_S/ave2_dli1.dat
185	/misc/RSR_03/SH3/30Jul96.2/ave2_dli1.dat
201	/misc/RSR_04/SH3/1Aug96.1_/ave2_dli1.dat
225	/misc/RSR_04/SH3/1Aug96.2_/ave2_dli1.dat
239	/misc/RSR_04/SH3/31Jul96_S/ave2_dli1.dat
269	/misc/RSR_03/SH3/30Jul96.1/ave2_dli1.dat
294	/misc/RSR_03/SH3/26Jul96_S/ave2_dli1.dat

4.1.2.6. Model Performance

The model is evaluated by computing the RMS (root mean square) between the RSR of a specific measured pixel and the RSR computed by the model (Equation 3).

$$RMS = \sqrt{\frac{\sum (observed\_RSR - model\_RSR)^2}{49}} \tag{3}$$

In equation 3, difference is defined as measured RSR– calculated RSR, and 49 is one less that the number of measurements (wavelengths in this case). Figures 11-13 show the RMS results for the three imagers at all seven temperatures respectively.

Figure 4.1.2.6-1 for the HRI shows that approximately 99% of the pixels have an RMS value of less than 1%. All pixels at all temperatures have an RMS residual less than 4% with one pixel at one temperature just under 5%. Figure 4.1.2.6-2 for the MRI demonstrates that approximately 99% of the pixels have an RMS value less than 1%. The error then creeps up, with a few pixels having an RMS residual as high as 8%. Figure 4.1.2.6-3 for the SLI shows that approximately 90% of pixels have an RMS value of 1%, while 99.9% of pixels have an RMS residual of approximately 2%. A few pixels at a couple of temperatures have an RMS residual as high as approximately 4%.

The AR-RSR and Ave model RMS residuals are included in Figure 4.1.2.6-1 for comparison. The relevant comparison is between the AR-RSR, Ave and hump ratio model for 239K (the yellow line). While the result is better for many pixels using the AR-RSR and Ave model, the RMS residuals are much higher for some pixels toward the right of the graph. The cross over is at approximately 99%. Recall the HRI has 40,640 pixels such that 1% of the total pixels represent over 400 pixels. The 239K line never exceeds a 2% RMS residual, while a significant number of pixels have higher RMS residuals for both the AR-RSR and Ave model. Thus, the hump ratio model yields the lowest RMS residuals of the 3 models for all pixels in the HRI.

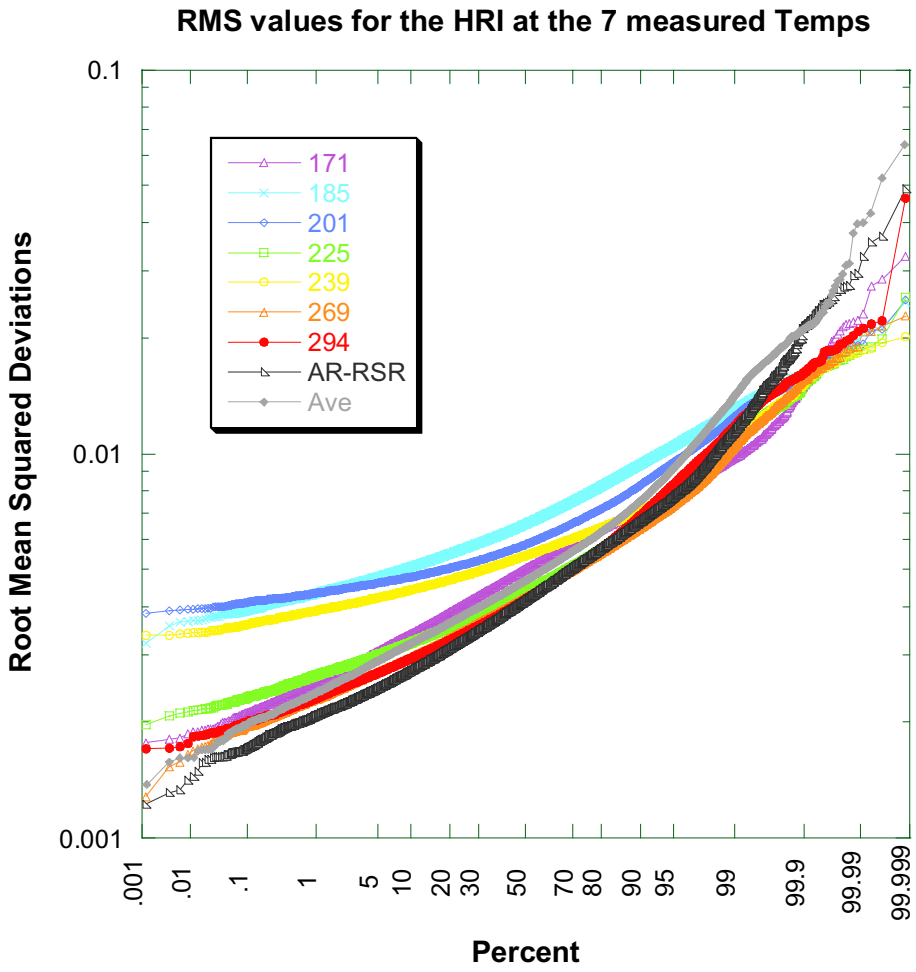

Figure 4.1.2.6-1 A probability plot of the RMS residuals for the HRI for every pixel at the 7 measured temperatures. Also included are the RMS residuals from the AR-RSR and Ave models for a temperature of 239K.

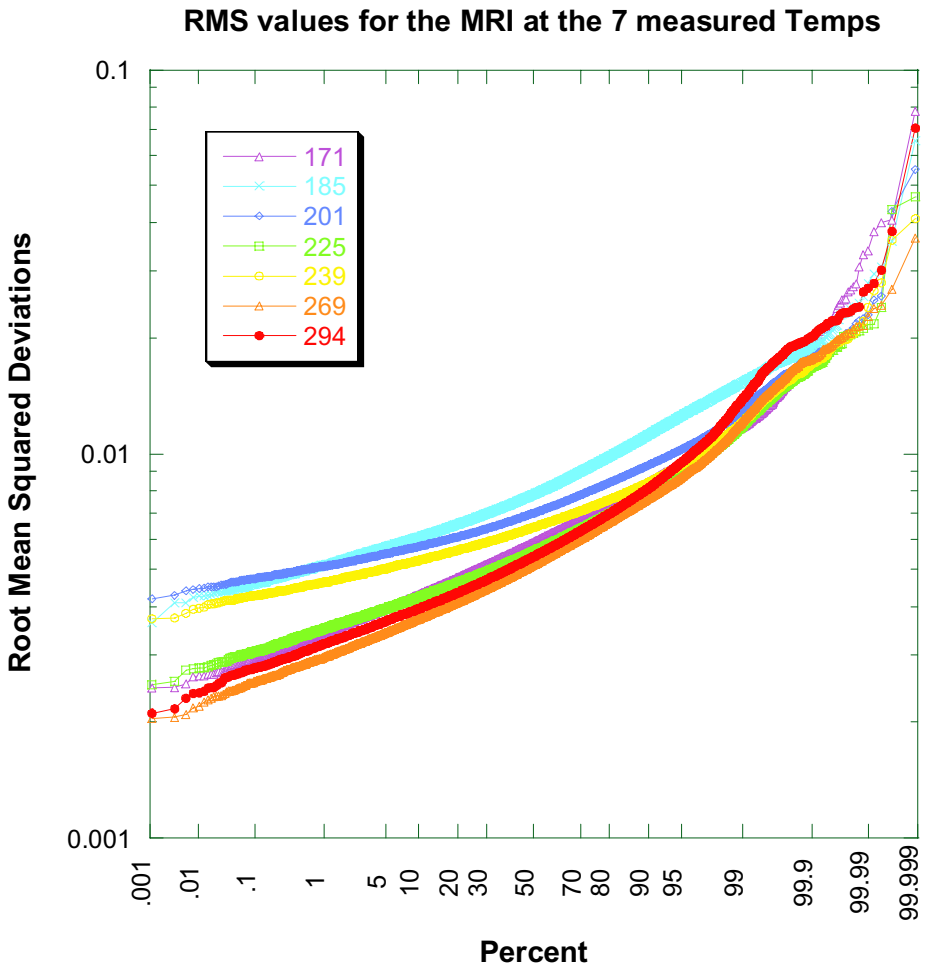

Figure 4.1.2.6-2 A probability plot of the RMS for the MRI for every pixel at the 7 measured temperatures.

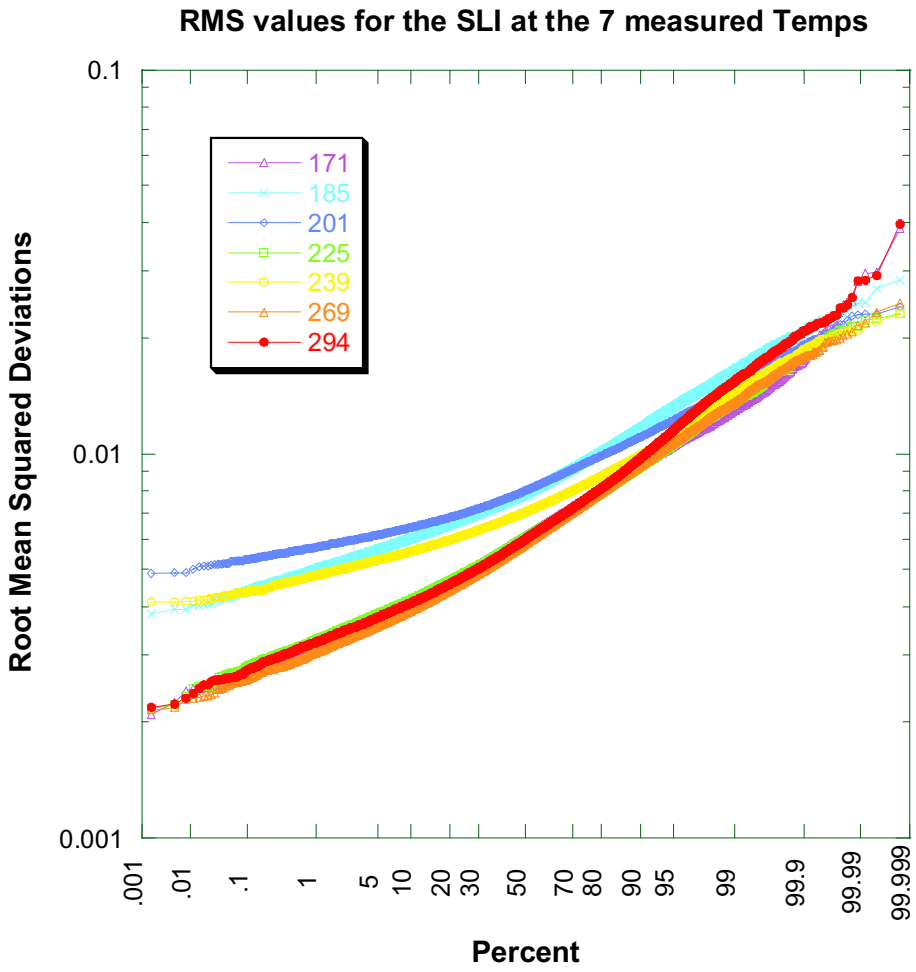

Figure 4.1.2.6-3 A probability plot of the RMS for the SLI for every pixel at the 7 measured temperatures.

4.1.3. Conclusion

Although there is some correlation between AR and RSR, there is significant scatter, and the correlation is not strong. Both the AR-RSR model and the Ave model yield appropriate RSR values for most pixels. However, both models yield high RMS residuals for a significant number of pixels. A better method for yielding the RSR of any pixel is a model based upon the ratio of the RSR at two wavelengths corresponding to the humps surrounding the RSR peak. The use of this hump ratio model yields results in the RSR that do not deviate more than 2% for the HRI at 239K and 5% for all pixels at all temperatures, 4% for the MRI at 239K and 8% for all pixels at all temperatures, and 3% for the SLI and 4% for all pixels at all temperatures.

4.2. Image Absolute Responsivity Reductions

The absolute responsivity of every pixel in all three imagers was measured at 15 temperatures ranging from 171.5K to 289.7K. The measurements were made in the large integrating sphere at the University of Arizona on July 24, 1996.

The method of computing the absolute responsivities is described in detail below. An IDL program was used to compute the responsivities of all pixels. The absolute responsivities of two pixels (at different temperatures) were verified by detailed computations described below and carried out in an Excel spreadsheet. The IDL and Excel results for these pixels agree to 5 significant figures. The following section describes this verification and the reduction method.

4.2.1. Method and Verification of Absolute Responsivity Reductions

Here we verify the reduction of absolute responsivity of two imager pixels, one from the DISR#3 HRI and one from the DISR#3 MRI. The "standard" reductions were done using IDL program imager_abs_resp_v4, located on cassini in directory /users/ldoose/idl_programs/imager_abs_resp_sw/new_2002.

As mentioned above, we repeat the reduction for these two pixels using an Excel spreadsheet with the intention of obtaining a result independent of the IDL program. Verification will be achieved if we arrive at the same absolute responsivity using both methods.

The count rate in an imager pixel in DN/sec is given by

$$r = A\int I(\lambda)RSR(\lambda)d\lambda, \tag{1}$$

where A is the absolute responsivity

$I(\lambda)$ is the intensity of the source which depends on wavelength

and $RSR(\lambda)$ is the relative spectral response of the imager pixel

The absolute responsivity is given by $A = \dfrac{r}{\int I(\lambda)RSR(\lambda)d\lambda}$ (2)

We arbitrarily choose column 100 and row 100 at 290K for the HRI and column 50, row 150 at 172K for the MRI. Other specifics for the test pixels are given in the table below:

Table 4.2.1-1

HRI verification information

Item		
Test Log	/disr3_cal/24Jul96/Log/absresp_cold_24Jul96.4	
Bright exposure seq. numbers	101	101
Dark exposure seq. numbers	90	102
Bright 0 sec exposure seq. numbers	98	98
Dark 0 sec exposure seq. numbers	95	107
Exposure times of Bright exposure	5.0 ms	5.0 ms
Exposure times of Dark exposure	5.0 ms	5.0 ms
CCD temperatures for Bright Exposure	289.73	289.73
CCD temperatures for Dark Exposure	289.73	289.73
Bright DNs for HRI pixel (100,100)	2448	2448
Dark DNs for HRI pixel (100,100)	38	35
Bright DNs for 0 exp. HRI pixel (100,100)	139	139
Dark DNs for 0 exp. HRI pixel (100,100)	35	36
Sphere silicon detector reading for bright exposure	123401	123401
Sphere silicon detector reading for dark exposures	16289	16318

Table 4.2.1-2

MRI verification information

Item		
Test Log	/disr3_cal/24Jul96/Log/absresp_cold_24Jul96.1	
Bright exposure seq. numbers	9	9
Dark exposure seq. numbers	2	14
Bright 0 sec exposure seq. numbers	6	6
Dark 0 sec exposure seq. numbers	3	15
Exposure times of Bright exposure	12.0 ms	12.0 ms
Exposure times of Dark exposure	12.0 ms	12.0 ms
CCD temperatures for Bright Exposure	171.51	171.51
CCD temperatures for Dark Exposure	171.39	171.51
Bright DNs for MRI pixel (50,150)	2207	2207
Dark DNs for MRI pixel (50,150)	9	9
Bright DNs for 0 exp. MRI pixel (50,150)	72	72
Dark DNs for 0 exp. MRI pixel (50,150)	9	9
Sphere silicon detector reading for bright exposure	124441	124441
Sphere silicon detector reading for dark exposures	16293	16293

For both pixels the absolute responsivities were computed for two sets of measurements listed in the two columns of tables 4.2.1-1 and 4.2.1-2.

The relative spectral response of the imager pixels was measured for each pixel at several temperatures and about 50 wavelengths. It has also been modeled assuming the relative spectral response falls into a discrete number of categories, based on the relative height of the left and right “bumps” in a plot of response vs. wavelength. The model description and a comparison of the model and measurements is given in another document.

The relative spectral response was measured at 171K, 185K, 201K, 225K, 239K, 269K, and 294K. The relative spectral response measurements at relevant temperatures are shown below in tabular and graphical form.

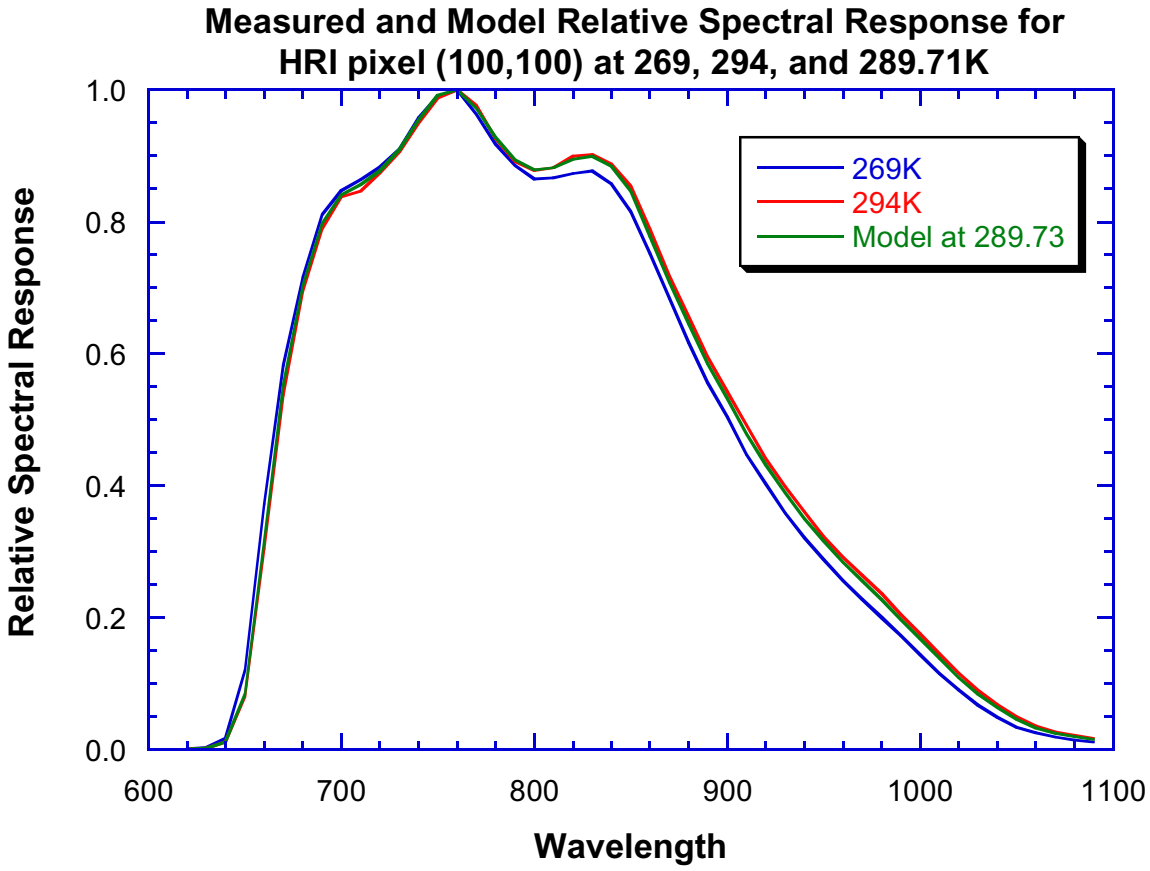

Figure 4.2.1-1 Measured and model relative spectral responses for the HRI pixel.

Table 4.2.1-3

Relative Spectral Response of HRI pixel (100,100) vs. Temperature

Wavelength	269K	294K	289.73K	Model at 289.73K
600	0.00022	0.00022	0.00022	0.00034
610	0.00047	0.00044	0.00045	0.00045
620	0.00094	0.00078	0.00081	0.00089
630	0.00291	0.00214	0.00227	0.00229
640	0.01730	0.01099	0.01207	0.01164
650	0.12050	0.08003	0.08694	0.08396
660	0.37222	0.30440	0.31598	0.31685
670	0.58265	0.53704	0.54483	0.55268
680	0.71644	0.69498	0.69865	0.70313
690	0.81114	0.78977	0.79342	0.79764
700	0.84711	0.83740	0.83906	0.84025

710	0.86408	0.84617	0.84923	0.85620
720	0.88271	0.87400	0.87549	0.87745
730	0.90994	0.90672	0.90727	0.90933
740	0.95680	0.94935	0.95062	0.95452
750	0.99001	0.98843	0.98870	0.99202
760	1.00000	1.00000	1.00000	1.00000
770	0.96272	0.97561	0.97341	0.97236
780	0.91849	0.92625	0.92492	0.92852
790	0.88535	0.89122	0.89022	0.89358
800	0.86488	0.87828	0.87599	0.87898
810	0.86694	0.88176	0.87923	0.88210
820	0.87306	0.89904	0.89460	0.89457
830	0.87713	0.90226	0.89797	0.89969
840	0.85709	0.88740	0.88222	0.88431
850	0.81556	0.85366	0.84715	0.84642
860	0.75204	0.78799	0.78185	0.77837
870	0.68397	0.71784	0.71206	0.70861
880	0.61653	0.65639	0.64958	0.64561
890	0.55652	0.59555	0.58888	0.58495
900	0.50429	0.54182	0.53541	0.53227
910	0.44692	0.49162	0.48399	0.47858
920	0.40274	0.44147	0.43485	0.43179
930	0.35822	0.39860	0.39170	0.38875
940	0.32116	0.35995	0.35332	0.35012
950	0.28805	0.32331	0.31729	0.31611
960	0.25589	0.29135	0.28529	0.28400
970	0.22766	0.26426	0.25801	0.25589
980	0.20008	0.23595	0.22982	0.22697
990	0.17252	0.20481	0.19929	0.19717
1000	0.14419	0.17588	0.17047	0.16765
1010	0.11491	0.14491	0.13979	0.13795
1020	0.09063	0.11622	0.11185	0.10963
1030	0.06759	0.08991	0.08610	0.08390
1040	0.04903	0.06772	0.06453	0.06318
1050	0.03417	0.04914	0.04658	0.04548
1060	0.02495	0.03576	0.03391	0.03294
1070	0.01873	0.02649	0.02516	0.02464
1080	0.01451	0.02137	0.02020	0.01944
1090	0.01148	0.01674	0.01584	0.01539
1100	0.00000	0.00000	0.00000	0.00034

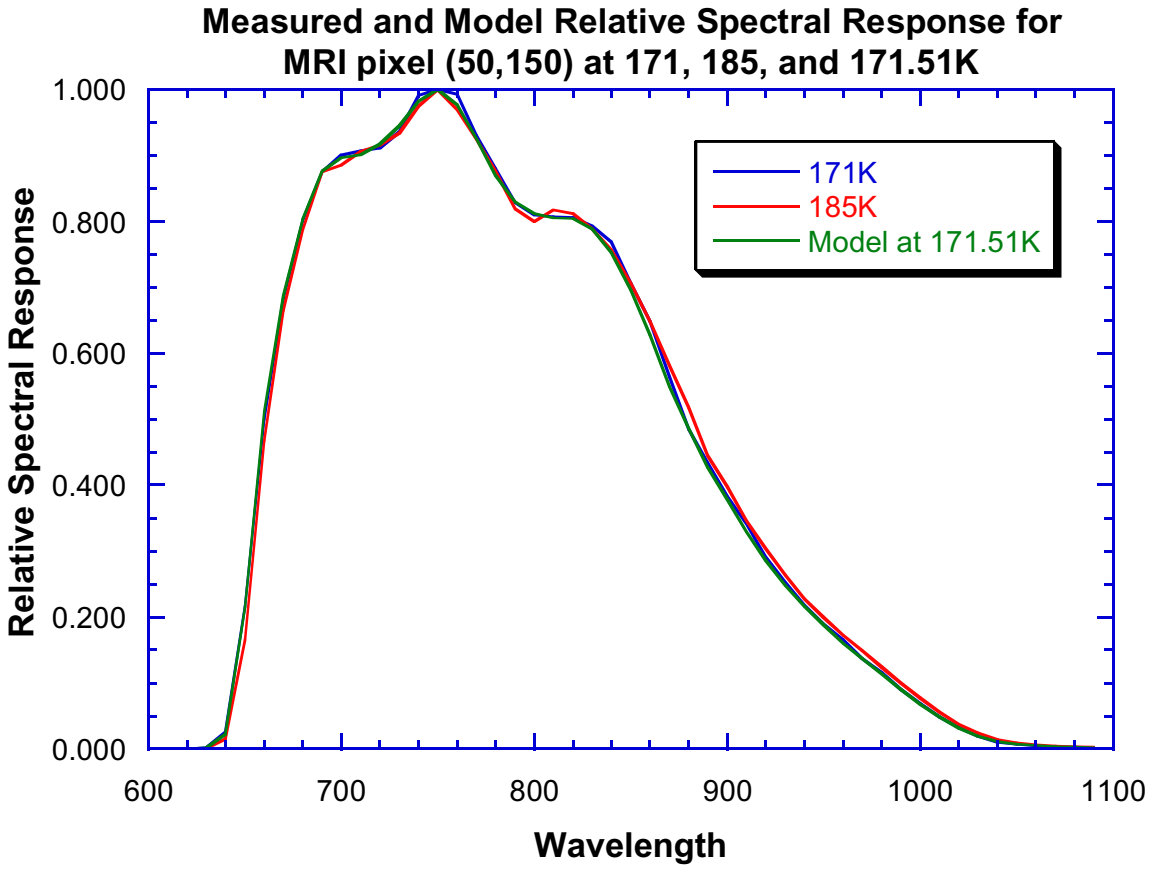

Figure 4.2.1-2 Measured and model relative spectral responses for the MRI pixel.

Table 4.2.1-4

Relative Spectral Response of MRI pixel (50,150) vs. Temperature

Wavelength	171K	185K	171.51K	Model at 171.51K
600	0.00039	0.00051	0.00039	0.00042
610	0.00045	0.00067	0.00046	0.00042
620	0.00045	0.00045	0.00045	0.00053
630	0.00157	0.00096	0.00155	0.00156
640	0.02565	0.01502	0.02526	0.02289
650	0.21618	0.16569	0.21434	0.21475
660	0.50008	0.46797	0.49891	0.51133
670	0.68313	0.66488	0.68247	0.68699
680	0.80203	0.78803	0.80152	0.80469
690	0.87495	0.87560	0.87497	0.87587
700	0.89993	0.88585	0.89942	0.89689
710	0.90701	0.90616	0.90698	0.90124
720	0.91172	0.91533	0.91185	0.91693
730	0.93554	0.93410	0.93549	0.94539

740	0.99089	0.97496	0.99031	0.98224
750	1.00000	1.00000	1.00000	1.00000
760	0.99296	0.96972	0.99211	0.97705
770	0.93001	0.92415	0.92980	0.92527
780	0.88023	0.87629	0.88009	0.86963
790	0.82808	0.81879	0.82774	0.82938
800	0.81022	0.79928	0.80982	0.81165
810	0.80750	0.81731	0.80786	0.80503
820	0.80577	0.81157	0.80598	0.80423
830	0.79316	0.78859	0.79299	0.78813
840	0.76898	0.75713	0.76855	0.75332
850	0.70633	0.70629	0.70633	0.69645
860	0.64816	0.64816	0.64816	0.62800
870	0.56424	0.58148	0.56487	0.54914
880	0.48534	0.51765	0.48652	0.48641
890	0.43408	0.44468	0.43447	0.42756
900	0.38219	0.39744	0.38275	0.37777
910	0.34170	0.34652	0.34188	0.32981
920	0.29125	0.30433	0.29173	0.28644
930	0.25317	0.26408	0.25357	0.24872
940	0.21869	0.22748	0.21901	0.21662
950	0.18958	0.19938	0.18994	0.18838
960	0.16541	0.17313	0.16569	0.16094
970	0.13747	0.14927	0.13790	0.13749
980	0.11548	0.12431	0.11580	0.11374
990	0.09054	0.10037	0.09090	0.09045
1000	0.06961	0.07775	0.06991	0.06822
1010	0.04905	0.05578	0.04930	0.04855
1020	0.03316	0.03768	0.03332	0.03211
1030	0.01942	0.02406	0.01959	0.01941
1040	0.01088	0.01431	0.01100	0.01096
1050	0.00749	0.00993	0.00758	0.00780
1060	0.00503	0.00687	0.00510	0.00549
1070	0.00351	0.00472	0.00355	0.00369
1080	0.00253	0.00352	0.00257	0.00267
1090	0.00172	0.00275	0.00176	0.00195
1100	0.00000	0.00000	0.00000	0.00000

The final quantity needed to determine the AR is the intensity of the integrating sphere. This is obtained from a scan of the sphere interior wall as illuminated by an incandescent lamp using the standard detector of the monochromator itself. Three bandpass detectors monitor the brightness of the sphere separately. The sphere brightness may change between the time of the monochromator scan and the DISR measurements. The brightness of the sphere is corrected for this change. Finally the spatial variations of

intensity within the sphere are considered. The intensity is different in the direction of the imager pixels as compared to the field of view of the standard detector. A correction is applied to account for this difference.

The brightness of the sphere interior is computed from readings on silicon and germanium detectors in the monochromator sensor.
The intensity of the portion of the sphere viewed by the monochromator detector at wavelength λ is computed as

$$I(\lambda) = \frac{D(\lambda)}{c(\lambda)}\left(\frac{L_0}{L_\lambda}\right)\left(\frac{B_t}{B_0}\right), \text{ where} \qquad (3)$$

$D(\lambda)$ is the detector reading at wavelength λ

$c(\lambda)$ is the monochromator calibration factor at wavelength λ, obtained from an appropriate calibration file

L_0 is the "luminosity constant" (e.g. = 12853)

L_λ is the luminosity constant actually measured during the determination of $c(\lambda)$ (e.g., usually 12853), so the quantity $\frac{L_0}{L_\lambda}$ is taken to be unity

$\frac{B_t}{B_0}$ is the ratio of the brightness at time *t* to the brightness at time t_0. This term allows for drift in the lamp between the times of the monochromator detector measurements and the DISR imager measurements.

$D(\lambda)$ is obtained from either the silicon or germanium standard detector of the monochromator. Only one detector is active at a given time. Values of $D(\lambda)$ are obtained from the "cal" file taken close in time to the DISR measurements. The units of these measurements are Amperes. Generally the monochromator is configured to measure the sphere brightness at a uniformly spaced grid of wavelengths.

$c(\lambda)$ is the detector responsivity in Amperes/[watt/(m^2 μm str)]. These values are obtained from the monochromator manufacturer during absolute calibration of the detectors. $c(\lambda)$ also depends on the slit configuration inside the monochromator. For the DISR#3 measurements the appropriate files are
cassini:/local/cal.cal/New_Std_Si_(Calcal_vers) and
cassini:/local/cal.cal/New_Std_Ge_(Calcal_vers). Only the slit configurations 5:5:5mm aperture for the Si detector and 5:5:3mm aperture for the Ge detector were used.

Details of the absolute calibration can be found in the document "A New DISR Absolute Standard" by Bashar Rizk.

Table 4.2.1-5, below, gives the intensity (in $\frac{Watts}{m^2 \cdot \mu m \cdot str}$) of the integrating sphere from the standard detector readings alone, i.e., without the corrections for time drift or spatial inhomogeneity.

Table 4.2.1-5

Brightness of the Integrating Sphere from Monochrometer Scan

Wavelength (nm)	D(λ)	c(λ)	I(λ)
600	8.269E-11	1.0459E-10	0.790611
610	9.749E-11	1.2036E-10	0.809987
620	9.852E-11	1.1846E-10	0.831673
630	9.388E-11	1.0988E-10	0.854387
640	9.249E-11	1.0470E-10	0.883381
650	1.136E-10	1.2550E-10	0.905179
660	1.284E-10	1.3863E-10	0.926206
670	1.310E-10	1.3816E-10	0.948176
680	1.271E-10	1.3129E-10	0.968086
690	1.208E-10	1.2214E-10	0.989029
700	1.140E-10	1.1321E-10	1.006978
710	1.072E-10	1.0460E-10	1.024857
720	1.006E-10	9.6846E-11	1.038763
730	9.428E-11	8.9465E-11	1.053820
740	8.799E-11	8.2488E-11	1.066701
750	8.199E-11	7.6033E-11	1.078348
760	7.616E-11	6.9893E-11	1.089666
770	7.063E-11	6.4270E-11	1.098958
780	6.553E-11	5.9079E-11	1.109193
790	6.081E-11	5.4488E-11	1.116026
800	5.686E-11	5.0673E-11	1.122097
810	5.378E-11	4.7783E-11	1.125505
820	5.170E-11	4.5872E-11	1.127049
830	5.076E-11	4.5038E-11	1.127048
840	5.095E-11	4.5303E-11	1.124650
850	5.222E-11	4.6628E-11	1.119928
860	5.439E-11	4.8841E-11	1.113614
870	7.085E-11	6.3255E-11	1.120070
880	9.348E-11	8.4091E-11	1.111653
890	1.224E-10	1.1135E-10	1.099237
900	1.577E-10	1.4541E-10	1.084520
910	1.997E-10	1.8575E-10	1.075101
920	2.525E-10	2.3586E-10	1.070550
930	3.236E-10	3.0449E-10	1.062761
940	4.032E-10	3.8449E-10	1.048662

950	4.686E-10	4.5668E-10	1.026101
960	5.186E-10	5.1171E-10	1.013465
970	5.569E-10	5.5491E-10	1.003586
980	5.917E-10	5.9505E-10	0.994370
990	6.210E-10	6.2993E-10	0.985824
1000	6.399E-10	6.5562E-10	0.976023
1010	6.444E-10	6.6810E-10	0.964526
1020	6.321E-10	6.6319E-10	0.953121
1030	6.001E-10	6.3821E-10	0.940286
1040	5.493E-10	5.9188E-10	0.928060
1050	4.852E-10	5.2955E-10	0.916250
1060	4.149E-10	4.5913E-10	0.903666
1070	3.572E-10	4.0006E-10	0.892866
1080	3.118E-10	3.5310E-10	0.883036
1090	2.709E-10	3.0874E-10	0.877437
1100	2.291E-10	2.6532E-10	0.863486

We first compute $\int I(\lambda)RSR(\lambda)d\lambda$ without the corrections for time drift and spatial inhomogeneity. Computations are done for the HRI pixel and the MRI pixel for both the interpolated (in temperature) measured and model RSR. Simpson's rule is used for the integration. The results (in $\frac{Watts}{m^2 \cdot str}$) are:

Table 4.2.1-6
$\int I(\lambda)RSR(\lambda)d\lambda$ **(uncorrected)**

RSR	HRI pixel (100,100)	MRI pixel (50,150)
Measured	0.254986	0.230221
Model	0.254939	0.228738

The count rates are obtained from

$$r = \frac{(DN_b - DN_{b0}) - (DN_d - DN_{d0})}{\Delta t}, \quad (4)$$

where

DN_b is the number of bright (shutter open) counts at the full exposure time

DN_{b0} is the number of bright (shutter open) counts at zero exposure time

DN_d is the number of dark (shutter closed) counts at the full exposure time

DN_{d0} is the number of dark (shutter closed) counts at zero exposure time

Δt is the exposure time in seconds

Where two measurements of the number of counts were made, we average them. The result for HRI pixel is

$$r = \frac{(2448 - 36.5) - (139 - 35.5)}{0.005} = 461600 \frac{counts}{sec} \tag{5}$$

The result for the MRI pixel is

$$r = \frac{(2207 - 72) - (9 - 9)}{0.012} = 177917 \frac{counts}{sec} \tag{6}$$

The resulting absolute responsivities (in $\frac{counts/\sec}{Watt/m^2 \cdot str}$) are

Table 4.2.1-7

Absolute responsivities (uncorrected)

RSR	HRI pixel (100,100)	MRI pixel (50,150)
Measured	1810295	772810
Model	1810629	777820
Current	1842440	753925

In this table the "Current" entry is from the files on cassini in /local. These values are from the reductions using the DISRSOFT program imager_abs_resp_v3, and they have been used in all reductions requiring absolute responsivity. They include the corrections mentioned below. Older algorithms were used for these corrections.

As mentioned above, small corrections must be applied for drift in the lamp during the monochromator scan, the drift in the lamp between the times of the monochromator scan and the DISR exposure, and difference in intensity caused by the inhomogeneity of the integrating sphere. We consider these in this section.

Early algorithms to correct for the lamp drift involved the consideration of three monitor detectors: a broadband silicon detector, a narrow band (violet) filtered silicon, detector, and an InGaAs detector (infrared). The three detectors theoretically provide information about the color temperature of the lamp as well as its luminosity. In practice it has been found that simple use of the broadband silicon detector as a scale factor correction is an adequate method. The broadband silicon detector output is found in column 10 of the "cal" file and in the header entry H_SPSI of the DISRSOFT image data sets.

The first step is to correct all the standard silicon reference detector readings for drift during the monochromator scan itself.

$$s_{corr}(\lambda) = s(\lambda) \cdot \left(\frac{Si_{mono-t_0-b} - Si_{mono-t_0-d}}{Si_{t_\lambda - b} - Si_{t_\lambda - d}} \right) \tag{7}$$

where

$s_{corr}(\lambda)$ is standard silicon reference detector reading at the standard time t_0

$s(\lambda)$ is the uncorrected standard silicon reference detector reading at the time wavelength λ was measured (t_λ)

Si_{mono-t_0-b} is the silicon monitor detector reading with the shutter open at t_0

Si_{mono-t_0-d} is the silicon monitor detector reading with the shutter closed at t_0

$Si_{t_\lambda-b}$ is the silicon monitor detector reading with the shutter open at the time when wavelength λ was measured (t_λ)

$Si_{t_\lambda-d}$ is the silicon monitor detector reading with the shutter closed at the time when wavelength λ was measured (t_λ)

In practice dark measurements were not usually made during a monochromator scan, but they were measured during the imager exposures. The quantity $Si_{t_\lambda-d}$ should not vary with time, except due to statistical fluctuations. The figure below shows the variation of $Si_{t_\lambda-d}$ vs. time while the images were exposed on 24 July, 1996.

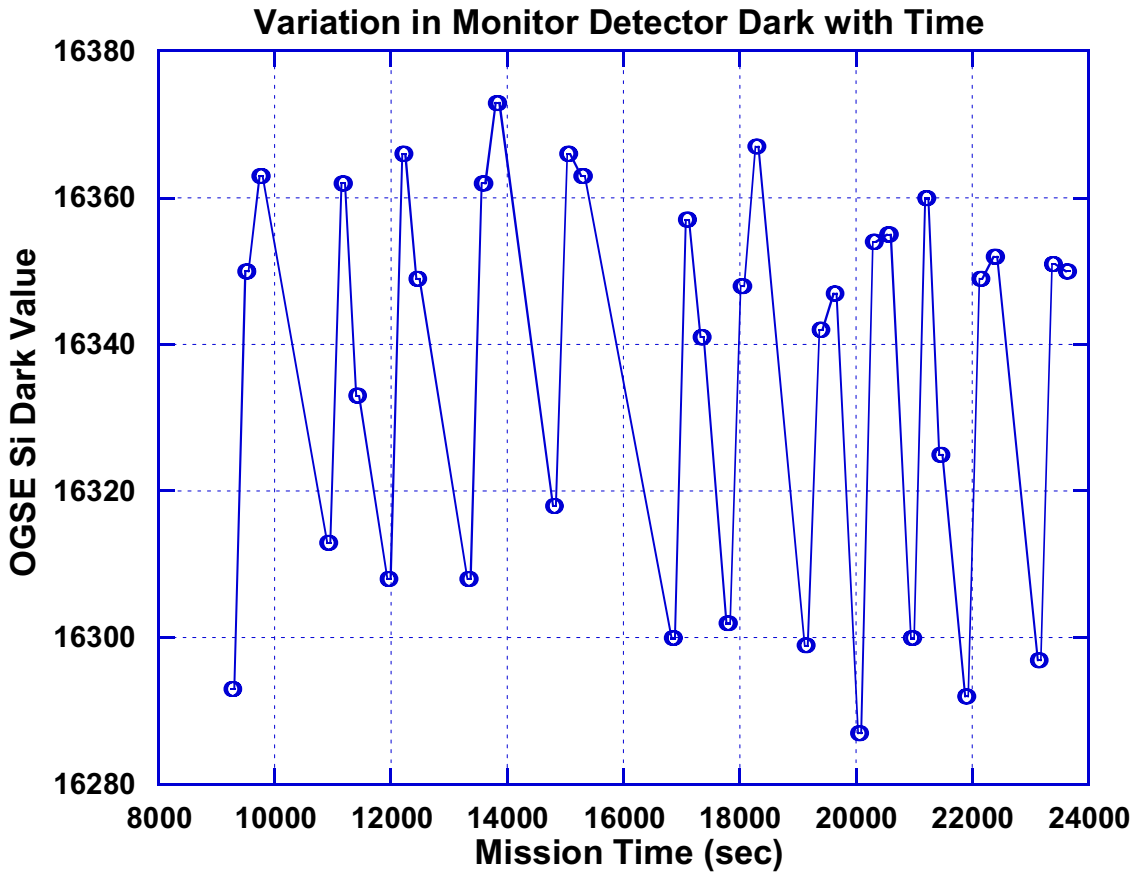

Figure 4.2.1-3 Silicon monitor detector readings with the shutter closed during DISR image taking.

The graph shows a cyclic change in the monitor detector dark readings, however the amplitude is very small. Typically the peak-to-peak variation is ±30 counts. The bright readings are about 123000. The variation in the dark is about ±0.03% of the signal. We choose to adopt a constant value for the dark readings equal to the average of the values in the plot. This average value is 16336.

We define t_0 by choosing the first DISR bright image as the reference, and we compute the silicon reference detector readings as if the whole monochromator scan were done at the time of this image, according to the equation above. From these readings we can compute the integrating sphere intensity $I(\lambda)$ as if the whole monochromator scan had been done at time t_0.

Using the numbers from the monochromator file for the bright silicon monitor detector readings and 16336 for the dark silicon monitor detector reading during the monochromator scan, we can re-compute the integrating sphere intensities in table 4.2.1-8.

Table 4.2.1-8

Brightness of the integrating sphere with drift corrections to HRI image

Wavelength (nm)	D(λ)	c(λ)	I(λ)	Bright Monitor Reading	Dark Monitor Reading	Correction Factor	Corrected I(λ)
600	8.269E-11	1.0459E-10	0.790611	123476	16336	0.999739	0.790404
610	9.749E-11	1.2036E-10	0.809987	123476	16336	0.999701	0.809745
620	9.852E-11	1.1846E-10	0.831673	123483	16336	0.999636	0.831370
630	9.388E-11	1.0988E-10	0.854387	123478	16336	0.999683	0.854116
640	9.249E-11	1.0470E-10	0.883381	123480	16336	0.999664	0.883084
650	1.136E-10	1.2550E-10	0.905179	123479	16336	0.999673	0.904883
660	1.284E-10	1.3863E-10	0.926206	123485	16336	0.999617	0.925852
670	1.310E-10	1.3816E-10	0.948176	123486	16336	0.999608	0.947804
680	1.271E-10	1.3129E-10	0.968086	123488	16336	0.999589	0.967688
690	1.208E-10	1.2214E-10	0.989029	123489	16336	0.999580	0.988614
700	1.140E-10	1.1321E-10	1.006978	123485	16336	0.999617	1.006593
710	1.072E-10	1.0460E-10	1.024857	123488	16336	0.999589	1.024436
720	1.006E-10	9.6846E-11	1.038763	123482	16336	0.999645	1.038395
730	9.428E-11	8.9465E-11	1.053820	123482	16336	0.999645	1.053446
740	8.799E-11	8.2488E-11	1.066701	123476	16336	0.999701	1.066382
750	8.199E-11	7.6033E-11	1.078348	123477	16336	0.999692	1.078016
760	7.616E-11	6.9893E-11	1.089666	123478	16336	0.999683	1.089320
770	7.063E-11	6.4270E-11	1.098958	123482	16336	0.999645	1.098568
780	6.553E-11	5.9079E-11	1.109193	123482	16336	0.999645	1.108800

790	6.081E-11	5.4488E-11	1.116026	123484	16336	0.999627	1.115609
800	5.686E-11	5.0673E-11	1.122097	123486	16336	0.999608	1.121657
810	5.378E-11	4.7783E-11	1.125505	123482	16336	0.999645	1.125106
820	5.170E-11	4.5872E-11	1.127049	123481	16336	0.999655	1.126660
830	5.076E-11	4.5038E-11	1.127048	123482	16336	0.999645	1.126648
840	5.095E-11	4.5303E-11	1.124650	123479	16336	0.999673	1.124283
850	5.222E-11	4.6628E-11	1.119928	123478	16336	0.999683	1.119573
860	5.439E-11	4.8841E-11	1.113614	123475	16336	0.999711	1.113292
870	7.085E-11	6.3255E-11	1.120070	123476	16336	0.999701	1.119735
880	9.348E-11	8.4091E-11	1.111653	123479	16336	0.999673	1.111290
890	1.224E-10	1.1135E-10	1.099237	123484	16336	0.999627	1.098827
900	1.577E-10	1.4541E-10	1.084520	123484	16336	0.999627	1.084115
910	1.997E-10	1.8575E-10	1.075101	123481	16336	0.999655	1.074730
920	2.525E-10	2.3586E-10	1.070550	123483	16336	0.999636	1.070160
930	3.236E-10	3.0449E-10	1.062761	123479	16336	0.999673	1.062414
940	4.032E-10	3.8449E-10	1.048662	123482	16336	0.999645	1.048290
950	4.686E-10	4.5668E-10	1.026101	123477	16336	0.999692	1.025785
960	5.186E-10	5.1171E-10	1.013465	123478	16336	0.999683	1.013143
970	5.569E-10	5.5491E-10	1.003586	123480	16336	0.999664	1.003249
980	5.917E-10	5.9505E-10	0.994370	123479	16336	0.999673	0.994045
990	6.210E-10	6.2993E-10	0.985824	123485	16336	0.999617	0.985447
1000	6.399E-10	6.5562E-10	0.976023	123490	16336	0.999571	0.975604
1010	6.444E-10	6.6810E-10	0.964526	123491	16336	0.999561	0.964103
1020	6.321E-10	6.6319E-10	0.953121	123496	16336	0.999515	0.952658
1030	6.001E-10	6.3821E-10	0.940286	123491	16336	0.999561	0.939874
1040	5.493E-10	5.9188E-10	0.928060	123482	16336	0.999645	0.927731
1050	4.852E-10	5.2955E-10	0.916250	123484	16336	0.999627	0.915908
1060	4.149E-10	4.5913E-10	0.903666	123488	16336	0.999589	0.903295
1070	3.572E-10	4.0006E-10	0.892866	123491	16336	0.999561	0.892474
1080	3.118E-10	3.5310E-10	0.883036	123486	16336	0.999608	0.882690
1090	2.709E-10	3.0874E-10	0.877437	123485	16336	0.999617	0.877101
1100	2.291E-10	2.6532E-10	0.863486	123485	16336	0.999617	0.863156

Table 4.2.1-9

$\int I(\lambda) RSR_{HRI}(\lambda) d\lambda$ for HRI with first drift correction

RSR	Uncorrected	Corrected
Measured	0.254986	0.254895
Model	0.254939	0.254834

Similarly we can compute the corrected monochromatic integrating sphere brightness for the MRI. We note that the brightness in the integrating sphere was slightly brighter (about 1%) for the MRI images, as indicated by the higher monitor detector reading (124441 vs. 123401).

Table 4.2.1-10

Brightness of the integrating sphere with drift corrections to MRI image

Wavelength (nm)	D(λ)	c(λ)	I(λ)	Bright Monitor Reading	Dark Monitor Reading	Correction Factor	Corrected I(λ)
600	8.269E-11	1.0459E-10	0.790611	123476	16336	1.009408	0.798049
610	9.749E-11	1.2036E-10	0.809987	123476	16336	1.009408	0.817608
620	9.852E-11	1.1846E-10	0.831673	123483	16336	1.009342	0.839443
630	9.388E-11	1.0988E-10	0.854387	123478	16336	1.009389	0.862409
640	9.249E-11	1.0470E-10	0.883381	123480	16336	1.009371	0.891659
650	1.136E-10	1.2550E-10	0.905179	123479	16336	1.009380	0.913670
660	1.284E-10	1.3863E-10	0.926206	123485	16336	1.009323	0.934841
670	1.310E-10	1.3816E-10	0.948176	123486	16336	1.009314	0.957007
680	1.271E-10	1.3129E-10	0.968086	123488	16336	1.009295	0.977085
690	1.208E-10	1.2214E-10	0.989029	123489	16336	1.009286	0.998213
700	1.140E-10	1.1321E-10	1.006978	123485	16336	1.009323	1.016367
710	1.072E-10	1.0460E-10	1.024857	123488	16336	1.009295	1.034383
720	1.006E-10	9.6846E-11	1.038763	123482	16336	1.009352	1.048477
730	9.428E-11	8.9465E-11	1.053820	123482	16336	1.009352	1.063675
740	8.799E-11	8.2488E-11	1.066701	123476	16336	1.009408	1.076737
750	8.199E-11	7.6033E-11	1.078348	123477	16336	1.009399	1.088483
760	7.616E-11	6.9893E-11	1.089666	123478	16336	1.009389	1.099897
770	7.063E-11	6.4270E-11	1.098958	123482	16336	1.009352	1.109235
780	6.553E-11	5.9079E-11	1.109193	123482	16336	1.009352	1.119566
790	6.081E-11	5.4488E-11	1.116026	123484	16336	1.009333	1.126442
800	5.686E-11	5.0673E-11	1.122097	123486	16336	1.009314	1.132548
810	5.378E-11	4.7783E-11	1.125505	123482	16336	1.009352	1.136030
820	5.170E-11	4.5872E-11	1.127049	123481	16336	1.009361	1.137599
830	5.076E-11	4.5038E-11	1.127048	123482	16336	1.009352	1.137588
840	5.095E-11	4.5303E-11	1.124650	123479	16336	1.009380	1.135199
850	5.222E-11	4.6628E-11	1.119928	123478	16336	1.009389	1.130443
860	5.439E-11	4.8841E-11	1.113614	123475	16336	1.009418	1.124102
870	7.085E-11	6.3255E-11	1.120070	123476	16336	1.009408	1.130608
880	9.348E-11	8.4091E-11	1.111653	123479	16336	1.009380	1.122080
890	1.224E-10	1.1135E-10	1.099237	123484	16336	1.009333	1.109496
900	1.577E-10	1.4541E-10	1.084520	123484	16336	1.009333	1.094642
910	1.997E-10	1.8575E-10	1.075101	123481	16336	1.009361	1.085165
920	2.525E-10	2.3586E-10	1.070550	123483	16336	1.009342	1.080551
930	3.236E-10	3.0449E-10	1.062761	123479	16336	1.009380	1.072730
940	4.032E-10	3.8449E-10	1.048662	123482	16336	1.009352	1.058469
950	4.686E-10	4.5668E-10	1.026101	123477	16336	1.009399	1.035745
960	5.186E-10	5.1171E-10	1.013465	123478	16336	1.009389	1.022981
970	5.569E-10	5.5491E-10	1.003586	123480	16336	1.009371	1.012990
980	5.917E-10	5.9505E-10	0.994370	123479	16336	1.009380	1.003697

990	6.210E-10	6.2993E-10	0.985824	123485	16336	1.009323	0.995015
1000	6.399E-10	6.5562E-10	0.976023	123490	16336	1.009276	0.985077
1010	6.444E-10	6.6810E-10	0.964526	123491	16336	1.009267	0.973464
1020	6.321E-10	6.6319E-10	0.953121	123496	16336	1.009220	0.961909
1030	6.001E-10	6.3821E-10	0.940286	123491	16336	1.009267	0.949000
1040	5.493E-10	5.9188E-10	0.928060	123482	16336	1.009352	0.936739
1050	4.852E-10	5.2955E-10	0.916250	123484	16336	1.009333	0.924801
1060	4.149E-10	4.5913E-10	0.903666	123488	16336	1.009295	0.912066
1070	3.572E-10	4.0006E-10	0.892866	123491	16336	1.009267	0.901140
1080	3.118E-10	3.5310E-10	0.883036	123486	16336	1.009314	0.891261
1090	2.709E-10	3.0874E-10	0.877437	123485	16336	1.009323	0.885618
1100	2.291E-10	2.6532E-10	0.863486	123485	16336	1.009323	0.871537

Table 4.2.1-11
$\int I(\lambda)RSR_{MRI}(\lambda)d\lambda$ for MRI with drift correction

RSR	Uncorrected	Corrected
Measured	0.230221	0.232375
Model	0.228738	0.230878

The second part of the drift correction is to correct the image count rates to what their values would have been at t_0. Because we have chosen t_0 to be the time of the first (and only) bright image of the sequence, this correction is unnecessary. We already know the intensity in the integrating sphere at this time.

The terms necessary to compute the absolute responsivity with the time drift corrections are now known, and equation 2 may be recomputed using the integrating sphere intensity at the time of the bright image.

$$A = \frac{r}{\int I(\lambda)RSR(\lambda)d\lambda} = \frac{461600}{0.254834} = 1811375 \frac{counts/sec}{Watt/m^2 \cdot str} \text{ for the HRI} \qquad (12)$$

and

$$A = \frac{r}{\int I(\lambda)RSR(\lambda)d\lambda} = \frac{177917}{0.230878} = 770611 \frac{counts/sec}{Watt/m^2 \cdot str} \text{ for the MRI,} \qquad (13)$$

where we have used the measured (rather than model) RSR values. These represent changes of +0.08% for the HRI and –0.87% for the MRI compared to the values

uncorrected for drift. Almost all of the drift correction comes from changes between t_0 and the DISR image taking. The effect of the drift during the monochromator scan is negligible.

The correction for non-uniformity of brightness in the integrating sphere begins with Bashar Rizk's document "Integrating Sphere Homogeneity and the Relative Brightness of each DISR Instrument's Calibration Field" (also available as http://disr.lpl.arizona.edu/Integrating%20Sphere%20Non-Uniformity%20Report.htm on the DISR team web site. This document describes the brightness in sphere-centered and DISR window-centered coordinate systems, concluding that the sphere is uniform to approximately 2% over most of the DISR fields of view. The intensity in the direction corresponding to each pixel must be compared to the intensity in the direction of the Silicon standard detector to obtain the actual sphere intensity for that pixel. A spreadsheet named Integrating_Sphere_Relative_Brightness.xls gives the sphere brightness on a 1° grid in zenith and azimuth angle over the entire sphere. This file is located on cassini in the directory /local/Integrating_Sphere. In this speadsheet the zenith angle varies from 0° to 180° with row number, and the azimuth angle increases counter-clockwise when looking down on the sphere (and DISR). 0° DISR azimuth corresponds to 90° sphere azimuth.

The monochromater standard reference detector views the "front" of integrating sphere, an area opposite the mounting position of the DISR. It has a finite field of view. For purposes of standardization, we adopt the value used by M. Tomasko for the Solar Aureole absolute responsivity of 0.987988.

$$I(col,row)_{corr} = \frac{1+\frac{S(col,row)}{100}}{0.987988} \cdot I(col,row), \text{ where} \qquad (14)$$

$I(col,row)_{corr}$ is the corrected intensity seen by a given column and row of the imagers

$S(col,row)$ is the sphere intensity factor from Bashar Rizk's tables for that column and row

$I(col,row)$ is the original, uncorrected intensity measured by the standard reference detector

The sphere inhomogeneity correction is assumed to be independent of wavelength.

The elevation and azimuth of the two pixels in this study can be found in Appendix II. This appendix contains the coordinates of every pixel in all three imagers. These coordinates are nadir angle and azimuth angle. Azimuth angle increases clockwise when looking down on the top of DISR (opposite from the convention for the sphere azimuth).

The conversion from DISR to sphere coordinates is as follows:

$$zenith\_angle_{rb} = 180^{\circ} - nadir\_angle_{DISR} \quad (15)$$

$$azimuth\_angle_{rb} = 90^{\circ} - azimuth\_angle_{DISR} \quad (16)$$

For HRI (column 100, row 100), the DISR azimuth is 6.098º, and the DISR nadir angle is 12.941º. These convert to a relative brightness (*rb*) azimuth of 83.902º and an *rb* zenith of 167.059º.

For MRI (column 50, row 150), the DISR azimuth is –7.711º, and the DISR nadir angle is 34.506º. These convert to *rb* azimuth of 97.711º and *rb* zenith of 145.491º.

Tables 4.2.1-12 and 4.2.1-13, below give the percentage differences from the field of view of the reference detector of the normalized sphere intensity at the 4 points surrounding these two directions.

Table 4.2.1-12

Sphere Intensity Factor for the HRI point

Zenith\Azimuth	83º	84º
167º	-7.87774	-7.85185
168º	-8.12122	-8.09307

Table 4.2.1-13

Sphere Intensity Factor for the MRI point

Zenith\Azimuth	97º	98º
145º	-1.71368	-1.78599
146º	-1.91588	-2.03303

Bilinear interpolation at the actual positions of the pixels yields –7.86863 for the HRI point and –1.88003 for the MRI point.

Equation 14 becomes $I(col,row)_{corr} = \frac{1+\frac{-7.86863}{100}}{0.987988} \cdot I(col,row) = 0.932515 \cdot I(col,row)$

for the HRI pixel and $I(col,row)_{corr} = \frac{1+\frac{-1.88003}{100}}{0.987988} \cdot I(col,row) = 0.993129 \cdot I(col,row)$

for the MRI pixel.

The absolute responsivities are divided by these factors to obtain the final calibration.

$$A = \frac{1811680 \dfrac{counts/sec}{Watt/m^2 \cdot str}}{0.932515} = 1942789 \frac{counts/sec}{Watt/m^2 \cdot str}$$ for HRI, and

$$A = \frac{770611 \dfrac{counts/sec}{Watt/m^2 \cdot str}}{0.993129} = 775943 \frac{counts/sec}{Watt/m^2 \cdot str}$$ for the MRI.

As mentioned above, the IDL program reproduces these results to five significant figures.

4.2.2. Results

The absolute responsivity of each pixel in all three imagers was computed using the method above. The results for the HRI at 236.84K, the MRI at 236.53K, and the SLI at 236.72K are given in tables X, Y, and Z below.

Similar computations were made at each of the other 14 temperatures. The absolute responsivity for each pixel in the three imagers at all 15 temperatures can be found on cassini (the computer) in the directory local/Imagers/Abs_Resp/DISR#3/new_reductions_ Oct2002. The file names are given in table 4.2.2-1.

Table 4.2.2-1

File Names of Absolute Responsivity Reductions

Imager	Temperature (K)	File Name
HRI	171.57	abs_resp_dli1_171.57
HRI	181.51	abs_resp_dli1_181.51
HRI	187.37	abs_resp_dli1_187.37
HRI	195.85	abs_resp_dli1_195.85
HRI	207.25	abs_resp_dli1_207.25
HRI	211.77	abs_resp_dli1_211.77
HRI	222.32	abs_resp_dli1_222.32
HRI	229.58	abs_resp_dli1_229.58
HRI	236.84	abs_resp_dli1_236.84
HRI	244.40	abs_resp_dli1_244.40
HRI	253.43	abs_resp_dli1_253.43
HRI	259.84	abs_resp_dli1_259.84
HRI	271.00	abs_resp_dli1_271.00
HRI	281.31	abs_resp_dli1_281.31
HRI	289.67	abs_resp_dli1_289.67
MRI	171.51	abs_resp_dli2_171.51

MRI	181.51	abs_resp_dli2_181.51
MRI	187.31	abs_resp_dli2_187.31
MRI	195.60	abs_resp_dli2_195.60
MRI	207.07	abs_resp_dli2_207.07
MRI	211.52	abs_resp_dli2_211.52
MRI	222.08	abs_resp_dli2_222.08
MRI	229.27	abs_resp_dli2_229.27
MRI	236.53	abs_resp_dli2_236.53
MRI	244.10	abs_resp_dli2_244.10
MRI	253.19	abs_resp_dli2_253.19
MRI	259.84	abs_resp_dli2_259.84
MRI	270.94	abs_resp_dli2_270.94
MRI	281.31	abs_resp_dli2_281.31
MRI	289.73	abs_resp_dli2_289.73
SLI	171.57	abs_resp_sli_171.57
SLI	181.39	abs_resp_sli_181.39
SLI	187.43	abs_resp_sli_187.43
SLI	195.66	abs_resp_sli_195.66
SLI	207.13	abs_resp_sli_207.13
SLI	211.65	abs_resp_sli_211.65
SLI	222.14	abs_resp_sli_222.14
SLI	229.46	abs_resp_sli_229.46
SLI	236.72	abs_resp_sli_236.72
SLI	244.28	abs_resp_sli_244.28
SLI	253.25	abs_resp_sli_253.25
SLI	259.84	abs_resp_sli_259.84
SLI	270.94	abs_resp_sli_270.94
SLI	281.31	abs_resp_sli_281.31
SLI	289.73	abs_resp_sli_289.73

These files are in DISRSOFT format, and they must be read with the d_read procedure through IDL. In these files bad pixels are given the flag value of –1.0.

Constructing a model for the temperature dependence of the absolute responsivity can reduce the large quantity of numbers. We expect the temperature dependence for all pixels to be very nearly the same. Therefore we have modeled the temperature dependence of the average responsivity of all good pixels in each imager. A polynomial is fitted to the temperature dependence of each imager. The results are shown in figures 4.2.2-1, 4.2.2-2, and 4.2.2-3.

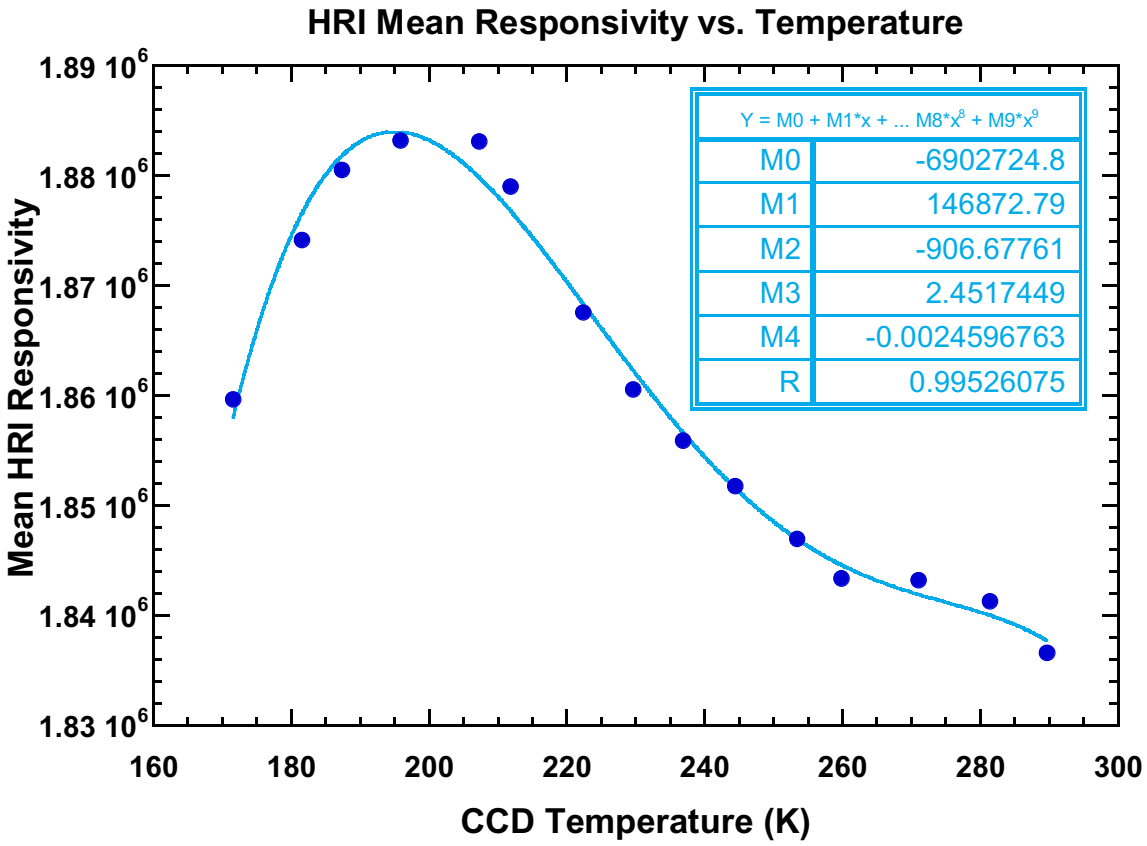

Figure 4.2.2-1 Temperature model of the absolute responsivity for all good HRI pixels. Dots are the measurements, and the curve is a fourth-order polynomial fit.

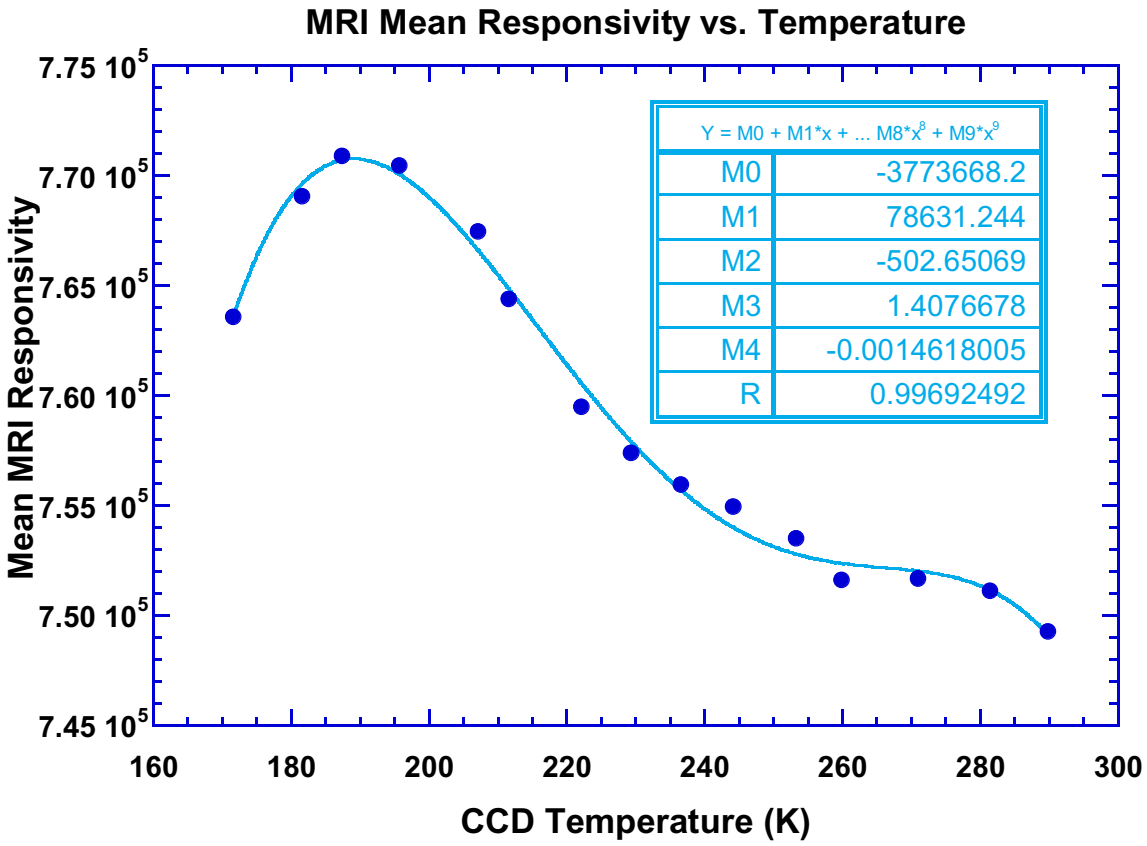

Figure 4.2.2-2 Temperature model of the absolute responsivity for all good MRI pixels. Dots are the measurements, and the curve is a fourth-order polynomial fit.

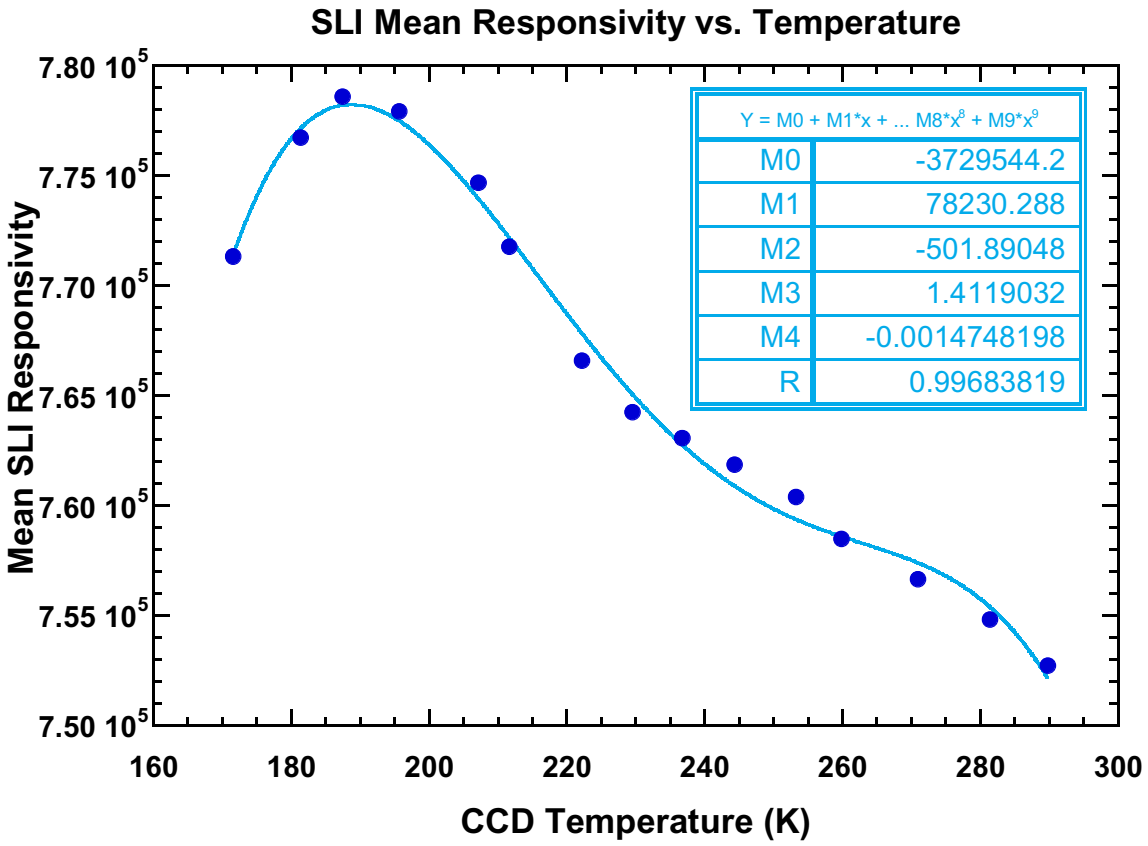

Figure 4.2.2-3 Temperature model of the absolute responsivity for all good SLI pixels. Dots are the measurements, and the curve is a fourth-order polynomial fit.

The principal temperature effect is a drop in the responsivity as the temperature increases. This is consistent with the narrowing of the imager relative spectral responses with decreasing temperature. We note that the responsivity of the HRI is a little over twice that of the other imagers. The HRI does not have the neutral density filter in the filter window that the other imagers have.

An obvious question is whether all pixels really do have the same temperature dependence. This is investigated below by comparing the measured and modeled absolute responsivity for each pixel. The model responsivity is computed by assuming the same shape for the temperature dependence found for all pixels for each imager independently. The responsivity at approximately 237K is used as a basis, and the responsivity at the other 14 temperatures is predicted using the shape of the model temperature dependence. At each of these 14 temperatures there will be a residual, the measured responsivity – the predicted responsivity. For each temperature we examine the distribution of these residuals in figures 4.2.2-4, 4.2.2-5, and 4.2.2-6.

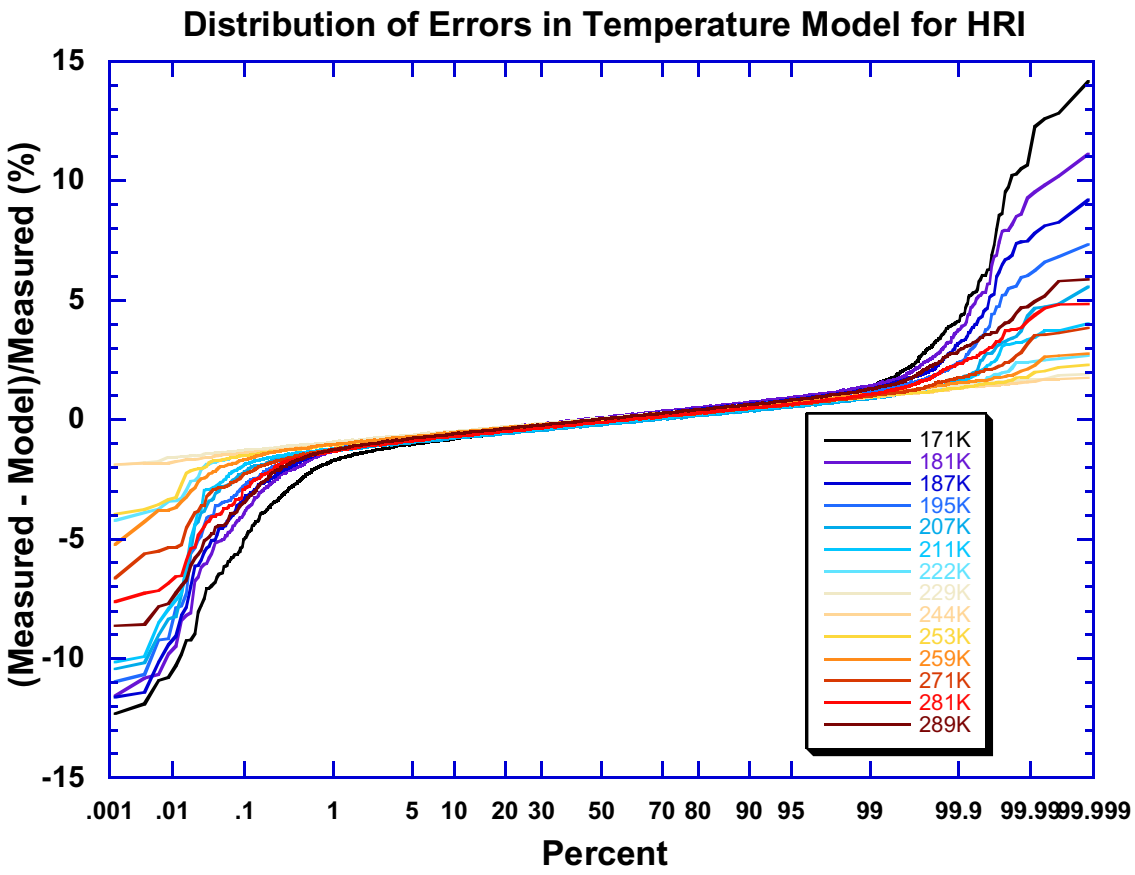

Figure 4.2.2-4 The distribution of absolute responsivity residuals expressed in percent as (measured – model) for the temperature dependence of the HRI.

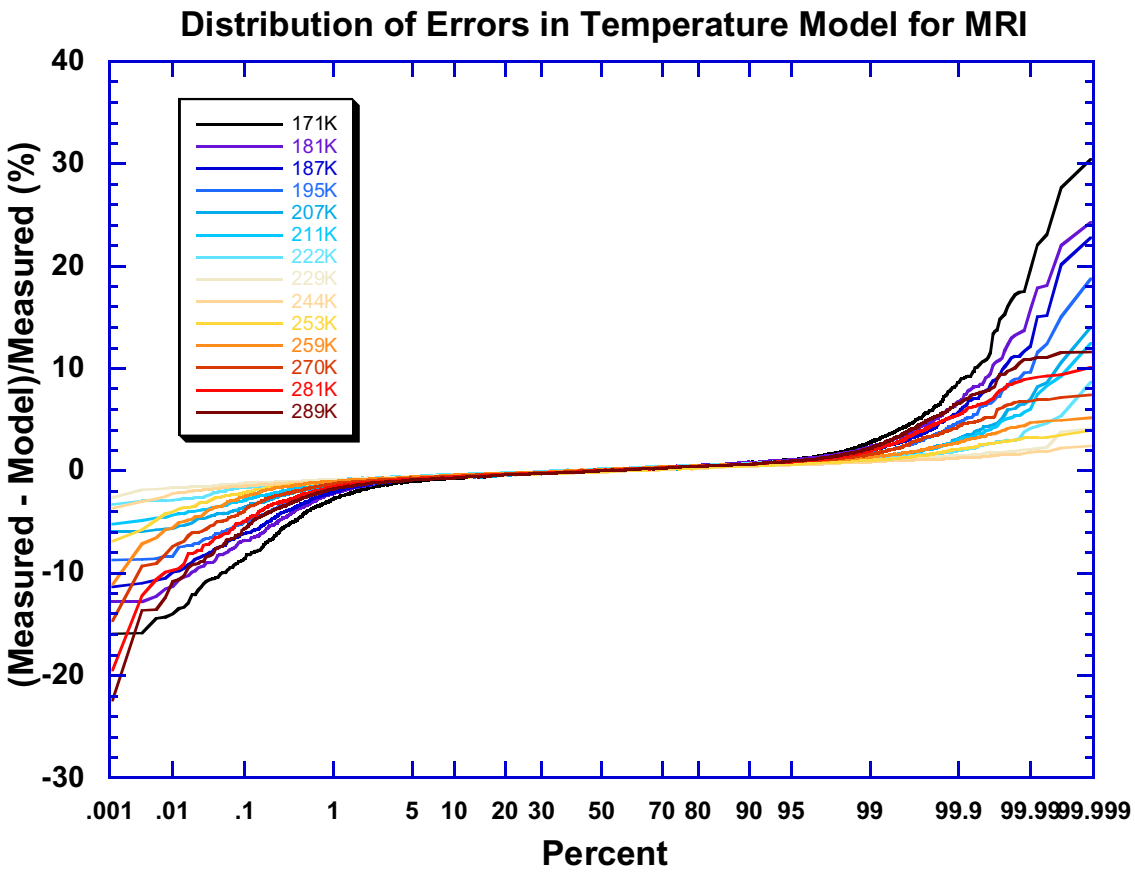

Figure 4.2.2-5 The distribution of absolute responsivity residuals expressed in percent as (measured – model) for the temperature dependence of the MRI.

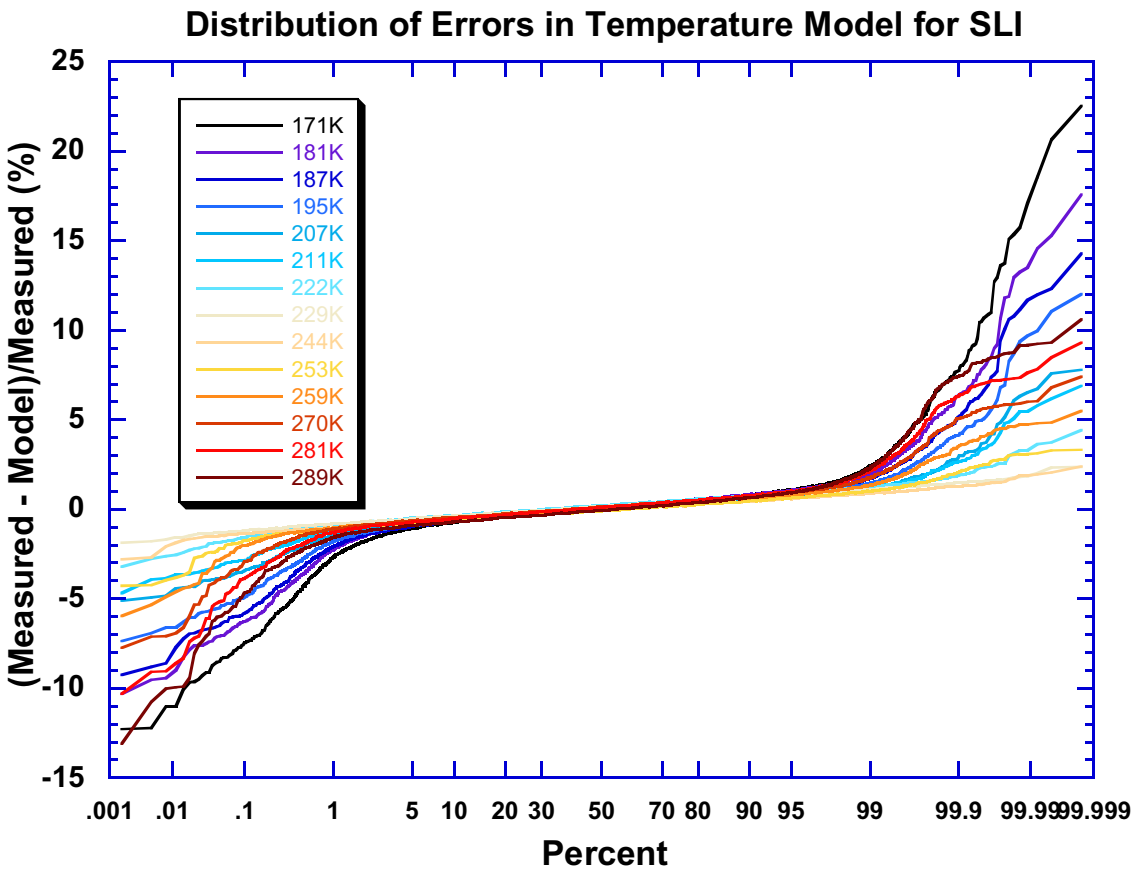

Figure 4.2.2-6 The distribution of absolute responsivity residuals expressed in percent as (measured – model) for the temperature dependence of the SLI.

The temperature model performs very well for almost all pixels. More than 98% of the pixels show residuals of <1.5%. The best performance is achieved for temperatures close to the base temperature of ≈237K, and the performance decreases as the temperature differs more from the base temperature. Errors exceed 10% for only a few pixels at the most extreme temperatures.

To gain insight about the pixels which do not fit the temperature model well, we examine their spatial distribution within the imagers in figures 11, 12, and 13. In these images poorly fitting pixels are color coded according to table 14.

Table 4.2.2-2

Color Codes of Poorly Fitting Pixels

Range of Residual	Color
<-10%	Blue
-5% to -10%	Blue-Green
-3% to –5%	Green

+3% to +5%	Magenta
+5% to +10%	Yellow
>+10%	Red

Figure 4.2.2-7 Spatial Distribution of Pixels that Fit the Temperature Model Poorly for the HRI

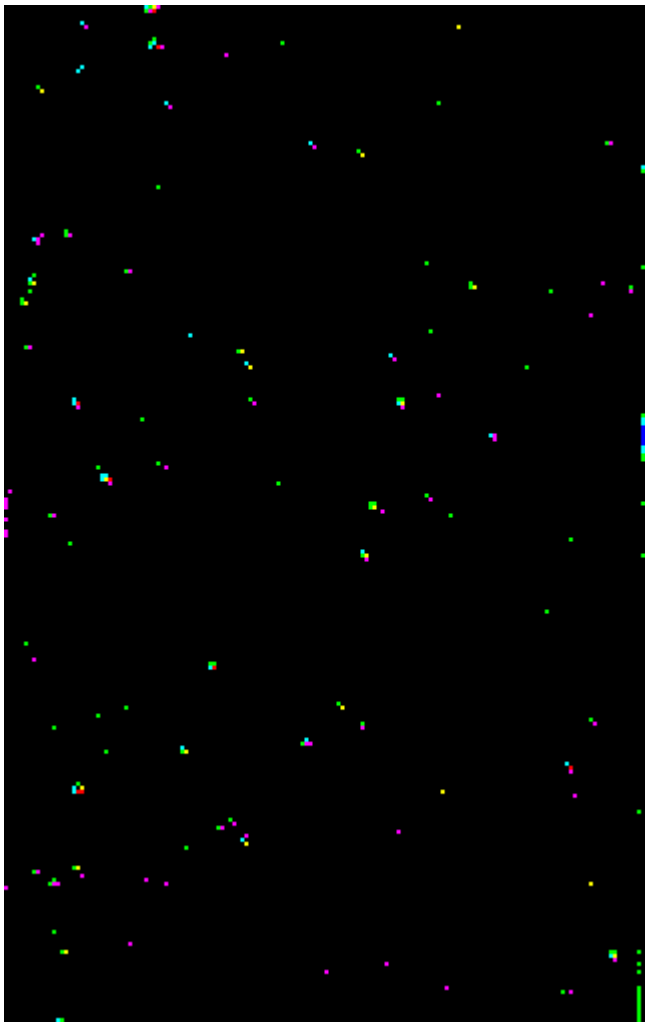

HRI at 171.57K

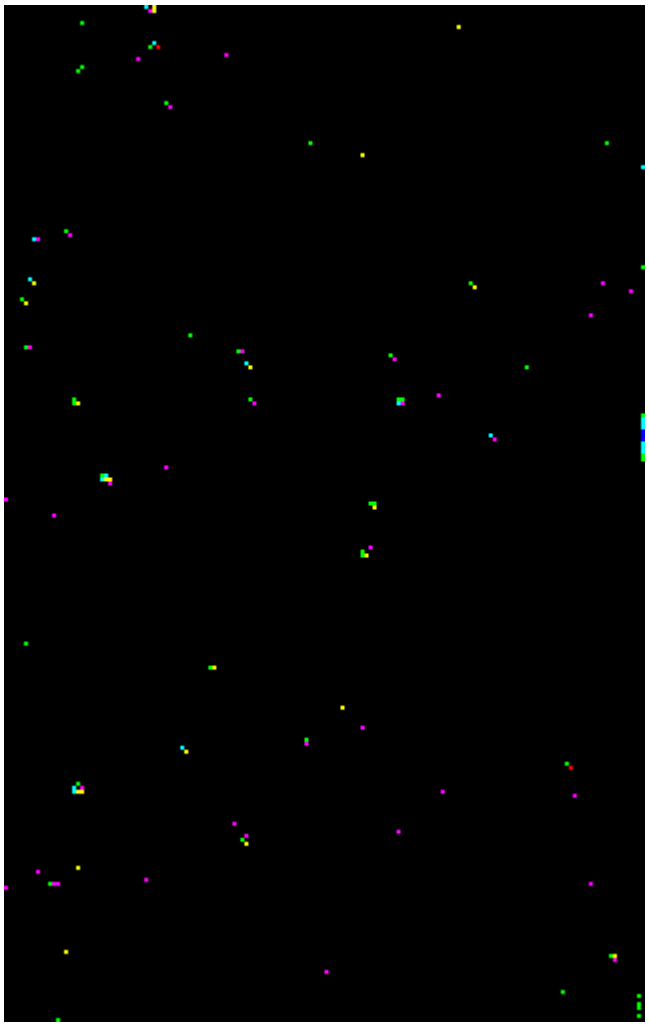

HRI at 181.51K

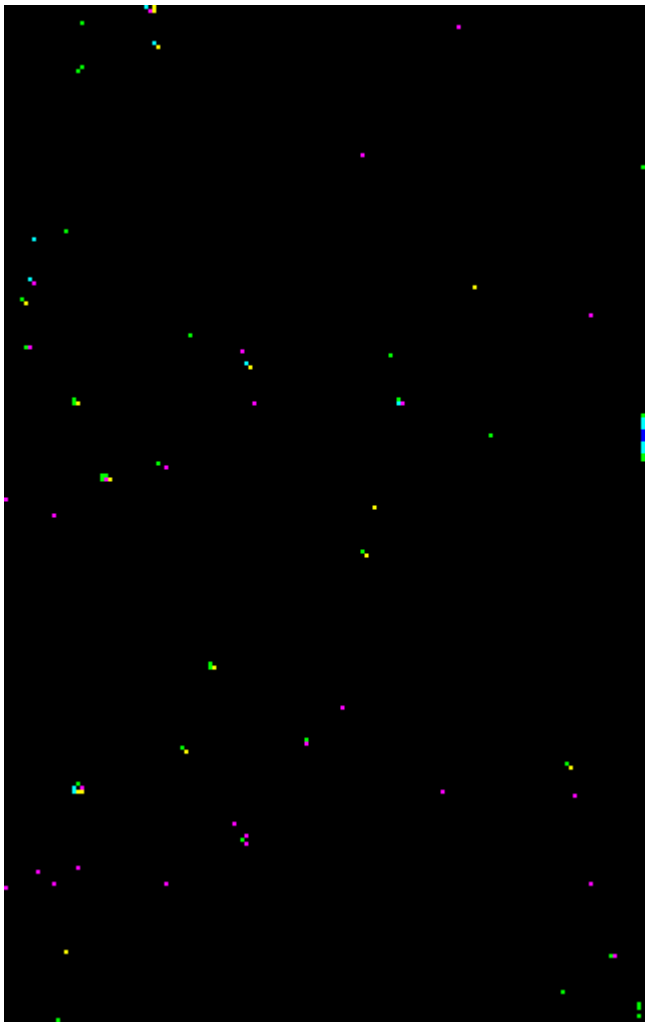

HRI at 187.37K

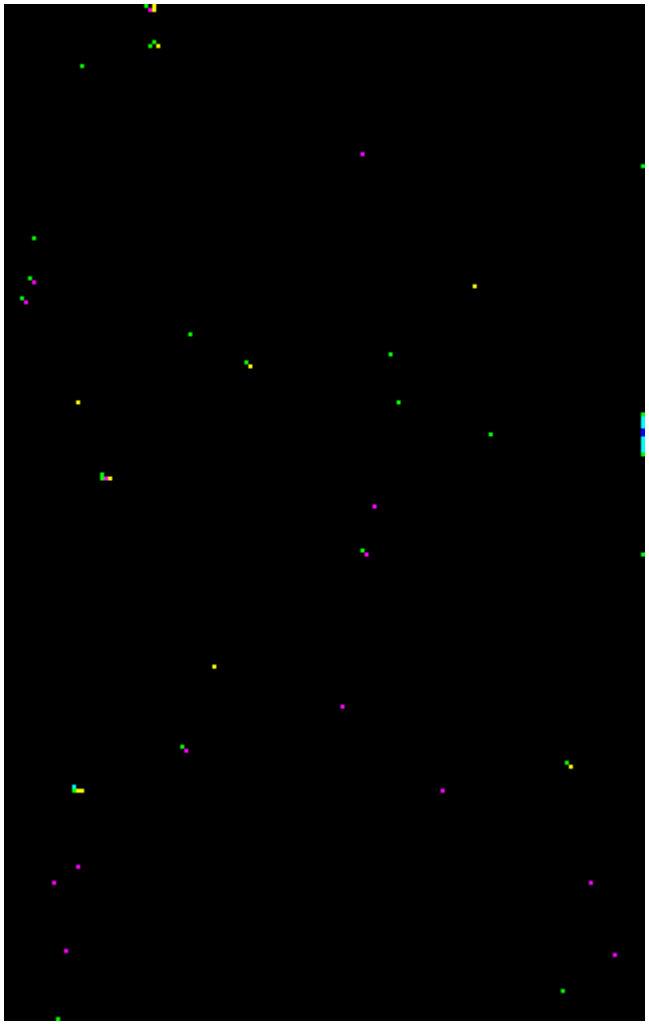

HRI at 195.85K

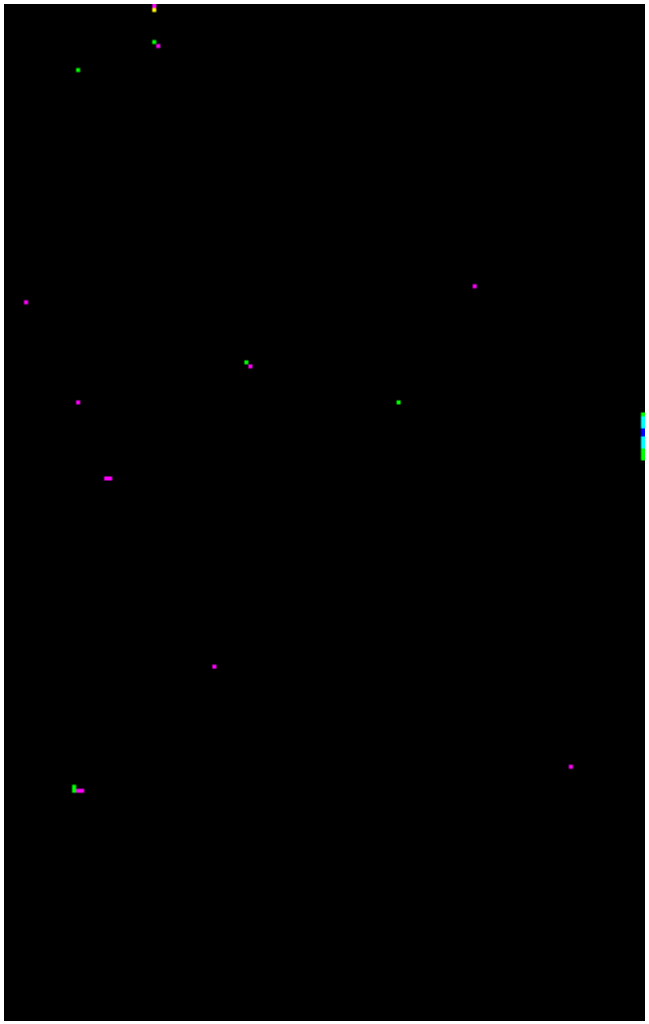

HRI at 207.25K

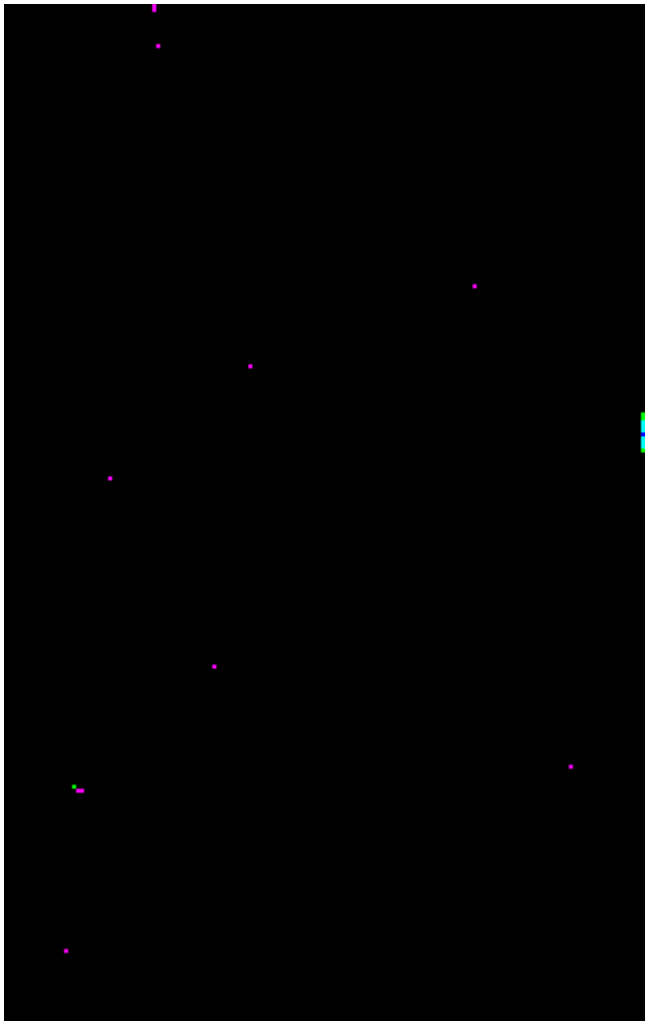

HRI at 211.77K

HRI at 222.32K

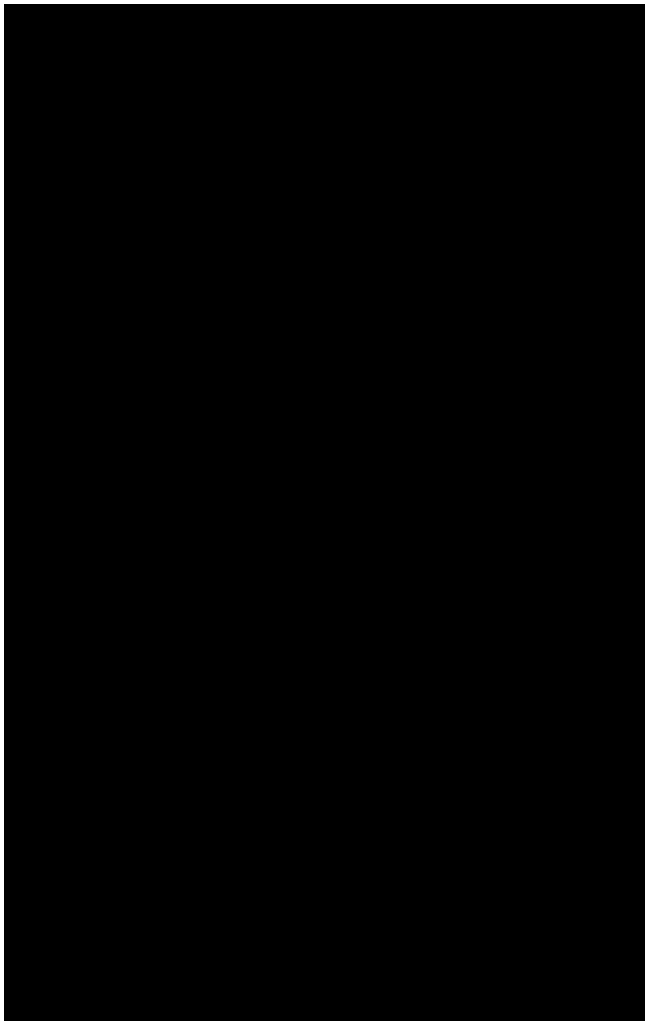

HRI at 229.58K

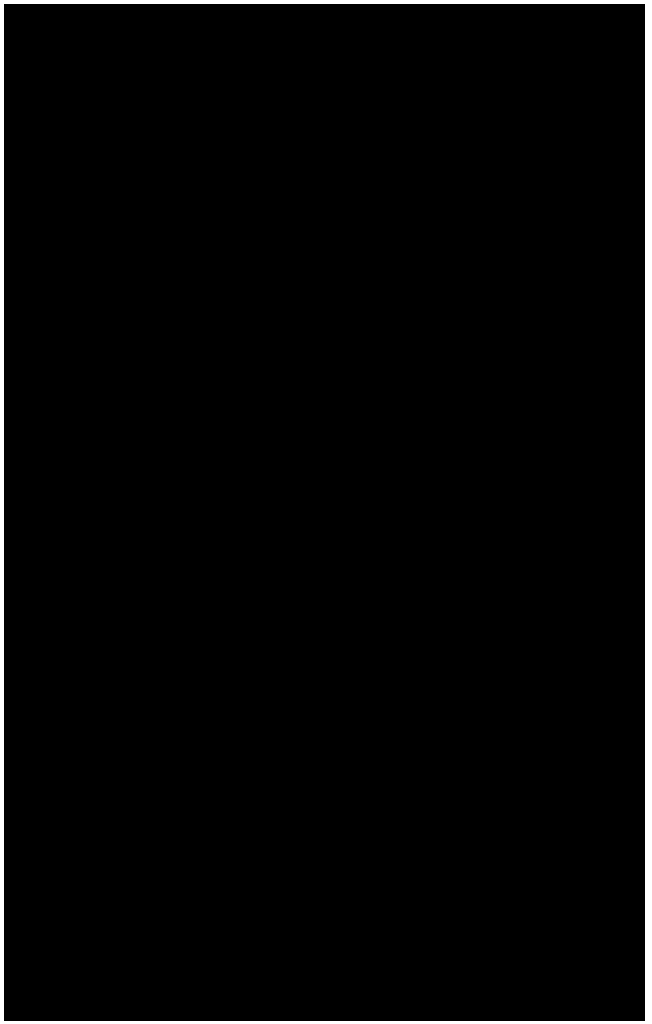

HRI at 236.84K

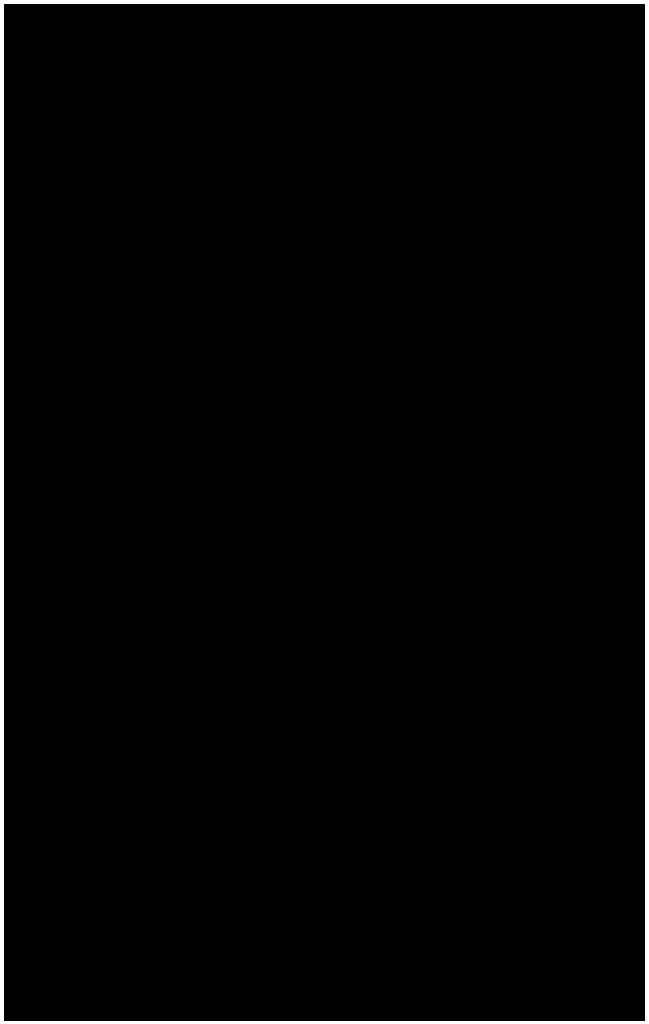

HRI at 244.40K

HRI at 253.43K

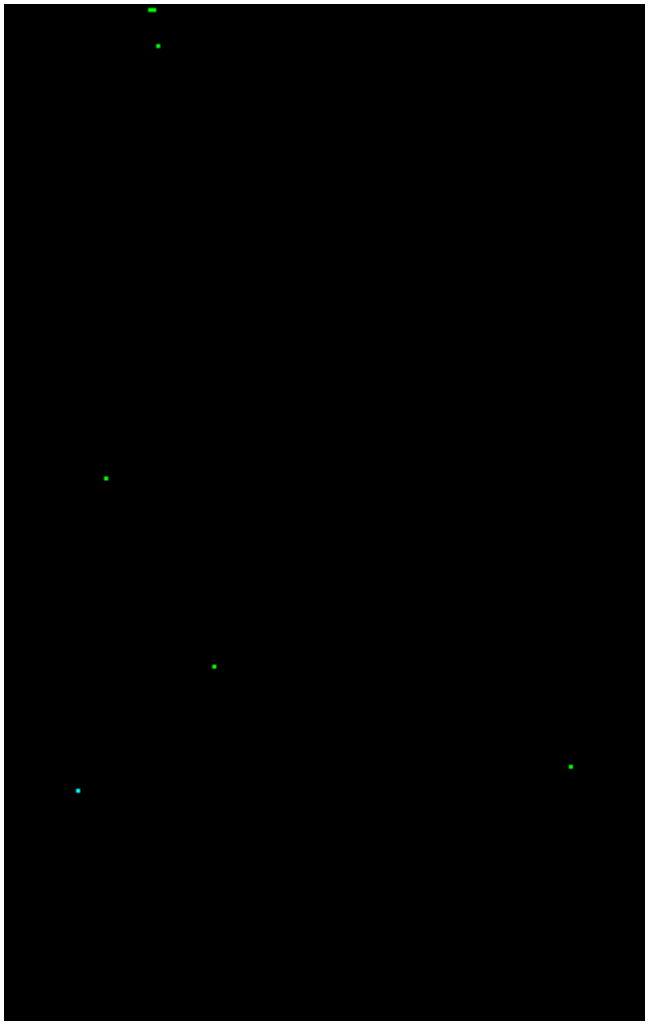

HRI at 259.84K

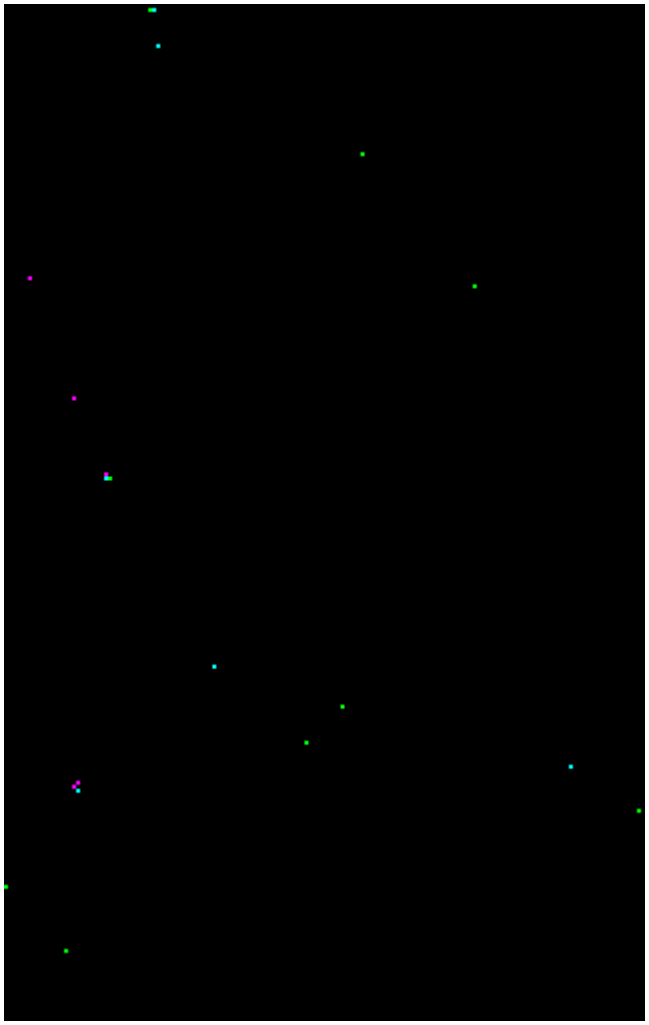

HRI at 271.00K

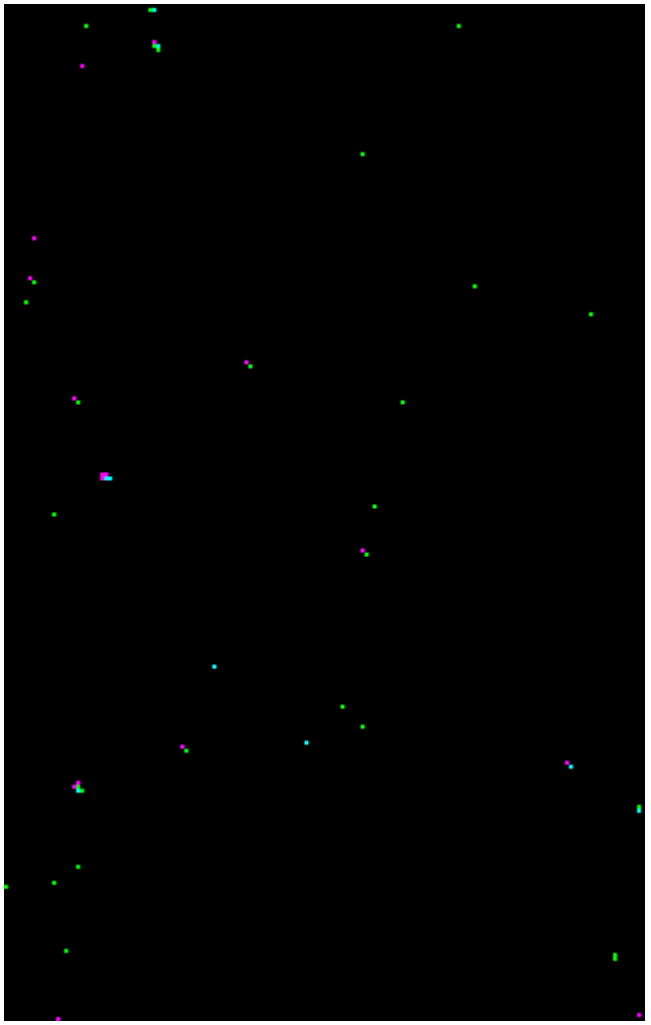

HRI at 281.31K

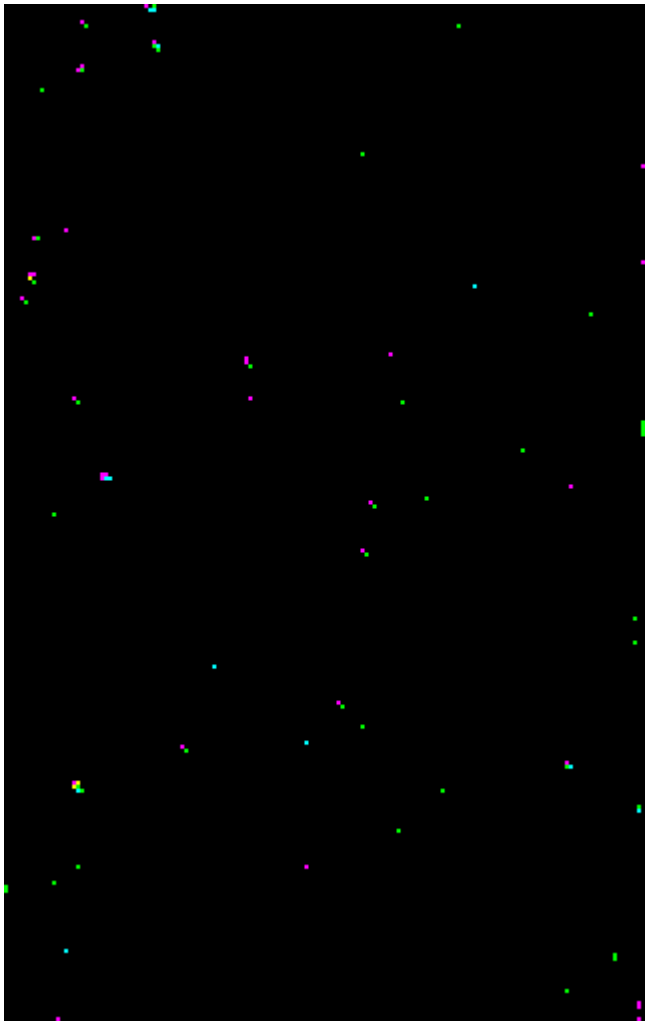

HRI at 289.67K

Figure 4.2.2-8 Spatial Distribution of Pixels which Fit the Temperature Model Poorly for the MRI

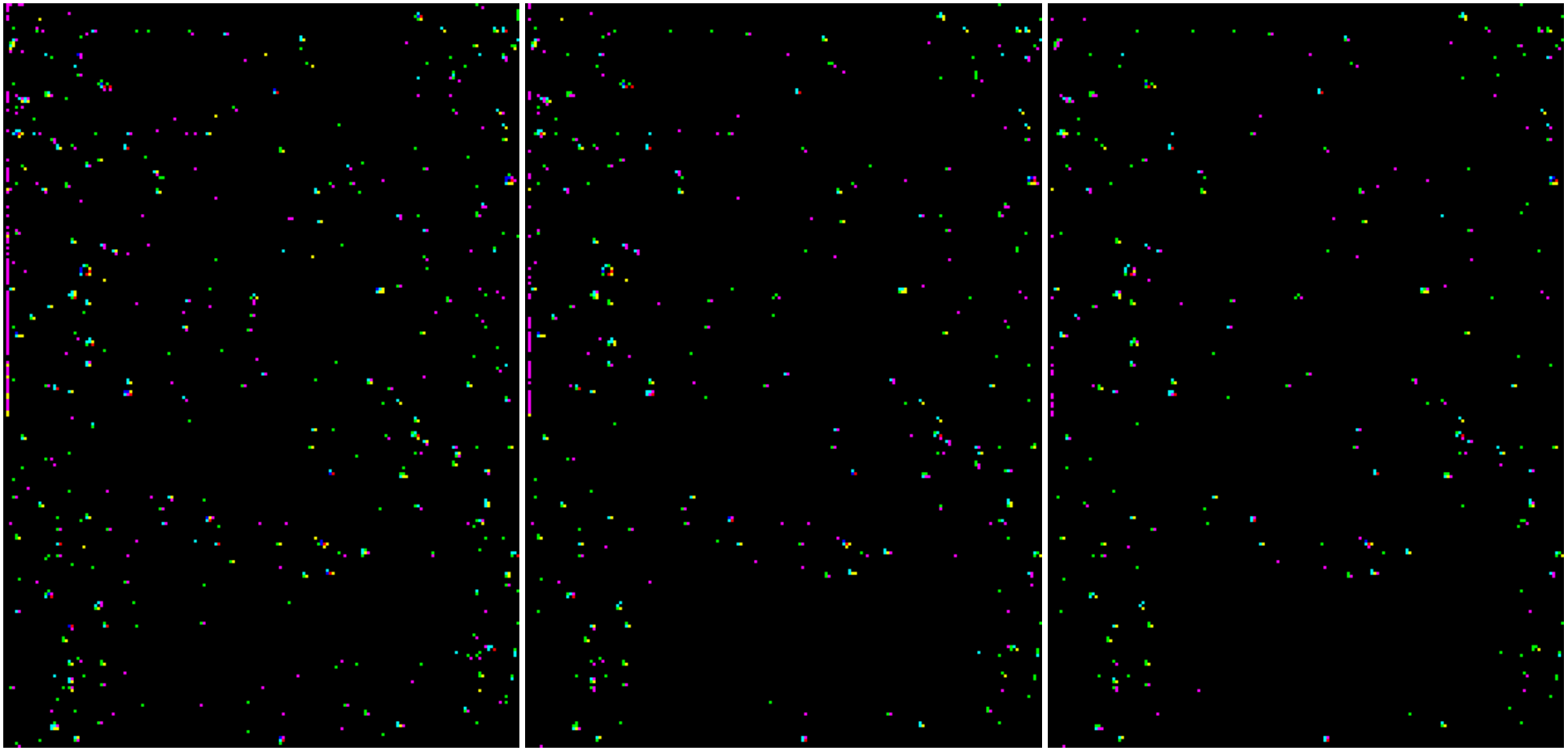

MRI at 171.51K MRI at 181.51K MRI at 187.31K

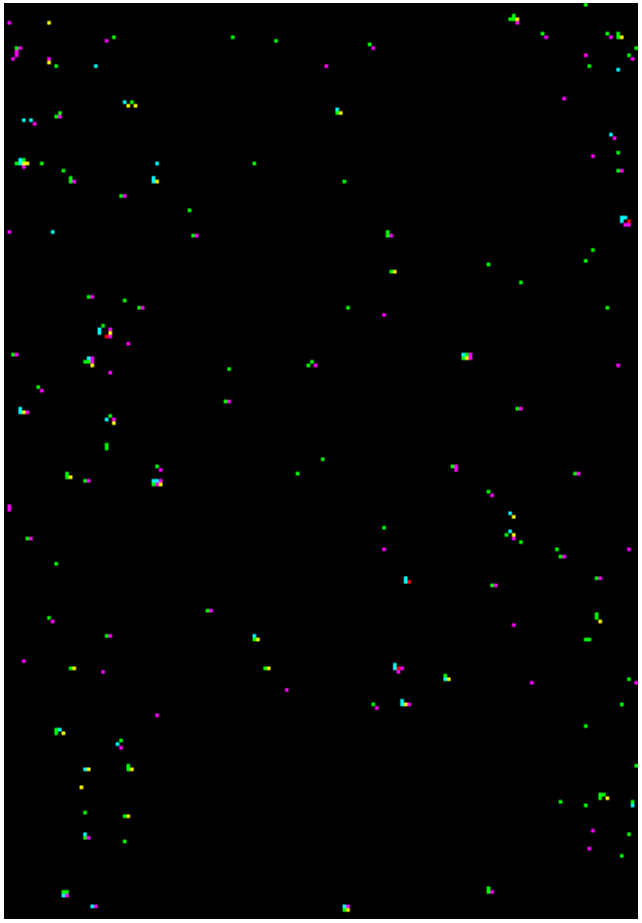

MRI at 195.60K

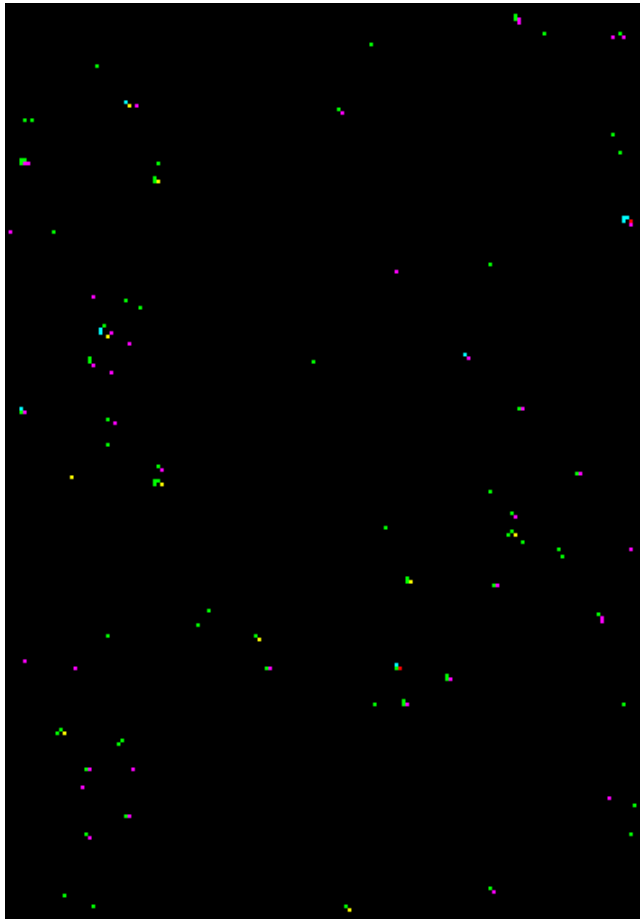

MRI at 207.07K

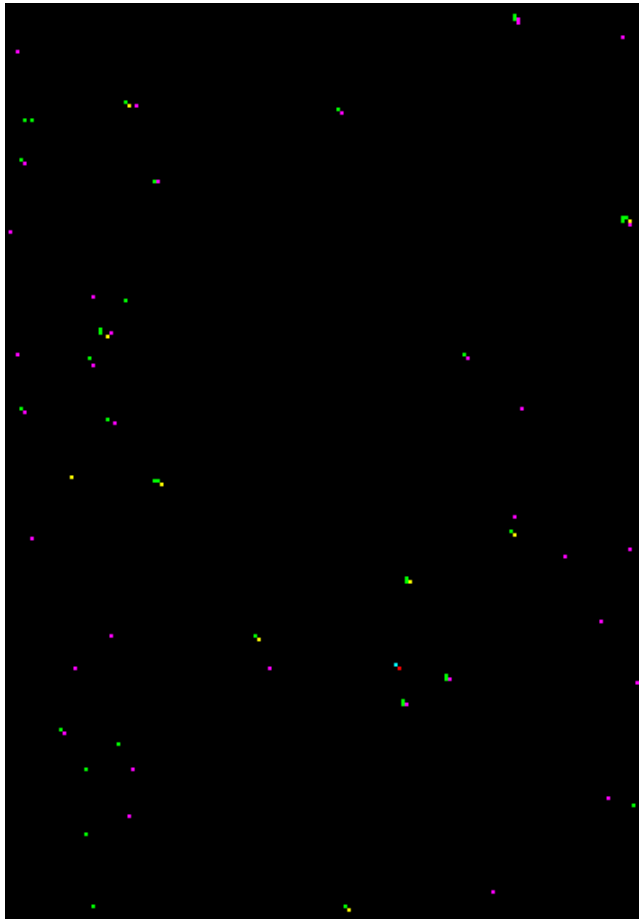

MRI at 211.52K

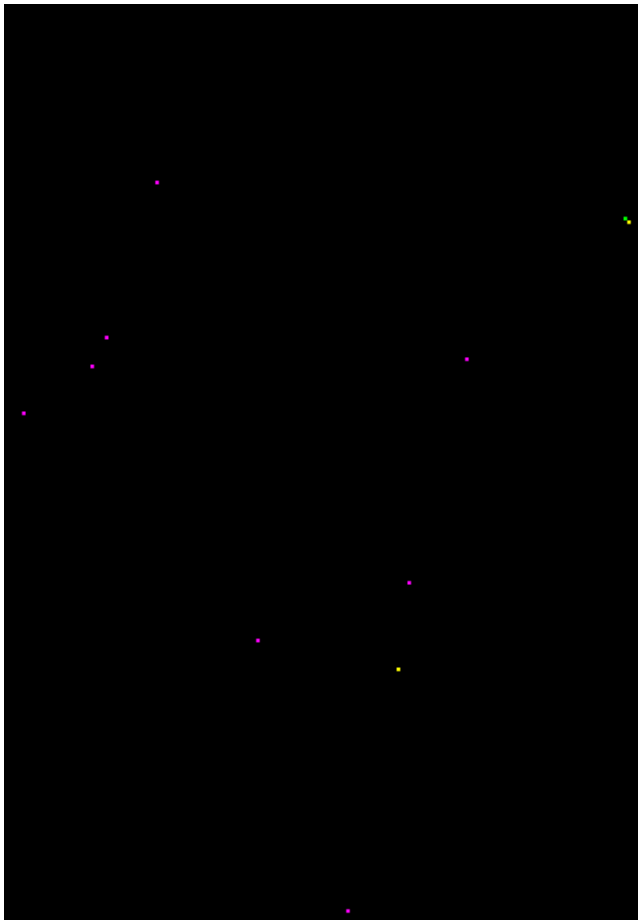

MRI at 222.08K

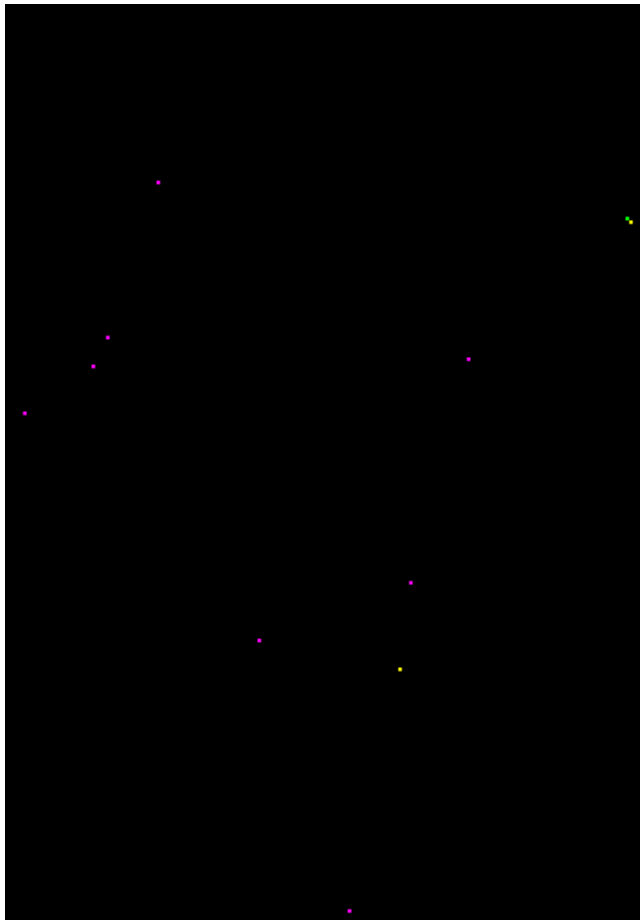

MRI at 229.27K

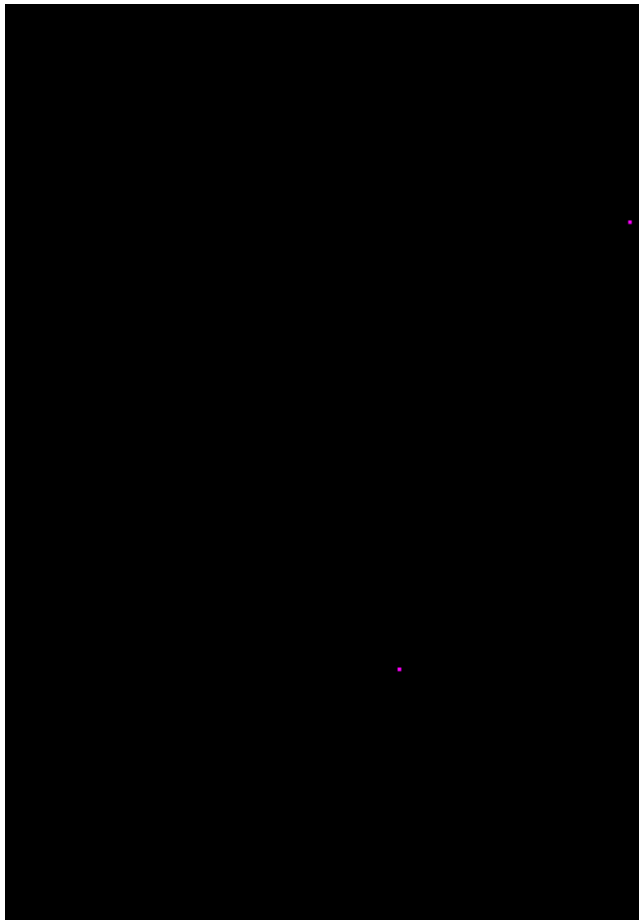

MRI at 236.53K

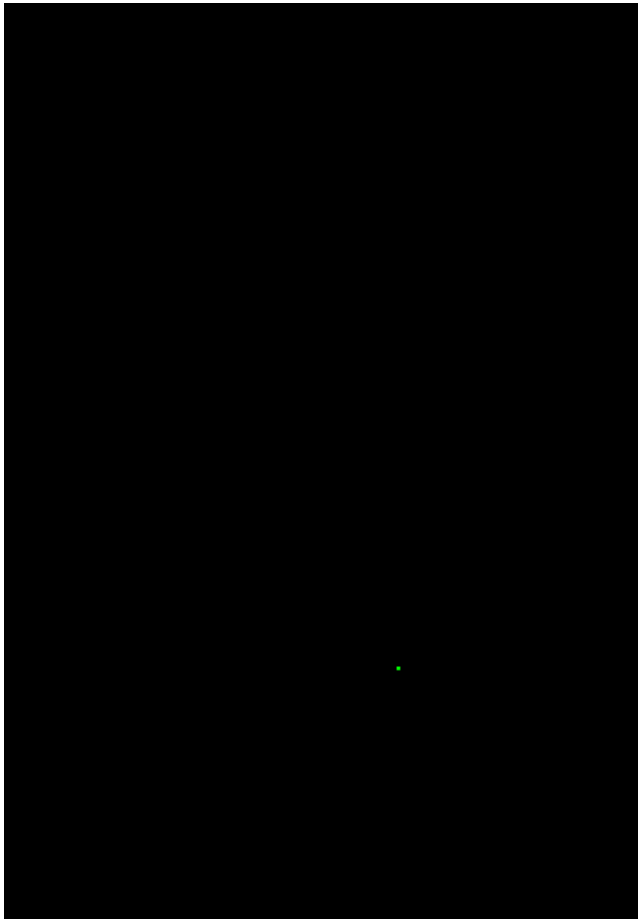

MRI at 244.10K

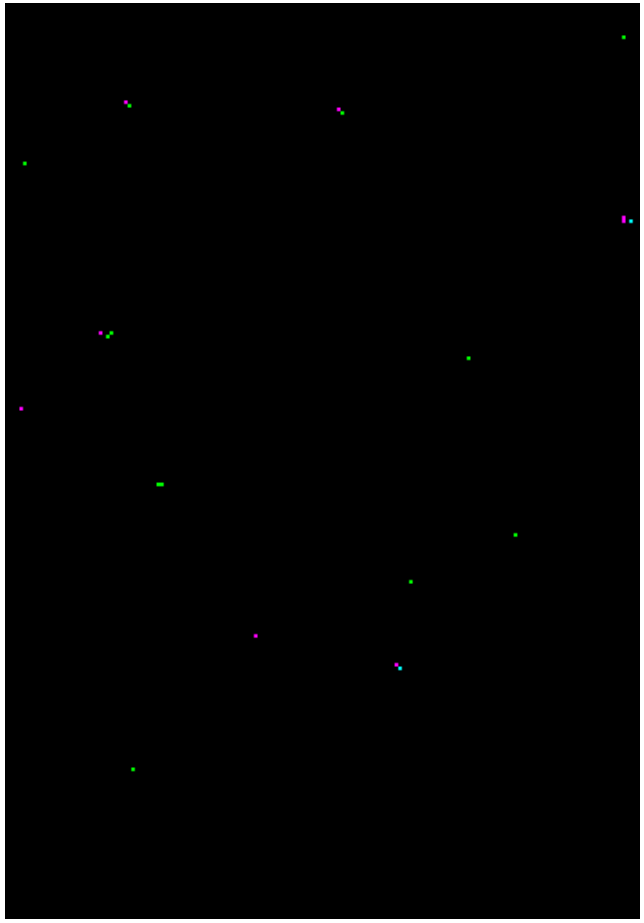

MRI at 253.19K

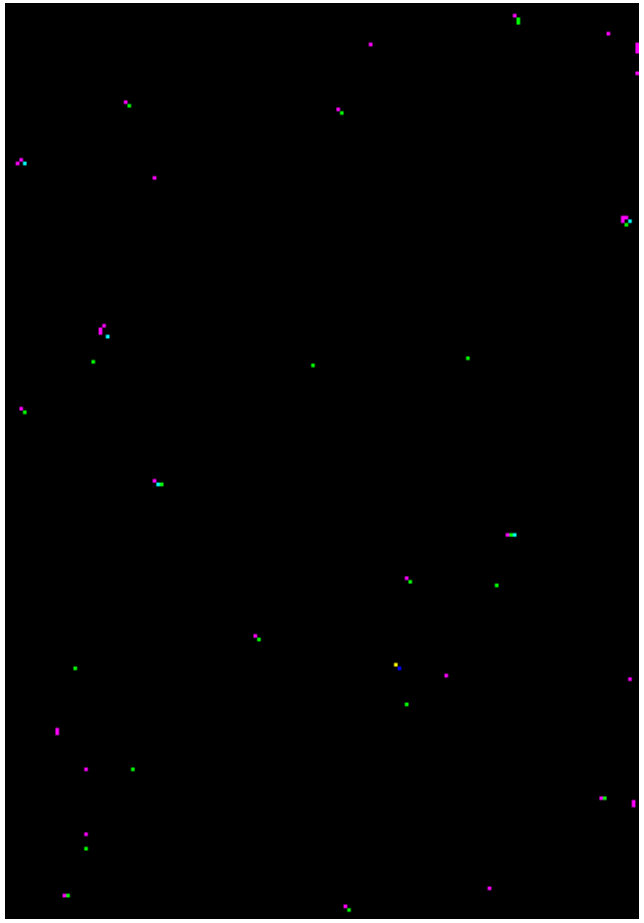

MRI at 259.84K

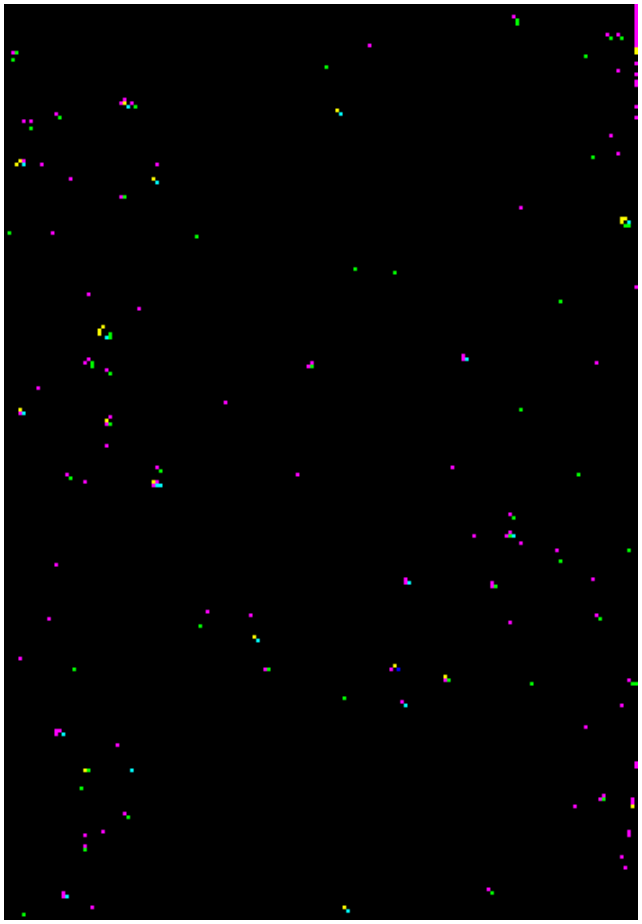

MRI at 270.94K

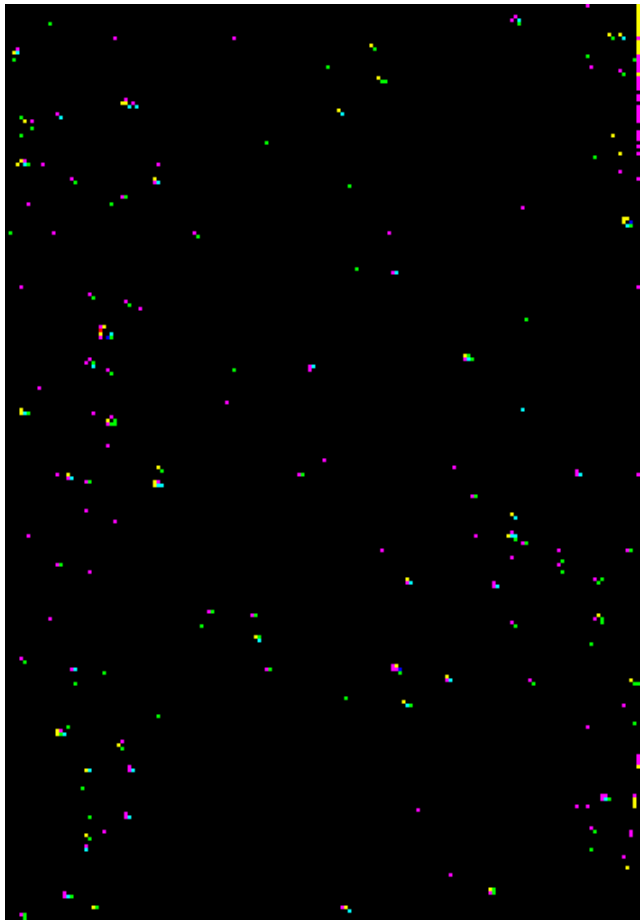

MRI at 281.31K

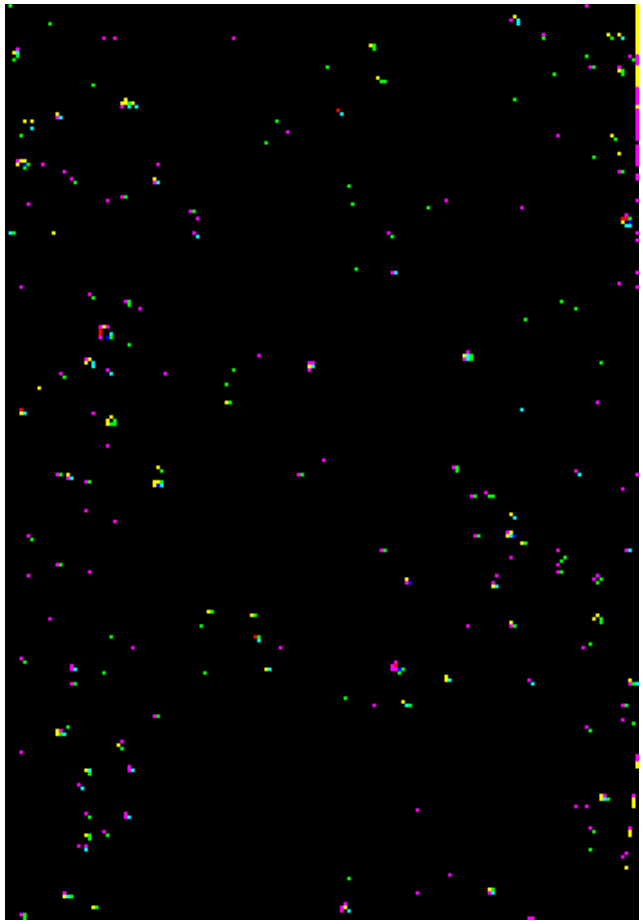

MRI at 289.73K

Figure 4.2.2-9 Spatial Distribution of Pixels which Fit the Temperature Model Poorly for the SLI

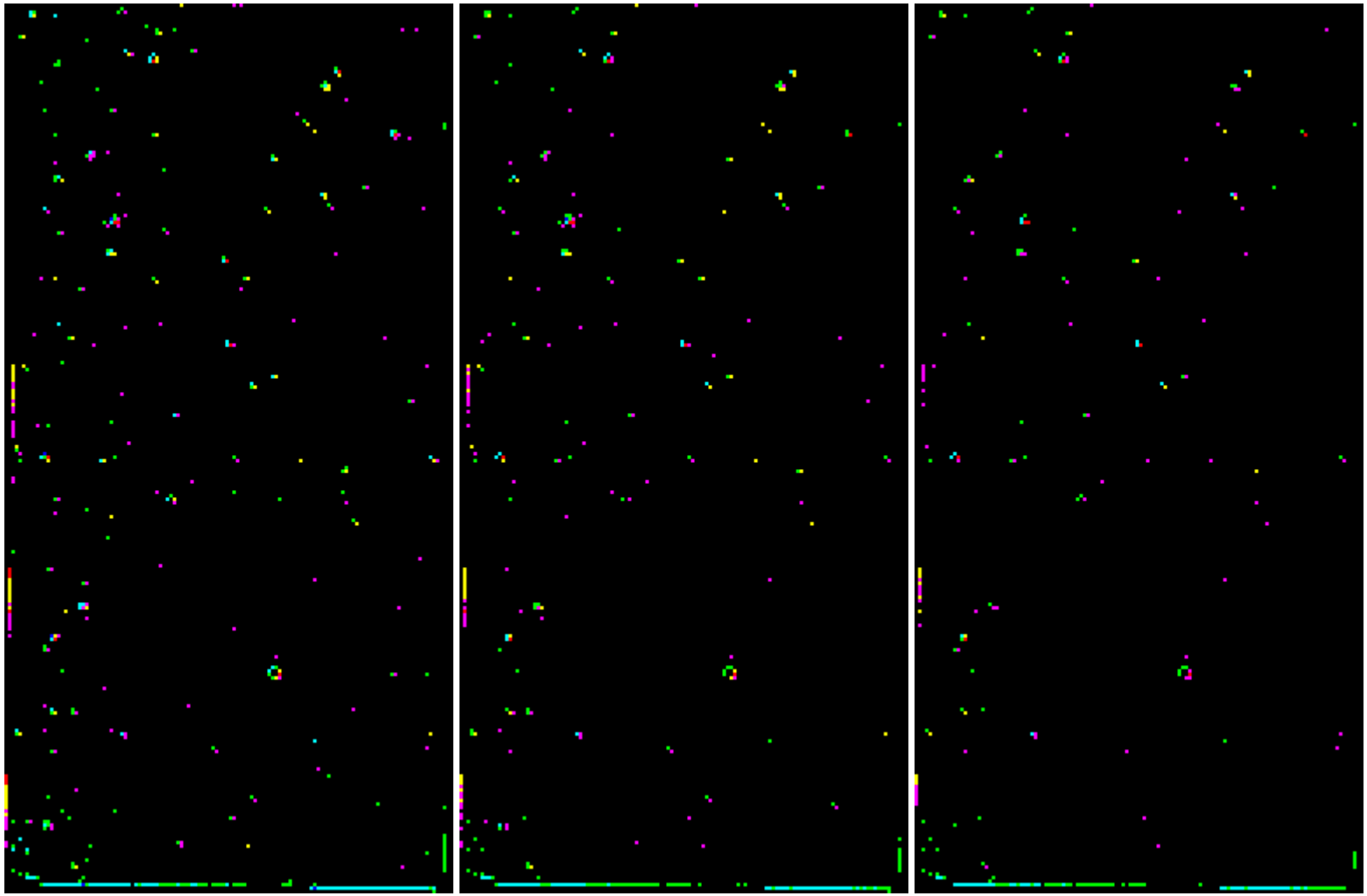

SLI at 171.57K SLI at 181.39K SLI at 187.43K

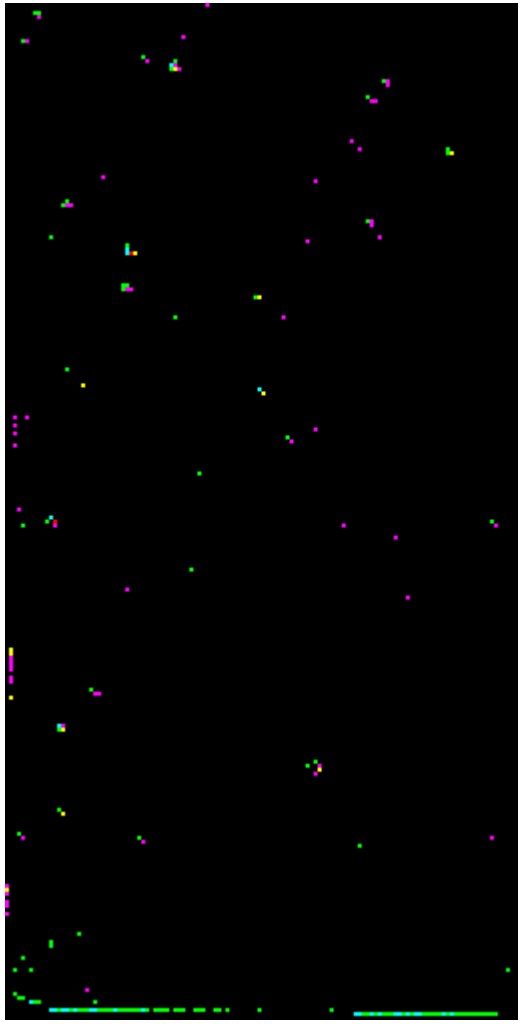

SLI at 195.66K

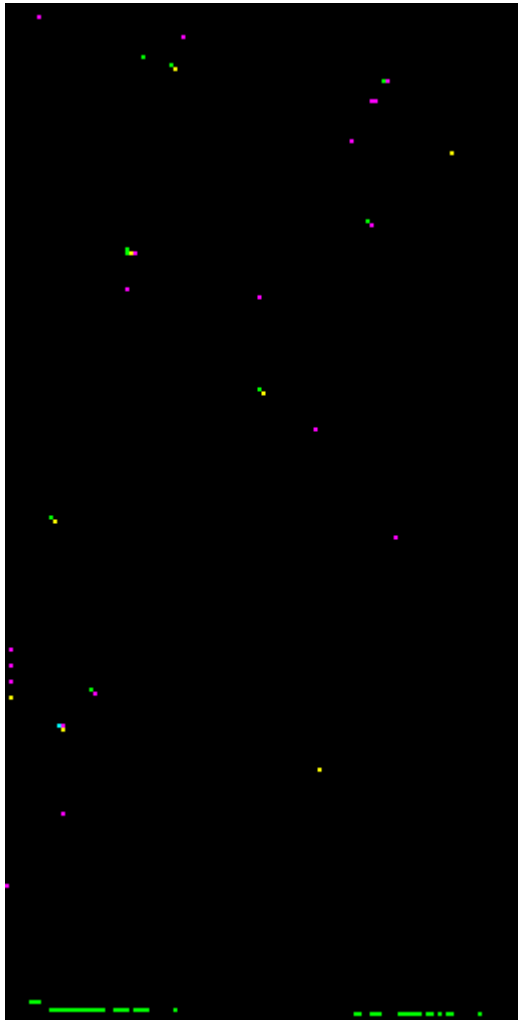

SLI at 207.13K

SLI at 211.65K

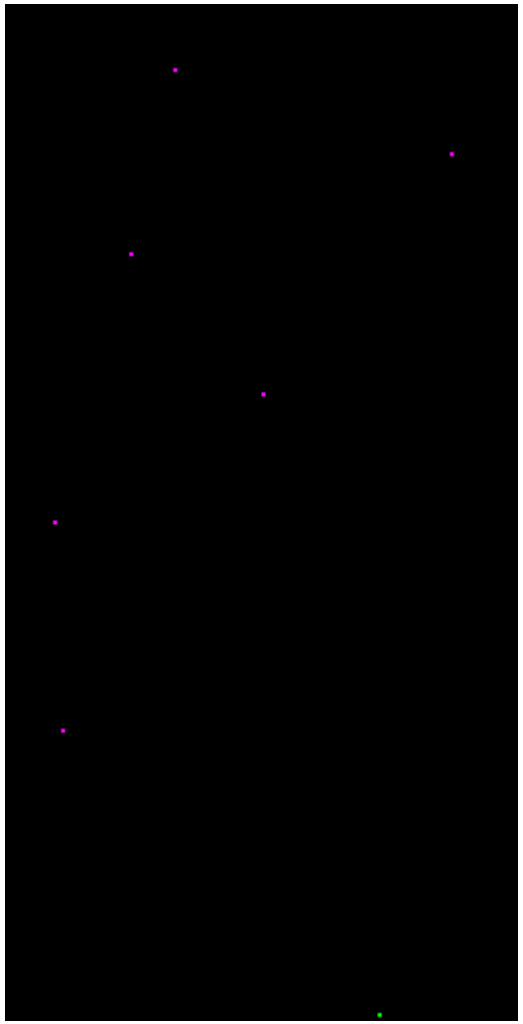

SLI at 222.14K

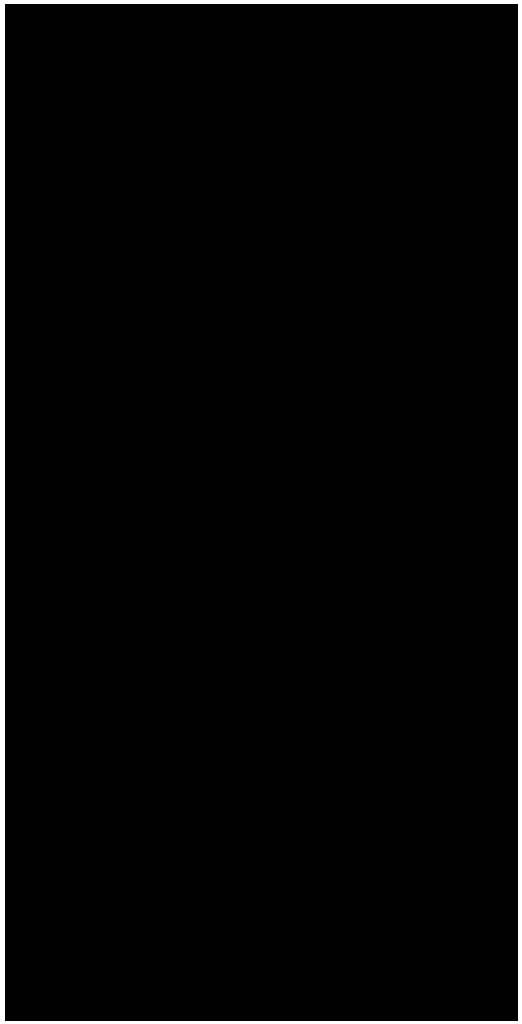

SLI at 229.46K

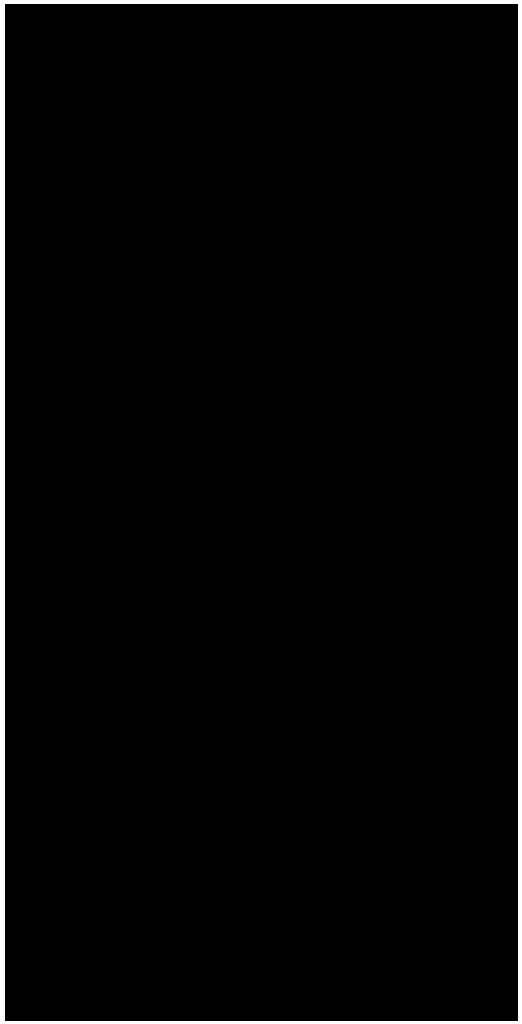

SLI at 236.72K

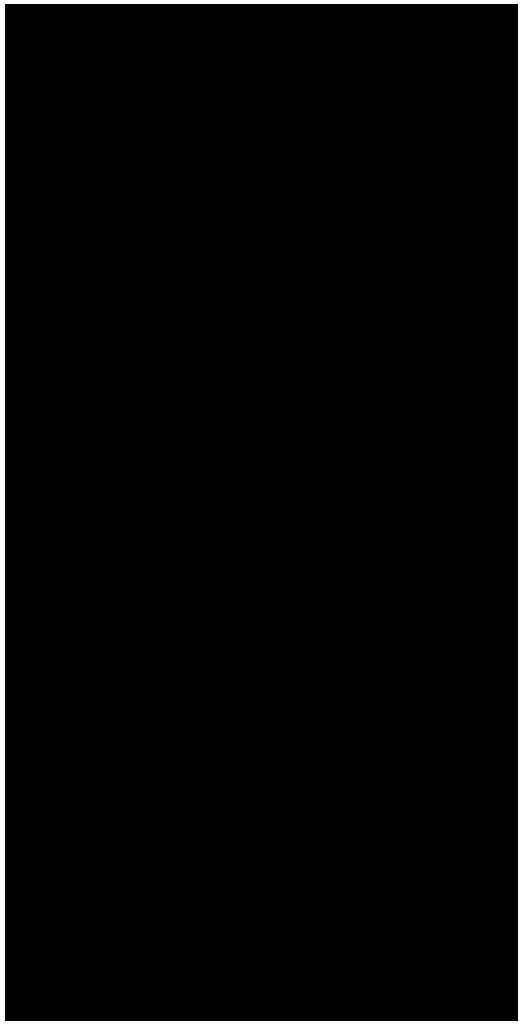

SLI at 244.28K

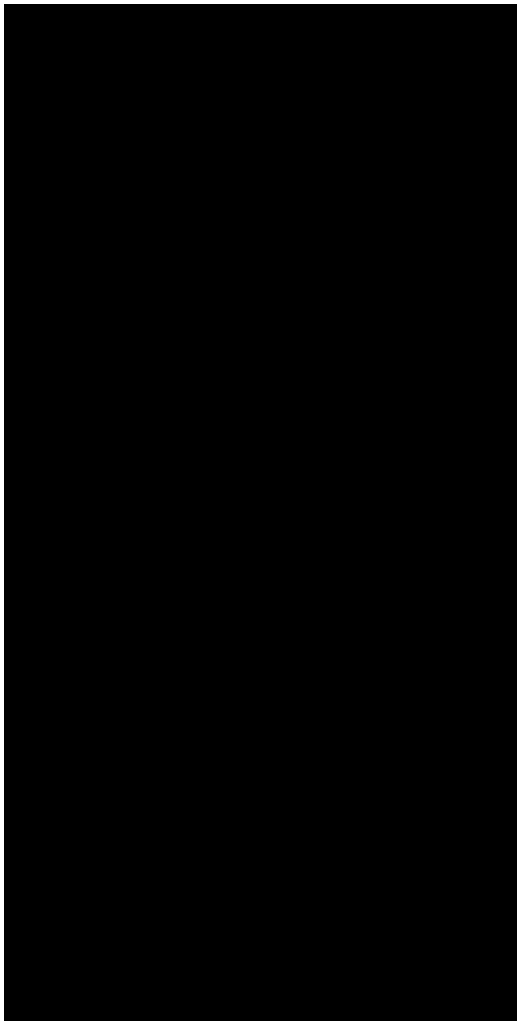

SLI at 253.25K

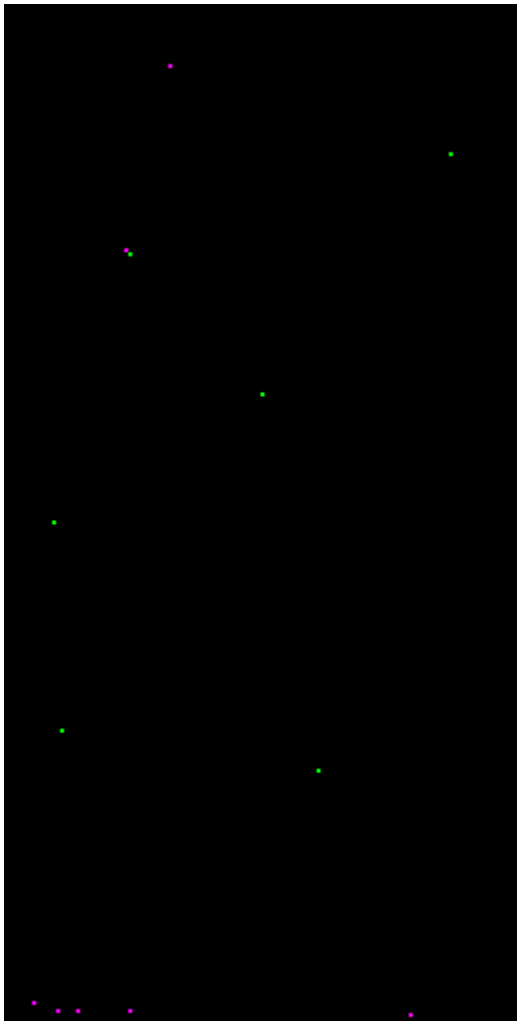

SLI at 259.84K

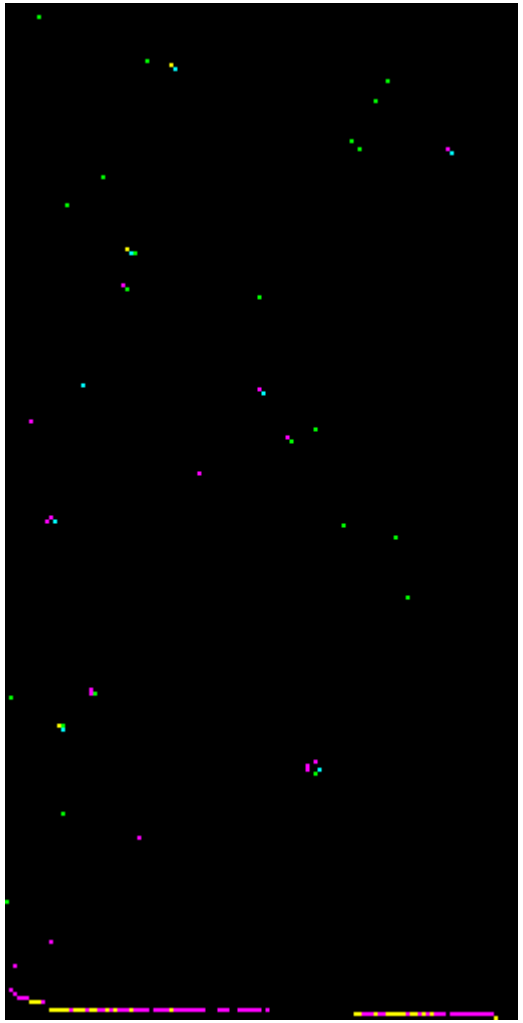

SLI at 270.94K

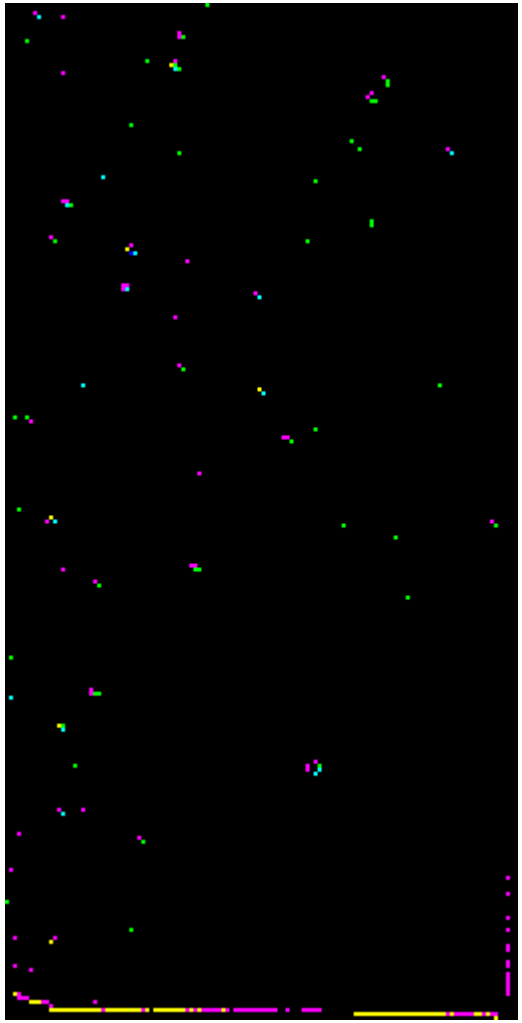

SLI at 281.31K

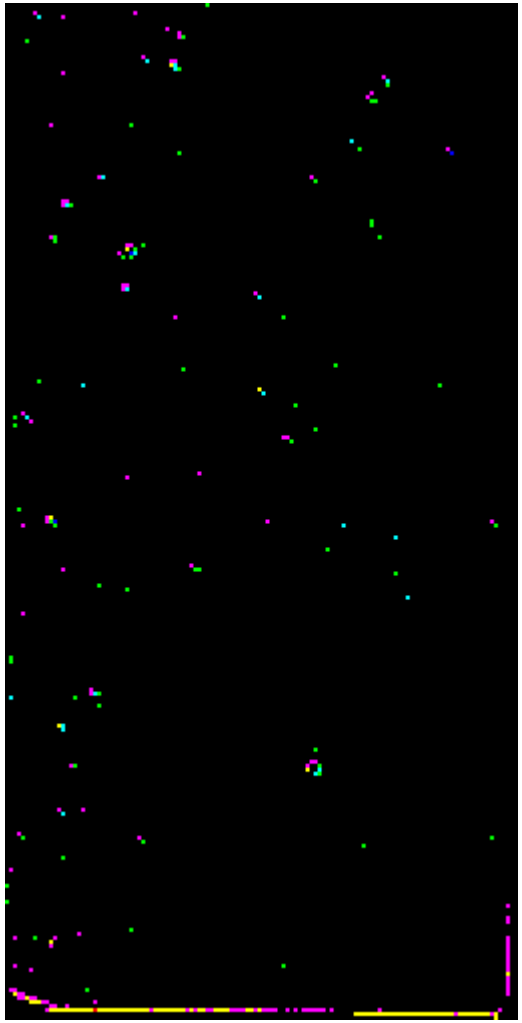

SLI at 289.73K

Conclusions from figures 4.2.2-7, 4.2.2-8, and 4.2.2-9 are as follows:

- Although many of the ill-fitting pixels are near the edges of the imagers, most of these pixels are distributed throughout the interior of each imager.
- These interior pixels remain anomalous over a wide range of temperature, i.e., the same pixels fit the temperature model poorly over the whole temperature range.
- Anomalous pixels occur in isolation or with anomalous neighbors with roughly the same frequency.

The persistence of the identity of the anomalous pixels suggests a familiar method of improving the model. These pixels could be assigned to different "bin" numbers, which have different temperature models. At this point we simply recognize this fact without actually developing such a model.

5.0. Flight and Ground Software Processing

The flight software both schedules the acquisition of images and processes the resulting data. Several types of image processing are possible, although during a descent all images are processed with hardware compressor.
The ground software (GSE) decompresses the images but not in an optimal way for photometric analysis.

5.1. Measurement scheduling

Images are taken according to cycle type, as described in Table 5.1-1. The target azimuths are referenced to the azimuth of the sun, and they can be achieved only when the Sun Sensor is locked on the sun.

Table 5.1-1

Image Scheduling During Descents

Cycle Type	No. HRIs	No. MRIs	No. SLIs	Target Azimuths
Image A	12	12	12	2º, 32º, 62º, 92º, 122º, 152º, 182º, 212º, 242º, 272º, 302º, 332º
Image B	12	12	12	17º, 47º, 77º, 107º, 137º, 167º, 197º, 227º, 257º, 287º, 317º, 247º
High Near Surface A	12	12	12	2º, 32º, 62º, 92º, 122º, 152º, 182º, 212º, 242º, 272º, 302º, 332º
High Near Surface B	12	12	12	17º, 47º, 77º, 107º, 137º, 167º, 197º, 227º, 257º, 287º, 317º, 247º
Calibration Cycle A	1	1	1	180º
Calibration Cycle B	1	1	1	180º

Medium Near Surface	1	1	1	Unconstrained
Low Near Surface	1	0	0	Unconstrained
Surface C	1	1	1	Unconstrained
Surface D	1	1	1	Unconstrained

Actual azimuths of the images are typically 1º - 2º less than the target azimuths.

5.2. Bad Pixel Maps

All descent images are processed by the flight software using the bad pixel maps. This is the first processing performed after the CCD readout. The bad pixel maps were intially created to remove hot pixels on the CCD. This removal is necessary to avoid poor performance of the hardware data compressor. A single hot pixel in a 16 x 16 block of pixels can produce a checkerboard pattern within that block on the decompressed image. As hot pixels develop during the mission modifications to the bad pixel map can be made to follow the changing spatial distribution of hot pixels.

After the instruments were built another obvious use for the bad pixel maps was discovered. The fiber optic bundles carrying the images to the CCD had imperfections (usually broken fibers) near the edges of the fields, and the CCD pixels which they were supposed to feed received little, if any, light. This problem also impacts the data compression, so these pixels have been mapped out. Two of the DISR instruments have exhibited small changes in this pattern of poorly fed pixels, probably due to cracking of additional fibers at the edges of the fields. This effect may also require updating of the bad pixel maps.

For the imagers bad pixel mapping really means bad pixel replacement. Each pixel identified as bad has its value replaced by the value of another pixel in the same row. A second method of accomplishing the same result is possible through the flat-fielding operation. A special flat fielding code specifies that the previous pixel's value should be used for the current pixel. Because the computer memory space for the bad pixel map is limited, much of the bad pixel mapping has been done using this flat-fielding function.

True bad pixel replacement is specified through EEPROM uploads. No modifications to the initial uploads have been made as of this writing. The locations of these uploads (slots) are shown in table 5.2-1.

Table 5.2-1

Bad Pixel Map Slots

Imager	EEPROM Slots
HRI	0x019 and 0x219
MRI	0x01A and 0x21A
SLI	0x01B – 0x029 and 0x21B and 0x229

The original bad pixel maps are given in tables 5.2-2, 5.2-3, and 5.2-4.

Table 5.2-2

DLI1 (HRI) Map in Imager Coordinates

Entry No.	Column	Replacement Column	First Row	Last Row
1	0	2	34	78
2	0	3	131	196
3	0	4	197	254
4	1	2	44	74
5	1	4	183	254
6	2	4	183	217
7	3	4	202	216

Table 5.2-3

DLI2 (MRI) Map in Imager Coordinates

Entry No.	Column	Replacement Column	First Row	Last Row
1	0	13	0	254
2	1	13	0	112
3	27	25	162	163
4	28	25	162	163
5	172	170	193	193

Table 5.2-4

SLI Map in Imager Coordinates

Entry No.	Column	Replacement Column	First Row	Last Row
1	87	86	73	254
2	0	122	0	7
3	0	3	34	253
4	1	3	93	253
5	2	3	151	253
6	76	74	62	63
7	77	74	62	63
8	1	122	**-1**	6
9	2	122	**-1**	5
10	3	122	0	4
11	4	122	0	4
12	5	122	0	4
13	6	122	0	3
14	7	122	0	3
15	8	122	0	3
16	9	122	0	2
17	10	122	0	1
18	11	122	0	1

19	12	122	0	1
20	13	122	0	1
21	14	122	0	1
22	15	122	0	1
23	16	122	0	1
24	17	122	0	1
25	18	122	0	1
26	19	122	0	1
27	20	122	0	1
28	21	122	0	1
29	22	122	0	1
30	23	122	0	1
31	24	122	0	1
32	25	122	0	1
33	26	122	0	1
34	27	122	0	1
35	28	122	0	1
36	29	122	0	1
37	30	122	0	1
38	31	122	0	1
39	32	122	0	1
40	33	122	0	1
41	34	122	0	1
42	35	122	0	1
43	36	122	0	1
44	37	122	0	1
45	38	122	0	1
46	39	122	0	1
47	40	122	0	1
48	41	122	0	1
49	42	122	0	1
50	43	122	0	1
51	44	122	0	1
52	45	122	0	1
53	46	122	0	1
54	47	122	0	1
55	48	122	0	1
56	49	122	0	1
57	50	122	0	1
58	51	122	0	1
59	52	122	0	1
60	53	122	0	1
61	54	122	0	1
62	55	122	0	1

63	56	122	0	1
64	57	122	0	1
65	58	122	0	1
66	59	122	0	1
67	60	122	0	1
68	61	122	0	1
69	62	122	0	1
70	63	122	0	1
71	64	122	0	1
72	65	122	0	1
73	66	122	0	1
74	67	122	0	1
75	68	122	0	1
76	69	122	0	1
77	70	122	0	1
78	71	122	0	1
79	72	122	0	1
80	73	122	0	1
81	74	122	0	1
82	75	122	0	1
83	76	122	0	1
84	77	122	0	1
85	78	122	0	1
86	79	122	0	1
87	80	122	0	1
88	81	122	0	1
89	82	122	0	1
90	83	122	0	1
91	84	122	0	1
92	85	122	0	1
93	86	122	0	1
94	87	122	0	0
95	88	122	0	0
96	89	122	0	0
97	90	122	0	0
98	91	122	0	0
99	92	122	0	0
100	93	122	0	0
101	94	122	0	0
102	95	122	0	0
103	96	122	0	0
104	97	122	0	0
105	98	122	0	0
106	99	122	0	0

107	100	122	0	0
108	101	122	0	0
109	102	122	0	0
110	103	122	0	0
111	104	122	0	0
121	105	122	0	0
123	106	122	0	0
124	107	122	0	0
125	108	122	0	0
126	109	122	0	0
127	110	122	0	0
128	111	122	0	0
129	112	122	0	0
130	113	122	0	0
131	114	122	0	0
132	115	122	0	0
133	116	122	0	0
134	117	122	0	0
135	118	122	0	0
136	119	122	0	0
137	120	122	0	0
138	121	122	0	0

The structure of the bad pixel map memory area is well described in the Experiment User's Manual.

We note that two entries for the SLI bad pixel map contain possibly inconsistent data. These are entries 8 and 9, which specify a first row of –1. The consequences of this must be investigated.

5.3. Square-root processing

The data compression hardware (DCS) is capable of processing only 8 bits/pixel data. The analog-to-digital converter for the CCD delivers 12 bits. A method of converting a 12-bit image to an 8-bit image was required.

We noted that the inherent accuracy in the imager data was limited by Shot noise, and that for high data numbers the standard deviation of a pixel value would be several DN. We therefore decided on a mapping of 12 to 8 bit data numbers which took advantange of this noise property. The 12-to-8 bit transfer function used is approximately a square root function. It differs from a square root because we also imposed the condition that signal-to-noise ratios in excess of 100 need not be retained. This condition permits a less dense mapping of 12 bit states into 8 bit states for high data numbers.

The final step was to make the transfer function adaptive in some cases. If an image has a narrow histogram, there is no point in assigning 8-bit codes to 12-bit DNs which do not

occur. Higher signal-to-noise ratios can be achieved by mapping fewer 12-bit DNs to the 256 8-bit codes. If the histogram is too broad, the original transfer function is used.

The non-adaptive transfer function is implemented as a lookup table in the flight software.

Table 5.3-1

Non-adaptive square root table in the flight software

12 bit DNs	8 bit DN	12 bit DNs	8 bit DN	12 bit DNs	8 bit DN	12 bit DNs	8 bit DN
0	0	170 - 173	64	480 - 485	128	1261 - 1282	192
1	1	174 - 177	65	486 - 491	129	1283 - 1305	193
2 - 3	2	178 - 181	66	492 - 497	130	1306 - 1328	194
4 - 5	3	182 - 185	67	498 - 503	131	1329 - 1352	195
6 - 7	4	186 - 189	68	504 - 509	132	1353 - 1376	196
8 - 9	5	190 - 193	69	510 - 515	133	1377 - 1400	197
10 - 11	6	194 - 197	70	516 - 522	134	1401 - 1425	198
12 - 13	7	198 - 201	71	523 - 529	135	1426 - 1450	199
14 - 15	8	202 - 205	72	530 - 536	136	1451 - 1476	200
16 - 17	9	206 - 209	73	537 - 543	137	1477 - 1503	201
18 - 19	10	210 - 213	74	544 - 550	138	1504 - 1530	202
20 - 21	11	214 - 217	75	551 - 557	139	1531 - 1558	203
22 - 23	12	218 - 221	76	558 - 565	140	1559 - 1586	204
24 - 25	13	222 - 225	77	566 - 573	141	1587 - 1615	205
26 - 27	14	226 - 229	78	574 - 581	142	1616 - 1644	206
28 - 29	15	230 - 233	79	582 - 589	143	1645 - 1674	207
30 - 31	16	234 - 237	80	590 - 597	144	1675 - 1704	208
32 - 33	17	238 - 241	81	598 - 605	145	1705 - 1735	209
34 - 35	18	242 - 245	82	606 - 614	146	1736 - 1767	210
36 - 37	19	246 - 249	83	615 - 623	147	1768 - 1799	211
38 - 39	20	250 - 253	84	624 - 632	148	1800 - 1832	212
40 - 41	21	254 - 257	85	633 - 641	149	1833 - 1866	213
42 - 43	22	258 - 262	86	642 - 650	150	1867 - 1900	214
44 - 45	23	263 - 267	87	651 - 660	151	1901 - 1935	215
46 - 47	24	268 - 272	88	661 - 670	152	1936 - 1971	216
48 - 49	25	273 - 277	89	671 - 680	153	1972 - 2007	217
50 - 51	26	278 - 282	90	681 - 690	154	2008 - 2044	218
52 - 53	27	283 - 287	91	691 - 700	155	2045 - 2082	219
54 - 56	28	288 - 292	92	701 - 711	156	2083 - 2121	220
57 - 59	29	293 - 297	93	712 - 722	157	2122 - 2161	221
60 - 62	30	298 - 302	94	723 - 733	158	2162 - 2201	222
63 - 65	31	303 - 307	95	734 - 744	159	2202 - 2242	223
66 - 68	32	308 - 312	96	745 - 756	160	2243 - 2284	224
69 - 71	33	313 - 317	97	757 - 768	161	2285 - 2327	225
72 - 74	34	318 - 322	98	769 - 780	162	2328 - 2371	226

75 - 77	35	323 - 327	99	781 - 792	163	2372 - 2415	227
78 - 80	36	328 - 332	100	793 - 805	164	2416 - 2460	228
81 - 83	37	333 - 337	101	806 - 818	165	2461 - 2506	229
84 - 86	38	338 - 342	102	819 - 831	166	2507 - 2553	230
87 - 89	39	343 - 347	103	832 - 844	167	2554 - 2601	231
90 - 92	40	348 - 352	104	845 - 858	168	2602 - 2650	232
93 - 95	41	353 - 357	105	859 - 872	169	2651 - 2700	233
96 - 98	42	358 - 362	106	873 - 886	170	2701 - 2751	234
99 - 101	43	363 - 367	107	887 - 900	171	2752 - 2803	235
102 - 104	44	368 - 372	108	901 - 915	172	2804 - 2856	236
105 - 107	45	373 - 377	109	916 - 930	173	2857 - 2910	237
108 - 110	46	378 - 382	110	931 - 945	174	2911 - 2965	238
111 - 113	47	383 - 387	111	946 - 961	175	2966 - 3021	239
114 - 116	48	388 - 392	112	962 - 977	176	3022 - 3079	240
117 - 119	49	393 - 397	113	978 - 993	177	3080 - 3138	241
120 - 122	50	398 - 402	114	994 - 1010	178	3139 - 3198	242
123 - 125	51	403 - 407	115	1011 - 1027	179	3199 - 3259	243
126 - 128	52	408 - 413	116	1028 - 1044	180	3260 - 3321	244
129 - 131	53	414 - 419	117	1045 - 1062	181	3322 - 3385	245
132 - 134	54	420 - 425	118	1063 - 1080	182	3386 - 3450	246
135 - 137	55	426 - 431	119	1081 - 1098	183	3451 - 3516	247
138 - 141	56	432 - 437	120	1099 - 1117	184	3517 - 3583	248
142 - 145	57	438 - 443	121	1118 - 1136	185	3584 - 3652	249
146 - 149	58	444 - 449	122	1137 - 1156	186	3653 - 3702	250
150 - 153	59	450 - 455	123	1157 - 1176	187	3703 - 3794	251
154 - 157	60	456 - 461	124	1177 - 1196	188	3795 - 3867	252
158 - 161	61	462 - 467	125	1197 - 1217	189	3868 - 3941	253
162 - 165	62	468 - 473	126	1218 - 1238	190	3942 - 4017	254
166 - 169	63	474 - 479	127	1239 - 1260	191	4018 - 4095	255

The algorithm for selecting an adaptive transfer function is complex. The reader is referred to the flight software (object O350_Image_Pic) and to the IDL program new_sqrt_sim.pro. Note that each adaptive transfer function is defined entirely by two values in the data set header, H_SQRT_MIN (=*img_min*) and H_SQRT_MAX(=*img_max*). The adaptive transfer function calculation is described by the following steps.

1. Construct a histogram of frequency of occurrence of each 12-bit DN
2. Determine the 12-bit DN values:
    a. Above which 95% of the image DN values lie (*img_min*)
    b. Below which 95% of the image DN values lie (*img_max*)
3. Redefine *img_min* and *img_max* by extending the range (= *img_max* – *img_min*) by 10%, i.e.,
    a. $img\_min_{new} = img\_min_{old} - 0.6(img\_max - img\_min)$
    b. $img\_max_{new} = img\_max_{old} + 0.6(img\_max - img\_min)$

4. Under the following conditions, use the original transfer function in table 5.3-1:
    a. (img_max_{new}-img_min_{new}) < 2000
    b. $img\_max_{new} = img\_min_{new}$
    c. All pixels have values ≤ img_min_{new}
5. The range of 12-bit DNs is then divided into three sections:
    a. Lower (DN < img_min_{new})
    b. Middle (img_min_{new} ≤ DN ≤ img_max_{new})
    c. Upper (DN > img_max_{new})
6. The number of new 8-bit codes in the middle section is set to the lesser of
    a. 10 times the number of codes in the middle section for the non-adaptive transfer function
    b. 128
    c. img_max_{new}-img_min_{new}+1
7. If the non-adaptive transfer function contained more 8-bit codes than the adaptive transfer function, the non-adaptive function is used throughout
8. The DN value boundaries of the three sections are calculated
    a. The largest DN in the lower section is the larger of
        i. img_min_{new}-1
        ii. 0
    b. The smallest DN in the middle section is img_min_{new}
    c. The largest DN in the middle section is img_max_{new}
    d. The smallest DN in the upper section is the lesser of
        i. img_max_{new}+1
        ii. 4095
9. Calculate the number of codes in the lower and upper sections
    a. Compute the fraction of all codes in the non-adaptive table for DN < *img_min*
    b. Set the number of codes in the lower section to this fraction times the number of codes left (256 – number of codes in the middle section)
    c. Set the number of codes in the upper section to the number of codes left (256 – number of codes in the middle section – number of codes in the lower section)
    d. Compute the number of codes in the non-adaptive table for DN > *img_max*
    e. If there are now more new codes in the upper section (from c) than there were old codes (from d):
        i. Reset the number of new codes in the upper section to be equal to the the old codes in the upper section
        ii. Reset the number of codes in the lower section to the number of codes left (256 – number of codes in the middle section – number of codes in the upper section
    f. Compute the number codes in the non-adaptive table for DN < *img_min*
    g. If there are now more new codes in the lower section than there were old codes (from f):
        i. Reset the number of new codes in the lower section to the number of old codes in the lower section

10. Generate the new codes in the lower section of the new table
    a. Compute the factor $f = \frac{new\_codes\_in\_lower\_section - 1}{old\_codes\_in\_lower\_section}$
    b. For all codes in the lower section $new\_code(DN) = f(old\_code(DN))$
11. Generate the new codes in the middle section of the new table
    a. If the number of new codes in the middle section is equal to the number of data numbers in the middle section, then assign one code to each data number, beginning with the first unused 8-bit code
    b. If the number of new codes in the middle section is less than the number of data numbers in the middle section:
        i. Compute the factor $f = \frac{new\_codes\_in\_lower\_section - 1}{old\_codes\_in\_lower\_section - 1}$
        ii. Let $start\_code$ be the first unused 8-bit code
        iii. For all codes in the middle section
        $new\_code(DN) = start\_code + 1 + f(old\_code(DN) - old\_code(img\_min))$
        iv. Reset the number of codes in the middle section to the total number of codes assigned so far less the number of codes in the lower section
12. Generate the new codes in the upper section of the new table
    a. Compute the number of codes left as 256 – number of codes already used
    b. If the number of codes left is greater than the number of codes in the upper section, reset the number of codes in the upper section to be the number of codes left
    c. Compute the factor *f* to be the lesser of:
        i. $\frac{new\_codes\_in\_upper\_section - 1}{255 - old\_codes(img\_max + 1)}$
        ii. 1.0
    d. Let $start\_code$ be the first unused 8-bit code
    e. For all codes in the upper section set $new\_code(DN)$ to the lesser of
        i. $start\_code + 1 + f(old\_code(DN) - old\_code(img\_max + 1))$
        ii. 255
13. Return to the middle section to fill in gaps, because the scheme of assigning codes above may skip some new code values
    a. Find the first DN values in the middle region which have code values larger than the code values for the previous DN, i.e., where *new_code*(DN) > *new_code*(DN-1)
    b. Reset the *new_codes* between the successive DN values found in a. using linear interpolation, i.e.,
    $$new\_code(DN) = \frac{new\_code(DN_2) - new\_code(DN_1)}{DN_2 - DN_1}(DN - DN_1) + new\_code(DN_1)$$

5.4. Flat-fielding

During the DISR development phase when the first imaging system contained both a fiber optic conduit and processing by the hardware data compressor, we noticed a serious problem. The fiber optic conduit introduced a distinct high spatial frequency pattern into the images consisting of the hexagonal "chicken wire" pattern as well as many poorly illuminated pixels fed by fibers with low transmission. Figure X, which shows images from the three imagers of the inside of 20-inch integrating sphere, illustrates the problem. For low contrast scenes the data compressor tended to preserve this fiber optic pattern much better than many features in the scene. The only cure available in the original design was to reduce the compression ratio. With the low contrast scenes expected on Titan, compression ratios of only 2:1 would be required.

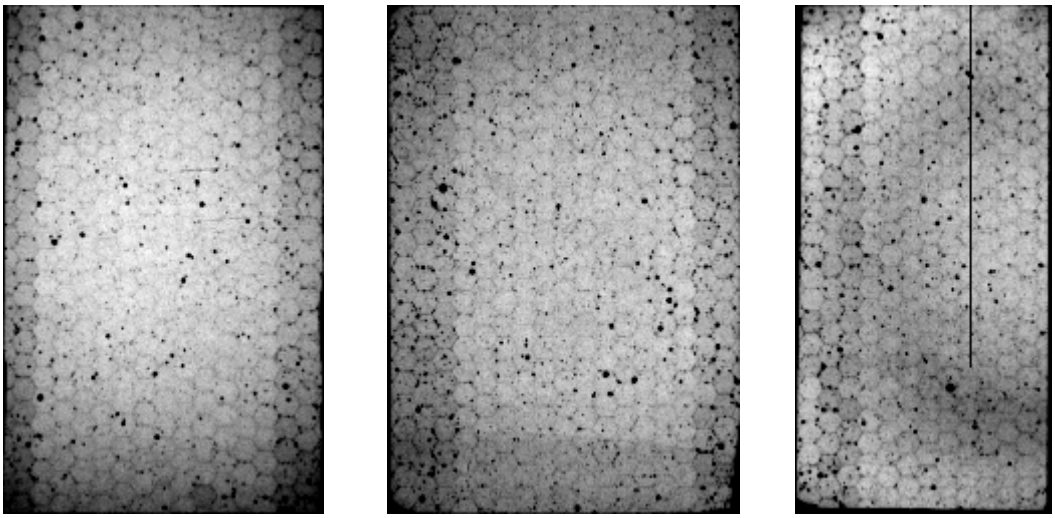

HRI MRI SLI

Fig. 5.4-1 Images of the 20-inch integrating sphere wall taken with the DISR flight model imagers. The contrast has been enhanced greatly to show the details of the flat field defects.

The design of the DISR electronics was modified to include EEPROM containing an 8-bit number for each imager pixel. This number describes how to modify that pixel's DN to provide a flat field correction. The flat field algorithm is implemented in the flight software as follows.

5.4.1. Flat Field Table

For each pixel in the three imagers a corresponding 8-bit code shall be stored in EEPROM. These codes shall be pre-loaded before instrument delivery. The flight software shall be capable of changing any of these codes by command upload.

5.4.2. Flat Field Lookup Table

A translation table containing 256 16-bit entries shall be defined in PROM. It shall be copied to data RAM during initialization. The flight software shall be capable of changing any of these table entries by command upload through the normal EEPROM upload mechanism.

Two table entries have special significance. A value of zero shall direct the flight software to make no alteration of the raw pixel value during the flat field correction operation. A value of 1 shall direct the flight software to replace the current pixel being corrected with the corrected value of the previous processed pixel.

The remaining 254 table entries shall contain values representing 1024/(pixel transmission) according the following formula:

$$Entry(i) = \frac{1024}{\left(\frac{i-2}{253} + 0.2\right)}$$

where *Entry* is the table value and i is the table index (from 0 through 255). For i = 2, the table entry shall be 5120 and for i = 255 the table entry shall be 853. The table entries shall be evaluated using floating point arithmetic and rounded to the nearest integer.

Figure X shows the relationship between flat field table entry and pixel correction factor, defined by

$$DN_{corr} = \frac{DN_{original}}{correction\_factor}.$$

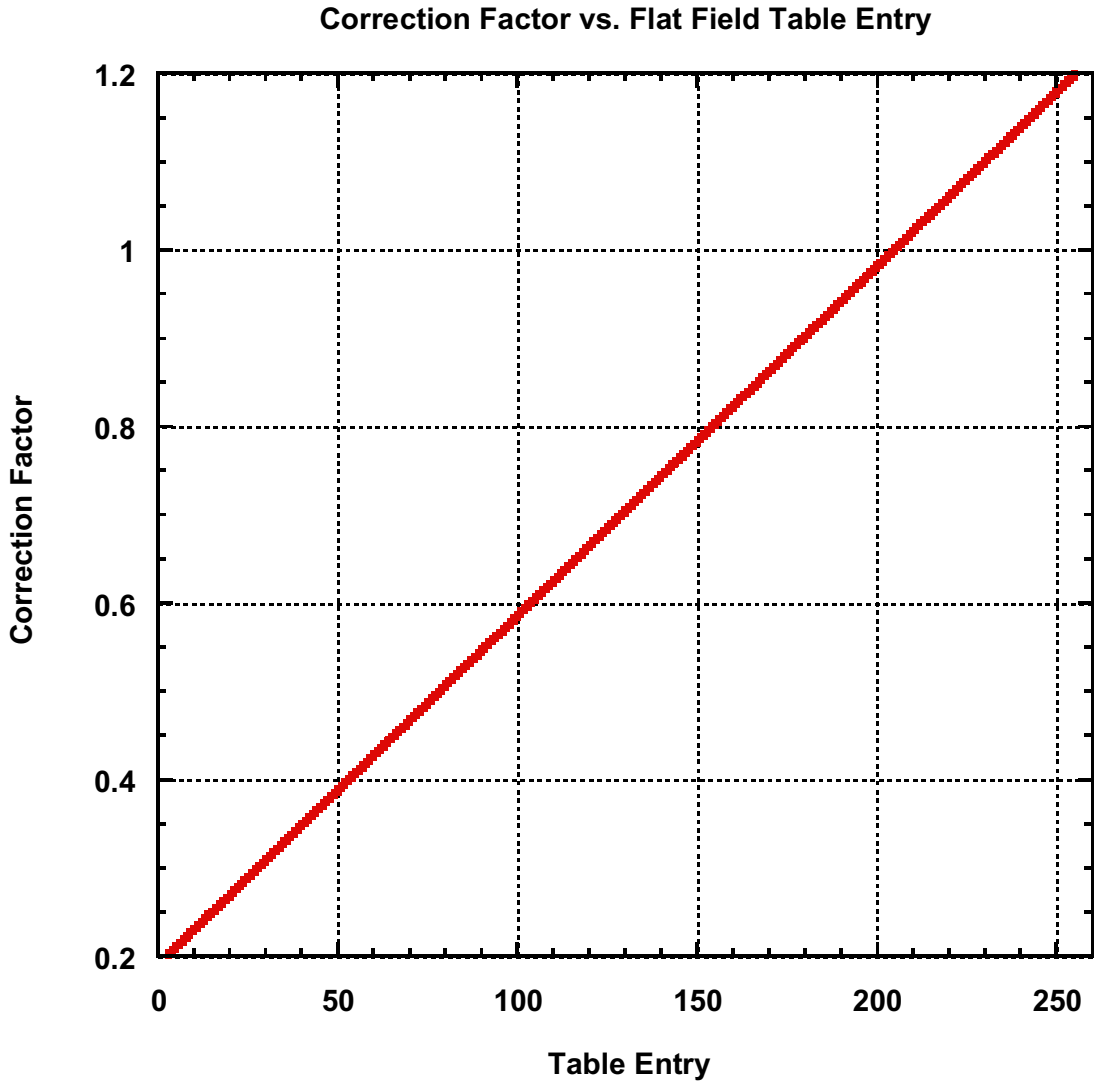

Figure 5.4.2-1 The relationship between correction factor and the flat field table entry for tabular values > 1.

5.4.3. Flat Field Correction Operation

The entire flat field correction operation shall be optional, dependent on the setting of a flag in data RAM. By default the flat field correction shall be enabled. It may be disabled by resetting this flag through a memory upload.

This operation shall be done prior to bad pixel replacement.

For each pixel in the imaging area of the CCD the corresponding flat field table entry shall be examined. If the value of this entry is 0, the pixel shall be left unchanged. If the value of this entry is 1, the pixel value shall be replaced by the previously corrected pixel value. If the value of this entry is more than 1, the corresponding value in the flat field

lookup table shall be retrieved. The raw pixel value shall first have a constant subtracted from it, then be multiplied by the flat field lookup table entry, and then shifted by 10 bits (to divide the result by 1024). If the result is larger than 4095, the result shall be set to 4095. The resulting value shall then replace the raw pixel value.

5.4.4. Method of Determining the Flat Field Table

20 sets of exposures of the 20-inch integrating sphere wall were made with each of the three imagers July 20, 1996. The test log for these data sets is flatfield_imagers_20July96.1. It is currently located on the computer cassini in directory /disr3_cal/20Jul96/Log.

The brightness of a given pixel is taken to be proportional to (the bright DN – the dark DN) – the electronic shutter correction. The electronic shutter correction is caused by the charge picked up as the image is shifted from the image zone to the memory zone. This charge is different when the chip is illuminated from when it is not. Therefore, two additional exposures are taken with zero exposure time, with the chip illuminated and not illuminated, to derive the complete auto-exposure correction. The corrected DN for each pixel is

$$DN_{corr} = \left(DN_{bright} - DN_{dark}\right) - \left(DN_{bright-0} - DN_{dark-0}\right)$$

The data sets, from the test log, used to derive the flat field correction are given in table 5.4.4.

Table 5.4.4-1a

Data Sets used to derive the High Resolution Imager flat field correction

No.	Bright	Dark
1	V_00054I.MMX_01:42:34_7586_Img	V_00048I.MMX_01:40:17_5079_Img
2	V_00060I.MMX_01:44:21_7577_Img	V_00066I.MMX_01:46:38_7584_Img
3	V_00078I.MMX_01:52:51_2573_Img	V_00072I.MMX_01:50:33_2585_Img
4	V_00084I.MMX_01:54:38_2584_Img	V_00090I.MMX_01:56:55_0073_Img
5	V_00102I.MMX_02:03:49_0071_Img	V_00096I.MMX_02:01:31_2586_Img
6	V_00108I.MMX_02:05:36_0096_Img	V_00114I.MMX_02:07:52_7570_Img
7	V_00126I.MMX_02:12:45_0086_Img	V_00120I.MMX_02:10:27_5077_Img
8	V_00132I.MMX_02:14:32_0091_Img	V_00138I.MMX_02:16:48_2585_Img
9	V_00150I.MMX_02:22:44_5069_Img	V_00144I.MMX_02:20:26_7584_Img
10	V_00156I.MMX_02:24:31_5080_Img	V_00162I.MMX_02:26:48_2589_Img
11	V_00174I.MMX_02:31:40_5083_Img	V_00168I.MMX_02:29:22_7574_Img
12	V_00180I.MMX_02:33:27_5074_Img	V_00186I.MMX_02:35:44_2582_Img
13	V_00198I.MMX_02:42:44_2581_Img	V_00192I.MMX_02:40:26_7575_Img
14	V_00204I.MMX_02:44:31_2572_Img	V_00210I.MMX_02:46:48_2579_Img
15	V_00222I.MMX_02:52:28_0084_Img	V_00216I.MMX_02:50:10_2582_Img
16	V_00228I.MMX_02:54:15_0082_Img	V_00234I.MMX_02:56:32_0083_Img
17	V_00246I.MMX_03:02:28_2575_Img	V_00240I.MMX_03:00:10_5088_Img
18	V_00252I.MMX_03:04:15_2584_Img	V_00258I.MMX_03:06:31_7573_Img
19	V_00270I.MMX_03:11:18_7589_Img	V_00264I.MMX_03:09:01_2580_Img
20	V_00276I.MMX_03:13:05_7602_Img	V_00282I.MMX_03:15:22_5089_Img

Table 5.4.4-1b

Data Sets used to derive the High Resolution Imager electronic shutter correction

No.	Bright – 0 Exposure	Dark – 0 Exposure
1	V_00059I.MMX_01:43:31_5081_Img	V_00053I.MMX_01:41:14_2573_Img
2	V_00065I.MMX_01:45:18_5070_Img	V_00071I.MMX_01:47:35_5079_Img
3	V_00083I.MMX_01:53:48_0103_Img	V_00077I.MMX_01:51:30_0094_Img
4	V_00089I.MMX_01:55:35_0079_Img	V_00095I.MMX_01:57:51_7587_Img
5	V_00107I.MMX_02:04:45_7587_Img	V_00101I.MMX_02:02:28_0094_Img
6	V_00113I.MMX_02:06:32_7577_Img	V_00119I.MMX_02:08:49_5087_Img
7	V_00131I.MMX_02:13:41_7581_Img	V_00125I.MMX_02:11:24_2587_Img
8	V_00137I.MMX_02:15:28_7572_Img	V_00143I.MMX_02:17:45_0079_Img
9	V_00155I.MMX_02:23:41_2584_Img	V_00149I.MMX_02:21:23_5077_Img
10	V_00161I.MMX_02:25:28_2575_Img	V_00167I.MMX_02:27:45_0082_Img
11	V_00179I.MMX_02:32:37_2578_Img	V_00173I.MMX_02:30:19_5070_Img
12	V_00185I.MMX_02:34:24_2569_Img	V_00191I.MMX_02:36:41_0077_Img
13	V_00203I.MMX_02:43:41_0076_Img	V_00197I.MMX_02:41:23_5069_Img
14	V_00209I.MMX_02:45:28_0100_Img	V_00215I.MMX_02:47:45_0074_Img
15	V_00227I.MMX_02:53:24_7586_Img	V_00221I.MMX_02:51:07_0077_Img
16	V_00233I.MMX_02:55:11_7576_Img	V_00239I.MMX_02:57:28_7584_Img
17	V_00251I.MMX_03:03:25_0089_Img	V_00245I.MMX_03:01:07_2582_Img
18	V_00257I.MMX_03:05:12_0092_Img	V_00263I.MMX_03:07:28_5089_Img
19	V_00275I.MMX_03:12:15_5084_Img	V_00269I.MMX_03:09:58_0088_Img
20	V_00281I.MMX_03:14:02_5075_Img	V_00287I.MMX_03:16:19_2584_Img

Table 5.4.4-2a

Data Sets used to derive the Medium Resolution Imager flat field correction

No.	Bright	Dark
1	V_00056I.MMX_01:43:11_2582_Img	V_00050I.MMX_01:40:54_0089_Img
2	V_00062I.MMX_01:44:58_2573_Img	V_00068I.MMX_01:47:15_2581_Img
3	V_00080I.MMX_01:53:27_7570_Img	V_00074I.MMX_01:51:09_7581_Img
4	V_00086I.MMX_01:55:14_7581_Img	V_00092I.MMX_01:57:31_5089_Img
5	V_00104I.MMX_02:04:25_5089_Img	V_00098I.MMX_02:02:07_7582_Img
6	V_00110I.MMX_02:06:12_5079_Img	V_00116I.MMX_02:08:29_2588_Img
7	V_00128I.MMX_02:13:21_5084_Img	V_00122I.MMX_02:11:04_0087_Img
8	V_00134I.MMX_02:15:08_5074_Img	V_00140I.MMX_02:17:24_7581_Img
9	V_00152I.MMX_02:23:21_0086_Img	V_00146I.MMX_02:21:03_2579_Img
10	V_00158I.MMX_02:25:08_0090_Img	V_00164I.MMX_02:27:24_7584_Img
11	V_00176I.MMX_02:32:17_0081_Img	V_00170I.MMX_02:29:59_2572_Img
12	V_00182I.MMX_02:34:04_0083_Img	V_00188I.MMX_02:36:20_7580_Img
13	V_00200I.MMX_02:43:20_7579_Img	V_00194I.MMX_02:41:03_2571_Img
14	V_00206I.MMX_02:45:07_7588_Img	V_00212I.MMX_02:47:24_7575_Img
15	V_00224I.MMX_02:53:04_5088_Img	V_00218I.MMX_02:50:46_7580_Img
16	V_00230I.MMX_02:54:51_5079_Img	V_00236I.MMX_02:57:08_5086_Img
17	V_00248I.MMX_03:03:04_7570_Img	V_00242I.MMX_03:00:47_0085_Img
18	V_00254I.MMX_03:04:51_7581_Img	V_00260I.MMX_03:07:08_2600_Img
19	V_00272I.MMX_03:11:55_2586_Img	V_00266I.MMX_03:09:37_7576_Img
20	V_00278I.MMX_03:13:42_2577_Img	V_00284I.MMX_03:15:59_0086_Img

Table 5.4.4-2b

Data Sets used to derive the Medium Resolution Imager electronic shutter correction

No.	Bright – 0 Exposure	Dark – 0 Exposure
1	V_00057I.MMX_01:43:31_5081_Img	V_00051I.MMX_01:41:14_2573_Img
2	V_00063I.MMX_01:45:18_5070_Img	V_00069I.MMX_01:47:35_5079_Img
3	V_00081I.MMX_01:53:48_0103_Img	V_00075I.MMX_01:51:30_0094_Img
4	V_00087I.MMX_01:55:35_0079_Img	V_00093I.MMX_01:57:51_7587_Img
5	V_00105I.MMX_02:04:45_7587_Img	V_00099I.MMX_02:02:28_0094_Img
6	V_00111I.MMX_02:06:32_7577_Img	V_00117I.MMX_02:08:49_5087_Img
7	V_00129I.MMX_02:13:41_7581_Img	V_00123I.MMX_02:11:24_2587_Img
8	V_00135I.MMX_02:15:28_7572_Img	V_00141I.MMX_02:17:45_0079_Img
9	V_00153I.MMX_02:23:41_2584_Img	V_00147I.MMX_02:21:23_5077_Img
10	V_00159I.MMX_02:25:28_2575_Img	V_00165I.MMX_02:27:45_0082_Img
11	V_00177I.MMX_02:32:37_2578_Img	V_00171I.MMX_02:30:19_5070_Img
12	V_00183I.MMX_02:34:24_2569_Img	V_00189I.MMX_02:36:41_0077_Img
13	V_00201I.MMX_02:43:41_0076_Img	V_00195I.MMX_02:41:23_5069_Img
14	V_00207I.MMX_02:45:28_0100_Img	V_00213I.MMX_02:47:45_0074_Img
15	V_00225I.MMX_02:53:24_7586_Img	V_00219I.MMX_02:51:07_0077_Img
16	V_00231I.MMX_02:55:11_7576_Img	V_00237I.MMX_02:57:28_7584_Img
17	V_00249I.MMX_03:03:25_0089_Img	V_00243I.MMX_03:01:07_2582_Img
18	V_00255I.MMX_03:05:12_0092_Img	V_00261I.MMX_03:07:28_5089_Img
19	V_00273I.MMX_03:12:15_5084_Img	V_00267I.MMX_03:09:58_0088_Img
20	V_00279I.MMX_03:14:02_5075_Img	V_00285I.MMX_03:16:19_2584_Img

Table 5.4.4-3a

Data Sets used to derive the Side-Looking Imager flat field correction

No.	Bright	Dark
1	V_00058I.MMX_01:43:31_5081_Img	V_00052I.MMX_01:41:14_2573_Img
2	V_00064I.MMX_01:45:18_5070_Img	V_00070I.MMX_01:47:35_5079_Img
3	V_00082I.MMX_01:53:48_0103_Img	V_00076I.MMX_01:51:30_0094_Img
4	V_00088I.MMX_01:55:35_0079_Img	V_00094I.MMX_01:57:51_7587_Img
5	V_00106I.MMX_02:04:45_7587_Img	V_00100I.MMX_02:02:28_0094_Img
6	V_00112I.MMX_02:06:32_7577_Img	V_00118I.MMX_02:08:49_5087_Img
7	V_00130I.MMX_02:13:41_7581_Img	V_00124I.MMX_02:11:24_2587_Img
8	V_00136I.MMX_02:15:28_7572_Img	V_00142I.MMX_02:17:45_0079_Img
9	V_00154I.MMX_02:23:41_2584_Img	V_00148I.MMX_02:21:23_5077_Img
10	V_00160I.MMX_02:25:28_2575_Img	V_00166I.MMX_02:27:45_0082_Img
11	V_00178I.MMX_02:32:37_2578_Img	V_00172I.MMX_02:30:19_5070_Img
12	V_00184I.MMX_02:34:24_2569_Img	V_00190I.MMX_02:36:41_0077_Img
13	V_00202I.MMX_02:43:41_0076_Img	V_00196I.MMX_02:41:23_5069_Img
14	V_00208I.MMX_02:45:28_0100_Img	V_00214I.MMX_02:47:45_0074_Img
15	V_00226I.MMX_02:53:24_7586_Img	V_00220I.MMX_02:51:07_0077_Img
16	V_00232I.MMX_02:55:11_7576_Img	V_00238I.MMX_02:57:28_7584_Img
17	V_00250I.MMX_03:03:25_0089_Img	V_00244I.MMX_03:01:07_2582_Img
18	V_00256I.MMX_03:05:12_0092_Img	V_00262I.MMX_03:07:28_5089_Img
19	V_00274I.MMX_03:12:15_5084_Img	V_00268I.MMX_03:09:58_0088_Img
20	V_00280I.MMX_03:14:02_5075_Img	V_00286I.MMX_03:16:19_2584_Img

Table 5.4.4-3b

Data Sets used to derive the Side-Looking Imager electronic shutter correction

No.	Bright – 0 Exposure	Dark – 0 Exposure
1	V_00058I.MMX_01:43:31_5081_Img	V_00052I.MMX_01:41:14_2573_Img
2	V_00064I.MMX_01:45:18_5070_Img	V_00070I.MMX_01:47:35_5079_Img
3	V_00082I.MMX_01:53:48_0103_Img	V_00076I.MMX_01:51:30_0094_Img
4	V_00088I.MMX_01:55:35_0079_Img	V_00094I.MMX_01:57:51_7587_Img
5	V_00106I.MMX_02:04:45_7587_Img	V_00100I.MMX_02:02:28_0094_Img
6	V_00112I.MMX_02:06:32_7577_Img	V_00118I.MMX_02:08:49_5087_Img
7	V_00130I.MMX_02:13:41_7581_Img	V_00124I.MMX_02:11:24_2587_Img
8	V_00136I.MMX_02:15:28_7572_Img	V_00142I.MMX_02:17:45_0079_Img
9	V_00154I.MMX_02:23:41_2584_Img	V_00148I.MMX_02:21:23_5077_Img
10	V_00160I.MMX_02:25:28_2575_Img	V_00166I.MMX_02:27:45_0082_Img
11	V_00178I.MMX_02:32:37_2578_Img	V_00172I.MMX_02:30:19_5070_Img
12	V_00184I.MMX_02:34:24_2569_Img	V_00190I.MMX_02:36:41_0077_Img
13	V_00202I.MMX_02:43:41_0076_Img	V_00196I.MMX_02:41:23_5069_Img
14	V_00208I.MMX_02:45:28_0100_Img	V_00214I.MMX_02:47:45_0074_Img
15	V_00226I.MMX_02:53:24_7586_Img	V_00220I.MMX_02:51:07_0077_Img
16	V_00232I.MMX_02:55:11_7576_Img	V_00238I.MMX_02:57:28_7584_Img
17	V_00250I.MMX_03:03:25_0089_Img	V_00244I.MMX_03:01:07_2582_Img
18	V_00256I.MMX_03:05:12_0092_Img	V_00262I.MMX_03:07:28_5089_Img
19	V_00274I.MMX_03:12:15_5084_Img	V_00268I.MMX_03:09:58_0088_Img
20	V_00280I.MMX_03:14:02_5075_Img	V_00286I.MMX_03:16:19_2584_Img

The actual numbers in the flat field tables for the DISR flight model are contained in Appendix B.

The flat field correction is assumed to be temperature independent, although this is not exactly the case. The calibration data used to derive the flat field was taken with focal plane temperatures in the range 240 – 251K.

Figures 5.4-1, 5.4-2, and 5.4-3 show original image, the image with bad-pixel replacement, and the image with both bad pixel replacement and flat field processing for each of the three imagers. The three processing steps are all shown with the same highly stretched contrast.

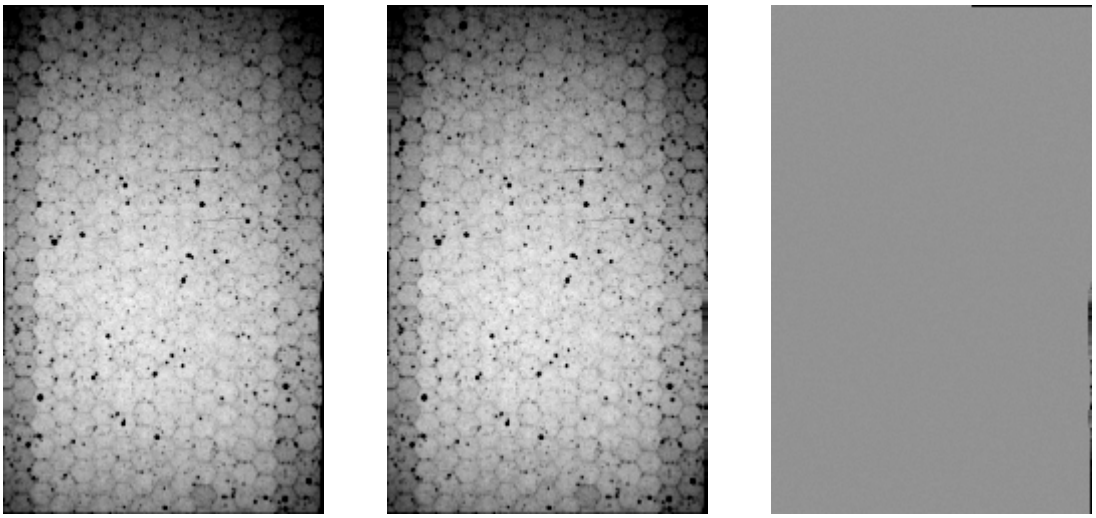

HRI original HRI bad pixel replacement HRI full processing

Figure 5.4-1 Bad pixel replacement and flat-field processing for the High Resolution Imager

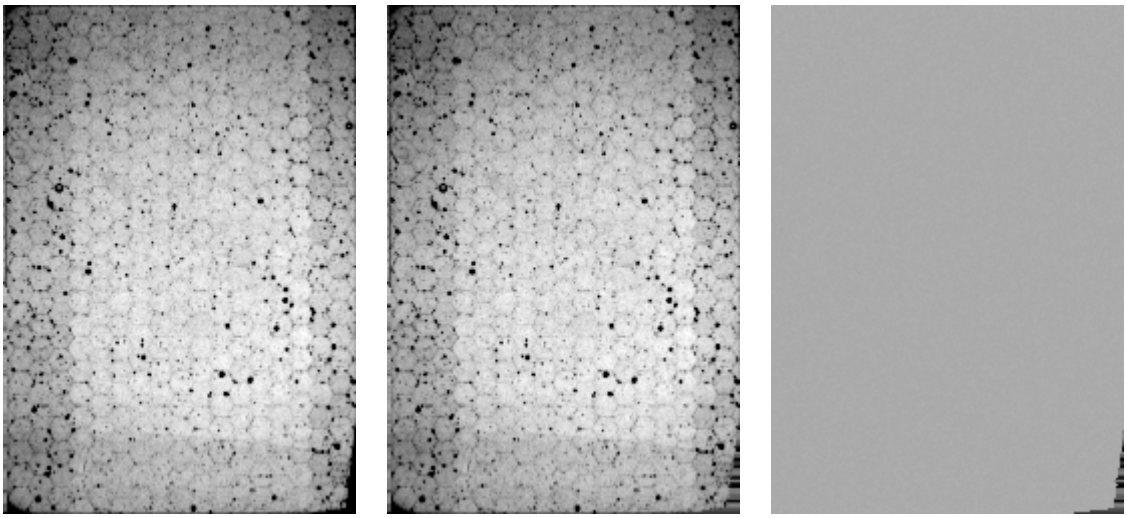

MRI original MRI bad pixel replacement MRI full processing

Figure 5.4-2 Bad pixel replacement and flat-field processing for the Medium Resolution Imager

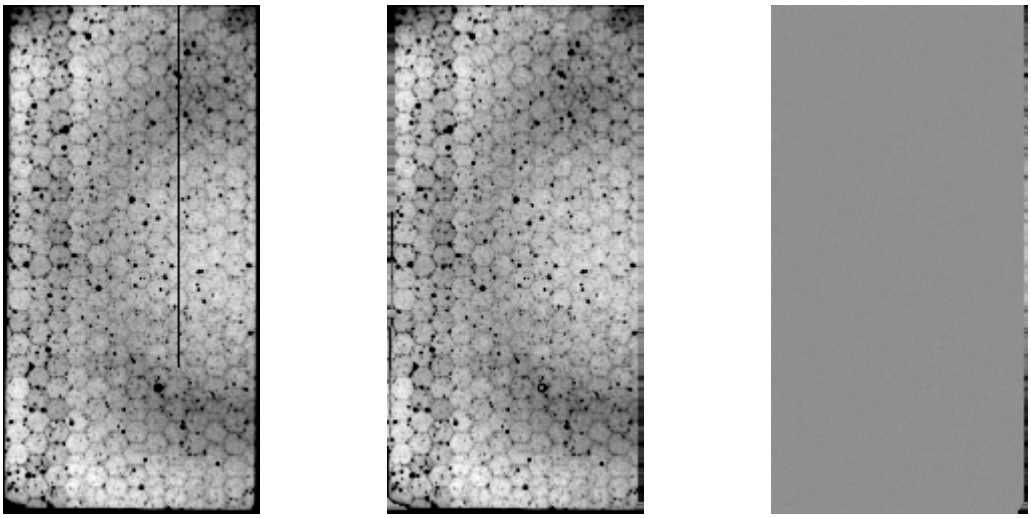

SLI original SLI bad pixel replacement SLI full processing

Figure 5.4-3 Bad pixel replacement and flat-field processing for the Side-Looking Imager

5.4.5. Flat Field Performance at Other Temperatures

As noted above the flat field was derived from measurements in the CCD temperature range 240 – 251K, and it is of interest to know how it performs at other temperatures. To investigate this we apply the flat field to images taken for the purpose of absolute responsivity calibration in the 20-inch integrating sphere at other temperatures. The figures below show images taken at different temperatures, then processed for the flat field correction and the bad pixel replacement. All images are scaled such that white is 10% larger than the image mean values and black is 10% less than the image mean value.

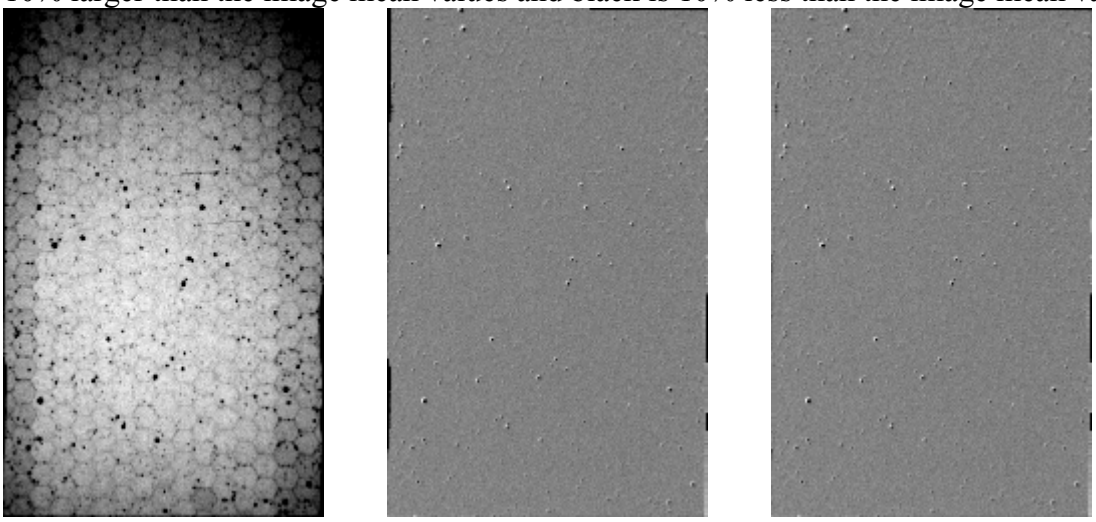

Figure 5.4.5-1 HRI original image, flat field processing, and ff+bpm at 176K

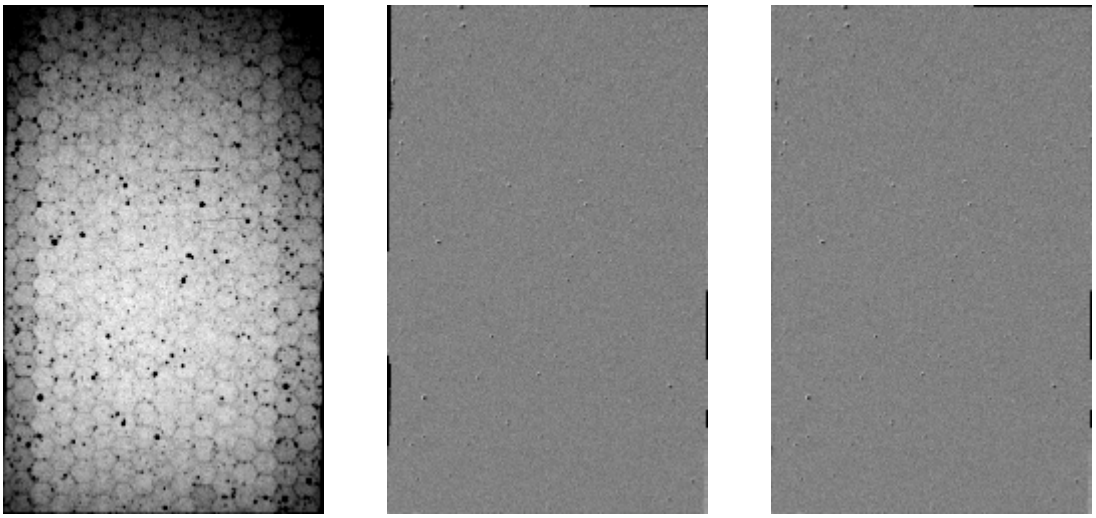

Figure 5.4.5-2 Same as figure 5.4.5-1 except at 208K

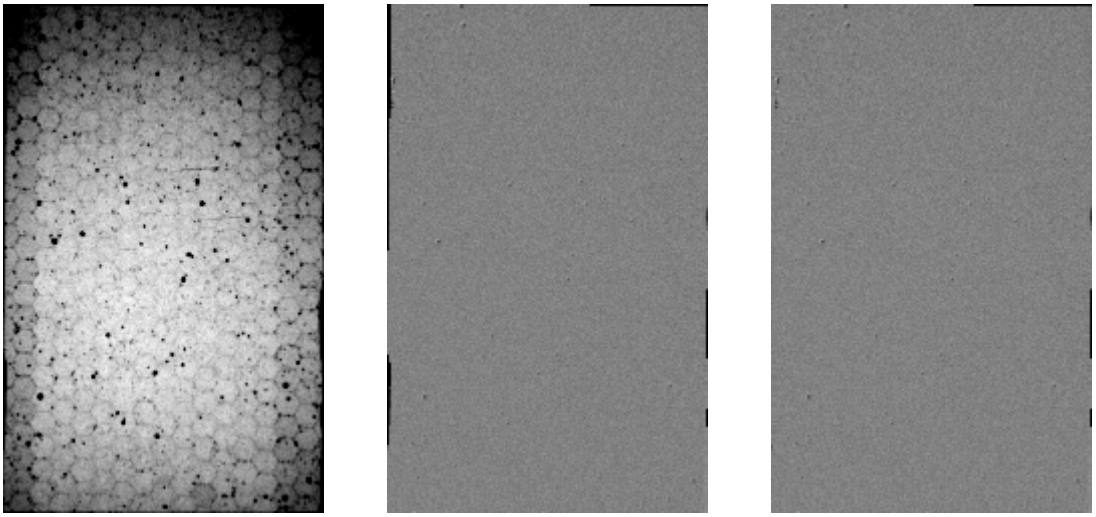

Figure 5.4.5-3 Same as figure 5.4.5-1 except at 223K

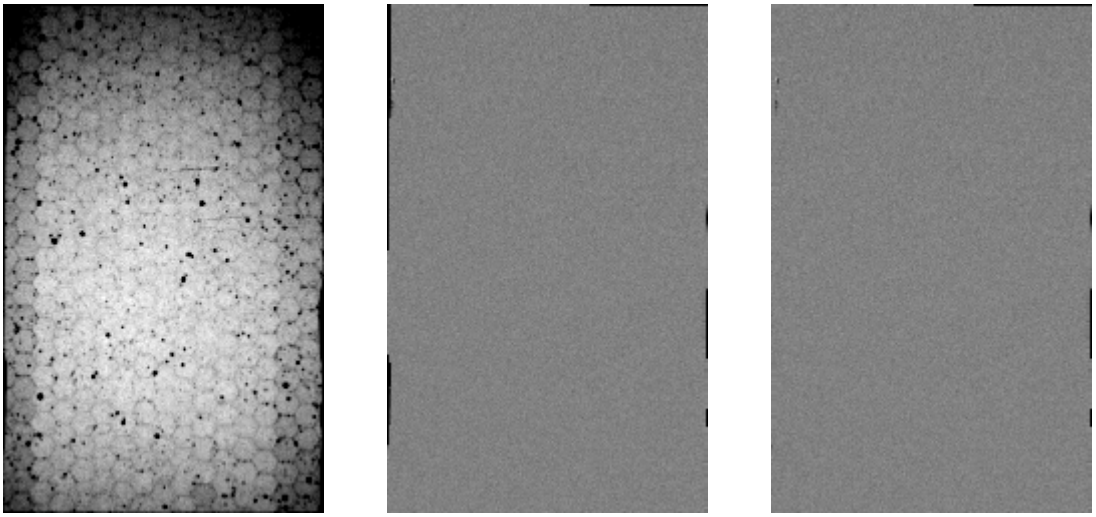

Figure 5.4.5-4 Same as figure 5.4.5-1 except at 245K

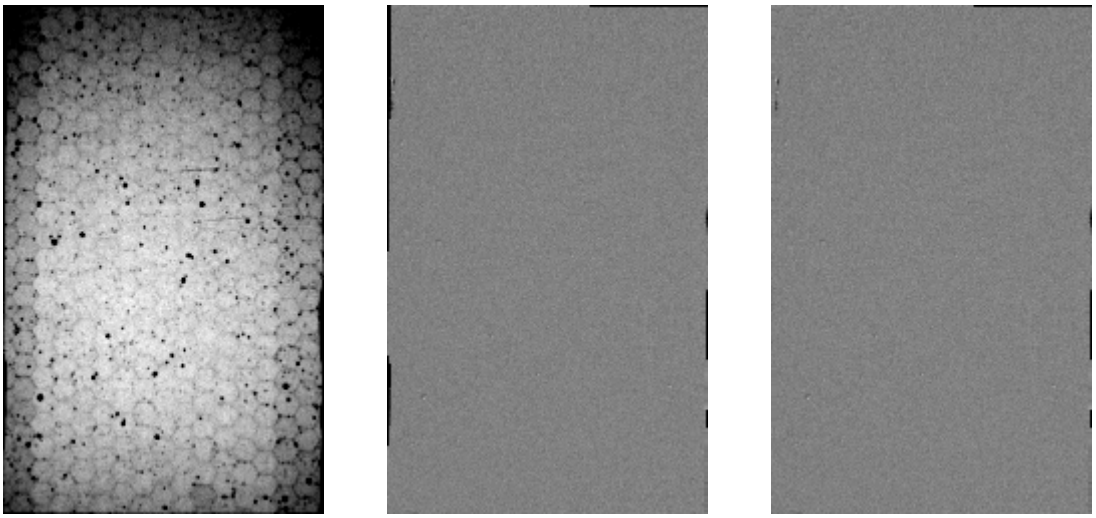

Figure 5.4.5-5 Same as figure 5.4.5-1 except at 260K

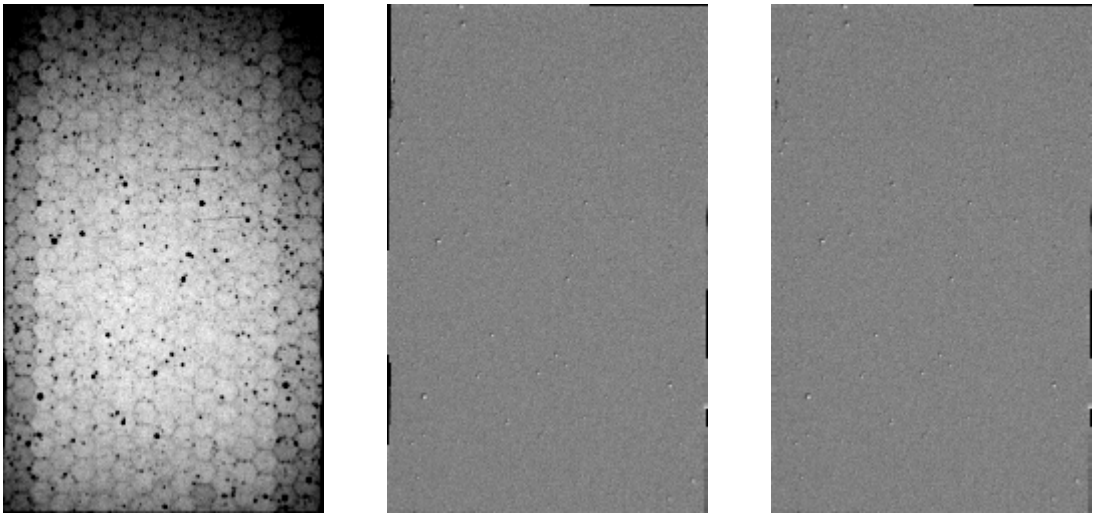

Figure 5.4.5-6 Same as figure 5.4.5-1 except at 281K

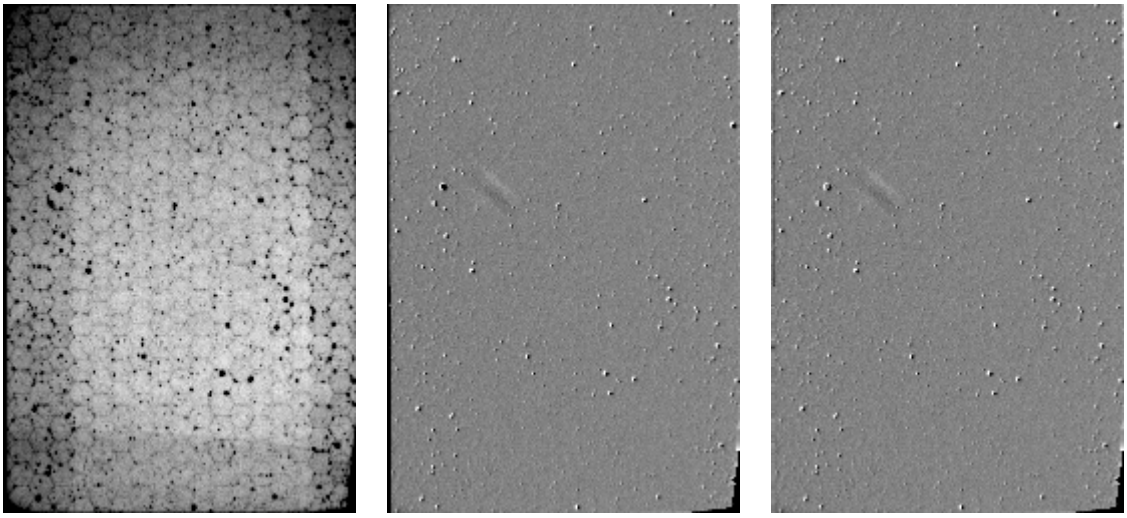

Figure 5.4.5-7 MRI original image, flat field processing, and ff+bpm at 176K

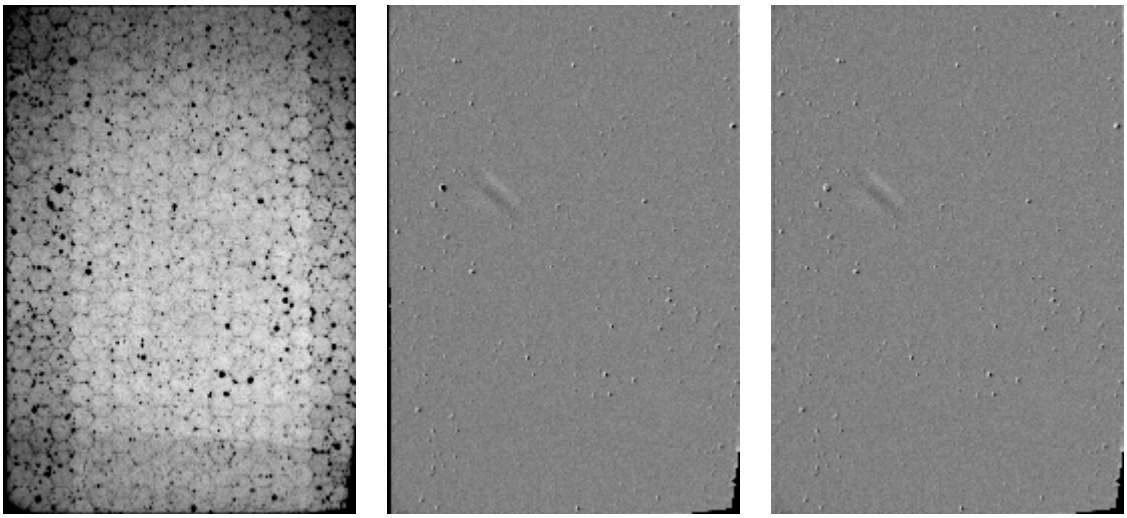

Figure 5.4.5-8 Same as figure 5.4.5-7 except at 208K

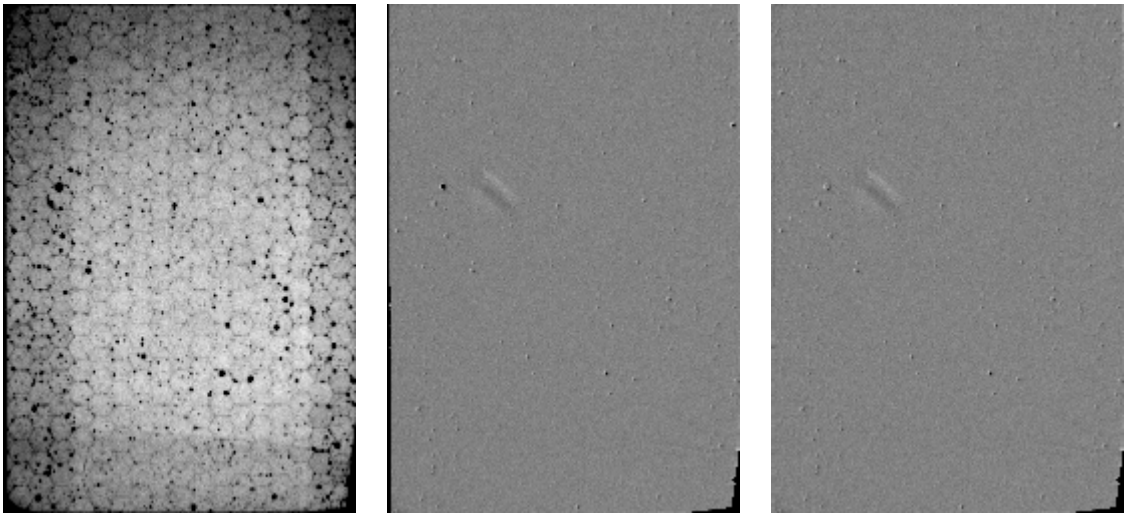

Figure 5.4.5-9 Same as figure 5.4.5-7 except at 223K

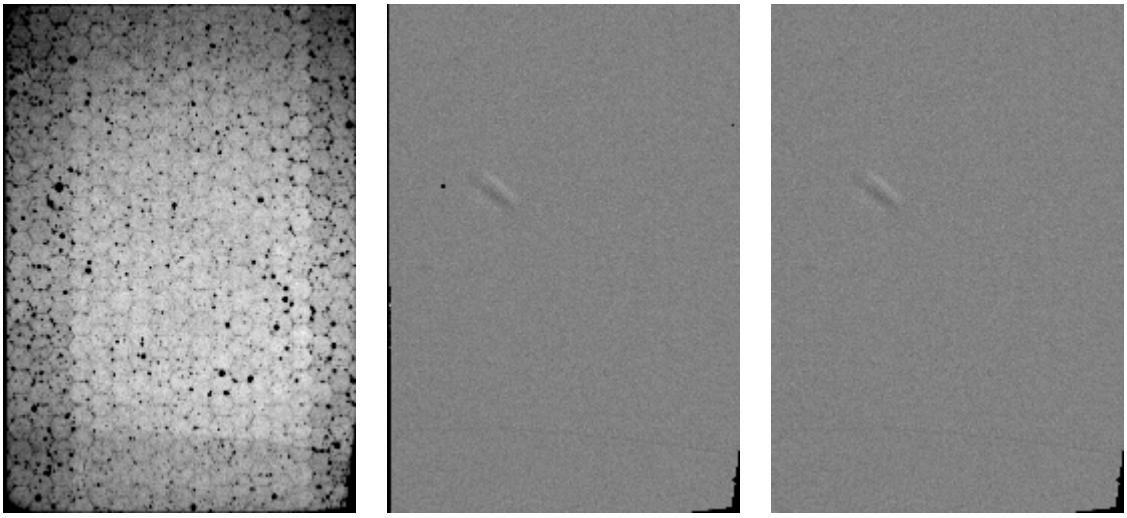

Figure 5.4.5-10 Same as figure 5.4.5-7 except at 245K

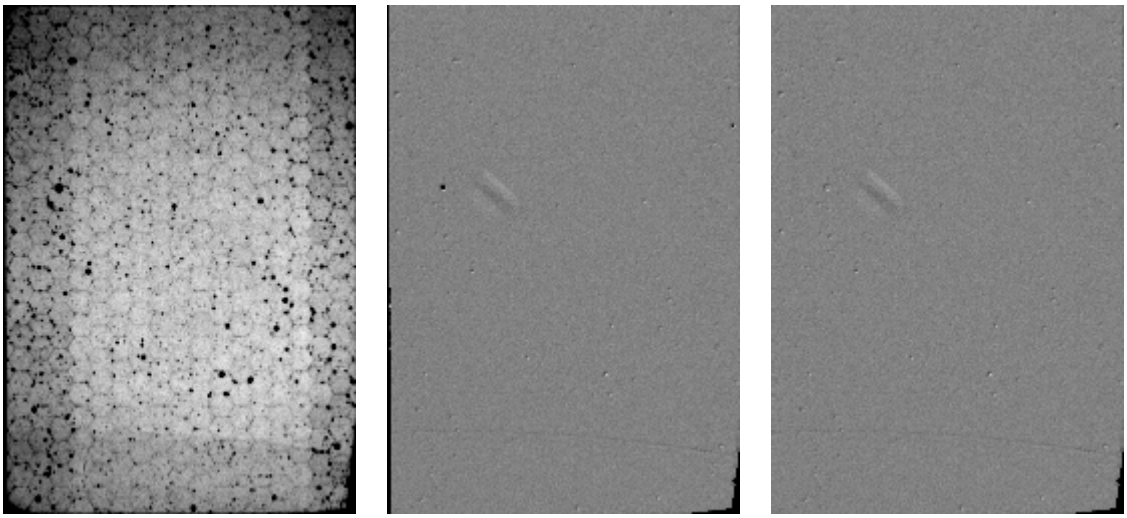

Figure 5.4.5-11 Same as figure 5.4.5-7 except at 260K

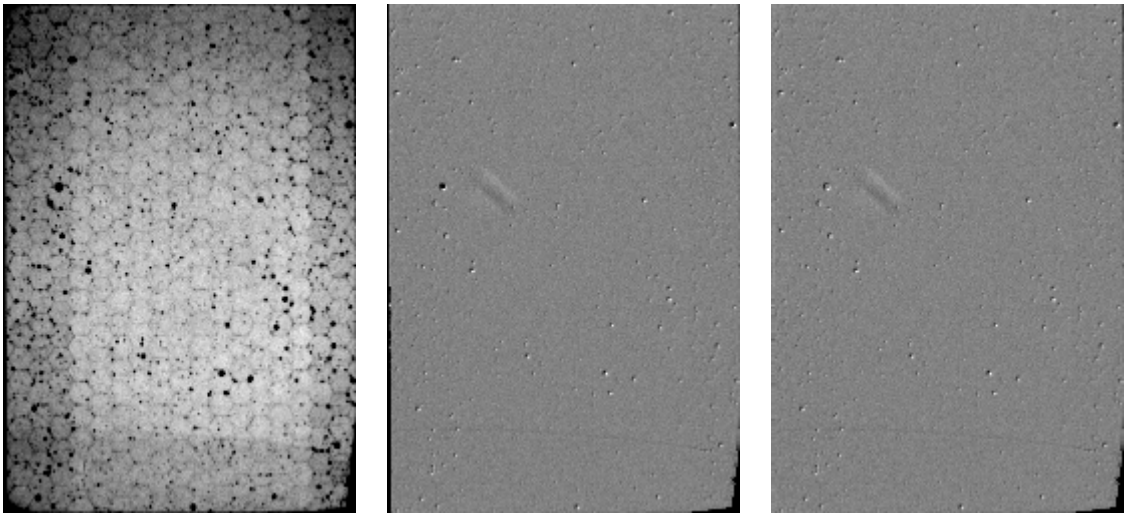

Figure 5.4.5-12 Same as figure 5.4.5-7 except at 281K

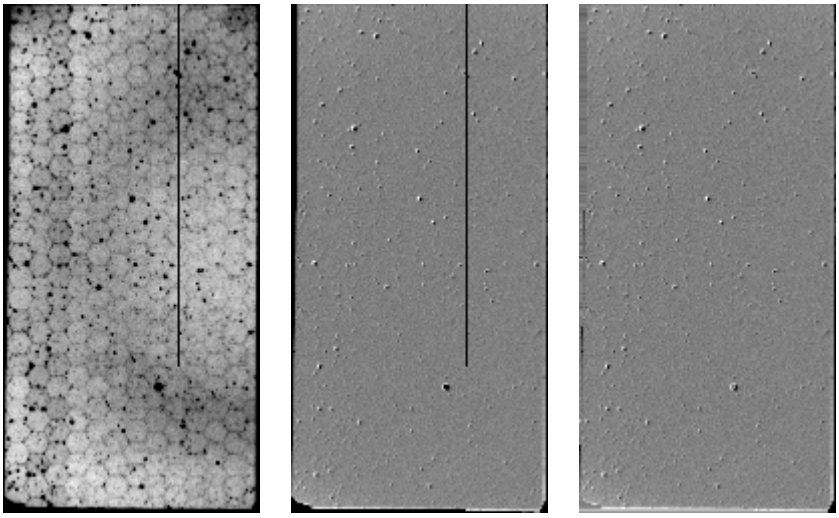

Figure 5.4.5-13 SLI original image, flat field processing, and ff+bpm at 176K

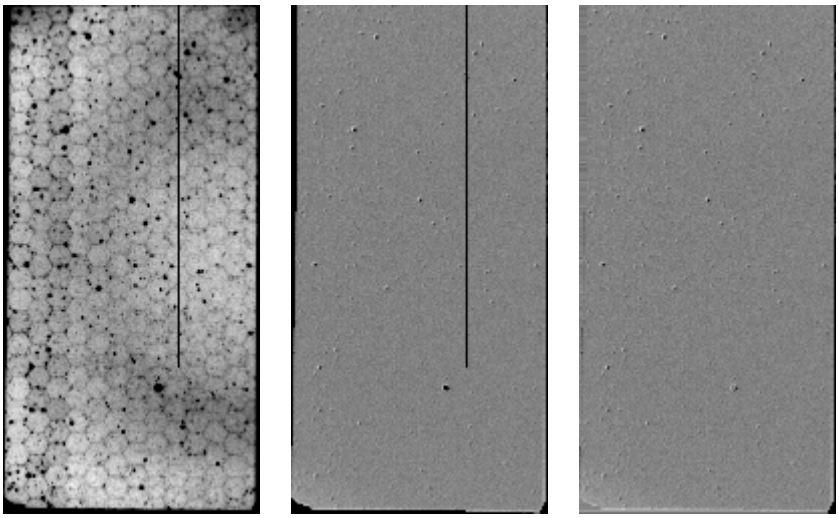

Figure 5.4.5-14 Same as figure 5.4.5-13 except at 208K

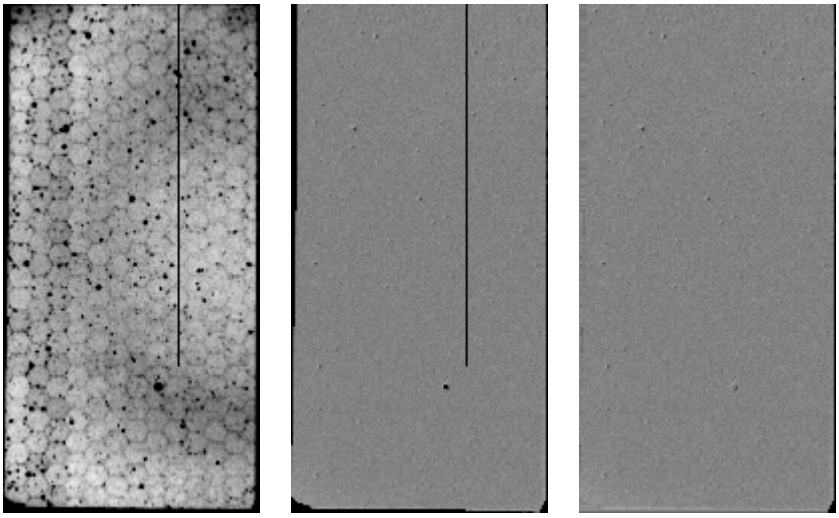

Figure 5.4.5-15 Same as figure 5.4.5-13 except at 223K

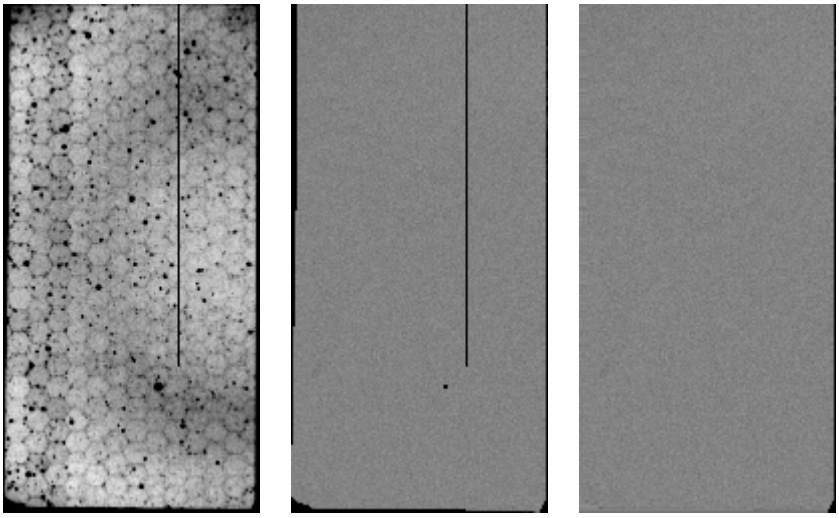

Figure 5.4.5-16 Same as figure 5.4.5-13 except at 245K

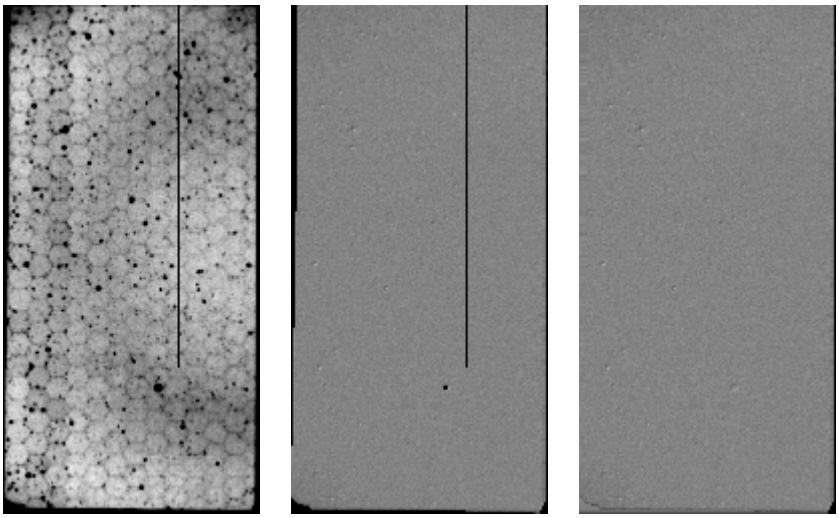

Figure 5.4.5-17 Same as figure 5.4.5-13 except at 260K

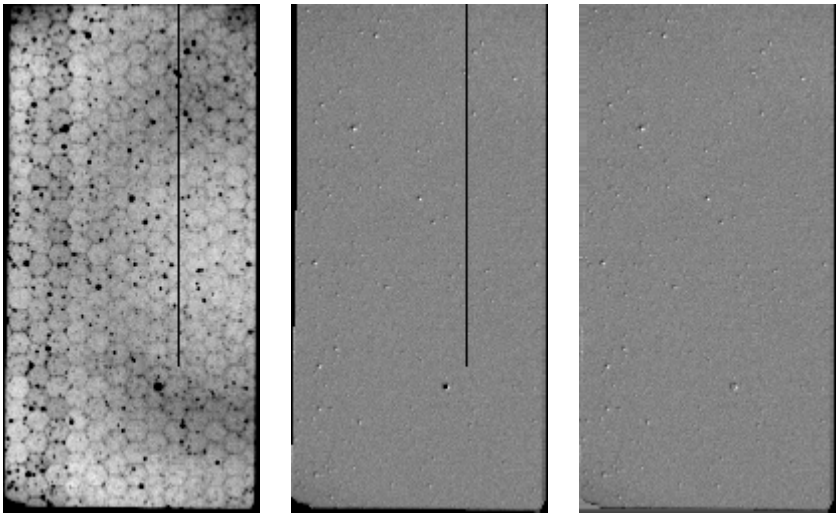

Figure 5.4.5-18 Same as figure 5.4.5-13 except at 281K

Correction of the integrating sphere images using the standard flat field results in systematic changes with temperature. Not surprisingly, the best result occurs at 245K, which is approximately the temperature at which the flat field correction was derived. Hotter and colder exposures produce corrected images with more features, with the number and visibility of features increasing for larger temperature differences.

The short conclusion from this study is that the flat field varies with temperature. The most accurate photometry from the images requires removing the flight software flat field correction and applications of the pixel-by-pixel responsivities to derive the intensities of field objects.

It is possible to draw some conclusion about what is producing this temperature dependence. The changes are very systematic. The coldest images show blemishes with a dark part at about “4 o’clock”, and the warmest images show blemishes with a dark part at about “10 o’clock”. Apparently as the fiber optic/CCD assembly changes temperature

the fibers move with respect to the CCD pixels in the 4 o'clock – 10 o'clock direction. All three imagers move in same direction, so the entire fiber optic bundle moves with respect to the CCD. Whatever the cause, removal of the flight software flat field correction followed by application of the pixel-by-pixel absolute responsivity at the focal plane temperature provides a fundamental correction.

One aspect of the images above is worthy of further note. The MRI displays a prominent, large feature just to be upper left of the center of the images at all temperatures. This feature is about 23 pixels long and 5 pixels wide. It does not correlate well with any fiber-optic structures. It appears to be a variation in CCD responsivity between the two days (July 20, 1996 and July 24, 1996), with an amplitude of 1 – 2%. The origin of this feature is unknown. It does appear in the integrating sphere data on September 11, 1996, so it does appear to be a permanent feature. This feature is contained in the absolute responsivity data, so it should be possible to correct for this accurately.

During the Titan descent no dark frames are available. For this reason the flight software "estimates" the dark DN to be 8 counts for each pixel, and it subtracts this number before applying the flat field correction. While this number may be close to accurate when the CCD is very cold, dark current growth during the mission will make it too small during a large part of the mission. Furthermore a wide variation in the dark currents of different pixels will exist. Both effects will degrade the flat field correction. The main effect of these will be to make images less compressible while the CCD cools.

5.5. Compression

DISR offers two methods for compressing images. Software compression, based on a row-by-row applicaton of the Rice ψ-f method, is available for lossless compression. It is used for compression of the Solar Aureole and spectrometer data sets during descent and will not be mentioned further here. By default, the imagers use the Data Compression Subsystem (DCS) compressor, which implements compression using a Discrete Cosine Transform method, for all image data sets during descent.

Discrete cosine transform compression is similar to JPEG compression, although for most scenes it is not quite as efficient. It was chosen over JPEG, because no space-qualified JPEG hardware compressor was available at the time of the DISR design. The DCS hardware was furnished by the Technische Universität Braunschweig, under the direction of Professor Fritz Gliem. The hardware design was executed by Dr. Frank Rabe.

The DISR implementation is described "A DCT Image Data Processor For Use On The Huygens Titan Probe", P. Rüffer, F. Rabe, and F. Gliem, International Geoscience and Remote Sensing Symposium, pp. 678 – 680, 1992.

The image is subdivided into 16x16 pixel blocks, and the discrete cosine transform of each is then computed. The resulting coefficients are then quantized (or eliminated) and coded using an arithmetic coding scheme.

A traditional problem with image compression has been its susceptibility to telemetry dropouts. A single lost packet in the telemetry stream for an entire image could cause loss of the entire image. To contain this problem the DISR implementation contains added "sync" markers, which contain pointers to the addresses of previous blocks. This limits the data loss from lost telemetry packets.

The DCS flight code and ground decompression software support dropped packet recovery only for version 3 of the algorithms. It is noted that the "gse" program, written by Martin Marietta, gives up trying to process any data set for which any data is missing. Therefore, the gse program will not currently process images with missing telemetry.

The Technische Universität Braunschweig has provided code (in C) to reconstruct images with missing data. It is located on cassini in the directory /users/ldoose/TUB/source_Mar95. The main source code module is named dcs.c. Software has also been provided which simulates operation of the hardware compressor. This is in the same directory, and the main source code module is named disrcmp3.c. Mike Bushroe has recently and successfully undertaken the task is to integrate the dcs program with the image telemetry stream to produce recovered images.

5.5.1. DCS automatic bad pixel replacement

A drawback of the DCS compression technique is its performance on hot pixels. If a 16x16 pixel block contains a single pixel very much brighter than the other pixels, the compressor/decompressor will produce a checker board pattern within the block. An example is shown in figure Z.

Sources of hot pixels include cosmic rays and pixels made hot through enhanced dark current. Because the point spread function of the imagers is generally larger than one pixel, real features are unlikely to produce such disturbances.

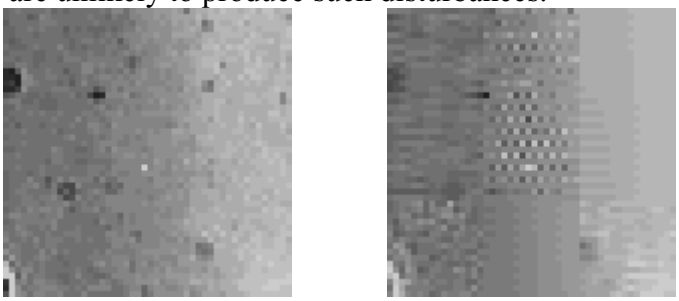

Figure 5.5.1-1 48x48 pixel sub-samples of an image before and after compression. The single bright pixel in the center causes the "checkerboard" pattern in its block.

E. Karkoschka suggested a method of replacing pixels hot enough to disturb the compressor, and this method was implemented in the compressor software. The algorithm is applied to the data as the compressor receives it, i.e., after flat-fielding, bad pixel removal, and square root processing.

The algorithm searches all 2x2 pixel squares. If the absolute difference between the sums of both diagonals is less than a given threshold, it does nothing. Otherwise it calculates for each of these four pixels the median of the four pixels directly bordering the offending pixel. If the absolute difference between the pixel value the median is less than the threshold, it again does nothing. Otherwise it changes the pixel value to the median plus threshold (if the pixel DN is too high) or the median minus threshold (if the pixel DN is too low).

The DCS implementation of this algorithm limits the number replaced pixels to about 400 – 500. I believe the adopted threshold value was 40 DN, although I have no proof of this.

5.6. Imaging system performance

A comprehensive look at the imaging system performance at different compression ratios is available in section 6 of this document, "Test for Suitable Selection of Compression Ratios for DISR Imagers", by Erich Karkoschka.

Here we present a more limited study. DCS performance depends on several factors, including image contrast, compression ratio, flat-fielding performance, and dark current. Overall performance of the onboard image processing software is more important than the compressor performance alone.

A software simulator has been written to reproduce the processing of the onboard and GSE software. This simulator has the advantage of operating on any concocted scene incident on the CCD.

Prior to launch test exposures were made using the HRI aimed at a projected slide. Contrast of the scene was degraded by illuminating the screen with a lamp, until this diluting illumination made the scene contrast approach zero. Compression ratios of 2, 3, 6, and 8 were used. Figure 5.6-1 shows the unprocessed, onboard software/GSE-processed images, and simulator images for two of the five contrast levels at compression ratios of 8. The purpose of this figure is to demonstrate the accuracy of the simulator.

Mean exposure levels are about 1800 DN. The detector temperature was about 277K for all exposures, so the dark current was only slightly above its nominal value of 8 DN.

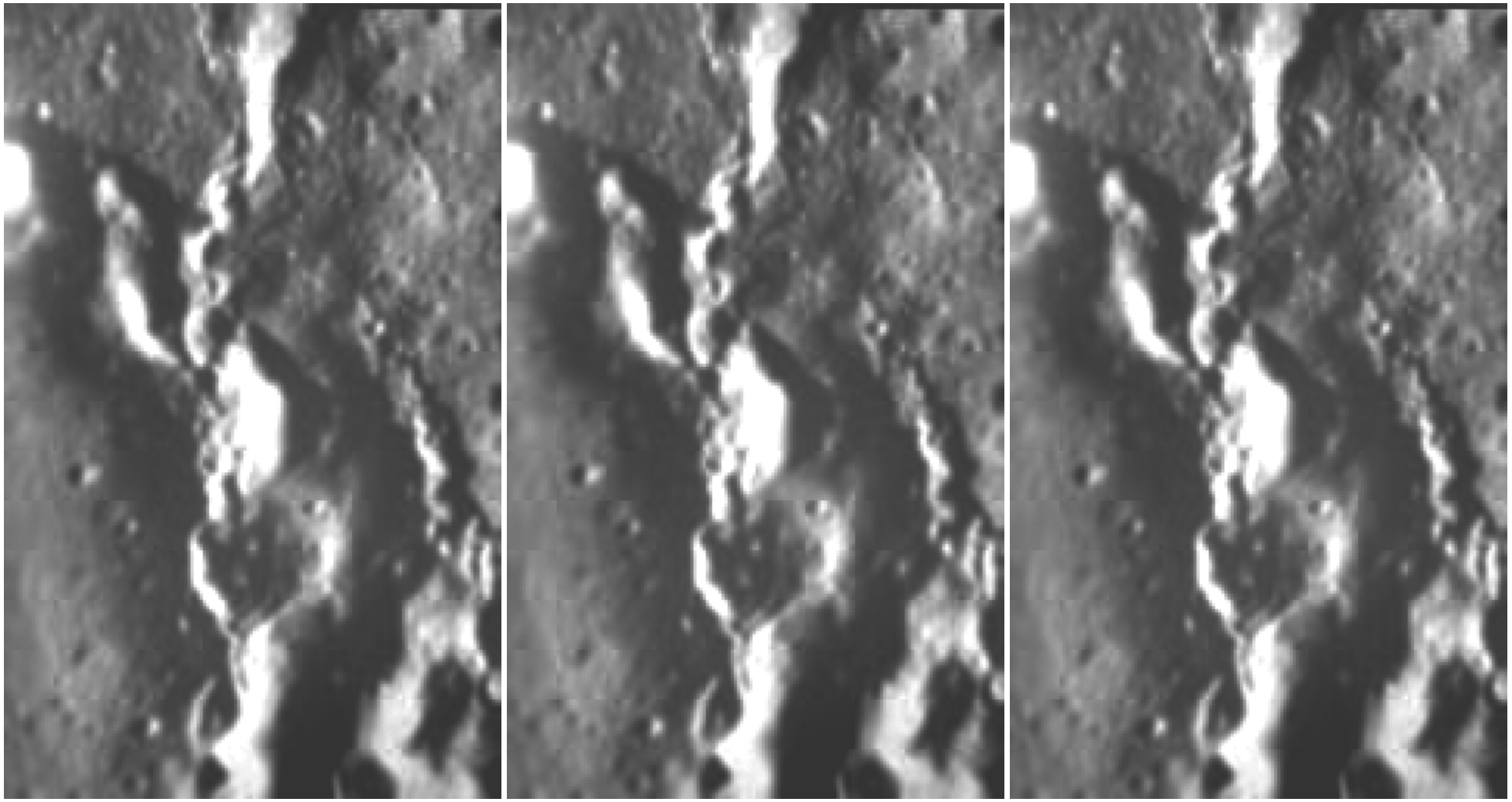

Figure 5.6-1a The original scene on the CCD (left), the image produced by the flight and GSE software (center), and the image produced by the simulator (right) for the highest contrast scene and compression ratio 8. The two right images are essentially identical, validating the simulator. For this high contrast scene a compression ratio of 8 is well tolerated.

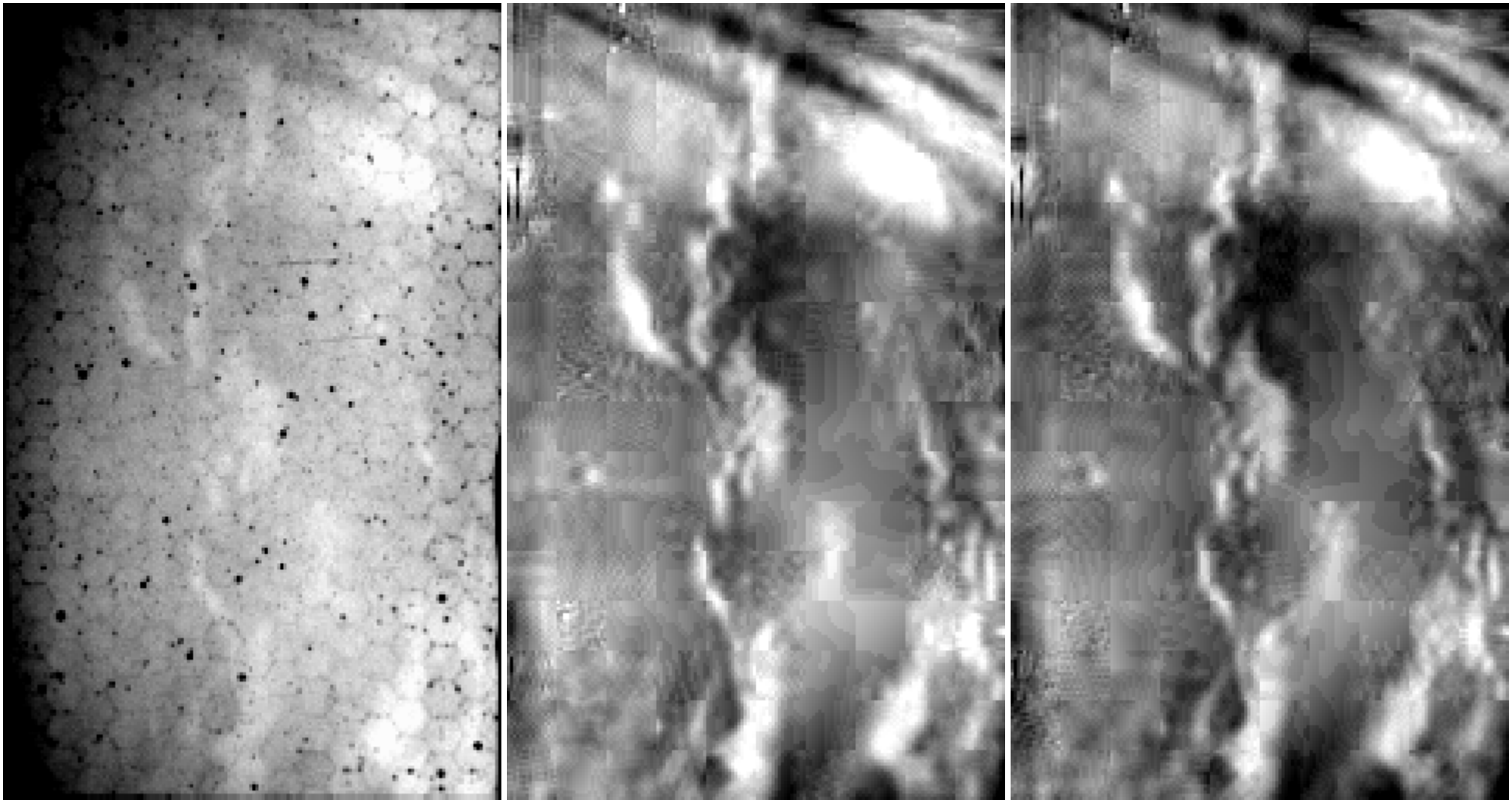

Figure 5.6-1b Same as figure 5.6-1a, except for a very low contrast scene. Reconstruction of the image suffers under the extreme contrast enhancement used to display this scene. The blockiness in the right two images is very obvious. Reconstruction quality from the

original scene is still remarkable. Minor differences in the two right images are seen. These are expected, because the source images are different.

In figure 5.6-1 the two processed images (on the right) have been divided by a best-fit cubic polynominal surface to remove large scale brightness gradients in the images. This division flattens the image brightness level and permits a higher contrast stretch. The histograms of the images with and without the division are shown in figure 5.6-2.

Figure Z2 validates the simulator. Exact agreement between the DISR system and simulator images is not expected, because they originate from different exposures which will be slightly different due to noise.

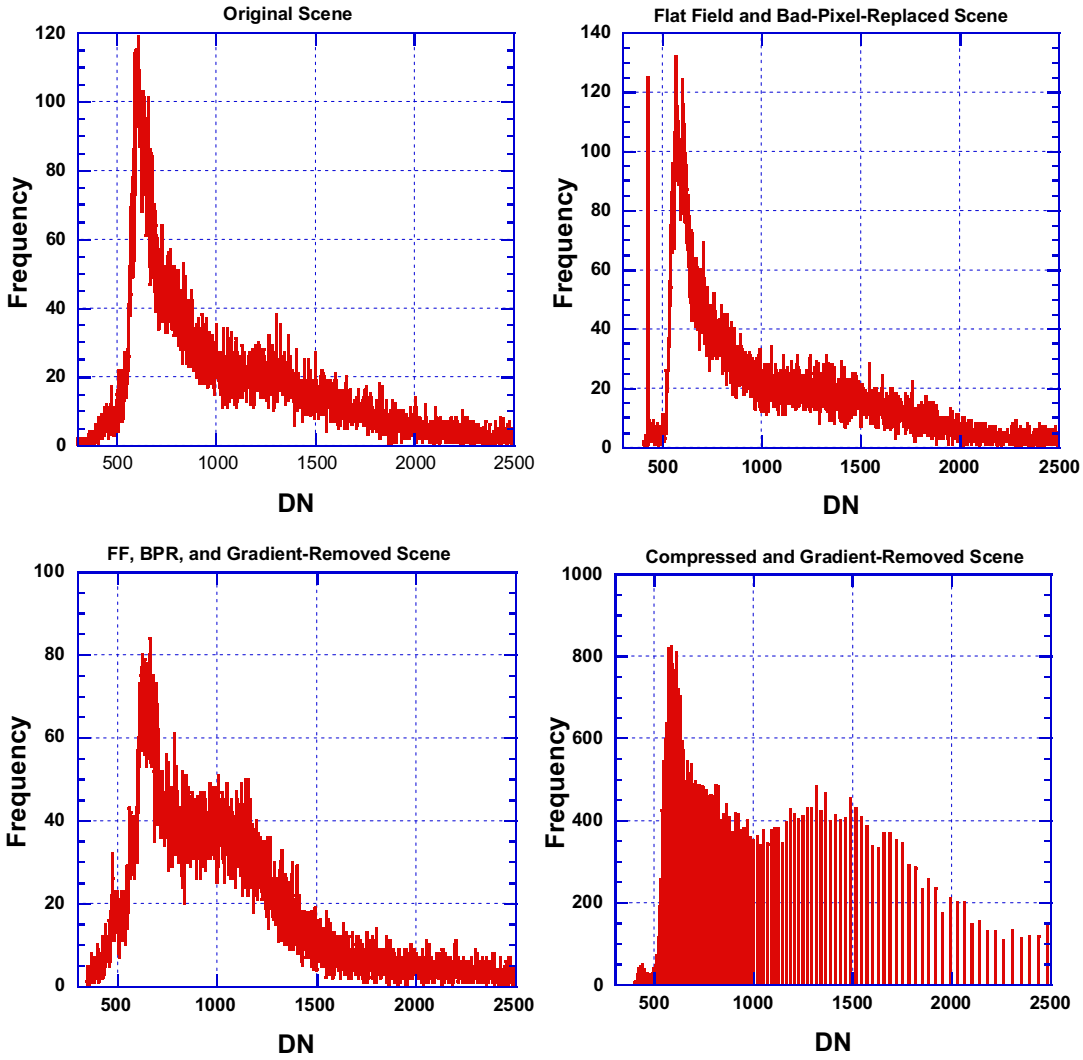

Figure 5.6-2a Histograms of the high contrast image at various stages of processing.

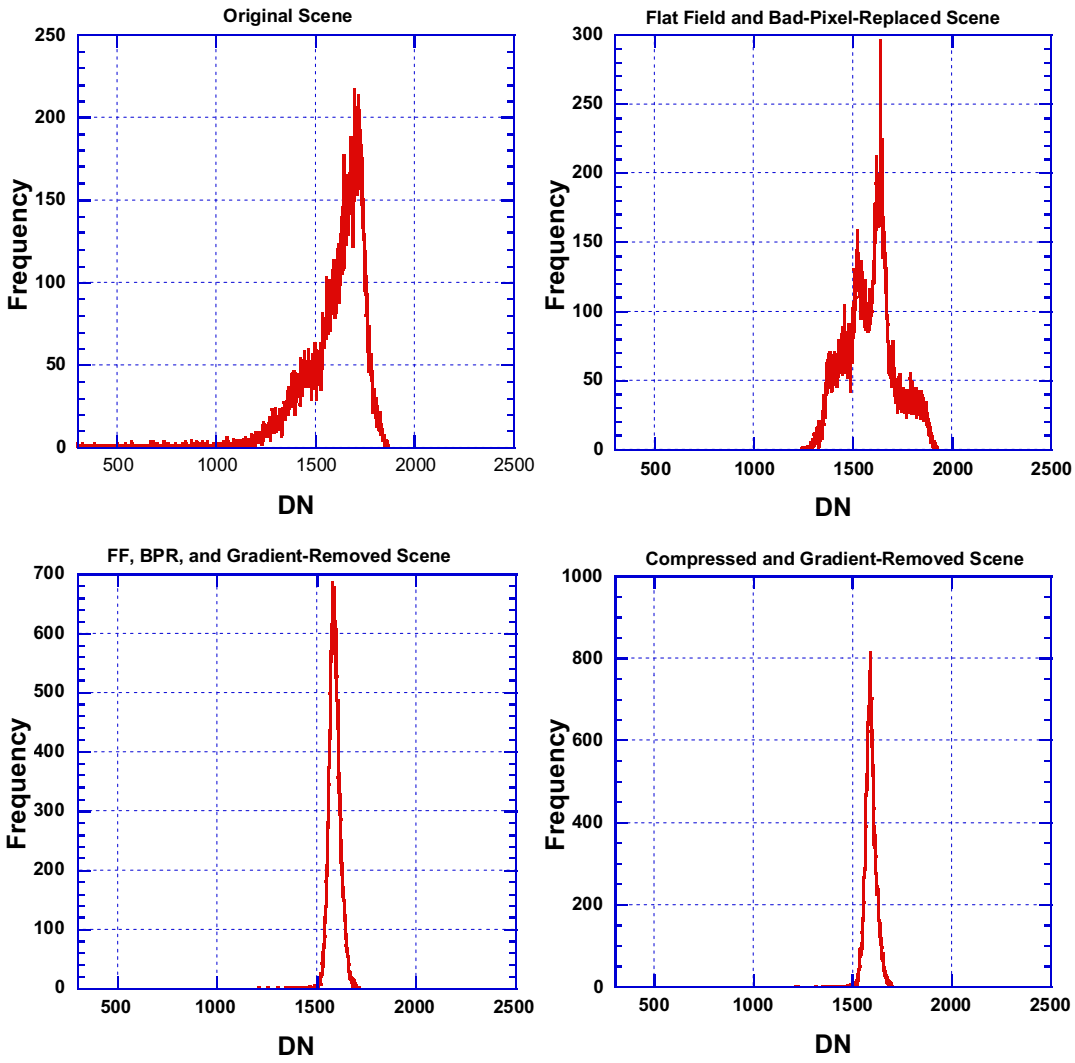

Figure 5.6-2b Histograms of the low contrast image at various stages of processing.

The histograms show significant changes during the processing. These are all expected. The flat field correction and bad pixel replacement alter the data number content substantially. Removal of the large scale gradients narrows the histograms. Square root processing reduces the number of permitted data numbers from 4096 to 256, and redistributes them so that relatively fewer high DN values are permitted. Compression certainly redistributes the data numbers; this will be shown better below. The adaptive square root algorithm allocates the number of DNs based on the flat-fielded, bad-pixel-replaced scene. For the low contrast image this means 128 8-bit DNs are assigned between approximate 1300 and 1900 12-bit DNs. On average one 8-bit DN covers about 5 12-bit DNs. This granularity of 5 DN in an image with a mean brightness of about 1600 DN does not significantly degrade the inherent 200:1 signal-to-noise ratio. We have removed the large scale gradients, which narrows the histogram dramatically. Most of the resulting image is then represented with only about 30 DN levels. This, combined

with the compression, accounts for the contouring seen in parts of the 8:1 compressed image of this scene.

Although the appearance of the images is very good except at the lowest contrasts and highest compression factors, it is important to know the quantitative size of the errors introduced by the onboard/GSE processing. We have no ground truth measurements of images containing structure. The closest we can come is to correct an unprocessed DISR image for dark current, flat field, and bad pixels. This can serve as our ground truth image, and it can be compared to DISR-processed images. The differences are presumably caused by square root processing, compression, inherent system noise, and any temporal differences between the two exposures.

In figure 5.6-3 we compare our ground truth image to processed images at several steps during the processing for row 106, as indicated in the figure.

The original data (red dashed line) is about 5% higher than all the other profiles. This is because the flat field for this line has a mean value of about 1.05. Dividing by the flat field correction leaves the result about 5% low. For the high contrast, 2X compression profile, errors introduced by both the square rooting and compression are very small. The errors introduced by the square rooting are also very small, causing the green line to cover the blue line almost everywhere. At 8X compression the compressor introduces errors as large as about 3%, seen as the difference between the orange and green lines. Typical errors are much smaller. There are differences also between the simulated compression and hardware-compressed images. As noted above some of these differences are caused by these images coming from different exposures.

In the low contrast image the errors introduced by the processing remain small, typically a few DN. The amplitude of the features is much smaller. The feature at column 137 has a contrast of about 2.5% when measured as $\frac{I_{\max} - I_{\min}}{I_{\max} + I_{\min}}$. The noise in the surrounding data is about 0.5% in these contrast units. The 2.5% feature is easily discernible.

Figure 5.6-4 shows the errors from each stage of the flight/GSE software processing. For 2X compression square rooting errors dominate, while for 8X compression the compressor errors dominate.

The optimum compression ratio for photometry should compress the image as much as possible without becoming a limiting error source. For the data studied here that compression ratio is certainly between 2X and 8X.

Figure 5.6-3 The horizontal lines show the location of row 106 in the low contrast image.

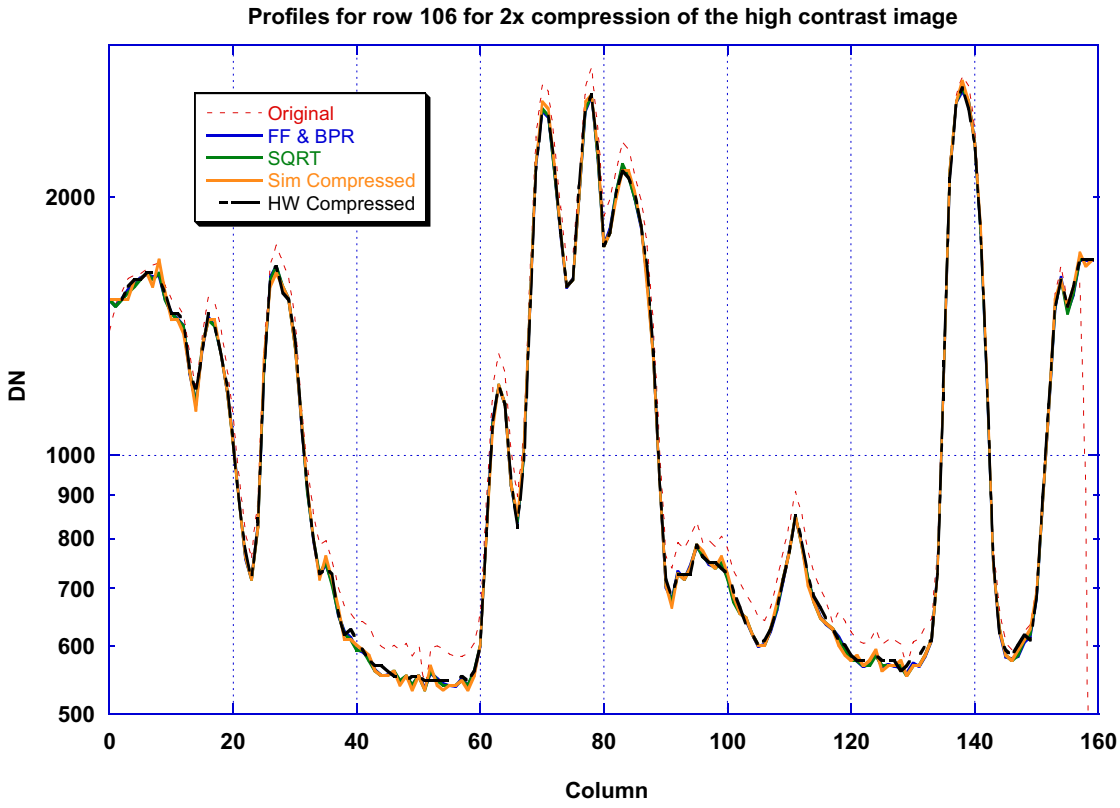
Profiles for row 106 for 2x compression of the high contrast image
Original
FF & BPR
SQRT
Sim Compressed
HW Compressed
DN
2000
1000
900
800
700
600
500
0
20
40
60
80
100
120
140
160
Column

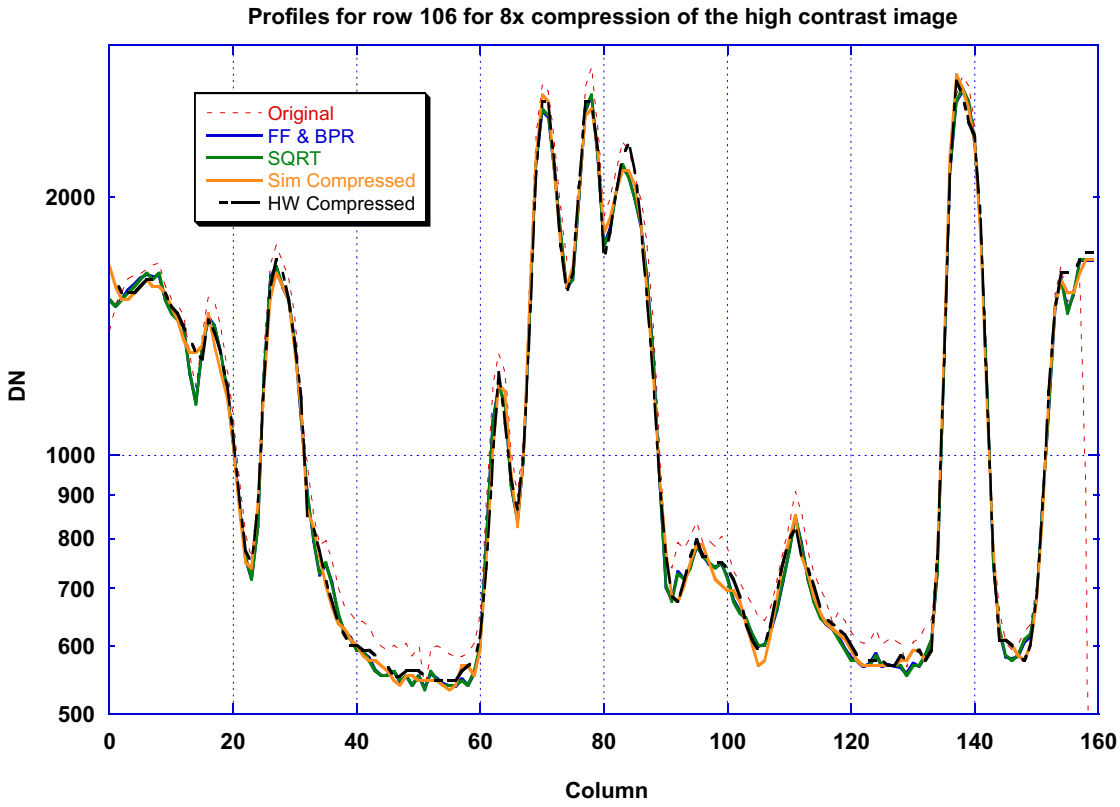
Profiles for row 106 for 8x compression of the high contrast image
Original
FF & BPR
SQRT
Sim Compressed
HW Compressed
DN
2000
1000
900
800
700
600
500
0
20
40
60
80
100
120
140
160
Column

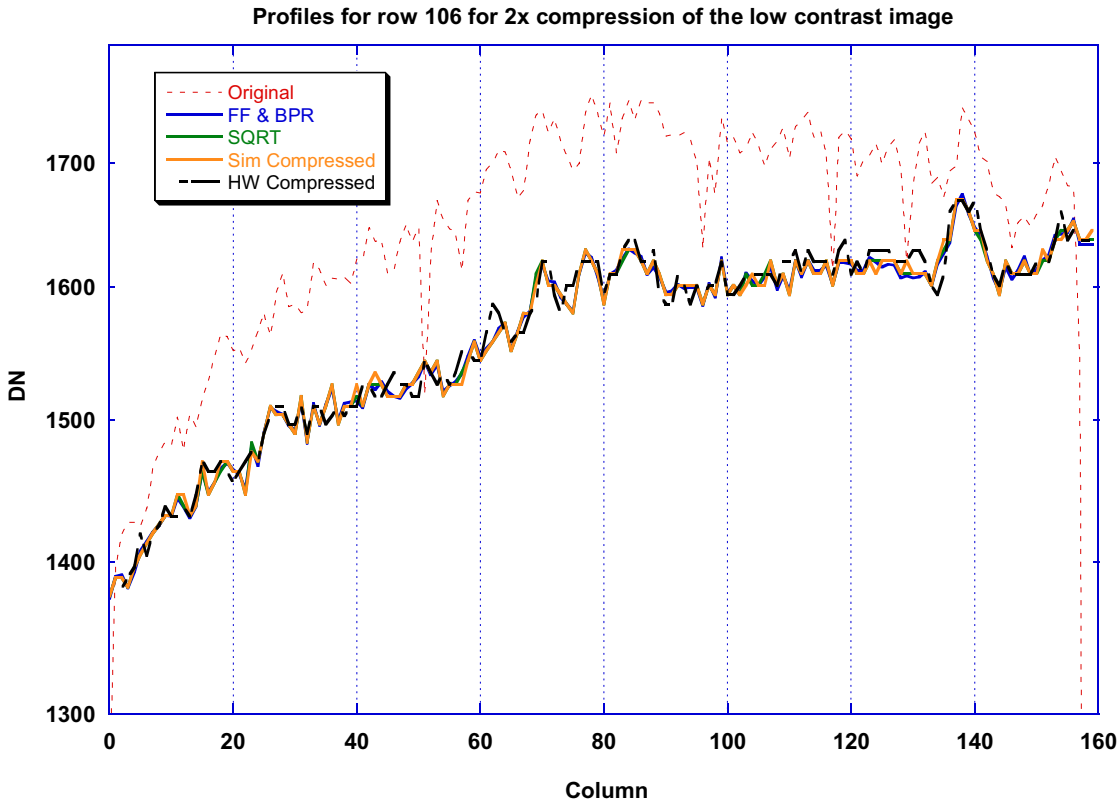
Profiles for row 106 for 2x compression of the low contrast image
Original
FF & BPR
SQRT
Sim Compressed
HW Compressed
DN
1300
1400
1500
1600
1700
0
20
40
60
80
100
120
140
160
Column

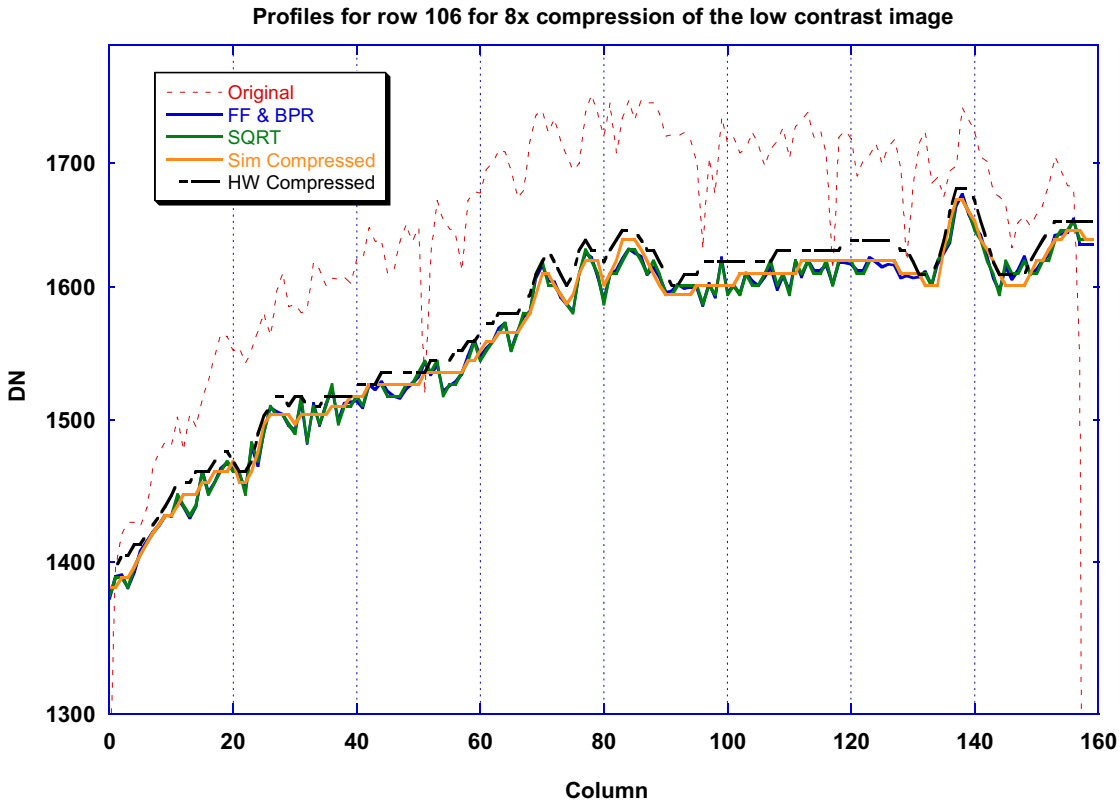
Profiles for row 106 for 8x compression of the low contrast image
Original
FF & BPR
SQRT
Sim Compressed
HW Compressed
DN
1300
1400
1500
1600
1700
0
20
40
60
80
100
120
140
160
Column

Figure 5.6-4a The data number in row 106 vs. column number in the HRI for four images (top to bottom): high contrast with 2X compression, high contrast with 8X compression, low contrast with 2X compression, and low contrast with 8X compression.

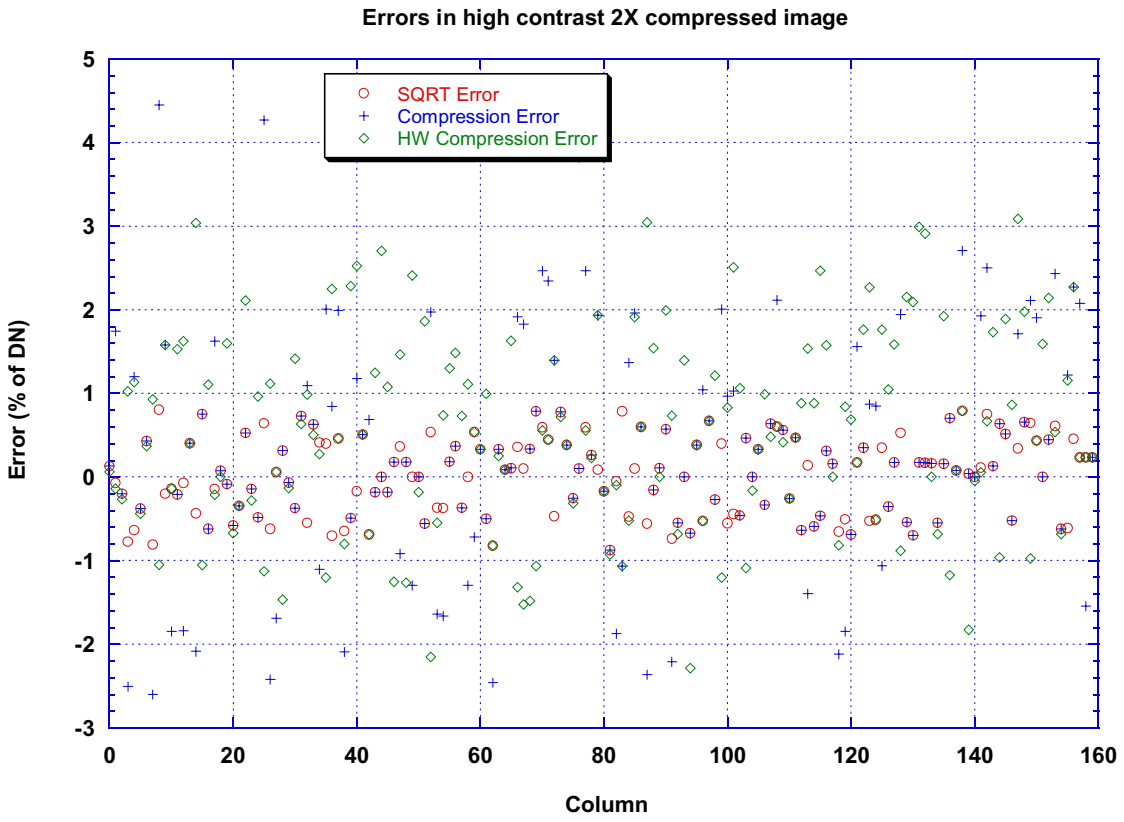

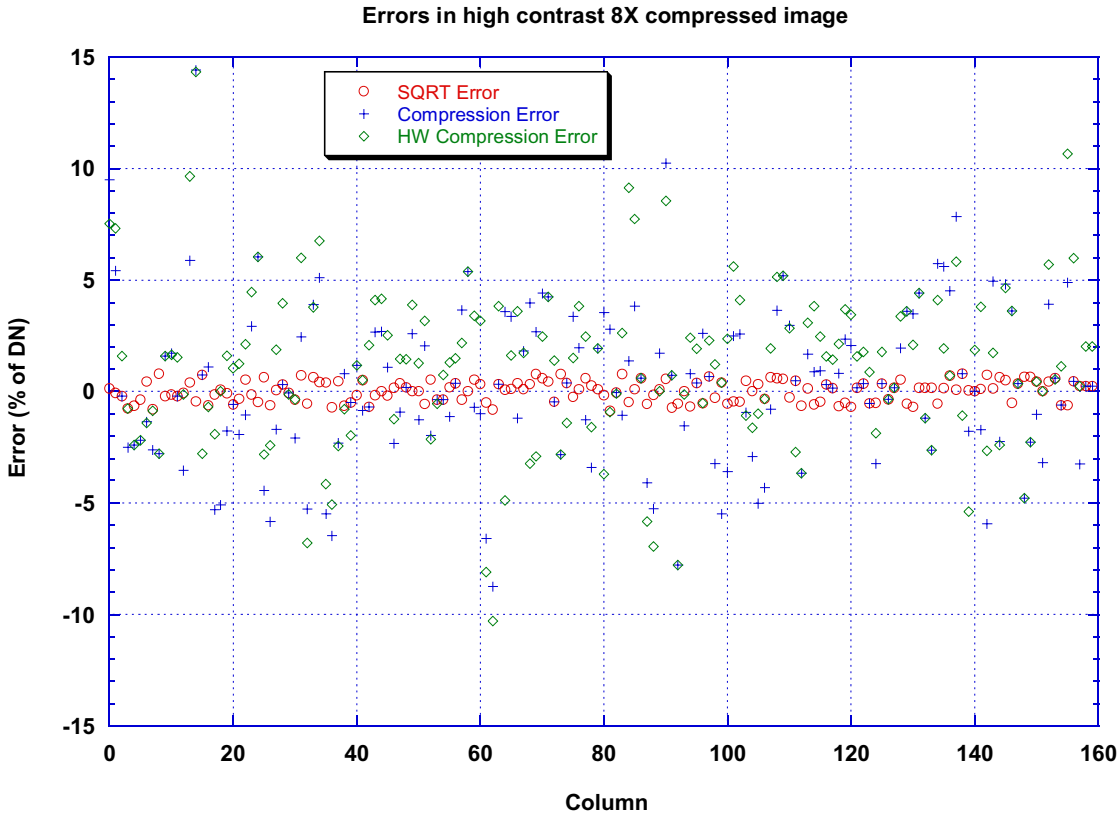
Errors in high contrast 8X compressed image
SQRT Error
Compression Error
HW Compression Error
Error (% of DN)
Column
15
10
5
0
-5
-10
-15
0
20
40
60
80
100
120
140
160

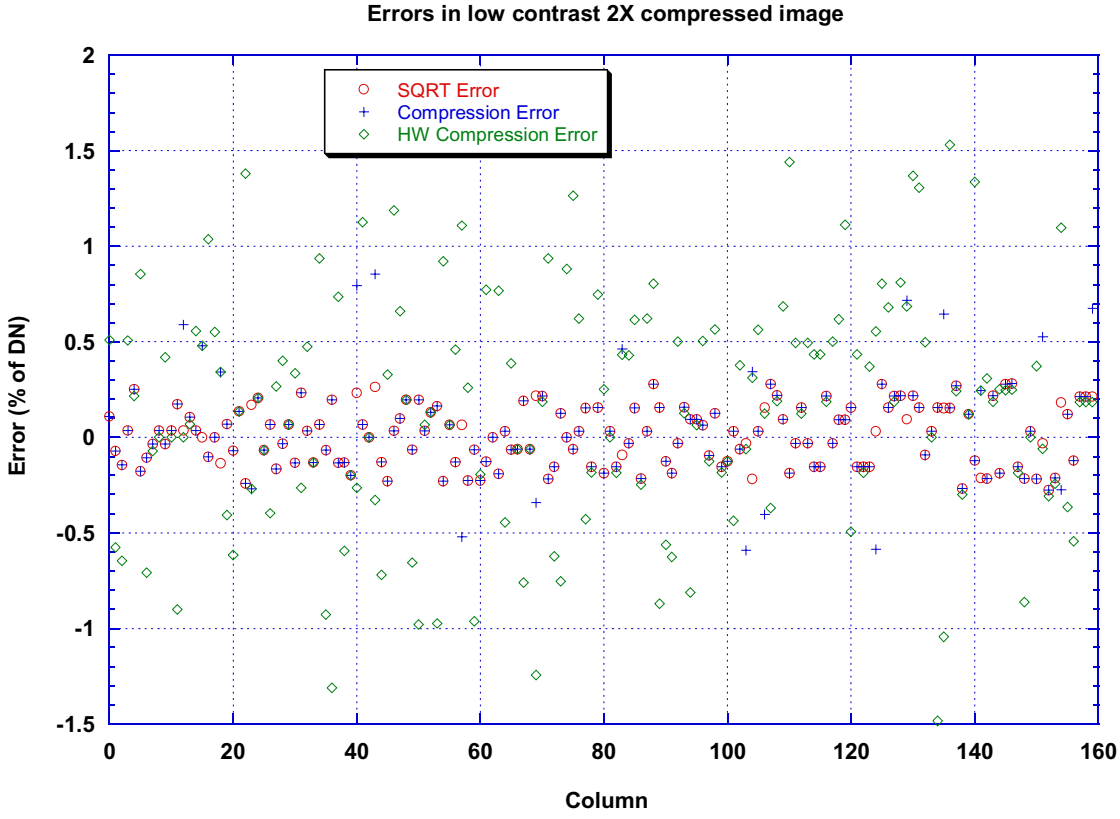
Errors in low contrast 2X compressed image
SQRT Error
Compression Error
HW Compression Error
Error (% of DN)
Column
2
1.5
1
0.5
0
-0.5
-1
-1.5
0
20
40
60
80
100
120
140
160

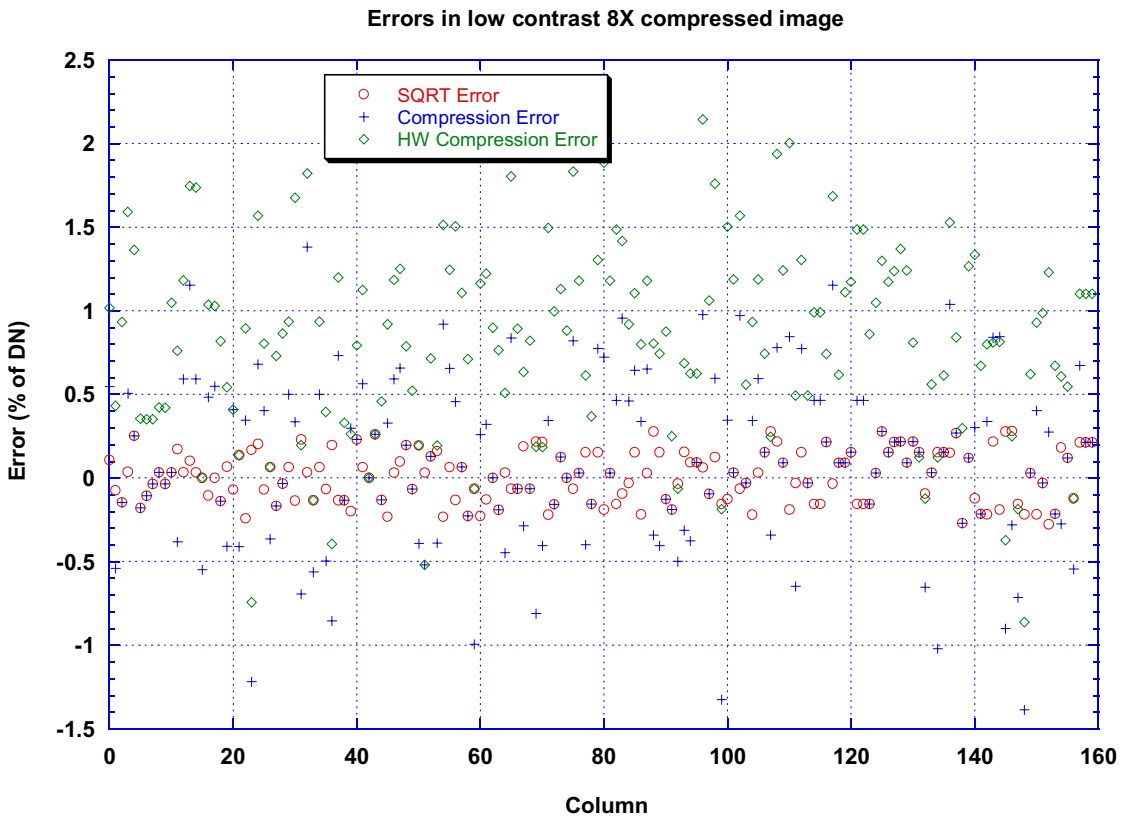

Figure 5.6-4b Errors introduced by flight/GSE software for two scene contrasts and two compression ratios for HRI row 106.

5.6.1. Compression in the presence of increased dark current

The mean CCD dark current has increased steadily during the mission. The dark current of some pixels has increased more than others, leading to a broadening of the image and memory zone dark current distributions. Although the dark current of each pixel is quite predictable, the onboard software does not have the capability to subtract dark current on a pixel-by-pixel basis – it simply subtracts 8 DN from all pixels. This may still be a reasonable correction when the CCD is very cold. At warmer temperatures the excess dark counts take the role of a scene-independent extra signal with a distribution similar to random noise. Because random noise is inherently incompressible, compression of the images suffers when the amplitude of the dark current is any significant fraction of the amplitude of the image scene.

We have studied this effect in two ways. First, using real data from the in-flight Health Checks we have searched for degradation of compressed images of the calibration lamps, using unprocessed images as ground truth. Second, we have simulated high dark current cases by adding synthetic dark current to existing pre-launch image scenes. These images can be processed with software that simulates onboard and GSE processing and compared with the original image.

Each in-flight Health Check contains an uncompressed image and a fully processed image with lamp B on. Each successive Health Check also contains more dark current than the previous one. The exposure times are 40 ms. At the present mean dark current rate of 25 DN/sec, the mean excess dark current is only about 1 DN, compared to mean signals of 600 to 1200 DN. The effect of the mean dark current will surely be negligible. Any visible effects must be caused by the smaller number of pixels with high dark current.

We show the effect on compression of the growth of dark current from F1 to F7 in figures 5.6-5, below. In these figures the contrast is stretched to show the features with high contrast. The difference image is scaled such that black is 10% lower intensity in the compressed image and white is 10% higher intensity in the compressed image.

MRI Compressed vs. Unprocessed for F1

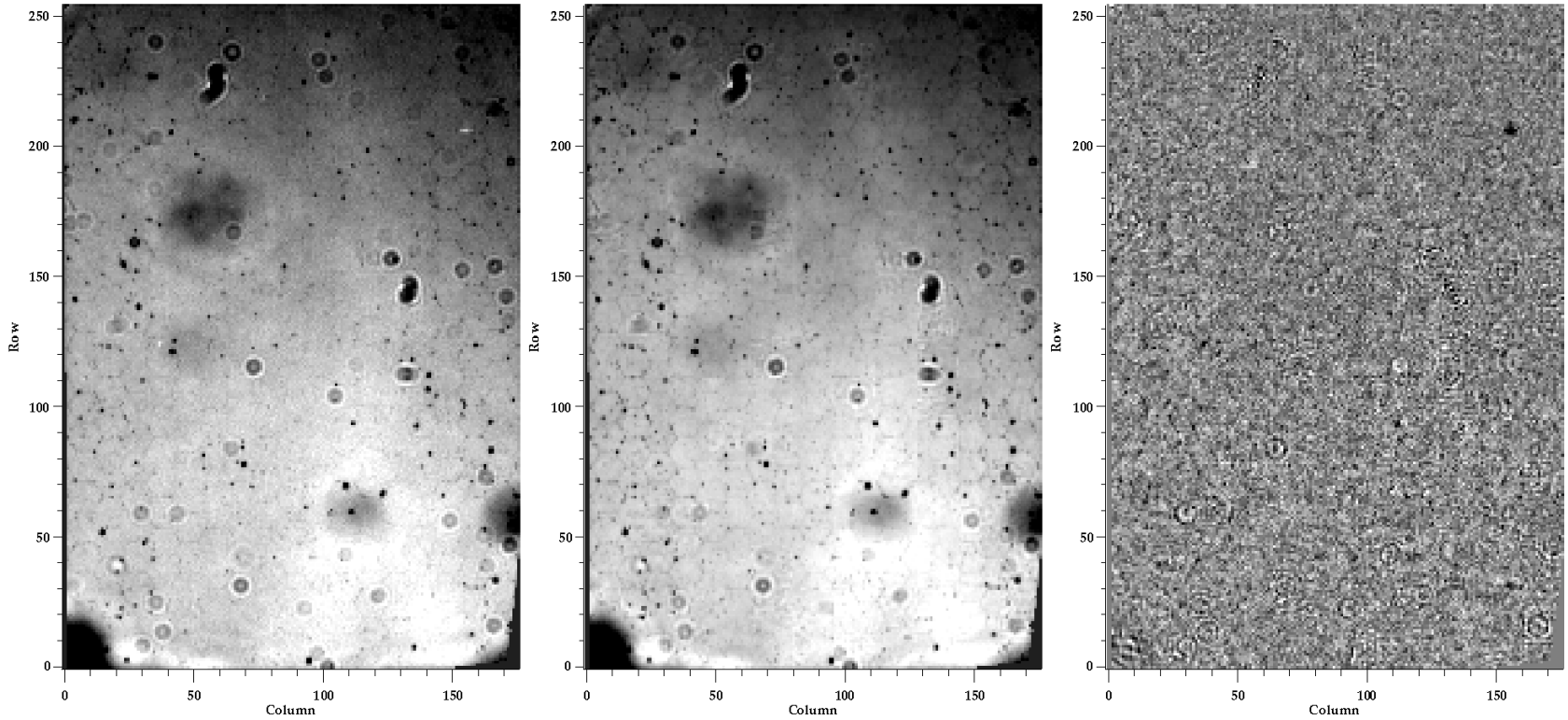

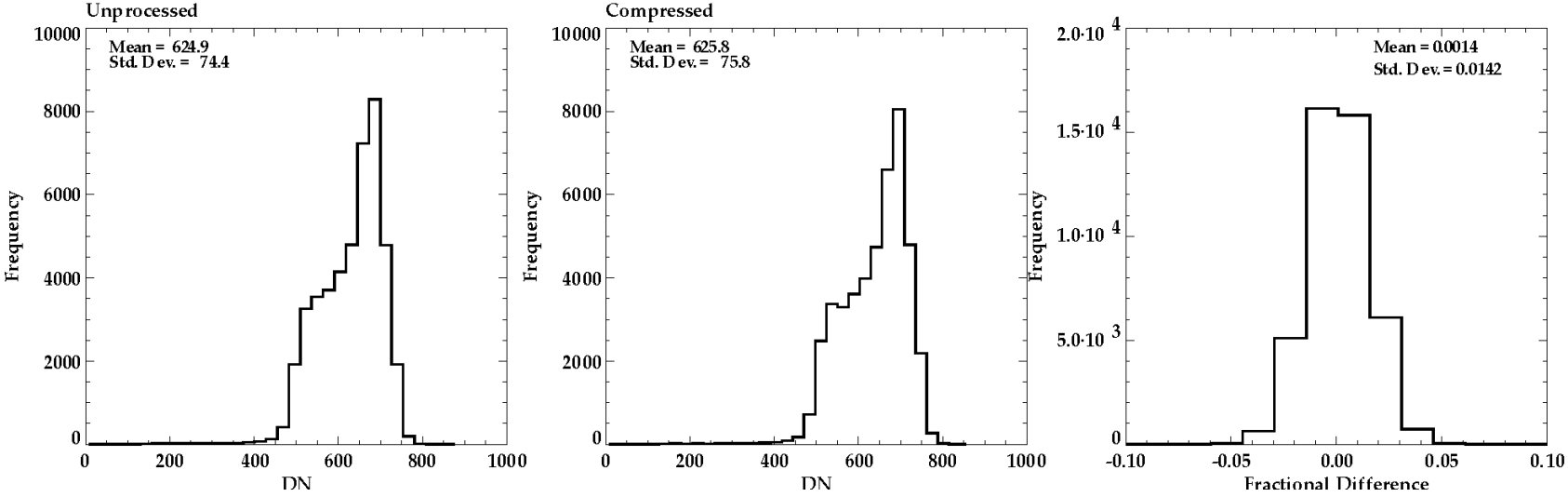

MRI Compressed vs. Unprocessed for F7

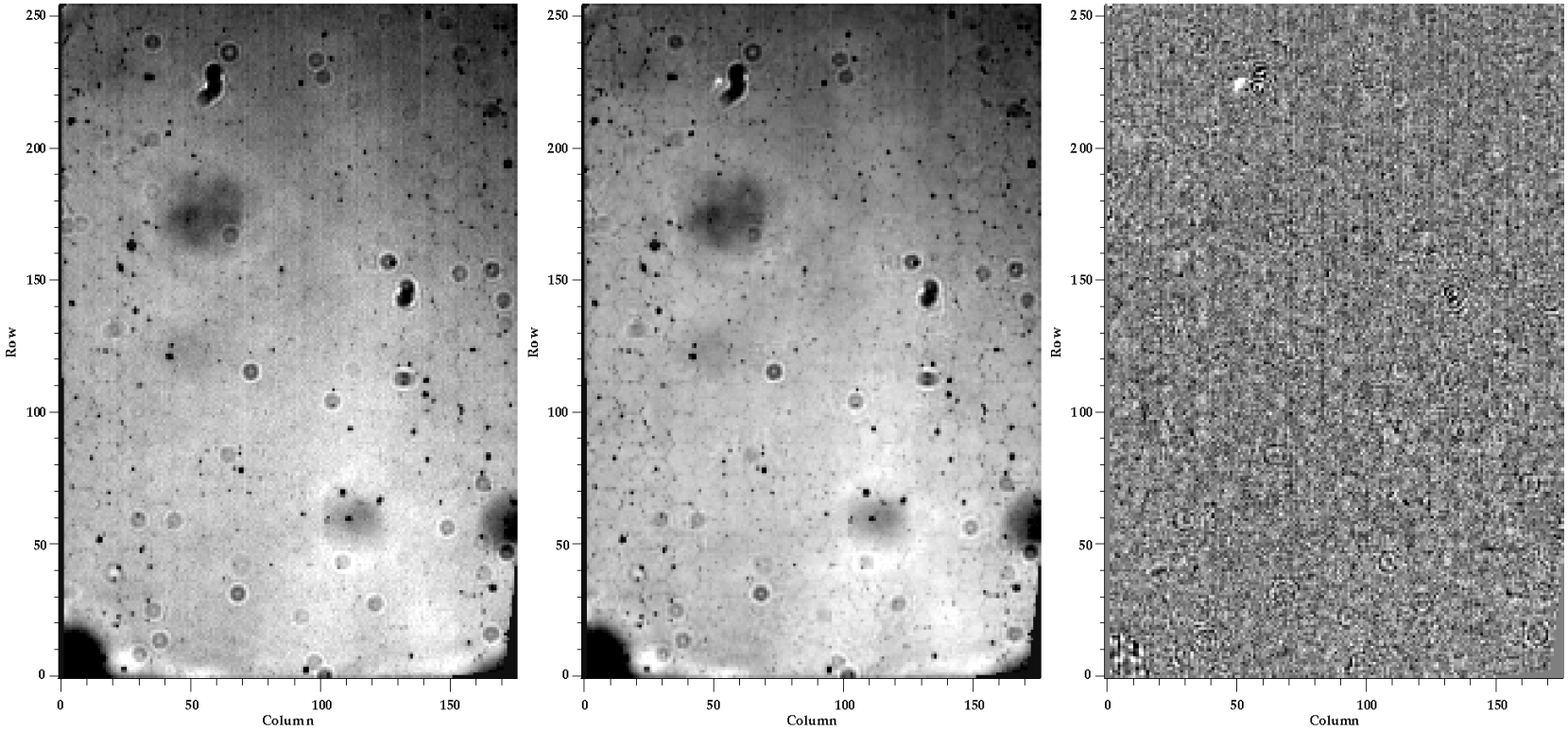

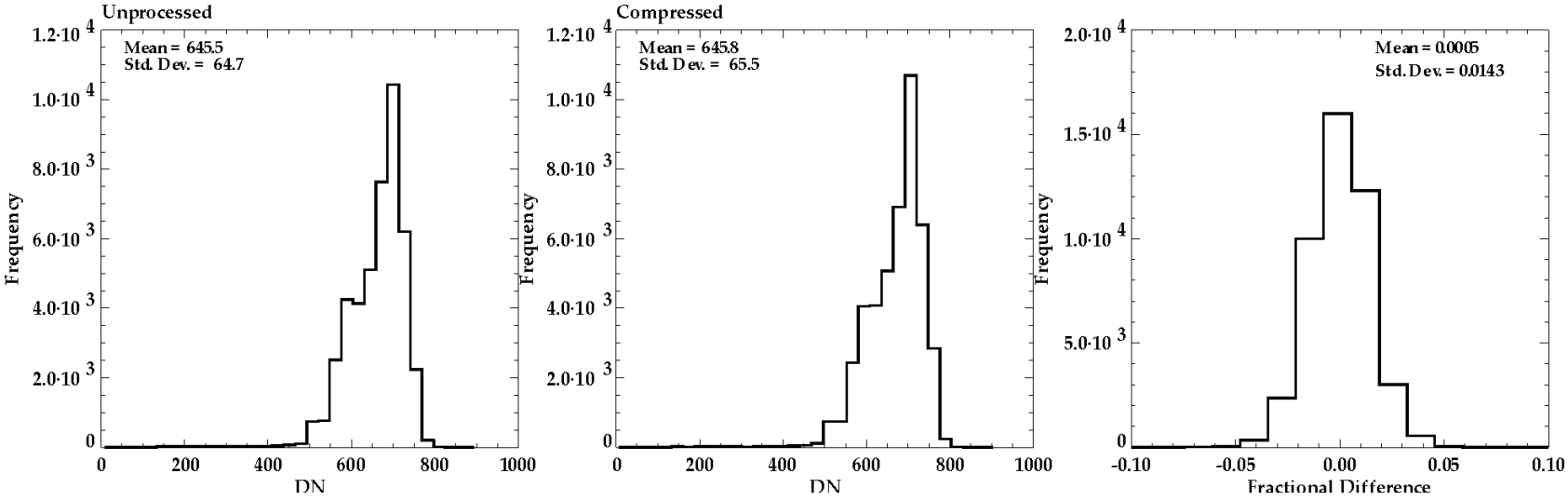

Three points can be made from figure 5.6-5:

1. The quantitative measure of agreement between the unprocessed and compressed image is almost exactly the same (0.0143 in the fractional difference) for both the F1 and F7. This indicates the damage done to compression by the rise in dark current is minimal.
2. Vertical stripes are visible in the difference image are more visible for the F7 than for the F1. These stripes originate in the memory zone dark current. The compression does not follow these linear features perfectly.
3. The 8x compression used introduces artifacts visible in both the F1 and F7 images:
    a. The fiber "chicken wire" pattern is emphasized in the compressed image.
    b. Larger, low-contrast features are lost or diminished in the compressed image.

Conclusions from HRI and SLI images are the same.

The situation during descent may not be much different, except the scene will certainly be very different. Although the mean dark current rate may double, the exposure times will typically be shorter by a factor of two or more. The situation will be worse in the memory zone. Here a few hot pixels have been created which cause vertical lines in the image as the pixels are shifted through them. These will get more numerous as the mission progresses. If the probe is heated significantly prior to entry, as is now being discussed, the first images may contain more dark current and the period of "warm" images will be slightly extended.

In order to extrapolate the dark current into the future, we build synthetic images. The true scenes for the three imagers are taken to be the projected slide images used in figure 5.6-1, above. The dark current is estimated from examination of the histograms of the dark current rates during the F3 (433 days after launch), F5 (841 days after launch), and F7 (1254 days after launch) checkouts. The descent occurs 2648 days after launch.

Cumulative histograms of the dark rates may be formed for each of these three checkouts for both the image and memory zones. The largest number of counts/sec which is truly due to dark current rather than cosmic rays is estimated at 700. This number has not changed appreciably over the checkout duration. We project the dark rate distributions to the time of descent by projecting the cumulative histograms vs. time. The results are shown in Figure 5.6.1-1.

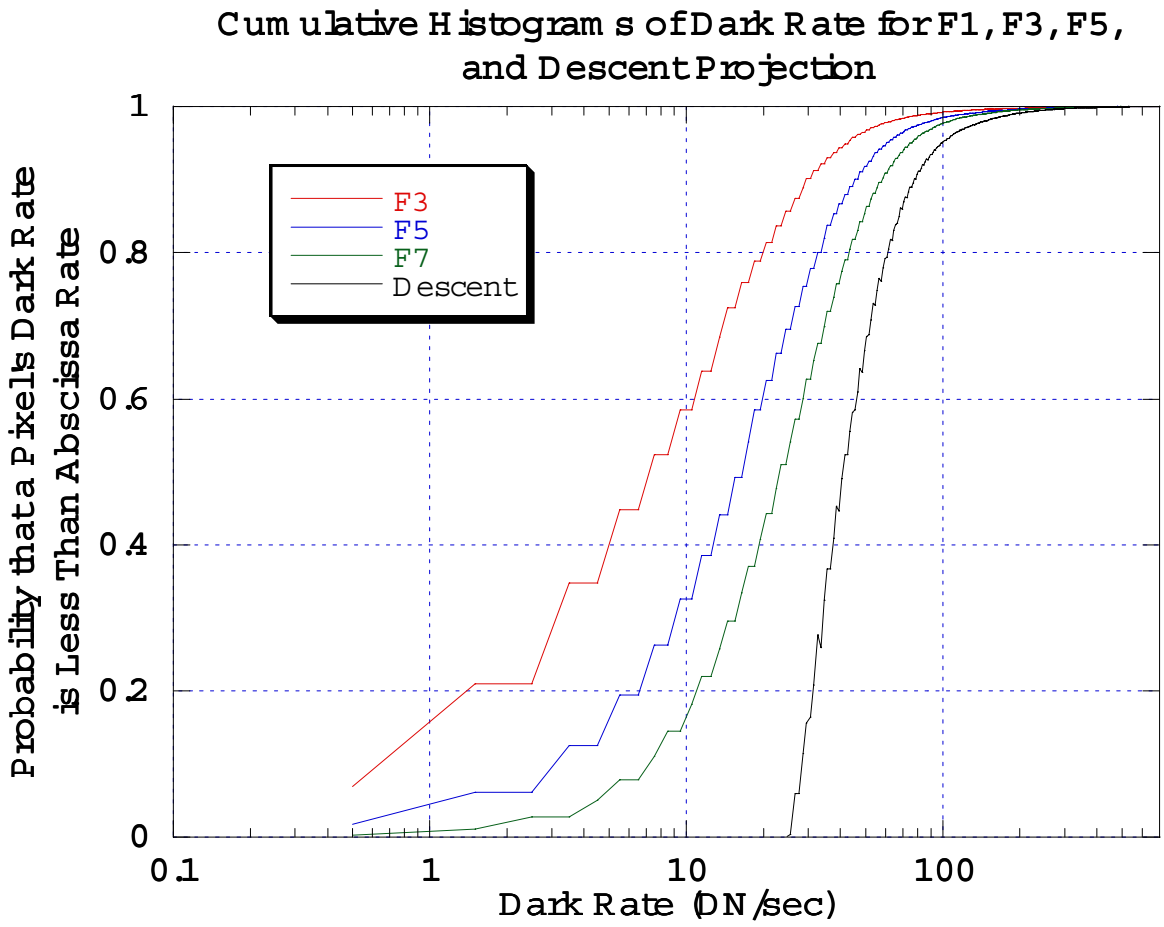

Figure 5.6.1-1 Cumulative histograms giving the probability than a pixel has dark current less than the abscissa value. The Descent curve is computed by extrapolating the best linear fit through the F3, F5, and F7 data downward at each abscissa value.

If the ordinate is divided by the number of pixels, the cumulative histogram shows the probability that a pixel will have a dark rate less than the ordinate. A dark rate "image" can then be constructed which satisfies these probabilities. That can be added to the "true scene", and the resulting image can be run through the onboard processing simulator.

The exposure time multiplies the dark rate for the image zone. Likewise, the temperature dependence of the dark scene can be included using the "known" dependence of the dark current for the image zone, memory zone, and serial register. The bias is assumed to be 8.9 DN.

Using these relationships a synthetic dark current at descent for any exposure time and temperature can be generated. This is added to the "true scene" image. For the projected slide images we perform the following steps in the simulation:

1. Generate the dark image for a specified exposure time and CCD temperature using the predicted descent dark rate probabilities.
2. Choose an unprocessed image of a projected slide with known scene contrast. (Here we have used only the 3% contrast images to provide worst case scenes).
3. Perform a flat field correction of the unprocessed image to eliminate blemishes.
4. Multiply the unprocessed, flat-fielded true scene image by a specified factor to control the brightness of the true scene.
5. Add the true scene image to the dark image.
6. Perform square root correction, compression by a specified factor, decompression, and "squaring" of the summed image, as the onboard and ground processing would do.
7. Subtract the dark image, leaving the reconstructed true scene.
8. Compare the original true scene to the reconstructed true scene.

The specifiable parameters in this process are:

1. Exposure time (to control the image zone dark current)
2. CCD temperature (to control the image, memory, and serial register dark current rates)
3. "Brightness" factor (by which the flat-fielded true scene is multiplied)
4. Compression factor

In the comparison images we fit a two-dimensional polynomial surface to the true scene to remove large-scale gradients. Both the true scene image and the reconstructed true scene image are divided by this fitted surface. Finally both scenes are contrast enhanced using the same linear stretch. This will likely be done during interpretation of the real images, so we felt it fair to do it here.

In the study below we fix the exposure time at 50 msec. This is probably an upper limit on the exposure time as imposed by the spin rate. For compression factors of 3, 6, and 8, we vary the CCD temperature (266K, 250K, and 220K), brightness factor (0.1 and 0.4), and contrast (3% and 13%), for a total of 36 cases. For each we produce two pages of comparison images as well as a plot comparing the photometric profiles. We consider these figures of merit: the RMS and maximum photometric deviation in DN between the original and reconstructed scenes for row 106 only, shown in figures 5.6.1-2 through 5.6.1-5.

During this study a minor flaw is the image decompression software was discovered. Dr. Frank Rabe graciously corrected this error, providing version 3.40 of the decompression software. In Table 5.6.1-1 we show a comparison of the decompression performance for version 3.30 vs. version 3.40. We also note that the version in the gse program which routinely decodes the telemetry is an earlier version yet. However we have no easy way to evaluate its performance.

Table 5.6.1-1

Comparison of performance of version 3.30 and 3.40 of the DCS decompressor

Signal	Contrast	Compression Ratio	Temperature	Version 3.30 RMS	Version 3.40 RMS	Change
Low	Low	3	266K	1.27	1.27	0.00
Low	Low	6	266K	2.03	2.03	0.00
Low	Low	8	266K	2.26	2.26	0.00
High	Low	3	266K	3.10	3.10	0.00
High	Low	6	266K	3.95	3.95	0.00
High	Low	8	266K	3.95	3.95	0.00
Low	Low	3	250K	0.71	0.71	0.00
Low	Low	6	250K	0.98	0.98	0.00
Low	Low	8	250K	0.98	0.98	0.00
High	Low	3	250K	2.85	2.85	0.00
High	Low	6	250K	3.46	3.46	0.00
High	Low	8	250K	3.46	3.46	0.00
Low	Low	3	220K	0.67	0.67	0.00
Low	Low	6	220K	0.94	0.94	0.00
Low	Low	8	220K	0.94	0.94	0.00
High	Low	3	220K	2.61	2.61	0.00
High	Low	6	220K	3.25	3.25	0.00
High	Low	8	220K	3.25	3.25	0.00
Low	High	3	266K	2.04	2.04	0.00
Low	High	6	266K	2.53	2.53	0.00
Low	High	8	266K	2.53	2.53	0.00
High	High	3	266K	4.37	4.37	0.00
High	High	6	266K	5.40	5.40	0.00
High	High	8	266K	5.61	5.45	-0.16
Low	High	3	250K	1.03	1.03	0.00
Low	High	6	250K	1.28	1.34	0.06
Low	High	8	250K	1.41	1.39	-0.02
High	High	3	250K	4.24	4.24	0.00
High	High	6	250K	4.93	4.93	0.00
High	High	8	250K	5.74	5.79	0.05
Low	High	3	220K	1.06	1.06	0.00
Low	High	6	220K	1.22	1.20	-0.02
Low	High	8	220K	1.28	1.26	-0.02
High	High	3	220K	4.08	4.08	0.00
High	High	6	220K	4.63	4.63	0.00
High	High	8	220K	5.13	5.32	0.19

Of 36 cases only 5 have difference RMS errors. Four of these are improvements with the newest software, and one is a degradation. Any changes are generally very small.

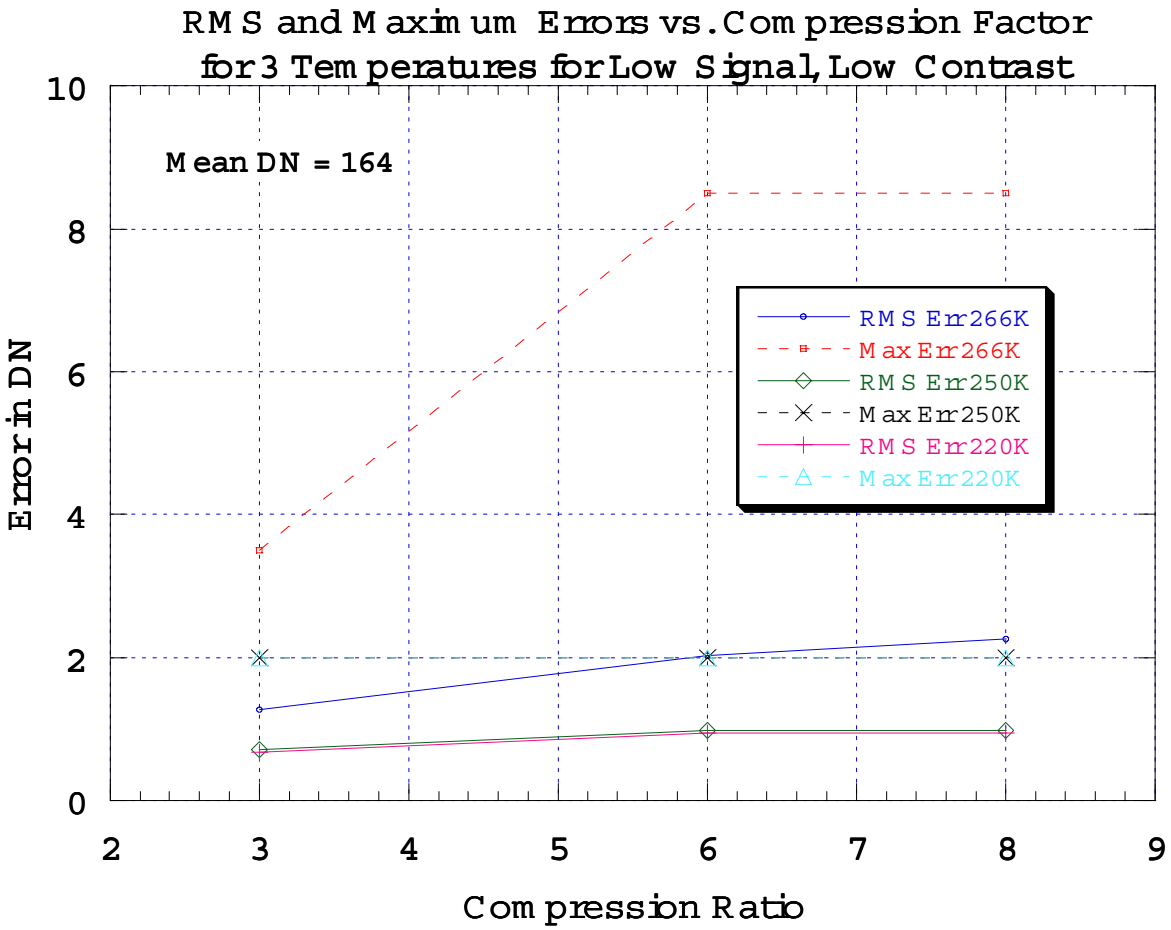

Figure 5.6.1-2 Errors (RMS and maximum) in data number caused by compression for a low signal, low contrast scene for three different compression ratios and three different temperatures.

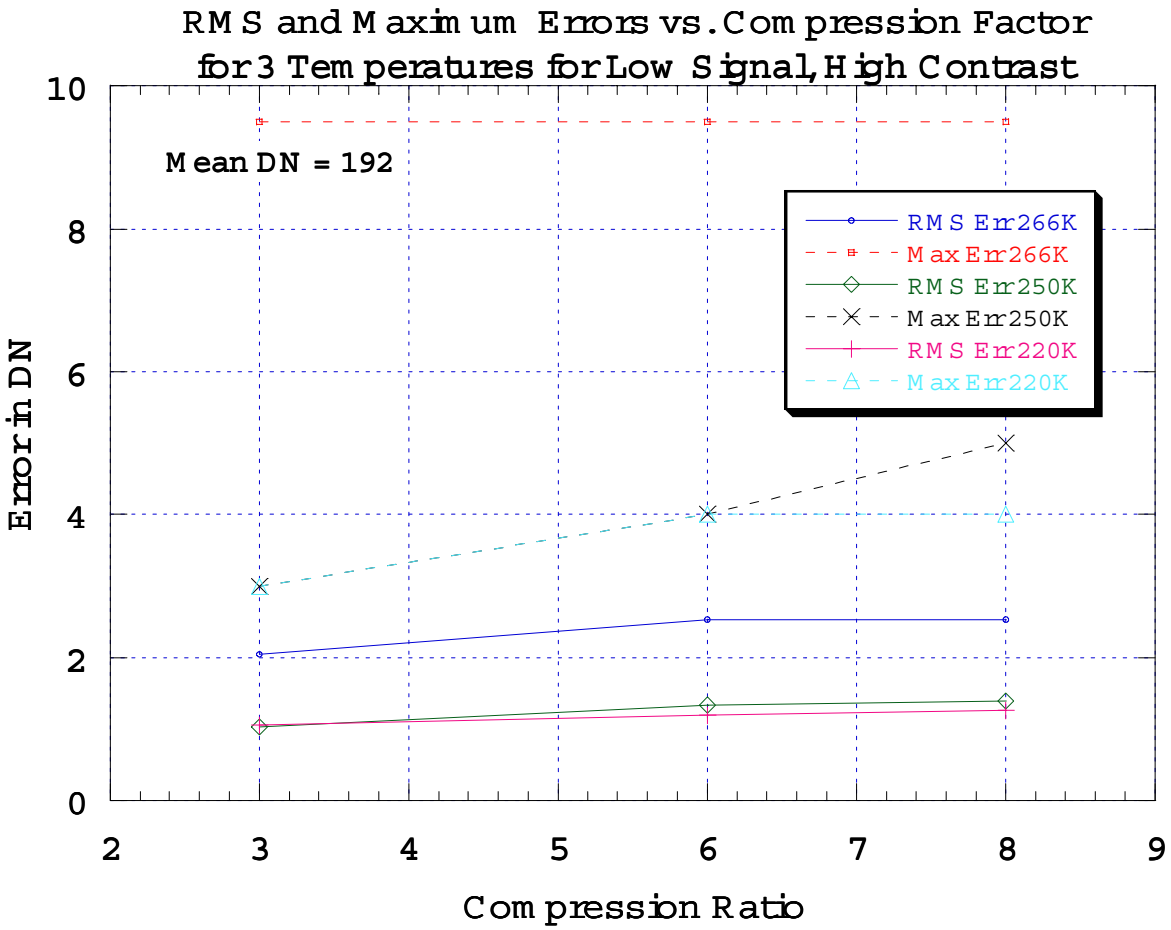

Figure 5.6.1-3 Errors (RMS and maximum) in data number caused by compression for a low signal, high contrast scene for three different compression ratios and three different temperatures.

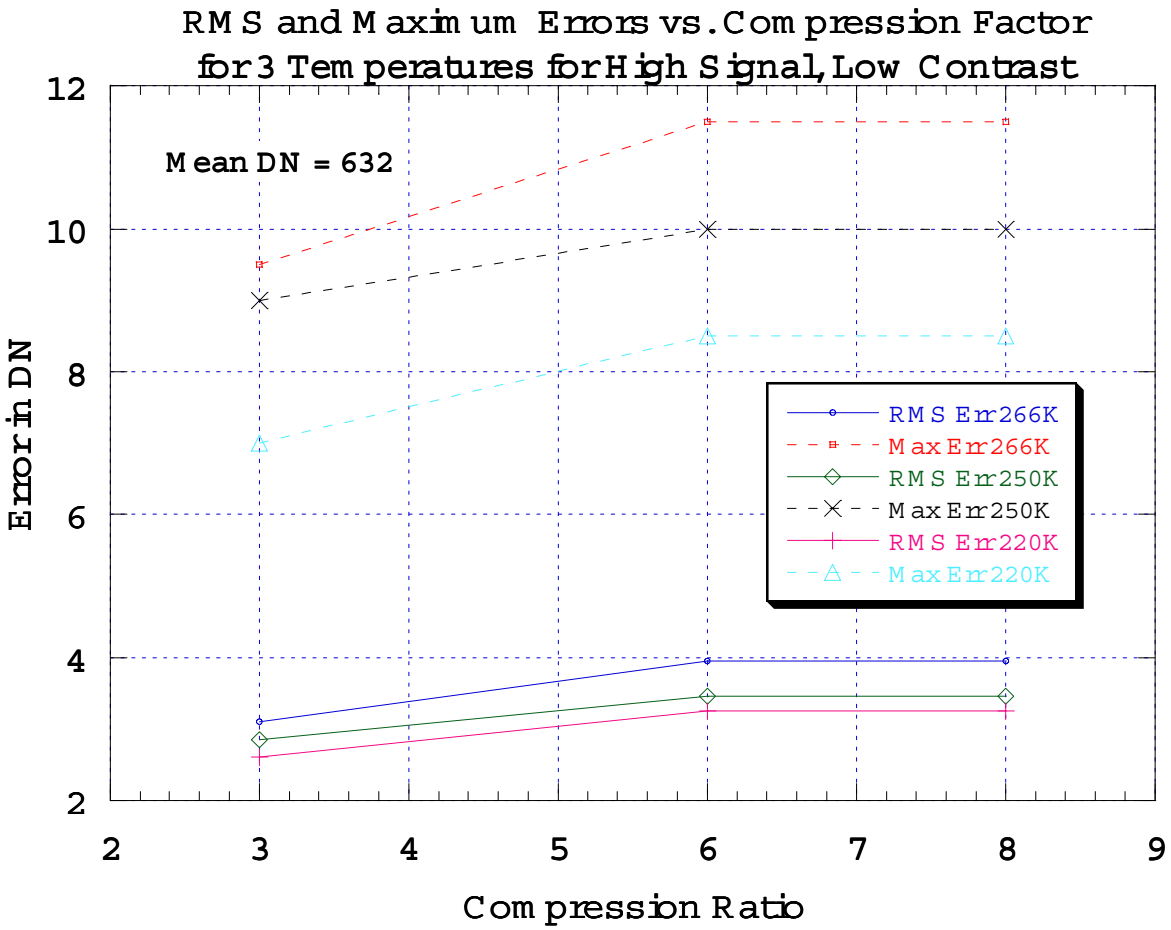

Figure 5.6.1-4 Errors (RMS and maximum) in data number caused by compression for a high signal, low contrast scene for three different compression ratios and three different temperatures.

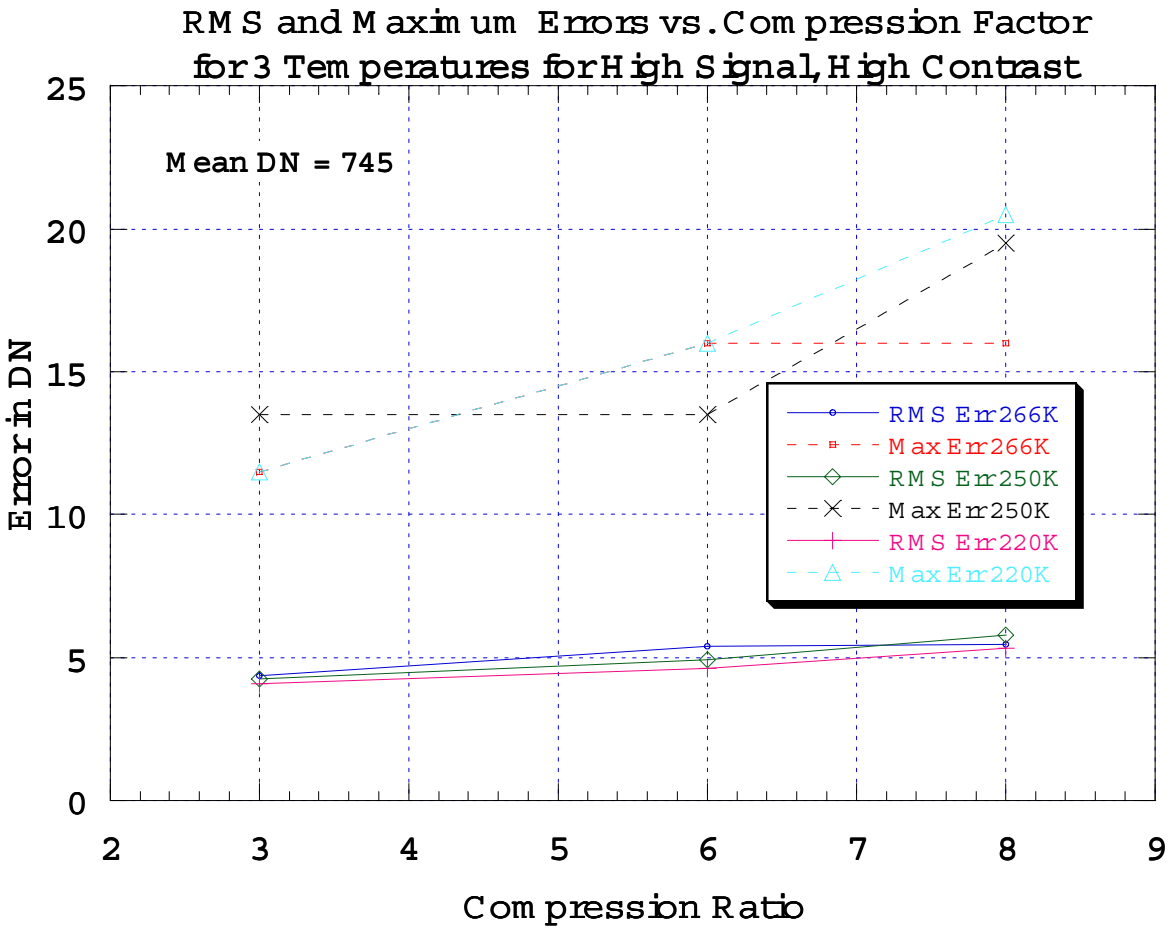

Figure 5.6.1-5 Errors (RMS and maximum) in data number caused by compression for a high signal, high contrast scene for three different compression ratios and three different temperatures.

5.7. Auto-exposure calculation

The flight software is capable of predicting the exposure time for the next exposure at the same azimuth (or at any azimuth if the azimuth of the next image is not constrained). This prediction is made if a flag (bit 3 in the general processing options word) is set. To make this prediction the flight software analyzes the histogram of DNs of the current image. A target is defined such that a specified fraction of the pixels exceeds a specified data number. For images 97% of the pixel DNs must be less than 60% of 4095 (=2457).

Normally the predicted exposure time is calculated using

$$exp\_time_{predicted} = exp\_time_{current} \frac{RF}{X}, \text{ where}$$

R = 0.6
F = 4095
X = the DN which 97% of the pixels are less than

X is determined by analyzing the histogram. As an example suppose 97% of pixels are found to have DNs less than 1500 for an exposure time of 12 ms. Then the predicted exposure time will be $exp\_time_{predicted} = 12.0ms \frac{0.6 \times 4095}{1500} = 19.5ms$.

Note that DNs actually contain a component which is independent of exposure time from the bias and memory zone dark current, whereas the algorithm above neglects this. This causes the algorithm to slightly underestimate the necessary change in exposure time. If a large fraction of the DN is generated by light and image zone dark current (components of the DN which do depend of exposure time), this underestimate makes a neglible error. However if a large fraction of the DN is generated by the bias and memory zone dark current, the underestimate of the correction will be larger.

The auto exposure algorithm also contains special cases for extreme under exposure and over exposure. These are necessary for cases where the algorithm above has insufficient information to work correctly. An example is an image which is entirely saturated. If all data values are 4095, then the algorithm will decrease the exposure time by less than a factor of 2. In fact the image may be overexposed by many times. Therefore a special test is done to see if more than 92% of the pixels exceed DN 4088. If they do, the exposure time is decreased by a factor 10. The criterion for the lower limit is 92% of the pixels less than DN 7.

If DCS compression is required, the pixel values have 8 subtracted from them before the tests are performed. If DCS compression is not required, the pixel values do not have 8 subtracted from them before the tests are performed. This appears to lead to some problems in the flight software.

Table 5.7-1

Consequences of subtracting 8 DN from images

Exp./Compression	Min possible DN	Max possible DN	Status
Under exposure with DCS compression	0	-	OK
Under exposure without DCS compression	8	-	Bad, because no pixel will have DN 7 or less
Over exposure with DCS compression	-	4087	Bad, because no pixel will have DN 4088 or more
Over exposure without DCS compression	-	4095	OK

The software does not provide for different limits depending on whether DCS compression is required or not. It should be designed for the case where DCS compression is required, because that it the case planned for descent. In this case the 4088 criterion should be reduce to (4087-8) = 4979. Probably this number should be reduced even more, because the fiber optic transmission is quite low for many pixels which are not mapped out in the bad pixel map. Fixing this flight software problem is currently under discussion.

5.8. Ground software processing

5.9. Photometric Reduction Summary

For DCS-compressed images the flight software performs the following operations on the raw data numbers:

1. Bad pixel replacement
2. Flat field correction (after subtracting 8 DN from each pixel for "dark current")
3. (Adaptive) square root translation to 8-bits/pixel
4. DCS bad pixel replacement
5. DCS image compression

The GSE software then

1. Decompresses the image
2. Translates from 8-bits/pixel back to 12-bits/pixel using the reverse square root table

Some steps, such as compression, are not accurately reversible, of course. Otherwise this process works, except for three problems: 1) the flat field at the correct temperature should have been used, 2) the dark current is probably not 8 DN for each pixel, and 3) compressor introduces defects which can be minimized. An improvement over the standard GSE processing may be made by decompressing the image with more than 8-bit precision (i.e., keeping fractional DN values upon decompression), then interpolating in the reverse square root table. This results in more than 256 gray levels for the reconstructed image.

A separate document on minimizing image defects, Processing of Compressed DISR Images, has been written by Erich Karkoschka. To enable use of Erich's algorithms, software has been written to extract the compressed data directly from the DISR data stream.

Following ground-based reconstruction of the image one needs to performs the following steps to obtain a photometrically calibrated image:

1. multiply by the flat field used by the flight software
2. add 8 DN to each pixel
3. subtract the actual dark current (from a dark current model) from each pixel
4. divide by the exposure time in seconds
5. divide by the absolute responsivity of each imager pixel at the correct CCD temperature

One might also consider flagging those image pixels which have been replaced, either through the bad pixel map or flat-fielding algorithm. Note that the derived radiance is within the spectral bandpass of the imager filter at the current temperature.

6.0. Improved Processing of Compressed DISR Images

E. Karkoschka

6.1. Abstract

DISR images of Titan will be transmitted with only about 1 bit/pixel, a compression ratio (CR) of 8. Most of our tests with such compression turned out more or less satisfactory, except that the compressed images contained many small-scale features that were not present in the original images. However, this unwanted property is not due to the compression but due to the decompression software that we used until now. By modifying the decompression algorithm, we successfully decreased or eliminated image defects and produced images resembling the original image significantly better.

6.2. The Discrete Cosine Transform

DISR images get divided into 16x16 pixel blocks. In each block, a discrete cosine transform is performed by the compressor, which produces 256 coefficients resembling the amplitudes of various spatial frequencies. The lowest frequency, the constant, is always transmitted accurately. The three highest frequencies are never transmitted. The remaining 252 coefficients are grouped into 63 quadruples. If a quadruple contains a coefficient with an absolute value larger than a certain threshold (which depends on the image and the CR), all four coefficients of the quadruple are transmitted, otherwise none is transmitted. All transmitted coefficients are rounded down to a certain binary digit, called the quantization (which also depends on the image and the CR). By knowing the quantization and threshold for a compressed image, one knows the compression method and thus for each coefficient the possible range of values. The current decompression software chooses the middle of the range. Note that previous versions had some errors, or they made a less optimal choice. Choosing the middle of the range is often not the best choice as explained below.

While the quantization is transmitted, the threshold is not, unfortunately. Thus, before one can give any uncertainty for a photometric or positional measurement, and before one can do image processing, one has to estimate the threshold.

6.3. Estimation of the Threshold

At first, the maximum absolute value of the four coefficients in each quadruple is evaluated. A histogram of these maxima clearly shows the threshold to the size of the quantization. For example, if the transmitted values are 0, ± 4, ±8, etc. , and no transmitted maximum is 0 or 4, but some are 8 and higher, then the threshold was between 6 and 10. The frequency of occurrence for the next three values (in our case 12,

16, and 20) is used to extrapolate for the frequency of occurrence between 6 and 10, using an almost exponential function. This yields to the estimation of threshold. For example, if values of 8 occur much less often than values of 12, then the cut-off was close to 10. On the other hand, if values of 8 occur as often as expected from the trend for 12, 16, and 20, then the cut-off was close to 6. Since an image has typically some 1000 transmitted quadruples, this statistical method works quite well. In some 100 test cases, the method found the exact threshold in 80 % of the cases and a value typically only some 5 % smaller or larger in the remaining cases, which is better than required for our purpose.

6.4. Unbiased Estimation of Coefficients

All investigated images have a distribution of amplitude coefficients strongly peaked at zero. For the high frequencies, the peak is narrower and higher than for low frequencies. Therefore, the original estimation of each coefficient by the middle between the minimum and maximum possible value is not an unbiased estimation. In the new software, the estimation is closer to zero in order to account for the distribution peaked at zero. For high frequencies, the modification is larger than for low frequencies due to the stronger peaked distribution. For simplicity, the modification is not based on the image.

This modification of coefficients is especially important for images with high dark current where the dark subtraction effectively adds a small constant to each amplitude. Thus, with the original decompression, all deleted coefficients are displayed in the final image as non-zero coefficients, producing high frequency noise. With the modification, the final amplitudes are much closer to zero.

6.5 Smoothing 16x16 Pixel Block Boundaries

The last step yields acceptable images within each 16x16 pixel block. The images are about as smooth as allowed within the constraints from the transmitted data. However, this is not the case across block boundaries where the noise is uncorrelated, which causes unwanted artificial features along the block boundaries. In order to smooth the image across the block boundaries, the image is divided into 32x32 pixel blocks, shifted by multiples of 16 pixels. Thus, the 16x16 pixel blocks away from the edges appear in four 32x32 pixel blocks each.

In each 32x32 pixel block, a discrete cosine transform is performed. The amplitudes are then decreased in a similar way as in the previous step. Then the image is transformed back. This method smoothes out the discontinuities across the two center boundaries in each 32x32 pixel block. The whole image is then constructed by weighted averaging the four data for each pixel from its four 32x32 pixel blocks.

This smoothing operation decreases amplitudes of features that are close to the noise limit. Thus, features that almost could be noise or could be introduced by compression artifacts will appear with decreased amplitudes. Investigation of many images indicated that this is superior for most purposes since noise and image artifacts are strongly reduced while features well above the noise level are not affected. Nevertheless, the amount of smoothing is left as a free input parameter (a parameter of 1 means standard smoothing, 2

means twice as much smoothing, etc.). In cases where one is interested in very subtle features, the smoothing should be less. On the other hand, if one wants to be sure that there are no visible image artifacts, the smoothing should be larger.

The smoothing operation actually takes place with square-rooted data numbers so that a specific amount of smoothing will causes the same amount relative to the CCD noise (which is constant in square-rooted data numbers). The software also evaluates how many more features there are across 16x16 block boundaries relative to the interior of a block. Based on this excess and on the known CCD noise, the program selects the standard amount of smoothing.

6.6 Rounding

The original decompression algorithm rounds all pixel values to integers, between 0 and 255. This means that the data numbers in the final image have only 256 possible values between 0 and 4095. In regions of the image with slowly changing data numbers, this causes disturbing steps. In the new version, data numbers are multiplied by 8, square-rooted values are multiplied by 128 (range 0-32767 in both cases) before rounding to integers occurs. This decreases the steps so that they are invisible.

6.7 Bad Rows at Top/Bottom

DISR gives images where a few CCD rows at the top and/or bottom are not exposed to light and thus have data numbers very different from the rest of the image, producing artificial sharp features. These edges do not exactly get transmitted causing ringing inside the exposed part of the image. The new decompression software has the ability to specify the number of bad rows at the bottom and top. This will cause the top and bottom 32x32 pixel blocks to be shifted accordingly towards the inside for smoothing so that the ringing is decreased. Therefore, accurate specification of the number of top and bottom bad rows is important.

Some images have also bad areas close to the left and/or right edge. The software is not designed to handle those. These areas should be replaced by data numbers of neighboring valid pixels so that all the high frequency information of these boundaries do not need to be transmitted over and over again.

6.8 Figures

The decompression algorithms are shown with three representative images: first, an image of a part of Ganymede taken by Galileo (which has higher contrasts than expected on Titan due to its low illumination angle), second, an image (repeated twice) of the forest in the Catalina Mountains (which also has higher contrasts than expected on Titan), and third, a low-contrast image with high dark current added, simulating the beginning of the descent. Each of the three images is shown in seven versions:

1: original CCD image

2: image with compression ratio of 4 with original decompression scheme

3: image with compression ratio of 8 with original decompression scheme

4: image with compression ratio of 8 with new decompression scheme, no smoothing

5: image with compression ratio of 8 with new decompression scheme, smoothing factor 0.5

6: image with compression ratio of 8 with new decompression scheme, nominal smoothing

7: image with compression ratio of 8 with new decompression scheme, smoothing factor 1.5.

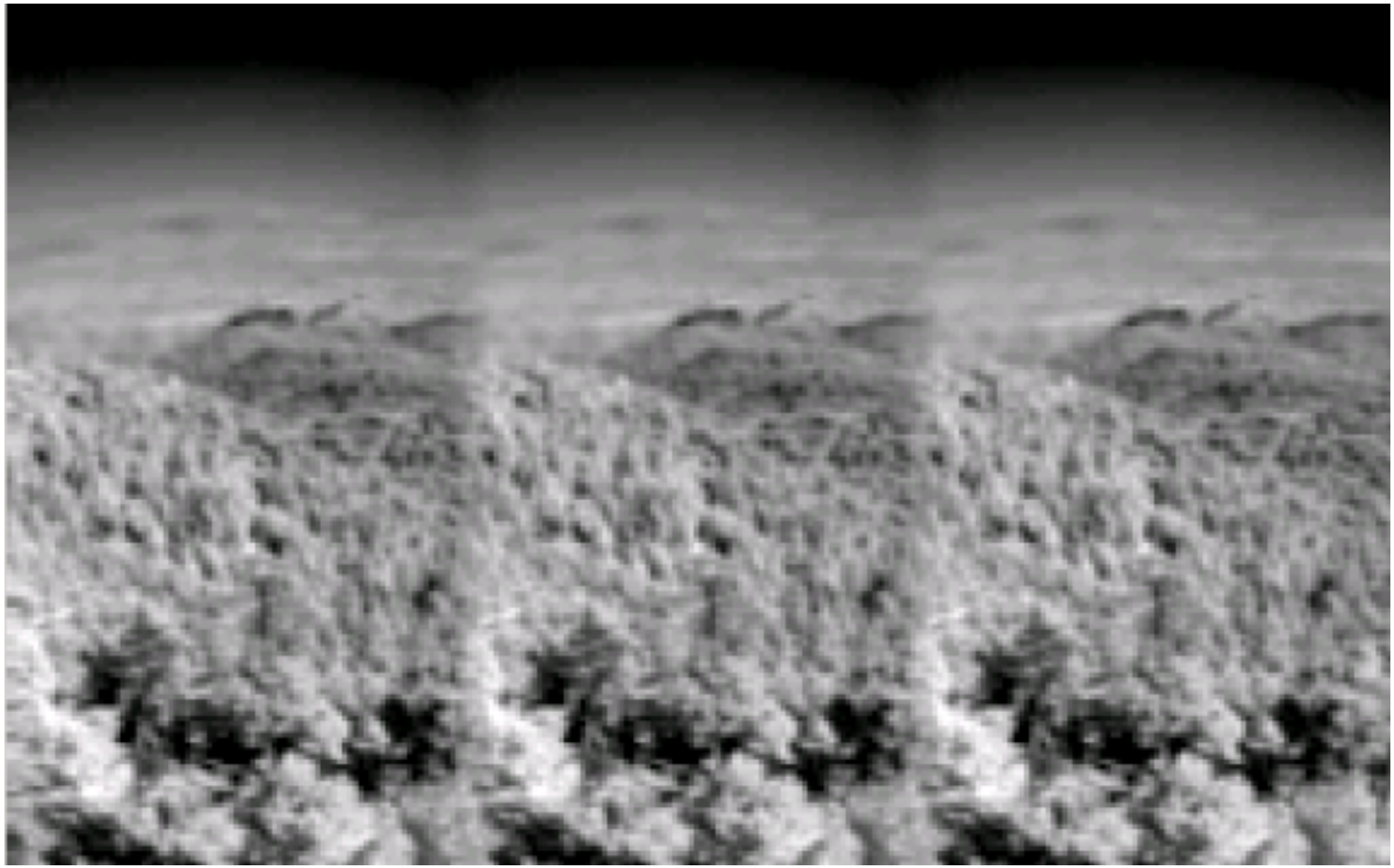

Figure 1a Original Mt. Bigelow scene.

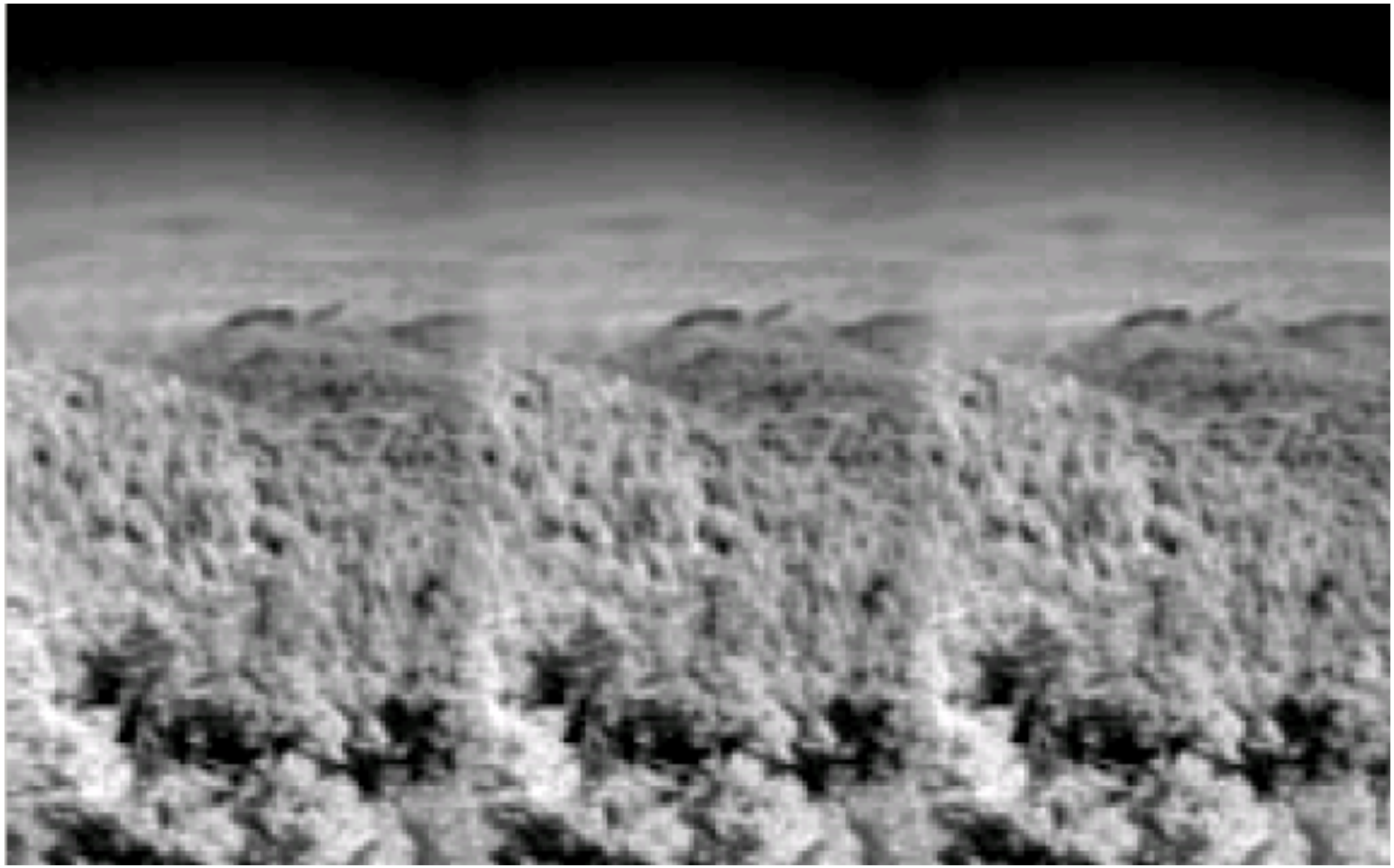

Figure 1b Compression ratio of 4 with original decompression scheme.

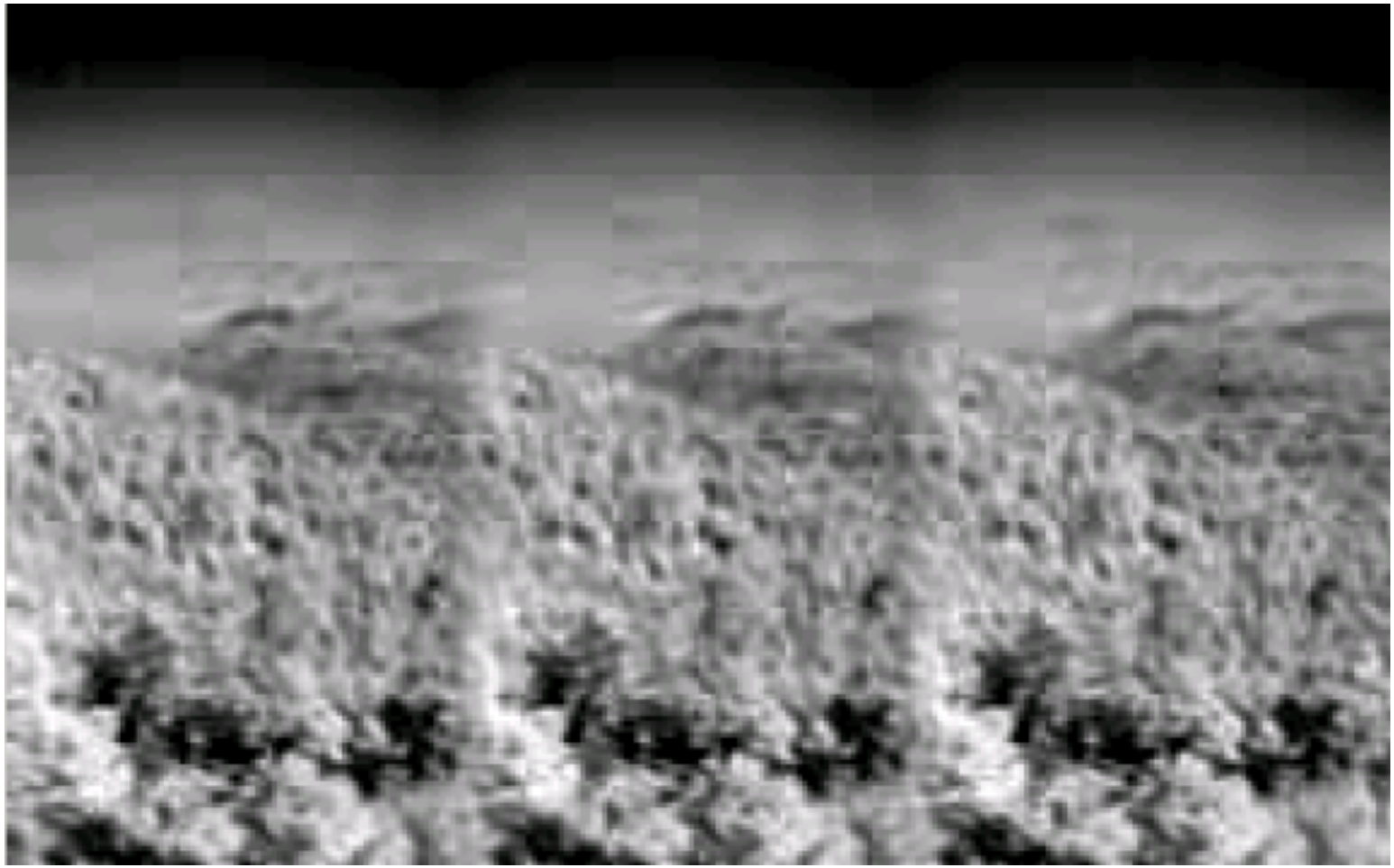

Figure 1c Compression ratio of 8 with original decompression scheme.

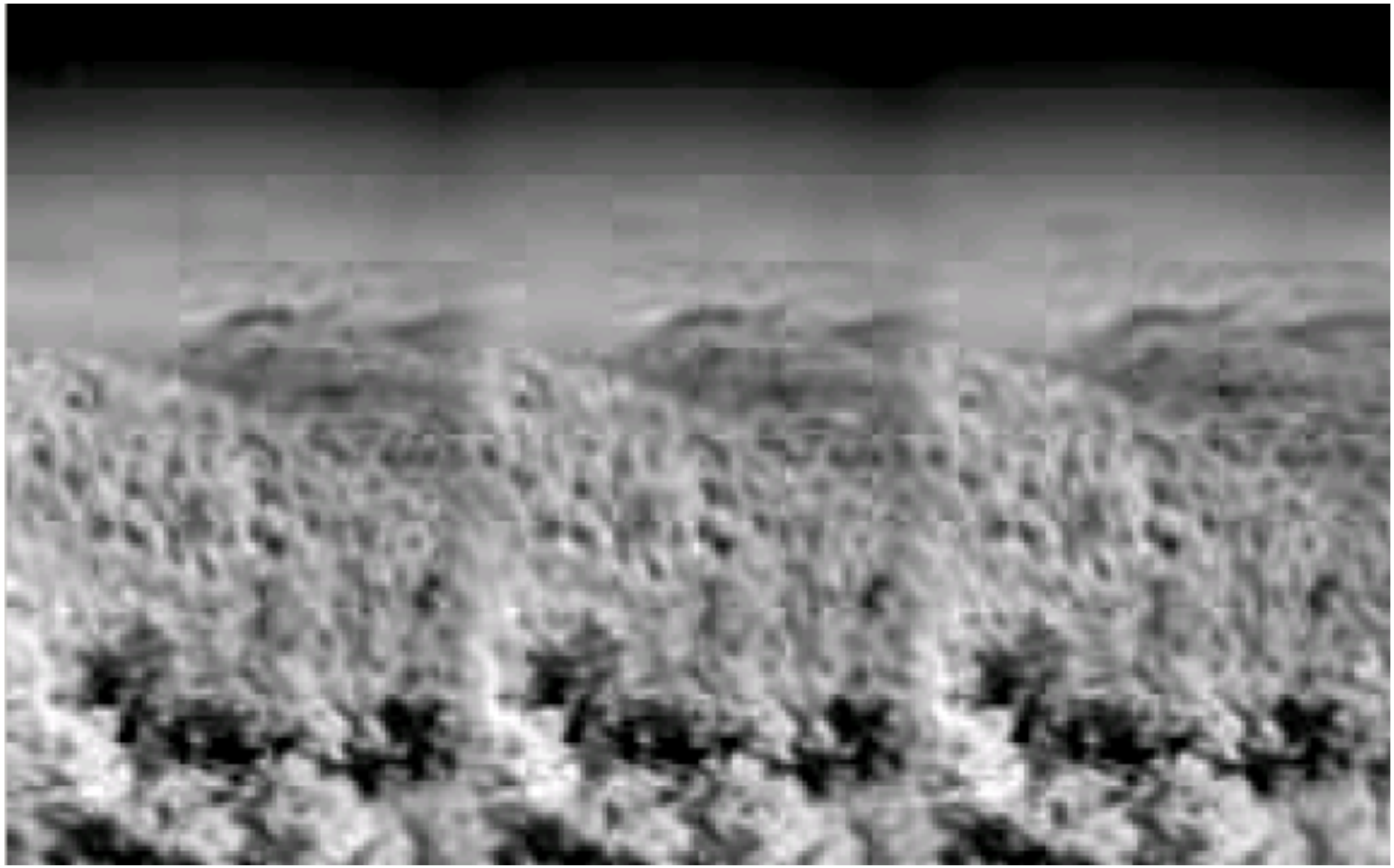

Figure 1d Compression ratio of 8 with new decompression scheme and no smoothing.

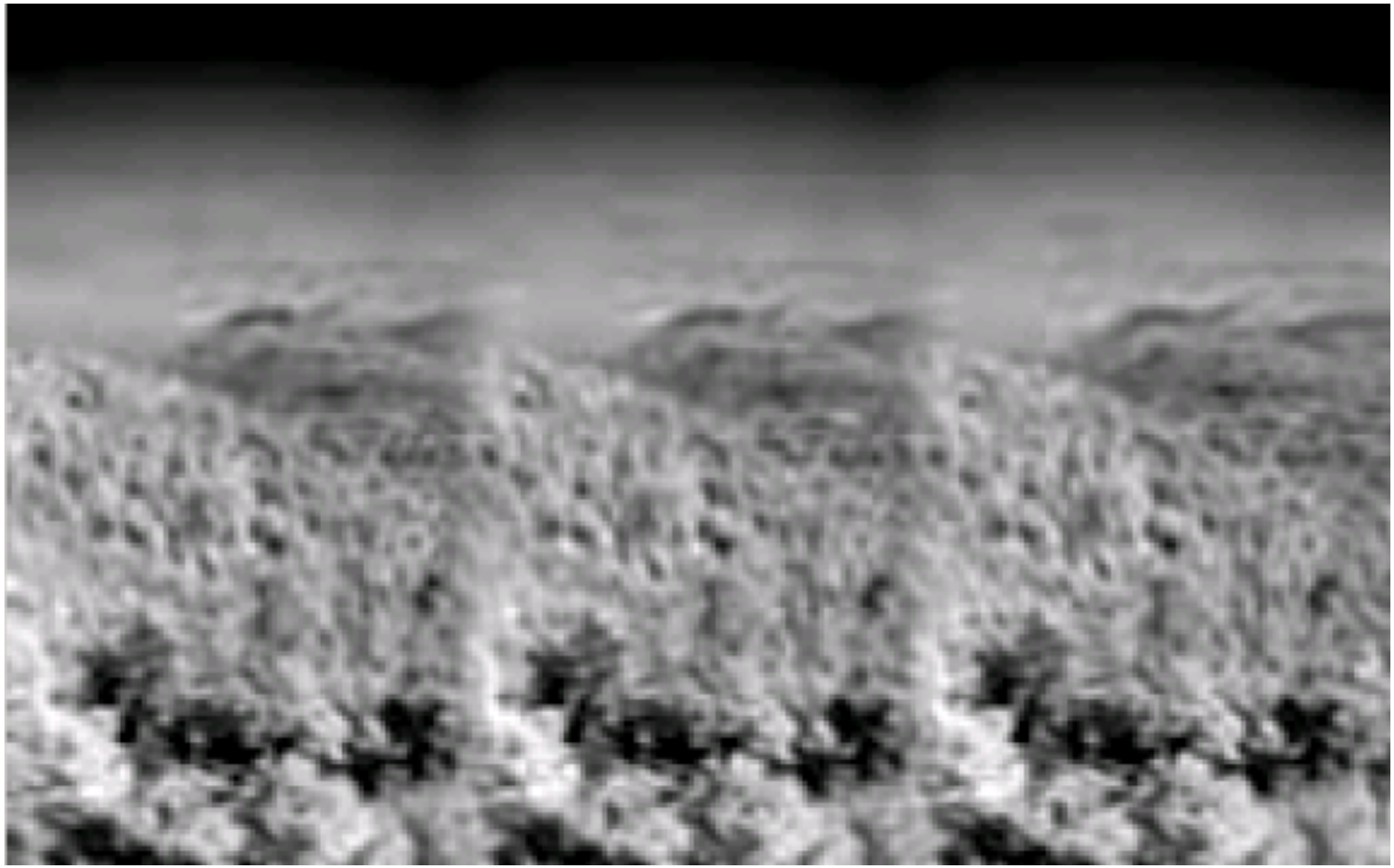

Figure 1e Compression ratio of 8 with new decompression scheme and smoothing factor of 0.5.

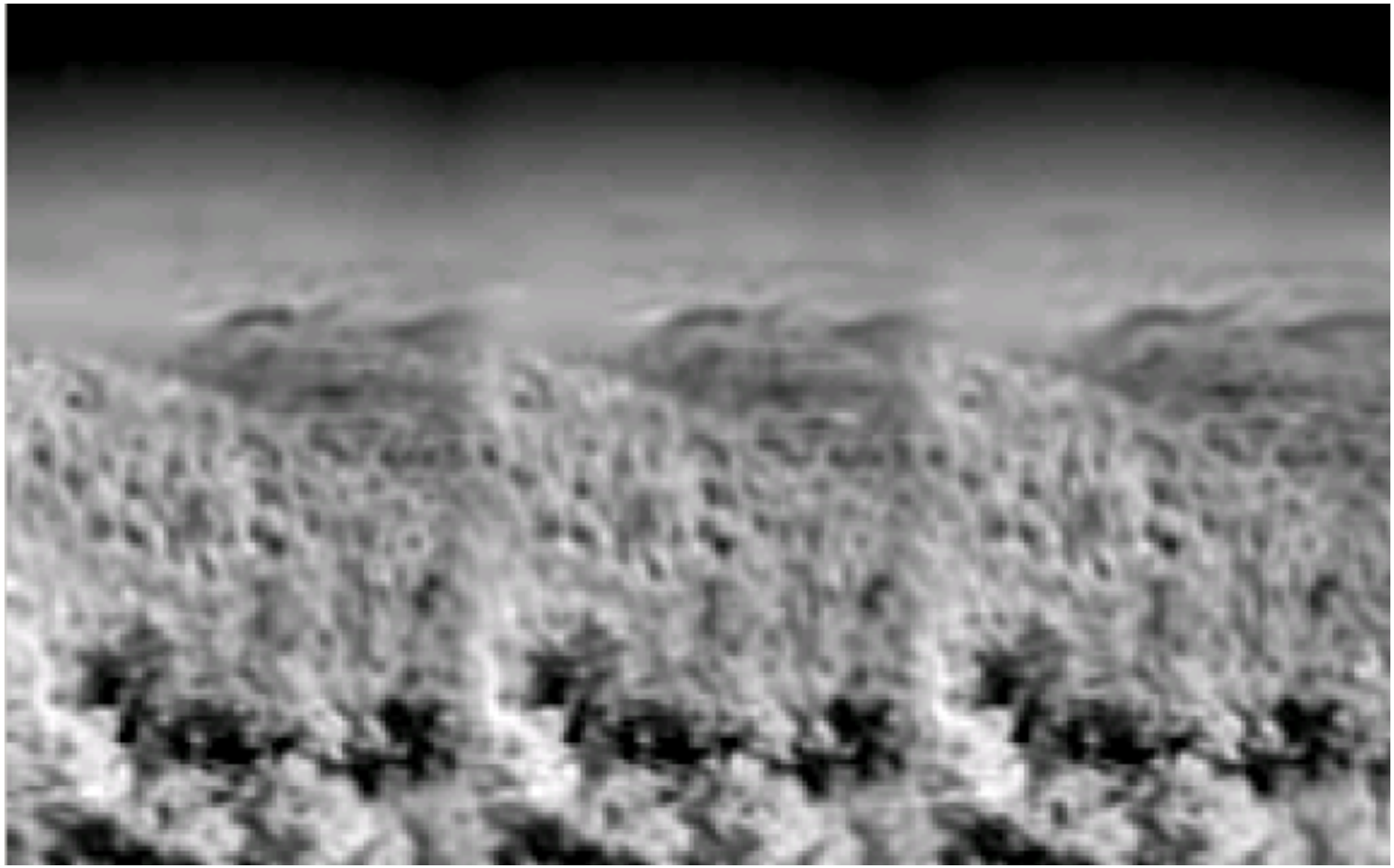

Figure 1f Compression ratio of 8 with new decompression scheme and nominal smoothing.

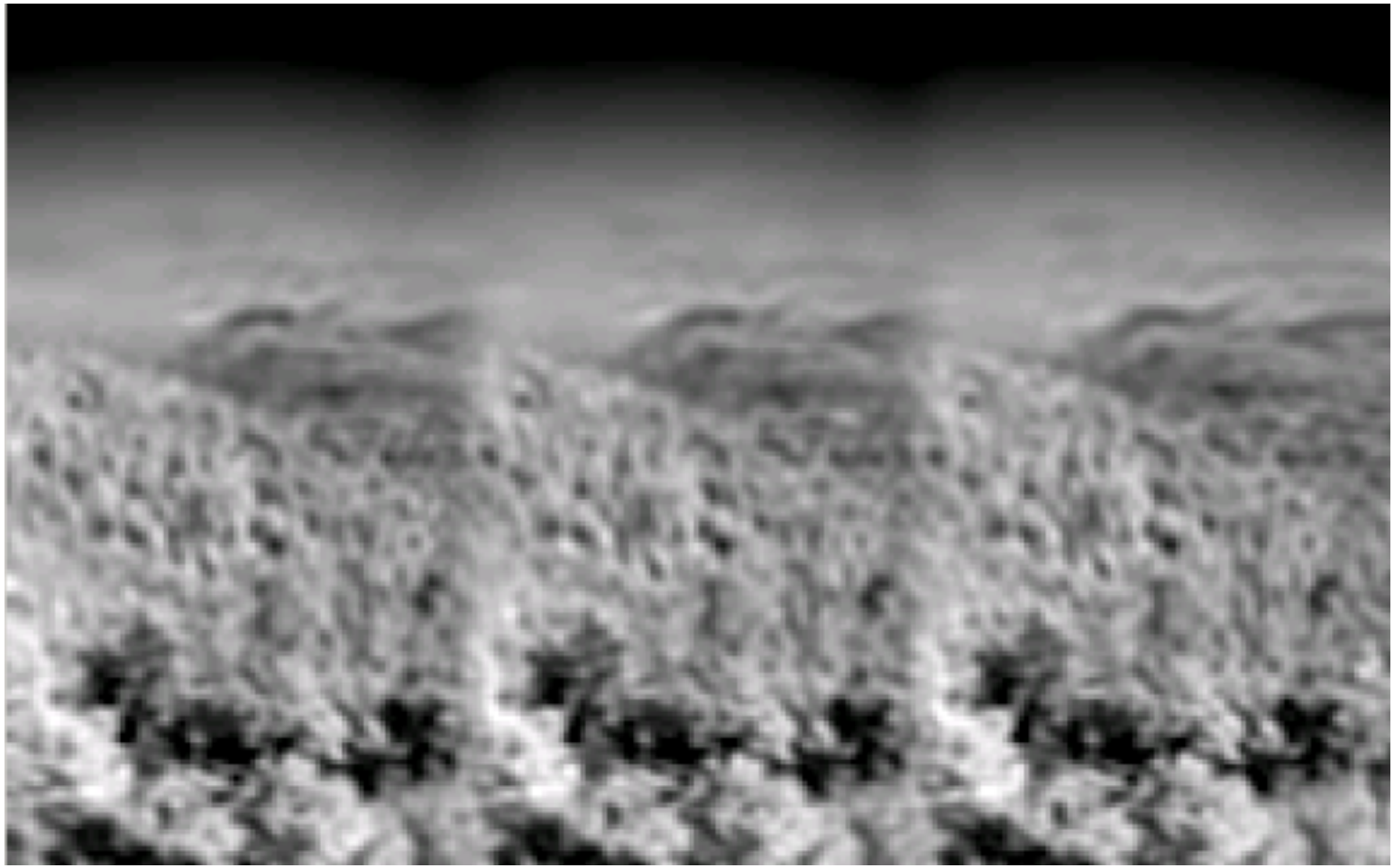

Figure 1g Compression ratio of 8 with new decompression scheme and smoothing factor of 1.5.

Figure 2a Original Ganymede scene.

Figure 2b Compression ratio of 4 with original decompression scheme.

Figure 2c Compression ratio of 8 with original decompression scheme.

Figure 2d Compression ratio of 8 with new decompression scheme and no smoothing.

Figure 2e **Compression ratio of 8 with new decompression scheme and smoothing factor of 0.5.**

Figure 2f **Compression ratio of 8 with new decompression scheme and nominal smoothing.**

Figure 2g **Compression ratio of 8 with new decompression scheme and smoothing factor of 1.5.**

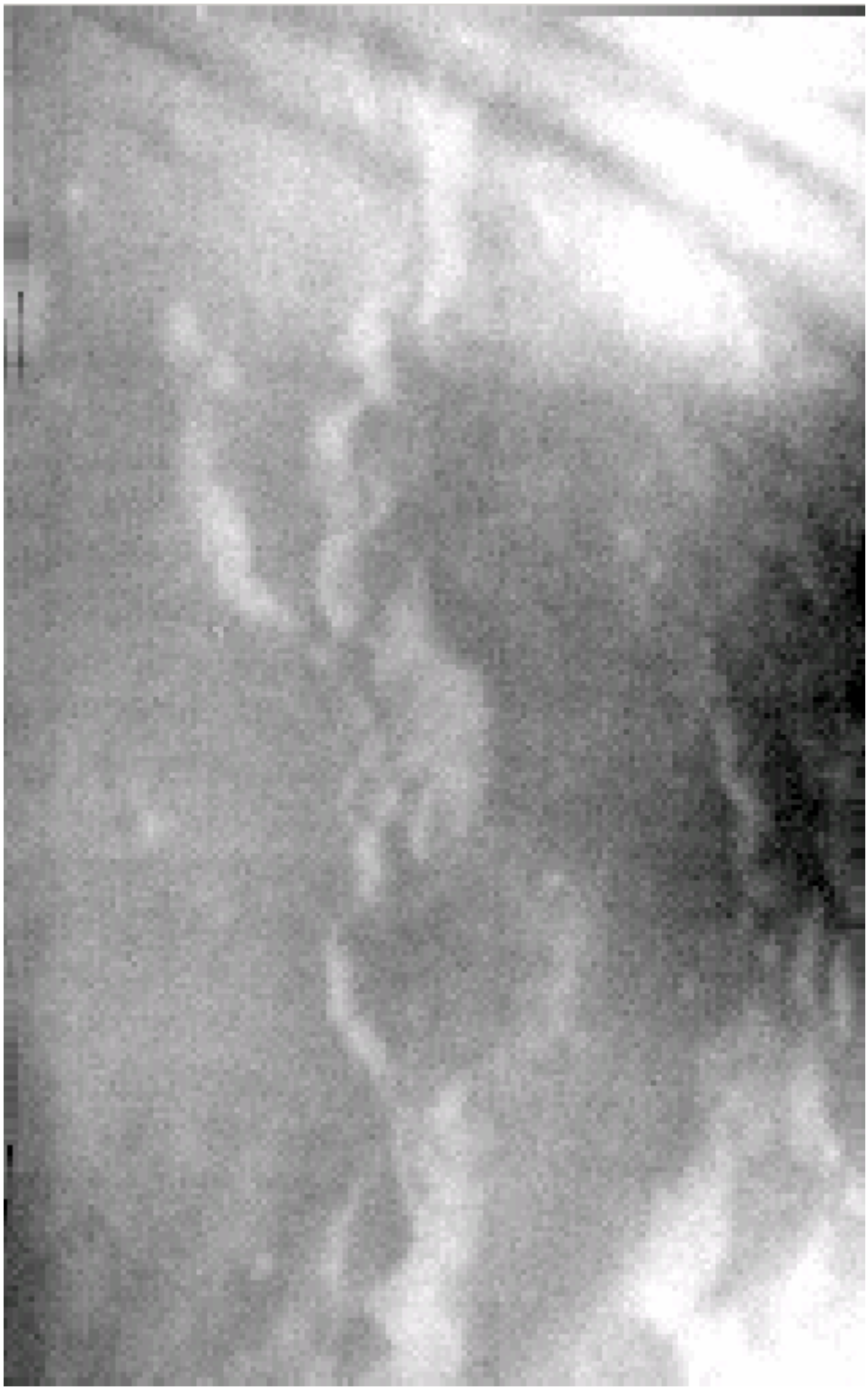

Figure 3a Original LANDSAT scene.

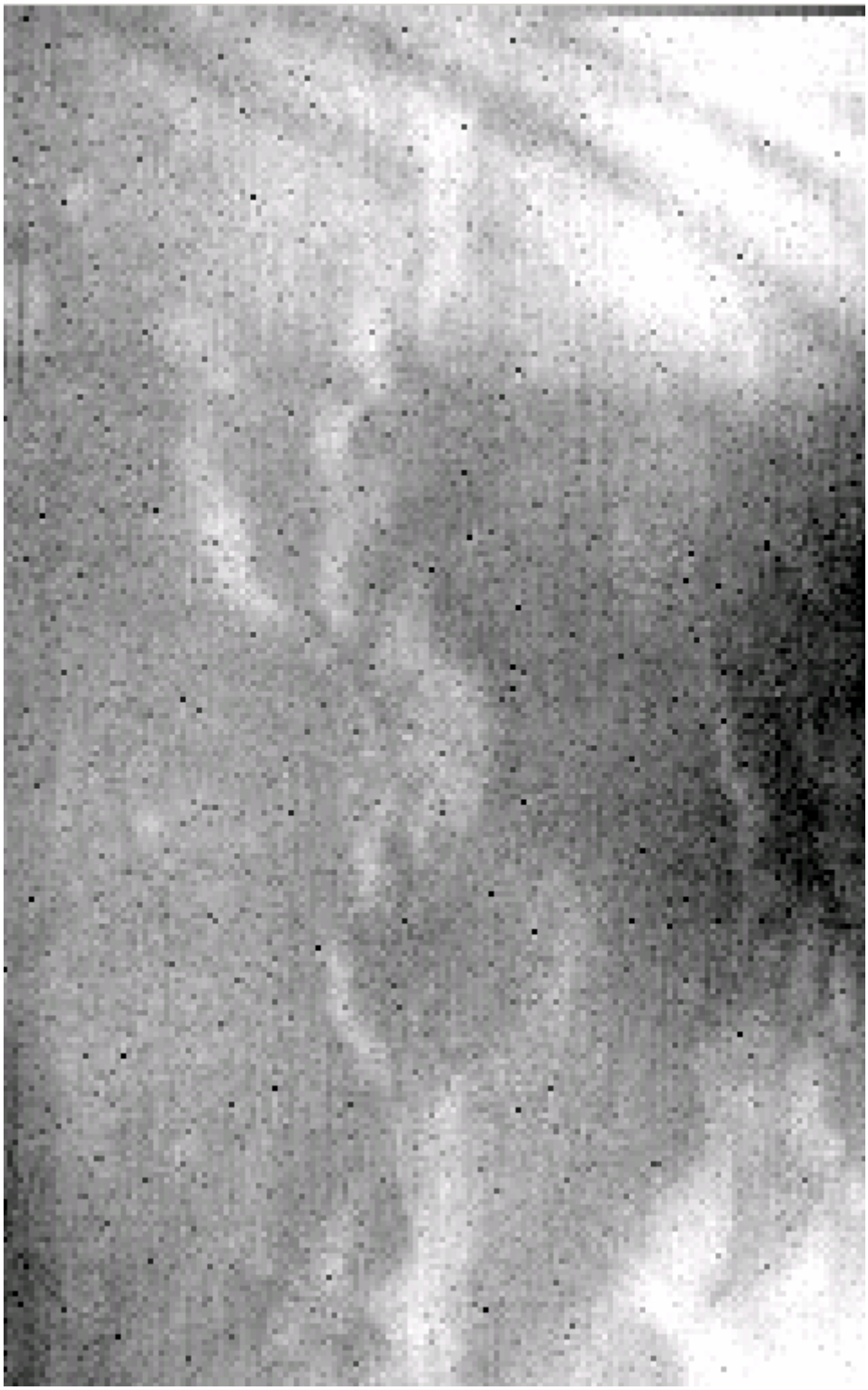

Figure 3b Compression ratio of 4 with original decompression scheme.

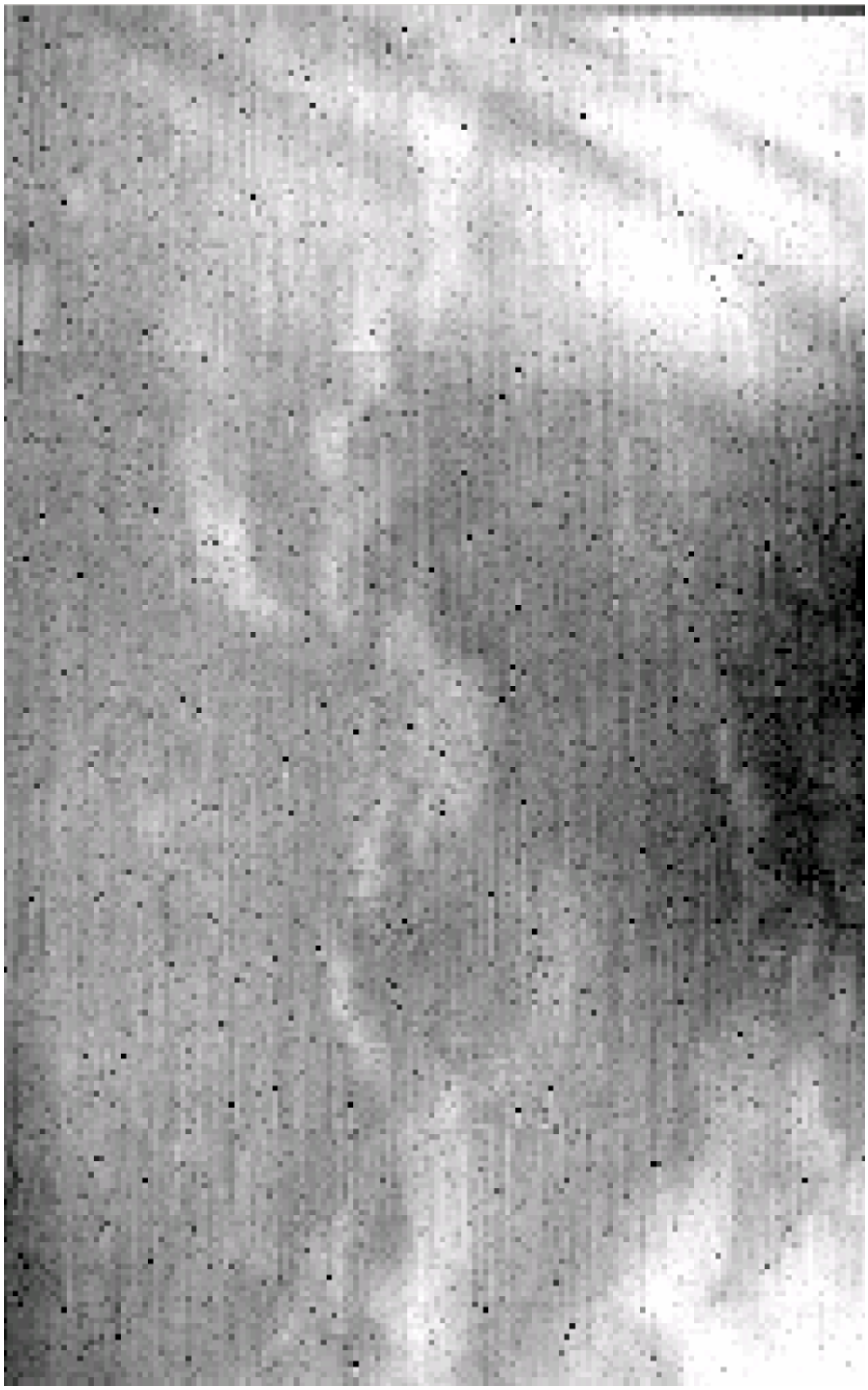

Figure 3c Compression ratio of 8 with original decompression scheme.

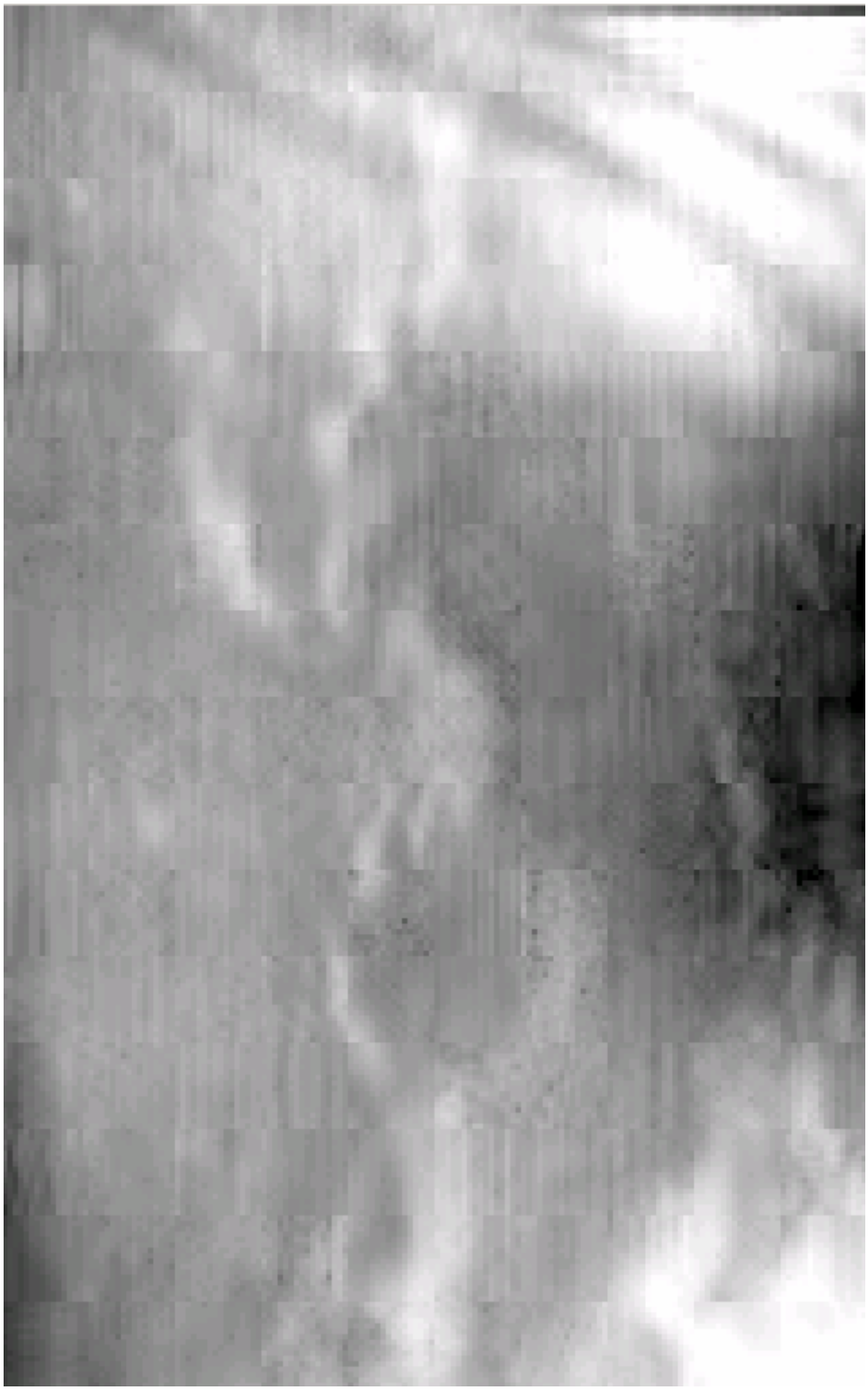

Figure 3d Compression ratio of 8 with new decompression scheme and no smoothing.

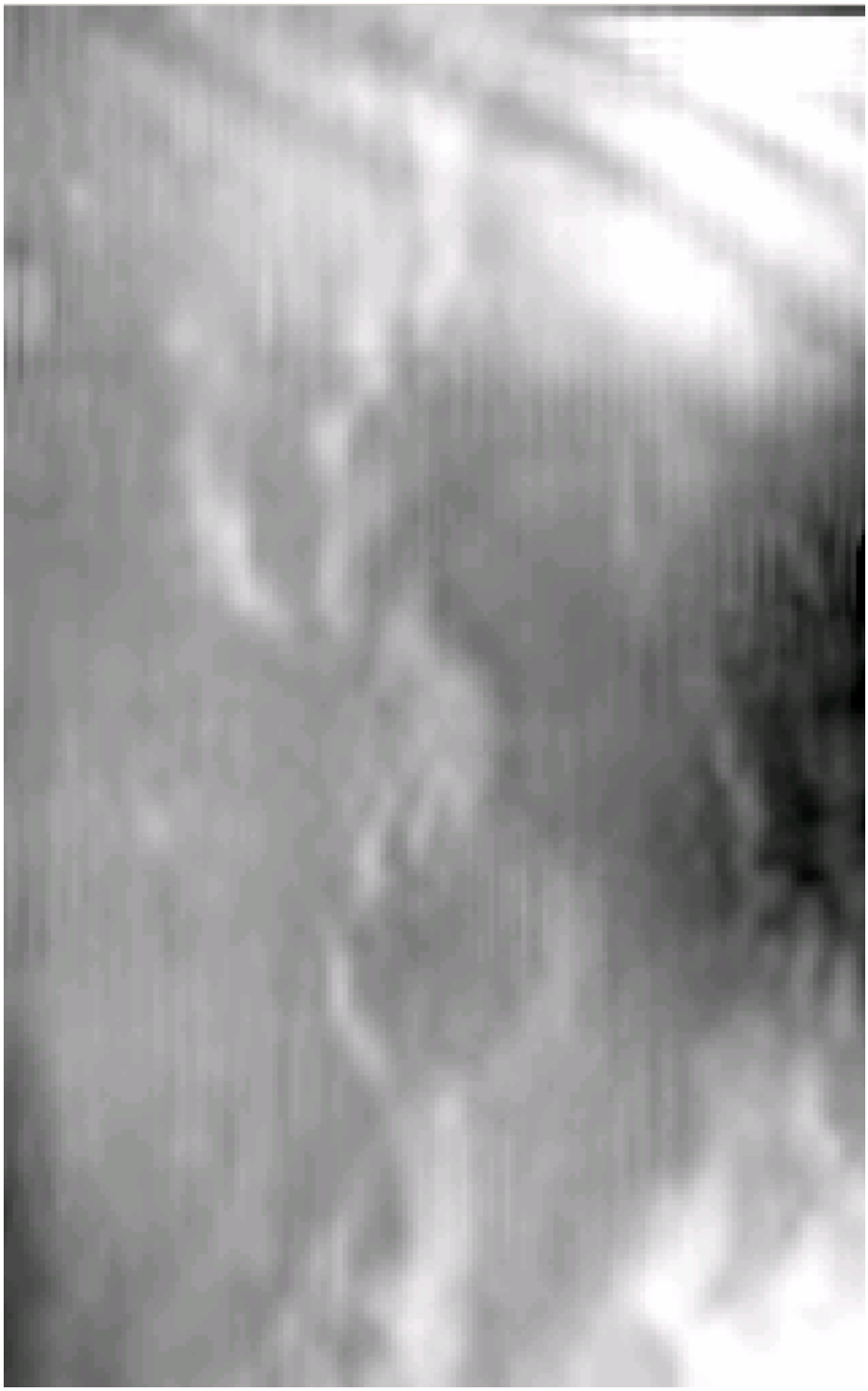

Figure 3e **Compression ratio of 8 with new decompression scheme and smoothing factor of 0.5.**

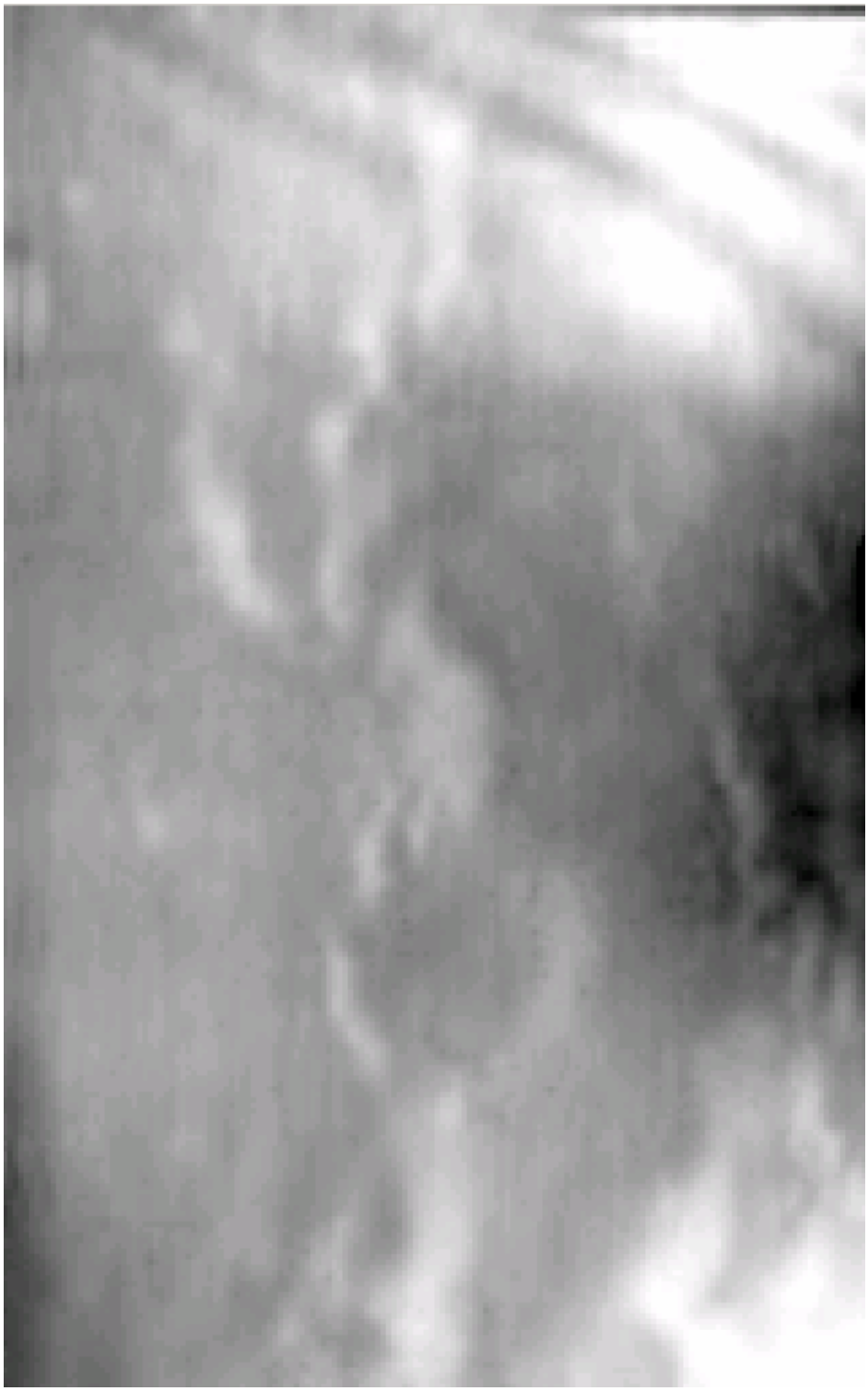

Figure 3f **Compression ratio of 8 with new decompression scheme and nominal smoothing.**

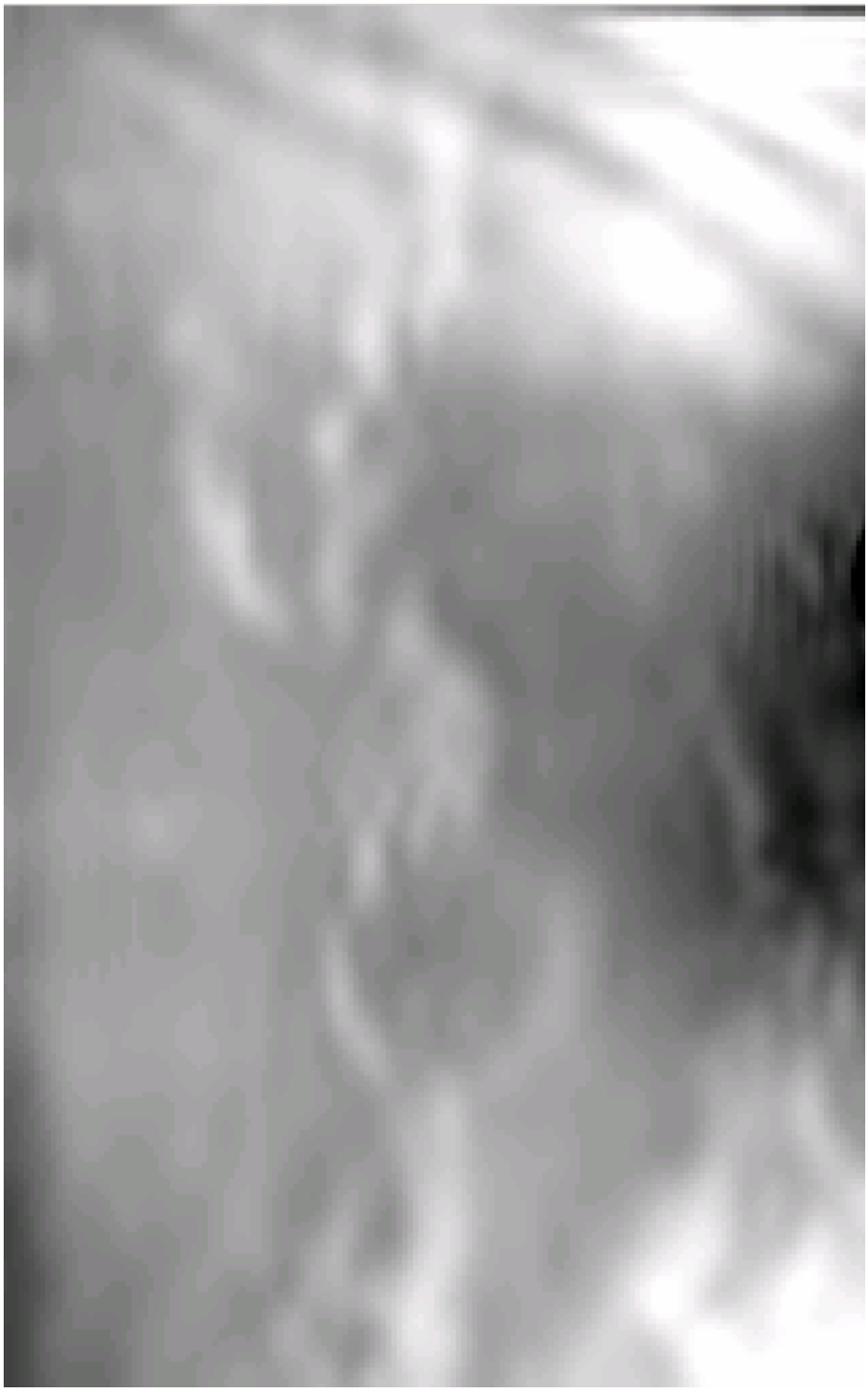

Figure 3g **Compression ratio of 8 with new decompression scheme and smoothing factor of 1.5.**

These examples show that features from the dark image (vertical stripes and black dots) are significantly suppressed with the new scheme even without smoothing. However, block boundaries require at least a smoothing factor of 0.5 in order to be reasonably suppressed. With a smoothing factor of unity, they are almost invisible. A smoothing factor of 1.5 makes them completely invisible, but it typically comes with the cost of reducing the visibility of real features more than necessary. Some images look better with compression ratio of 8 and a smoothing factor of unity than with the original scheme at compression ratio of 4, although in other images, the higher compression ratio looses fine detail that cannot be brought back.

6.8. Equations and the Fortran Code

6.8.1. Estimation of Threshold

We denote h_k as the number of times in the image that the maximum absolute value of a transmitted quadruple has the smallest absolute maximum within the image. h_{k+1}, h_{k+2}, and h_{k+3} are the number of times in the image that the maximum absolute values of a transmitted quadruple has the next values. Thus, the index denotes the rounded absolute maximum of a quadruple (which is multiplied by a power of 2 which respect to real amplitudes according to the quantization q where q takes values of 1, 2, 4, etc.). The threshold t is then between k-0.5 and k+0.5. It is estimated the following way:

$$t = k - 0.5 - \ln\{1+[1-\exp(-fq)]\, h_k / h_{k+1}\} / fq$$

where

$$f = 0.75 \ln[(1+h_{k+1}) / (1+h_{k+3})] /(q+0.2).$$

t is then rounded to the next possible value.

6.8.2. Decrease of Small Amplitudes

We denote the amplitude as a, and half of the possible range as d. Thus, the amplitude before compression must have been between a-d and a+d. We denote i and j are the frequency indices in both axes, ranging between 1 and 16. To calculate decreased amplitudes, the following iteration is performed twice:

$$a_{new} = 0.2\, a_{old} + 0.8\, a_{old} / \max\left[\, 1 \,,\, (a_{old}/d)^2\, 16/\max(i,j)\right].$$

Note that in cases with a non-zero dark image, the zero amplitude is based with respect to the un-square-rooted image, and the scaling of amplitudes between the square-rooted and un-square-rooted image is based on the average bin size of data numbers. Since the bin size is not constant, the first estimate may not be perfect, but by the second iteration, it is close to perfect.

6.8.3. Determination of Standard Smoothing Amplitude

The standard smoothing amplitude s, used in the 32x32 pixel block smoothing, is determined by the rms of the CCD noise and a value dependent on the size of excessive features at block boundaries. Thus,

$s = \sqrt{(\sigma^2 + 3\Delta^2)}$.

The CCD noise σ was assumed to be 1 data number for an exposure level of 30 data numbers, increasing with the square-root of the exposure level.

The horizontal and vertical feature size δ at each pixel is evaluated by DN(i,j) – 0.5 DN(i-1,j) – 0.5 DN(i+1,j) and DN(i,j) – 0.5 DN(i,j-1) – 0.5 DN(i,j+1), respectively, where DN(i,j) is the data number at pixel i,j. The rms of all feature sizes where the three pixels go across a 16x16 pixel block boundary is called Δ_e. The rms of all remaining feature sizes is called Δ_i. Then:

$\Delta = \Delta_e - \Delta_i$.

6.8.4. Decrease of amplitudes in 32x32 pixel blocks

Again, we denote the amplitude as a and the frequency indices i and j, now ranging between 1 and 32. Then, the amplitudes are decreased according to the equation:

$a_{new} = a_{old} - a_{old} / \max [1 , (a_{old}/s)^2 \, 32/\max(i,j)]$.

This calculation is performed on an image where all data numbers have been square-rooted (the mathematical square-root).

6.8.5. Interpolation between neighboring 32x32 pixel blocks

For the horizontal interpolation, the contribution from each 32x32 pixel square is unity at the center of the square and zero at the edge. The contribution function is $\cos^2(r\ 90°)$ where r goes from –1 at the left edge of the square to 0 at the center to 1 at the right edge. The vertical interpolation is performed in the same way.

7.0. Test for Suitable Selection of Compression Ratios for DISR Imagers

November 2001, by Erich Karkoschka with help by
Martin Tomasko, Lyn Doose, and Bashar Rizk

7.1. Scientific Background

7.1.1. Introduction

The DISR imagers were designed to be used with compression ratio (CR) 8(1 bit/pixel) in order to give sufficient coverage for the limited data rate. However, in 1995, we found that for low-contrast scenes, images compressed with CR 8 looked very bad since almost all compressed data were data about the flatfield, not data about the scene. Only at CR2-3 did the images look good. Thus, we considered CR of 3 and 6 for half of the images each. This way, at least half of the images would look good, and we would get half of the original coverage. Fortunately, flatfielding was installed before compression which caused some low-contrast scenes returned at CR 16 to look as well as scenes obtained at CR 3 without the flatfielding.

During the last years, we collected many image sequences on the roof of the building, on a fire tower in the forest, and on a helicopter. These tests raised our appetite for higher quality since CR of 8 give some unwanted artifacts. The worst artifacts are discontinuities at16x16 pixel block boundaries. They are always bad at CR 16, they can be disturbing at CR 8, and they may be noticeable at CR 4. An example is shown in figure 7.1.1-1.

Figure 7.1.1-1a An original test image with low signal and high contrast.

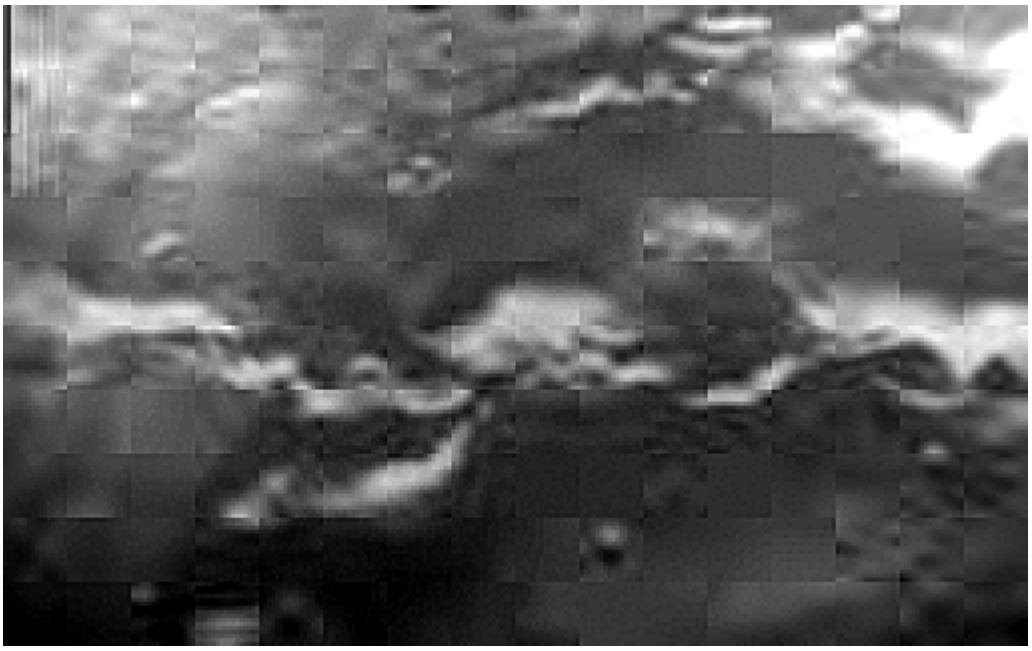

Figure 7.1.1-1b The scene in figure 1a with a compression ratio of 16.

Recently, we created software which smoothes the images at those boundaries in such a way that the resulting image is still consistent with the compressed data, which means that the

unsmoothed and the smoothed images would give exactly the same compressed data stream. With images run through our software, 16x16 block boundaries cannot be detected any more even at CR 16, not even by detectives who are trained to detect those boundaries. Details on the software which removes the artifacts are found in a separate document.

Other artifacts are periodic features introduced by incomplete transmission of the CCD noise. We created software which targets specific coefficients in order to reduce those artifacts. Further reduction of these artifacts is possible by setting a parameter in our software, but this would decrease the visibility of small, real features.

For about the first half hour of the descent, the dark current is expected to be significant. This causes damage in low-contrast scenes which are expected during the beginning of the descent. We created software which lets the decompressor "know" about the dark current. This way, we can decrease this damage to insignificant levels.

In studying image artifacts introduced by compression, it became clear that the resulting image becomes better and better the more the parameters of the software are tuned to the appropriate values. This can be done by testing the software with a few representative test images, which have similar noise, similar range of data numbers, similar contrast, and similar types of features as the compressed images. Currently, we do not have images representative of Titan's surface. However, these images could be taken during the descent by using low CR for 5-10 percent of the images. We expect that those images will tell what the compressor does at higher CR which then can be used to significantly improve the other images and to yield error estimates for measurements of features such as photometry or position measurements. Without a few very good representative images, the decompression software produces "mean" images but does not provide any information about the uncertainty of each data number. We think that a sufficient set of "perfect" representative images would be obtained by setting the CR for one or two out of the 24 azimuths to a value 1.5-2 times lower than for most of the other azimuths. This would only cost about 3-6 percent of the data rate. We propose to use two azimuths with low CR.

Our image sequences during the past years were all taken with an essentially stationary camera where lower CR produce better images, of course. However, on Titan, the expected strong wind carries Huygens over the terrain so that lower CR give less coverage. Actually, we don't expect to lose many features by using low CR, but the imaged resolution is expected to decrease due to further distance, due to imaging in a camera of worse pixel scale (e.g. MRI instead of HRI), or due to less optimal positioning within the field of view (each imager produces sharper images near the center of the field of view than towards the corners). Furthermore, even if the coverage were perfect, higher CR would yields more images of the same feature which would increase the signal-to-noise (S/N) ratio.

There is clearly a trade-off. At very low CR, the compressor produces little damage, but the resolution is so bad that even uncompressed images do not show much. At very high CR, the compressor produces only disappointing images. In order to find the best compromise, we designed a set of test images which show the degradation due to compression, resolution, and

noise at the same time.

For our test, we consider the area of the terrain which is visible to the HRI between the first and last panorama. The area outside the visibility of the HRI is imaged reasonably well, and the resulting resolution is not very dependent on the choice of the CR. The terrain imaged after the last panorama has such a poor coverage that we never considered lowering the CR below the original number of 8.

7.2. Resolution

The imaged resolution of a feature depends on the distance between the feature and the camera, on the image scale (degrees/pixel) of the camera, and the width of the point spread function (pixels) at that location. For features close to the horizon, foreshortening decreases the resolution in the vertical direction.

The best resolution is achieved when imaging is in the center of the HRI. The shortest distance is achieved when looking back about 75 degrees below horizontal since the descent angle is typically about 15 degrees down from horizontal. The resolution for all images of the same feature is expressed here relative to the best resolution, thus this number is 1.0 or larger. For the descent angle of 15 degrees, the resolution in the HRI can vary between 1.0 and 1.8 due to a factor of 1.3 in the variation of distance and a similar factor for the variation of the point-spread-function. The median value is about 1.3. The relative resolution in the MRI can vary between 2.2 and 11 due to variations of factors of about 2 in distance and in point-spread-function each. The median is about 4. The relative resolution in the SLI is 5 or more.

According to simulated descent runs, the coverage is about CR times 10 percent for the HRI and about four times as much for the MRI. Thus, for CR = 8, for example, about 80 percent of the terrain is imaged by the HRI and about 320 percent by the MRI which means that for most surface features, one gets one HRI image and three MRI images (again, these numbers are valid for the terrain which is visible to the HRI between the first and last panorama). The HRI image will have a relative resolution between 1.0 and 1.8, the MRI images between 2.2 and 11. If we only consider the image of best resolution, then 80 percent of the features have a relative resolution between 1.0 and 1.8 and the remaining 20 percent above 2.2, but probably not much above 2.2 since we chose the best of the three MRI images. We now divide the terrain in eight parts: one eighth which happened to be imaged at the best relative resolution (1.0), one eighth which happened to be imaged close to the best resolution (1.1), and so on until the last eighth which happened to be imaged at a resolution of about 2.3. In our test image, each eighth is represented by a 32-pixel wide stripe, ordered from the best to the worst. In reality, the terrain will be irregularly divided up with regions well resolved bordering regions very poorly resolved.

We estimated the distribution of relative resolutions for each eighth of the terrain for CR of 2, 3, 4, 6, 8, 12, and 16 (Table 7.4-1). Is obvious that for low CR, the relative resolution for part of the terrain is 4 or more and thus so bad that many features are lost. For CR of 8, the relative

resolution becomes good for most of the terrain. For higher CR, the relative resolution does not improve much further.

7.3. Noise

A specific scene can give high or low data numbers (DN) depending on the exposure time. The scene can also give high or low contrast depending on the amount of haze between Huygens and the ground, since haze absorbs some of the signal and adds an additional signal which we will assume to be featureless for the test. While the DN for a dark high-contrast scene and a bright low-contrast scene are very different, it turns out that the 8-bit numbers the compressor sees may be almost identical because the adaptive square-root scheme. What matters is the size of the noise relative to the full range of data numbers, or the numbers of noise steps between the minimum and maximum DN. For example, an image with DN between 20 and 40 has 20 noise steps since the noise is about 1 DN, while an image with DN between 2900 and 3100 has also 20 noise steps since the noise is about 10 DN.

The number of noise steps is critical to the amount of damage the compressor does. As a rough guide, the mean error due to compression is almost negligible as long as it is smaller than the noise, but the error due to compression is roughly proportional to CR once it is larger than the noise. Thus, an image with twice the noise can roughly be compressed twice as much before the damage due to compression becomes noticeable. Note, however, that twice the CR allows transmission of two images which cuts the noise by the square-root of 2. Thus, twice the noise causes only a loss of a factor of square-root of 2 if the CR is adjusted.

The optimal CR for each image is in the transition region where the error by compression is similar to the noise. The exact optimum depends slightly on other factors such as relative resolution, but it never makes sense to have a much lower CR where one uses most of the data stream to transmit noise, nor does is make sense to have a much higher CR where one loses many features. In principle, a compressor could use the optimal CR if it knew the size of the noise. However, the design of the data transmission called for a predetermined CR. Thus, we have to estimate how many noise steps we expect in the images in order to design the CR for near optimal performance.

The basis of our estimation is a model of Titan's atmosphere with aggregate particles which predicts the amount of light from the atmosphere in the appropriate passband for several altitudes and several directions. These numbers were fit to simple functions of altitude for evaluation at each altitude. The predicted intensities are tabulated as I/F values with the flux taken from the surface (Table 7.3-1).

Table 7.3-1

Estimation of brightness, data numbers, and signal-to-noise ratios for a bright surface (top), average surface (middle), and dark surface (bottom) for various altitudes.

1) Surface geometric albedo = 0.5

#	Alt.	Exp	I/F (-90°)		I/F (-45°)		I/F(5°)	DN (-90°)		DN (-45°)		DN(5°)	S/N		0.4* S/N	
	km	ms	surf	haze	surf	haze	haze	surf	haze	surf	haze	haze	-90°	-45°	-90°	-45°
A	146	7	0.035	+1.168	0.019	+1.606	2.998	39	1308	11	+899	1679	6	2	2	1
B	139	7	0.037	+1.112	0.021	+1.529	2.990	41	1245	12	+856	1674	6	2	2	1
C	94	11	0.059	+0.752	0.040	+1.034	2.624	104	1324	35	+910	2309	15	6	6	2
D	66	10	0.078	+5.28	0.060	+0.726	2.154	125	845	48	+581	1723	22	10	9	4
E	42	23	0.108	+3.36	0.083	+0.462	1.600	397	1236	153	+850	2944	54	26	22	10
F	33	31	0.110	+2.64	0.095	+0.363	1.260	546	1309	236	+900	3125	69	38	28	15
G	27	38	0.115	+2.16	0.103	+0.297	1.184	699	1313	313	+903	3599	85	49	34	20
H	21	44	0.122	+1.88	0.112	+0.231	1.004	859	1324	394	+813	3534	101	62	40	24
I	15	52	0.129	+1.20	0.122	+0.165	0.812	1073	998	508	+686	3378	129	81	52	32
J	12	55	0.133	+0.96	0.127	+0.132	0.714	1170	845	559	+581	3142	143	91	57	36
K	9	61	0.137	+0.72	0.132	+0.099	0.614	1337	703	644	+483	2996	162	105	65	42
L	6	64	0.141	+0.48	0.138	+0.066	0.512	1444	492	707	+338	2621	180	120	72	48
M	3	68	0.146	+0.24	0.144	+0.033	0.408	1588	261	783	+180	2220	202	138	81	55
N	1	70	0.149	+0.08	0.148	+0.011	0.336	1669	90	829	+62	1882	218	152	87	61

2) Surface geometric albedo = 0.2

#	Alt.	Exp	I/F (-90°)		I/F (-45°)		I/F(5°)	DN (-90°)		DN (-45°)		DN(5°)	S/N		0.4* S/N	
	km	ms	surf	haze	surf	haze	haze	surf	haze	surf	haze	haze	-90°	-45°	-90°	-45°
A	146	7	.012	+1.168	.006	+1.606	2.998	13	+1308	3	+899	1679	2	1	1	0
B	139	7	.012	+1.112	.007	+1.529	2.990	13	+1245	4	+856	1674	2	1	1	0
C	94	11	.020	+.752	.013	+1.034	2.624	35	+1324	11	+910	2309	5	2	2	1
D	66	10	.026	+.528	.020	+.726	2.154	42	+845	16	+581	1723	8	4	3	2
E	42	23	.036	+.336	.028	+.462	1.600	132	+1236	52	+850	2944	20	9	8	4
F	33	31	.037	+.264	.032	+.363	1.260	184	+1309	79	+900	3125	26	14	11	6
G	27	38	.038	+.216	.034	+.297	1.184	231	+1313	103	+903	3599	32	18	13	7
H	21	44	.041	+.188	.037	+.231	1.004	289	+1324	130	+813	3534	39	23	16	9
I	15	52	.043	+.120	.041	+.165	.812	358	+998	171	+686	3378	53	32	21	13
J	12	55	.044	+.096	.042	+.132	.714	387	+845	185	+581	3142	60	37	24	15
K	9	61	.046	+.072	.044	+.099	.614	449	+703	215	+483	2996	72	45	29	18
L	6	64	.047	+.048	.046	+.066	.512	481	+492	236	+338	2621	84	54	34	22
M	3	68	.049	+.024	.048	+.033	.408	533	+261	261	+180	2220	104	68	42	27
N	1	70	.050	+.008	.049	+.011	.336	560	+90	274	+62	1882	120	82	48	33

3) Surface geometric albedo = 0.05

#	Alt.	Exp	I/F (-90°)		I/F (-45°)		I/F(5°)	DN (-90°)		DN (-45°)		DN(5°)	S/N		0.4* S/N	
	km	ms	surf	haze	surf	haze	haze	surf	haze	surf	haze	haze	-90°	-45°	-90°	-45°
A	146	7	.0014	+1.168	.0008	+1.606	2.998	2	+1308	0	+899	1679	0	0	0	0
B	139	7	.0015	+1.112	.0009	+1.529	2.990	2	+1245	0	+856	1674	0	0	0	0
C	94	11	.0023	+.752	.0016	+1.034	2.624	4	+1324	1	+910	2309	1	0	0	0
D	66	10	.0031	+.528	.0024	+.726	2.154	5	+845	2	+581	1723	1	0	0	0
E	42	23	.0039	+.336	.0033	+.462	1.600	14	+1236	6	+850	2944	2	1	1	0
F	33	31	.0043	+.264	.0038	+.363	1.260	21	+1309	9	+900	3125	3	2	1	1
G	27	38	.0046	+.216	.0041	+.297	1.184	28	+1313	12	+903	3599	4	2	2	1
H	21	44	.0049	+.188	.0045	+.231	1.004	34	+1324	16	+813	3534	5	3	2	1
I	15	52	.0052	+.120	.0049	+.165	.812	43	+998	20	+686	3378	7	4	3	2
J	12	55	.0053	+.096	.0051	+.132	.714	47	+845	22	+581	3142	9	5	4	2
K	9	61	.0055	+.072	.0053	+.099	.614	54	+703	26	+483	2996	11	6	4	2
L	6	64	.0057	+.048	.0055	+.066	.512	58	+492	28	+338	2621	14	8	6	3
M	3	68	.0058	+.024	.0058	+.033	.408	63	+261	32	+180	2220	19	12	8	5
N	1	70	.0059	+.008	.0059	+.011	.336	66	+90	33	+62	1882	29	19	12	8

Column header explanations:

#: Panorama number for CR = 4

Alt: Altitude (km)

Exp: Exposure time for constant image smear (ms)

I/F: Reflectivity between straight down (-90°) and 5 degrees up (5)

surf: Contribution from the surface

haze: Contribution from the haze

DN: Data number

S/N: Signal from the surface divided by the CCD noise

0.4*S/N: Number of noise steps for +/- 20 percent contrast

The model also predicts the extinction between the surface and Huygens. The light from the surface is estimated by phase functions of asteroids with three cases, one of the brightest asteroids, (44) Nysa, with a geometric albedo of 0.5 and a relatively flat phase function, asteroids with a geometric albedo of 0.2 (which is close to Titan's geometric albedo) and a slightly steeper phase function, and a dark asteroid (53) with a geometric albedo of 0.05 and a steep phase function. Since the current landing site is expected to be in the dark terrain, one can expect an albedo somewhere between the average and dark case, but the bright case is still possible on small scales. The bright case is typical of relatively clean, icy surfaces, while some satellites are still brighter. The dark case matches Hyperion's dark side, Titan's outer neighbor. There are a few satellites and a fair fraction of asteroids with geometric albedos less than 0.05. We assumed that half of the light is direct sunlight and half of the light is diffuse skylight, although resulting

numbers are very insensitive to this assumption.

For an object at Titan's surface with an I/F = 1, we assume a sensitivity of 160 DN/ms for the HRI and 80 DN/ms for the MRI and SLI because of their filters with 50 percent transmission. We then calculated the expected DN for various altitudes for the three kinds of surfaces and for three directions: straight down (representative for all HRI images), 45 degrees down with am azimuth 90 degrees away from the azimuth of the sun (representative of most of the MRI and SLI images, although in some directions, DN can easily get twice as high and half as high), and 5 degrees up with an azimuth 90 degrees away from the azimuth of the sun (representative for the sky in the SLI). We then calculated S/N values where the signal is the contribution of DN from the surface and the noise is the CCD noise. The S/N data show that there is a very large increase from the highest to the lowest altitudes, but the actual values are difficult to predict since they depend a lot on the surface albedo which we do not know (Table 7.3-1).

We assume that the albedo varies between the assumed value minus 20 percent and the assumed value plus 20 percent in every image. The true contrasts can easily be twice as high, but much higher contrasts are rare with the sun high in the sky and with part of the illumination from diffuse skylight. The contrast can be easily half as much as the ± 20 percent, but much lower contrasts would mean that we are exceptionally unlucky. I/F variations due to topography with moderate slopes are on the order of 10 percent. The last columns of Table 7.3-1 show the number of noise steps for each considered case. For altitudes above 20 km, the number of noise steps will probably stay below 20 (HRI) and 10 (MRI) with more typical numbers on the order of 4 (HRI) and 2 (MRI). Below 20 km altitude, the typical number of noise steps will be about 20 (HRI) and 10 (MRI), but there is a good chance that it can get as high as about 100 (HRI) and 50 (MRI).

Table 7.3-1 shows that the noise for the MRI is typically twice as high as for the HRI. Thus, for a test images, we use twice the noise for the terrain which is not imaged by the HRI. The right side of Table 7.4-1 lists the scaled noise, usually 1.0 for the HRI and 2.0 for the MRI. For high CR, one gets several images at similar scales which can be used to decrease the noise. The lower adopted values on the right side of Table 7.3-1 account for this fact.

For the test, we use three images. The first image is based on a Ganymede scene imaged by Galileo with 100 noise steps (HRI) and 50 noise steps (MRI). Such a case is possible at the lowest altitudes with the brightest surface. The second image is the same as the first one but with five times the noise which is typical for intermediate altitudes (0 km for the dark case, 15 km for the average case, and 40 km for the bright case). The last image is a different scene with only 4 and 2 noise steps (HRI and MRI, respectively). This is typical for higher altitudes (10 km for the dark case to 100 km for the bright case). This artificial scene, looking like a set of many lakes, was chose since it has most DN near the maximum or near the minimum DN and thus the best chance to be recognized under very noisy conditions. The three test images are listed in Table 7.3-2. This table also lists some previous test images. Note that most of the test images including most of the images from the building roof, fire tower, and helicopter have many more noise steps than what we can expect.

Table 7.3-2
Noise steps for test images

Image	HRI	MRI	Object
Low Noise Image	100	50	Ganymede
Medium Noise Image	20	10	Ganymede
High Noise Image	4	2	Lakes

Previous tests:	620	Jupiter
	420	Forest
	250-300	Ganymede
	140	Dark test
	45	Dark test + noise

The HRI and MRI have a significant overlap. If features are imaged at the HRI and MRI simultaneously, the HRI collects eight times as much signal than the MRI because its aperture area is four times as much as that of the MRI and because of the filter with 50 percent transmission in front of the MRI. Thus, very large features are imaged with one HRI image as well as eight repetitions with the MRI. For smaller features, the ratio is much higher since the MRI smoothes out features much more due to its point-spread-function which is about three times as wide as that of the HRI in the overlapping region. This consideration shows the most important aspect of the choice of CR, the loss from an HRI image to an MRI image of the same terrain.

7.4. Evaluation

We have not found a parameter which describes how much an image has been degraded due to worse image scale, due to CCD noise, and due to compression. Thus, the evaluation has to be done by comparing images. However, we have a parameter which gives a rough guide about the damage. We take the root mean square of the DN between the original image at the best scale (1.0) without noise and the final image. We use averages of 2x2 pixels for this comparison since this is about the size of the point-spread-function. For each 2x2 pixel square, we calculate the difference between the DN in the original image at resolution 1.0 and the DN in the actual image (which may have worse resolution, which has added CCD noise and compression artifacts). We then calculate the root-mean-square of these differences across each eighth of the image. We scale this value to the value expected for the CCD noise of a single HRI image. The bottom part of Table 7.4-1 lists this number for each section of each of the three images and each CR.

Table 7.4-1

Relative distribution of resolution, noise, and total damage parameter for each of the eight panels of terrain, ordered from best to worst resolution, and the total damage

	Relative resolution distribution								Noise							
CR	1	2	3	4	5	6	7	8	1	2	3	4	5	6	7	8
2	1.3	2.0	3.0	4.0	5.0	6.0	7.0	8.0	1.0	2.0	2.0	2.0	2.0	2.0	2.0	2.0
3	1.2	1.5	2.2	2.8	3.4	4.0	4.8	5.6	1.0	1.0	2.0	2.0	2.0	2.0	2.0	2.0
4	1.1	1.3	1.6	2.0	2.5	3.0	3.5	4.0	1.0	1.0	1.0	2.0	2.0	2.0	2.0	2.0
6	1.1	1.2	1.3	1.5	1.8	2.2	2.6	3.0	1.0	1.0	1.0	1.0	1.0	2.0	2.0	2.0
8	1.0	1.1	1.2	1.3	1.4	1.6	2.0	2.3	1.0	1.0	1.0	1.0	1.0	1.0	1.6	1.6
12	1.0	1.1	1.1	1.2	1.3	1.4	1.5	1.6	0.9	0.9	0.9	0.9	0.9	0.9	0.9	0.9
16	1.0	1.0	1.1	1.1	1.2	1.2	1.3	1.3	0.8	0.8	0.8	0.8	0.8	0.8	0.8	0.8

Total damage for low noise image

CR scheme	1	2	3	4	5	6	7	8	Average	Weighted Average
2	4.6	8.6	12	15	18	23	21	14	14.5	11.4
3	4.5	5.5	10	13	15	21	19	14	12.7	9.7
3,6	4.1	4.0	6.7	10	13	20	17	12	10.8	7.9
2-6	4.1	4.0	6.7	10	13	20	17	12	10.8	7.9
4	4.1	3.9	6.8	10	13	20	17	12	10.8	7.9
6	4.5	3.7	4.9	7.0	9.9	16	15	12	9.0	6.9
8	3.2	4.1	5.2	6.5	7.4	11	13	11	7.7	6.1
12	4.9	5.9	6.1	7.3	8.0	10	11	9.3	7.8	7.3
16	6.5	6.2	7.8	7.7	9.0	9.3	10	8.9	8.2	8.0

Total damage for medium noise image

CR scheme	1	2	3	4	5	6	7	8	Average	Weighted Average
2	1.4	2.8	3.4	3.8	4.5	5.4	4.8	3.9	3.7	3.2
3	1.5	1.8	3.2	3.6	4.1	5.0	4.7	4.0	3.5	3.0
3,6	1.5	1.5	2.0	3.5	3.8	5.0	4.7	3.8	3.2	2.6
2-6	1.5	1.5	2.0	3.5	3.8	4.9	4.7	3.8	3.2	2.6
4	1.4	1.4	2.0	3.1	3.5	4.8	4.4	3.5	3.0	2.5
6	1.4	1.4	1.6	2.1	2.6	4.0	3.5	3.3	2.5	2.1
8	1.1	1.3	1.5	1.7	1.9	2.6	3.1	2.6	2.0	1.8
12	1.1	1.4	1.4	1.7	1.8	2.3	2.3	2.0	1.7	1.6
16	1.3	1.3	1.6	1.6	1.8	1.9	2.0	1.8	1.7	1.6

Total damage for high noise image

CR scheme	1	2	3	4	5	6	7	8	Average	Weighted Average
2	1.0	2.3	2.5	2.9	3.2	3.0	3.0	3.0	2.6	2.3
3	0.9	1.0	2.2	2.7	2.8	2.6	3.1	3.3	2.3	1.9
3,6	1.0	1.0	1.1	2.7	3.0	3.2	3.1	3.2	2.3	1.7
2-6	1.0	1.0	1.0	2.8	2.9	3.1	3.0	3.0	2.2	1.7
4	0.9	0.9	0.9	2.3	2.5	2.5	2.5	2.5	1.9	1.5
6	0.9	1.0	1.0	1.1	1.3	2.4	2.3	2.6	1.6	1.3
8	0.8	0.8	0.9	1.1	1.1	1.1	1.7	1.7	1.2	1.1
12	0.8	0.8	0.7	0.9	0.9	1.0	1.0	1.0	0.9	0.9
16	0.7	0.7	0.7	0.8	0.9	0.9	0.9	0.9	0.8	0.8

This parameter may be a rough guide, but we have found cases where the subjective judgment does not agree with the results based on this parameter. The last two rows give the average of the preceding eight values and a weighted average, the inverse of the average of the inverse values. The latter average is strongly weighted towards values with little damage which is probably appropriate since good images will be more looked at than bad ones.

After looking at the test images, it is clear that some types of features or regions improve with higher CR, other degrade. Thus, depending on each person's subjective preference, the votes for optimal CR will definitely scatter. Nevertheless, there are certain cases which look so bad that most people will agree that those cases need to be avoided. The images with CR of 2 and 3, and probably even 4, have very poor resolution for some of the terrain. This can be significantly improved with higher CR without losing much. For the low noise image, CR of 12 and 16 loses too many small features. Thus, for low altitudes, the CR probably should be around 6 or 8. By setting a higher priority for quality than for quantity, the preferred choice is 6. For higher altitudes, higher CR give the better images overall, but the gain is small, so that it is not clear how much one should push for higher CR.

Taking the total-damage parameter one step further, one can define the image quality as the number of noise steps divided by the weighted average damage. Table 7.4-2 lists those values for the case of average surface albedo (0.2). Again, it is clear that one gains a lot by increasing the CR from 2 to 8, but there is no significant gain for CR larger than 8.

Table 7.4-2

Expected quality as function of altitude and compression ratio for average surface brightness (geometric albedo 0.2)

#	Alt	Noise steps	(Noise steps)/Weighted Average Damage for CR =								
	km	-90°	2	3	3,6	2-6	4	6	8	12	16
A	146	1	1	1	1	1	1	1	1	1	1
B	139	1	1	1	1	1	1	1	1	1	1
C	94	2	1	1	2	2	2	2	2	2	2
D	66	3	1	2	2	2	2	3	3	3	3
E	42	8	3	3	4	4	4	5	6	7	7
F	33	11	4	5	5	5	6	6	7	8	8
G	27	13	4	5	6	6	6	7	8	9	9
H	21	16	5	6	6	6	7	8	10	12	12
I	15	21	6	7	8	8	8	10	12	13	13
J	12	24	6	7	8	8	9	11	13	13	13
K	9	29	7	8	9	9	9	11	13	14	13
L	6	34	8	9	10	10	10	12	14	14	13
M	3	42	8	9	10	10	10	12	14	14	13
N	1	48	9	10	11	11	11	13	15	14	13

7.5. Variation of CR

We also tested two alternatives for CR of 4 which produce the same number of images (the same time-averaged CR): the first alternative is half the azimuths at CR of 3 and half at CR of 6. With respect to the CR = 4 case, one seems to lose more between CR of 4 and 6 than one gains between CR of 4 and 3. However, a variation of CR has some benefit. For example, some complicated feature many never be clear at one specific CR but at a somewhat smaller CR. Thus, by varying the CR, one gets the feature at least half the time. Currently, we feel that some smaller variation, say half of the images at about 1.5 times the CR than the other half, has still advantages, but a variation by a factor of two loses too much for the higher CR.

The other tested alternative for an average CR of 4 is 1/7 at CR of 2, 3/7 at CR of 4, and 3/7 at CR of 6. With respect to the all CR of 4 case, only a small region is improved but a large region degraded. Thus, such a distribution is probably not recommended unless the small region with low CR is important. As stated near the beginning, we prefer to have a few percent of the images at a low CR, but these are so few images that they hardly affect the coverage of the remaining ones. We do not show the images with mixed CR, since variation of the CR is much less important than selection of the average CR.

During the descent, the best and probably second-best image of the area only visible to the MRI and SLI are taken at azimuths more than 90 degrees away from the direction of motion. This is simply due to the angle of descent where the closest approach to any feature occurs by looking back. Furthermore, the forward-looking azimuths see the surface at higher phase angles which makes the I/F lower. Together with the larger distance, the best views will almost certainly occur looking back. Thus, if one chooses to vary the CR somewhat, the backward azimuths should probably get the lower CR.

7.6. Additional Considerations

This test is designed for interpretations which require just one good image of any region. However, some studies, such as stereo imaging or studies of phase functions, require more than one image. In that case, a slightly higher CR may be preferable so that the second best image of a region is at least at somewhat similar resolution.

This test does not consider a variation of haze within each test case. However, especially at higher altitudes, the regions imaged from larger distances will not only have worse resolution but also lower contrast due to the additional haze. Thus, the real loss at the poorly resolved regions is larger than in the test images. This may favor slightly larger CR at higher altitudes than the test suggests, but the change is expected to be minimal.

7.7. The Test

There are three images, a Ganymede image of low noise (figure 7.7-1), a Ganymede image of

moderate noise (figure 7.7-2), and an image of lakes of high noise (figure 7.7-3). Each image comes in seven different compression ratios (CR) of 2, 3, 4, 6, 8, 12, and 16, in addition to the uncompressed image. While we cannot control the scene we get, we can choose the CR. Thus, the question is: which is the best choice of CR? This may difficult to judge since some parts of the terrain improve with higher CR, others improve with lower CR. Nevertheless, we need to choose. Which one is the best compromise for each of the three images? Or better, which range of CR is acceptable for each of the three images?

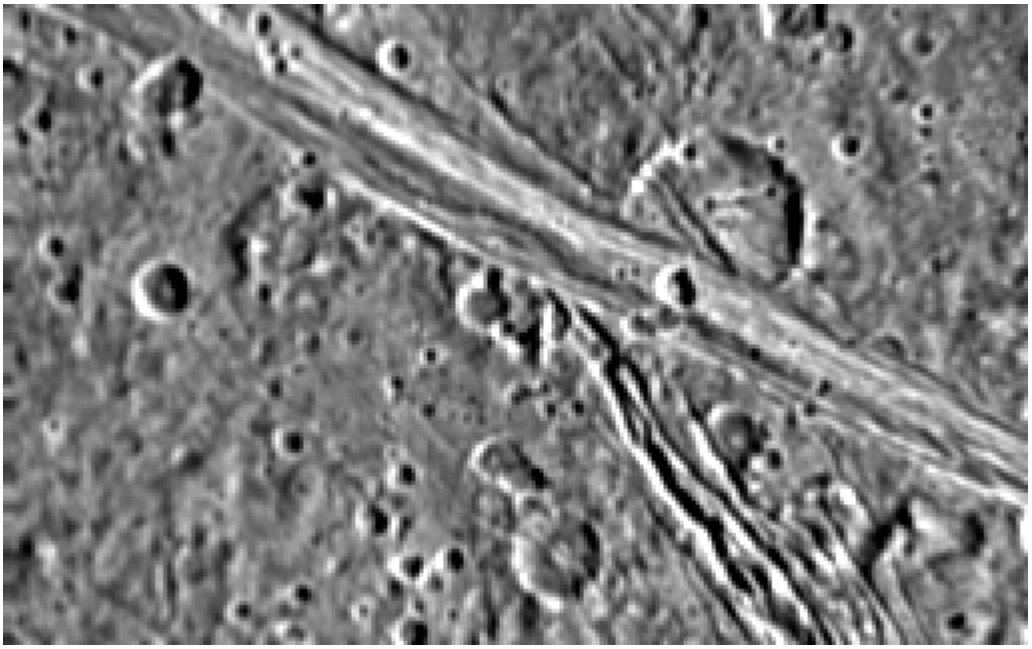

Figure 7.7-1a Original Ganymede image smoothed with no noise

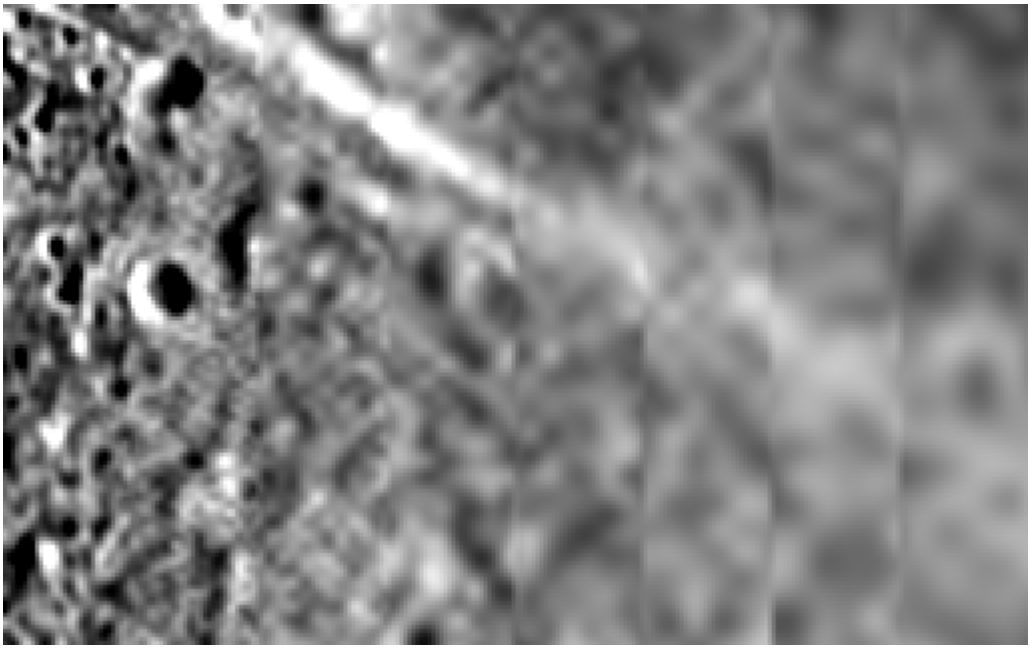

Figure 7.7-1b Low noise with CR 2

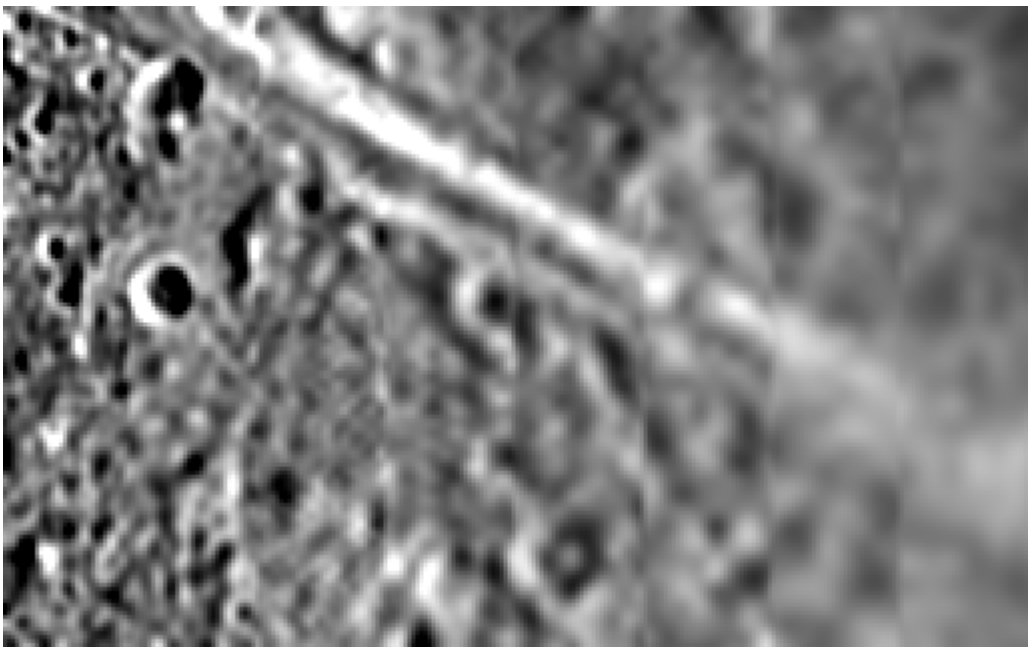

Figure 7.7-1c Low noise with CR 3

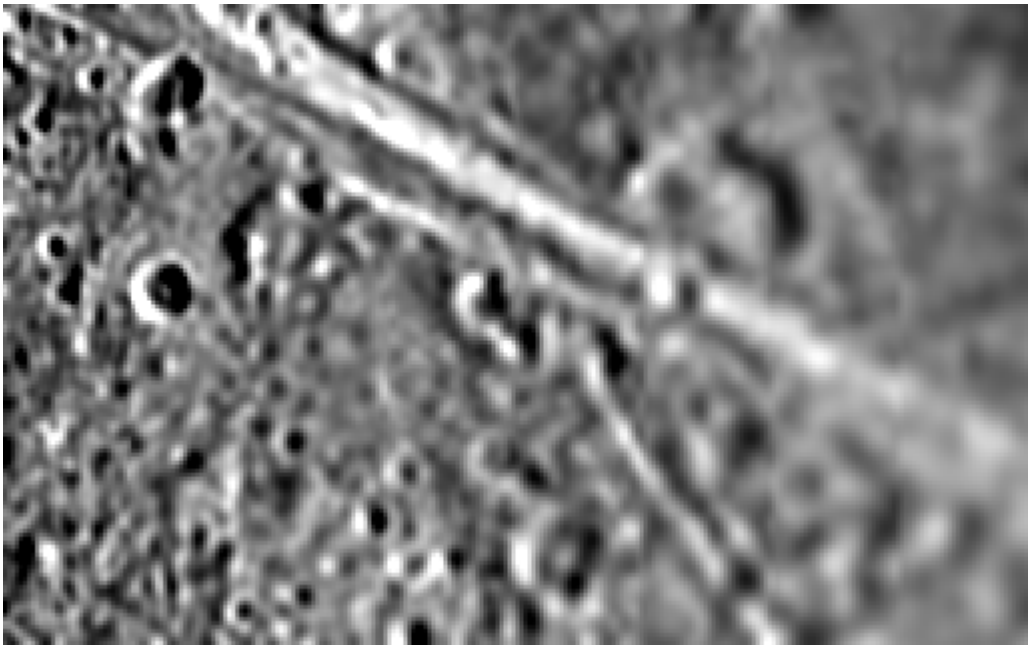

Figure 7.7-1d Low noise with CR 4

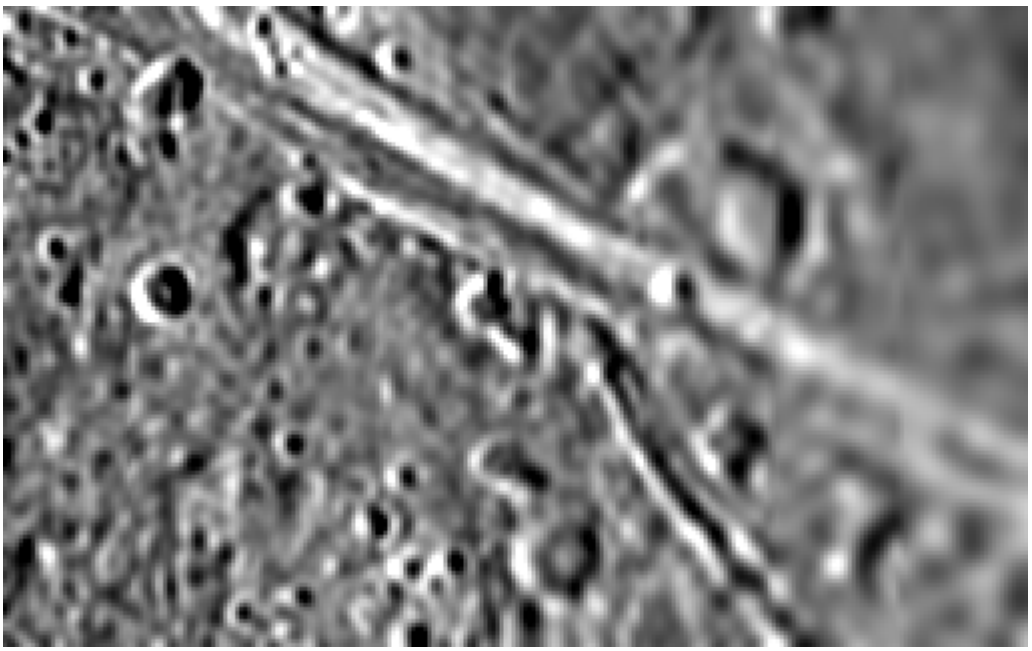

Figure 7.7-1e Low noise with CR 6

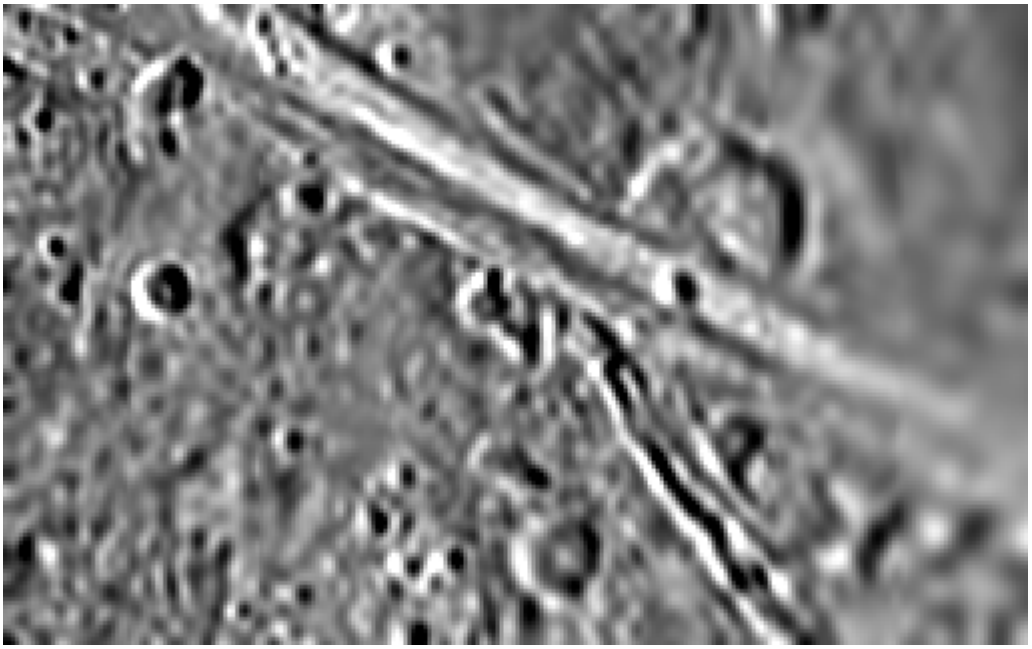

Figure 7.7-1f Low noise with CR 8

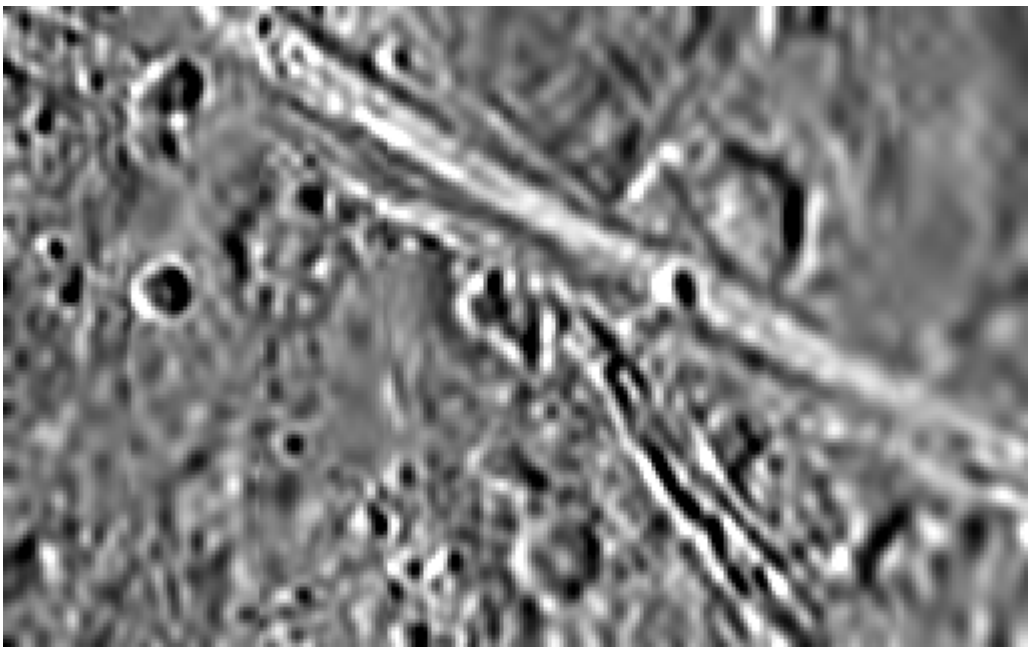

Figure 7.7-1g Low noise with CR 12

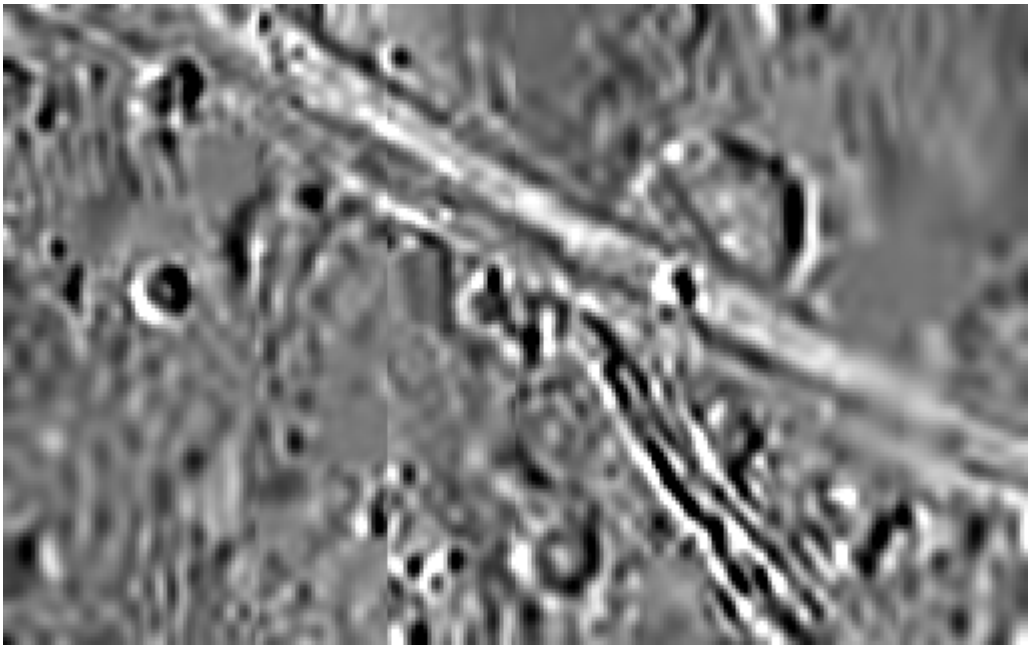

Figure 7.7-1h Low noise with CR 16

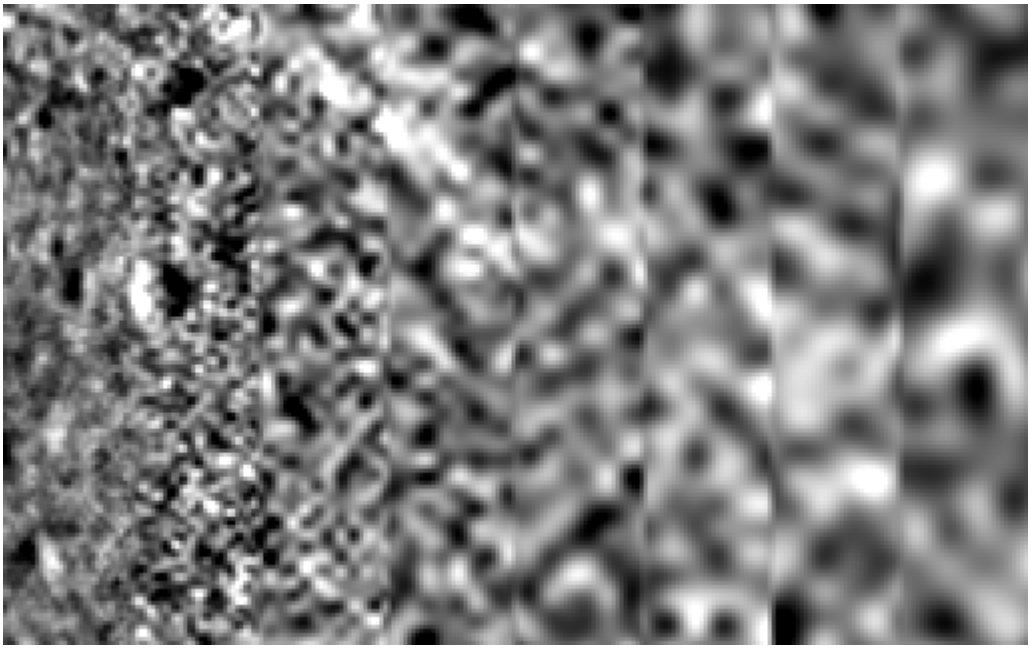

Figure 7.7-2a Moderate noise with CR 2

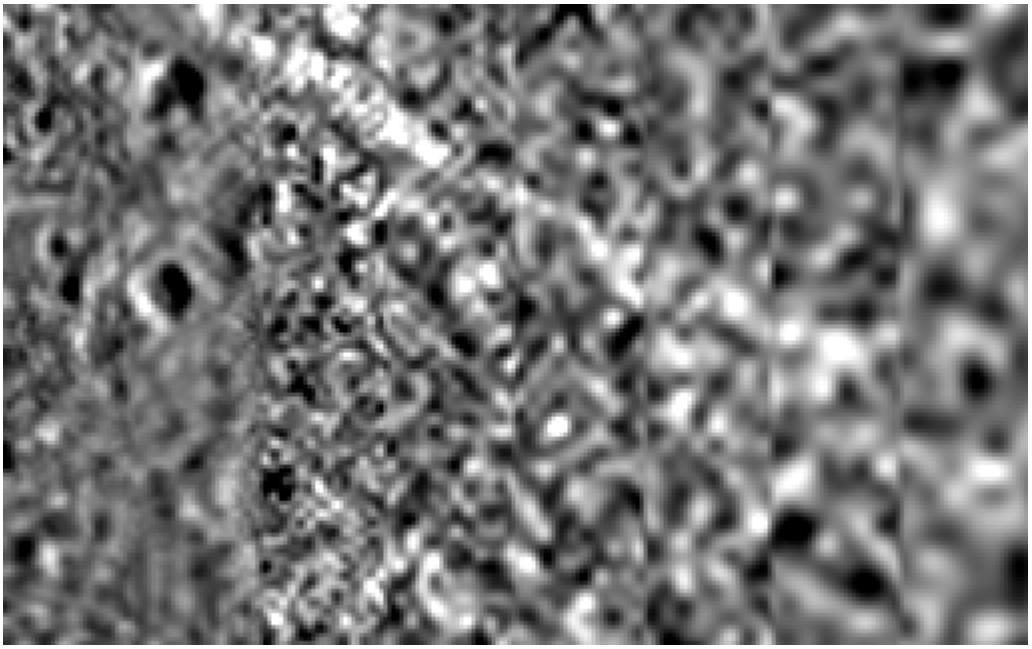

Figure 7.7-2b Moderate noise with CR 3

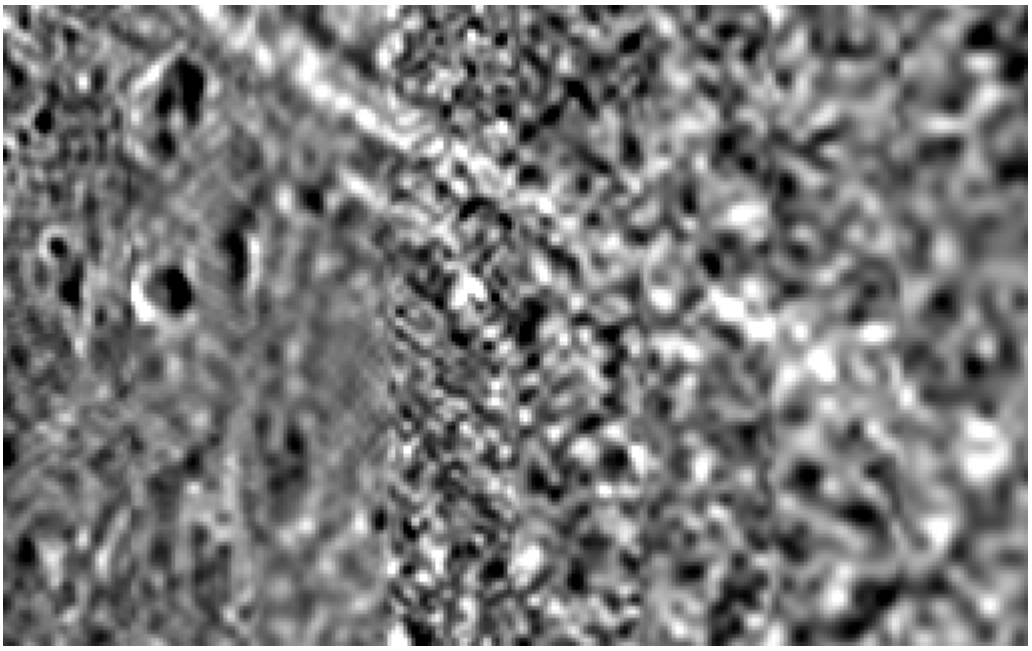

Figure 7.7-2c Moderate noise with CR 4

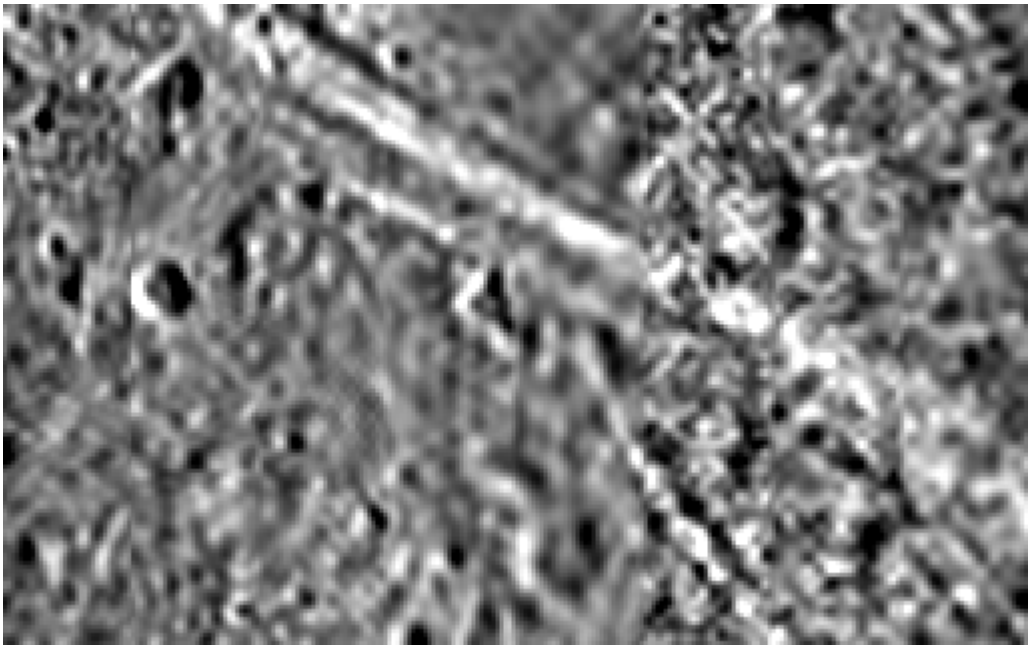

Figure 7.7-2d Moderate noise with CR 6

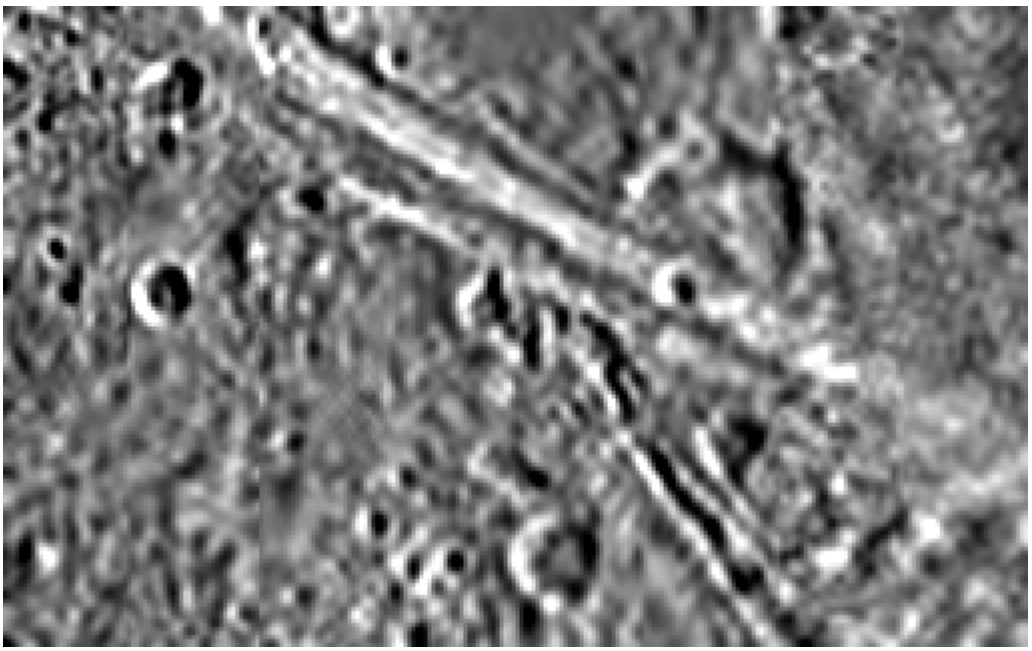

Figure 7.7-2e Moderate noise with CR 8

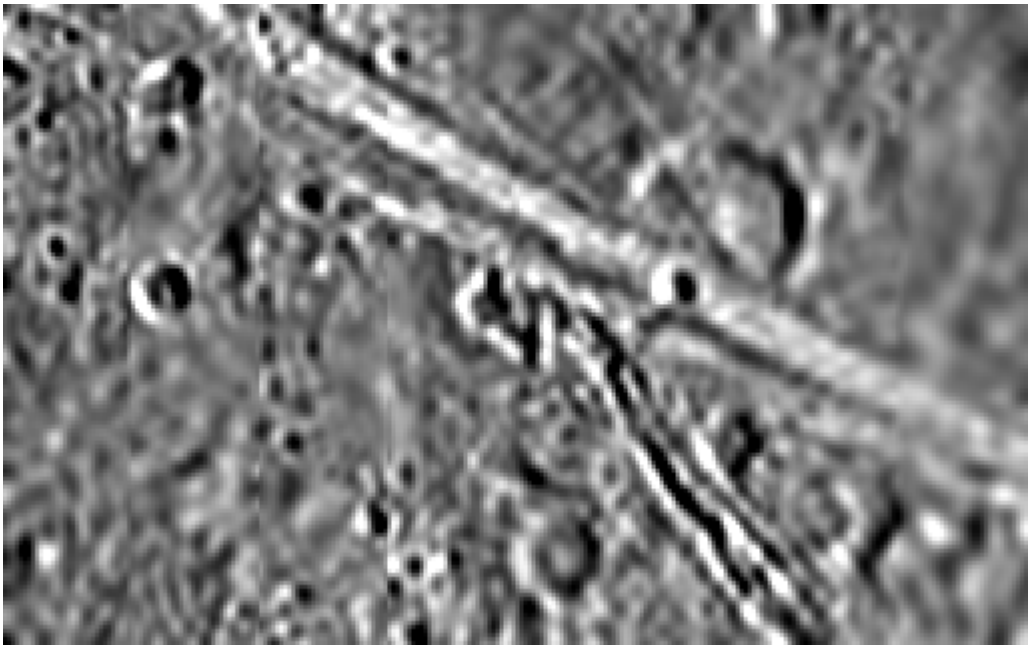

Figure 7.7-2f Moderate noise with CR 12

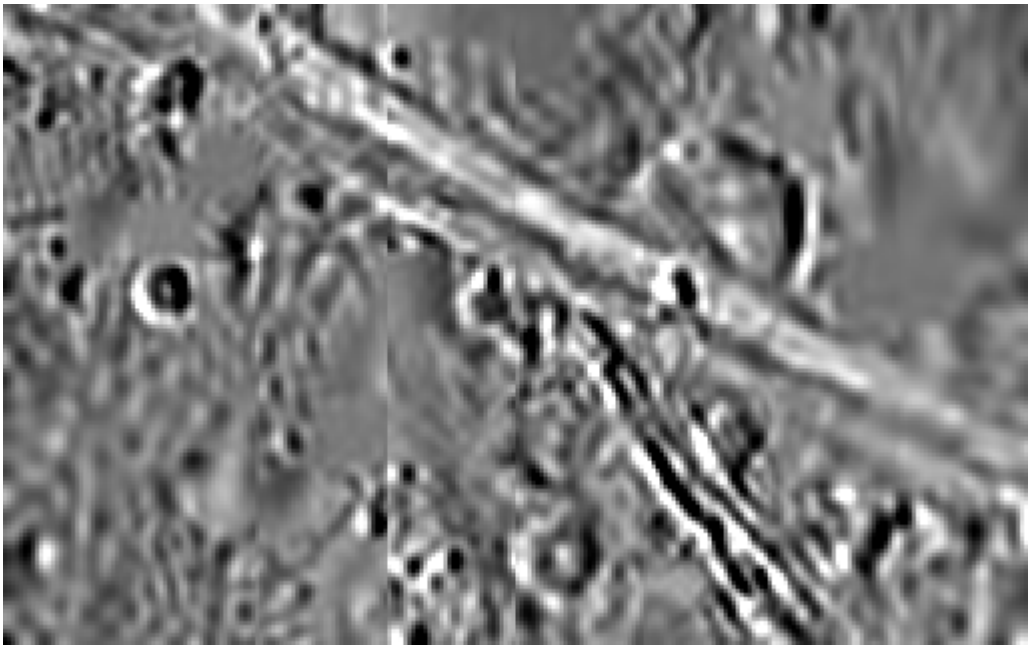

Figure 7.7-2g Moderate noise with CR 16

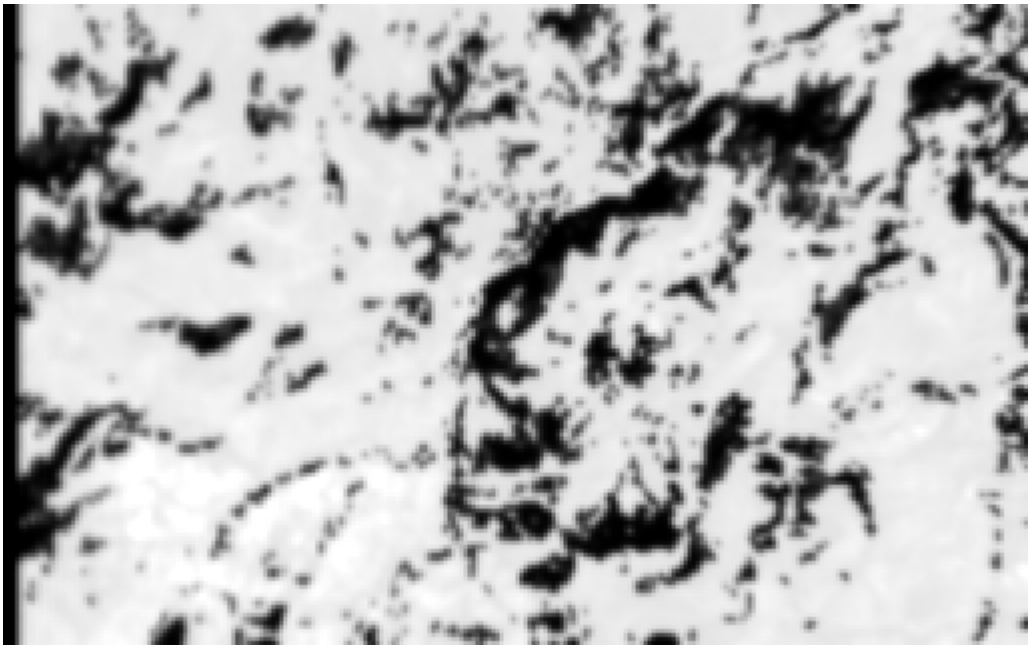

Figure 7.7-3a Original “lakes” image smoothed with no noise

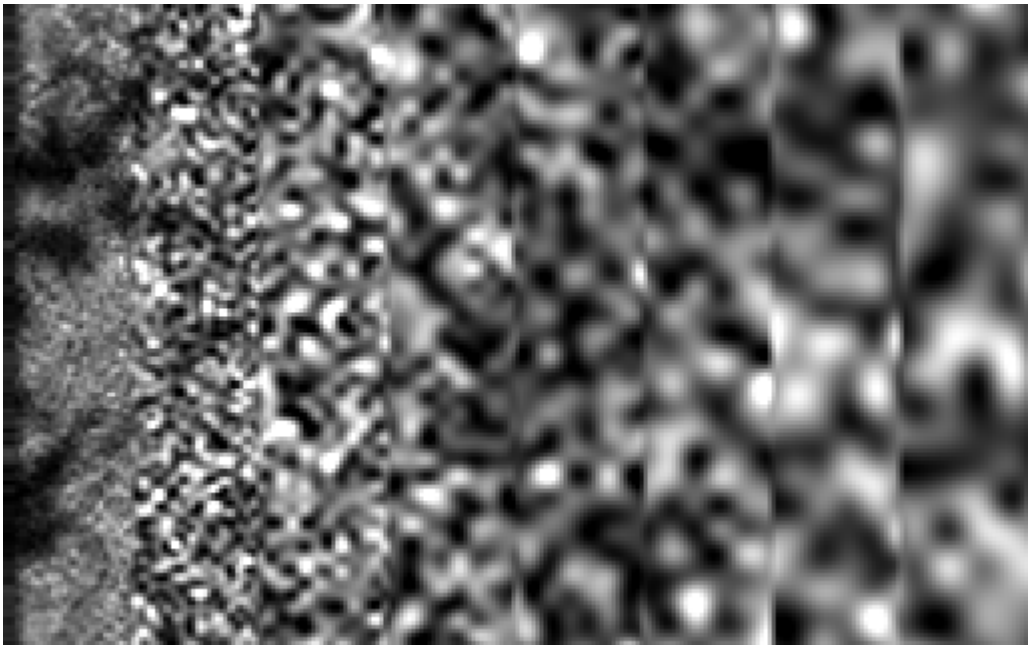

Figure 7.7-3b High noise with CR 2

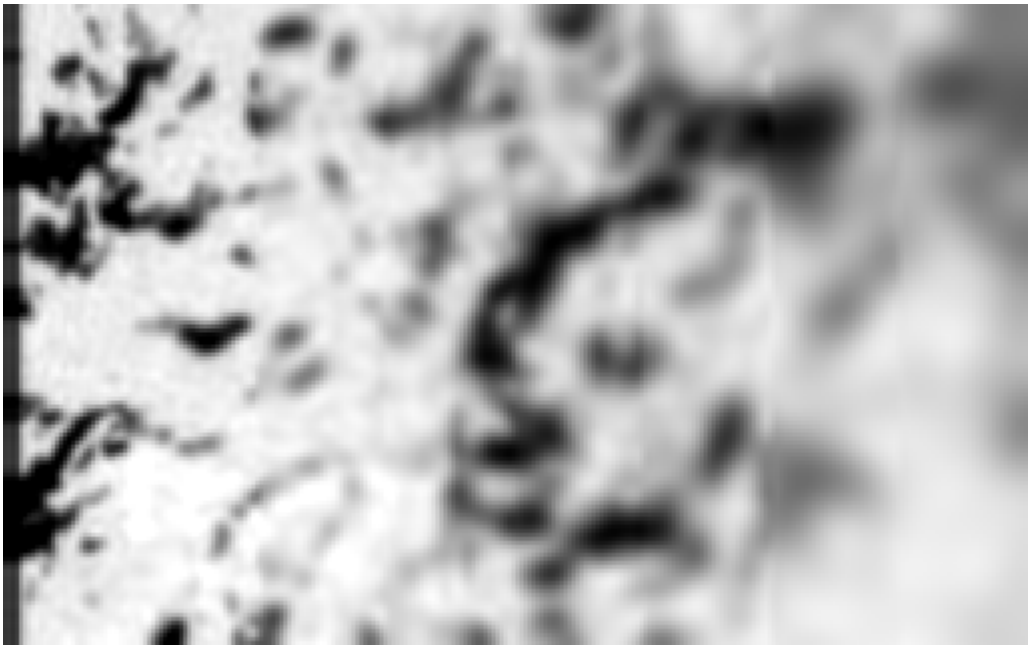

Figure 7.7-3c High noise with CR 3

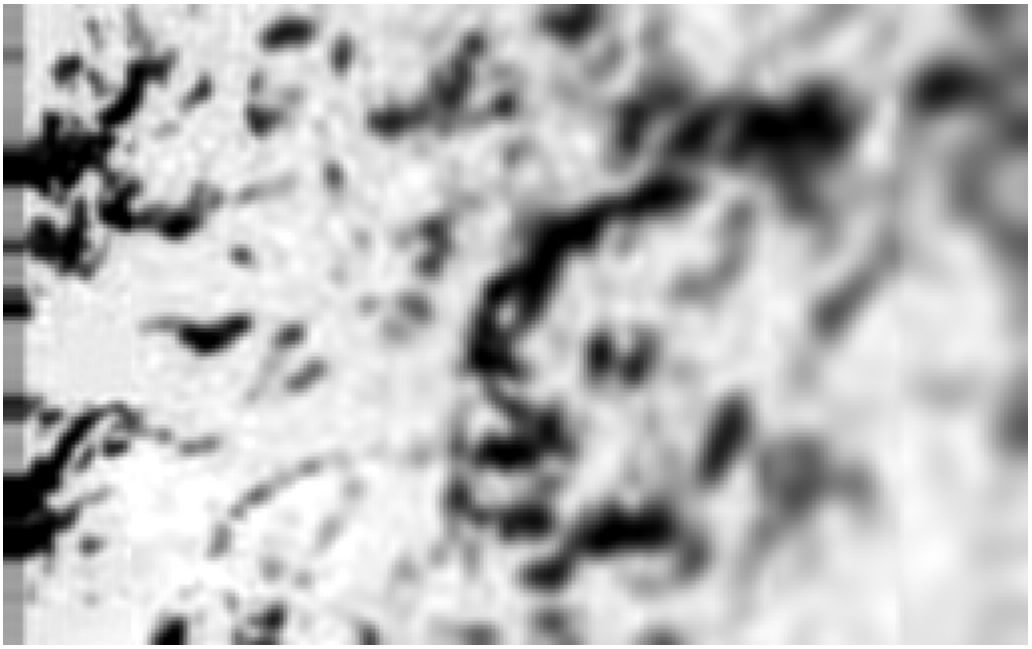

Figure 7.7-3d High noise with CR 4

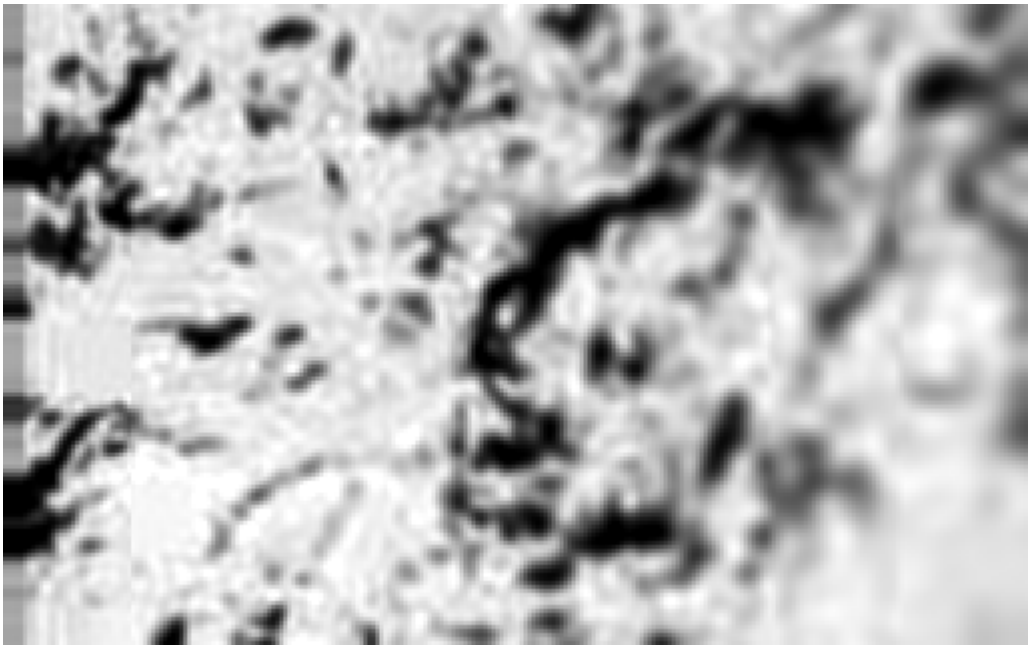

Figure 7.7-3e High noise with CR 6

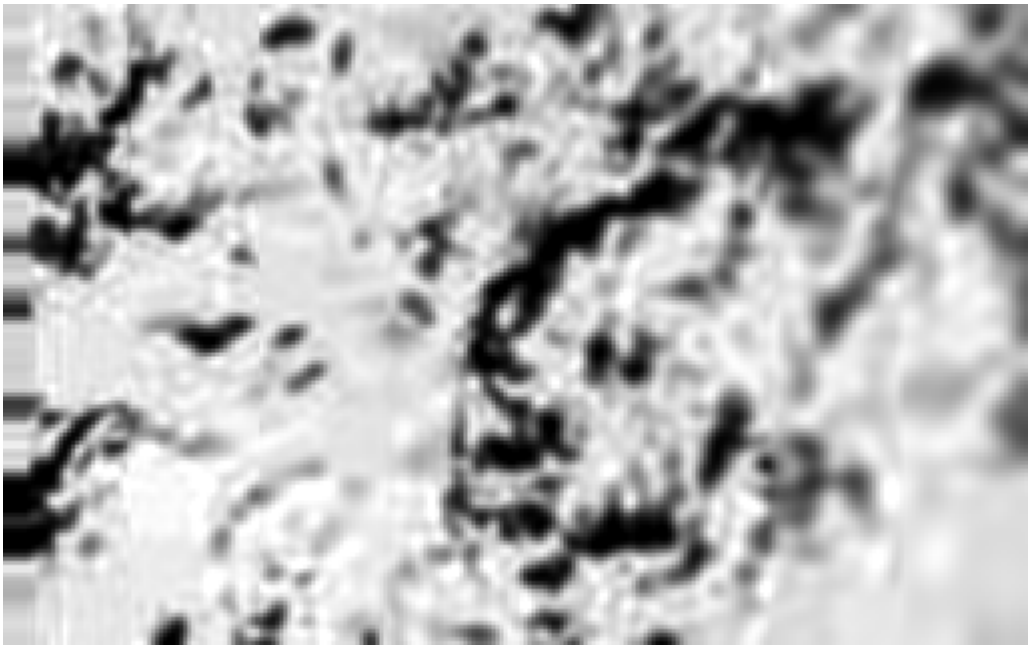

Figure 7.7-3f High noise with CR 8

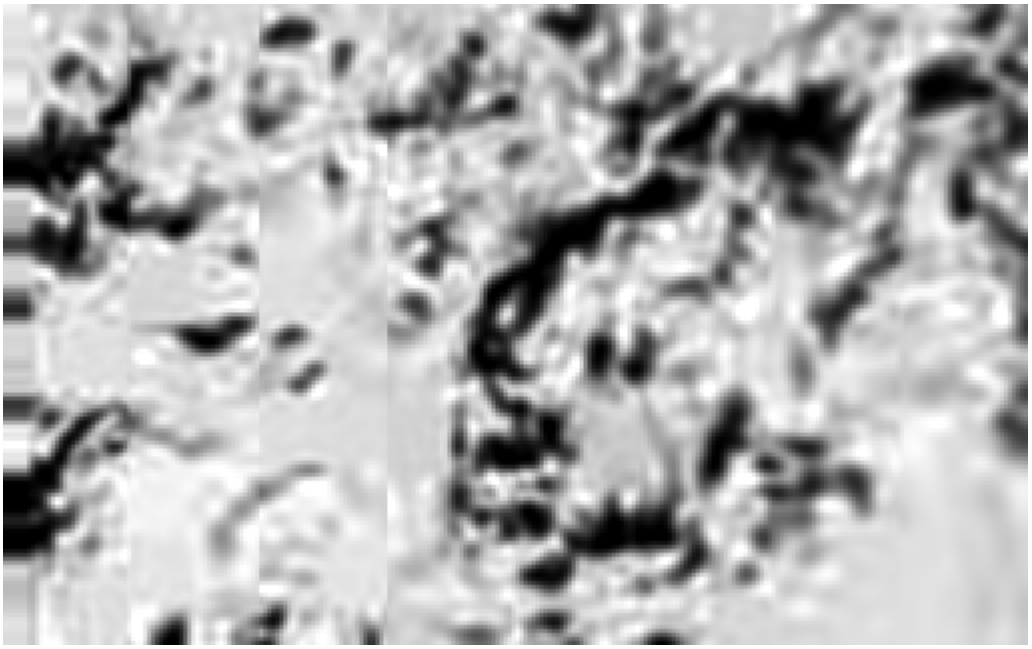

Figure 7.7-3g High noise with CR 12

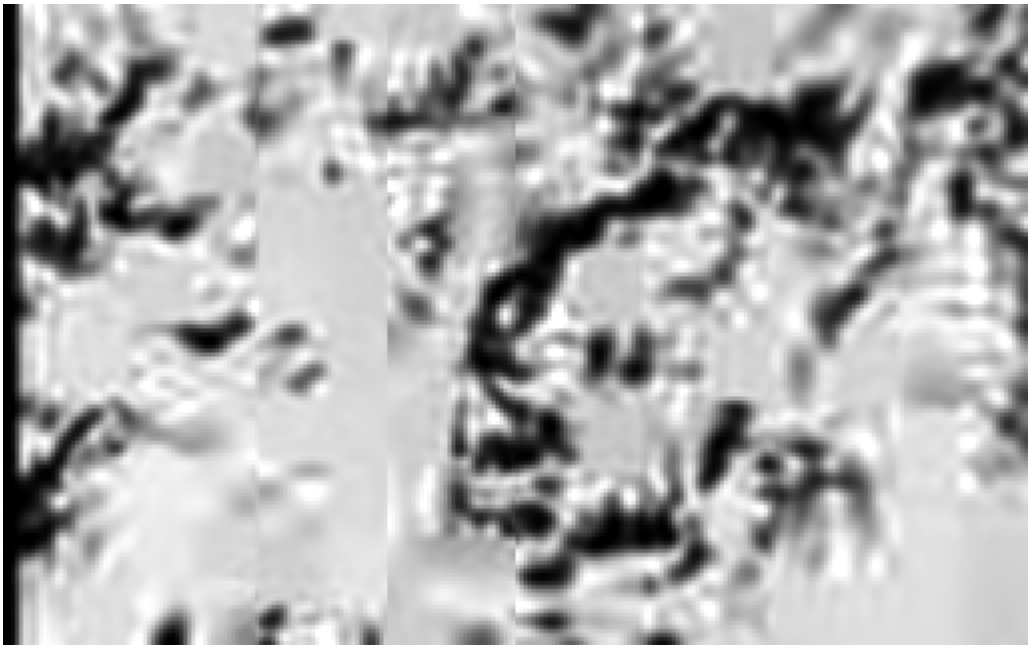

Figure 7.7-3h High noise with CR 16

Table 7.7-1

File names, all in pirl:/pirl1/erich/mrim/:

	Original	2x	3x	3x & 6x	2,4,6x*	4x	6x	8x	12x	16x
#1:	ganzh	ganvg2	ganvg3	ganvg36	ganvg26	ganvg4	ganvg6	ganvg8	ganvg12	ganvg16
#2:	ganzh	ganwg2	ganwg3	ganwg36	ganwg26	ganwg4	ganwg6	ganwg8	ganwg12	ganwg16
#3:	lakeh	lakwg2	lakwg3	lakwg36	lakwg26	lakwg4	lakwg6	lakwg8	lakwg12	lakwg16

* 1/7 at 2x (top), 3/7 and 4x (middle), and 3/7 at 6x (bottom)

8.0. Area Coverage and Image Statistics for a Simulated Descent

The simulated descent of 17 Sept. 1996 was performed with the flight-model, DISR#3, in the calibration laboratory a few days before ship. The sensor head and flight electronics were mounted so as to receive a simulated image of the Sun at Titan moving past the field of view. The speed of the moving solar image was adjusted so as to mimic the nominal predicted rate of the rotation of the Huygens descent module within Titan's atmosphere. Hence, a realistic lock was achieved by the Sun Sensor, which performed flawlessly under these simulated conditions, and provided a baseline for the scheduling of all DISR measurements. A full suite of DISR measurements was acquired.

Some 13 image panoramas were recorded under these simulated conditions and they were fully flight-processed using the current hardware compression scheme (compression ratios alternating between 3 and 6) and tagged with the simulated altitudes of the nominal time-altitude table. Table 1 shows their locations in time, vertical and horizontal space. Figures 8.0-1 through 8.0-9 show the same information in graphical form.

After modifying the image compression scheme as described above (alternating between compression ratios of 6 and 8 with a single image at a compression ratio of 4 acquired per panorama), the arrangement of panoramas listed in Table 8.0-2 and displayed in Figures 8.0-10 through 8.0-20 resulted.

Only the HRI image footprints are shown.

Table 8.0-1

List of Panoramas acquired during simulated descent of 17 Sept. 1996, along with times, altitudes (km) and estimated sub-probe longitudes on Titan assuming an entry point of 162^{o} E longitude and a nominal Flasar *et al* wind model.

Panorama	Time (min)	Altitude	Sub-P Lng
A	1.7-3.7	143-150	162.2-162.5
B	3.8-6.0	135-142	162.6-162.9
C	18.3-20.4	90-98	164.6-164.8
D	27.9-29.9	64-68	165.7-165.9
E	46.9-49.2	41-43	167.6-167.8
F	58.2-60.4	32-34	168.5-168.7

G	68.0-70.5	26-27	169.2-169.3
H	78.3-80.8	21-22	169.8-169.9
I	91.7-94.1	14.5-16	170.4-170.6
J	98.5-100.7	11.8-12.7	170.7-170.8
K	107.1-109.2	8.4-9.4	171.1
L	114.3-117.0	5.8-6.8	171.2-171.3
M	123.4-125.8	2.8-3.6	171.4

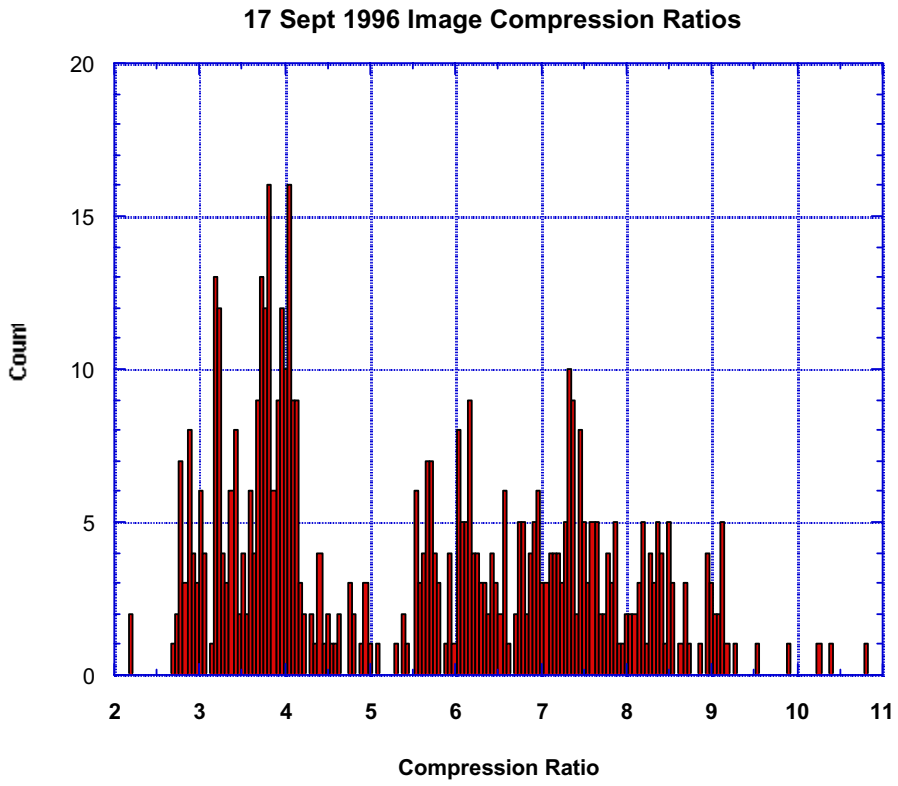

Figure 8.0-3 Histogram of image compression ratios for original compression scheme.

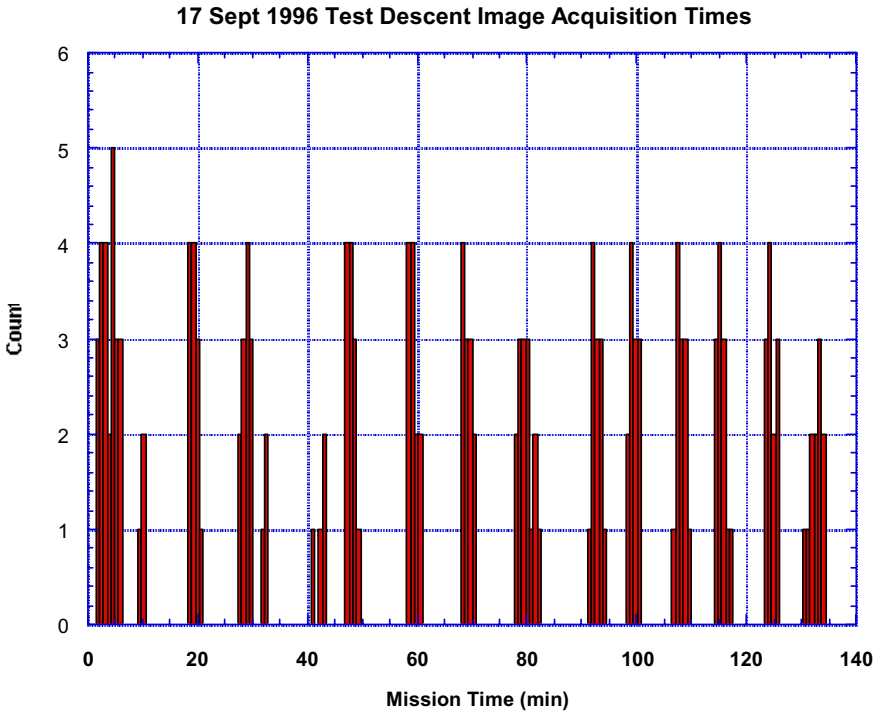

Figure 8.0-4 Distribution of image acquisition times for original compression scheme.

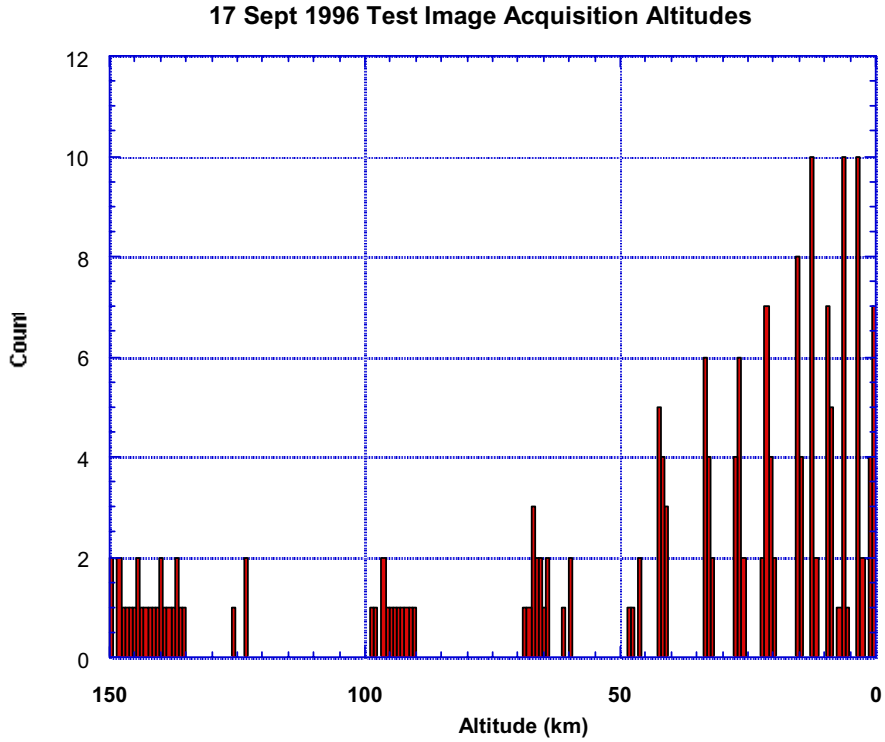

Figure 8.0-5 Distribution of image acquisition altitudes for original compression scheme.

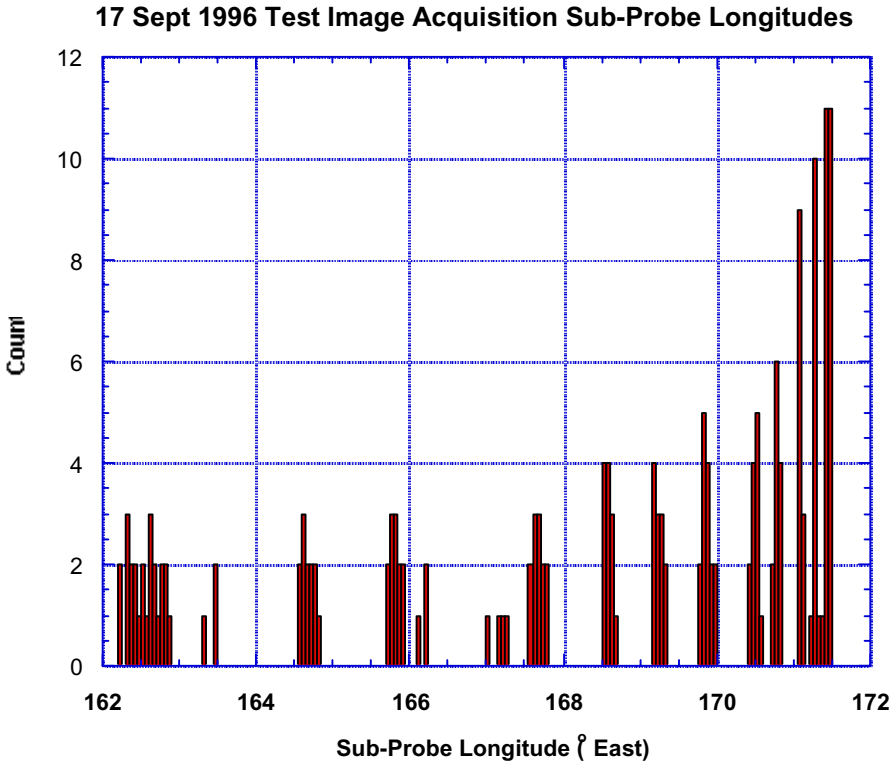

Figure 8.0-6 Distribution of image sub-probe longitudes for original compression scheme.

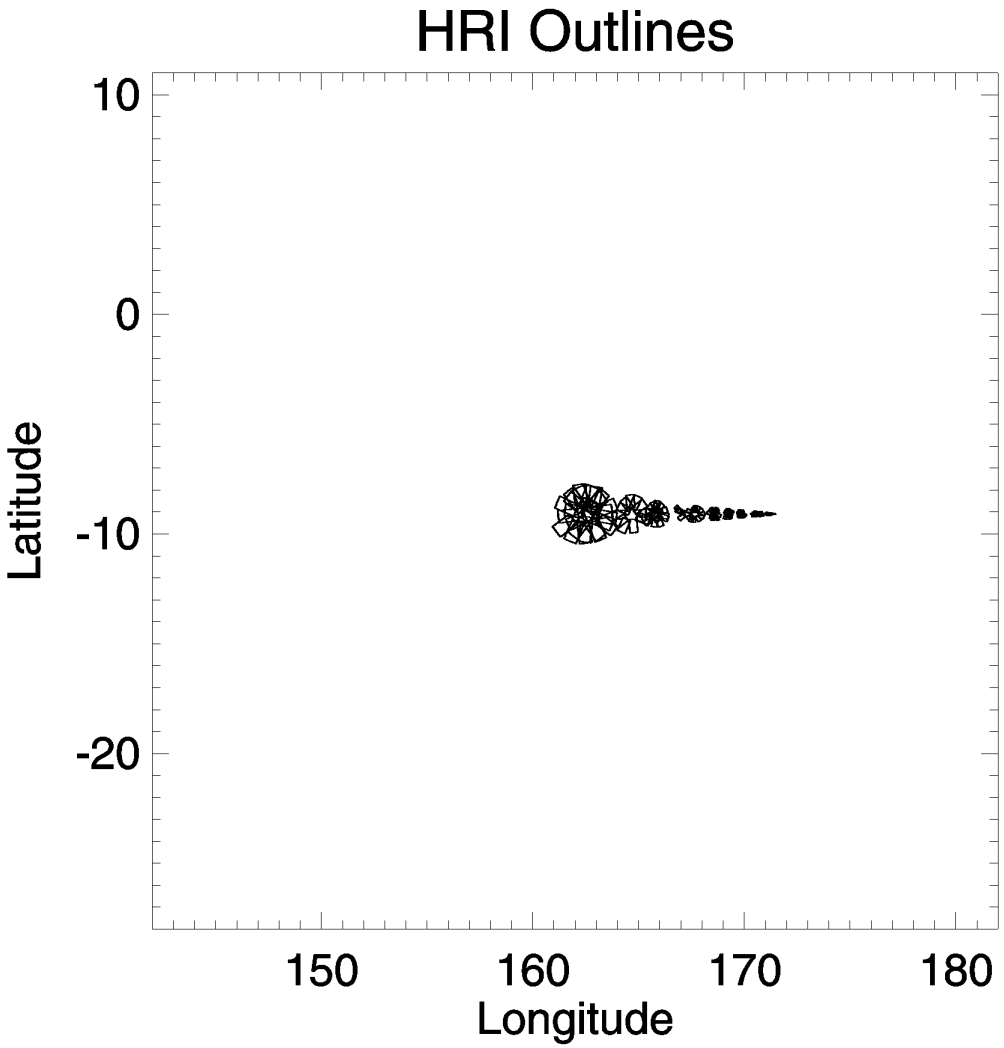

Figure 8.0-7 HRI footprint outlines for all HRI images for original compression scheme.

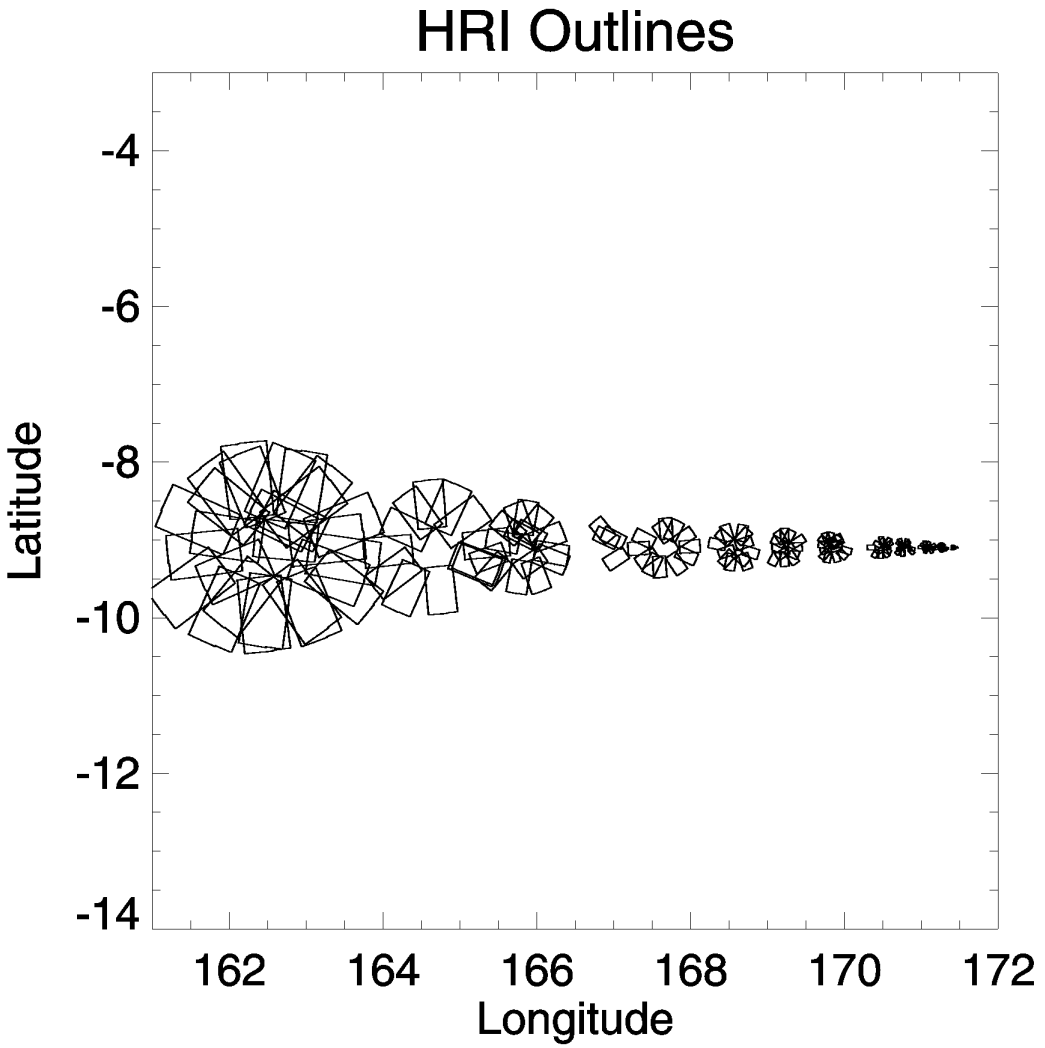

Figure 8.0-8 HRI footprint outlines for all HRI images (magnified view) for original compression scheme.

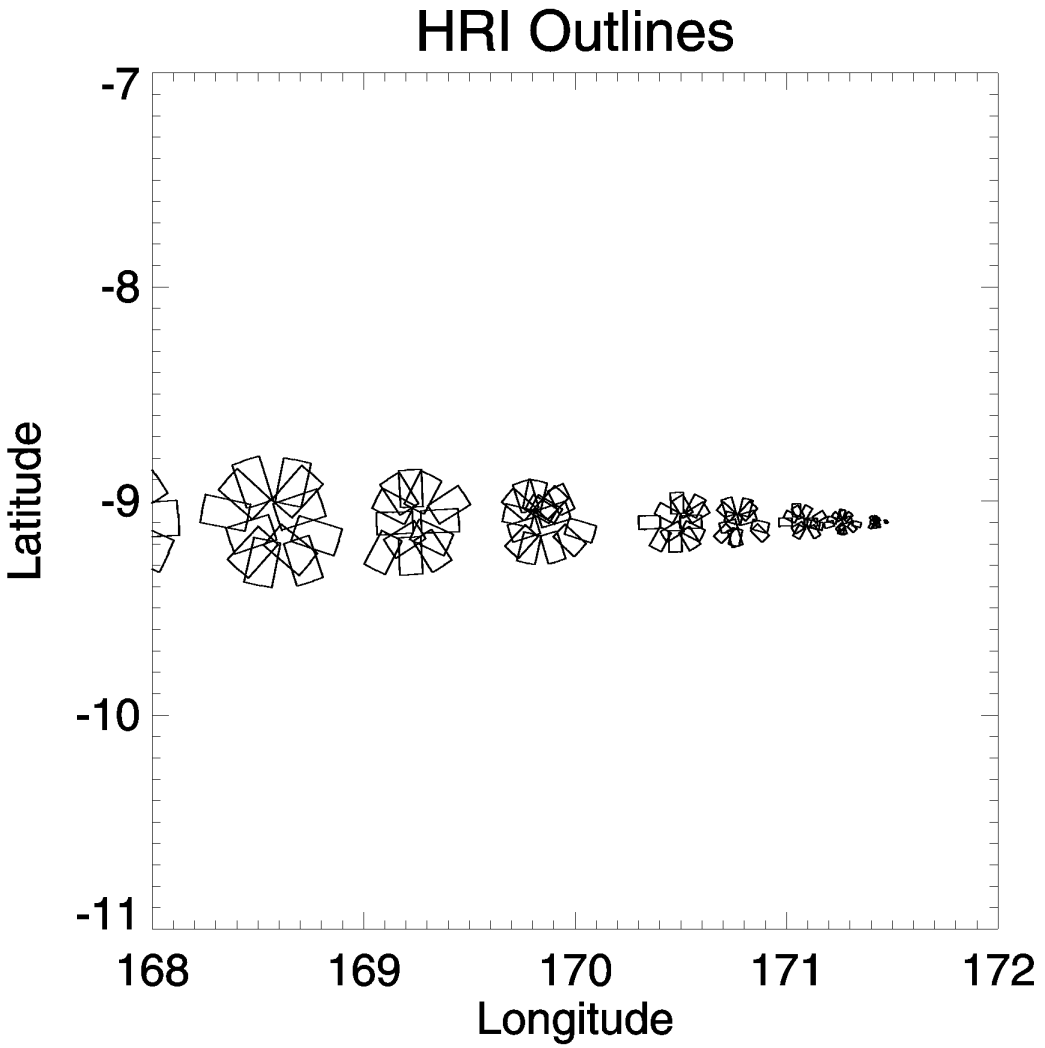

Figure 8.0-9 HRI footprint outlines for mid to low altitude panoramas for original compression scheme.

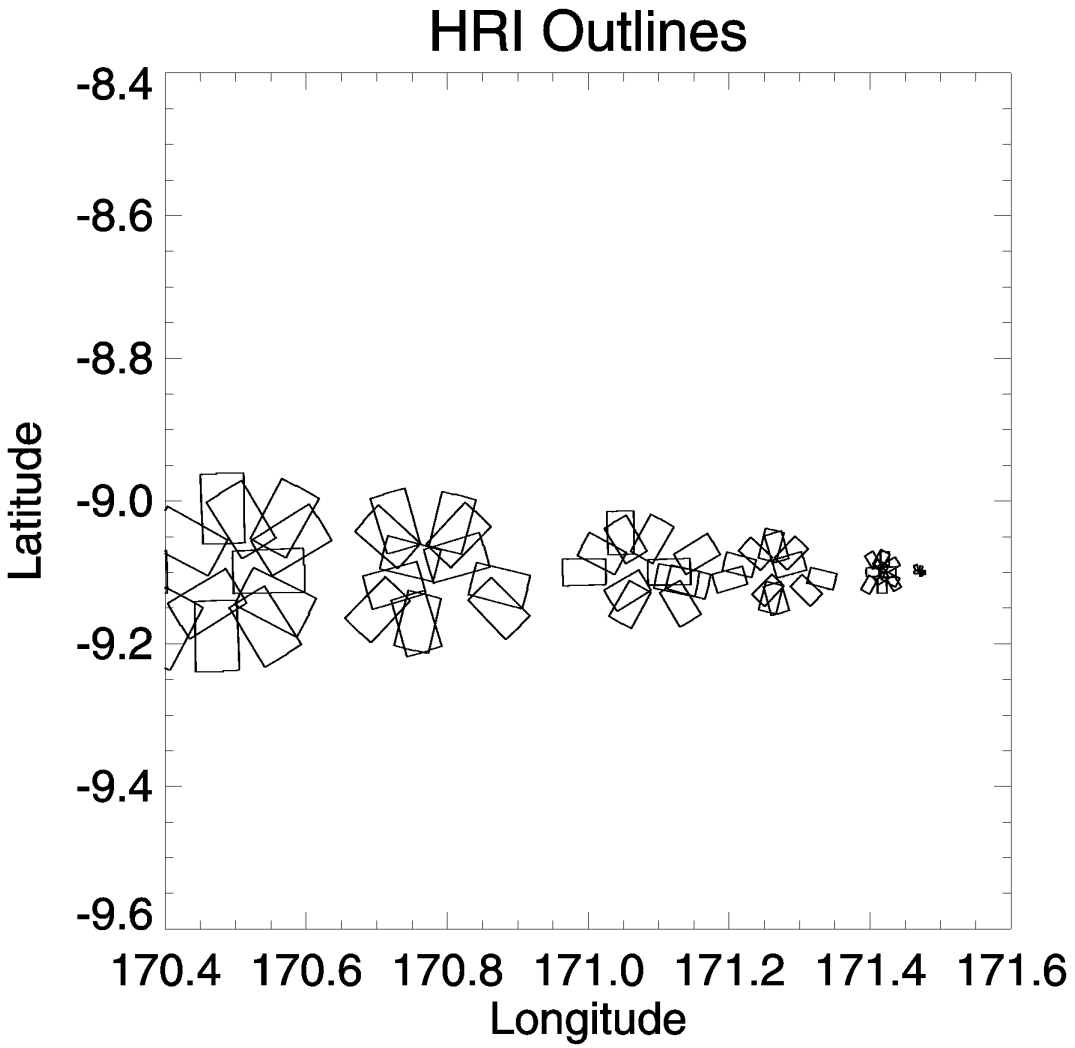

Figure 8.0-10 HRI footprint outlines for low panoramas for original compression scheme.

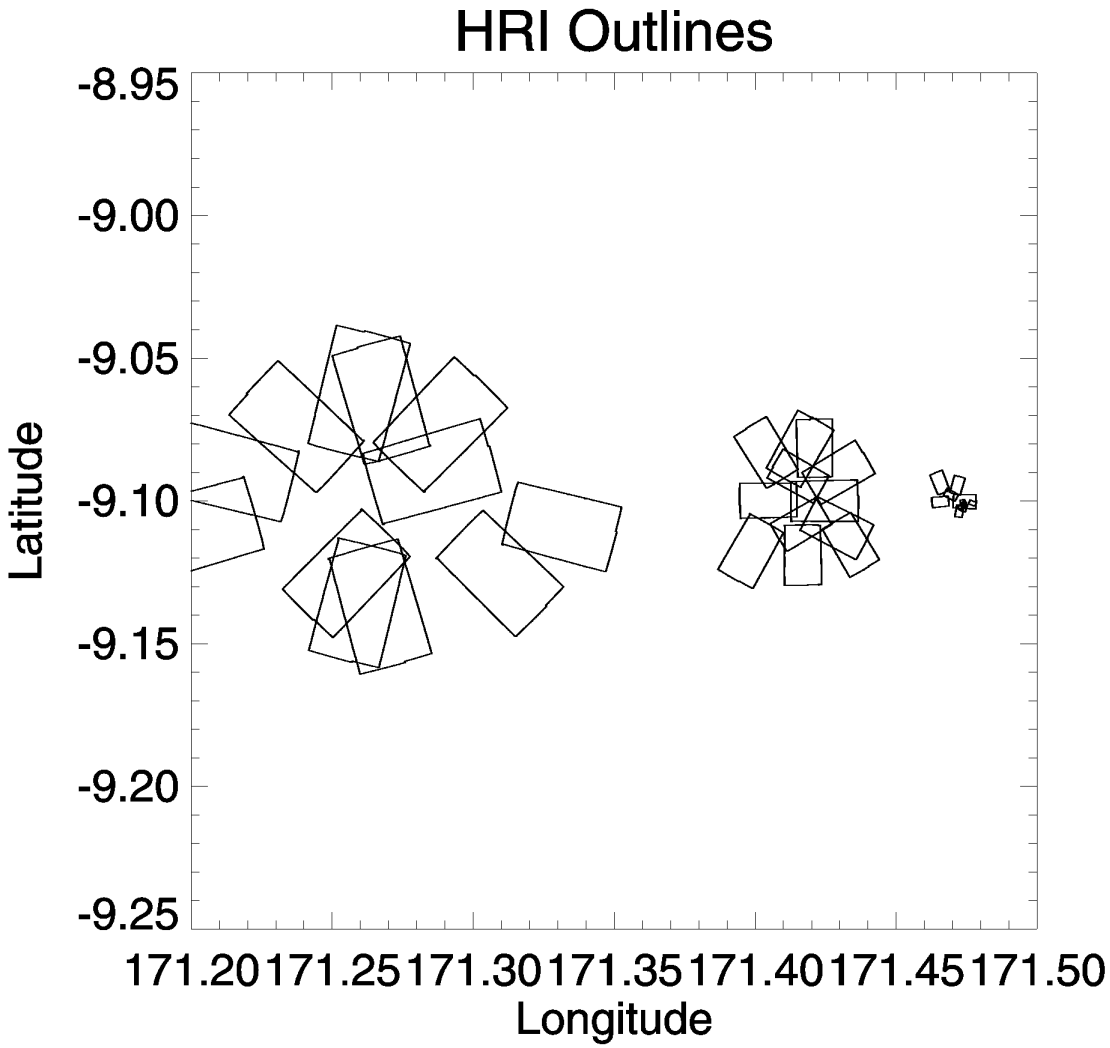

Figure 8.0-11 HRI footprint outlines for lowest panoramas and non-panoramic images for original compression scheme.

Table 8.0-2

List of Panoramas acquired during simulated descent of 17 Sept. 1996, along with times, altitudes (km) and estimated sub-probe longitudes on Titan assuming an entry point of 162^{o} E longitude and a nominal Flasar *et al* wind model for the modified compression scheme.

Panorama	Time (min)	Altitude	Sub-P Lng
A	2.52-4.64	146.7-139.6	162.4-162.7
B	4.92-6.95	138.8-132.6	162.7-163.0
C	8.5-10.5	128.3-123.1	163.2-163.5

D	16.8-18.8	105.5-96.3	164.3-164.6
E	23.4-25.4	80.2-74.6	165.2-165.4
F	29.9-31.9	64.2-60.7	165.9-166.1
G	36.7-38.8	53.8-51.2	166.6-166.8
H	46.7-48.8	42.8-41.0	167.6-167.7
I	53.4-55.7	37.2-35.4	168.1-168.3
J	58.8-61.0	33.2-31.8	168.5-168.7
K	65.5-68.0	28.8-27.4	169.0-169.2
L	71.1-73.3	25.6-24.4	169.4-169.5
M	78.5-80.6	21.7-20.6	169.8-169.9
N	87.9-90.3	17.2-16.2	170.3-170.4
O	92.9-95.5	15.1-14.0	170.5-170.6
P	97.8-100.0	13.0-12.2	170.7-170.8
Q	102.6-104.8	11.1-10.3	170.9-171.0
R	109.7-112.2	8.4-7.6	171.1-171.2
S	114.6-117.2	6.7-5.8	171.2-171.3
T	121.8-124.4	4.2-3.3	171.4

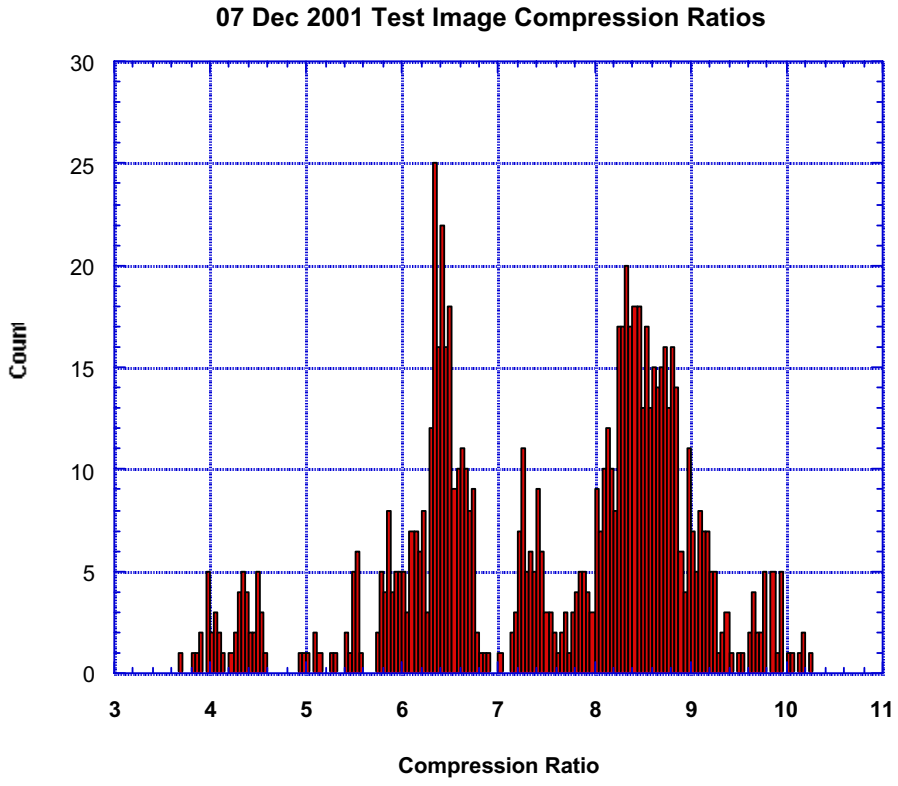

Figure 8.0-12 Distribution of image acquisition times for new compression scheme.

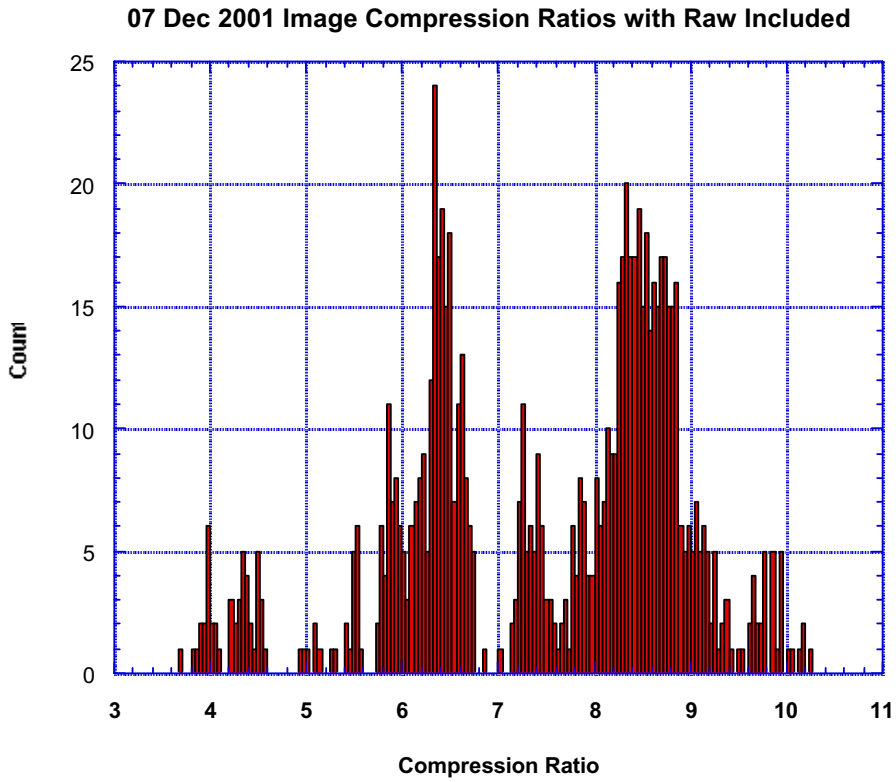

Figure 8.0-13 Distribution of image compression ratio (with raw image data sets included) for new compression scheme.

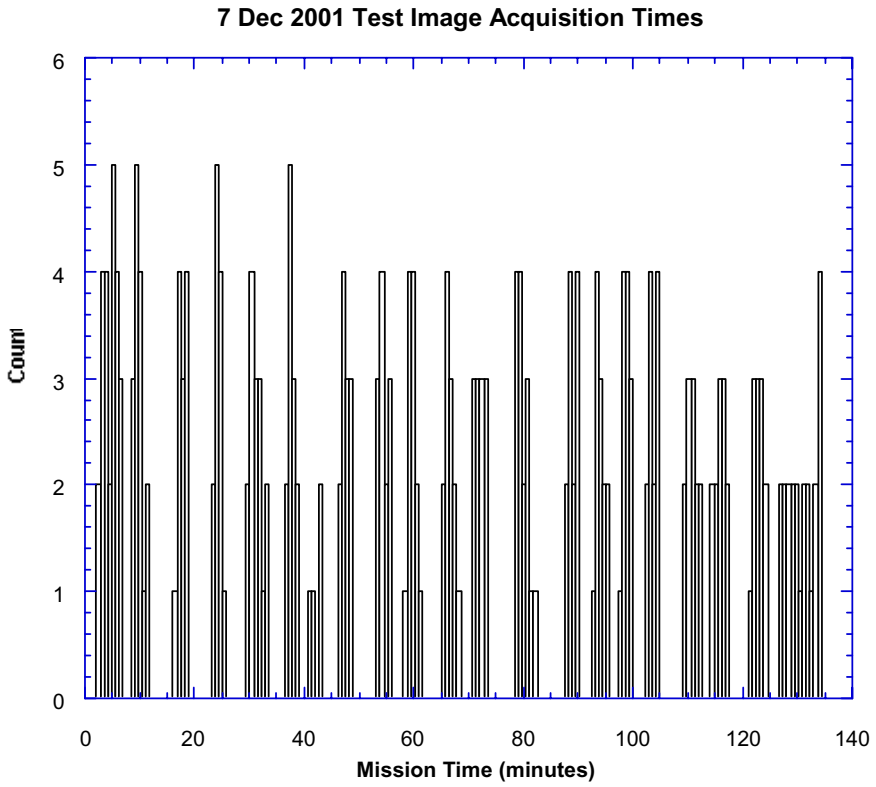

Figure 8.0-14 Distribution of image acquisition times for new compression scheme.

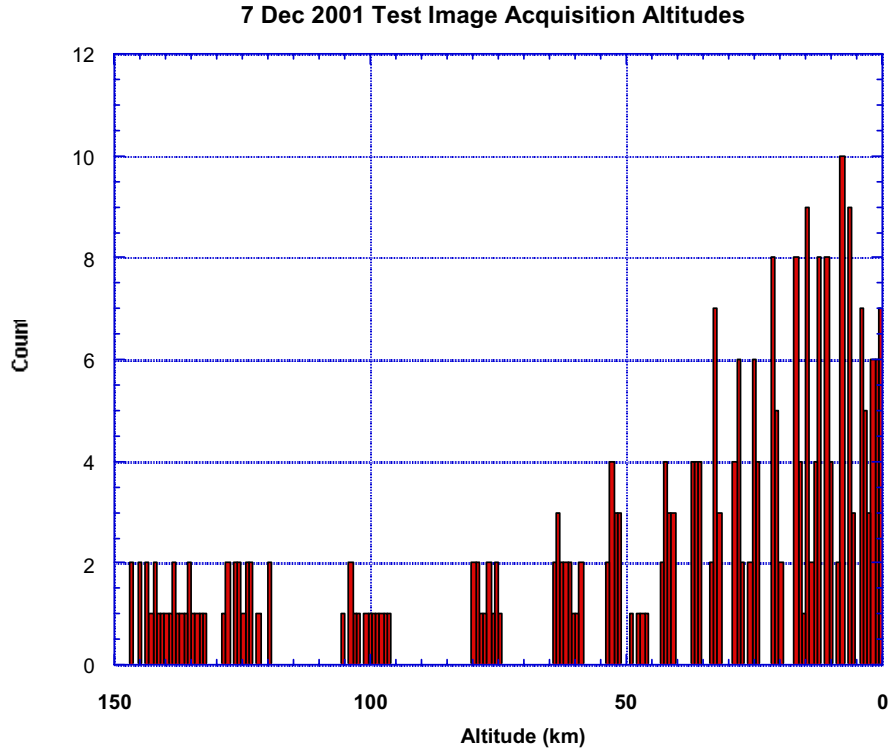

Figure 8.0-15 Distribution of image acquisition altitudes for new compression scheme.

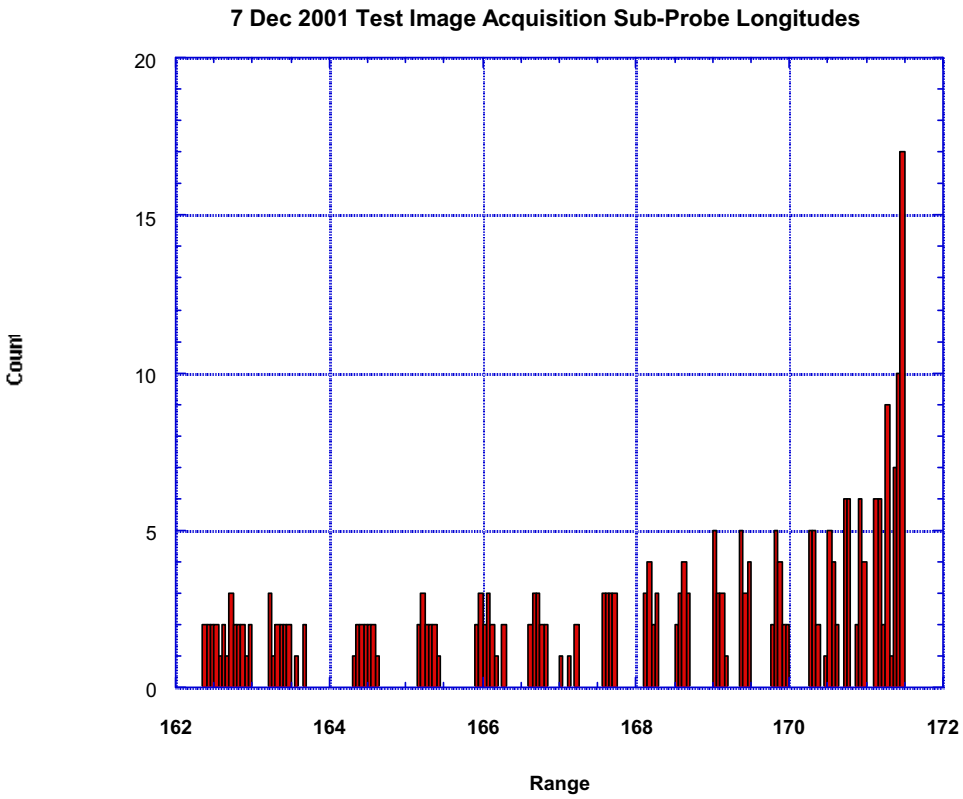

Figure 8.0-16 Distribution of image sub-probe longitudes for new compression scheme.

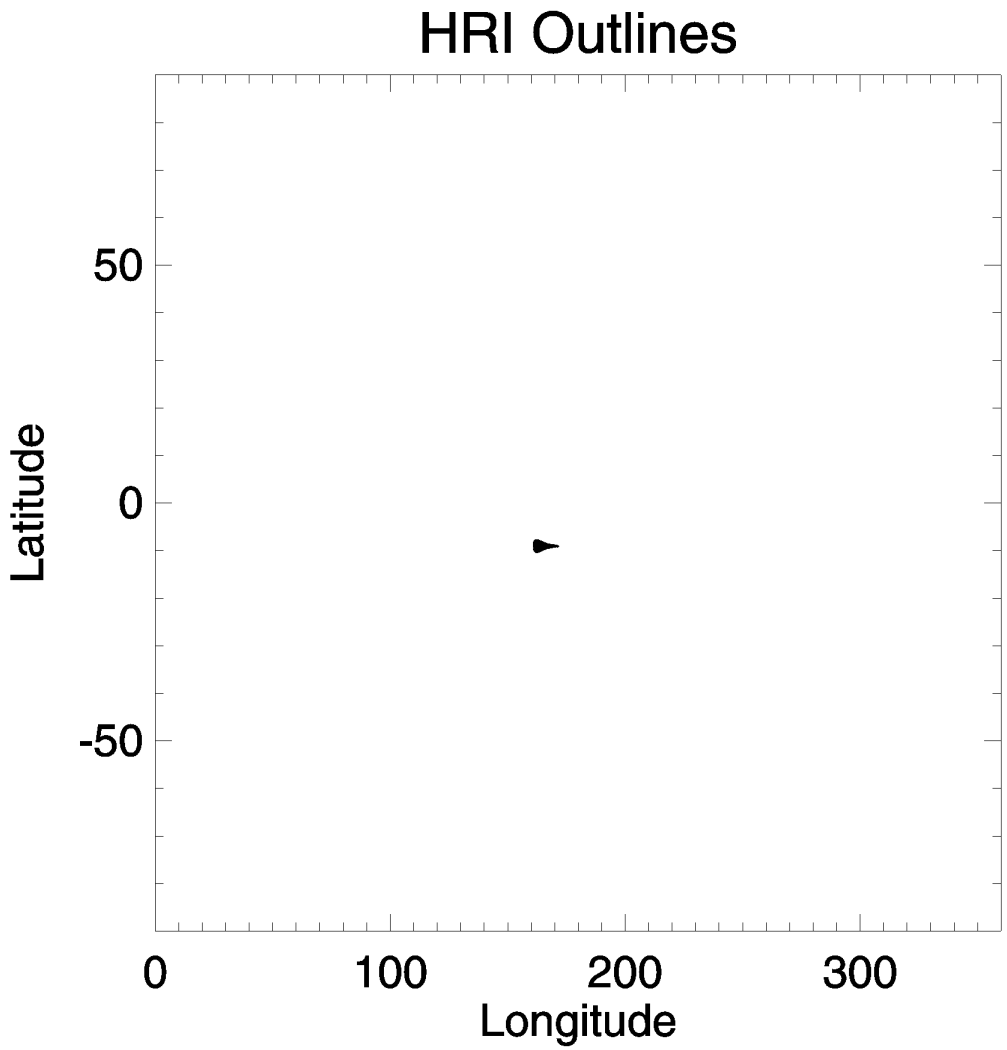

Figure 8.0-17 HRI footprint outlines for all HRI images for new compression scheme.

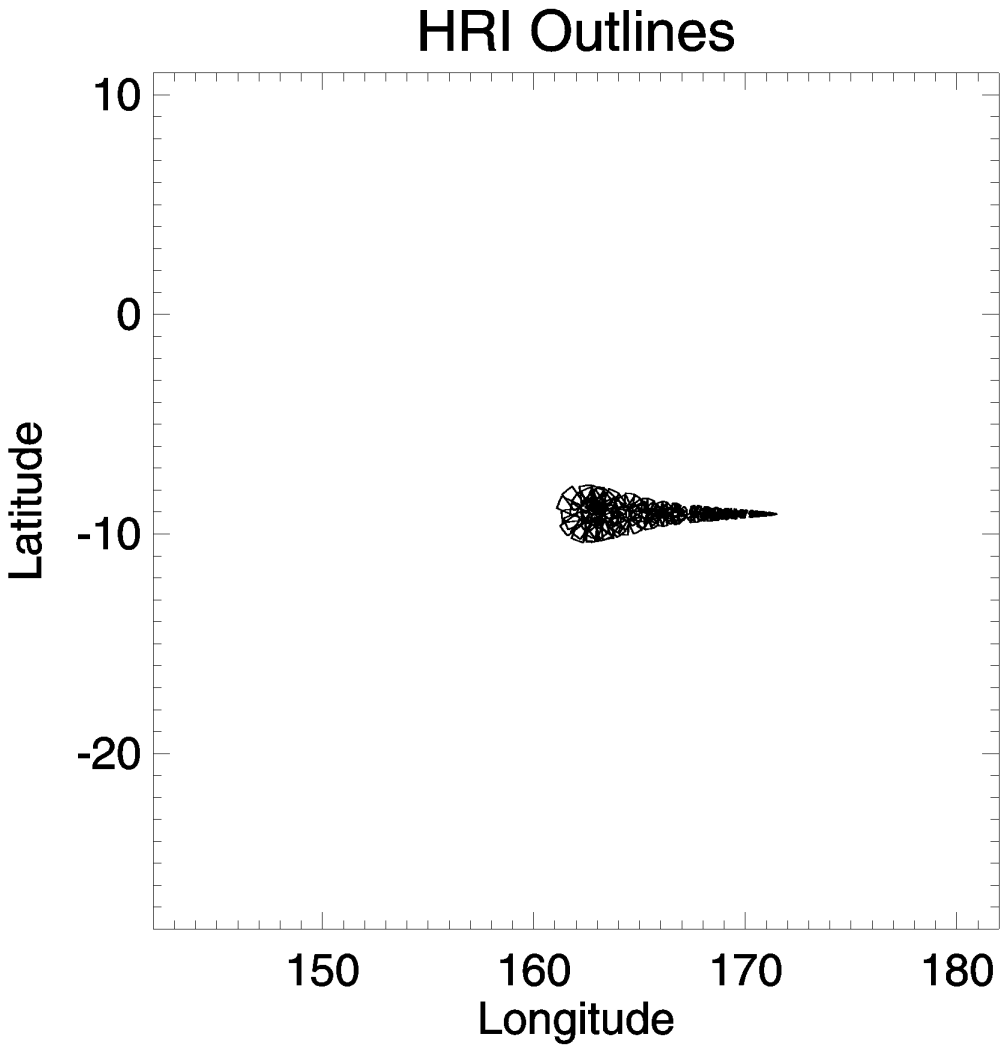

Figure 8.0-18 HRI footprint outlines for all HRI images (magnified view) for new compression scheme.

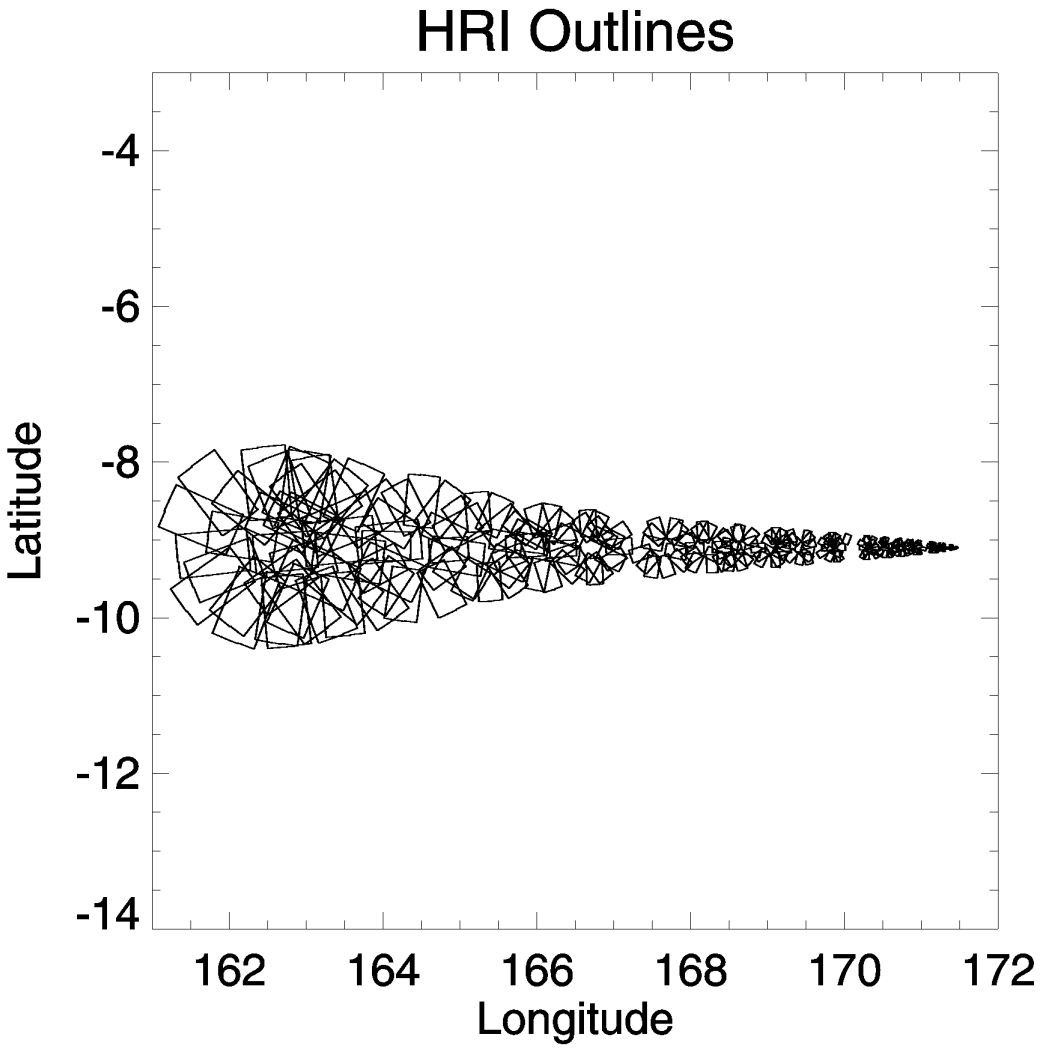

Figure 8.0-19 HRI footprint outlines for mid to low altitude panoramas for new compression scheme.

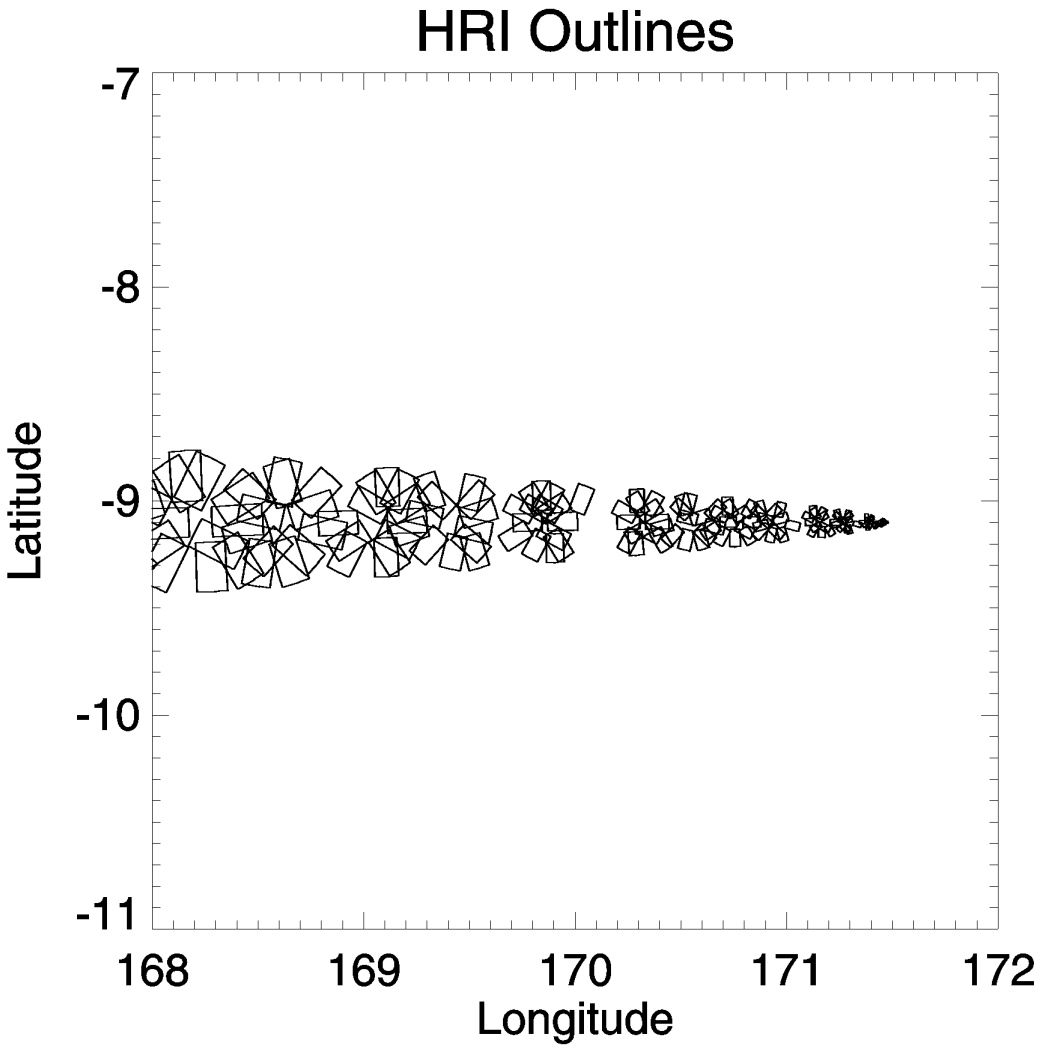

Figure 8.0-120 HRI footprint outlines for low panoramas for new compression scheme.

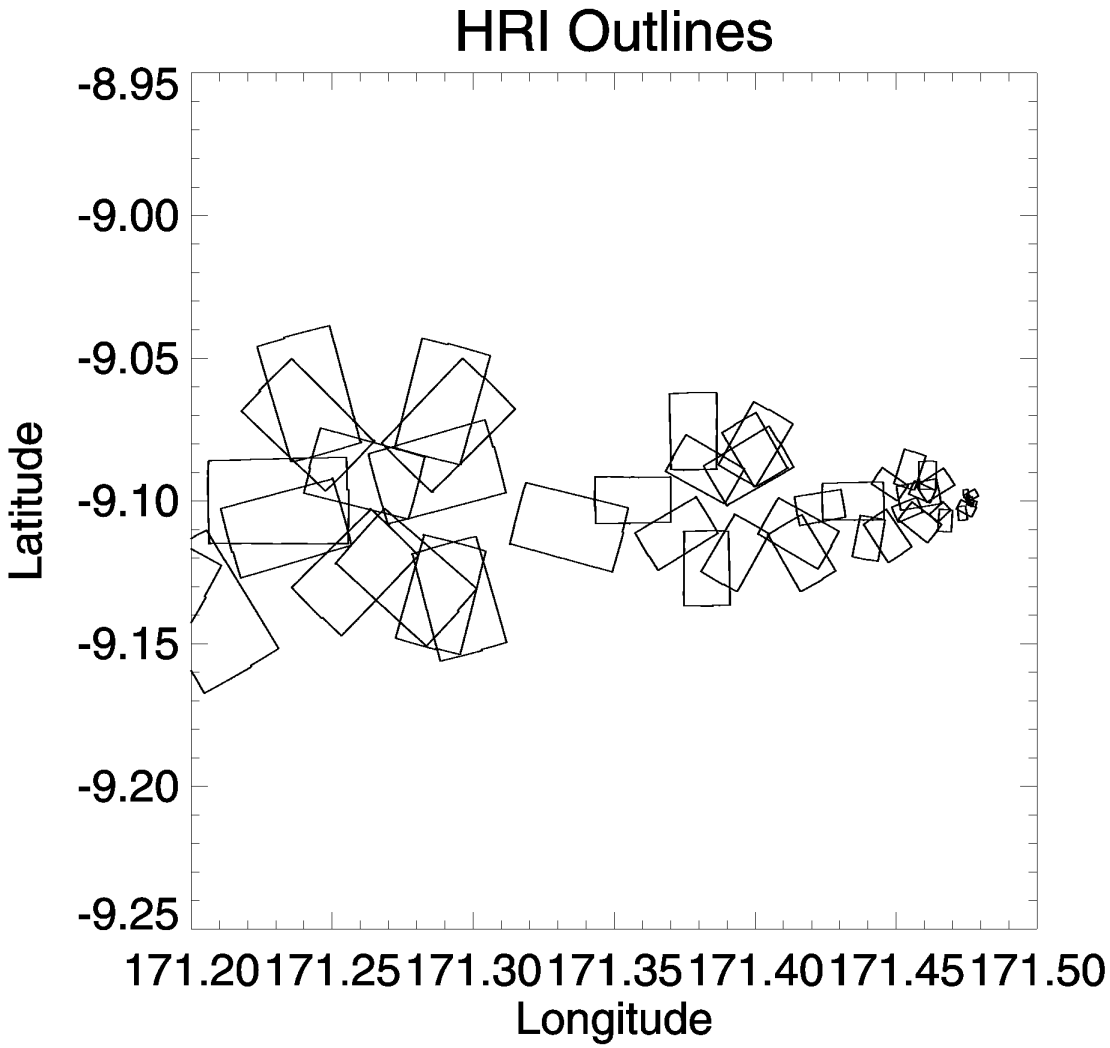

Figure 8.0-21 HRI footprint outlines for lowest panoramas and non-panoramic images for new compression scheme.

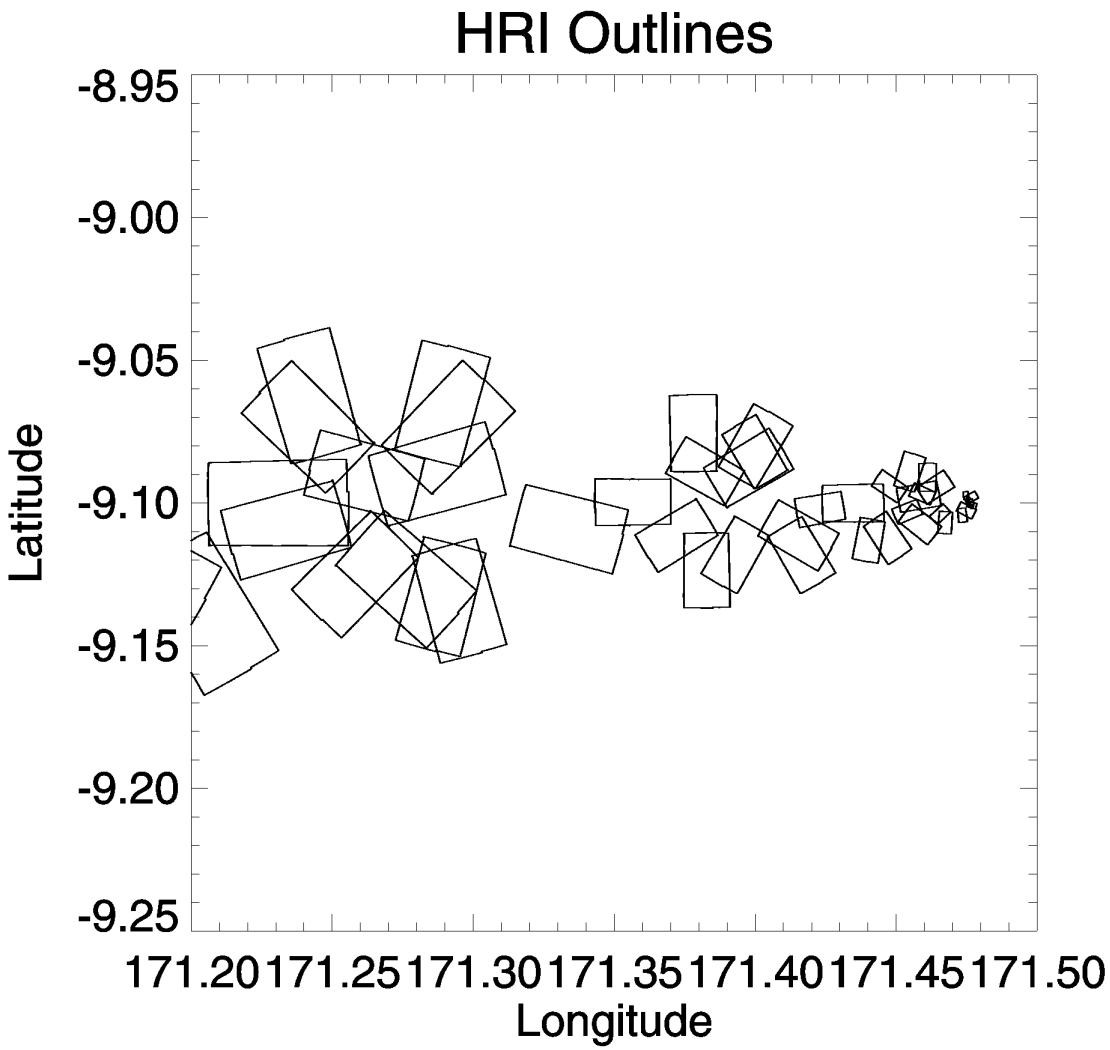

Figure 8.0-22 HRI footprint outlines for lowest panoramas and non-panoramic images (magnififed) for new compression scheme.